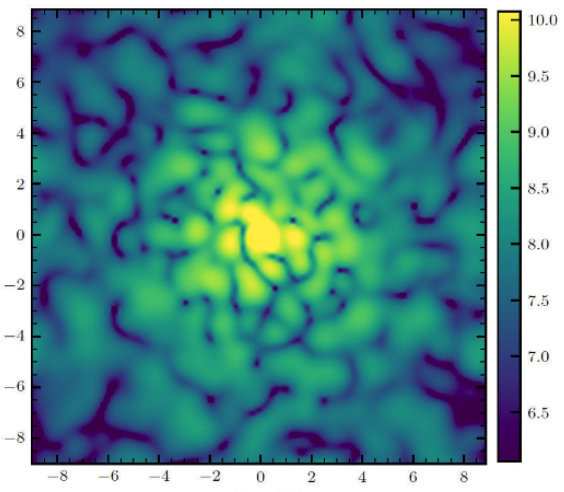
eISSN
2683-2224

REVISTA MEXICANA DE FÍSICA

Publicación bimestral de la
Sociedad Mexicana de Física



Granular structure and local de Broglie wavelength in fuzzy dark matter halos

Rosales-Infante, Quiñonez-Guerrero, Álvarez-Rios and Francisco S. Guzmán

Volume 72
Number 6
Nov-Dec 2026

© Sociedad Mexicana de Física

Volume 72, Número 6, Nov-Dec 2026

Editorial Staff

Revista Mexicana de Física

Editorial Direction

EDITOR-IN-CHIEF
Ramón Castañeda-Priego
División de Ciencias e Ingenierías,
Universidad de Guanajuato
chief.editor.rmf@ciencias.unam.mx

SECRETARY
María Magdalena López Reynoso
Sociedad Mexicana de Física, A. C.
rmf@ciencias.unam.mx

JOURNAL MANAGER
Edgar Iván Preciado Govea
División de Ciencias e Ingenierías,
Universidad de Guanajuato
ei.preciadogovea@ugto.mx

JOURNAL MANAGER
Fidencio Pérez Hernández
División de Ciencias e Ingenierías,
Universidad de Guanajuato
fisicafide27@gmail.com

TECHNICAL STAFF

Julio César Pérez Pedraza
Universidad Michoacana
de San Nicolás de Hidalgo

Juan Domingo García Muñoz
Universidad Michoacana
de San Nicolás de Hidalgo

Efraín R. Garrido
Sociedad Mexicana de Física, A. C.

Editorial Board

ADVANCES IN LIGHT SOURCES

Abel Moreno Cárcamo
Instituto de Química, UNAM

Mayra Cuellar Cruz
Universidad de Guanajuato

ATOMIC AND MOLECULAR PHYSICS

John Alexander Franco
Instituto de Física, UASLP

CONDENSED MATTER

Alfredo Tlahuice Flores
Facultad de Ciencias Físico-Matemáticas,
Universidad Autónoma de Nuevo León

FLUID DYNAMICS AND GRANULAR MATTER

Sergio Cuevas García
Instituto de Energías Renovables,
UNAM

Anne Cros
Departamento de Física,
Universidad de Guadalajara

Felipe Pacheco Vázquez
Instituto de Física,
Benemérita Universidad Autónoma de
Puebla

GRAVITATION, MATHEMATICAL PHYSICS AND FIELD THEORY

David J. Fernández
Departamento de Física,
Cinvestav

Francisco S. Guzmán Murillo
Instituto de Física y Matemáticas,
UMSNH

Alonso Contreras Astorga
Departamento de Física,
Cinvestav

Oscar Miguel Sabido
Departamento de Física,
Universidad de Guanajuato

Efraín Rojas Marcial
Facultad de Física,
Universidad Veracruzana

HIGH ENERGY PHYSICS

J. Lorenzo Díaz Cruz
Benemérita Universidad Autónoma de
Puebla

ASTROPHYSICS

Alma Xóchitl González Morales
División de Ciencias e Ingenierías,
Universidad de Guanajuato

Lucero Uscanga Aguilera
Departamento de Astronomía,
Universidad de Guanajuato

Héctor Bravo Alfaro
Departamento de Astronomía,
Universidad de Guanajuato

INSTRUMENTATION

Angélica Hernández Rayas
Universidad de Guanajuato

COMPLEX SYSTEMS

Leonardo Dagdug Lima
Universidad Autónoma Metropolitana

Guillermo Chacón Acosta
Departamento de Matemáticas Aplicadas y
Sistemas, UAM

Enrique Hernández Lemus
Departamento de Genómica
Computacional,
INMEGEN

MATERIALS SCIENCES

Ismeli Alfonso López
Instituto de Investigaciones en Materiales,
Unidad Morelia, UNAM

Miguel Angel Vallejo Hernández
Departamento de Ingeniería Física,
Universidad de Guanajuato

Subhash Sharma

Volume 72, Número 6, Nov-Dec 2026

Centro de Nanociencias y Nanotecnología, UNAM

MEDICAL PHYSICS

Héctor Alva Sánchez
Instituto de Física, UNAM

Francisco Miguel Vargas Luna
Departamento de Ingeniería en Física, Universidad de Guanajuato

Hilda Mercado Uribe
Unidad Monterrey, Cinvestav

NUCLEAR PHYSICS

Daniele Dell'Aquila
Federico II University, Italia

Roelof Bijker
Universidad Nacional Autónoma de México

OPTICS

David Bermúdez
Departamento de Física, Cinvestav

Lorena Berenice Velázquez Ibarra
Departamento de Física, Universidad de Guanajuato

PLASMA PHYSICS

Julio Herrera
Instituto de Ciencias Nucleares, UNAM

SOLID STATE PHYSICS

Juan Carlos Martínez Orozco
Unidad Académica de Física
Universidad Autónoma de Zacatecas

Esteban Cruz Hernández
Universidad Autónoma de San Luis Potosí

Máximo López López
Cinvestav

THERMODYNAMICS AND STATISTICAL PHYSICS

Pavel Castro Villarreal
Universidad Autónoma de Chiapas

Ricardo Román Ancheyta
Universidad Nacional Autónoma de México

Rosario Esperanza Moctezuma Martiñón
Universidad Autónoma de San Luis Potosí

NANOTECHNOLOGY

Elder de la Rosa Cruz
Universidad De La Salle Bajío

QUANTUM PHYSICS

Ana María Cetto
Universidad Nacional Autónoma de México
Instituto de Física

Jose Luis Lucio Martínez
Universidad de Guanajuato,
División de Ciencias e Ingenierías

ARTIFICIAL INTELLIGENCE ON PHYSICS

Nidiyare Hevia Montiel
Universidad Nacional Autónoma de México

Huziel Enoc Sauceda Félix
Universidad Nacional Autónoma de México

REVISTA MEXICANA DE FÍSICA, year 72, issue 6, Nov-Dec 2026. Scientific journal published by Sociedad Mexicana de Física, A. C. Departamento de Física, 2º Piso, Facultad de Ciencias, Universidad Nacional Autónoma de México, Ciudad Universitaria, Alcaldía Coyacán, C.P. 04510, Ciudad de México. Apartado Postal 70-348. Tels. (+52)55 5622 4946, (+52) 5622 4848, https://rmf.smf.mx/ojs/, e-mail: rmf@ciencias.unam.mx. Chief Editor: Ramón Castañeda Priego. INDAUTOR Certificate of Reserve: 04-2021-102913424600-203, e-ISSN: 2683-2224, granted by Instituto Nacional del Derecho de Autor. Responsible for the last update of this issue, Technical Staff of Sociedad Mexicana de Física, A. C., 2o. Piso, Facultad de Ciencias, Universidad Nacional Autónoma de México, Ciudad Universitaria, C.P. 04510, Coyoacán, CDMX. Date of last modification, May 1st, 2026.

The responsibility of the materials published in Revista Mexicana de Física rests solely with their authors and their content does not necessarily reflect the criteria of the Editorial Committee or the Sociedad Mexicana de Física. The total or partial reproduction of the texts hereby published is authorized as long as the complete source and the electronic address of the publications are cited.

There is no fee for article submission, processing or publication.

Revista Mexicana de Física by Sociedad Mexicana de Física, A. C. is distributed under a Creative Commons Attribution-NonCommercial-NoDerivatives 4.0 International License.

Volume 72, Número 6, Nov-Dec 2026

Índice

Ionization of atoms by positron impact: Applcations of the Scaled Born Method **1**
Jorge L. S. Lino

A DFT+U theoretical study of the effect of aluminum quantities on the structural, electronic, elastic and optic properties of Zinc oxide compound **5**
S. Haireche, M. Elbaa, M. Habireche and M. Bouchenafa

A gauge-invariant spectral scale from covariant diffusion in d-dimensional Yang–Mills backgrounds **20**
A. Escamilla-Aké

Dimensional consistency of derivatives with non-singular kernels **27**
J. J. Rosales García L. A. Ramírez Garza F. Hernández Cabrera F. A. Godínez Rojano

Granular structure and local de Broglie wavelength in fuzzy dark matter halos **35**
F. Rosales-Infante, I. Álvarez-Rios, A. Quiñonez-Guerrero and F. S. Guzmán

Investigation of impact of calcination temperature on the structural, microstructural, and functional properties of MgO nanoparticles using Williamson Hall method **43**
A. Tanveer, M. M. Haseeb Awan, M. Sajjad Mehmood, and M. Ahmad

Structural, electronic, magnetic, and optical properties of $CuMnInSe_3$ chalcogenide compound **56**
W. Menasri, S. Fetah, S. Didaoui, and A. Djerad

Studying the properties of prepared kaolin/epoxynanocomposites for flame retardancy **63**
M. T. Abd, I. N. Kashkool, and Saif Khalel Jasim

The pH effect on PEDOT: PSS/GO as a potential hole transport layer **69**
M. D. Nurhafizah, Tan You Zi, and B. Afzalina

Structural, morphological, optical and electrical properties ofAl-doped ZnO thin films prepared by Sol-Gel spin coating **79**
A. Carrero, P. Perillo, D. Rodríguez, and M. Barrera

Improvement I-V characteristics of (GaAs/Ge) heterojunction at differentthicknesses and annealing temperatures by thermal evaporation method **85**
I. N. Kashkool, A. K. Mohammed, M. T. Abd, A. M. Shano, and S. Khalel Jasim

Ising-type ferroelectric switching and piezoelectric response in wurtzite KMgP: First-principles study **92**
A. Labdelli and A. Benbedra

Antenas pre-fractales en medicina: fundamentos geométricos,desempeño electromagnético y aplicaciones diagnósticas **102**
L. González-Zamora, S. S. Hidalgo-Tobón y M. A. Quiroz-Juarez

Wavelength-dependent optical bleaching in Al_2O_3:C nanoDot optically stimulated luminescence dosimeters **112**
Isabel Morales-Peña et al.,

A dynamical system approach to modified point kinetics equations **120**
T. M. Tiscareño Sánchez, S. L. Hinojosa Ruiz, and H. Tototzintle Huitle

Numerical modeling of spin-dependent phase shifts in nucleon-nucleon scattering **127**
P. Sahoo

Testing the effects of ultraviolet radiation on biological samples using laser interferometry **134**
G. Frausto-Rea and M. del S. Hernández-Montes

Topological modes for light propagation inside a 2D photonic square lattice crystal with $p4$ symmetry **142**
M. A. Tun-Carrillo, J. A. Medina-Vázquez, M. E. Mora-Ramos, H. A. Gómez-Urrea and I. V. Pérez-Quintana

Plasma-Activated Fenton Chemistry for Acid Blue 9 dye removal: Kinetics, physicochemical dynamics, and G_{50} optimization **151**
J. Vergara et al.,

Deep learning based identification of solvents from post-desiccation patterns **158**
J. I. Morán-Cortés and F. Pacheco-Vázquez

Ionization of atoms by positron impact: Applications of the Scaled Born Method

Jorge L. S. Lino

Instituto Lino de Educação, Dept. de Assessoria e Orientação Estudantil, 12242000, São José dos Campos, São Paulo, Brazil

Received 17 March 2026; accepted 9 June 2026

Positron emission tomography (PET) scans can be used to investigate the pathogenesis of neurological disorders and diseases such as Alzheimer's and Parkinson's. PET scans use positrons to resolve an image of the internal biochemical process occurring inside the body, *i.e.*, ionization cross sections. Knowledge of ionization cross sections for atoms is evidently crucial in PET technology. We will discuss some recent developments of the scaled Born positron (SBP) method for ionization of atoms. The SBP method was originally proposed for electronic excitations of atoms (J.L.S. Lino, $Chin.J.Phys.\mathbf{54}$ (2016)504). First Born approximation (FBA) and the atomic orbital wavefunctions have been approximated by Roothaan-Hartree-Fock, and the scattered positron and ejected electron have been approximated by a plane wave and Coulomb wave as proposed by Barlett $etal.$ (Atomic Data Tables **86** (2004) 235). It is shown that the SBP method combined with an analytical factor results in a efficient method when compared with the sophisticated and traditional binary-encounter-dipole (BED) model. Results of ionization cross sections of H, He, Ne, and C atoms using the new representation are presented to illustrate the applicability of the improved SBP method.

Keywords: Born; positron; ionization; atoms.

DOI: https://doi.org/10.31349/RevMexFis.72.060401

1. Introduction

Positron-impact ionization cross sections represent a powerful tool for biomedical research and enable the imaging of internal molecular process occurring in vivo in real time [1]. A database of ionization cross sections can be used, for example, as a starting to investigate the pathogenesis of neurological disorders and diseases such as Alzheimer's disease [1]. For example, positherapy utilizes positrons to destroy cancer cells [1] and has proven useful in treating cancers where conventional methods are less effective. Positherapy also is a safer alternative to current radiotherapy approaches due the low range of the emitted positron. In recent years, there has been increasing interest in studying biological molecules such as DNA by electrons and positrons impact ionization cross sections of atoms. It is worth mentioning that after losing sufficient energy, positrons undergo annihilation and release gamma rays which can be observed by "positron emission tomography (PET)" scans and their applicability in medicine is imperative, which justifies further studies on the topic. A series of experiments involving positron impact with several atoms has been conducted recently (see Ref.[2-4]) and evidently theoretical calculations are extremely important for an adequate comparison. Some methods, such as Born approximation [5], the distorted plane wave method [6], and the binary-encounter-Bethe (BEB) dipole model [7,8] have been used to calculate ionization cross sections by positron impact. Accurate ionization cross sections still remain an important and challenging endeavor. The scaled Born positron (SBP) method was originally proposed by Lino [9-12] for studies involving electronic excitation of atoms and molecules by positron impact. As we will demonstrate, the SBP method can be adapted for ionization cross sections of atoms (the merit of SBP method is important, *i.e.*, avoid arduous mathematical equations, and computational complexity [13]). In Sec. 2 we identify the SBP method and in Sec. 3 computational procedures and results are discussed. Conclusions are presented in Sec. 4.

2. Theory

The well-known FBA was first applied to treat electron scattering at high incident energies in 1926. Since then significant effort and investment have been made carried out by several researchers involving the FBA as a suitable starting point [5]. As is well known, for sufficiently fast electrons (or positron) the cross sections for a collision with an atomic target are expected to be promising but for low and intermediate energies the FBA is not sufficient. In this article, we will show that the SBP method is appropriate for low, intermediate, and high incident positron energies. In the FBA the plane wave represents the correct function at infinity for a positron colliding with a target and also represent the simplest collision theory that uses target wave function explicitly. The FBA does not properly incorporate target distortion and resonances. We will see that the SBP method include such possibilities. The traditional FBA can be written as

$$\sigma = \left[\frac{(4\pi {a_o}^2 R)}{E}\right] f_{\rm FBA}, \tag{1}$$

where

$$f_{\rm FBA} = \left(-\frac{1}{2}\pi\right) < S_{kf}\,|\,V\,|\,S_{ki} > . \tag{2}$$

The SBP method represent an improved version of FBA and as observed in Eq. (1) the SBP method replaces the E (energy) that appears in the denominator of Eq. (1), by $E + (E_{\rm exc} + E_{\rm Ps})$ and the Eq. (1) turning Eq. (1) into

$$\sigma_{\rm SBP} = \left(\frac{f_{\rm acc}}{f_{\rm Born}}\right) \cdot f(E)\sigma_{\rm Born}, \tag{3}$$

where

$$f(E) = \frac{E}{(E + E_{\rm Ps} + E_{\rm ex})}. \tag{4}$$

It is important to mention that the SBP method has important aspects that can be highlighted. First, E_{Ps} is the positronium energy of the target and is used only when the incident particle is a positron which is not identical to the target electrons. Second, E_{exc} is the excitation energy, f_{accur} is an accurate dipole value from experiments or from accurate wavefunctions, and f_{Born} is the dipole value from the FBA (these parameters are not of adjustable and this is very important in a mathematical development). Third, the constant $(E_{\rm Ps} + E_{\rm exc})$ has also some pratical consequences to the performance of the SBP method, *i.e.*, the constant is related with energy of the incident positron in the field of the nucleus and the bound electrons of the target (also can be seen as the scaling factor to represent the correlation between the positron and electrons of the target). Finally, the "scaling factor" here proposed suggests a similarity with polarization effects (Lino has shown many examples [9-12] in which the SBP method for dipole-allowed excitation into very reliable cross sections when compared with sophisticates methods). The Coulombic attraction between positrons and electrons makes an enormous difference from the always repulsive interaction between electrons. The SBP method does not incorporate real positronium formation, but it explicitly considers virtual positronium formation, *i.e.*,

$$E_{Ps} = B - 6{,}8 \ \text{eV}, \tag{5}$$

where B is the binding energy of the electron of target. As observed, the $f(E)$ factor reduces the FBA at low energies while keeping the validity of the Born approximation at high energies [5]. Studies using the SBP method for electronic excitation of the targets by positron impact are conclusively satisfactory [9] and the method is not computationally intensive. The FBA is calculated from the sum of the partial ionization cross sections of each occupied orbital,

$$\sigma = \frac{\sum(N_{\rm nlm}\sigma_{\rm nlm})}{(2l+1)}, \tag{6}$$

where nlm orbital and it is assumed that electrons are equally shared among the available m quantum states. Mathematically the FBA for ionization may be expressed as

$$[e^{-iqr}]_{\rm nml} = \int \psi^* e^{-{\rm iqr}}\phi_{\rm nml} d^3r, \tag{7}$$

where $\varphi_{\rm nlm}$ is the target orbital wave function with the usual nlm labels for orbital, angular momentum and magnetic quantum numbers, respectively, and ψ is a Coulomb wave used to model the ejected electron. There are no arbitrary parameters or fitting constants. The SBP method does not provide differential cross sections in energy loss or angle of scattering, and no positronium formation was considered. The total ionization cross sections for the target atom is the sum over all accupied orbitals, *i.e.*, $\sigma_{\rm total} = \sigma_\sigma(1s + 2s + 2p + ...)$.

For ionization cross sections the Eq. (3) can be written as

$$\sigma_{\rm SBP} = \left(\frac{f_{\rm acc}}{f_{\rm Born}}\right) \cdot f(E)\sigma_{\rm Born}, \tag{8}$$

where

$$f(E) = \frac{E}{(E + E_{\rm Ps})}. \tag{9}$$

3. Results and discussion

We have investigated ionization cross sections by positron impact of H, He, Ne, and C atom. In Table I, we show the data for ionization energy (B) and positronium formation energy (E_{Ps}). In Table II, we shows results for all atoms (ionization cross sections by positron impact) using the SBP method.

TABLE I. Ionization and positronium energies.

Atom	B(eV)	E_{Ps}(eV)
H	13.6	6.8
He	24.50	17.70
Ne	21.56	14.76
C	11.26	4.40

TABLE II. Ionization cross sections for H, He, Ne, and C atom by positron impact using the SBP method (10^{-16} cm^2).

Energy(eV)	H	He	Ne	C
20	0.288	0.0008	0.0016	0.523
30	0.618	0.0378	0.087	1.117
40	0.743	0.140	0.196	1.571
50	0.779	0.230	0.287	1.821
60	0.771	0.296	0.364	1.941
70	0.746	0.342	0.429	1.991
80	0.714	0.372	0.484	1.985
90	0.681	0.391	0.528	1.958
100	0.648	0.409	0.565	1.918
150	0.515	0.424	0.660	1.660
200	0.423	0.367	0.676	1.464
250	0.359	0.351	0.660	1.276
300	0.310	0.304	0.625	1.134

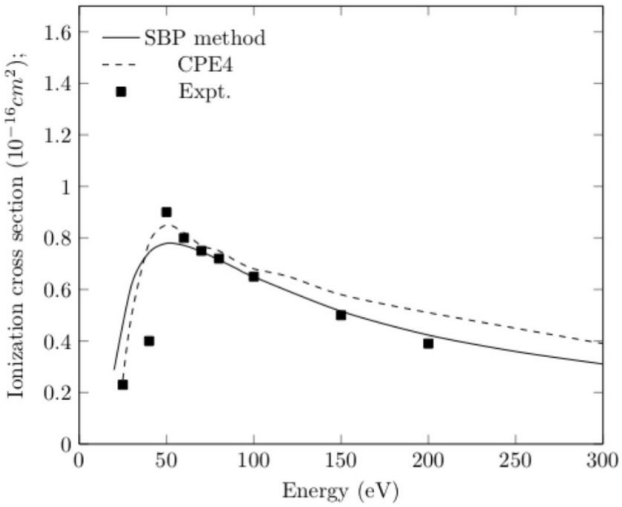


FIGURE 1. Positron-hydrogen atom ionization cross sections.

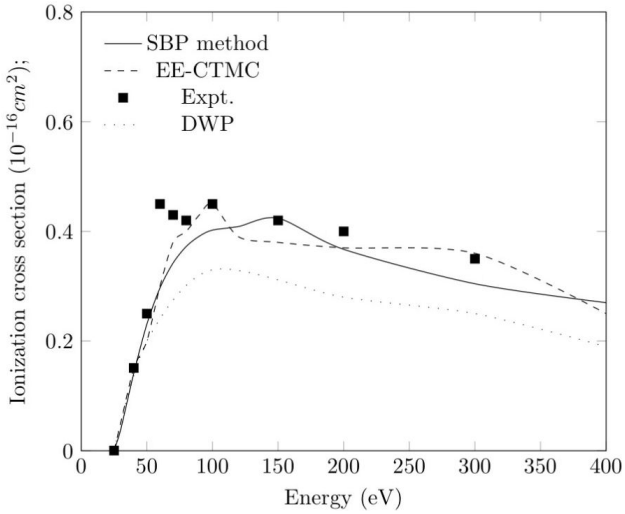


FIGURE 2. Positron-helium atom ionization cross sections.

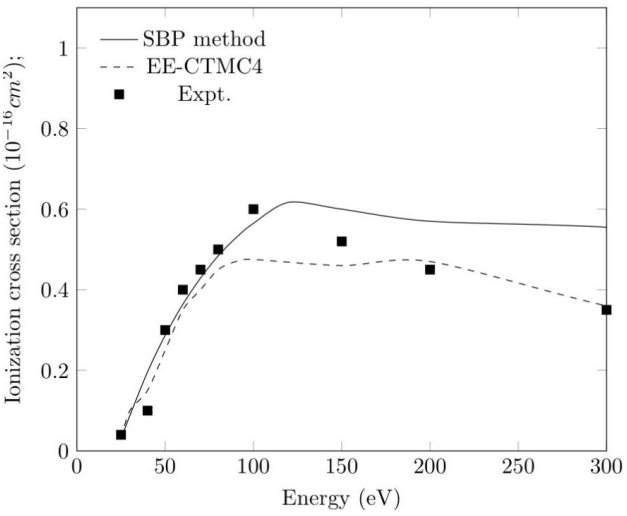


FIGURE 3. Positron-neon atom ionization cross sections.

In Fig. 1 we present positron-hydrogen atom ionization cross sections using the SBP method compared with the efficient distorted wave method (CPEA) [14], and experimental data [15]. As observed the SBP method is very similar with the CPEA [14]. The agreement with the CPEA [14] theory provides direct evidence of the accuracy of our structure model. As observed also our cross sections are in good agreement with the experimental data [14].

In Fig. 2 we shows positron-helium atom ionization cross sections using the SBP method compared with distorted wave plane (DWP) method [16], the sophisticate classical trajectory Monte Carlo (EE-CTMC) model (see Ref. [16]), and experimental data [16]. As observed in Fig. 2 the agreement in the shape and magnitude between the SBP method and EE-CTMC model is encouraging. This is of special relevance for the SBP method, since the EE-CTMC model demands great computational effort. From Fig. 2 can be clearly seen that the SBP method is in very good agreement with the experimental data [16]. At high energies the methods converge to the traditional FBA, validating the procedure.

Figure 3 shows positron-Ne atom ionization cross sections. Ionization of neon atom by positron impact is a fundamental process which atomic structure, positronium formation, and particle-antiparticle interactions are not fully understood in the literature. Positron scattering from neon atom is very important for the interpretation of astrophysical data [17]. Because neon is a noble gas with a high ionization potential (21.56 eV), it serves as a rigorous test for the SBP method. Fig. 3 shows our SBP method compared again with the sophisticate classical trajectory Monte Carlo (EE-CTMC4) model [17] and experimental data [17]. As observed again the theoretical results are in good agreement. The agreement between the methods are consistently good, giving confidence that the set of atomic parameters used in our SBP method are the best available set.

Finally, in Fig. 4 we show a preliminary study on the positron-carbon atom ionization cross sections. As cited before, ionization cross sections help the investigate the pathogenesis of neurological disorders and diseases such as Alzheimer's and Parkinson's. The carbon atom represent 18 % of the human body and is the major component of biomolecules such as DNA. Preliminarily, in Fig. 4 we shows ionization cross sections calculated using the SBP method compared with the BEB method for electron case only [17]. As observed, the cross sections calculated using the SBP method for positrons are in ery good agreement with those obtained using the BEB method for electrons [17]. This scenario is obviously not found for several other atoms. It is important to observe that the convergence between the cross sections using SBP method (positron) and BEB method (electron) suggests new comparative studies (for high incident positron energies, numerical convergence to the FBA is expected). The carbon atom shows signs of the presence of excitation-autoionization [17], which represents an interesting question for the future using the SBP method [19].

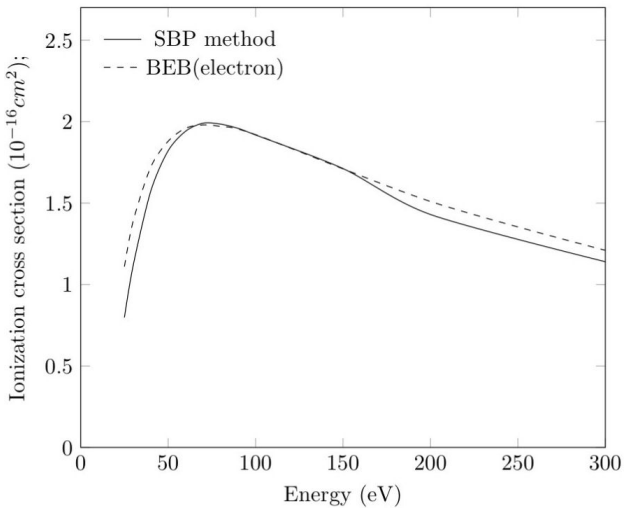


FIGURE 4. Positron-carbon atom ionization cross sections.

4. Conclusions

The scaled Born positron (SBP) method provides in conclusion good results for all the targets studied. The SBP method not diminish the value of more sophisticated methods that produce highly accurate results, though they requires orders of magnitude more computational effort than SBP cross sections. First, the SBP method will not work well on angular distribution because the scaling only change the E dependence of first Born approximation (FBA) cross sections. It is well known that the FBA cross sections do not reproduce large angle scattering well at any E, and the SBP method will not change the shape of FBA angular distributions. However, the SBP method described here will facilitate the calculation of integrated excitation, ionization, excitation-autoionization cross sections, and studies on positronium formation for targets in general, which pose difficulties to more computer-intensive theories. In conclusion the SBP method for ionization cross sections is relatively simple and efficient when compared to state-of-art ab initio theories.

1. S. D. Bass, S. Mariazzi, P. Moskal, E. Stepien, Positronium Physics and Biomedical Applications. $Rev.Mod.Phys.$ **95** (2023) 021002.
2. L. Wymer, S. Kumar, T. J. Gay, S. Hodgman, S. J. Buckman, J. R. Machacek, Excitation of metastable helium atoms by positron impact. $Eur.Phys.J.D$ **80** (2026) 12.
3. C. M. Surko, G. F. Gribakin, S. J. Buckman, Low-energy positron interactions with atoms and molecules. $J.Phys.B$ **38** (2005) R57.
4. K. Ratnavelu, M. J. Brunger, S. J. Buckman, Recommended positron scattering cross sections for atomic systems. $J.Phys.Chem.Ref.Data$ **48** (2019) 023103.
5. J. L. S. Lino, PhD, Thesis, Instituto Tecnológico de Aeronáutica, ITA, Centro Técnico Aeroespacial-CTA (1996).
6. S. A. Abdel-Naby, C. P. Ballance, T. G. Lee, S. D. Loch, M. S. Pindzola, Electron-impact ionization of the C atom , $Phys.Rev.A$ **87** (2013) 022708.
7. K. Ratnavelu, M. J. Brunger, S. J. Buckman, Recommended positron scattering cross sections for atomic systems, $J.Chem.Ref.Data$ **48** (2019) 023102.
8. Y.-K. Kim, M. E. Rudd, Binary-encounter-dipole model for electron-impact ionization. $Phys.Rev.A$ **50** (1994) 3954.
9. J. L. S. Lino, An investigation of the scaling of plane wave Born cross sections for positron-H_2 considering the positronium formation channel, $Chin.J.Phys.$ **54** (2016) 104.
10. J. L. S. Lino, Scaling of plane-wave Born cross sections for positron-impact excitations of He, and H_2, $Chin.J.Phys.$ **54** (2016) 223.
11. J. L. S. Lino, Electronic excitation of H_2, CO, and N_2 by positron impact. $Rev.Mex.Fis.$ **63** (2017) 303.
12. J. L. S. Lino, Scaling plane wave Born cross sections for positron-impact excitations of H_2, $Rev.Mex.Fis.$ **62** (2016) 596.
13. N. A. Mori, L. H. Scarllet, I. Bray, D. V. Fursa, Convergent close-coupling calculations of positron scattering from atomic carbon, $Phys.Rev.A$ **107** (2023) 032817.
14. P. Acacia, R. I. Campeanu, M. Horbatsch, R. P. McEachran, A. D. Stauffer, Positron impact ionization of atomic hydrogen, $Phys.Lett.A$ **179** (1993) 205.
15. T. S. Stein, M. Harte,J. Jiang, W. E. Kauppila, C. K. Kwan, H. Li, S. Zhou, Measurements of positron scattering by hydrogen, alkali metal, and other atoms. $Nucl.Instr.Meth.Phys.Res.B$ **143** (1998) 68.
16. M. Basu, P. S. Mazumdar, A. Ghosh, Ionisation cross sections in positron-helium scattering. $J.Phys.B$ **18** (1985) 369.
17. P. Stone, P.; Y. -K. Kim, An overview of the BEB method for electron-impact ionization of atoms and molecules, *Surf. Interface Analysis* **37** (2005) 966.
18. J. L. S. Lino, Ionization cross section in positron-boron, and carbon atom scattering, in preparation, (2026).

A DFT+U theoretical study of the effect of aluminum quantities on the structural, electronic, elastic and optic properties of Zinc oxide compound

S. Haireche[a,*], M. Elbaa[b], M. Habireche[a] and M. Bouchenafa[c]

[a] *Laboratory of Mechanics, Physics, and Mathematical Modelling, University of Medea, Medea 26000, Algeria.*

[b] *Department of Material Sciences, Faculty of Sciences and Technology, Djilali Bounaama University of Khemis Miliana, 44225, Algeria.*

[c] *Laboratoire de Matériaux pour Application et Valorisation des Energies Renouvelable (LMAVER), Département de Sciences de la Matière, Université Amar Telidji Laghouat, BP 3000, Algeria.*

Received 10 August 2025; accepted 2 July 2026

This work presents a comprehensive ab initio investigation of the structural, electronic, elastic, and optical properties of aluminum-doped zinc oxide ($Zn_{1-x}Al_xO$) using the DFT+U framework. A realistic 2×2×2 supercell model is employed to simulate substitutional doping at various Al concentrations (up to 25 %). The results reveal a systematic reduction in band gap energy, reaching 2.216 eV at the highest doping level, which reflects enhanced electrical conductivity. Density of states analysis highlights the emergence of Al-3p states near the conduction band, contributing to donor-like behavior and supporting n-type conductivity. The elastic properties show a progressive decrease in stiffness and an increase in anisotropy with Al content, indicating mechanical softening of the ZnO matrix. Optically, the doped systems exhibit improved transparency, a blue shift in the absorption edge, and modulation of the dielectric response, consistent with the Burstein Moss effect. These findings suggest that Al doping significantly tailors the multifunctional behavior of ZnO, making it a promising candidate for transparent conducting electrodes, optoelectronic components, and sensor technologies. The theoretical insights presented herein provide useful guidelines for experimental optimization of Al doped ZnO-based materials.

Keywords: GGA+U; $Zn_{1-x}Al_xO$; DFT; gap energy; transmission; supercell.

DOI: https://doi.org/10.31349/RevMexFis.72.060501

1. Introduction

For many years, Zinc oxide has been used in the chemical and pharmaceutical industries [1, 2]. Zinc oxide (ZnO) holds significant potential in the medical field, particularly in drug delivery systems and cancer treatments, due to its biocompatibility, antimicrobial properties, and ability to target cancerous cells effectively [3, 4]. New avenues of research in optoelectronics are beginning to advance with the evolution of technology like photoluminescence applications [5–7]. The latest technological trend shows that zinc oxide doping with transition metals such as Sc, Ti, V, Cr, Mn, Fe, Co, Ni and Cu can be used as a ferromagnetic material and also has great interest in spintronic applications [8–10]. After industrial interest in this material became more prominent, research into its physical properties was extensively studied not only for the development of the microelectronics industry but also to collect as much information as possible on its energy behavior concerning the preparation conditions. ZnO, with its wide gap (3.37 eV) and its high binding energy (60 meV), is considered one of the most promising semiconductor materials for technological applications such as laser diodes emitting in blue and UV spectra [11–13]. Moreover, the thermoelectric field extensively uses ZnO with metallic impurities such as aluminum [14, 15]. Zinc oxide in thin films has enjoyed considerable importance in various fields of research in recent decades due to its multiple potential applications in optoelectronics, such as solar cells [16], spintronics [17–19], gas sensors [20], and photodetector applications [21]. Doping ZnO with suitable elements can improve its optical characteristics with increased transmission in the visible ($T \sim 90\,\%$) and accelerate the run for its practical applications [22–28]. Also, oxygen vacancies improve both optical and electrical properties, particularly electrical conductivity ($\sigma \sim 10^{-3}\ \Omega^{-1}\ \mathrm{cm}^{-1}$) [29–32]. Moreover, thermal treatment plays a crucial role in improving the electrical properties of ZnO, as demonstrated by the work of Abdullin *et al*. [33]. Furthermore, sintering and precursor concentration have a greater impact on ZnO physical properties [34]. In particular, the doping of ZnO with Aluminum considerably modifies its physical properties [35–37]. Al-doped ZnO compounds exhibit high transparency in the visible range [38, 39]. It has been shown that the gap can be controlled by introducing a small amount of aluminum [40]. Several research groups are currently working on developing more efficient solar cells by doping zinc oxide with aluminum [41, 42]. For three decades, the number of publications addressing the doping of ZnO has failed to fundamentally understand the effect of doping with metallic elements on electrical, optical, and electronic properties. This work focuses on the microscopic aspect of doping on band gap energy, elasticity, and optical absorption. This study aims to deepen the understanding of the atomic-scale effects

of aluminum doping in ZnO, with a focus on its structural and mechanical behavior relevant to advanced technological applications. By employing a realistic $2 \times 2 \times 2$ supercell model, we sought to closely mimic experimental conditions and generate reliable data on dopant-induced changes. Special emphasis was placed on comparing ZnO:Al with other transparent conducting oxides to assess its standing within this family of materials. The findings help categorize the material based on its directional performance and mechanical stability. They also offer valuable theoretical insights to support high-efficiency experimental design.

2. Computational methods and geometric model

In this study, ab initio calculations are performed using the plane wave method, incorporating the pseudopotential approach within the framework of density functional theory (DFT) [43]. To improve the accuracy of the results, the Generalized Gradient Approximation (GGA) was adopted, specifically using the Perdew-Purke-Ernzerhof (PBE) functional [44]. Simulations are carried out using the CASTEP code, leveraging Vanderbilt pseudopotentials to efficiently model electron-ion interactions [45]. The pseudo-potential of Vanderbilt-type ultra-soft was used to compute the potential seen by the valence electrons [46]. This choice of potential enables the following valence configurations to be used: ($3d^{10}4s^2$) for Zn, ($3s^23p^1$) for Al and ($2s^22p^4$) for O. To improve the description of localized electrons (*e.g.*, Zn 3d), we used the DFT+U method formulated by Dudarev *et al*., where the total energy is expressed as [47]:

$$E_{\mathrm{DFT}+U} = E_{\mathrm{DFT}} + \frac{U_{\mathrm{eff}}}{2} \sum_{\sigma} \left[\mathrm{Tr}\left(\rho^{\sigma}\right) - \mathrm{Tr}\left(\rho^{\sigma}\rho^{\sigma}\right) \right], \quad (1)$$

where $U_{\mathrm{eff}} = U - J$ is the effective Hubbard parameter (U : On-site Coulomb interaction and J : Hund's exchange parameter), ρ^{σ} is the occupation matrix for localized orbitals with spin σ, E_{DFT} is the standard DFT energy without corrections and Tr is the Trace of a matrix (sum of diagonal elements). Hubbard corrections are also applied, with optimized values of 5.5 eV for d-electrons and 8.5 eV for p-electrons, in order to improve the treatment of electronic correlation effects. These U values have been widely optimized and reported in the literature [40, 48–50]. Unless otherwise stated, we use GGA+U with U^d for Zn and *Up* for O in the literature validated AZO window seen in the study of Shabani *et al*. [51] and report a U sensitivity analysis confirming that all qualitative trends versus Al content are robust. We employ GGA+U with the previously cited, in house optimised parameters calibrated to the band gap, Zn(3d) binding energy, and equilibrium a and c, and no U is applied to Al(3p), and the qualitative trends remain robust within ± 0.5 eV.

In ab-initio calculation, it is necessary to test the convergence of the results with respect to the cut-off energy ($E^{\text{cut-off}}$) and the K-points mesh configuration in the first Brillouin zone (1BZ). According to the optimization operation, a good convergence is obtained for a plane-wave energy of Ecut-off values of 500 eV and $6 \times 6 \times 4$ K- points mesh configuration. In this study, Al atoms are introduced into the hexagonal wurtzite structure of ZnO via a substitutional doping mechanism. Figure 1 illustrates a 2×2×2 ZnO supercell consisting of 16 zinc and 16 oxygen atoms, designed to allow the systematic substitution of Zn atoms with Al at different doping concentrations. Specifically, Al atoms substitute Zn atoms at atomic ratios of $x = 6{,}25\,\%$, 12.5 %, 18.75 % and 25 %, corresponding to 1, 2, 3, and 4 Al atoms, respectively, within the supercell. This method preserves the overall hexagonal symmetry while allowing investigation of the effects of increasing dopant content on the structural and electronic properties of zinc oxide. The substitution of Zn^{2+} with smaller Al^{3+} ions introduces extra free electrons into the system, making it suitable for n-type conductivity enhancement. The supercell approach facilitates accurate modeling of local distortions, charge distribution, and band structure modifications resulting from Al incorporation. Compositions up to 25 % Al are modeled in a 2×2×2 supercell to sample defect-defect interactions and provide an upper bound on electronic/elastic trends. This does not assert bulk equilibrium solubility at 25 % rather, it reflects non-equilibrium thin film processing windows where high nominal Al contents are reported while wurtzite reflections persist in XRD. Experimental evidence for such regimes (FCM-CVD) and a discussion of possible phase separation at very high Al are provided in the references.

Similar criteria were employed by Damente *et al*., who also selected doping sites to maintain the symmetry of the hexagonal lattice [37]. Other studies, such as those by Jafarova *et al*., have selected the dopant-receiving sites based

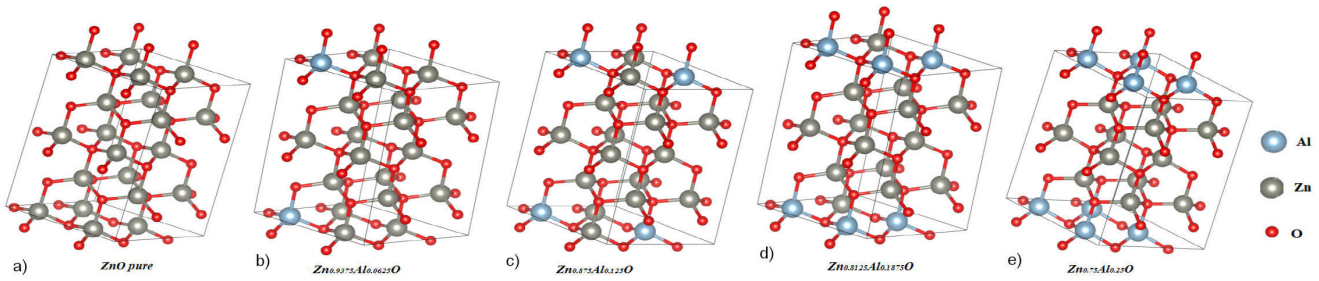


FIGURE 1. 2×2×2) supercell models of a) pure ZnO and Al-doped ZnO with x(%) = Al/Zn: b) 6.25 %, c) 12.5 %, d) 18.75 %, and e) 25 %.

TABLE I. Optimised lattice parameters a (Å) and c(Å), cell volume V (Å^3) for ZnO compared with other experimental and theoretical results ($\Delta a/a$ and $\Delta c/c$: Relative error without units on the lattice parameters a and c, respectively).

	$Zn_{1-x}Al_xO$						Reference
Our results	x	a (Å)	$\Delta a/a$ (%)	c (Å)	Δc/(%)	**V(Å^3)**	
	0	3.284	1.64	5.299	2.39	49.491	GGA
	0.0625	3.251		5.294		48.119	
	0.125	3.249		5.205		47.259	
	0.1875	3.268		5.369		57.339	
	0.25	3.172		5.877		59.131	
	0	3.219	0.37	5.184	0.17	46.519	GGA+U
	0.0625	3.249		5.205		47.252	
	0.125	3.188		5.607		49.007	
	0.1875	3.233		5.190		46.653	
	0.25	3.219		5.180		49.088	
Other (Exp.)	0	3.231	-	5.175	-	46.785	[17]
Other (Theo.)	0	3.240	6.93	5.190	0.08	47.183	[54]
		3.340	7.29	5.350	0.58	51.687	[55]
		3.184	10.23	5.147	3.16	45.184	[56]
		2.940	6.85	5.070	0.74	37.952	[57]
		3.225	0.33	5.174	0.27	46.603	[58]
		3.186	6.44	5.150	0.23	45.272	[59]
		3.240	5.15	5.190	0.69	47.183	[60]

on the criterion of minimizing the system's total energy [52, 53]. Finally, self-consistency calculations were considered converged when the system's total energy become stable, ensuring the results' reliability. Graphical representations and crystal structure visualizations are performed using the Origin software and the VESTA applications.

3. Results and discussions

3.1. Structural properties

The first and fundamental step in *ab initio* calculations is the determination of a material's structural properties. This phase is crucial as it provides key insights into the material microstructure, serving as the basis for subsequent calculations related to electronic and elastic properties. The optimized lattice parameters of ZnO are essential for understanding its structure and impact on various physical properties. These parameters offer valuable information about the atomic arrangement within the crystal lattice, ultimately influencing its mechanical, thermal, and electronic behavior. Table I provides an overview of the structural properties, comparing them with existing experimental and theoretical data. To validate our findings, we meticulously compared our optimized values with existing experimental and theoretical data. Our results for the undoped and Al-doped ZnO lattice parameters and volumes are in excellent agreement with the existing experimental and theoretical data. The relative errors in the lattice parameters Δa/a and Δc/c, calculated using DFT-GGA for the undoped ZnO, are 1.64 % and 2.39 %, respectively. In contrast, the corresponding deviations obtained using the DFT-GGA+U approach are significantly reduced to 0.37 % and 0.17 %, respectively. These results demonstrate that the inclusion of the Hubbard U correction in the GGA framework enhances the accuracy of the structural predictions and yields better agreement with experimental data.

Within GGA+U, the lattice-parameter response to Al doping results from an interplay of the local chemical pressure shorter Al–O bonds contract AlO^4 tetrahedra followed by anisotropic relaxation through the wurtzite framework and electronic changes Al donor electrons increase screening and ionicity, softening bond-bending and coupling a-c via the internal coordinate u. This balance yields small, composition dependent shifts and non-monotonic features in a and c, which we attribute to how specific Al configurations in the $2\times2\times2$ supercell redistribute local strain between basal and axial directions.

In DFT, the GGA+U approximation is generally more suitable for the geometric optimization of materials that exhibit strong electronic correlation effects, such as those containing transition elements with d-orbitals or f-orbitals. The GGA alone may underestimate the band gap and fail to accurately capture strongly correlated electronic interactions. In contrast, adding the U term (Hubbard correction) in GGA+U enhances the description of these interactions by correcting the energy of localized electrons, often leading to more precise geometric optimizations for these types of systems [49, 50]. According to the DFT criteria outlined by Damonte *et al*., our results exhibit strong agreement with both experimental and theoretical data [37]. For undoped Zinc oxi-

de, our study yielded a value of 3.219 Å and 5.184 Å for *a* and *c*, aligning closely with theoretical values of 3.225 Å and 5.174 Å [58] and 3.184 Å and 5.147 Å [56]. This result also demonstrated favorable agreement with the experimental values of 3.231 Å and 5.175 Å for *a* and *c*, respectively [20]. In the case of doping, the lattice parameters *a* and *c* of aluminum doped ZnO change only slightly, and the crystal structure approximately retains its hexagonal lattice, despite the absence of experimental values for a proper comparison.

These findings highlight the complexity of crystalline behavior in these compounds and stress the significance of integrating both theoretical and experimental perspectives. This comprehensive comparative study enhances our understanding of the structural properties of both undoped and Al doped ZnO, contributing to the broader knowledge of their unique crystalline behaviors.

3.2. Electronic properties

Band structure of undoped and Al doped ZnO

The band structure is composed of permitted and prohibited energy bands. The permitted energy bands, also called valence and conduction bands, determine the electrical properties of the material. The valence band is the lowest energy band and is generally occupied by electrons. The conduction band is the highest energy band, which can be partially or completely empty. From an energetic point of view, a material band gap corresponds to the lowest energy needed for an electron to transition from the valence band to the conduction band. Materials can be classified based on the size of this bandgap into insulators (large bandgap), semiconductors (medium-sized bandgap), and conductors (zero or near-zero bandgap). The graphs in Figs. 2a) to 2e) represent the band structures of ZnO and Al doped ZnO at various atomic ratios of Al/Zn from 0 to 25 % Al impurity quantities. In this graph, the gap energy between the valence and conduction bands is distinctly observable. The Fermi level lies in the middle of the bandgap, indicating it's an intrinsic semiconductor. In the undoped ZnO, the material exhibits a direct band gap located at the Γ point, consistent with the known semiconducting behavior of pure wurtzite ZnO.

As Al is introduced into the ZnO lattice, a systematic reduction in the band gap is observed across the series (b–e), accompanied by a noticeable shift of the conduction band minimum (CBM) toward lower energies, especially near the Γ M points. This narrowing is attributed to the incorporation of Al-3p orbitals, which contribute additional conduction states and introduce donor-like behavior, effectively lowering the CBM.

While the valence band maximum (VBM) remains relatively stable in energy, slight changes in its curvature and dispersion are observed, reflecting the perturbation of the electronic structure due to local lattice distortions and Al–O bonding. The shift is most pronounced at 25 % doping, where the band gap becomes significantly reduced and the bands exhibit increased overlap and dispersion, suggesting a transition toward a more conductive regime.

In previous results, it is observed that replacing a certain percentage of zinc with aluminum leads to a decrease in the energy gap as the doping level increases [63]. By comparing our results with the theoretical ones, we see an improvement in the value of the gap for $Zn_{1-x}Al_xO$. K. Dakhsi's study showed that the gap energy of films decreases from 3.29 eV for undoped ZnO to 3.27 eV for 5 % Al-doped ZnO [64]. This decrease is attributed to distortions of the crystal lattice caused by the introduction of impurities and the increase in the concentration of free electrons. Additionally, the gap decreases as the concentration of metal doping increases [65]. In contrast, results from FCM-CVD reveal a relatively stable bandgap around 3.1-3.2 eV for doping levels between 0 %

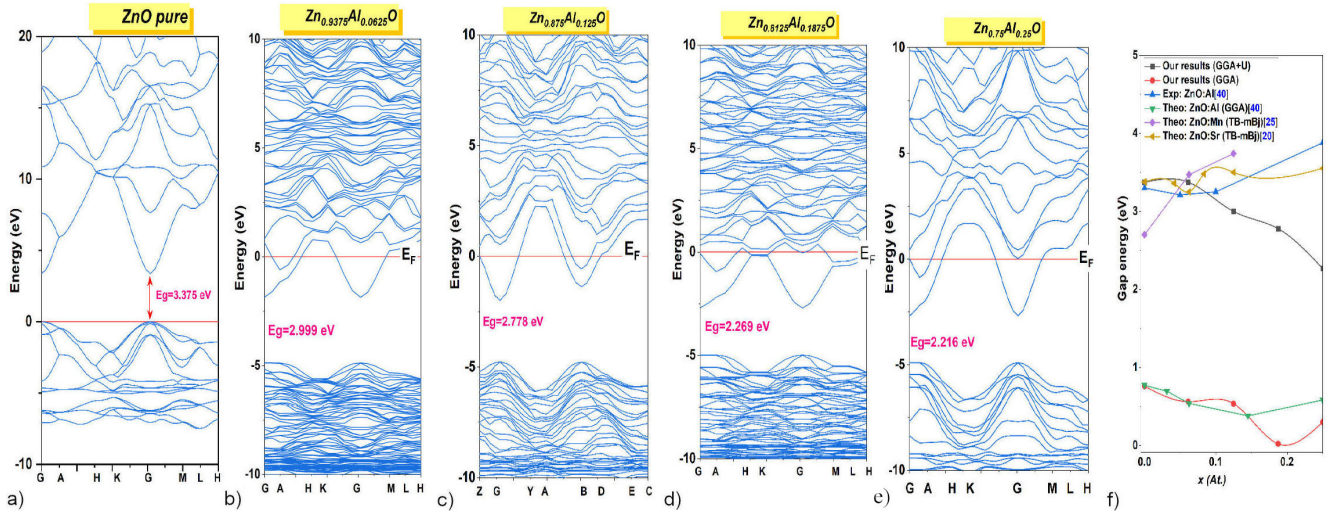


FIGURE 2. Band structure for: a) the undoped ZnO and Al doped ZnO with different atomic ratios of doping b) 6.125 %, c) 12.5 %, d)18.75 % and e) 25 %, f) Evolution of the band gap energy as a function of dopant concentration in previous research.

and 5 %, indicating limited Al solubility or incorporation under those processing conditions [40]. Figure 2f) illustrates the variation in band gap energy as a function of aluminum doping concentration in ZnO. The trend shows a significant decrease in Eg with increasing Al doping from the undoped ZnO to 25 % Al doped ZnO. Initially, for pure ZnO (x = 0), the band gap is around 3.375 eV. As Al is introduced (x = 0, 0.06125, 0.125, 0.1875, 0.25), the band gap decreases, reaching a minimum at $x = 0{,}25$, dropping to approximately 2.216 eV. This reduction is attributed to introducing free carriers and changes in the electronic structure caused by Al substitution. The observed trend suggests that controlled Al doping allows for tuning ZnO electronic properties, making it suitable for various optoelectronic and transparent conductive applications.

TDOS and PDOS of Undoped and Al doped ZnO

The density of states (DOS) is a fundamental physical quantity that provides deep insights into the electronic band structure of materials. Understanding DOS is essential because it influences many of the material electronic properties, such as electrical conductivity, optical absorption, and thermal properties. By examining the DOS, particularly the total density of states (TDOS) and partial density of states (PDOS), researchers can infer critical information about the distribution of electrons at various energy levels within a material. This understanding is especially important for materials like ZnO, which have widespread applications in electronics and optoelectronics due to their specific properties. Figure 3 shows the Total Density of States (TDOS) and Projected Density of States (PDOS) for both undoped and doped ZnO, with different atomic ratios of x =Al/Zn ($x = 0$, 0.0625, 0.125, 0.1875 and 0.25). Peaks in the PDOS indicate significant contributions from specific orbitals at corresponding energies. In the context of zinc oxide (ZnO), in its pure and aluminum-doped forms, the DOS analysis reveals intricate details about how doping affects the material's electronic structure. Typically, the energy origin in these analyses is fixed at the Fermi level, which serves as a reference point for measuring the energy distribution of electrons. The undoped ZnO is also presented for comparison purposes. The total and partial density of states (TDOS and PDOS) of Al-doped ZnO, evaluated over the energy range from -15 eV to +15 eV, reveal substantial modifications in the electronic structure with increasing Al concentration. In the deep valence region (-15 eV to -5 eV), the PDOS is dominated by oxygen 2s states, showing minimal sensitivity to doping levels. Between -5 eV and 0 eV, the valence band is primarily composed of O-2p states, with a minor contribution from Zn-3d orbitals, which remain relatively stable across different doping ratios. However, as the Al content increases, a slight shift and broadening in this region indicate perturbations in the local bonding environment, particularly due to Al–O interactions. Around the Fermi level (set at 0 eV), the undoped ZnO displays a clear band gap characterized by the absence of electronic states, while the doped structures exhibit a progressive narrowing of this gap. For doping levels starting from 6.25 % up to 25 %, the conduction band minimum shifts closer to the Fermi level, with Al-3p states contributing significantly to the conduction region just above 0 eV. In some cases, shallow donor states appear within the gap, indicating the possibility of n-type conductivity enhancement. The conduction band (0 to +5 eV) becomes increasingly populated with Al-derived states, which hybridize partially with Zn-4s and O-2p orbitals, suggesting an improved carrier mobility. At higher energies (beyond +5 eV), the contributions of Zn and Al states remain notable but less structured, indicating a convergence toward free-electron-like behavior. Overall, the TDOS and PDOS profiles demonstrate that Al doping modifies both the valence and conduction band edges, introduces new states near the Fermi level, and thus significantly influences the optoelectronic properties of ZnO. Zhou *et al*. obtained similar results in their study on the bonding mechanism of ZnO using the LDA+U method [66]. A detailed analysis of the PDOS for undoped ZnO reveals that the oxygen atom's p orbitals dominate the valence band, contributing more significantly than the zinc atom's s orbitals. The valence band of ZnO is predominantly shaped by the electronic contributions of oxygen atoms, indicating that O-2p orbitals govern the bonding interactions in this region.

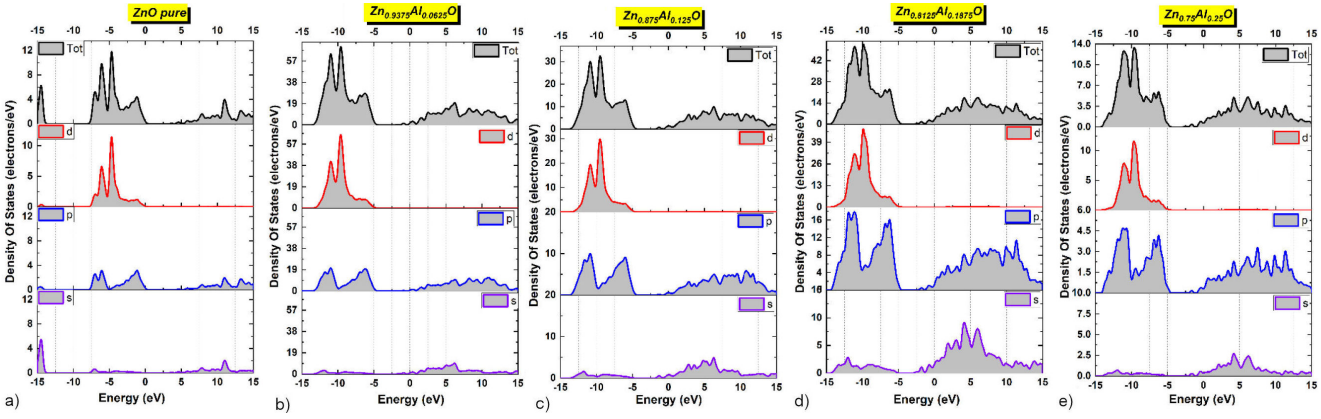


FIGURE 3. TDOS and PDOS for a) undoped ZnO and with different atomic ratios of Al/Zn b) 6.25 %, c) 12.5 %, d) 18.75 % and e)25 %.

In contrast, the conduction band is mainly influenced by the Zn-4s orbitals, which are critical to the material's electrical conductivity [67]. In the case of ZnO doped with 25 % Al, the total and partial density of states (TDOS and PDOS) reveal the electronic effects of aluminium incorporation.

Doping with Al alters the electronic structure by shifting energy levels and modifying the intensity and distribution of DOS peaks, thereby impacting the material's electronic and conductive properties [68].

As depicted in Fig. 3, the upper energy states of the doped system are primarily derived from the Zn d-orbitals, O p-orbitals, and Al p-orbitals. A detailed comparison between the PDOS of doped and undoped ZnO highlights pronounced differences, particularly near the valence band maximum, where Zn and O exhibit distinct modifications. The emergence of new electronic states at the valence band edge is attributed to interactions between Al and its nearest-neighbor Zn and O atoms. These findings confirm that Al doping effectively tailors the DOS of ZnO, in agreement with the observations reported by Khuili *et al*. [67].

To quantitatively connect the DOS to the band-structure evolution and the ensuing n-type conductivity, we note the following trends across $x = 0 \rightarrow 0{,}25$. For undoped ZnO, EF lies within the gap and the TDOS at EF vanishes, consistent with a direct-gap semiconductor. Upon Al substitution ($Al^{+}3 \rightarrow Zn^{+2}$), one excess electron per Al is donated to the conduction manifold. In the PDOS this appears as Al(3p) driven spectral weight that hybridises with Zn(4s) and O(2p) at the conduction band edge. As x increases, these Al(3p) derived states move into and broaden the CBM region, while EF shifts upward toward and at higher x, into the onset of these states. The net effect is a progressive increase of the DOS at near EF (N(E)> 0), which is the electronic signature of donor filling and explains the measured expected rise in n-type conductivity. This DOS evolution is fully consistent with the band structure trends and with optics: the Burstein Moss blue shift observed in $\varepsilon 2$/absorption follows naturally from EF entering low-lying conduction states, which blocks the lowest interband transitions even as the many-body/electrostatic perturbation narrows the fundamental gap in the calculations. Importantly, the PDOS shows no prominent deep mid-gap resonances, indicating that Al acts as a shallow donor rather than introducing compensating traps hence the finite N(EF) and Al(3p)/Zn(4s) character at the CB edge are the microscopic origin of the enhanced n-type transport.

3.3. Elastic properties

A material elastic constants offer crucial information about the types of forces operating within it as well as a connection between its mechanical and dynamic properties. Specifically, they offer insights into the stability and rigidity of materials [69,70]. The elastic constants C_{ij} are obtained from the second-order derivative of the total energy with respect to strain [71]:

$$C_{ij} = \frac{1}{V}\frac{\partial^2 E_{\text{tot}}}{\partial\varepsilon_i \partial\varepsilon_j}, \tag{2}$$

where V is the equilibrium volume of the unit cell, E_{tot} is the total energy, and ε_i, ε_j are the applied strain components.

In Young's notation, $Zn_{1-x}Al_xO$ compounds exhibit a hexagonal crystal structure, with their elasticity tensor comprising five independent components: C^{11}, C_{12}, C_{13}, C_{33} and C_{44} [60].

These constants represent different components of the stiffness tensor, which describe how the material deforms under various stress conditions. Specifically, C^{11} quantifies the stiffness in the direction parallel to the crystallographic axis, indicating the material's resistance to deformation along this axis. C_{12} and C_{13} describe the interactions between perpendicular stress and strain components, providing insight into how the material reacts when stress is applied in one direction but strain occurs in another [72]. C_{33} represents the stiffness along the crystallographic c-axis, which is particularly rele-

TABLE II. Elasticity constants C_{ij} (in GPa) of $Zn_{1-x}Al_xO$ with $x = 0$, 0.0625, 0.125, 0.1875 and 0.25 compounds compared with other theoretical and experimental results.

Elasticity constants C_{ij} (GPa)		C_{11}	C_{12}	C_{13}	C_{33}	C_{44}	Ref.
Our results	ZnO	214.987	114.654	106.872	194.142	34.052	
	$Zn_{0,9375}Al_{0,0625}O$	195.452	92.740	100.840	165.887	18.633	
	$Zn_{0,875}Al_{0,125}O$	183.288	98.143	92.854	172.214	20.547	
	$Zn_{0,8125}Al_{0,1875}O$	170.915	95.190	91.732	140.756	31.805	
	$Zn_{0,75}Al_{0,25}O$	150.193	89.124	98.540	171.232	21.241	
Exp. data	ZnO	206 ± 4	118 ± 10	211 ± 4	$44{,}3 \pm 4$	$44{,}6 \pm 4$	[58]
Theo. data	ZnO	293.31	104.24	73.55	278.27	54.63	[54]
		210	121	105.1	210.9	–	[27]
		191.16	111.96	85.63	190.57	36.89	[56]
		222	118	127	215	51	[74]
		199.7	104.3	92.9	192	43.2	[55]
		240	161	135	253	39.5	[59]

TABLE III. Mechanical properties of Zn1-xAlxO compounds for varying compositions x (x=0, 0.0625, 0.125, 0.1875 and 0.25).

Mechanical	properties		of	$Zn_{1-x}Al_xO$	
x	0	0.0625	0.125	0.1875	0.25
Bulk modulus B (GPa)	142.32	135.80	127.74	118.03	117.80
shear-modulus μ (GPa)	43.369	41.881	36.509	36.149	33.250
Lame λ (GPa)	113.41	109.00	103.40	99.68	95.64
Young modulus E (GPa)	118.11	112.99	100.00	94.17	91.17
Poisson ratio ν	0.362	0.365	0.369	0.368	0.371
Compressibility $\beta.10^{-3}$ (GPa^{-1})	7.06	7.54	7.830	8.05	8.54
Universal anisotropy index A^U	0.181	0.214	0.059	0.698	0.867
Hardness H (GPa)	3.436	3.228	2.828	2.667	2.610

vant for hexagonal materials like ZnO, which have distinct properties along this axis. Finally, C_{55} and C_{66} are the shear moduli, describing the material's resistance to shear deformation. This is crucial for understanding how the material behaves under forces that cause sliding or twisting. The C_{11}, C_{12}, C_{13}, C_{33}, and C_{44} elastic constants of undoped ZnO and Al-doped ZnO are reported in Table II for $Zn_{1-x}Al_xO$ compounds, comparing our results with experimental data and results from other theoretical methods. The mechanical stability of a solid is one of the most crucial characteristics to be inferred from its elastic properties. The mechanical strength of the crystalline lattice was initially formulated by Born and Huang, who demonstrated that stability criteria can be derived based on conditions imposed on the elastic constants, assuming that the internal energy of a crystal remains positive under small deformations. For the hexagonal system, these criteria are given by the following relations of Born and Kuang [73]:

$$C_{11} > |C_{12}, \quad 2C_{13}^2 < C_{33}\left(C_{11} + C_{12}\right), \\ C_{44} > 0, \quad C_{66} > 0. \tag{3}$$

The elastic constants C_{ij} obtained for $Zn_{1-x}Al_xO$ reveal a clear decrease in overall mechanical stiffness as the aluminum doping concentration increases. The progressive reduction of C^{11} (from 214.99 to 150.19 GPa) and C^{33} (from 194.14 to 171.23 GPa) indicates a weakening of the crystal bonding both within the basal plane and along the c-axis. The sharp drop in C^{44} at low doping levels, followed by moderate fluctuations, highlights a pronounced sensitivity to shear deformation. Although less systematic, the changes in C^12 and C^{13} also reflect a gradual disturbance in transverse elasticity caused by the substitution of $Zn^{+}2$ with $Al^{+}3$. Compared to experimental data and other theoretical works, the values remain consistent while capturing the specific effects of the GGA+U method and the use of a supercell model. Overall, the results point to increased mechanical anisotropy and reduced structural robustness with doping, which must be carefully considered when selecting optimal Al concentrations for TCO-based device applications.

Our study determined the elastic constants for $Zn_{1-x}Al_xO$ compounds, with results such as $C_{11} = 191{,}8$ GPa and $C_{33} = 193{,}4$ GPa. These values are compared with experimental data from reference [74], where the experimentally measured elastic constants for C_{11} and C_{33} are 206 GPa and 211 GPa, respectively, both with an uncertainty of $\pm$4GPa. Other theoretical methods and calculations, such as PBE-GGA Tb-mBJ and PBE-GGA+U, provide further comparisons. For instance, PBE-GGA Tb-mBJ from references [60,73] reports C^{11} = 293.31 GPa and C_{33} = 278.27 GPa, demonstrating the variations in results based on different computational methods. Including methods like LDA+U and PBE-GGA+U helps to explore the impact of Coulomb interactions on the material's elastic properties. Table III reports the calculated mechanical properties of $Zn_{1-x}Al_xO$ compounds for varying aluminum concentrations (x=0, 0.0625, 0.125, 0.1875, and 0.25). The results reveal a clear trend of decreasing mechanical strength with increasing Al content, indicating that aluminum incorporation gradually softens the ZnO matrix.

Specifically, the bulk modulus, which reflects the material's resistance to uniform compression, decreases from 142.3 GPa (pure ZnO) to 117.8 GPa at x=0.25, suggesting reduced volumetric stiffness. Similarly, the shear modulus and Young's modulus indicators of resistance to shape change and uniaxial stress, respectively, also exhibit a consistent decline, confirming the weakening of mechanical rigidity upon doping. For instance, the shear modulus drops from 43.4 GPa to 33.3 GPa, and Young's modulus declines from 118.1 GPa to 91.2 GPa. Poisson's ratio slightly increases with doping, from 0.362 to 0.371, implying a more ductile behavior at higher Al concentrations. This is further supported by the Lame parameter, which also decreases, and the compressibility, which increases with doping, indicating enhanced deformability under pressure. A significant observation is the sharp rise in the universal anisotropy index, from 0.181 for undoped ZnO to 0.867 at $x = 0{,}25$. This indicates increasing elastic anisotropy as aluminum is introduced, likely due to lattice distortion and local inhomogeneity caused by the size and charge differences between Zn^{+2} and Al^{+3} ions. Finally, the Vickers hardness decreases from 3.44 GPa (ZnO) to 2.61 GPa

at the highest doping level, confirming a drop in mechanical hardness with Al incorporation.

Physically, the mechanical softening upon Al substitution arises from a combination of electronic and bonding effects. First, Al acts as a donor, and the added free carriers enhance screening of long-range Coulomb interactions that dominate stiffness in polar wurtzite lattices, thereby reducing the effective interatomic force constants. Second, replacing Zn (whose filled 3d states contribute to Zn(3d)/O(2p) hybridization) with Al (lacking 3d) increases bond ionicity and diminishes directional covalency; this selectively weakens bond bending responses and explains the pronounced reduction in shear-related constants (C_{44}) and the drop in G. Third, the size/charge mismatch (Al^{+3} vs Zn^{+2}) introduces local strain fields and heterogeneity, which elevate elastic anisotropy and open softer deformation pathways. These mechanisms rationalize our computed trends C_{11} and C_{33} decrease with x, B, G, and E decline, Vickers hardness is reduced, and the universal anisotropy index increases indicating a transition toward a more compliant yet still Born stable lattice as Al content rises.

3.4. Optical properties

The study of optical properties of solid materials, including phenomena like absorption, reflection, transmission, and so on, is a basic means of understanding the properties of the materials under the influence of incident light beams. Furthermore, the bandgap of the materials directly affects several optical characteristics, including the absorption coefficient and refraction. The optical properties of materials can be characterized by the transverse dielectric function, represented as $\varepsilon(\omega)$ or complex refractive index *N*, which is expressed as $\varepsilon(\omega) = \varepsilon_1(\omega) + i\varepsilon_2(\omega)$. This function is a fundamental parameter in describing how a material interacts with incident photons across different energy or frequency ranges [38, 43]. The ε_2 is obtained by summing the jumps from occupied to unoccupied states within the selection rule of the Brillouin zone Eq. (1). ε_2 yields ε_1 are calculated from the Kramers-Kronig relationship Eq. (4), and ε_1 is related to the electron polarization rate of the material. The imaginary part of the dielectric function ε_2, is determined by summing the transitions from occupied to unoccupied states, following the selection rules within the Brillouin zone Eq. (4). The real part, ε_1 is then derived from ε_2 using the Kramers-Kronig relation Eq. (5), where ε_1 corresponds to the electron polarization rate of the material [75]:

$$\varepsilon_2(\omega)\left(\frac{4\pi^2e^2}{m^2\omega^2}\right)\sum_{ij}\int |\langle i|M|j\rangle|^2 f_i(1-f_i) \times \delta(E_f - E_i - \omega), d^3k. \quad (4)$$

$$\varepsilon_1(\omega)1 + \frac{2}{\pi}P\int_0^\infty \frac{\omega'\varepsilon_2(\omega')}{\omega'^2-\omega^2}, d\omega'. \quad (5)$$

The real part, $\varepsilon_1(\omega)$, quantifies the amount of electromagnetic wave energy stored as potential energy within the material. In contrast, the imaginary part, $\varepsilon_2(\omega)$, indicates the energy absorbed and dissipated as heat. The refractive index n(ω), the extinction coefficient $k(\omega)$ the absorption coefficient $\alpha(\omega)$, reflectivity $R(\omega)$ and loss function $L(\omega)$ are calculated using the following equations Eqs. (6)-(10) of undoped and Al doped zinc oxide are calculated using the following equations [56]:

$$n(\omega) = \left[\frac{\varepsilon_1(\omega)}{2} + \frac{\sqrt{\varepsilon_1^2(\omega)+\varepsilon_2^2(\omega)}}{2}\right]^{\frac{1}{2}}, \quad (6)$$

$$n(\omega) = \frac{\omega}{c}\sqrt{\frac{\varepsilon_2(\omega)}{2}}, \quad (7)$$

$$\alpha(\omega) = \sqrt{2}\,\omega\left[\sqrt{\varepsilon_1^2(\omega)+\varepsilon_2^2(\omega)} - \varepsilon_1(\omega)\right]^{\frac{1}{2}}, \quad (8)$$

$$R(\omega) = \left|\frac{\sqrt{\varepsilon_1(\omega)+j\varepsilon_2(\omega)}-1}{\sqrt{\varepsilon_1(\omega)+j\varepsilon_2(\omega)}+1}\right|^2, \quad (9)$$

$$L(\omega) = \frac{\varepsilon_2(\omega)}{\varepsilon_1^2(\omega)+\varepsilon_2^2(\omega)}. \quad (10)$$

Figure 4 illustrates the complete set of optical properties of Al doped ZnO for aluminum concentrations ranging from 0 % to 25 %. The spectral analysis of the optical response reveals pronounced changes in the dielectric behavior, refractive index, optical conductivity, and absorption coefficient, all evolving consistently with increasing Al content ($x = 0$, 0.0625, 0.125, 0.1875, and 0.25).

The real $\varepsilon_1(\omega)$ and imaginary $\varepsilon_2(\omega)$ components of the complex dielectric function, shown in Fig. 4a), serve as primary indicators of electronic polarizability and absorption mechanisms, respectively. In undoped ZnO ($x = 0$), ε_1 exhibits a prominent peak around 3 eV, followed by a gradual decline, indicating strong interband polarization and moderate dispersion. Upon Al incorporation, this peak shifts toward higher photon energies and its magnitude decreases progressively, suggesting enhanced electronic screening and reduced static polarization.

Simultaneously, the ε_2 component displays a distinct absorption edge corresponding to the fundamental bandgap of ZnO. As the Al concentration increases, this absorption edge undergoes a blue shift, indicating an apparent widening of the optical bandgap. This shift is attributed to the Burstein Moss effect, wherein the increased carrier concentration fills the lower conduction band states, thereby raising the onset energy of optical transitions.

The static permittivity (ε_1 at zero frequency) decreases as Al doping increases, reflecting a reduced polarization response under low electric fields. This trend is consistent with findings from the studies of Almeida, Rosely [76] and Haireche [77], although contrary results have been reported by Issam Derkaoui [23]. The refractive-index (n) response in Fig. 4b) similarly confirms the trend. In pure ZnO, the refractive index starts at a relatively high static value ($\sim$ 2,1) in the

low-energy limit and decreases monotonically with increasing photon energy. As the doping level increases, the peak value of n diminishes, and the overall curve flattens slightly, suggesting that the material becomes optically less dense and more transparent in the visible region. This behavior is consistent with a reduced dielectric constant and increased free carrier contribution.

In some phases, the refractive index stabilizes at high doping levels, indicating that the material becomes less sensitive to further increases in Al concentration. Our results represent an advancement over the study conducted by Dada and Mochena [78]. As depicted in Fig. 4c), the optical conductivity (photon-induced current response) rises sharply across the near-UV ($\sim 3-6$ eV), consistent with dominant interband transitions. While the undoped ZnO shows a sharp onset of conductivity just after the band gap, the doped compounds demonstrate a shift of this onset toward higher energies, along with a broadening of the spectral width and intensity. This again confirms the widening of the optical band gap and suggests increased participation of free carriers due to Al-induced doping. The spectra of the absorption coefficient in Fig. 4d) provide a particularly clear readout of doping effects on light matter interactions. For undoped ZnO, the onset of absorption occurs just above 3 eV, in agreement with the band structure results. As the Al content increases, the absorption edge shifts significantly to higher energies another manifestation of the Burstein Moss shift. Moreover, the intensity of the absorption peaks also varies, reflecting changes in the joint density of states and transition matrix elements. Notably, at higher Al concentrations, a secondary absorption feature appears at higher energies ($\sim 8-10$ eV), likely related to deeper interband transitions involving Zn-3d or Al-3p states. The optical absorption coefficient is a crucial parameter in determining the shape of a solar cell's spectral response curve [79]. The absorption spectrum ranges from 0 eV to 40 eV. Since chalcogenide materials hold great potential for photovoltaic applications, examining the optical absorption spectra under different doping levels is crucial for enhancing their optoelectronic performance [80]. The reflectivity spectra in Fig. 4e) further corroborate these trends: undoped ZnO shows a characteristic semiconductor response with a modest UV peak of $\sim 10-12\,\%$. With increasing Al doping, the reflectivity in the visible and Near-UV regions slightly decreases, suggesting improved anti-reflective properties and enhanced transmittance desirable for optoelectronic and transparent conducting applications. Reflectivity

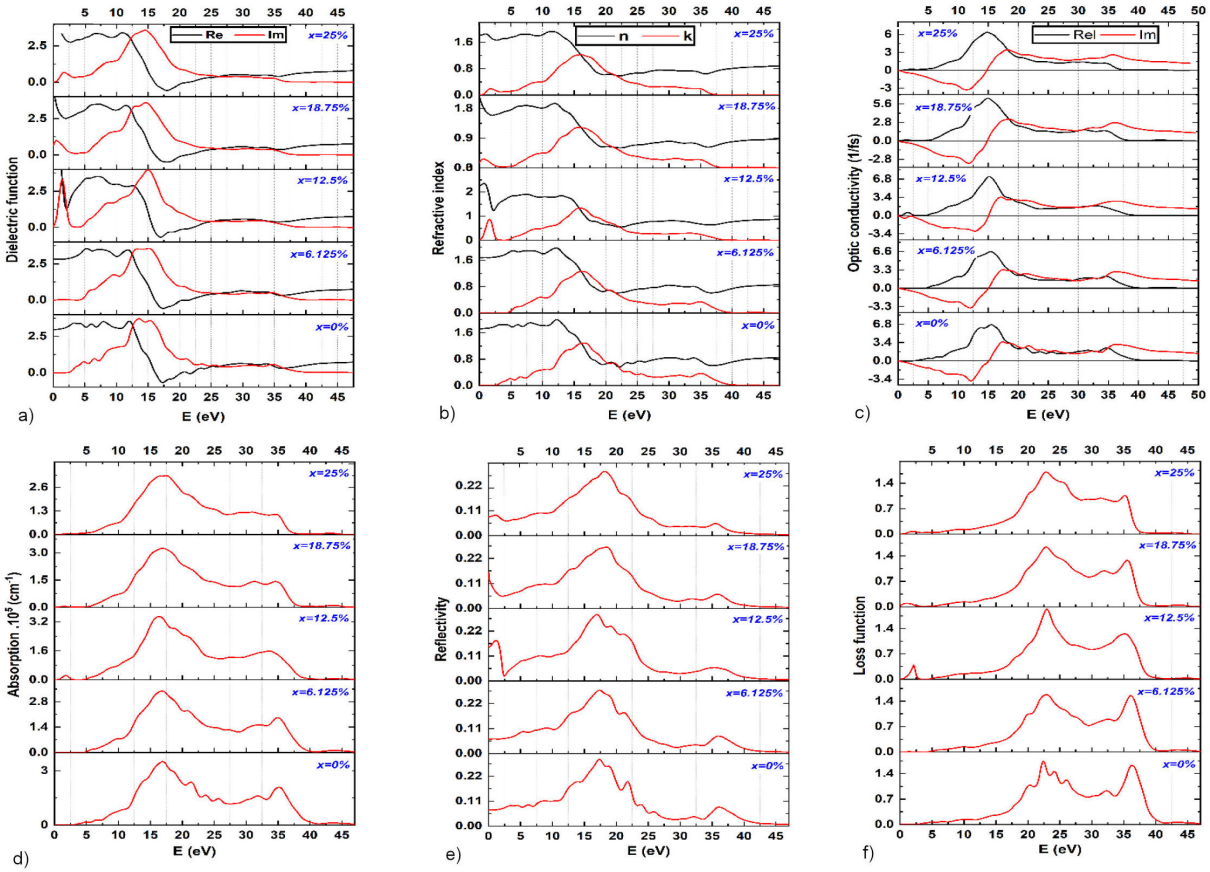


FIGURE 4. Optic properties as a function of energy for $Zn_{1-x}Al_xO$ compounds with $x = 0$, 0.0625, 0.125, 0.1875 and 0.25. a) Dielectric function ε_1 and ε_2 b), refractive index c), optical conductivity, d) Absorption, e) Reflectivity f) Loss function.

TABLE IV. The static absorption coefficient, reflectivity, loss function and gap energy for undoped and Al doped ZnO. $^{(*)}$ band gap calculated with Tauc's method.

x	α_0,10^{-6} cm^{-1}	R_0	n_0	F_0,10^{-3}	E_g (eV)	E_g (eV)$^{(*)}$
0	0.0	0.070	1.72	0.00	3.375	3.382
0.0625	0.6	0.064	1.67	0.14	2.999	3.102
0.125	27.2	0.152	2.28	2.84	2.778	3.532
0.1875	226.0	0.157	2.31	22.7	2.269	2.759
0.25	234.0	0.083	1.81	0.48	2.216	2.525

measures the percentage of light reflected off the material's surface rather than being absorbed or transmitted. A notable aspect is the slight shift observed in the reflectivity spectra as the incident photon energy nears the band gap energy, emphasizing the material's responsiveness to specific energy ranges [81]. Lastly, the energy loss function, which characterizes the energy loss of fast electrons traversing the material and is directly linked to the plasmonic behavior, shows a sharp peak in undoped ZnO around 11 eV. This feature is attributed to the collective oscillation of electrons (bulk plasmons). As Al concentration rises, the position of this loss peak shifts slightly toward higher energies, and its intensity increases, indicating a higher carrier density and modified plasmon frequency due to Al-induced free electrons. This plasmonic tunability could be leveraged in advanced photonic applications. The inelastic interaction of electrons with a material is strongly linked to the energy loss function, which defines the likelihood of inelastic scattering, the energy loss distribution, and the angular scattering distribution [46]. The energy loss spectrum illustrates the energy lost by a fast electron as it traverses the material, as shown in Fig. 4f). Peaks in the loss function usually indicate strong plasmonic excitations or other electron excitation phenomena. A weak peak is observed at 37.5 eV, followed by a maximum energy loss of around 22 eV, which coincides with a sharp decline in reflectivity [82]. In the general case, these optical spectra demonstrate that Al doping not only modulates the band structure but also leads to significant tunability in dielectric response, transparency, light absorption, and carrier-induced optical transitions. Such tunability reinforces the potential of Al doped ZnO for applications in transparent electrodes, UV photodetectors, plasmonic devices, and optoelectronic components operating in the UV-visible region.

For band gap estimation, a widely adopted approach relies on analyzing the optical absorption spectra of semiconductors. This method is applicable to materials exhibiting either direct or indirect allowed electronic transitions and is commonly expressed by the following relation [83].

$$(\alpha h\nu)^n = A\,(h\nu - E_g)\,, \tag{11}$$

where α is the absorption coefficient, $h\nu$ is the photon energy, E_g is the optical band gap, A is a constant, and n depends on the nature of the electronic transition: $n = 2$ for direct allowed transitions (as in ZnO), and $n = 1/2$ for indirect ones.

To determine gap energy E_g, one plots $(\alpha.h\nu)^2$ versus $h\nu$ and extrapolates the linear region of the curve to intersect the energy axis. The intercept gives the value of the band gap. This method allows for a simple graphical evaluation of band gap changes due to doping, strain, or defects, and is extensively used in optical characterization of semiconducting thin films and nanomaterials. The Tauc plots presented in Fig. 5 are used to estimate the optical band gap of Al doped ZnO by analyzing the absorption spectra. With increasing aluminum concentration, a clear blue shift in the absorption edge is observed, indicating a progressive widening of the optical band gap. This shift is mainly attributed to the Burstein Moss effect, where additional electrons from Al doping raise the Fermi level, filling low-energy conduction band states and

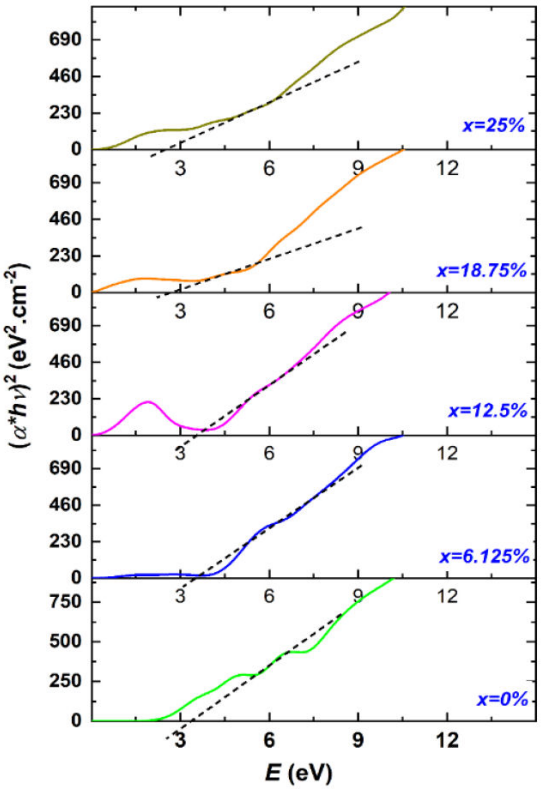


FIGURE 5. Optical band gap estimation by extrapolating the linear region of $(\alpha.h\nu)^2$ versus photon energy $(h\nu)$ plot. The intercept on the energy axis indicates the optical band gap of the $Zn_{1-x}Al_xO$ material.

requiring higher photon energies for electronic transitions. As

a result, the band gap decreases from $\sim$ 3,3 eV for undoped ZnO to $\sim$ 2,5 eV at high doping levels ($x = 0{,}25$). The observed reduction in band gap suggests that doping induces significant modifications in the electronic structure of ZnO, which may enhance its absorption in the visible range but at the expense of its UV selectivity.

Table IV summarises the static optical properties of both undoped and Al-doped ZnO, including the absorption coefficient (α_0), reflectivity (R_0), refractive index (n_0), energy loss function (F_0), and optical band gap energy (Eg), obtained through direct calculation and extrapolation from absorption spectra. In the undoped state, ZnO exhibits negligible absorption at zero frequency, consistent with its known transparency and wide band gap. As the doping concentration increases, particularly beyond $x = 0{,}125$, the absorption coefficient rises significantly, suggesting the introduction of localised states within the band gap that enable additional optical transitions. Reflectivity initially decreases slightly with low doping levels, then increases at higher concentrations, which may reflect changes in free carrier concentration or dielectric behavior. The refractive index follows a similar non-linear trend, reaching a maximum at $x = 0{,}1875$, indicating a stronger polarization response of the material under static fields.

The non-monotonic evolution of the static refractive index n_0 with Al doping (maximum at $x = 0{,}1875$) reflects a balance between the Burstein Moss shift which raises the apparent optical gap and tends to lower the bound electron polarizability and a concomitant increase in low-energy oscillator strength due to band structure renormalization and spectral weight transfer, which raise $\varepsilon 1(0)$ and n_0. In our dataset, n_0 slightly decreases at very low Al content, then increases to a maximum at $x = 0{,}1875$ alongside marked rises in A0 and F0, before dropping at $x = 0{,}25$ as free carrier screening and local field effects reduce the bound polarizability. This interpretation is consistent with classical polarizability relationships and with the joint evolution of R0, A0, F0, and Eg summarized in Table IV.

A sharp increase in the energy loss function is observed at the same concentration, highlighting enhanced plasmonic interactions or collective electron oscillations induced by higher doping. The optical band gap shows a decreasing trend as doping increases, shifting from 3.375 eV in the undoped sample to 2.216 eV at x = 0.25, which can be attributed to band tailing and the incorporation of impurity states despite the potential presence of the Burstein Moss effect. The band gap values obtained via the Tauc method are generally slightly higher than the directly calculated ones, which may be due to the extrapolation assumptions inherent to this method. Overall, these results confirm that aluminum doping significantly modifies the optical response of ZnO, making it a tunable material for applications in optoelectronics and transparent conductive devices.

4. Conclusion

In this work, a detailed first-principles investigation based on the DFT+U formalism was conducted to examine the structural, electronic, elastic, and optical properties of Al doped ZnO. The results demonstrate that aluminum substitution at Zn sites induces measurable variations in lattice parameters while preserving the wurtzite hexagonal symmetry. The electronic structure reveals a systematic narrowing of the band gap with increasing Al concentration, reaching 2.216 eV at 25 % doping, highlighting the effectiveness of Al as an n-type dopant. The emergence of Al-3p states near the conduction band enhances electronic conductivity and introduces donor-like behavior. Elastic property analysis confirms a gradual reduction in mechanical stiffness and a rise in anisotropy, suggesting a trade-off between electronic tunability and structural robustness at higher doping levels. Optical characterization reveals substantial modulation of the dielectric function, refractive index, absorption edge, and energy loss spectra, driven by both the Burstein–Moss effect and the formation of impurity states. The improved optical transparency and tunable electronic properties position Al doped ZnO as a strong candidate for applications in transparent conductive oxides (TCOs), UV photodetectors, and optoelectronic devices. The use of a 2×2×2 supercell model allows for a realistic depiction of local atomic distortions and supports the reliability of the predicted trends. These findings offer valuable insights for the design and optimization of Al doped ZnO materials, particularly for photovoltaic, sensing, and biomedical applications. Future work may explore the impact of temperature, defects, and co-doping strategies, as well as experimental validation of the proposed theoretical framework.

Acknowledgments

The authors thank Pr A. El Hdiy (ITheMM/EA7548), Université de Reims Champagne-Ardenne, Reims, France, for valuable discussions. This work was supported by the Algerian Ministry of Higher Education and Scientific Research (MESRS) and the General Directorate of Scientific Research and Technological Development (DGRSDT).

1. C. Shipra, M. Satyabrata, Efficient photocatalytic degradation of antibiotic levofloxacin and organic pollutants in water by Pr doped ZnO nanorods. *Chemical Physics Impact* **9** (2024) 100687, https://doi.org/10.1016/j.chphi.2024.100687

2. A. F. Abdulrahman, A. N. Abdulqodus, M. A. Almessiere, Biosynthesis of Al-doped ZnO nanoparticles with different Al doping ratio for methylene orange dye degradation activity. *Ceramics International* **49** (2023) A:34920-34936, https://doi.org/10.1016/j.ceramint.2023.08.165

3. Y. Slimani, S. Caliskan, F. A. Khan, A. Baykal, Anti-cancer activity and optoelectronic properties via DFT calculations of rare-earth dually doped wurtzite-type ZnO nano-systems. *Nano-Structures & Nano-Objects* **40** (2024) 101348, https://doi.org/10.1016/j.nanoso.2024.101348

4. H. R. Abd El-Mageed, Zinc oxide nanoclusters and nanoparticles as a drug carrier for cisplatin and nedaplatin anti-cancer drugs, insights from DFT methods and MC simulation. *Molecular Physics* (2020) e1842533, https://doi.org/10.1080/00268976.2020.1842533

5. P. Latthiwan, P. Sikam, P. Moontragoon, R. Klinkla, A. Watcharapasorn, T. Hussain, T. Kaewmaraya, Controllable terahertz intersubband absorptions in ZnO/(Sb,N) co-doped ZnO quantum wells: First-principles study. *Journal of Physics and Chemistry of Solids* **185** (2024) 111765, https://doi.org/10.1016/j.jpcs.2023.111765

6. I. Musa, R. Faqi, Structural, electrostatic force microscopy, work function, and optical characterization of pure and Al-doped ZnO nanoparticles. *Results in Materials* **22** (2024) 100570, https://doi.org/10.1016/j.rinma.2024.100570

7. U. Jinendra, D. Bilehal, B. M. Nagabhushana, A. P. Kumar, M. Afzal, C. Shivamallu, M. S. Sanjay, S. P. Kollur, Synthesis, characterization, and photoluminescence investigations of Al/Co-doped ZnO nanopowder. *Journal of Molecular Structure* **1305** (2024) 137701, https://doi.org/10.1016/j.molstruc.2024.137701

8. F. Pan, C. Song, X. J. Liu, Y. C. Yang, F. Zeng, Ferromagnetism and possible application in spintronics of transition-metal-doped ZnO films. *Materials Science and Engineering R: Reports* **62** (2008) 1-35, https://doi.org/10.1016/j.mser.2008.04.002

9. Vusala Nabi Jafarova, High Curie temperature and half-metallic ferromagnetism in Cr- and V-doped ZnSe in wurtzite phase: First-principles study, *Solid State Communications,* **369** (2023) 115197, https://doi.org/10.1016/j.ssc.2023.115197.

10. Vusala Nabi Jafarova, Sevda Sabir Rzayeva, First-principles prediction of higher Curie temperature, metallic and half-metallic ferromagnetism in Zn1-x(Vx,Nix)O systems. *Chinese Journal of Physics* **87** (2024) 592-607, https://doi.org/10.1016/j.cjph.2023.11.022

11. A. S. Javaid, W. S. Javaid, M. Adnan, M. Usman, M. A. Akram, N. Bashir, A. Khalid, A. Pervaiz, M. M. Hossin, I. Liaqat, M. A. Ismail, H. Dib, N. Arshad, Synthesis and characterization of efficient Sr-doped ZnO nanostructures for optoelectronic and photocatalytic applications. *Inorganic Chemistry Communications* **162** (2024) 112175, https://doi.org/10.1016/j.inoche.2024.112175

12. X. Huang, S. Chen, J. Pan, Z. Wei, X. Ye, Q. Wang,L. A. Ma, Field emission properties of LIG/ZnO heterojunction prepared by ultrafast laser direct writing. *Ceramics International* **50** 13 Part B (2024) 24205-24216, https://doi.org/10.1016/j.ceramint.2024.04.152

13. S. Jessadaluk, N. Khemasiri, P. Rattanawarinchai, N. Kayunkid, S. Rahong, A. Rangkasikorn, S. Wirunchit, A. Klamchuen, J. Nukeaw, Electroreflectance study of antimony doped ZnO thin films grown by pulsed laser deposition. *Optical Materials* **120** (2001) 111461, https://doi.org/10.1016/j.optmat.2021.111461

14. S. Jantrasee, S. Pinitsoontorn, P. Moontragoon, *journal of electronic materials* **43** (2014) 1689, https://doi.org/10.1007/s11664-013-2834-2

15. U. Ur Rehman, K. Ul Sahar, O. Cherniushok, K. T. Wojciechowski, C. Wang, Wedge-shape Al and Mg co-doped zinc oxide thin films: A Facile Route to achieve high thermoelectric power factor. *Ceramics International* **50** 19 Part B (2024) 36394-36401, https://doi.org/10.1016/j.ceramint.2024.07.022

16. H. Benali, B. Hartiti, F. Lmai, A. Batan, S. Fadili, P. Thevenin, Synthesis and characterization of Al-doped ZnO thin-films for photovoltaic applications. Materials Today: Proceedings (2024) In Press Corrected Proof, https://doi.org/10.1016/j.matpr.2024.06.012.

17. E. B. Buzok, S. Yalcin, G. Demircan, D. Yılmaz, B. Aktas, and E. Aytar, The structural, optical, electrical and radiation shielding properties of Co-doped ZnO thin films. *Radiation Physics and Chemistry* **222** (2024) 111840, https://doi.org/10.1016/j.radphyschem.2024.111840.

18. V. N. Jafarova, U. S. Abdurahmanova and S. S. Rzayeva, Ab initio prediction of half-metallic and metallic ferromagnetism in ZnO:(Co,Cr) systems. *Phys. Scr.* **99** (2024) 065927, https://doi.org/10.1088/1402-4896/ad43a1.

19. V. N. Jafarova, G. S. Orudzhev, S. S. Huseynova et al, Magnetic Properties of Vacancies and Doped Chromium in a ZnO Crystal. *Semiconductors* **52** (2018) 1047-1050, https://doi.org/10.1134/S1063782618080055

20. R. Bhattarai, R. B. Thapa, D. D. Mulmi, R. R. Ghimire, Fabrication of alcohol sensor using undoped and Al doped ZnO nanostructure film with polymer electrolyte gating. *Heliyon,* **10** (2024) e32281, https://doi.org/10.1016/j.heliyon.2024.e32281

21. S. Tekin, B. U. Begum Abdioglu, Er. I. Karaduman, S. Acar, Performance evaluation of SILAR deposited Rb-Doped ZnO thin films for photodetector applications. *J Sol-Gel Sci* **111** (2024) 891-908 https://doi.org/10.1007/s10971-024-06493-8

22. A. Virdian, S. Muhammady, A. M. Naradipa, R. Widita, A. Rusydi, Y. Darma, Enhancing photon absorption and conductivity of ZnO film by Fe doping: Experimental and first-principle perspectives. *Ceramics International* **46** 17 (2020) 27110-27118, https://doi.org/10.1016/j.ceramint.2020.07.188

23. I. Derkaoui, M. Achehboune, I. Boukhoubza, E. El Allam, Z. El Adnani, L. Henrard, A. Rezzouk, Effect of strontium (Sr) doping on the structural, electronic and optical properties of ZnO, by first-principles calculations. *Physica B Condensed Matter* **660** (2023) 414903, https://doi.org/10.1016/j.physb.2023.414903

24. Y. Liu, S. Jiang, X. Zhou, C. Xia, Q. Wu, X. Ma, L. Chen, J. Yao, J. Xu, High-concentration F-incorporated ZnO thin films doped via femtosecond-laser hyperdoping. *Surfaces and Interfaces* **42** Part A (2023) 103367, https://doi.org/10.1016/j.surfin.2023.103367

25. A. Slassi, Physical properties of Mo-doped ZnO by first principles and Boltzmann equations. *Opt Quant Electron* **47** (2015) 2465-2477, https://doi.org/10.1007/s11082-015-0131-4

26. Y. Miao, H. Wang, H. Li, K. He, Q. Wang, The GGA+U method studied the effects of Cu doping on the formation energy, electronic and optical properties of V-doped ZnO. *Opt Quant Electron* **49** (2017) 286, https://doi.org/10.1007/s11082-017-1128-y

27. L. Qiao, C. Chai, Y. Yang, X. Yu, C. Shi, First-principles theoretical study on band of strained wurtzite Nb-doped ZnO. *J Wuhan Univ Technol-Mat Sci Edit* **30** (2015) 467-472, https://doi.org/10.1007/s11595-015-1173-y

28. V. Ribić *et al*., New inversion boundary structure in Sb-doped ZnO predicted by DFT calculations and confirmed by experimental HRTEM. *Acta Materialia* **199** (2020) 633-648, https://doi.org/10.1016/j.actamat.2020.08.035

29. H. Liu, F. Zeng, Y. Lin, G. Wang, F. Pan, Correlation of oxygen vacancy variations to band gap changes in epitaxial ZnO thin films. *Appl Phys Lett* **102** (2013) 181908, https://doi.org/10.1063/1.4804613

30. S. Haireche, M. Bouchenafa, M. A. Fadla, A. Benmakhlouf, S. Maabed, M. Sidoumou, *Acta Physica Polonica A*, **142** (2022), https://doi.10.12693/APhysPolA.142.216

31. B. B. Nasab, A. Kosarian, N. A. Sheini, Effect of oxygen flow rate in zinc oxide radio frequency magnetron sputtering on the structural and optical properties of ZnO/PEDOT. PSS Inorganic|Organic Hetero-Junction. *Fizika i Tekhnika Poluprovodnikov* **54** (2020) 707, https://doi.10.1134/S1063782620080151

32. V. N. Jafarova, I. C. Scurtu, C. Stanca, N. Acomi and G. Raicu, Defect influence on the electronic and magnetic properties of silver doped (6,0) single-walled ZnO nanotubes: a first-principles study. *Indian J Phys* **98** (2024) 2335-2346, https://doi.org/10.1007/s12648-023-03044-9.

33. Kh. A. Abdullin, M. T. Gabdullin, L. V. Gritsenko, D. V. Ismailov, Zh. K. Kalkozova, S. E. Kumekov, Zh OMukash, A. YuSazonov, E. I. Terukov, Electrical, optical, and photoluminescence properties of ZnO films subjected to thermal annealing and treatment in hydrogen plasma. *Semiconductors* **50** (2016) 1010-1014, https://doi.org/10.1134/S1063782616080029

34. Ma. Tianlei, Effect of precursor concentration and sintering on functional properties of ZnO thin films deposited by aerosol-assisted chemical vapour deposition (AACVD). *Materials Science in Semiconductor Processing* **121** (2021) 105413, https://doi.org/10.1016/j.mssp.2020.105413

35. T. Nachaithong, P. Sikam, P. Moontragoon, T. Kaewmaraya, P. Thongbai, W. Busayaporn, Z. Ikonic, DFT and experimental approaches of effect of (Al, Ga) doping ions on colossal dielectric properties of ZnO ceramic. *Ceramics International* **50** 23 Part C (2024) 52134-52143, https://doi.org/10.1016/j.ceramint.2024.05.336

36. P. Sikam, P. Moontragoon, Z. Ikonic, T. Kaewmaraya, P. Thongbai, The study of structural, morphological and optical properties of (Al, Ga)-doped ZnO: DFT and experimental approaches. *Applied Surface Science* **480** (2019) 621-635, https://doi.org/10.1016/j.apsusc.2019.02.255

37. L. C. Damonte, G. N. Darriba, M. Rentería, Structural and electronic properties of Al-doped ZnO semiconductor nanopowders: Interplay between XRD and PALS experiments and first-principles/DFT modeling. *Journal of Alloys and Compounds* **735** (2018) 2471-2478, https://doi.org/10.1016/j.jallcom.2017.11.072

38. G. El Hallani, M. Khuili, N. Fazouan, A. Liba, H. Abou El Makarim, E. H. Atmani, Experimental and DFT investigations of Al-doped ZnO nanostructured thin films. *Chemical Physics Impact* **8** (2024) 100648, https://doi.org/10.1016/j.chphi.2024.100648

39. Y. Larbah, M. Adnane, B. Rahal, Growth and Characterization of ZnO and Al-Doped ZnO Thin Films by a Homemade Spray Pyrolysis. *Semiconductors* **54** (2020) 1439-1444, https://doi.org/10.1134/S1063782620110184

40. I. Jellal, H. Ahmoum, Y. Khaaissa, K. Nouneh, M. Boughrara, M. Fahoume, S. Chopra, J. Naja. Experimental and ab-initio investigation of the microstructure and optoelectronic properties of FCM-CVD-prepared Al-doped ZnO thin films. *Appl Phys A* **125** (2019) 650, https://doi.org/10.1007/s00339-019-2947-4

41. V. Khayrudinov *et al*., Hybrid GaAs nanowire-polymer device on glass: Al-doped ZnO (AZO) as transparent conductive oxide for nanowire-based photovoltaic applications. *Journal of Crystal Growth* **548** (2020) 125840, https://doi.org/10.1016/j.jcrysgro.2020.125840

42. P. Sahoo, C. Tiwari, S. Kukreti, A. Dixit, All oxide lead-free bismuth ferrite perovskite absorber based FTO/ZnO/BiFeO3/Au solar cell with efficiency $\{}sim$ 12 %: First principle material and macroscopic device simulation studies. *Journal of Alloys and Compounds* **981** (2024) 173599, https://doi.org/10.1016/j.jallcom.2024.173599

43. W. Kohn , L. J. Sham, Self-consistent equations including exchange and correlation effects. *Phys Rev* **140** (1965) A1133-A1138, https://doi.org/10.1103/PhysRev.140.A1133

44. J. P. Perdew, K. Burke, M. Ernzerhof, Generalized gradient approximation made simple. *Phys Rev Lett* **77** (1996) 3865, https://doi.org/10.1103/PhysRevLett.77.3865

45. M. D. Segall, P. J. D. Lindan, M. J. Probert, C. J. Pickard, P. J. Hasnip, S. J. Clark, First-principles simulation: ideas, illustrations and the CASTEP code. *J Phys Condens Matter* **14** (2002) 2717, https://doi.org/10.1088/0953-8984/14/11/301

46. D. Vanderbilt, Soft self-consistent pseudopotentials in a generalized eigenvalue formalism. *Physical Rev B* **41** (1990) 7892-7895, https://link.aps.org/doi/10.1103/PhysRevB.41.7892

47. S. L. Dudarev, G. A. Botton, S. Y. Savrasov, C. J. Humphreys, A. P. Sutton, Electron-energy-loss spectra and the structural stability of nickel oxide: An LSDA+U study. *Physical Review B.* **57** (1998) 1505-1509, https://link.aps.org/doi/10.1103/PhysRevB.57.1505

48. Q. V. Duong, Investigation of structural and electronic properties of ZnO using first principle calculations. *HPU2 Journal of Science: Natural Sciences and Technology,* **3** (2024) 78-87, https://doi.org/10.56764/hpu2.jos.2024.3.1.78-87

49. V. Anisimov, J. Zaanen, O. K. Andersen, Band theory and Mott insulators: Hubbard U instead of Stoner I. *Physical Review B* **44** (1991) 943, https://doi.org/10.1103/PhysRevB.44.943

50. M. Cococcioni, S. De. Gironcoli, Linear response approach to the calculation of the effective interaction parameters in the LDA U method. *Phys Rev B* **71** (2005) 035105, https://doi.org/10.1103/PhysRevB.71.035105

51. A. Shabani, M. Khazaei Nezhad, N. Rahmani, Y. K. Mishra, B. Sanyal and J. Adam, Revisiting the Optical Dispersion of Aluminum-Doped Zinc Oxide: New Perspectives for Plasmonics and Metamaterials. *Advanced Photonics Research,* **2** (2021), https://doi.org/10.1002/adpr.202000086

52. Vusala Nabi Jafarova, Nazim T Mamedov and Musaver A Musaev, High Curie Temperature and Half-Metallic Ferromagnetism in ZnSe:Co,Ni with Wurtzite Structure: First-Principles Study. *Phys. Status Solidi B,* **260** (2023) 2200360, https://doi.org/10.1002/pssb.202200360

53. Vusala Nabi Jafarova, Structural, electronic and magnetic properties of pure and Fe-doped ZnSe: first-principles investigation. *Pramana - J. Phys.* **98** (2024) 82, https://doi.org/10.1007/s12043-024-02752-z

54. R. Manotum, R. Klinkla, N. Phaisangittisakul, U. Pinsook, T. Bovornratanaraks, Effect of Pressure on the Stability and Electronic Structure of ZnO0.5S0.5 and ZnO0.5Se0.5. *J Electron Mater* **46** (2017) 6856-6863, https://doi.org/10.1007/s11664-017-5708-1

55. L. A. Valdez, M. A. Caravaca, R. A. Casali, Ab-initio study of elastic anisotropy, hardness and volumetric thermal expansion coefficient of ZnO, ZnS, ZnSe in wurtzite and zinc blende phases. *Journal of Physics and Chemistry of Solids* **134** (2019) 245-254, https://doi.org/10.1016/j.jpcs.2019.05.019

56. F. Wang, J. Wu, C. Xia, C. Hu, C. Hu, P. Zhou, L. Shi, Y. Ji, Z. Zheng, X. Liu, Thermodynamic and elastic properties of hexagonal ZnO under high temperature. *J Alloys Compd* **597** (2014) 50-57, https://doi.org/10.1016/j.jallcom.2013.12.212

57. Y. S. Liu, W. Zeng, Z. T. Liu, Q. J. Liu, J. Gao, Z. Jiao, Geometrical, electronic and optical properties of seven types ZnO from first-principles calculation. *Opt Quant Electron* **55** (2023) 1177, https://doi.org/10.1007/s11082-023-05332-4

58. G. Carlotti, D. Fioretto, G. Socino, E. Verona, Brillouin scattering determination of the whole set of elastic constants of a single transparent film of hexagonal symmetry. *J Phys Condens Matter* **7** (1995) 9147-9153, https://doi.org/10.1088/0953-8984/7/48/006

59. M. K. Yaakob, N. H. Hussin, M. F. M. Taib, T. I. T. Kudin, O. H. Hassan, A. M. MAli, M. Z. A. Yahya, First Principles LDA+U Calculations for ZnO Materials. *Integrated Ferroelectrics* **155** (2014) 15-22, http://dx.doi.org/10.1080/10584587.2014.905086

60. R. Moussa, Y. Djalab, M. Maache, R. Khenata, S Bin-Omran, SA Rouf, MW Iqbal, A Abdiche, W. Ahmed, M. Manzour, An investigation using DFT methods on the electronic and optical properties, and mechanical behavior of the wurtzite ZnO1-xTex ternary alloy. *Current Applied Physics* **55** (2023) 82-92, https://doi.org/10.1016/j.cap.2023.09.004

61. K. Meliani, S. Haireche, M. Bouchenafa, M. Elbaa, S. Douakh, R. Chiker, Comprehensive Analysis of the Structural, Electronic, Elastic, and Optical Properties of SrS Compound Under Pressure: First-Principles Calculations. *Braz J Phys* **54** (2024) 46, https://doi.org/10.1007/s13538-024-01419-9

62. M. J. Akhtar, A. H. Alhadlaq, A. Alshamsan, M. A. M. Khan, M. Ahamed, Aluminum doping tunes band gap energy level as well as oxidative stress-mediated cytotoxicity of ZnO nanoparticles in MCF-7 cells. *Sci Rep* **5** (2015) 13876, https://doi.org/10.1038/srep13876

63. P. Anup, S. Heath, D. A. Drabold, Density functional theory model of amorphous zinc oxide (a-ZnO) and a-X0.375Z0.625O (X= Al, Ga and In). *Journal of Non-Crystalline Solids* **455** (2017) 98-101, http://dx.doi.org/10.1016/j.jnoncrysol.2016.10.035

64. S. Haireche, A. Benmakhlouf, M. Bouchenafa, S. Maabed, M. Bouhamida, M. Sidoumou, First principles study of structural and electronic properties of binary strontium chalcogenides under pressure. *Sigma J Eng Nat Sci* **41** (2023) 1231-1242, http://dx.doi.org/10.14744/sigma.2023.00142

65. N. Kamarulzaman, M. F. Kasim, R. Rusdi, Band Gap Narrowing and Widening of ZnO nanostructures and doped materials. *Nanoscale Res Lett* **10** (2015) 346, https://doi.org/10.1186/s11671-015-1034-9

66. G. C. Zhou, L. Z. Sun, X. L. Zhong, X. Chen, Lu Wei, J. B. Wang, First-principle study on bonding mechanism of ZnO by LDA+U method. *Physics Letters A* **368** 1-2 (2007) 112-116, https://doi.org/10.1016/j.physleta.2007.03.061

67. M. Khuili, N. Fazouan, H. Abou El Makarim, G. El Halani, E. H. Atmani, Comparative first principles study of ZnO doped with group III elements. *Journal of Alloys and Compounds* **688 Part B** (2016) 368-375, https://doi.org/10.1016/j.jallcom.2016.06.294

68. A. Jemmy Cinthia, G. Sudhapriyang, R. Rajeswarapalanichamy, M. Santhosh, Structural, electronic and elastic properties of ZnO and CdO: A first-principles study. *Procedia Materials Science* **5** (2014) 1034-1042, https://doi.org/10.1016/j.mspro.2014.07.394

69. F. Mouhat, F. X. Coudert, Necessary and sufficient elastic stability conditions in various crystal systems. *Physical Review B* **90** (2014) 224104, https://link.aps.org/doi/10.1103/PhysRevB.90.224104

70. J. Wang, J. Li, S. Yip, S. Phillpot, D. Wolf, Mechanical instabilities of homogeneous crystals. *Phys Rev B* **52** (1995) 12627, https://link.aps.org/doi/10.1103/PhysRevB.52.12627

71. O. H. Nielsen and R. M. Martin, First-principles calculation of stress. *Physical Review B* **32** (1985) 3780-3791, https://doi.org/10.1103/PhysRevB.32.3780

72. F. Silvearv, A. L. Rosa, S. Lebègue, R. Ahuja, An ab-initio study of (Mn,Al) doped ZnO including strong correlation effects. *Physica E: Low-dimensional Systems and Nanostructures* **44** (2012) 1095-1097, https://doi.org/10.1016/j.physe.2010.12.007.

73. R. Manotum, R. Klinkla, N. Phaisangittisakul, U. Pinsook, K.Bovornratanaraks, Effect of pressure on the stability and electronic structure of ZnO0.5S0.5 and ZnO0.5Se0.5. *J Electron Mater* **46** (2017) 6856-6863, https://doi.org/10.1007/s11664-017-5708-1

74. G. Carlotti, D. Fioretto, G. Socino, E. Verona, Brillouin scattering determination of the whole set of elastic constants of a single transparent film of hexagonal symmetry. *Journal of Physics: Condensed Matter* **7** (1995) 9147-9153, urlhttps://doi.org/10.1088/0953-8984/7/48/006

75. B. Huang, Doping of RE ions in the 2D ZnO layered system to achieve low-dimensional upconverted persistent luminescence based on asymmetric doping in ZnO systems. *Physical Chemistry Chemical Physics* **19** (2017) 12683-12711, https://doi.org/10.1039/C7CP01623A

76. MV. SA. Rosely, DR. A. Luisa, F. Thomas, S. DA. Jailton, Optoelectronic Properties of Zinc Oxide: A First-Principles Investigation Using the Tran-Blaha Modified Becke-Johnson Potential. *Physica Status Solidi (b)* **256** (2019) 4, http://dx.doi.org/10.1002/pssb.201800380

77. S. Haireche, S. Douakh, M. Elbaa, M. Bouchenafa, K. Meliani, Influence of phase transition on the mechanical and optical properties of SrSe and SrTe compounds via ab initio calculations. *Physica B* **696** (2025) 416610, https://doi.org/10.1016/j.physb.2024.416610

78. D. Dada, M. DA. Mochena, DFT+U Study of Absorption Spectra and Localized Surface Plasmon Resonances of few electrons in Doped ZnO Quantum Dots. *Cond Mat Mtrl-sci*. (2023), https://arxiv.org/abs/2401.00074

79. M. Khuili, N. Fazouan, H. Abou El Makarim, E. H. Atmani, P. RaiD, M. Houmad, DFT study of rare earth (Tm, Yb, Ce) doped ZnO: structural, optoelectronic and electrical properties. *Cond Mat Mtrl-sci*. (2020), https://arxiv.org/abs/2004.10728

80. A. G. Alharshan, A. M. Aboraia, Uosif AM, Sharaf MI, Shaaban RE, Saad M, ALMohiy H, Elsenety MM Optical Band Gap Tuning, DFT Understandings, and Photocatalysis Performance of ZnO Nanoparticle-Doped Fe Compounds. *Materials* **16** (2023) 2676, https://doi.org/10.3390/ma16072676

81. W. M. Murphy, R. W. Diebel, Y. M. Yiu, T. K. Sham, Cr doped ZnO nanostructures: synthesis, electronic structures, and magnetic properties. *Canadian Journal of Chemistry* **95** (2017), https://doi.org/10.1139/cjc-2017-0143

82. M. Irungu, S. Kiprotich, M. M. Winfred, A DFT Investigation of RE (Ce, Dy, Eu) Doped Monolayer ZnO for Potential Application in Dye Sensitized Solar Cells Application. *Nanoscience and Nanotechnology* **13** (2024) 17-27, https://doi.org/10.5923/j.nn.20241302.01

83. J. Tauc, R. Grigorovici and A. Vancu, Optical Properties and Electronic Structure of Amorphous Germanium. *Physica Status Solidi (b),* **15** (1966) 627-637, https://doi.org/10.1002/pssb.19660150224

A gauge-invariant spectral scale from covariant diffusion in d-dimensional Yang–Mills backgrounds

A. Escamilla-Aké

Unidad Multidisciplinaria de Docencia e Investigación, Facultad de Ciencias, Universidad Nacional Autónoma de México, Puerto de Abrigo, Sisal, 97356, Yucatán, México.

Centro para el Desarrollo Educativo, Científico, Tecnológico y Ambiental (CEDECTYA A.C.), Calle 23, Dzidzantún, 97506, Yucatán, México.

Received 21 January 2026; accepted 3 June 2026

We introduce a simple gauge-invariant spectral diagnostic for Euclidean Yang–Mills backgrounds based on covariant diffusion. Using the gauge-covariant Laplacian Δ_A, we consider heat-kernel trace observables built from the semigroup $e^{-t\Delta_A}$ and address the infinite-volume divergence through two complementary normalizations: a trace per unit volume in a finite domain followed by the thermodynamic limit, and a relative trace with respect to the trivial background $A = 0$ that cancels the leading volume contribution. From these trace observables we define an effective spectral scale via a logarithmic derivative in diffusion time, yielding a mass-squared-like parameter that characterizes the large-t decay of covariant diffusion when the limit exists. In parallel, we outline a diffusion-based spectral-dimension diagnostic and discuss basic invariance and positivity properties of the construction. The framework is formulated in general dimension d and is intended as a clean, continuum starting point for connecting gauge-invariant long-time diffusion behaviour with spectral information of the covariant operator, without discretization or lattice input.

Keywords: Yang–Mills theory; covariant Laplacian; heat kernel; gauge invariance; spectral diagnostics.

DOI: https://doi.org/10.31349/RevMexFis.72.060701

1. Introduction

The emergence of macroscopic scales from microscopic gauge dynamics is a central theme in non-Abelian field theory. In Euclidean Yang–Mills settings, one often seeks gauge-invariant diagnostics that translate structural information about a background connection into quantitative long-distance behaviour [1]. Spectral methods provide a natural route: the spectrum of gauge-covariant elliptic operators encodes how fields relax, diffuse, and coarse-grain under heat-type evolution, in a manner stable under smooth deformations and (when defined appropriately) insensitive to gauge choice [2].

Heat-kernel methods and spectral analysis of elliptic operators have a long history in spectral geometry, mathematical physics, and quantum field theory. Classical results relate geometric and analytic properties of differential operators to the asymptotic structure of heat traces, while covariant heat kernels play a central role in effective actions, anomaly calculations, background-field methods, and spectral constructions in gauge theories [2–6]. More recently, diffusion-based observables have been employed to characterize scale-dependent geometric properties through the notion of spectral dimension, particularly in approaches to quantum gravity and random geometries [7–9].

The present work is not intended to introduce a new heat-kernel formalism, a new covariant operator, or a new notion of spectral dimension. Rather, it combines standard ingredients—covariant diffusion, infrared-safe heat-trace normalizations, and logarithmic diffusion-time derivatives—into a gauge-invariant diffusion-based spectral scale associated with the covariant Laplacian. The emphasis is on providing a continuum diagnostic of the infrared spectral behaviour of Yang–Mills backgrounds while remaining independent of gauge choice, discretization schemes, or lattice-specific constructions.

A particularly convenient probe is covariant diffusion generated by a gauge-covariant Laplacian. Given a connection A_μ on $\mathbb{R}^d$ (or on a large finite domain), the semigroup $e^{-t\Delta_A}$ defines a heat kernel that is gauge covariant in its spatial arguments, while trace observables built from it are gauge invariant. The diffusion time t plays the role of a coarse-graining scale: small t probes ultraviolet structure, whereas large t probes infrared spectral information [2].

A technical issue is immediate in infinite volume: $\mathrm{Tr}(e^{-t\Delta_A})$ diverges proportionally to the volume, even for $A = 0$ [2]. We therefore employ two complementary infrared-safe normalizations: (i) an intensive trace per unit volume in a finite domain followed by the thermodynamic limit, and (ii) a relative trace (subtracting the $A = 0$ contribution) which cancels the leading extensive term.

From either normalized trace we extract an *effective spectral scale* via a logarithmic derivative in diffusion time. When a large-t limit exists after taking the thermodynamic limit, the resulting quantity behaves like a mass-squared parameter controlling long-time decay in the diffusion channel under

consideration. This is not asserted to be a physical pole mass; rather, it is a gauge-invariant spectral diagnostic tied to the low end of the spectrum of Δ_A in the chosen representation.

The goals of this paper are sharply defined:

- define a clean gauge-invariant diffusion observable in general dimension d,
- control its infrared normalization and thermodynamic limit,
- define an effective spectral scale from its t-dependence,
- establish basic positivity/monotonicity properties,
- provide benchmarks clarifying what the large-t behaviour can and cannot imply.

The paper is organized as follows. Section 2 introduces covariant diffusion, heat–trace observables, and the two infrared–safe normalizations. Section 3 presents the effective spectral scale (and a complementary spectral–dimension diagnostic), including monotonicity constraints from spectral representations. Section 4 discusses benchmark cases and clarifies finite–volume artifacts versus genuine infrared behaviour. Section 5 summarizes implications and extensions.

2. Covariant diffusion and infrared-safe trace observables

2.1. Set-up and gauge covariance

We work in Euclidean space $\mathbb{R}^d$ (or a bounded domain $\Omega_L \subset \mathbb{R}^d$ of linear size L), with compact gauge group G and Lie algebra $\mathfrak{g}$. Fix a unitary representation ρ acting on a complex vector space V. Let $A_\mu(x)$ be a sufficiently regular background connection, understood as a matrix field in $\mathrm{End}(V)$, and define the covariant derivative

$$D_\mu \equiv \partial_\mu + A_\mu. \tag{1}$$

Under a gauge transformation $g(x) \in G$,

$$\begin{aligned} A_\mu &\mapsto A_\mu^g = gA_\mu g^{-1} - (\partial_\mu g)\, g^{-1}, \\ D_\mu &\mapsto D_\mu^g = gD_\mu g^{-1}. \end{aligned} \tag{2}$$

We consider the gauge-covariant Laplacian acting on V-valued scalar fields,

$$\Delta_A \equiv -D_\mu D_\mu, \tag{3}$$

which is elliptic and nonnegative on appropriate domains and boundary conditions.

For $t > 0$, the semigroup $e^{-t\Delta_A}$ defines covariant diffusion. Formally,

$$\left(e^{-t\Delta_A}\phi\right)(x) = \int_{\Omega_L} \mathrm{d}^d y\, K_A(t; x, y)\, \phi(y), \qquad t > 0, \tag{4}$$

where $K_A(t; x, y)$ is the heat kernel. Gauge covariance implies $K_{A^g}(t; x, y) = g(x)K_A(t; x, y)g(y)^{-1}$, and hence trace observables are gauge invariant.

2.2. Finite-volume heat trace

Let Ω_L be a bounded region of volume $V_L = \mathrm{Vol}(\Omega_L)$, with boundary conditions (periodic/Dirichlet/Neumann) chosen so that Δ_A is self-adjoint and has discrete spectrum $\{\lambda_n(A; L)\}_{n\geq 1}$ with $\lambda_n \geq 0$ [2]. The heat trace is

$$\begin{aligned} \mathrm{Tr}_{\Omega_L}\left(e^{-t\Delta_A}\right) &= \sum_{n\geq 1} \mathrm{e}^{-t\lambda_n(A;L)} \\ &= \int_{\Omega_L} \mathrm{d}^d x\ \mathrm{Tr}_V\ K_A(t; x, x). \end{aligned} \tag{5}$$

Gauge covariance of $e^{-t\Delta_A}$ implies gauge invariance of the trace:

$$\mathrm{Tr}_{\Omega_L}\left(e^{-t\Delta_{A^g}}\right) = \mathrm{Tr}_{\Omega_L}\left(e^{-t\Delta_A}\right), \tag{6}$$

for gauge transformations compatible with the chosen boundary conditions.

2.3. Two infrared-safe normalizations

In infinite volume, $\mathrm{Tr}(e^{-t\Delta_A})$ diverges extensively. We therefore consider:

(i) Intensive trace density. Define the normalized heat-trace density

$$\mathcal{T}_A(t; L) \equiv \frac{1}{V_L}\,\mathrm{Tr}_{\Omega_L}\left(e^{-t\Delta_A}\right). \tag{7}$$

When the thermodynamic limit exists at fixed $t > 0$, we define

$$\mathcal{T}_A(t) \equiv \lim_{L\to\infty} \mathcal{T}_A(t; L). \tag{8}$$

(ii) Relative trace density. Let $\Delta_0 \equiv -\partial^2$ denote the free Laplacian with the *same* boundary conditions on Ω_L. Define

$$\mathcal{R}_A(t; L) \equiv \frac{1}{V_L}\Big[\mathrm{Tr}_{\Omega_L}\left(e^{-t\Delta_A}\right) - \mathrm{Tr}_{\Omega_L}\left(e^{-t\Delta_0}\right)\Big], \tag{9}$$

and, when it exists,

$$\mathcal{R}_A(t) \equiv \lim_{L\to\infty} \mathcal{R}_A(t; L). \tag{10}$$

The relative normalization often improves infrared behaviour by cancelling the leading extensive contribution [2].

2.4. Relation between the two normalizations

The intensive trace density $T_A(t)$ and the relative trace $R_A(t)$ are designed to remove the same extensive volume divergence, but they do not necessarily encode identical information at finite diffusion times.

When the thermodynamic limit exists, the two normalizations provide complementary information about the infrared spectrum, but they need not identify the same asymptotic exponential scale. Their large-t behaviours can differ because $R_A(t) = T_A(t) - T_0(t)$ may be affected by cancellations or by the slower-decaying contribution.

However, the two constructions emphasize different aspects of the spectrum. The intensive trace density $T_A(t)$ remains positive by construction and therefore naturally admits logarithmic derivatives and monotonicity properties. By contrast, the relative trace $R_A(t)$ measures deviations from the free background and may change sign depending on the spectral redistribution induced by the gauge field. As a consequence, logarithmic derivatives based on $R_A(t)$ may become singular or may fail to provide a useful diagnostic in diffusion-time intervals where cancellations occur.

For this reason, $T_A(t)$ will be regarded as the primary spectral observable throughout this work, while $R_A(t)$ is viewed as a complementary quantity that highlights departures from free diffusion. Agreement between the two normalizations in the large-t regime provides evidence that the extracted spectral scale reflects genuine infrared spectral behaviour rather than a normalization artifact.

2.5. Remarks on existence and boundary effects

For fixed $t > 0$, the heat kernel is effectively local on length scale $\ell(t) \sim \sqrt{t}$, and boundary contributions are typically subextensive as $L \to \infty$ [2]. In favorable settings one expects

$$\mathcal{T}_A(t; L) = \mathcal{T}_A(t) + \mathcal{O}\left(\frac{|\partial\Omega_L|}{V_L}\right), \qquad L \to \infty, \tag{11}$$

and similarly for $\mathcal{R}_A(t; L)$. We do not attempt the sharpest minimal hypotheses here; our emphasis is a clean continuum definition and its robust structural consequences.

3. Spectral scale from diffusion: effective mass and spectral dimension

3.1. Effective spectral scale

Assume $\mathcal{T}_A(t; L) > 0$ for $t > 0$ (true at finite volume for standard positive semigroups). We define the diffusion-time dependent effective spectral scale

$$m^2_{\text{eff}}(t; L) \equiv -\frac{\mathrm{d}}{\mathrm{d}t} \ln \mathcal{T}_A(t; L). \tag{12}$$

Using functional calculus,

$$m^2_{\text{eff}}(t; L) = \frac{\frac{1}{V_L}\mathrm{Tr}_{\Omega_L}\left(\Delta_A\, \mathrm{e}^{-t\Delta_A}\right)}{\frac{1}{V_L}\mathrm{Tr}_{\Omega_L}\left(\mathrm{e}^{-t\Delta_A}\right)}, \tag{13}$$

so $m^2_{\text{eff}}(t; L)$ is a heat-kernel weighted average of the spectrum: small t weights higher eigenvalues, while large t concentrates toward the low end of the spectrum.

If the thermodynamic limit exists at fixed t, define

$$m^2_{\text{eff}}(t) \equiv \lim_{L\to\infty} m^2_{\text{eff}}(t; L). \tag{14}$$

When, in addition, the large-t limit exists, we define the macroscopic diffusion spectral scale

$$m^2_{\infty} \equiv \lim_{t\to\infty} m^2_{\text{eff}}(t), \tag{15}$$

provided the order of limits is taken as written (thermodynamic limit first).

Relative version (optional). When $\mathcal{R}_A(t; L)$ has definite sign on a t-window, one may analogously define

$$m^2_{\text{eff,rel}}(t; L) \equiv -\frac{\mathrm{d}}{\mathrm{d}t} \ln|\mathcal{R}_A(t; L)|\,, \tag{16}$$

and its thermodynamic-limit counterpart when it exists. Because $\mathcal{R}_A$ can cross zero, we treat the relative logarithmic derivative as auxiliary.

3.2. Spectral representation and monotonicity (thermodynamic limit)

When the thermodynamic-limit trace density admits a spectral-density representation per unit volume,

$$\mathcal{T}_A(t) = \int_0^\infty \mathrm{e}^{-t\lambda}\, \rho_A(\lambda)\, \mathrm{d}\lambda, \qquad \rho_A(\lambda) \geq 0, \tag{17}$$

in Ref. [2], one can introduce the t-dependent probability measure

$$\mathrm{d}\pi_{A,t}(\lambda) = \frac{\mathrm{e}^{-t\lambda}\rho_A(\lambda)\, \mathrm{d}\lambda}{\mathcal{T}_A(t)}. \tag{18}$$

Then

$$m^2_{\text{eff}}(t) = -\frac{\mathrm{d}}{\mathrm{d}t} \ln \mathcal{T}_A(t) = \int_0^\infty \lambda\, \mathrm{d}\pi_{A,t}(\lambda), \tag{19}$$

and

$$\frac{\mathrm{d}}{\mathrm{d}t} m^2_{\text{eff}}(t) = -\mathrm{Var}_{A,t}(\lambda) \leq 0. \tag{20}$$

Thus, whenever Eq. refeq:Laplace holds, $m^2_{\text{eff}}(t)$ is nonincreasing in t and can approach a finite limit only from above. This provides a robust constraint and a practical consistency check.

3.3. A diffusion-based spectral dimension (complementary diagnostic)

Define the diffusion-based spectral-dimension diagnostic by

$$d_s^A(t;L) \equiv -2\,\frac{\mathrm{d}}{\mathrm{d}\ln t}\ln \mathcal{T}_A(t;L) = -2t\,\frac{\mathrm{d}}{\mathrm{d}t}\ln \mathcal{T}_A(t;L) = 2t\,m_{\mathrm{eff}}^2(t;L), \tag{21}$$

in Ref. [7]. In regimes where $\mathcal{T}_A(t)$ exhibits approximate power-law scaling in t, $d_s^A(t)$ can develop plateaus which diagnose intermediate scaling windows. In contrast, when $\mathcal{T}_A(t)$ contains strong exponential suppression (as in genuinely gapped toy models), $d_s^A(t)$ is typically not the cleanest infrared descriptor; in that case the primary infrared diagnostic is the plateau (or lack thereof) in $m_{\mathrm{eff}}^2(t)$.

The quantity $d_s(t)$ is closely related to the spectral dimension commonly employed in spectral geometry, diffusion processes, and quantum-gravity approaches based on scale-dependent effective geometries [7–9]. In those settings, diffusion observables are used to probe how the effective dimensionality perceived by a random walker changes with scale. The role of $d_s(t)$ in the present work is more modest: it serves as a complementary diagnostic accompanying the effective spectral scale $m_{\mathrm{eff}}^2(t)$. While both quantities are derived from the same heat-trace observable, $m_{\mathrm{eff}}^2(t)$ provides a more direct characterization of infrared spectral suppression, whereas $d_s(t)$ offers additional information regarding the scale dependence of the underlying spectral structure.

3.4. Order of limits and an operational criterion

At fixed finite L, the large-t limit is dominated by the lowest eigenvalue:

$$T_A(t;L) \propto e^{-t\lambda_1(A;L)}, \qquad t\to\infty,$$
$$m_{\mathrm{eff}}^2(t;L) \xrightarrow[t\to\infty]{} \lambda_1(A;L) \tag{22}$$

Ref. [2]. Therefore a plateau at finite L is *not* evidence of a genuine infrared scale unless it remains nonzero after the thermodynamic limit. The operational criterion advocated here is:

$$m_\infty^2 = \lim_{t\to\infty}\Big(\lim_{L\to\infty} m_{\mathrm{eff}}^2(t;L)\Big), \tag{23}$$

and $m_\infty^2 > 0$ is interpreted as a robust infrared spectral scale in the diffusion channel probed by Δ_A.

4. Benchmarks and interpretation

This section provides calibrating examples clarifying how the diffusion diagnostics behave in simple settings and how finite-volume artifacts appear.

4.1. Pure gauge backgrounds

As a first gauge-theoretic benchmark, consider a pure gauge connection

$$A_\mu = -(\partial_\mu g)g^{-1}, \tag{24}$$

where $g(x)$ is a smooth gauge transformation. The corresponding field strength vanishes identically,

$$F_{\mu\nu} = 0. \tag{25}$$

In this case the covariant derivative is related to the ordinary derivative by conjugation,

$$D_\mu = g\,\partial_\mu\, g^{-1}, \tag{26}$$

and therefore the covariant Laplacian satisfies

$$\Delta_A = g\,\Delta_0\,g^{-1}. \tag{27}$$

Consequently, Δ_A and Δ_0 are unitarily equivalent and possess identical spectra. Whenever boundary conditions are compatible with the gauge transformation, the associated heat traces coincide,

$$\mathrm{Tr}\big(e^{-t\Delta_A}\big) = \mathrm{Tr}\big(e^{-t\Delta_0}\big)\,. \tag{28}$$

It follows that the intensive trace density, the effective spectral scale, and the spectral-dimension diagnostic all reduce to their free-background counterparts. Thus the proposed observables are insensitive to gauge-equivalent descriptions of the trivial connection and respond only to genuine spectral information. This benchmark provides a simple consistency check of the gauge-invariant character of the construction.

4.2. Free background $A = 0$

For $A = 0$ in $\mathbb{R}^d$, the heat kernel is Gaussian and the thermodynamic-limit heat-trace density takes the standard form

$$\mathcal{T}_0(t) = (4\pi t)^{-d/2}\,\dim(V), \tag{29}$$

Ref. [2]. Consequently,

$$m_{\mathrm{eff},0}^2(t) = -\frac{\mathrm{d}}{\mathrm{d}t}\ln \mathcal{T}_0(t) = \frac{d}{2t}, \tag{30}$$

which decays algebraically and has no nonzero infrared plateau:

$$\lim_{t\to\infty} m_{\mathrm{eff},0}^2(t) = 0. \tag{31}$$

The corresponding diagnostic spectral dimension is constant:

$$d_s^0(t) = -2\frac{\mathrm{d}}{\mathrm{d}\ln t}\ln \mathcal{T}_0(t) = d. \tag{32}$$

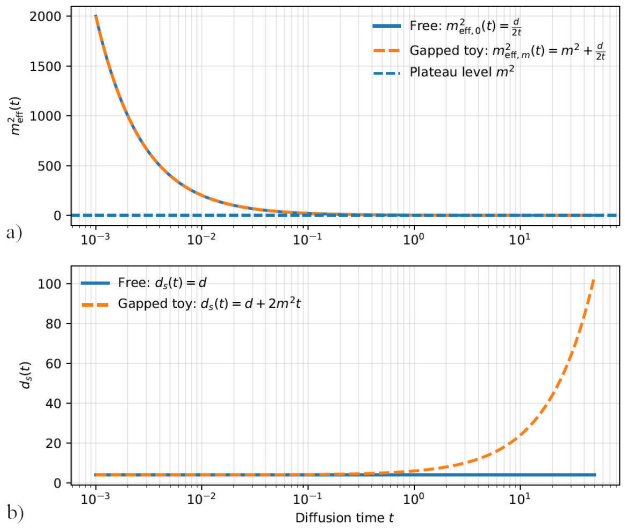


FIGURE 1. Benchmarks for the diffusion-based diagnostics in d dimensions. a) Effective spectral scale $m^2_{\mathrm{eff}}(t)$ for the free background $A = 0$, showing algebraic decay with no infrared plateau, and for the gapped toy operator $-\partial^2+m^2$, illustrating the emergence of a genuine infrared plateau at m^2. b) Corresponding diffusion-based spectral dimension $d_s(t) = 2t\, m^2_{\mathrm{eff}}(t)$, which remains constant in the free case and is dominated by the exponential regime in the gapped benchmark. The contrast highlights the role of a true spectral gap in producing a stable infrared plateau in the diffusion channel.

4.3. A gapped toy benchmark: $-\partial^2 + m^2$

Consider the scalar operator $-\partial^2 + m^2$ (not necessarily arising as Δ_A, but useful for calibration). One has

$$\mathcal{T}_m(t) = (4\pi t)^{-d/2}\, \dim(V)\, \mathrm{e}^{-m^2 t} \tag{33}$$

Ref. [2], so

$$m^2_{\mathrm{eff},m}(t) = m^2 + \frac{d}{2t},$$
$$\lim_{t\to\infty} m^2_{\mathrm{eff},m}(t) = m^2 > 0. \tag{34}$$

This is the canonical signature of a genuine infrared scale: the effective spectral scale approaches a positive constant. Figure 1 illustrates this canonical behaviour, contrasting the algebraic decay of the free case with the genuine infrared plateau arising in a gapped toy model.

4.4. Finite-volume pseudo-plateaus and stability in L

Equation (22) shows that at fixed L, $m^2_{\mathrm{eff}}(t; L)$ always approaches $\lambda_1(A; L)$ as $t \to \infty$. Therefore, the practical distinction is:

- **Finite-volume artifact:** a plateau in t at fixed L that drifts toward 0 as $L \to \infty$ (typical of gapless spectra).
- **Genuine infrared scale:** a plateau in $m^2_{\mathrm{eff}}(t)$ obtained after $L \to \infty$, converging to $m^2_\infty > 0$ as $t \to \infty$.

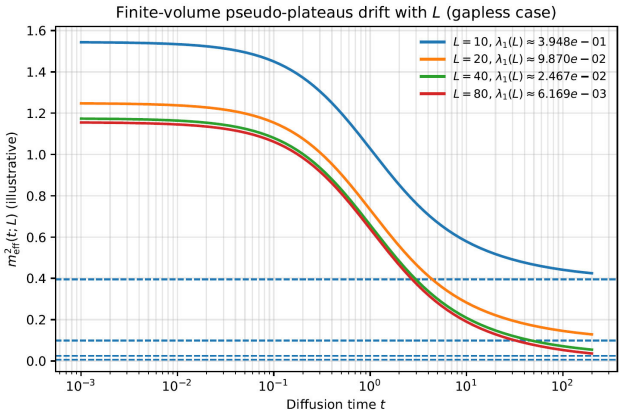


FIGURE 2. Illustration of finite-volume pseudo-plateaus. At fixed L, the effective spectral scale $m^2_{\mathrm{eff}}(t; L)$ approaches the lowest eigenvalue $\lambda_1(A; L)$ as $t \to \infty$, producing an apparent plateau. In a gapless situation, the plateau level drifts toward zero as L increases, motivating the order of limits used to define the macroscopic diffusion scale m^2_∞.

This is precisely why the order of limits in (23) is essential. Figure 2 illustrates this mechanism: at fixed L a plateau in $m^2_{\mathrm{eff}}(t; L)$ is unavoidable, but its level drifts with increasing L, so stability under the limit $L \to \infty$ is the operative criterion for identifying a genuine infrared spectral scale.

4.5. Relative trace as a complementary diagnostic

The relative quantity $\mathcal{R}_A(t) = \mathcal{T}_A(t) - \mathcal{T}_0(t)$ isolates departures from free diffusion and can be useful for identifying t-windows where the background significantly suppresses diffusion. However, since $\mathcal{R}_A(t)$ need not have definite sign for all t, logarithmic derivatives of $\mathcal{R}_A(t)$ can develop spurious singularities near zeros. For this reason, we recommend using $\mathcal{R}_A(t)$ primarily as a qualitative companion to the main diagnostic $m^2_{\mathrm{eff}}(t)$.

It is instructive to emphasize that the appearance of a plateau in $m^2_{\mathrm{eff}}(t)$ is tightly linked to the infrared structure of the spectrum of Δ_A. A genuine plateau arises only when the spectral density exhibits a true infrared gap, leading to an exponential suppression of the heat–trace density at large diffusion times. By contrast, gapless spectra extending down to $\lambda = 0$, such as in the free case, produce an algebraic decay of $T_A(t)$ and therefore prevent the formation of a plateau. Intermediate situations, where the low–lying spectrum is strongly suppressed but not gapped, may lead to a rapid decay of $T_A(t)$ without a well–defined exponential regime. Finally, at finite volume, apparent plateaus are unavoidable but correspond to the lowest discrete eigenvalue and must not be interpreted as genuine infrared scales unless they persist after taking the thermodynamic limit. These possibilities are illustrated in Fig. 3, which compares simple toy spectral densities with and without a true infrared gap and shows how their distinct low–lying spectral structures translate into qualitatively different large–t behaviours of the effective spectral scale $m^2_{\mathrm{eff}}(t)$.

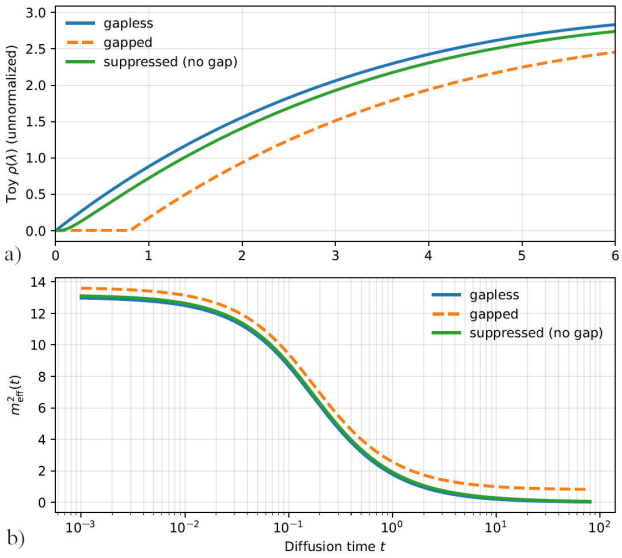


FIGURE 3. Toy spectral densities $\rho(\lambda)$ a) and the resulting effective spectral scale $m^2_{\mathrm{eff}}(t)$ obtained from the Laplace representation $\mathcal{T}(t) = \int_0^\infty \mathrm{e}^{-t\lambda}\rho(\lambda)\,\mathrm{d}\lambda$ b). A true infrared gap, corresponding to spectral support starting at $\lambda_0 > 0$, leads to the emergence of a positive infrared plateau in $m^2_{\mathrm{eff}}(t)$. By contrast, gapless spectra extending down to $\lambda = 0$ yield algebraic decay and prevent the formation of a plateau. Strong suppression of low-lying modes without a strict gap can produce rapid decay of $\mathcal{T}(t)$ without a clean exponential regime, illustrating intermediate infrared behaviour.

5. Discussion and outlook

We have defined a gauge-invariant, continuum diffusion framework for extracting spectral information from Euclidean Yang–Mills backgrounds in general dimension d. The central observable is the intensive heat-trace density $\mathcal{T}_A(t)$ (or, complementarily, the relative trace $\mathcal{R}_A(t)$), from which we define an effective spectral scale $m^2_{\mathrm{eff}}(t)$ by a diffusion-time logarithmic derivative. When the thermodynamic limit exists and is taken before the large-t limit, a nonzero plateau $m^2_\infty > 0$ provides a clean and robust infrared spectral scale in the diffusion channel probed by the covariant Laplacian.

Several structural points are worth emphasizing:

- The construction is manifestly gauge invariant, since it is based on traces of covariant operators.
- When a positive spectral-density representation holds in the thermodynamic limit, $m^2_{\mathrm{eff}}(t)$ is monotone nonincreasing in t and admits the variance identity (20), providing strong constraints on possible behaviours.
- Finite-volume plateaus are inevitable but can be diagnosed and removed by enforcing the order of limits (23).

Relation to physical mass scales. The diffusion scale m^2_∞ is a spectral diagnostic of Δ_A in a chosen representation and is not, by itself, a statement about a specific gauge-invariant particle mass (*e.g.* a glueball pole). Bridging from diffusion spectra to correlator spectra requires additional input (choice of gauge-invariant operator channels, Osterwalder–Schrader reconstruction, and comparison of decay rates). Nevertheless, the diffusion scale provides a clean continuum quantity that can be compared across ensembles, representations, and deformations, and can serve as a disciplined starting point for such comparisons.

Spectral scales versus physical masses. It is worth emphasizing that the existence of a nonzero diffusion scale m^2_∞ does not necessarily imply the presence of a corresponding physical particle mass. From a purely spectral perspective, an exponential suppression of the heat–trace density at large diffusion time may arise from the collective behaviour of the low–lying spectrum of Δ_A, even in the absence of an isolated pole in any gauge–invariant two–point function. In such situations, the quantity m^2_∞ should be interpreted strictly as a gauge–invariant infrared *spectral scale* associated with covariant diffusion, rather than as the mass of a physical excitation. Establishing a direct relation between diffusion scales and particle masses requires additional dynamical input, such as the analysis of specific gauge–invariant correlator channels and their long–distance decay properties.

Extensions. Natural extensions include: (i) studying other covariant operators (adjoint Laplacian, Dirac-type operators, or Faddeev–Popov operators in suitable formulations), (ii) analyzing background ensembles (rather than fixed backgrounds) and defining disorder-averaged trace densities, (iii) comparing continuum predictions with lattice-measured heat-trace observables as a consistency check, while keeping the definition itself non-discrete.

What would constitute decisive evidence. Within this framework, decisive evidence for a genuine diffusion infrared scale is a stable nonzero plateau in $m^2_{\mathrm{eff}}(t)$ after taking $L \to \infty$, together with robustness under changes of boundary conditions and (when available) cross-checks against decay rates of suitable gauge-invariant correlators.

Acknowledgements

The author acknowledges support from a SECIHTI (formerly CONAHCYT) postdoctoral fellowship (CVU 489483).

1. K. Osterwalder and R. Schrader, Axioms for Euclidean Green's Functions, *Commun. Math. Phys.* **31** (1973) 83–112.

2. D. V. Vassilevich, Heat kernel expansion: user's manual, *Phys. Rept.* **388** (2003) 279–360, https://doi.org/10.1016/S0370-1573(03)00111-4.

3. M. Kac, Can One Hear the Shape of a Drum?, *Am. Math. Monthly* **73** (1966) 1–23, https://doi.org/10.1080/00029890.1966.11970915.

4. P. B. Gilkey, *Invariance Theory, the Heat Equation, and the Atiyah-Singer Index Theorem*, 2nd ed. (CRC Press, Boca Raton, 1995).

5. I. G. Avramidi, *Heat Kernel and Quantum Gravity* (Springer, Berlin Heidelberg New York, 2000).

6. A. H. Chamseddine and A. Connes, The Spectral Action Principle, *Commun. Math. Phys.* **186** (1997) 731–750, https://doi.org/10.1007/s002200050126.

7. J. Ambjørn, J. Jurkiewicz and R. Loll, The Spectral Dimension of the Universe is Scale Dependent, *Phys. Rev. Lett.* **95** (2005) 171301, https://doi.org/10.1103/PhysRevLett.95.171301.

8. O. Lauscher and M. Reuter, Fractal Spacetime Structure in Asymptotically Safe Gravity, *JHEP* **10** (2005) 050, https://doi.org/10.1088/1126-6708/2005/10/050.

9. M. Reuter and F. Saueressig, Fractal Space-Times under the Microscope: A Renormalization Group View on Monte Carlo Data, *JHEP* **12** (2011) 012, https://doi.org/10.1007/JHEP12(2011)012.

Dimensional consistency of derivatives with non-singular kernels

J. J. Rosales García

Centro de Investigación en Ciencias Físico Matemáticas,
Universidad Autónoma de Nuevo León, UANL.
Pedro de Alba s/n, 66451, San Nicolás de los Garza, Nuevo León, México.
Departamento de Ingeniería Eléctrica, DICIS, Universidad de Guanajuato.
Carretera Salamanca-Valle de Santiago, km. 3.5 + 1.8 km.
Comunidad de Palo Blanco, Salamanca Guanajuato, México.

F. A. Godínez Rojano

Instituto de Ingeniería, Universidad Nacional Autónoma de México.
Ciudad de México, C.P. 04510,
Unidad de Investigación y Tecnología Aplicadas,
Universidad Nacional Autónoma de México,
Vía de la Innovación No. 410, Autopista Monterrey-Aeropuerto,
km. 10 PIIT, C.P. 66629, Apodaca Nuevo León, México.

L. A. Ramírez Garza

Centro de Investigación en Ciencias Físico Matemáticas,
Universidad Autónoma de Nuevo León, UANL.
Pedro de Alba s/n, 66451, San Nicolás de los Garza Nuevo León, México.

F. Hernández Cabrera

Centro de Investigación en Ciencias Físico Matemáticas,
Universidad Autónoma de Nuevo León, UANL.
Pedro de Alba s/n, 66451, San Nicolás de los Garza Nuevo León, México.

Received 11 March 2026; accepted 8 June 2026

The Caputo-Fabrizio (CF) and Atangana-Baleanu (AB) derivatives were proposed as alternatives to the usual Caputo and Riemann-Liouville fractional derivatives. An advantage of CF and AB derivatives is that they are defined in terms of non-singular kernels, such as the exponential function and the Mittag-Leffler function, respectively. However, the use and application of fractional derivatives with non-singular kernels has resulted in many models in terms of fractional differential equations that do not comply with the principle of dimensional homogeneity and therefore their solutions are not entirely satisfactory. In this work, we propose New Derivatives of the Caputo-Fabrizio (NDCF) and Atangana-Baleanu (NDAB) types, derive their Laplace transforms and apply them to the solution of an RC circuit as an illustrative example. Furthermore, we confirm that the price to pay for attempting to avoid the singularity of the Caputo derivative is that the initial condition is not satisfied for kernels without singularities. The initial condition depends on the order of the fractional derivative γ and only reduces to the initial condition when $\gamma = 1$. To provide a more realistic response, a shift in the dynamic variable was introduced, yielding physical solutions consistent with the dimensionality, the initial condition, and the steady state.

Keywords: Caputo fractional derivative; Caputo-Fabrizio derivative; Atangana-Baleanu derivative; RC circuit.

DOI: https://doi.org/10.31349/RevMexFis.72.060702

1. Introduction

Fractional calculus (FC), which might be considered a generalization of ordinary calculus, deals with derivatives and integrals of non-integer order [1-3]. Although fractional derivatives and integrals appeared almost at the same time as ordinary derivatives, it was not until about 40 years ago that they gained wide acceptance in the scientific community, particularly in applied sciences. Solutions obtained from fractional differential equations have been shown to fit experimental data better [4-10]. Despite the efforts to have a physical and geometrical interpretation of fractional derivatives and integrals, today there is no fully accepted answer to this issue [11, 12]. A further aspect that requires attention and is overlooked in many works is the dimensional homogeneity of equations, particularly when physical processes are modeled. It is very common to find, in the literature, equations that do not comply with the principle of homogeneity, which states that the dimensions of each of the terms of a dimensional equation on both sides should be the same [13, 14]. The

standard procedure for converting an integer-order model into its corresponding fractional-order model consists of replacing the classical differential operator(s) with those of non-integer order. This method, however, unbalances the units in the equations. One possibility to overcome this difficulty is to change the ordinary derivative d/dt by the fractional one $1/\sigma^{1-\gamma}d^{\gamma}/dt^{\gamma}$, introducing a parameter, commonly denoted as σ, first introduced in Refs. [15-17]. The units of this parameter depend on the variable to which the derivative is applied (time or space). Thus, if we are dealing with a dynamic process, where time derivative is required, σ must have units of time $[T]$. The above strategy has yielded dimensionally consistent results in models of different processes in the fields of electric circuits, physics, biology and engineering, among others [18-25]. Because the fractional Riemann-Liouville and Caputo derivatives have a weak singularity at $t = \tau$, in recent times the Caputo-Fabrizio derivative (CFD) [26] and the Atangana-Baleanu derivative (ABD) [27], were proposed as alternatives to solve this problem. However, it has been observed that, by starting from a dimensionally consistent fractional differential equation the resulting solutions are not dimensionally consistent [6, 28, 29]. This does not occur when applying the fractional Caputo derivative, in this case, dimensionally consistent solutions are obtained [6, 29]. The growing interest in these non-singular operators motivates a deeper examination of their properties, including the issue of dimensional consistency addressed in the present work.

2. Basic concepts

Definition 1: Given the function $f \in C^m[a,b]$ and γ a positive real parameter, let $n \in \mathbb{N}$ be such that $\gamma \in (n-1, n)$, then the Caputo fractional derivative of f of order γ and $n = 1$, is defined by the integral [1],

$$ {}^{C}D^{\gamma}f(t) = \frac{1}{\Gamma(1-\gamma)}\int_0^t \frac{f'(\tau)}{(t-\tau)^{\gamma}}d\tau, \tag{1}$$

where, $f' = df/d\tau$, and, $\Gamma(x) = \int_0^{\infty} e^{-t}t^{x-1}dt$, are the ordinary derivative and the Gamma function, respectively.

Definition 2: The Caputo-Fabrizio derivaitive is obtained from (1) by replacing the power law kernel $(t-\tau)^{-\gamma}$ with the exponential function $\exp(-[\gamma/(1-\gamma)]t)$ and $1/\Gamma(1-\gamma)$ with $M(\gamma)/[1-\gamma]$, then, we have [26],

$$ {}^{CF}D^{\gamma}f(t) = \frac{M(\gamma)}{1-\gamma}\int_0^t f'(\tau)\exp\left(-\frac{\gamma(t-\tau)}{1-\gamma}\right)d\tau, \tag{2}$$

where $M(\gamma)$ is a normalization function, such that, $M(0) = M(1) = 1$. The above is to ensure that, when $\gamma \to 1$, the Caputo-Fabrizio derivative should be reduced to a first-order ordinary derivative.

Definition 3: The Atangana-Baleanu (AB) derivative is defined in terms of a Mittag-Leffler function as a kernel, such as [27],

$$ {}^{AB}D^{\gamma}f(t) = \frac{B(\gamma)}{1-\gamma}\int_0^t f'(\tau)E_{\gamma}\Big[-\frac{\gamma(t-\tau)^{\gamma}}{1-\gamma}\Big]d\tau, \tag{3}$$

where $B(\gamma)$ has the same properties as in the CF case, and $E_{\gamma}(\cdot)$, is the one-parameter Mittag-Leffler function, defined in Ref. [1],

$$ E_{\gamma}(z) = \sum_{n=0}^{\infty}\frac{z^n}{\Gamma(\gamma n+1)}. \tag{4}$$

The advantage of the CF and AB derivatives is that, we do not have to deal with singular kernels at $t = \tau$, as is the case of (1).

Definition 4: The Laplace transform of a function $f(t) : [0,\infty) \to \mathbb{R}$ is the function $F(s)$, defined by

$$ F(s) = L[f(t)] = \int_0^{\infty} f(t)e^{-st}dt. \tag{5}$$

The Laplace transform in the case of the Caputo, CF and AB derivatives, are, respectively:

$$ \mathcal{L}[{}^{C}D^{\gamma}f(t)] = s^{\gamma}F(s) - s^{\gamma-1}f(0), \tag{6}$$

$$ \mathcal{L}[{}^{CF}D^{\gamma}f(t)] = \frac{sF(s)-f(0)}{s+\gamma(1-s)}, \tag{7}$$

$$ \mathcal{L}[{}^{AB}D^{\gamma}f(t)] = \frac{1}{1-\gamma}\frac{s^{\gamma}F(s)-s^{\gamma-1}f(0)}{s^{\gamma}+\frac{\gamma}{1-\gamma}}, \tag{8}$$

where $f(0)$ represents the initial condition at $t = 0$, and we have taken $M(\gamma) = B(\gamma) = 1$. In this work, we will only analyze the case where the order of the derivative satisfies the inequality $0 < \gamma \leq 1$. It is clear that γ is a dimensionless quantity.

3. Dimensional analysis of fractional derivatives

First, note that an ordinary derivative has the physical units

$$ \Big[\frac{df}{dt}\Big] = \Big[\frac{f}{T}\Big]. \tag{9}$$

If f represents position and is measured in length $[L]$ and t has units of time $[T]$, then (9) represents the velocity of an object at a given point. Every ordinary or partial differential equation that represents a physical system must comply with the principle of dimensional homogeneity [13, 14].

On the other hand, the Caputo fractional derivative, as defined in Eq. (1), has the following physical units, [28, 30],

$$ \Big[{}^{C}D^{\gamma}f(t)\Big] = \Big[\frac{1}{T^{\gamma}}\times\frac{f}{T}\times T\Big] = \Big[\frac{f}{T^{\gamma}}\Big] \quad \Longrightarrow$$
$$ \Big[\frac{f}{T^{\gamma}}\Big] = \Big[\frac{f}{T^{\gamma}}\Big]. \tag{10}$$

This expression complies with the principle of dimensional homogeneity [13, 14]. If f represents position and t represents time, then the fractional derivative would represent "fractional"velocity. But, what would the physical interpretation be? This question still lacks a satisfactory and universal answer. On the other hand, the Caputo-Fabrizio, Eq. (2),

and Atangana-Baleanu, Eq. (3), derivatives do not satisfy the principle of dimensional homogeneity, because the kernels; exponential function and Mittag-Leffler function do not have well-defined dimensions [28].

It is clear that we cannot use the definition of a fractional derivative in an ordinary differential equation simply by changing the ordinary derivative to a fractional derivative, since, as we have seen, they have different units. One way to go from an ordinary derivative to a fractional derivative was first presented in [15-17], as follows

$$\frac{df}{dt} \neq \frac{d^\gamma f}{dt^\gamma} \quad \Longrightarrow \quad \frac{df}{dt} = \frac{1}{\sigma^{1-\gamma}} \frac{d^\gamma f}{dt^\gamma} \quad \Longrightarrow$$
$$\Big[\frac{f}{T}\Big] = \Big[\frac{1}{T^{1-\gamma}} \cdot \frac{f}{T^\gamma}\Big] = \Big[\frac{f}{T}\Big], \tag{11}$$

provided that σ has units of time $[T]$. As can be seen in (11), the principle of dimensional homogeneity [13,14] is fulfilled. In (11), the right-hand side corresponds to a fractional derivative which can be any of the known ones, such as Caputo, Caputo-Fabrizio, Atangana-Baleanu, conformable derivative [31], etc.

Taking into account the expressions (11) and (1), we have

$$\frac{df}{dt} = \frac{1}{\sigma^{1-\gamma}} {}^C D^\gamma f(t)$$
$$= \frac{1}{\sigma^{1-\gamma}} \frac{1}{\Gamma(1-\gamma)} \int_0^t \frac{f'(\tau)}{(t-\tau)^\gamma} d\tau. \tag{12}$$

It is easy to see that the expression (12), has the following dimensionality,

$$\Big[\frac{f}{T}\Big] = \Big[\frac{1}{T^{1-\gamma}} \times \frac{f}{T} \times \frac{1}{T^\gamma} \times T\Big] = \Big[\frac{f}{T}\Big]. \tag{13}$$

This method of converting an ordinary derivative into a fractional derivative, using the Caputo derivative, has been used in different physical systems, resulting in a more general solution that is homogeneously consistent with the physical units of the system [15-17]. As we can see, starting from an ordinary derivative of time or space, by means of the transformation (11), we can obtain dimensionally homogeneous fractional differential equations, and therefore their solutions will be consistent with the physical units.

4. A new derivative of the Caputo-Fabrizio type

For the relation (12) to hold, in the case of the Caputo-Fabrizio derivative, we define a New Derivative of the Caputo-Fabrizio type (NDCF),

$${}^{NDCF} Df(t) = \frac{1}{(1-\gamma)} \frac{1}{\sigma} \int_0^t \frac{df}{d\tau}$$
$$\times \exp\Big[-\frac{\gamma}{1-\gamma}\Big(\frac{t-\tau}{\sigma}\Big)\Big] d\tau. \tag{14}$$

Unlike the Caputo-Fabrizio derivative, in this expression the exponential is dimensionless. The dimensionality of this new derivative is the same as in (13), that is, it is seen as an ordinary derivative (9). Its corresponding Laplace transform has the form

$$\mathcal{L}\{{}^{NDCF} D(t)\} = \frac{1}{\sigma(1-\gamma)s + \gamma}\Big(sF(s) - f(0)\Big). \tag{15}$$

Due to the dimensionality of the new derivative (14), the direct transformation of an ordinary differential equation into a fractional differential equation can be performed, thanks to its construction. To verify this, let us look at a simple example, such as the RC electrical circuit.

The ordinary differential equation that describes the behavior of an RC circuit with a constant source V_0, is given by

$$RC\frac{dv}{dt} + v(t) = V_0, \qquad v(0) = 0. \tag{16}$$

Now, we change the derivative in (16) by the NDCF (14), then, the corresponding new differential equation is given by

$${}^{NDCF} Dv(t) + \frac{1}{RC} v(t) = \frac{1}{RC} V_0. \tag{17}$$

Applying the Laplace transform (15),

$$\mathcal{L}[{}^{NDCF} Dv(t)] + \frac{1}{RC}\mathcal{L}[v(t)] = \frac{V_0}{RC}\mathcal{L}[1],$$
$$v(0) = 0, \tag{18}$$

we get,

$$\frac{1}{\sigma(1-\gamma)s+\gamma} sV(s) + \frac{1}{RC} V(s) = \frac{V_0}{RC}\frac{1}{s}. \tag{19}$$

Factoring out $V(s)$

$$V(s) = \frac{V_0}{s} \frac{\sigma(1-\gamma)s + \gamma}{[RC + \sigma(1-\gamma)]s + \gamma}. \tag{20}$$

Now, applying the inverse Laplace transform, we get

$$v(t;\gamma)_{NDCF} = V_0\Bigg[1 - \frac{RC}{RC + \sigma(1-\gamma)}$$
$$\times \exp\Big(-\frac{\gamma}{RC + \sigma(1-\gamma)} t\Big)\Bigg]. \tag{21}$$

The solution (21) is dimensionally consistent, since σ has units of time. However, when $t \to 0$, we have

$$v(0;\gamma)_{NDCF} = \Big[\frac{\sigma(1-\gamma)}{RC + \sigma(1-\gamma)}\Big] V_0 \neq 0. \tag{22}$$

In other words, the initial condition is not satisfied. Initial condition is satisfied only when $\gamma = 1$. However, when $t \to \infty$, from (21), we have $V(t \to \infty) = V_0$. This fact had already been observed in Refs. [6,29], however, it differs a little from this work, since the dimensionality of the CF derivative was not defined. That is, the definition (2) was used there. It can easily be verified that, when $\gamma = 1$ the expression (21) reduces to the well-known solution.

5. A new derivative of the Atangana-Baleanu type

Because the Atangana-Baleanu derivative is a generalization of the Caputo-Fabrizio derivative, then we can define a New Derivative of the Atangana-Baleanu type (NDAB), as follows,

$$ {}^{NDAB}Df(t) = \frac{1}{(1-\gamma)}\frac{1}{\sigma}\int_0^t \frac{df}{d\tau} \times E_\gamma\Big[-\frac{\gamma}{1-\gamma}\Big(\frac{t-\tau}{\sigma}\Big)^\gamma\Big]d\tau. \tag{23}$$

Its dimensionality is the same as in (13). Therefore, the Laplace transform in this case, is

$$\mathcal{L}\{{}^{NDAB}Df(t)\} = \frac{1}{\sigma(1-\gamma)s^\gamma + \gamma\sigma^{1-\gamma}} \times \Big(s^\gamma F(s) - s^{\gamma-1}f(0)\Big). \tag{24}$$

Now, applying the Laplace transform (24) to the same RC electrical circuit (16), we have

$$\frac{1}{as^\gamma + b}s^\gamma V(s) + \frac{1}{RC}V(s) = \frac{V_0}{RC}\frac{1}{s}, \tag{25}$$

where $a = \sigma(1-\gamma)$ and $b = \gamma\sigma^{1-\gamma}$. Solving for $V(s)$, we have

$$V(s) = \frac{V_0 a\Big(s^\gamma + \frac{b}{a}\Big)}{(RC+a)s\Big(s^\gamma + \frac{b}{RC+a}\Big)}. \tag{26}$$

Taking the inverse Laplace transform, we can write the solution as follows

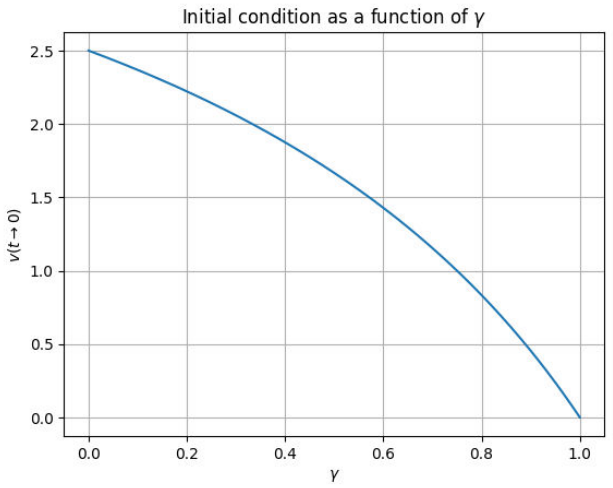


FIGURE 1. This graph represents the initial condition (22), for certain values of γ, with the following physical parameter values: $R = 1000, \Omega$; $C = 1 \times e^{-3}$, F; $\sigma = 1$, s; $V_0 = 5$, volts.

$$v(t;\gamma)_{NDAB} = V_0\Big[1 - \frac{RC}{RC+\sigma(1-\gamma)} \times E_\gamma\Big(-\frac{\gamma\sigma^{1-\gamma}}{RC+\sigma(1-\gamma)}t^\gamma\Big)\Big]. \tag{27}$$

It was expected that in this case the initial condition would not be satisfied, when $t = 0$, as in the case of the Caputo-Fabrizio derivative (22). From Eq. (22) and Fig. 1, we can see that the initial condition is also a function of γ. We can see that, when $\gamma = 1$, the expression (27) reduces to the ordinary solution.

$$v(t) = V_0\Big[1 - \exp\Big(-\frac{t}{RC}\Big)\Big]. \tag{28}$$

6. Applying the Caputo fractional derivative

To analyze and compare the different derivatives, we will solve the same RC circuit problem using Caputo's derivative (1) and its corresponding Laplace transform (6), we have

$$\frac{d^\gamma v}{dt^\gamma} + \frac{\sigma^{1-\gamma}}{RC}v(t) = \frac{\sigma^{1-\gamma}}{RC}V_0. \tag{29}$$

Applying the Laplace transform and its inverse, we finally obtain the solution

$$v(t,\gamma)_C = V_0\Big[1 - E_\gamma\Big(-\frac{\sigma^{1-\gamma}}{RC}t^\gamma\Big)\Big]. \tag{30}$$

In this case the conditions, $v(0,\gamma)_C = 0$, $v(\infty;\gamma)_C = V_0$ are satisfied.

7. Discussion

So far, starting from the transformation (11), the new derivatives NDCF (14) and NDAB (23) have been defined, which are dimensionally consistent and also preserve the dimensionality of the ordinary time derivative. Their corresponding Laplace transforms, (15) and (24) were also obtained and applied to a simple example, the RC circuit with a constant source, yielding the solutions (21), (27) and for the Caputo fractional derivative (30), which are dimensionally consistent, unlike those obtained in Ref. [6, 29]. However, only the Caputo derivative satisfies the conditions $v(0;\gamma) = 0$ and $v(\infty,\gamma) = V_0$, as can be seen in Fig. 2.

Figure 2 clearly shows that the initial condition only holds in the case of Caputo's derivative; in the other two cases, a jump occurs. Furthermore, from Fig. 2, we can observe that the NDCF has a behavior similar to that of the ordinary integer derivative, which implies that this derivative does not contribute anything new to the description of the system, in total agreement with [32]. In particular, the decay pattern follows an exponential trend, indicating that the memory introduced by the NDCF is effectively finite and rapidly attenuated, and the behavior of the system is more like that of an integer-order RC circuit. Unlike the NDCF, the NDAB uses

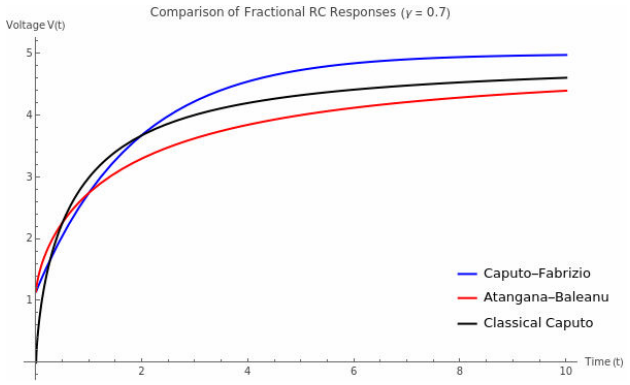


FIGURE 2. This graph represents the different solutions given by the equations (21), (27) and (30), respectively. Here, $R = 1\,\Omega$hm, $C = 1\,$F, $\sigma = 1\,$s and $V_0 = 5\,$V.

the Mittag-Leffler kernel, specifically designed to overcome the short-memory limitations of exponential kernels. The log-log representation in Fig. 3, makes this distinction explicit: while NDCF curves bend downward due to exponential decay, both Caputo and NDAB maintain nearly linear behavior in the asymptotic region, revealing algebraic relaxation. This confirms that NDAB preserves genuine long-memory effects comparable to those of Caputo.

Let us define a shifted physical variable as

$$\tilde{v}(t) = v(t) - v(0). \tag{31}$$

Then, using the NDCF operator, the initial value problem (16) is described by

$${}^{NDCF}D[v(t) - v(0)] + \frac{1}{RC}[v(t) - v(0)] = \frac{V_0}{RC}. \tag{32}$$

Taking into account the initial condition $v(0) = 0$, we get

$${}^{NDCF}D[v(t)] + \frac{1}{RC}v(t) = \frac{V_0}{RC}. \tag{33}$$

This equation is the same as in (17), therefore the solution is given by (21) with the initial condition (22). Now, taking the relation (31), we have

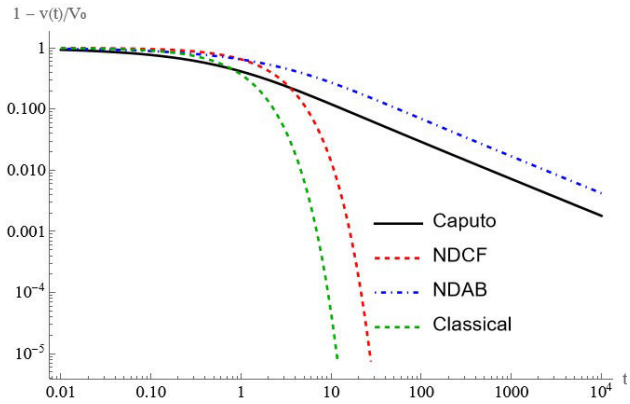


FIGURE 3. Log-log comparison of the asymptotic residual $1 - V/V_0$ for the fractional RC circuit $\gamma = 0{,}6$. The NDCF model exhibits exponential decay, indicating a short memory.

$$\begin{aligned}\tilde{v}(t;\gamma)_{NDCF} &= V_0\Big[1 - \frac{RC}{RC + \sigma(1-\gamma)} \\ &\times \exp\Big(-\frac{\gamma}{RC + \sigma(1-\gamma)}t\Big)\Big] \\ &\times -\Big[\frac{\sigma(1-\gamma)}{RC + \sigma(1-\gamma)}\Big]V_0 = \frac{RC}{RC + \sigma(1-\gamma)} \\ &\times \Big[1 - \exp\Big(-\frac{\gamma}{RC + \sigma(1-\gamma)}t\Big)\Big]V_0. \end{aligned} \tag{34}$$

In this case, when $t = 0$, we have

$$\tilde{v}(0,\gamma)_{NDCF} = 0, \tag{35}$$

and the initial condition holds. But, in the limit $t \to \infty$, we get

$$\lim_{t\to\infty} \tilde{v}(\infty,\gamma)_{NDCF} = \frac{RC}{RC + \sigma(1-\gamma)}V_0. \tag{36}$$

If we choose

$$N_{NDCF} = \frac{RC + \sigma(1-\gamma)}{RC}, \tag{37}$$

as the normalization parameter, then the physical voltage $\tilde{v}^{phys}(t;\gamma)_{NDCF} = N_{NDCF} \cdot \tilde{v}(t;\gamma)$, will be given by

$$\begin{aligned}&\tilde{v}^{phys}(t;\gamma)_{NDCF} \\ &= V_0\Big[1 - \exp\Big(-\frac{\gamma}{RC + \sigma(1-\gamma)}t\Big)\Big]. \end{aligned} \tag{38}$$

In this case, the conditions

$$\begin{aligned}\tilde{v}^{phys}(0;\gamma)_{NDCF} &= 0, \\ \tilde{v}^{phys}(\infty;\gamma)_{NDCF} &= V_0. \end{aligned} \tag{39}$$

are hold, and, when $\gamma = 1$ the solution (38) becomes (28). In the case of the NDAB, the system is described by

$${}^{NDAB}D[v(t) - v(0)] + \frac{1}{RC}[v(t) - v(0)] = \frac{V_0}{RC}. \tag{40}$$

Following the similar procedure, we get the solution

$$\begin{aligned}&\tilde{v}^{phys}(t;\gamma)_{NDAB} \\ &= V_0\Big[1 - E_\gamma\Big(-\frac{\gamma\sigma^{1-\gamma}}{RC + \sigma(1-\gamma)}t^\gamma\Big)\Big]. \end{aligned} \tag{41}$$

The solution (41) satisfies the conditions

$$\begin{aligned}\tilde{v}^{phys}(0;\gamma)_{NDAB} &= 0, \\ \tilde{v}^{phys}(\infty;\gamma)_{NDAB} &= V_0. \end{aligned} \tag{42}$$

and, in the case $\gamma = 1$ it becomes (28).

Even after enforcing structural normalization to guarantee physical consistency (39) and (42), the intrinsic asymptotic nature of each operator remains unchanged, Fig. 4.

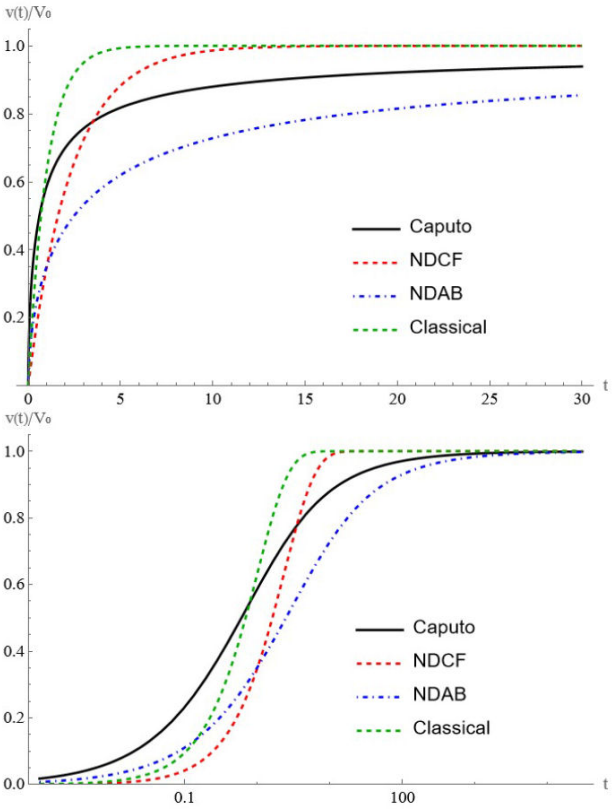


FIGURE 4. Time-domain response $v(t)/V_0$ of the fractional RC circuit corresponding to solutions (30), (38) and (41). After structural normalization, the solutions (38) and (41) satisfy the physical initial condition, $\tilde{v}^{phys}(0;\gamma) = 0$, as can be seen in the first graph, and in the second it can be seen that it converges to the steady-state value $\tilde{v}^{phys}(\infty;\gamma) = V_0$. In the second graph, a logarithmic scale is used on the horizontal axis to clearly illustrate convergence toward the steady state.

NDCF modifies the effective time scale but does not alter the exponential character of the relaxation. In contrast, Caputo and NDAB maintain heavy-tailed decay, which is the defining structural property of fractional-order systems.

In summary, while Caputo is suitable for modeling systems with persistent memory, NDAB refines this behavior through a non-singular Mittag-Leffler kernel, NDCF behaves as a short-memory approximation. From a dynamical perspective, only Caputo and NDAB generate true nonlocal fractional behavior in the RC circuit, whereas Caputo-Fabrizio reduces effectively to a time-rescaled integer-order model.

8. Conclusions

In this work, starting from the transformation (11), the New Derivatives of the Caputo-Fabrizio type NDCF (14) and of Atangana-Baleanu NDAB (23) were defined, as well as their corresponding Laplace transforms. Because these new derivatives have units of $\left[f/T\right]$, just like an ordinary derivative, they can be used directly in physical problems without altering their physical units. This was verified in the RC system, where the solutions are dimensionally consistent; however, the initial condition results as a function of the fractional order of the derivative. From a physical point of view, the above is incorrect, since the capacitor was initially discharged. To obtain a more physically realistic response, a shift was made in the dynamic variable (31) and the physical solutions are obtained. The solutions (38) and (41) are now dimensionally consistent and the initial conditions are maintained at $t \to 0$, as well as the steady state, when $t \to \infty$.

We hope that these New Derivatives of the Caputo-Fabrizio and Atangana-Baleanu type, will find applications in various physical problems, where dimensionality is important.

Appendix A

In this appendix we will explicitly obtain the Laplace transform of the Atangana-Baleanu derivative (23). Expression (23) can be written as a convolution

$$ {}^{NDAB}Df(t) = \frac{1}{\sigma(1-\gamma)} \cdot \Big[f'(t) * E_\gamma\Big(-\frac{\gamma}{(1-\gamma)\sigma^\gamma}t^\gamma\Big)\Big]. \quad \text{(A.1)}$$

Then, applying the Laplace transform, we have

$$ \mathcal{L}\{{}^{NDAB}Df(t)\} = \frac{1}{\sigma(1-\gamma)}\mathcal{L}[f'(t)] \cdot \mathcal{L}\Big[E_\gamma\Big(-\frac{\gamma}{(1-\gamma)\sigma^\gamma}t^\gamma\Big)\Big]. \quad \text{(A.2)}$$

Taking into account the formulas

$$ \mathcal{L}\Big[E_\gamma(-at^\gamma)\Big] = \frac{s^{\gamma-1}}{s^\gamma + a}, \qquad \mathcal{L}[f'(t)] = sF(s) - f(0). \quad \text{(A.3)}$$

We get

$$ \mathcal{L}\{{}^{NDAB}Df(t)\} = \frac{1}{\sigma(1-\gamma)}\Big[sF(s) - f(0)\Big] \cdot \frac{s^{\gamma-1}}{s^\gamma + \frac{\gamma}{(1-\gamma)\sigma^\gamma}} = \frac{1}{\sigma(1-\gamma)s^\gamma + \gamma\sigma^{1-\gamma}} \times \Big(s^\gamma F(s) - s^{\gamma-1}f(0)\Big), \quad \text{(A.4)}$$

which is the expression (24). The process for obtaining the Laplace transform of the NDCF (15) is similar to that shown here.

Appendix B

In this appendix we will explicitly obtain the Laplace transform of the Atangana-Baleanu derivative (23). Expres-

sion (23) can be written as a convolution

$$ {}^{NDAB}Df(t) = \frac{1}{\sigma(1-\gamma)} \cdot \Big[f'(t) * E_\gamma\Big(-\frac{\gamma}{(1-\gamma)\sigma^\gamma} t^\gamma \Big) \Big]. \quad \text{(B.1)} $$

Then, applying the Laplace transform, we have

$$ \mathcal{L}\{{}^{NDAB}Df(t)\} = \frac{1}{\sigma(1-\gamma)} \mathcal{L}[f'(t)] \cdot \mathcal{L}\Big[E_\gamma\Big(-\frac{\gamma}{(1-\gamma)\sigma^\gamma} t^\gamma \Big) \Big]. \quad \text{(B.2)} $$

Taking into account the formulas

$$ \mathcal{L}\Big[E_\gamma(-at^\gamma) \Big] = \frac{s^{\gamma-1}}{s^\gamma + a}, \qquad \mathcal{L}[f'(t)] = sF(s) - f(0). \quad \text{(B.3)} $$

We get

$$ \mathcal{L}\{{}^{NDAB}Df(t)\} = \frac{1}{\sigma(1-\gamma)} \Big[sF(s) - f(0) \Big] \cdot \frac{s^{\gamma-1}}{s^\gamma + \frac{\gamma}{(1-\gamma)\sigma^\gamma}} = \frac{1}{\sigma(1-\gamma)s^\gamma + \gamma\sigma^{1-\gamma}} \times \Big(s^\gamma F(s) - s^{\gamma-1} f(0) \Big), \quad \text{(B.4)} $$

which is the expression (24). The process for obtaining the Laplace transform of the NDCF (15) is similar to that shown here.

Acknowledgments

J. Juan Rosales thanks CONAHCyT for its support within the framework of the Sabbatical Stays: BP-BSNAC20250411170404044-10573580. He also thanks the Autonomous University of Nuevo León for its hospitality.

Author contributions

Each of the authors contributed to each part of this study equally and read and approved the final version of the manuscript.

Conflict of interest

The authors declare no potential conflict of interests.

1. I. Podlubny, Fractional differential equations, (Academic Press, New York, 1999).
2. S.G. Samko, A.A. Kilbas, O.I. Marichev, Fractional integrals and derivatives: theory and applications, (Gordon and Breach, New York, 1993).
3. E. Capelas de Oliveira and J. A. Tenreiro Machado, A review of definitions for fractional derivatives and integrals, Mathematical Problems in Engineering, (2014), ID:238459.
4. L. Martínez Jiménez, J.M. Cruz Duarte, J.J. Escalante Martínez, J. J. Rosales García, Analytical and experimental study for mechanical vibrations of a two couples spring masses system via Caputo-based derivatives, *Math. Meth. Applied Sciences*, (2021), https://doi.org/10.1002/mma.7421
5. J. J. Rosales, F. A. Godínez, L. Martínes, O. Chávez, Combining fractional derivatives to predict blood alcohol concentration, *Fractals*, **29** (2021) 2150063, https://doi:10.1142/S0218348X21500638
6. Da lin, Xiaoshong Liao, Lei Dong, Ruocen Yang, Samson S. Yu, Herbert Ho-Ching Iu, Tyrone Fernando, Zhen Li, Experimental study of fractional-order RC circuit model using the Caputo and Caputo-Fabrizio derivatives, *IEEE Transactions on Circuits and Systems-I*, **68** (2021) 1034, https://doi.org/10.1109/TCSI.2020.3040556
7. J. Rosales García, J. J. Andrade Lucio, O. Shulika. Conformable derivative applied to experimental Newton's law of cooling, *Rev. Mex. Fís.* **66** (2020) 224, https://doi.org/10.31349/RevMexFis.66.224
8. Juan Rosales, Israel Velázquez, Francisco Godínez. Modeling a Real Electrical Circuit with Fractional Calculus, in J. Rosales at all Eds., Advances in Fractional Calculus: Modeling and optimization in science and technology (Springer Nature Switzerland, 2026) pp. 183-193, https://doi.org/10.1007/978-3-031-83989-$4_1$3
9. F.C. Meral, T.J. Royston, R. Magin. Fractional calculus in viscoelasticity: An experimental study, *Commun Nonlinear Sci. Numer. Simulation*, **15** (2020) 939, https://doi:10.1016/j.cnsns.2009.05.004
10. B.A. Paez Sierra. A fractional calculus approach to analyze physicochemical relaxation processes of charge trapping in organic based nano-photodiodes, *Alexandria Engineering Journal*, **130** (2025) 47, https://doi.org/10.1016/j.aej.2025.09.005
11. I. Podlubny, Geometric and physical interpretation of fractional integration and fractional differentiation, arXiv:math/0110241v1[math.CA] (2021) 22 Oct.
12. Ruby, M. Mandal, The geometrical and physical interpretation of fractional order derivatives for a general class of functions, *Math. Methods Appl. Sci*. **47** /2024) 8400, https://doi.org/10.1002/mma.10020
13. Clive L. Dym, Principle of mathematical modeling, 2nd ed. (Elsevier Academic Press, 2004).
14. J. C. Gibbings, Dimensional analysis, (Springer-Verlag London, 2011).
15. J.J. Rosales; J. F. Gómez; M. Guía; V.I. Tkach. Fractional electromagnetic waves, 2011 11th International Conferen-

ce on Laser and Fiber-Optical Networks Modeling (LFNM), https://doi.org/10.1109/LFNM.2011.6144969

16. J.J. Rosales, M. Guía, J.F. Gómez, V.I. Tkach, Fractional electromagnetic wave, *Discontinuity, Nonlinearity, and Complexity,* **1** (2012) 325, https://doi.org/10.5890/DNC.2012.09.004
17. JF. Gómez–Aguilar, JJ. Rosales–García, JJ. Bernal–Alvarado, T. Córdova–Fraga, and R. Guzmán-Cabrera, Fractional mechanical oscillators, *Rev. Mexi. de Fís.* **58** (2012) 348.
18. J. Juan Rosales, M. Guía, Juan Martínez, Dumitru Baleanu, Motion of a particle in a resisting medium using fractional calculus approach, *Proceedings of the Romanian Academy, Series A.* **14** (2013) p. 42-47.
19. Fahad M. Alharbi. Analysis of logistic model with constant harvesting in a view of non-integer derivative, *Journal of Mathematics and System Science*, **10** (2020). doi: 10.17265/2159-5291/2020.02.004
20. Won Sang Chunga, S. Zareb, H. Hassanabadi, J. Kriz and E. Maghsoodid, The investigation of a classical particle in the presence of fractional calculus, *Rev. Mex. Fís.* **66** (2020) 840
21. F. Gómez, J. Rosales, M. Guía, RLC electrical circuit of non-integer order, *Cent. Eur. J. Phys*., (2013), https://doi.org/10.2478/s11534-013-0265-6
22. D. Baleanu, M. Hassan Abadi, A. Jajarmi, K. Zarghami Vahid, J.J. Nieto, A new comparative study on the general fractional model of COVID-19 with isolation and quarantine effects, *Alexandria Engineering Journal*, **61** (2022) 4779
23. F. Gómez, J. Bernal, J. Rosales, T. Córdova, Modeling and simulation of equivalent circuits in description of biological systems: A fractional calculus approach, *J. Electr. Bioimp*, **3** (201) 2
24. Savita Rathee, Yogeeta Narwal, Komal Bansal, Homan Emadifar, Sensitivity analysis of fractional order SVEIR lumpy skin disease model, *Alexandria Engineering Journal*, **119** (2025) 609, https://doi.org/10.1016/j.aej.2025.01.076
25. Asiyeh Ebrahimzadeh, Amin Jajarmi, Mehmet Yavuz, Fractional optimal control of anthroponotic cutaneous leishmaniasis with behavioral and epidemiological extensions, *Math. Comput. Appl.* **122** (2025) 1, https://doi.org/10.3390/mca30060122
26. M. Caputo and M. Fabrizio, A new definition of fractional derivative without singular kernel, *Progr. Fract. Differ, Appl*. **1** (2015) 73
27. Atangana A, Baleanu D, New fractional derivatives with nonlocal and non-singular kernel, theory and application to heat transfer model, Thermal Science, **20** (2016) 763
28. B. Ghosh, Fractional order modeling of ecological and epidemiological systems: ambiguities and challenges, *The Journal of Analysis*, **33** (2015) 341
29. J.J. Rosales, J.D. Filoteo, and A. Gonzalez, A comparative analysis of the RC circuit with local and non-local fractional derivatives, *Rev. Mex. de Fís*. **64** (2018) 647
30. A. Atangana, Fractional derivatives, dimensions, and geometric interpretation: A answer to your worries, *AIMS, Mathematics*, **10**(2) (2025) 2562, https://doi.org/10.3934/math.2025119
31. R. Khalil, M.A.I. Horani, A. Yousef, M. Sababheh, A new definition of fractional derivative, *J. Comp. Appl. Math*, **264** (2014) 65
32. Kai Diethelm, Roberto Garrappa, Andrea Giusti, Martin Stynes, Why fractional derivatives with nonsingular kernels should not be used, *Fractional Calculus and Applied Analysis*, **23**(3) (2020) 610, https://www.degruyter.com/view/j/fca

Granular structure and local de Broglie wavelength in fuzzy dark matter halos

F. Rosales-Infante*, I. Álvarez-Rios⋆ and F. S. Guzmán†

Instituto de Física y Matemáticas, Universidad Michoacana de San Nicolás de Hidalgo,
Edificio C-3, Cd. Universitaria, 58040 Morelia, Michoacán, México.
**e-mail: flavio.rosales.infante@umich.mx; ORCID: 0009-0006-9275-1427*
⋆*e-mail: ivan.alvarez@umich.mx; ORCID: 0000-0003-4266-3374*
†*e-mail: francisco.s.guzman@umich.mx. ORCID: 0000-0002-1350-3673*

A. Quiñonez-Guerrero

Facultad de Ciencias Físico Matemáticas, Universidad Michoacana de San Nicolás de Hidalgo,
Edificio ALFA, Cd. Universitaria, 58040 Morelia, Michoacán, México.
e-mail: 1827746x@umich.mx. ORCID: 0009-0000-4940-7731

Received 31 March 2026; accepted 7 July 2026

We study the granular structure that emerges in a Fuzzy Dark Matter (FDM) halo formed through kinetic relaxation. After the system reaches a virialized core-halo structure, we separate the density field into a smooth spherical component and a residual density that contains the interference pattern characteristic of FDM halos. The power spectrum of this residual field shows a well defined dominant scale, different from the characteristic scale of the total density and of the smooth core-halo model. We compare this granular scale with a local de Broglie wave-lenght calculated from the velocity field obtained from the density current of the system. We find that both scales remain of the same order of magnitude, with the granular scale systematically smaller than the de Broglie wavelength. The radial behavior of the de Broglie wavelength also reveals a non-uniform internal structure, it decreases from the core and reaches its minimum near the transition between the solitonic core and the outer halo. These results provide a quantitative connection between density fluctuations, the local velocity field, and the core-halo morphology of FDM halos.

Keywords: Self-gravitating systems; dark matter; Bose condensates.

DOI: https://doi.org/10.31349/RevMexFis.72.060703

1. Introduction

Fuzzy Dark Matter (FDM), consisting of ultra-light bosonic particles, provides an alternative to the standard cold dark matter paradigm in which quantum wave effects become relevant on astrophysical scales. In this framework, dark matter is described by a coherent wavefunction obeying the Schrödinger-Poisson system, leading to a phenomenology different from that of classical particle dynamics. The wave nature of the field introduces a characteristic length scale set by the de Broglie wavelength, suppressing small-scale structure formation and giving rise to cored density profiles in gravitationally bound structures. These features have motivated the study of FDM as a possible solution to small-scale tensions in ΛCDM, with implications ranging from dwarf galaxy structure to large-scale cosmological observables [1-7].

One of the most important results from numerical simulations is the emergence of core–halo structures, in which a central solitonic core is embedded within an extended halo. The core corresponds to a self-gravitating, coherent configuration supported by quantum pressure corresponding to the ground state solution of equilibrium configurations, while the outer halo is characterized by a superposition of excited modes. This outer region exhibits a complex and time-dependent interference pattern, giving rise to a granular structure as seen in structure formation simulations [8-12] as well as at local scale collapse [13].

These granules are a distinctive signature of the wave nature of FDM and are commonly associated with the de Broglie wavelength of the system, suggesting a direct link between the velocity field and the spatial scale of density fluctuations. However, this association is typically qualitative. In particular, the spatial variation of the relevant wavelength within halos, and its precise relation to the core-halo structure, can be explored in detail.

Recent work has emphasized the dynamical impact of these fluctuations, showing that the time-dependent interference pattern can induce stochastic and chaotic motion of test particles within FDM halos [14,15]. This highlights the fact that the small-scale structure is not merely a visual feature, but has direct consequences for the dynamics of baryonic tracers and the evolution of embedded systems. At the same time, a systematic characterization of the spectral properties of these fluctuations is still lacking, especially in a form that directly connects to physical length scales.

This gap is particularly relevant in the context of potential observational signatures. Fluctuations at sub-galactic scales may affect stellar streams, induce dynamical heating (*e.g.* [16]), and leave imprints on the phase-space structure of galaxies [15]. Establishing a quantitative connection between

the fluctuation spectrum and observable effects is therefore important for testing FDM at local scale scenarios.

In this work we analyze the small-scale structure of FDM halos through the power spectrum of density fluctuations. The density field is decomposed into a smooth core-halo component and a residual field that isolates the interference pattern. From this residual, we compute the power spectrum both globally and within radial shells, allowing us to extract a characteristic scale as a function of radius.

This procedure defines a position-dependent wavelength, which we interpret as a local de Broglie scale. Our central result is that this scale is not uniform across the halo. Instead, it exhibits a non-monotonic radial dependence, with a well-defined minimum that coincides with the transition between the solitonic core and the outer halo.

This analysis also provides a perspective on the internal structure of FDM halos. It shows the radial dependence of the de Broglie wavelength from the core to the outskirts of the configuration. We establish a direct connection between spectral properties, velocity fields, and the core-halo morphology, which may open the possibility of linking small-scale fluctuations to observable signatures in galactic systems.

The paper is organized as follows. In Sec. 2 we describe the spectral analysis of a structure and in Sec. 3 we describe the local de Broglie wavelength. Finally, in Sec. 4 we draw some conclusions.

2. Analysis of one structure

2.1. The system of equations

The FDM dynamics is modeled as a coherent bosonic field described by a macroscopic wavefunction Ψ, which plays the role of an order parameter. The system evolves under its own gravitational potential V, generated by the density distribution of the bosonic gas itself, so that the dynamics of Ψ is governed by the coupled Schrödinger-Poisson (SP) equations

$$i\hbar\frac{\partial\Psi}{\partial t} = -\frac{\hbar^2}{2m_B}\nabla^2\Psi + m_B V\Psi, \tag{1}$$

$$\nabla^2 V = 4\pi G\left(\rho - \bar{\rho}\right), \tag{2}$$

where the mass density is given by $\rho = m_B|\Psi|^2$, and $\bar{\rho}$ denotes the spatial average over the computational domain. We solve and analyze this system on a uniformly discretized three dimensional domain described in Cartesian coordinates, and use adimensional code units defined by the transformations $t = t_0\tilde{t}, \vec{x} = x_0\tilde{\vec{x}}, V = V_0\tilde{V}, \Psi = \Psi_0\tilde{\Psi}$ and $\rho = \rho_0\tilde{\rho}$, which leaves the SP system in dimensionless code units that only depend on the length scale parameter x_0, for a given boson mass m_B. A useful choice of scaling parameters is based on the boson mass $m_B = m_{22}\times 10^{-22}\,\mathrm{eV}/c^2$ and a characteristic length scale $x_0 = \mathrm{kpc}/\lambda$, where λ is a free parameter. From these, the following scale factors are derived:

$$t_0 = \frac{m_B x_0^2}{\hbar} \approx 50{,}96\times 10^{-3}\left(\frac{m_{22}}{\lambda^2}\right)\,\mathrm{Gyr}, \tag{3}$$

$$V_0 = \left(\frac{\hbar}{m_B x_0}\right)^2 \approx 368{,}6\left(\frac{\lambda}{m_{22}}\right)^2\,(\mathrm{km/s})^2, \tag{4}$$

$$\rho_0 = \frac{\hbar^2}{4\pi G m_B^2 x_0^4} \approx 6{,}820\times 10^6\left(\frac{\lambda^4}{m_{22}^2}\right)\frac{M_\odot}{\mathrm{kpc}^3}. \tag{5}$$

Other useful physical quantities are the velocity and mass, whose scale factors are:

$$v_0 = \frac{\hbar}{m_B x_0} \approx 19{,}20\left(\frac{\lambda}{m_{22}}\right)\,\mathrm{km/s}, \tag{6}$$

$$M_0 = \frac{\hbar^2}{4\pi G m_B^2 x_0} \approx 6{,}820\times 10^6\left(\frac{\lambda}{m_{22}^2}\right)M_\odot, \tag{7}$$

that will proof useful for the physical description of the halo during the analysis below.

2.2. The workhorse core-halo structure

We are interested in the analysis of a galactic type of structure made of FDM, and there are various methods to produce a core-halo structure of FDM. One is based on the multi-merger of ground state solutions of the SP system of equations described in Ref. [17], that relaxes towards a virialized configuration as shown in Refs. [13,18-20]. A second method involves the construction of nearly stationary multimode solutions to the SP system that in solid-angle average provide radial density profiles that serve to model realistic LSB galaxies as illustrated in Ref. [21]. A third method, the one we use for the analysis in this paper, is based on the collapse of FDM through kinetic relaxation [22-28], that was later used to study the collapse of FDM together with a black hole [29] and with an ideal gas [28], where it was shown that the cooling of the FDM structure via kinetic relaxation is universal.

The kinetic relaxation eventually leads to the collapse of overdensities that in turn promote bosonic gas condensation. The systematic study of this collapse process is understood from local simulations defined in Refs. [22,24], where various distributions in the momentum domain are proposed. In our analysis, we use a Gaussian distribution $\Psi(\vec{p}) = Ae^{-p^2/2}e^{iS}$ in the momentum space, with S a random phase in the range $[0, 2\pi]$ at each point of the momentum space, with A a normalization factor.

The randomness of this method offers a rich variety of possibilities to produce structures. Nevertheless, for our study, instead of using a bundle of simulations, we use a single representative workhorse simulation that has become a standard setup for studies of the kinetic relaxation process. This is one of the simulations designed in Ref. [24], specifically on a box of side $L = 18$, with resolution $\Delta x = L/128$ and total FDM mass in the numerical domain $M = 1005{,}3$ as in Ref. [24], all in code units as defined above. Moreover,

the simulation lasts 250 dimensionless code units, sufficient for the bosonic gas to collapse and relax.

As an example in physical units, using a boson mass $m_B = 10^{-23}$eV, and initial average FDM density $\bar{\rho} \sim \lambda^4\ 1{,}18 \times 10^8 \mathrm{M}_\odot/\mathrm{kpc}^3$, the integrated FDM mass in the numerical domain is $M = \lambda\ 6{,}86 \times 10^{11}\mathrm{M}_\odot$, the numerical resolution and domain size for this boson mass are $\Delta x \sim 140\lambda$pc and $L = 18\ \mathrm{kpc}/\lambda$, respectively. Each time unit translates into $5{,}1/\lambda^2$ Myr, and the evolution time of 250 time units translates into $1{,}27/\lambda^2$ Gyr. Finally, the distribution in the momentum space uses a width of $\sigma = 1$, so that at one sigma radius $p = 1$, the associated velocity is $\sim 192\,\lambda\mathrm{km\,s}^{-1}$ for this value of m_B, which, for the purposes of dark matter, lies within a cold regime.

The solution of the SP system is carried out using our code CAFE-FDM described in Ref. [30], with the following combination of numerical methods. The evolution uses the Method of Lines with a fourth order Runge-Kutta integrator, spatial discrete Fourier transform discretization of the right hand side of Schödinger equation, and periodic boundary conditions on Ψ; the Poisson equation is solved using a Fast-Fourier-Transform based method over each intermediate step of the Runge-Kutta integrator. The evolution time-step uses the Courant-type condition $\Delta t/\Delta x^2 < 1/6\pi$, as recommended in Ref. [24], that guarantees stability.

The evolution of these initial data using the SP system (1)-(2) leads to virialized configurations that approach a virialized core-halo structure [24,29]. The central region forms a solitonic core whose density profile, when averaged in space and time, closely matches the ground-state solution of the SP system obtained under isolated boundary conditions [17]. Surrounding this core, the outer halo is typically approximated with a Navarro-Frenk-White (NFW) profile, from structure formation simulations [8,9], as well as in local collapse [13,31].

In order to monitor the virialization, we compute the kinetic and potential energy observables inside a sphere of radius r_t, where r_t denotes the transition radius between the solitonic core and the outer halo:

$$K_t = -\frac{1}{2}\int_{R\le r_t} \Psi^*\nabla^2\Psi\, d^3x, \tag{8}$$

$$W_t = \frac{1}{2}\int_{R\le r_t} V|\Psi|^2\, d^3x. \tag{9}$$

For a virialized configuration, ideally these quantities combine to satisfy the relation $2K_t + W_t = 0$. We therefore define

$$\eta_t := \frac{|2K_t + W_t|}{|W_t|}, \tag{10}$$

as the relative deviation from the ideal virial condition, normalized by the magnitude of the potential energy inside a sphere of radius r_t. The central structure is considered virialized when η_t falls below a chosen tolerance threshold η_{thr}, which is set here to $\eta_{\mathrm{thr}} = 0{,}02$. The Fig. 1a) shows the evolution of η_t and identifies the first time at which $\eta_t < \eta_{\mathrm{thr}}$. This defines the transition time $t_{\mathrm{tr}} \simeq 0{,}153\,\mathrm{Gyr}/\lambda^2$. For later times, η_t remains close to the threshold and oscillates around it. This diagnostic quantity shows that t_{tr} marks the beginning of a relaxed core-halo stage and provides a suitable reference time for the subsequent analysis. The Fig. 1b) shows the density distribution on the xy plane at time t_{tr}, where a condensed central core is already present. The core is not a smooth, spherically symmetric distribution, but a region where the density is high in angular average, whereas the surroundings composing the halo are lower density, however dominated by smaller granules, with higher kinetic energy and actually -although not seen in a snapshot- evolve in time moving around.

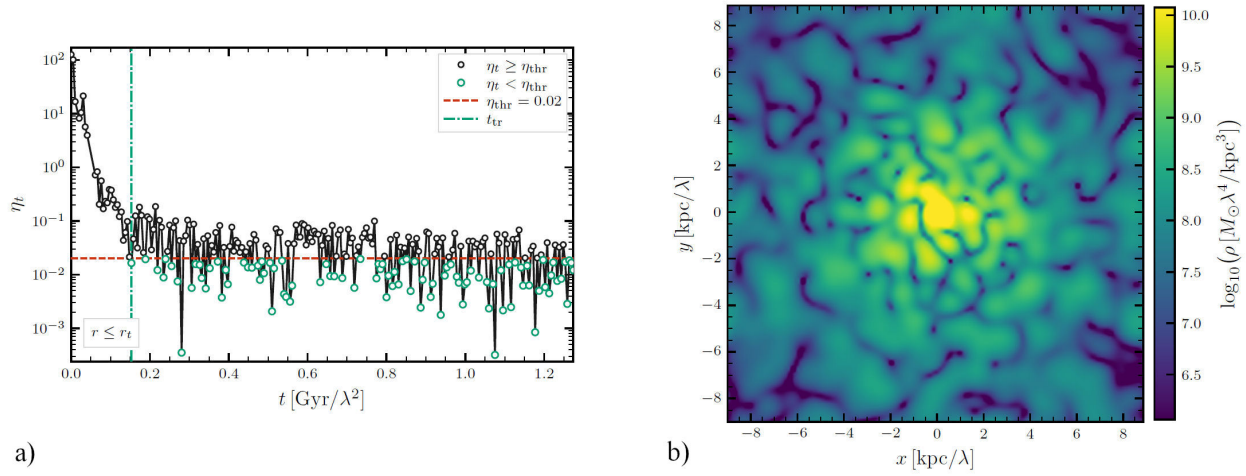


FIGURE 1. Virialization diagnostic and density structure at the transition time. a) Evolution of the virial deviation parameter $\eta_t = |2K_t + W_t|/|W_t|$ calculated inside the transition radius r_t. The horizontal dashed line marks the adopted threshold $\eta_{\mathrm{thr}} = 0{,}02$, and the vertical dash-dotted line indicates the first crossing time $t_{\mathrm{tr}} \simeq 0{,}153\,\mathrm{Gyr}/\lambda^2$. b) Density on the xy plane at t_{tr}.

2.3. Centering the core for analysis

The result of the workhorse simulation defined above, is the space-time dependent complex wave function Ψ, from which the density is obtained as $\rho = |\Psi|^2$. A first step in the core-halo fitting is the identification of the halo center. Rather than using a simple maximum or center-of-mass over the full numerical domain, we construct a density-weighted centroid. In practice, this is implemented by selecting grid points above a given density threshold and calculating

$$\mathbf{x}_c = \frac{\sum \rho(\mathbf{x})\,\mathbf{x}}{\sum \rho(\mathbf{x})}. \tag{11}$$

This method provides a useful estimate of the core center. All radius dependent quantities are then calculated with respect to this center.

2.4. Spherical averaging and density model

To separate large-scale structure from fluctuations, we construct a spherically averaged density profile. This is done by binning the density field in radial shells, where a solid angle average is calculated as

$$\rho_{\rm model}(r) = \langle\rho\rangle_\Omega = \frac{1}{4\pi}\int_\Omega \rho\, d\Omega, \tag{12}$$

at a given time during the evolution, taken over all grid points within a shell centered at radius r measured from the center location Eq. (11), where $\Omega := [0,\pi]\times[0,2\pi]$ denotes the solid angle over which the averaging is performed. The resulting angularly averaged density profile defines a radial density and a gravitational potential $\langle V\rangle$ through the Poisson equation (2) that depends only on r.

Once the structure has collapsed and virialized, this averaged density profile is characterized by a central solitonic core surrounded by an outer region that decays like an NFW-like halo (see *e.g.* [31]). In the Fig. 1b) we show a slice of a snapshot of the already virialized workhorse structure with this core-halo distribution.

In the angular average, the solitonic core is modeled using the radius dependent profile [8]

$$\rho_{\rm core}(r) = \rho_c\left[1+0{,}091\left(\frac{r}{r_c}\right)^2\right]^{-8}, \tag{13}$$

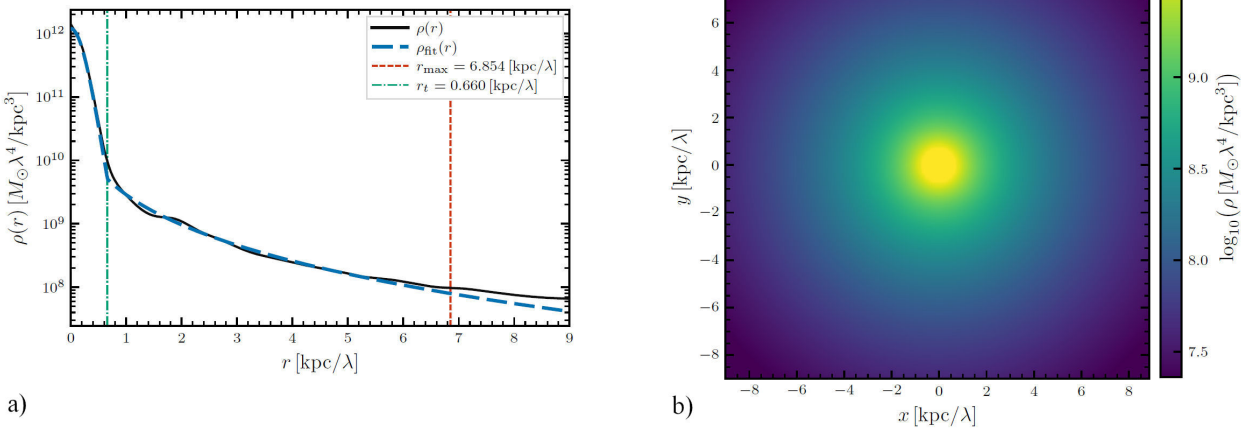
that mimics the ground state stationary solution of the SP system [17]. This density model was proposed in Ref. 8, as the result of structure formation simulations. In this formula, ρ_c is the central density of the core whereas r_c is the core radius, the radius at which the density is half the peak density. On the other hand, the outer region defined after a transition radius r_t, that is, for $r > r_t$, the distribution can be described in solid-angle average by the NFW profile

$$\rho_{\rm NFW}(r) = \frac{\rho_s}{\frac{r}{r_s}\left(1+\frac{r}{r_s}\right)^2}. \tag{14}$$

Adding these two components, the resulting angularly averaged density can be described by profile $\rho_{\rm model}(r) = \rho_{\rm core}(r)\Theta(r_t-r)+\rho_{\rm NFW}(r)\Theta(r-r_t)$, where Θ is the Heavisside step function and r_t denotes the transition radius between the core and the halo.

In this way, $\rho_{\rm model}(r)$ captures the global core-halo structure, including the solitonic inner region and the extended halo. The profile is then interpolated back onto the full grid to construct a three-dimensional density $\rho_{\rm model}(\mathbf{x}) = \rho_{\rm model}(r(\mathbf{x}))$. This technical step is important since it defines a smooth background that can be removed if desired in order to study the fluctuations.

In Fig. 2a) we show the radial density profile along r, where the transition radius r_t between the core and the NFW profile is indicated, as well as the radius $r_{\rm máx}$ at which we perform an accurate fitting, trying to avoid the effect of the



a) b)

FIGURE 2. a) Density profile along r at time $t_{\rm tr}$ with the values of the fitting parameters $r_s = 3{,}529$ kpc/λ, $r_t = 0{,}660$ kpc/λ, $\rho_c = 1{,}31\times10^{12}{\rm M}_\odot\lambda^4/{\rm kpc}^3$ and $\rho_s = 1{,}03\times10^9{\rm M}_\odot\lambda^4/{\rm kpc}^3$. b) Model density $\rho_{\rm model}(r)$ mapped back to the Cartesian domain.

periodic boundary, which can be noticed from this radius on. At the same figure we show the smooth version $\rho_{\rm model}(r)$ embedded back into the 3D domain. The quality of the fit is evaluated over the fitting region $0 < r \leq r_{\rm máx}$.

The value $r_{\rm máx}$ is estimated from the smoothed radial profile by identifying the point where the outer profile begins to flatten, which indicates that the boundary effects start to become relevant. The parameters of the model are then obtained through a least squares fit over the interval of confidence, leaving three free parameters, the core radius r_c, NFW scale r_s and transition radius r_t, at time $t_{\rm tr}$ the best fit values are $r_s = 3{,}529\ {\rm kpc}/\lambda$, $r_t = 0{,}660\ {\rm kpc}/\lambda$, $\rho_c = 1{,}31 \times 10^{12} {\rm M}_\odot \lambda^4/{\rm kpc}^3$ and $\rho_s = 1{,}03 \times 10^9 {\rm M}_\odot \lambda^4/{\rm kpc}^3$. The fitted core-halo profile $\rho_{\rm model}$ uses a least squares algorithm, and reproduces the density profile with a normalized RMS deviation of $\sim 5\,\%$, which improves when a smaller $r_{\rm max}$ is used.

It is worth mentioning that, even after virialization, the structure continues to evolve, never reaches a stationary state, and the granules in the halo never smooth out. This implies that granule positions and sizes evolve in time, therefore the fitted profile $\rho_{\rm model}$ also changes in time, and structures must be analyzed at various time slices to capture an average behavior of the structure in time as well.

2.5. Residual density and spectral analisys

We define the residual field as the difference between the full density and the spherical density model

$$\rho_{\rm res}(\mathbf{x}) = \rho(\mathbf{x}) - \rho_{\rm model}(\mathbf{x}), \tag{15}$$

which isolates the fluctuations associated with interference patterns developed during the evolution.

Using a Fast Fourier Transform $\mathcal{F}$, to ρ, $\rho_{\rm model}$ and $\rho_{\rm res}$, we calculate the power spectrum defined as

$$P(\mathbf{k}) = \left| \mathcal{F}\left[\frac{\alpha - \bar{\alpha}}{\bar{\alpha}} \right] \right|^2, \tag{16}$$

where α represents the three densities ρ, $\rho_{\rm model}$, $\rho_{\rm res}$, and $\bar{\alpha}$ is the average of α in the numerical domain. We then calculate the dimensionless isotropic spectrum of these densities in spherical shells in Fourier space

$$\Delta^2(k) = \frac{k^3}{2\pi^2} P(|\mathbf{k}|). \tag{17}$$

The resulting spectra are shown in Fig. 3 for the total density ρ, the model density $\rho_{\rm model}$ and the granules $\rho_{\rm res}$ for 30 snapshots taken after the structure is virialized, between $t_{\rm tr}$ and the final time. First notice that the dynamics of the FDM changes with time for all three densities, including the model density. However that the granular envelope has a more variable spectrum since it is more dynamic due to the dominant kinetic energy contribution in that region.

In order to clearly distinguish a difference between the peak frequencies of the whole structure with respect to that

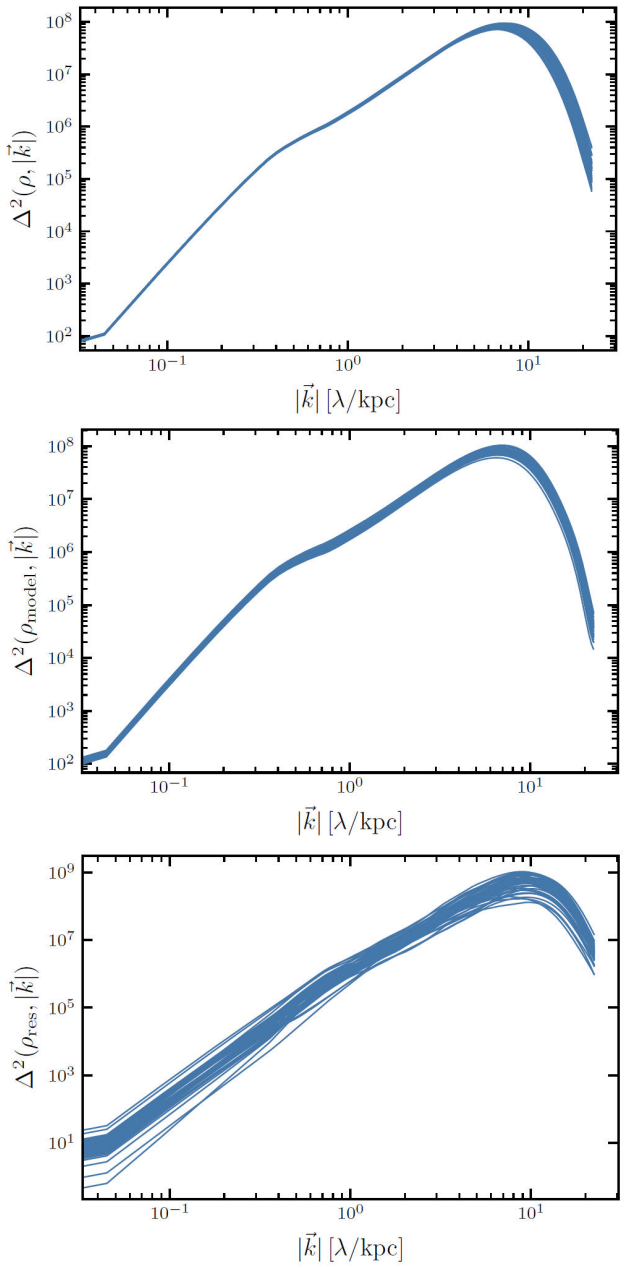


FIGURE 3. Dimensionless power spectrum $\Delta^2(k)$ computed for ρ, $\rho_{\rm model}$ and $\rho_{\rm res}$. Each line corresponds to a different snapshot during the evolution in a lapse time when the configuration is already virialized. Notice that the evolution actually produces a time dependent spectrum more noticeable in $\rho_{\rm res}$, associated to the granular structure.

of the granular fluctuations, we show in Fig. 4 a linear scale plot of the mean of the spectra. For the density ρ, as well as for the model density $\rho_{\rm model}$, there are similar peaks at $|\vec{k}| \sim 0{,}7$, whereas for the granules this dominant peak appears at $|\vec{k}| \sim 0{,}95$, which indicates preferred scales in the three fluctuation fields. This confirms the expected result that small fluctuations prefer a higher $|\vec{k}|$, and our analysis quantifies the difference between the two peaks.

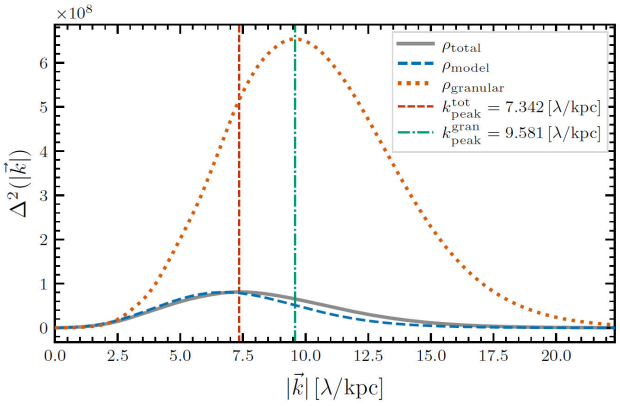


FIGURE 4. Time average across the snapshots, of the dimensionless power spectra $\Delta^2(k)$ of the densities ρ, $\rho_{\rm model}$ and $\rho_{\rm res}$. Unlike the traditional log-scale spectrum, this one allows one to clearly observe the peak separation between peak frequencies.

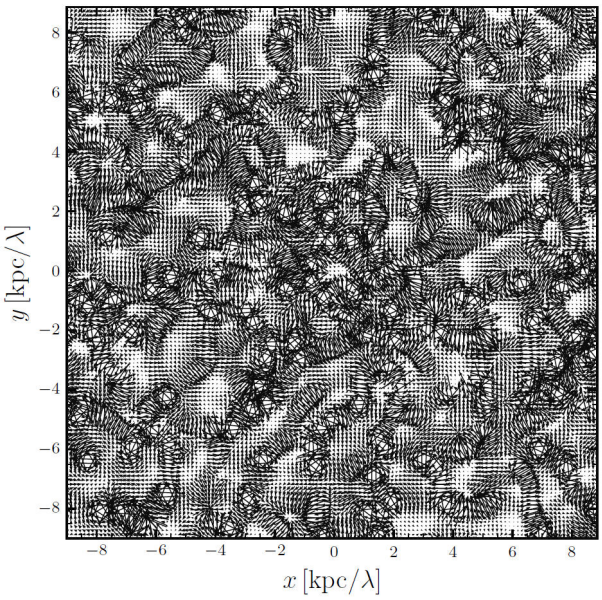


FIGURE 5. Slice of the velocity field on the $xy-$plane for $m_B = 10^{-23}$ eV at time $t_{\rm tr}$, that illustrates how anisotropic the velocity field is.

3. Estimating the de Broglie wavelength

The granular structure already implies that the velocity field across the structure has different directions and magnitudes. This suggests that, since $\lambda_{\rm dB}$ is velocity dependent, then its value depends on the region of the core-halo being considered. In order to estimate $\lambda_{\rm dB}$, we evaluate the density current

$$j_k = \frac{1}{2i}\left(\Psi^*\partial_k\Psi - \Psi\partial_k\Psi^*\right),$$

where $k = x, y, z$, then estimate the magnitude of the velocity at each grid point of the numerical domain as

$$\mathbf{v} = \frac{\mathbf{j}}{\rho}, \qquad v = \frac{\sqrt{|j_x|^2 + |j_y|^2 + |j_z|^2}}{\rho}, \tag{18}$$

which finally is used to estimate a position dependent de Broglie wavelength

$$\lambda_{\rm dB}(r) = \frac{2\pi}{m_b\sigma_v(r)}. \tag{19}$$

Here $\sigma_v(r)$ denotes the velocity dispersion computed over spherical shells at fixed radius

$$\sigma_v(r) = \left(\langle v^2\rangle_\Omega - \langle v\rangle_\Omega^2\right)^{1/2}, \tag{20}$$

where $\langle\cdot\rangle_\Omega$ represents the angular average. In order to have an idea of how the velocity field (18) looks like in the snapshot we have been working with, in Fig. 5 we show the case for $m_B = 10^{-23}$eV.

Figure 6 shows the radial dependence of the velocity dispersion $\sigma_v(r)$ and the corresponding de Broglie wavelength $\lambda_{\rm dB}(r)$ from the transition time $t_{\rm tr}$ to the final time of the simulation t_f. Since $\lambda_{\rm dB}$ is inversely proportional to σ_v, regions with smaller velocity dispersion correspond to larger de Broglie wavelengths. Inside the solitonic core, $\lambda_{\rm dB}$ is various orders of magnitude larger than in the outer halo, indicating that the core is dominated by long wavelength modes.

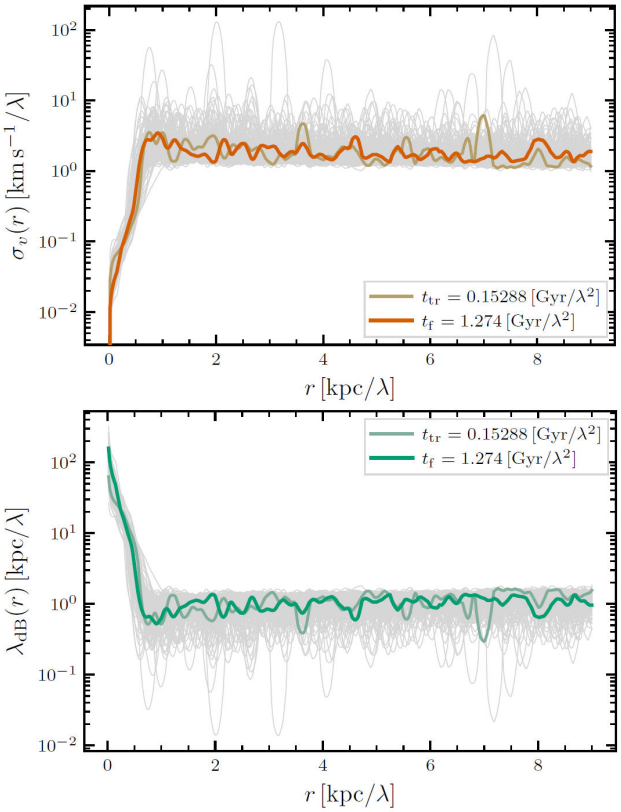


FIGURE 6. Radial profile of the velocity dispersion $\sigma_v(r)$ and the associated de Broglie wavelength $\lambda_{\rm dB}(r)$ from $t_{\rm tr}$ to t_f. Gray lines correspond to intermediate snapshots, while colored lines highlight $t_{\rm tr}$ and t_f.

The radial profile of $\lambda_{\rm dB}(r)$ exhibits a nontrivial behavior, it decreases from the center, reaches a minimum at an intermediate radius, and increases again in the outer halo. Explicitly, $\lambda_{\rm dB}$ is maximum at the center of the configuration, within the core, as expected, since it is the region where the FDM is colder than the halo, since the kinetic energy and thus the velocity are smaller there than in the halo. At large radii, where the granules carry high kinetic energy, the velocity is expected to be higher and therefore $\lambda_{\rm dB}$ should be smaller. This result allows one to **quantify** the difference in wavelength between the core and the halo. For the case of $m_B = 10^{-23}$ eV and the initial conditions used in the momentum space for our workhorse structure, we find that the minimum $\lambda_{\rm dB}$ at the interface is of $0{,}338\ {\rm kpc}/\lambda$, whereas an average $\lambda_{\rm dB}$ from the transition region to the outskirts of the halo and averaged also in time is $\langle\lambda_{\rm dB}\rangle = 1{,}033\ {\rm kpc}/\lambda$.

The dominant peak of the granular spectrum provides a characteristic length scale, $2\pi/k^{\rm gran}_{\rm peak}$, which can be directly compared with the de Broglie wavelength. During the relaxed stage, we find $\langle\lambda_{\rm dB}\rangle = 1{,}033\,{\rm kpc}/\lambda$, while the mean granular size scale is $0{,}753\,{\rm kpc}/\lambda$. Their ratio has a mean value of $\approx 0{,}714$. This shows that the characteristic scale extracted from the granular spectrum is systematically smaller than, but comparable to, the de Broglie wavelength. Therefore, the spectral peak scale and the de Broglie wavelength are connected at the same order of magnitude, supporting the interpretation that the observed granules are associated with de Broglie scale interference.

What is unexpected, is that there is a minimum precisely at the transition region between the core and the halo. The straightforward interpretation is that there the velocity should be higher than in the center and in the outer kinetic envelope. This is intriguing, although we find a precedent for the need of a high velocity at the transition sphere in the construction of core-halo FDM configurations within the Madelung frame [32].

4. Discussion and conclusions

We have presented a quantitative analysis of the small-scale structure of FDM halos, focusing on both the spectral properties of density fluctuations and the local velocity field.

From the decomposition of the density into a smooth core-halo component and a residual field, we showed that the interference pattern can be isolated and characterized through its power spectrum. The residual spectrum shows a well-defined peak that is clearly separated from the peak of the total and model densities, which identifies the characteristic scale of granules.

Independently, we estimated a local de Broglie wavelength from the velocity field derived from the wavefunction. The resulting radial profiles reveal that $\lambda_{\rm dB}$ is strongly position-dependent and evolves in time, but consistently shows a non-monotonic behavior within the core and halo. In particular, we find that the wavelength reaches a minimum at an intermediate radius, close to the transition between the solitonic core and the outer halo.

These results add to the picture of the internal structure of FDM halos, where the core-halo boundary plays a central dynamical role. The identification of a preferred scale for fluctuations, together with its radial dependence, opens the possibility of connecting the granular structure to observable effects in real galaxies, such as dynamical heating or perturbations of stellar tracers.

Future work should extend this analysis to different halo masses, environments, and initial conditions, as well as explore the impact of these fluctuations on baryonic matter.

Acknowledgments

This research is supported by SECIHTI Grant No. CFB-2025-I-759, Laboratorio Nacional de Cómputo de Alto Desempeño Grant No. 2026-8, and CIC-UMSNH Grant No. 4.9.

1. T. Matos and L. A. Urena-Lopez, A Further analysis of a cosmological model of quintessence and scalar dark matter, *Phys. Rev. D* **63** (2001) 063506, https://doi.org/10.1103/PhysRevD.63.063506
2. W. Hu, R. Barkana, and A. Gruzinov, Cold and fuzzy dark matter, *Phys. Rev. Lett.* **85** (2000) 1158, https://doi.org/10.1103/PhysRevLett.85.1158
3. P.-H. Chavanis, Self-gravitating Bose-Einstein Condensates, pp. 151-194 (Springer International Publishing, Cham, 2015), https://doi.org/10.1007/978-3-319-10852-0_6.
4. L. Hui *et al.*, Ultralight scalars as cosmological dark matter, *Phys. Rev. D* **95** (2017) 043541, https://doi.org/10.1103/PhysRevD.95.043541
5. E. G. M. Ferreira, Ultra-Light Dark Matter, arXiv e-prints (2020) arXiv:2005.03254
6. J. C. Niemeyer, Small-scale structure of fuzzy and axion-like dark matter, *Progress in Particle and Nuclear Physics* **113** (2020) 103787, https://doi.org/10.1016/j.ppnp.2020.103787
7. L. Hui, Wave Dark Matter, *Annual Review of As- tronomy and Astrophysics* **59** (2021) 247, https://doi.org/10.1146/annurev-astro-120920-010024
8. H.-Y. Schive, T. Chiueh, and T. Broadhurst, Cosmic Structure as the Quantum Interference of a Coherent Dark Wave, *Nature Phys.* **10** (2014) 496, https://doi.org/10.1038/nphys2996
9. P. Mocz, et al., Galaxy formation with BECDM I. Turbulence and relaxation of idealized haloes, *Mon. Not. Roy. Astron. Soc.* **471** (2017) 4559, https://doi.org/10.1093/mnras/stx1887
10. J. Veltmaat, J. C. Niemeyer, and B. Schwabe, Formation

and structure of ultralight bosonic dark matter halos, *Physical Review D* **98** (2018), https://doi.org/10.1103/physrevd.98.043509

11. S. May and V. Springel, Structure formation in large-volume cosmological simulations of fuzzy dark matter: impact of the non-linear dynamics, *Monthly Notices of the Royal Astronomical Society* **506** (2021) 2603, https://doi.org/10.1093/mnras/stab1764
12. B. Schwabe and J. C. Niemeyer, Deep Zoom-In Simulation of a Fuzzy Dark Matter Galactic Halo, *Phys. Rev. Lett*. **128** (2022) 181301, https://doi.org/10.1103/PhysRevLett.128.181301
13. I. Álvarez-Rios, F. S. Guzmán, and P. R. Shapiro, Effect of boundary conditions on structure formation in fuzzy dark matter, *Phys. Rev. D* **107** (2023) 123524, https://doi.org/10.1103/PhysRevD.107.123524
14. I. Álvarez-Rios and F. S. Guzman, Unveiling Orbital Chaos: The Wild Heart of Fuzzy Dark Matter Structures (2025), URL https://arxiv.org/abs/2502.20205.
15. Y. Zhao, A. Benson, and X. Du, A semi-analytic model for effects of fuzzy dark matter granule perturbations on orbital motion, *Monthly Notices of the Royal Astronomical Society* **542** (2025) 508, https://doi.org/10.1093/mnras/staf1281
16. D. J. Marsh and J. C. Niemeyer, Strong Constraints on Fuzzy Dark Matter from Ultrafaint Dwarf Galaxy Eridanus II, *Physical Review Letters* **123** (2019), https://doi.org/10.1103/physrevlett.123.051103
17. F. S. Guzmán and L. A. Ureña López, Evolution of the Schrödinger-Newton system for a self-gravitating scalar field, *Phys. Rev. D* **69** (2004) 124033, https://doi.org/10.1103/PhysRevD.69.124033
18. H.-Y. Schive *et al.*, Understanding the Core-Halo Relation of Quantum Wave Dark Matter from 3D Simulations, *Phys. Rev. Lett.* **113** (2014) 261302, https://doi.org/10.1103/PhysRevLett.113.261302
19. B. Schwabe, J. C. Niemeyer, and J. F. Engels, Simulations of solitonic core mergers in ultralight axion dark matter cosmologies, *Phys. Rev. D* **94** (2016) 043513, https://doi.org/10.1103/PhysRevD.94.043513
20. P. Mocz *et al.*, First Star-Forming Structures in Fuzzy Cosmic Filaments, *Phys. Rev. Lett*. **123** (2019)
21. I. Álvarez-Rios *et al.*, Galactic rotation curves of low surface brightness galaxies using core-halo fuzzy dark matter configurations, *Phys. Rev. D* **110** (2024) 063502, https://doi.org/10.1103/PhysRevD.110.063502
22. D. G. Levkov, A. G. Panin, and I. I. Tkachev, Gravitational Bose-Einstein Condensation in the Kinetic Regime, *Phys. Rev. Lett.* **121** (2018) 151301, https://doi.org/10.1103/PhysRevLett.121.151301
23. B. Eggemeier and J. C. Niemeyer, Formation and mass growth of axion stars in axion miniclusters, *Phys. Rev. D* **100** (2019) 063528, https://doi.org/10.1103/PhysRevD.100.063528
24. J. Chen *et al*., New insights into the formation and growth of boson stars in dark matter halos, *Phys. Rev. D* **104** (2021) 083022, https://doi.org/10.1103/PhysRevD.104.083022
25. J. Chen *et al*., Gravitational Bose-Einstein condensation of vector or hidden photon dark matter, *Phys. Rev. D* **108** (2023) 083021, https://doi.org/10.1103/PhysRevD.108.083021
26. K. J. Purohit *et al*., Formation of a Bose star in a rotating cloud, *Astrophysics and Space Science* **368** (2023), https://doi.org/10.1007/s10509-023-04253-8
27. J. Chen and H.-Y. Zhang, Novel structures and collapse of solitons in nonminimally gravitating dark matter halos, *Journal of Cosmology and Astroparticle Physics* **2024** (2024) 005, https://doi.org/10.1088/1475-7516/2024/10/005
28. I. Álvarez-Rios, F. S. Guzmán, and J. Niemeyer, Fermion- Boson Stars as Attractors in Fuzzy Dark Matter and Ideal Gas Dynamics, *Phys. Rev. Lett*. **135** (2025) 161003, https://doi.org/10.1103/4tkh-7hjs
29. C. Palomares-Chavez, I. Alvarez-Rios, and F. S. Guzman, Black Holes as Condensation Points of Fuzzy Dark Matter Cores (2024), https://arxiv.org/abs/2412.15465.
30. I. Álvarez-Rios and F. S. Guzmán, Exploration of simple scenarios involving fuzzy dark matter cores and gas at local scales, *Monthly Notices of the Royal Astronomical Society* **518** (2022) 3838, https://doi.org/10.1093/mnras/stac3395
31. I. Álvarez-Rios, et al., Galactic rotation curves of low surface brightness galaxies using core-halo fuzzy dark matter configurations, *Phys. Rev. D* **110** (2024) 063502, https://doi.org/10.1103/PhysRevD.110.063502
32. I. Álvarez-Ríos and F. S. Guzmán, Construction and Evolution of Equilibrium Configurations of the Schrödinger-Poisson System in the Madelung Frame, *Universe* **8** (2022) 432, https://doi.org/10.3390/universe8080432

Investigation of impact of calcination temperature on the structural, microstructural, and functional properties of MgO nanoparticles using Williamson Hall method

A. Tanveer, M. M. Haseeb Awan, and M. Sajjad Mehmood

Department of Physical Sciences, University of Engineering and Technology, 47050, Taxila, Pakistan.

M. Ahmad

Department of Physics, International Islamic University Islamabad, Pakistan.

Received 3 December 2025; accepted 26 May 2026

Magnesium oxide (MgO) nanoparticles were synthesized using a co-precipitation method and then calcined at 450 °C, 650 °C, and 700 °C to study the effects of different calcination temperatures on the structure and microstructure. The phase composition of the synthesized samples was studied using X-ray diffraction (XRD), which showed that all samples were composed of single-phase cubic MgO, and no secondary phases were detected. The Williamson-Hall (W–H) analysis using Lorentzian and Gaussian peak-profile functions was employed to investigate the effects of calcination temperature on the crystallite size and lattice microstrain. The results demonstrated that the calcination temperature significantly affected the MgO nanoparticles. With increasing temperature, the microstrain decreased, the crystallite size increased, and the thermal stability and ordering of the lattice improved. The study also revealed that increasing the calcination temperature led to a significant increase in the unit-cell volume and lattice ordering. When comparing the Lorentzian and Gaussian profiles, it was observed that both profiles produced very similar effects on the crystallite size; however, their effects on strain were different. Therefore, it was concluded that the calcination temperature used during the synthesis of MgO nanoparticles has a direct effect on the crystallite size, defect concentration, and the structural quality of the final product.

Keywords: Magnesium oxide nanoparticles; calcination temperature; Williamson-Hall analysis; X-ray diffraction; crystallite size; lattice microstrain; defect evolution; nanocrystalline oxides.

DOI: https://doi.org/10.31349/RevMexFis.72.061006

1. Introduction

Magnesium oxide (MgO) nanoparticles have great potential for multiple applications due to their unique characteristics arising from their diverse physicochemical properties. Some applications of MgO nanomaterials include catalysis, optoelectronics, energy storage systems, refractory materials, antibacterial coatings, and biomedical engineering [1-3]. Compared with bulk materials, nanoscale MgO has a higher surface-to-volume ratio, a denser concentration of surface active sites, and defect-mediated functional properties. MgO nanoparticles exhibit enhanced catalytic, dielectric, and optical properties [4,5]. The microstructural characteristics of oxide nanoparticles are affected by the synthesis methods and heat treatments employed. The condensation and calcination of the oxide precursor are particularly important, as they can significantly alter the final microstructure of the nanoparticles by changing the concentration and morphology of surface defects [6-8]. Other factors also influence the microstructure of MgO nanoparticles, such as calcination temperature, which can affect the migration and diffusion of atoms and thereby reduce defects. Previous studies have shown that as the calcination temperature increases, crystallinity improves while both defect density and microstrain decrease until an optimal temperature is reached [9,10]. Beyond this point, higher calcination temperatures may lead to particle agglomeration and a reduction in active surface area, thereby decreasing particle efficiency [11].

MgO nanoparticles are useful for studying microstructural changes at elevated temperatures because of their simplicity and stability. MgO crystal structures contain defects that exhibit distinct behavioral features [12,13]. Therefore, precise measurements of the microstructural features of MgO nanostructures are essential to understanding the relationship among processing, structure, and material properties [14,15]. This is particularly important for parameters such as crystallite size, dislocation density, internal stress, and microstrain.Among the various techniques used to investigate nanocrystalline materials, X-ray Diffraction (XRD) is one of the most prominent. Traditionally, the Scherrer equation has been used to estimate crystallite size from the broadening of XRD peaks, often neglecting the contribution of internal strain [16,17]. In contrast, the Williamson-Hall (W-H) equation allows peak broadening to be decomposed into size and strain contributions [18]. The W–H method can be further improved through the use of Lorentzian or Gaussian peak-profile functions, which help distinguish the two broadening mechanisms. Furthermore, the W–H approach can be applied to describe defect behavior and structural relaxation in oxide materials [19-22].

Recently, extensive research has focused on the influence of calcination temperature on the properties of nanosca-

le oxides, particularly Mg-based ferrites [23,24]. Mansouri and co-workers reported that chromium substitution in magnesium ferrites caused lattice distortion and defect engineering, thereby affecting both structural and optical properties of Mg–Co ferrite nanoparticles [25]. Zarai and colleagues observed that thermal treatment of $Mg_{0,6}Co_{0,4}FeAlO_4$ spinel ferrites enhanced crystallinity and optoelectronic properties while reducing the optical band gap [26]. Similarly, Chebbi and co-workers investigated the influence of chromium substitution and thermal treatment on the structural, optical, and electrical properties of Mg–Co ferrite nanoparticles [27]. Jdey and colleagues demonstrated that dielectric properties of Mg-based ferrites improved with enhanced lattice ordering, reduced microstrain, and higher calcination temperatures [17,28,29]. Numerous studies have also shown that thermal treatment of nanoscale oxides promotes hierarchical grain growth, reduction of lattice imperfections and structural defects, stress relaxation, and improved crystallinity quality and stability [30,31]. However, only a limited number of studies have focused specifically on MgO nanoparticles, and even fewer have investigated the relationship between calcination temperature, crystallite growth, lattice strain, and defect density [32]. Moreover, detailed Williamson-Hall analyses using both Lorentzian and Gaussian peak fitting methods remain scarce in studies concerning thermally treated MgO nanoparticles [25]. Understanding these parameters is essential for improving the application of MgO nanostructures in catalytic, optical, dielectric, and biomedical fields [17,33].

The present study investigates the effects of calcination temperature on the structure and microstructure of MgO nanoparticles synthesized using the co-precipitation method. MgO nanoparticles were prepared and calcined at different temperatures to evaluate the impact of calcination temperature on nanoparticle microstructure. The crystallite size and stress of the calcined MgO nanoparticles were analyzed using X-ray Diffraction (XRD), while Williamson-Hall (W–H) modeling methods were employed to estimate microstrain and dislocation density. Both Lorentzian and Gaussian peak-profile fitting methods were utilized in the W–H analysis. Additionally, the study evaluates the effects of synthesis methods on the thermal and microstructural properties of MgO nanoparticles prepared via co-precipitation. The Lorentzian and Gaussian methods were also used to explain peak-profile positioning and estimate crystallite size and microstrain. Finally, the study provides insights into microstructural stabilization and defect evolution in MgO nanomaterials.

2. Experimental details

2.1. Chemicals and materials

All chemicals used were of analytical grade, as this guarantees high purity MgO nanoparticle synthesis. Magnesium sulfate heptahydrate ($MgSO_4{\cdot}7H_2O$, $\geq$99 %, Sigma-Aldrich) was used as the magnesium source for nanoparticle synthesis because of its convenient solubility. $MgSO_4{\cdot}7H_2O$ was selected because Mg^{2+} ions precipitate completely under alkaline conditions.As the precipitating agent, Ammonium Hydroxide (NH_4OH, analytical grade, Sigma-Aldrich) was employed to control the pH and facilitate the formation of magnesium hydroxide precipitates. Distilled water was used throughout the synthesis process in order to minimize side reactions and ionic contamination. The observed changes in the structural and microstructural properties of the MgO nanoparticles were attributed solely to the effects of calcination. This was ensured by taking utmost care to avoid the presence of precursor impurities during the synthesis process.

2.2. Synthesis of MgO Nanoparticles by co-precipitation method

The synthesis of MgO nanoparticles was carried out using a simple and effective controlled co-precipitation route. This method was selected because it offers low synthesis cost, high purity of the final product, and excellent control over the size and morphology of the nanoparticles. Magnesium sulfate heptahydrate ($MgSO_4 \cdot 7H_2O$, Sigma Aldrich, 99 %) was used as the magnesium source. A measured quantity of $MgSO_4 \cdot 7H_2O$ was dissolved in 100 mL of freshly distilled water to prepare a 0.5 M magnesium precursor solution. The solution was stirred continuously at 700 rpm and heated to 80–90 °C for 24 h to ensure complete dissolution of the precursor salts. This process enabled uniform ion distribution within the solution and promoted homogeneous nucleation.To form magnesium hydroxide ($Mg(OH)_2$), ammonium hydroxide (NH_4OH, analytical grade, Sigma Aldrich) was used as the precipitation agent and added dropwise:

$$MgSO_4 + 2NH_4OH \rightarrow Mg(OH)_2 + (NH_4)_2SO_4$$

NH_4OH was used because it creates a controlled alkaline environment and sublimates during calcination, thereby keeping the final MgO product free from impurities. During the experiments, the reaction medium was maintained at an alkaline pH of approximately 10–11 to ensure complete precipitation of all Mg^{2+} ions as $Mg(OH)_2$ and to achieve a homogeneous particle-size distribution.The homogeneous white suspension obtained was centrifuged at 6000 rpm for 10 min, and the resulting precipitate was washed several times with distilled water to remove sulfate and ammonium ions. The $Mg(OH)_2$ precipitate was then dried at 100 °C for 12 h. This drying process was carried out to remove moisture and prepare the sample for subsequent calcination. The $Mg(OH)_2$ powder was calcined at different temperatures to obtain various morphologies and structural characteristics. Prior to calcination, the powder was finely ground to reduce agglomeration and promote a more homogeneous distribution of particles.

2.3. Calcination at different temperatures

The researchers divided the dried $Mg(OH)_2$ powder into three batches, which were then placed in high-purity alumina

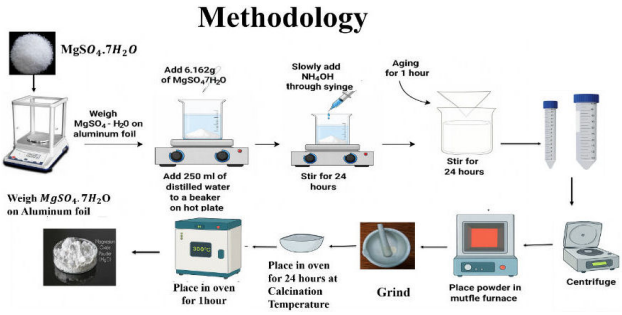


FIGURE 1. Schematic for the preparation steps followed for all samples preparation

crucibles to prevent contamination during thermal treatment. Each sample was then placed in a programmable muffle furnace to convert $Mg(OH)_2$ into MgO under an open-air atmosphere:

$$Mg(OH)_2 \rightarrow MgO + H_2O. \quad (1)$$

The calcination process was carried out at temperatures of 450 °C, 650 °C, and 700 °C using a controlled heating rate of 5 °C min^{-1}. An isothermal holding time of 24 h was maintained to ensure complete phase transformation and crystallization. The selected calcination temperatures were chosen to investigate the temperature-dependent structural evolution of MgO nanoparticles. The lower calcination temperature of 450 °C was used to examine the initial stage of crystallization, which generally results in smaller crystallite sizes and higher defect density. The higher calcination temperatures of 650 °C and 700 °C were selected to promote grain growth, lattice relaxation, reduction of structural defects, and improved lattice ordering. These temperatures also lie within the range reported in the literature where significant microstructural changes in MgO nanoparticles are commonly observed.After calcination, the furnace was allowed to cool naturally to room temperature in order to minimize thermal shock and prevent particle cracking. The obtained MgO powder samples were then gently ground to break weak agglomerates and stored in sealed glass containers to avoid moisture absorption.The samples were labeled as MgO-450, MgO-650, and MgO-700, respectively, and were further characterized using the Williamson-Hall (W-H) method to investigate their structural and microstructural properties.

2.4. X-Ray diffraction (XRD) characterization

To evaluate the impact of calcination temperature on MgO nanoparticles, X-ray Diffraction (XRD) analysis was performed. The analysis was carried out using a Philips X'Pert PRO X-ray diffractometer equipped with a Cu Kα radiation source. The X-ray source operated at 40 kV and 40 mA. Prior to analysis, the instrument accuracy was verified and calibrated using a commercial silicon standard.The XRD scans were recorded over an angular range of 10° to 80° with a step size of 0,02°, a counting time of 1 s per step, and a scanning rate of 2° min^{-1}. The obtained diffraction patterns were indexed, and the Joint Committee on Powder Diffraction Standards (JCPDS) database was used to identify the periclase phase of MgO and confirm the complete removal of secondary phases from the calcined $Mg(OH)_2$ products.The diffraction peak broadening was analyzed using Line Profile Analysis (LPA) with combined Lorentzian and Gaussian peak-profile fitting approaches. LPA was employed because it provides reliable estimations of crystallite size and microstrain-induced broadening effects within the samples. Line profile analysis and peak broadening techniques are widely applied in the microstructural characterization of nanostructured materials.

2.5. Williamson-Hall method

The Williamson-Hall (W-H) method is used to evaluate the broadening of X-ray diffraction peaks caused by finite crystallite size and lattice microstrain. Assuming the strain is uniform and anisotropic, the total peak broadening (β) can be expressed using the Williamson-Hall equation as follows:

$$\beta \cos\theta = \frac{k\lambda}{D} + 4\epsilon \sin\theta, \quad (2)$$

where β is the full width at half maximum (FWHM) of the diffraction peak after instrumental correction, k is the shape factor ($k = 0{,}94$), λ is the X-ray wavelength, D is the crystallite size, ϵ is the uniform elastic microstrain of the crystal, and θ is the Bragg diffraction angle. In this equation, $k\lambda/D$ represents size broadening, whereas $4\epsilon \sin\theta$ corresponds to strain broadening.In the Williamson-Hall analysis, the FWHM values of the most intense diffraction peaks corresponding to different crystallographic planes were extracted from the corrected XRD patterns after removing instrumental broadening. The quantities $\beta\cos\theta$ and $4\sin\theta$ were linearly fitted to separate the contributions of crystallite size and lattice strain. The crystallite size was determined from the intercept of the fitted line, while the lattice microstrain was obtained from the slope.This method enables the quantitative determination of crystallite size and lattice imperfections in MgO nanoparticles synthesized at different calcination temperatures and further characterized using thermal analysis [34].

3. Results and discussion

3.1. XRD analysis

The X-ray diffraction (XRD) patterns of MgO nanoparticles calcined at 450 °C, 650 °C, and 700 °C (Fig. 2) reveal significant structural evolution with increasing calcination temperature. The diffraction peaks observed at approximately $2\theta \approx 36{,}9°$, $42{,}8°$, and $62{,}1°$ correspond to the (111), (200), and (220) crystallographic planes of cubic periclase MgO, respectively. These results are consistent with JCPDS/PDF card No. 45–0946 and previously reported MgO

diffraction studies [25,35,36]. The absence of secondary impurity peaks confirms the formation of phase-pure MgO nanoparticles.

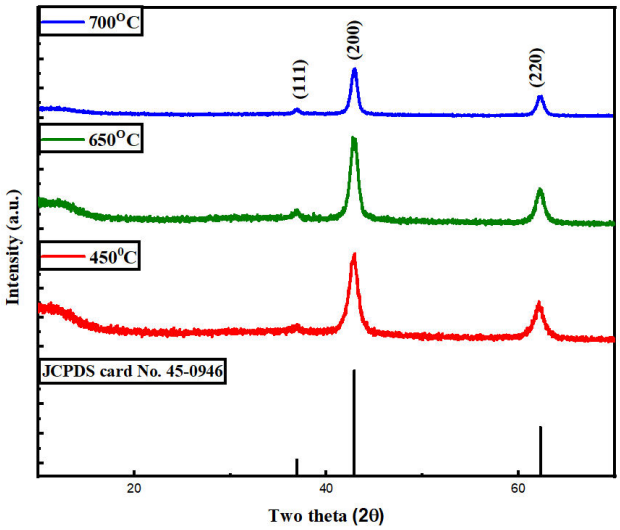


FIGURE 2. XRD patterns of MgO nanoparticles at different calcination temperatures (JCPDS No. 45-0946).

Similar calcination-temperature-dependent structural behavior has also been reported for MgO-based nanomaterials and spinel ferrite systems [25,26,28,37]. At a calcination temperature of 450 °C, the diffraction peaks are relatively broad with lower intensity, indicating smaller crystallite size, lower crystallinity, and higher lattice microstrain. Peak broadening is generally associated with lattice distortion, structural defects, and incomplete crystallization resulting from insufficient thermal energy during heat treatment [35,36]. The restricted atomic mobility at lower temperatures suppresses crystallite growth and enhances internal lattice strain. Similar observations have been reported for Mg-based ferrite systems [24,25]. With increasing calcination temperature to 650 °C and 700 °C, the diffraction peaks become sharper and more intense, indicating improved crystallinity and enhanced structural ordering. The increased thermal energy promotes atomic diffusion, lattice relaxation, and grain growth, thereby reducing defect density and lattice strain [28,36]. Grain growth occurs through the coalescence of smaller crystallites into larger grains in order to minimize the total grain boundary energy. Similar improvements in structural ordering and crystallinity at elevated temperatures were also reported by Zarai *et al.* [26], Jdey *et al.* [38], and Harrabi *et al.* [37] for Mg-based spinel ferrite systems. Unlike previous studies mainly focused on structural, optical, and dielectric enhancements, the present work systematically correlates crystallite growth, lattice strain reduction, and lattice expansion with calcination temperature using Williamson-Hall analysis. A gradual shift of the diffraction peaks toward lower 2θ values was observed with increasing calcination temperature. According to Bragg's law,

$$n\lambda = 2d\sin\theta, \tag{3}$$

the decrease in 2θ values indicates an increase in interplanar spacing (d-spacing), suggesting lattice expansion within the cubic MgO structure. The crystallographic parameters summarized in Table I further confirm this trend, where the lattice parameter increased from 4.214 Å to 4.229 Å, while the unit cell volume increased from 74.84 Å^3 to 75.64 Å^3 as the calcination temperature increased from 450 °C to 700 °C. The observed lattice expansion may be attributed to thermally induced defect relaxation and structural reorganization within the MgO lattice [28,36,39].

TABLE I. Crystallographic parameters of MgO nanoparticles at varying calcination temperatures, derived from XRD analysis of the (200) reflection, including diffraction angle (2θ), interplanar spacing (d), lattice parameter (a), and unit cell volume (V).

Parameters	**450 °C**	**650 °C**	**700 °C**
$2\theta_{(200)}$ (deg.)	42.8854	42.8063	42.7273
d-spacing, d (Å)	2.1071	2.1108	2.1146
Lattice parameter, a (Å)	4.2142	4.2216	4.2291
Unit cell volume, V (Å^3)	74.8431	75.2390	75.6387

With increasing calcination temperature, the (200) diffraction peak shifted toward lower 2θ values, indicating lattice expansion in cubic MgO. The data presented in Table I show that the interplanar spacing (d-spacing) increased from 2.1071 Å to 2.1146 Å. A slight increase in the lattice parameter and unit-cell volume was also observed, suggesting reduced lattice distortion and improved structural ordering.These changes in the crystallographic parameters are consistent with findings reported in the literature. Previous studies have shown that higher calcination temperatures enhance the structural stability of MgO nanoparticles and improve lattice uniformity due to defect reduction and lattice relaxation [37,40-45].

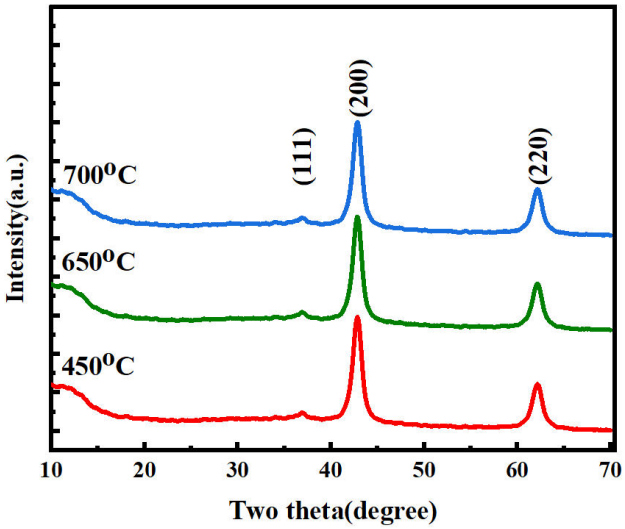


FIGURE 3. XRD patterns of MgO nanoparticles calcined at 450-700°C, showing a (200) peak shift to lower 2θ from lattice expansion and strain relaxation (FCC MgO, JCPDS 45-0946).

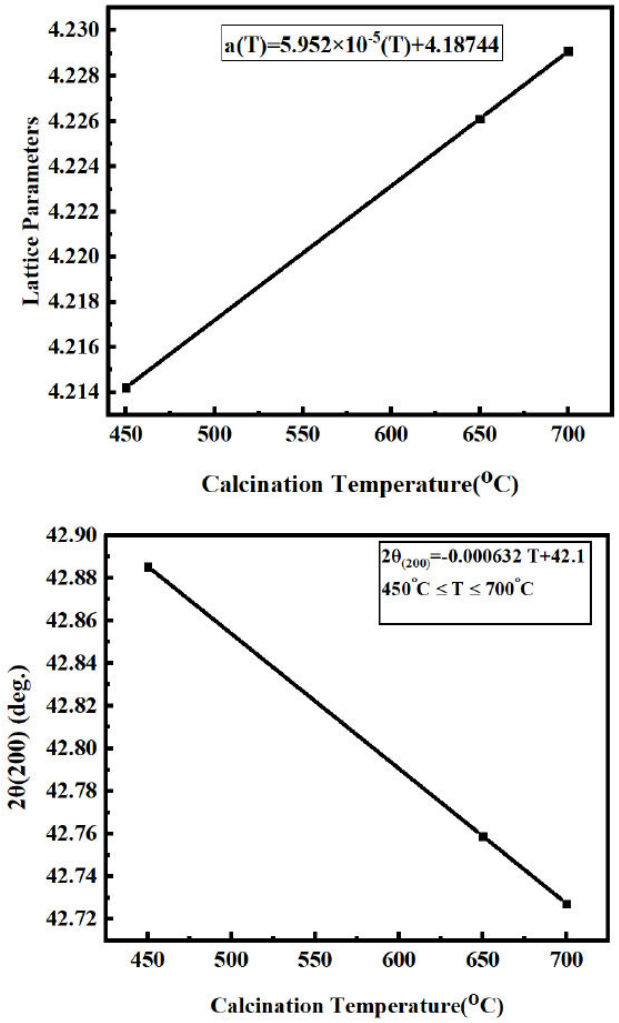


FIGURE 4. Systematic shift of the (200) diffraction peak toward lower angles and corresponding linear increase of the lattice parameter with calcination temperature, confirming thermally induced expansion of the MgO cubic lattice.

3.2. Lattice parameters

The lattice parameter was determined using the cubic relation

$$a = d\sqrt{(h^2 + k^2 + l^2)}, \tag{4}$$

in Fig. 4 show that X-ray diffraction (XRD) on MgO nanoparticles calcined at 450 °C, 650 °C, and 700 °C suggested the high crystallinity single-phase FCC structure (JCPDS 45-0946) formation [46]. With the increase in calcination temperature, the (200) diffraction peak shifted towards lower 2θ values which indicated that the lattice of cubic MgO was expanded. As noted, the d-spacing increased from 2.1071 Å to 2.1146 Å. Similarly, the lattice parameter increased from 4.2142 Å to 4.2291 Å, and the unit-cell volume was noted to increase from 74.843 Å^3 to 75.639 Å^3 and calcination temperature increased. This increase in the temperature showed that the lattice was less and less distorted and more and more ordered. This is in agreement with other studies that noted that as the temperature of calcined MgO nanoparticles was increased, the MgO nanoparticles remained thermally stable, and that the uniformity and stability of the MgO nanoparticles' lattice were improved [37,39,44,47]. Most of these studies focused on the fabrication of MgO and the improvement of the MgO's functional properties, as well as the degree of crystallinity of the MgO; however, little consideration was made to the relationship of the lattice parameters and the microstructural behavior of the MgO. The current study for MgO suggested a temperature-dependent XRD analysis of crystallographic parameters, a comparative analysis for MgO, and provided MgO lattice behavior.

From Table I and Fig. 4, the diffraction angle (2θ) corresponding to the (200) plane decreased systematically from $42{,}08°$ at 450 °C to $41{,}67°$ at 700 °C, while the corresponding lattice parameter increased from $4{,}187$ to $4{,}192$, indicating lattice expansion with increasing calcination temperature. The relationship is given by:

$$2\theta_{(200)} = -0{,}000565\,T + 43{,}145. \tag{4}$$

Similarly, the corresponding linear increase in the lattice parameter with temperature follows:

$$a(T) = 5{,}952 \times 10^{-5}T + 4{,}18744,$$
$$450°\text{C} \leq T \leq 700°\text{C}. \tag{5}$$

The decrease in 2θ values and expansion of the lattice parameter are indicative of the thermal relaxation of the MgO lattice and thermal expansion of the crystal structure. This behavior is associated with the reduction of lattice defects and distortion at elevated calcination temperatures [41]. The linear relationship between lattice parameter and calcination temperature indicates that thermal treatment induces predictable changes in lattice dimensions in accordance with Vegard's law. This phenomenon has also been observed in MgO nanocrystals, where increasing calcination temperature resulted in improved crystallinity, reduced lattice defects and distortion, and lattice expansion [48,49].

3.3. Nelson–Riley method

The Nelson–Riley extrapolation method was employed to determine the accurate lattice parameter by minimizing systematic errors associated with X-ray diffraction measurements. The Nelson–Riley function is expressed as

$$f(\theta) = \frac{1}{2}\left(\frac{\cos^2\theta}{\sin\theta} + \frac{\cos^2\theta}{\theta}\right), \tag{6}$$

where θ is the Bragg angle expressed in radians according to the method proposed by Nelson and Riley [50]. The true lattice parameter was obtained by linear extrapolation of the apparent lattice parameter to $f(\theta) = 0$, thereby minimizing systematic errors arising from specimen displacement, sample transparency, and instrumental effects.

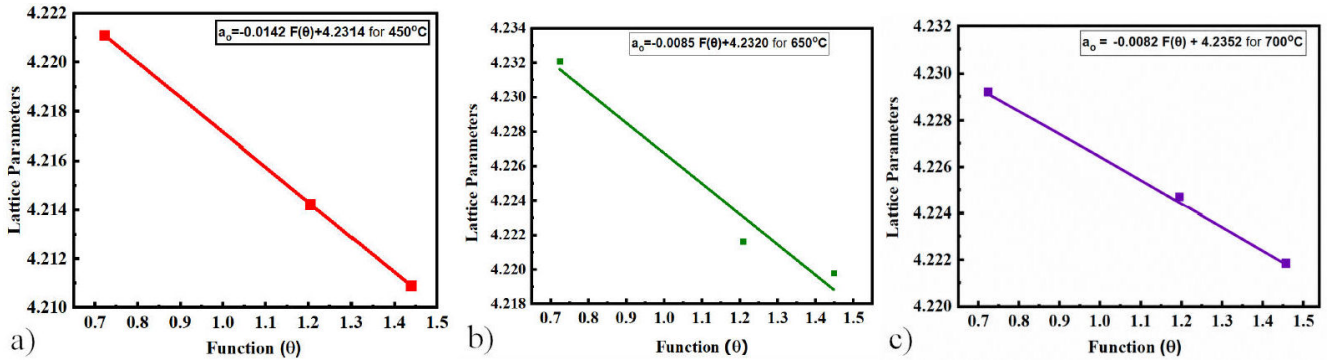


FIGURE 5. Nelson-Riley plot for MgO nanoparticles calcined at 450°C, 650 °C, and 700 °C.

The corresponding Nelson–Riley plots for MgO nanoparticles calcined at 450, 650, and 700°C are presented in Figs. 5a) – 5c). The extrapolated lattice parameter increased from 4.2314 Å at 450°C to 4.2352 Å at 700°C, indicating lattice strain relaxation, improved crystallinity, and enhanced crystal ordering. The excellent linearity observed for all three temperatures confirms the consistency of the diffraction data and the applicability of the Nelson–Riley method for accurate lattice parameter determination.

The gradual increase in the extrapolated lattice parameter with increasing calcination temperature is attributed to the reduction of lattice imperfections, relaxation of residual microstrain, and thermally assisted grain growth. As the calcination temperature increases, atomic diffusion becomes more effective, allowing Mg^{2+} and O^{2-} ions to occupy energetically favorable lattice positions, thereby reducing defect concentration and improving long-range structural ordering.

Furthermore, the intercept values obtained from the linear fits are in close agreement with the lattice expansion trend observed from the XRD analysis, providing independent confirmation of the structural evolution induced by calcination. The consistent increase in lattice parameter also supports the crystallite size enhancement and strain relaxation obtained from the Williamson–Hall analysis, indicating that higher calcination temperatures promote the formation of well-crystallized MgO nanoparticles with improved structural stability [22,36].

3.4. Microstructural parameters analysis

Crystallite size and microstrain are critical factors in determining the microstructural and physical properties of materials. X-ray diffraction (XRD) line profile analysis is among the most reliable methods for estimating crystallite size and the non-uniform lattice strain arising from atomic displacements relative to ideal lattice positions [51]. The broadening of diffraction peaks corresponding to a given (hkl) reflection is mainly attributed to finite crystallite size and lattice strain induced during partial crystallization. For samples exhibiting multiple diffraction peaks, as in the present study, the Williamson-Hall (W-H) method is considered the most appropriate approach [52]. The integral breadth (area-normalized peak width) of each diffraction peak was determined experimentally. The observed peak broadening (B) contains contributions from instrumental effects (b), crystallite size, and microstrain.To obtain physically meaningful microstructural parameters, instrumental broadening must first be corrected using a standard crystalline reference sample.

Instrumental Broadening Correction:

Depending on the assumed peak profile, two different correction approaches are used:

(1) **Gaussian peak profile (strain-dominated broadening):**

$$\beta = \sqrt{B^2 - b^2}. \tag{7a}$$

This quadratic subtraction is valid when peak shapes follow a Gaussian distribution, where broadening contributions are statistically independent.

(2) **Lorentzian (Cauchy) peak profile (size-dominated broadening):**

$$\beta = B - b. \tag{7b}$$

This linear subtraction is appropriate when peak broadening follows a Lorentzian shape, typically associated with finite crystallite size effects. Here, β represents the corrected integral breadth after removing instrumental contribution. After instrumental correction, the total physical broadening can be expressed as the sum of size and strain contributions:

$$\beta_{\text{hkl}} = \beta_{\text{size}} + \beta_{\text{strain}} + \beta_{\text{inst}}. \tag{8}$$

After correction:

$$\beta_{\text{corr}} = \begin{cases} \sqrt{B^2 - b^2}, & \text{(Gaussian assumption)}, \\ B - b, & \text{(Lorentzian assumption)}. \end{cases} \tag{9}$$

For further analysis using the Williamson-Hall method, the corrected broadening is separated into size and strain components:

$$\beta_{\text{corr}} = \beta_{\text{size}} + \beta_{\text{strain}}, \tag{10}$$

or, in squared form for Gaussian-type analysis:

$$\beta^2_{\text{corr}} = \beta^2_{\text{size}} + \beta^2_{\text{strain}}. \tag{11}$$

3.5. Williamson-Hall equation

The Williamson-Hall (W-H) method separates size- and strain-induced broadening by plotting peak broadening against diffraction angle. It relates total broadening (β) to crystallite size (D) and microstrain (ε) [53]:

$$\beta = \frac{k\lambda}{D\cos\theta} + 4\varepsilon\tan\theta, \tag{12}$$

$$\beta\cos\theta = \frac{k\lambda}{D} + 4\varepsilon\sin\theta. \tag{13}$$

For Gaussian approximation, the squared form is:

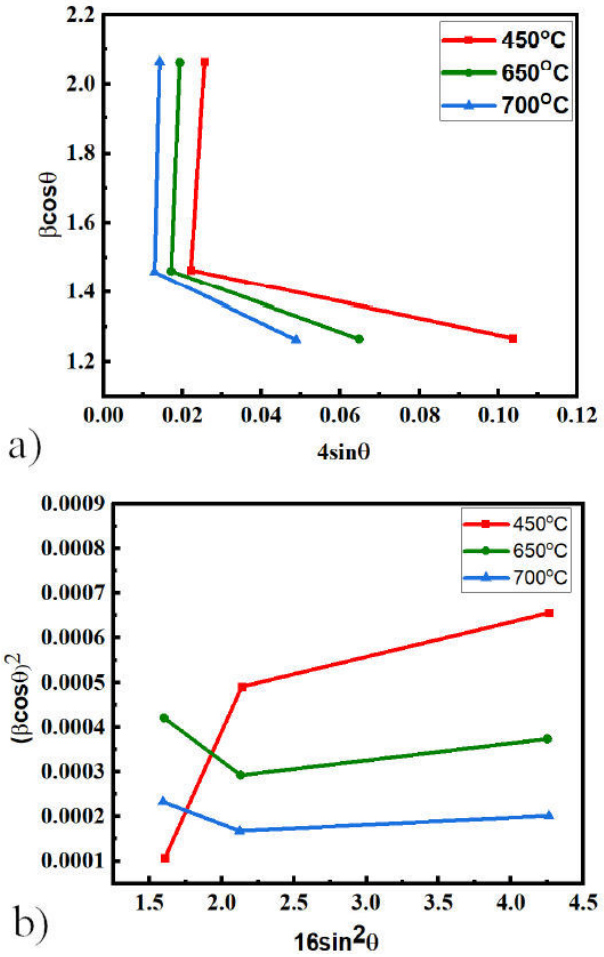


FIGURE 6. Williamson–Hall plots of MgO nanoparticles calcined at 450, 650, and 700°C: a) Lorentzian W–H plots of $\beta\cos\theta$ versus $4\sin\theta$, and b) Gaussian squared-form W–H plots of $(\beta\cos\theta)^2$ versus $16\sin^2\theta$, showing the effect of calcination temperature on crystallite size and lattice microstrain.

$$\beta^2\cos^2\theta = \left(\frac{k\lambda}{D}\right)^2 + 16\varepsilon^2\sin^2\theta, \tag{14}$$

where β is the full width at half maximum (FWHM) after instrumental correction (in radians), θ is the Bragg diffraction angle, k is the shape factor ($k = 0{,}94$), λ is the X-ray wavelength, D is the crystallite size, and ε is the microstrain. The Williamson-Hall (W-H) analysis was conducted to investigate the effect of calcination temperature on the crystallite size and lattice strain of MgO nanoparticles synthesized at 450 °C, 650 °C, and 700 °C (Fig. 6). The plots of $\beta\cos\theta$ versus $4\sin\theta$ and $(\beta\cos\theta)^2$ versus $16\sin^2\theta$ revealed that increasing calcination temperature resulted in larger crystallite size and lower lattice microstrain. At 450 °C, the W-H plots exhibited a higher slope and smaller intercept, indicating significant lattice strain and smaller crystallite size due to incomplete crystallization, lattice distortion, and defect-rich grain boundaries [53]. Limited atomic diffusion at lower calcination temperatures restricts crystallite growth and promotes structural disorder. With increasing calcination temperature to 650 °C and 700 °C, the slope of the W-H plots decreased while the intercept increased, confirming progressive strain relaxation and crystallite growth. Enhanced thermal diffusion at elevated temperatures promotes atomic rearrangement within the MgO lattice, reducing defect density and improving structural ordering. Similar behavior has been reported for Mg-based nanomaterials [26,54]. At 700 °C, the W-H analysis showed the lowest microstrain and the largest crystallite size, indicating improved lattice stability and enhanced long-range atomic ordering. These results demonstrate that calcination temperature plays a critical role in controlling the microstructural evolution and structural quality of MgO nanoparticles.

The Williamson-Hall (W-H) analysis shows that both Lorentzian and Gaussian fittings indicate that crystallite size and lattice microstrain depend on calcination temperature (Fig. 7). For samples calcined at 450 °C, the crystallite sizes were 5.9 nm (Lorentzian) and 6.5 nm (Gaussian). Correspondingly, the microstrain values were recorded as $3{,}7 \times 10^{-3}$ and $0{,}91 \times 10^{-3}$. The relatively high crystallite size and large microstrain indicate incomplete crystallization and lattice distortion due to a high defect density, primarily caused by insufficient atomic diffusion during densification.The microstrain and crystallite size were observed to change with calcination temperature. At 650 °C, the values were $2{,}82 \times 10^{-3}$ (microstrain, Lorentzian) and 7.5 nm (crystallite size), while for Gaussian fitting the corresponding values were $0{,}71 \times 10^{-3}$ and 8.3 nm. Similar temperature-dependent grain growth and strain reduction have also been reported by Chebbi *et al.* for Mg-based ferrite nanomaterials. Contrarily, most studies focus primarily on crystallinity improvement, whereas the present study correlates crystallite growth and W-H microstrain using both Lorentzian and Gaussian fittings of the W-H model. At 700 °C, the crystallite sizes increased to approximately 10.0 nm (Lorentzian)

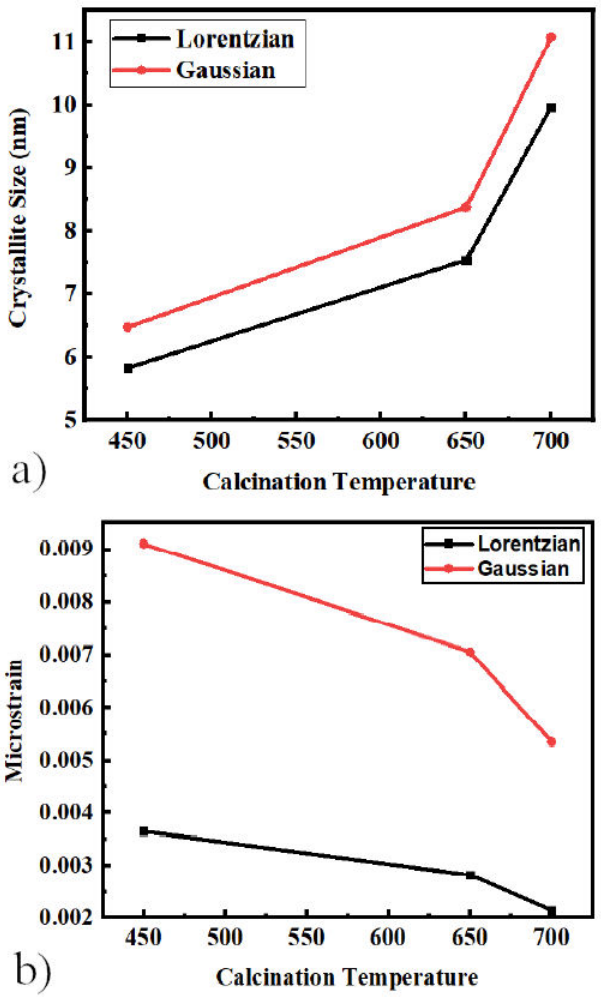


FIGURE 7. Williamson-Hall analysis of MgO nanoparticles showing a) average crystallite size versus calcination temperature and b) microstrain change with calcination temperature based on Lorentzian and Gaussian profile fittings.

and 11.0 nm (Gaussian), while the microstrain values significantly decreased to $2{,}1372 \times 10^{-3}$ and $0{,}5343 \times 10^{-4}$, respectively. The increase in crystallite size and reduction in strain confirm thermally induced grain coalescence, reduced defect concentration, and improved atomic ordering. Similar phenomena have also been reported by Pathak *et al*. for nanomaterials [55]. Overall, the W-H analysis shows that the observed trend is consistent with increased crystallinity and structural stability of MgO nanoparticles, accompanied by internal stress reduction and improved lattice ordering.

3.6. Intrinsic surface stress

Intrinsic surface stress reflects the influence of lattice distortion and surface effects on the structural stability of MgO nanoparticles. Following the reported methodology, the intrinsic surface stress was estimated using [56]

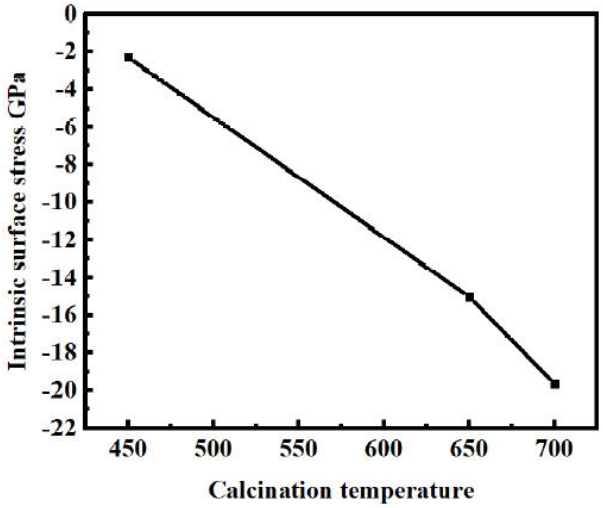


FIGURE 8. Variation of intrinsic surface stress of MgO nanoparticles as a function of calcination temperature.

$$\sigma = \frac{Y}{2\gamma}\left(\frac{a_0 - a}{a_0}\right), \tag{16}$$

where σ is the intrinsic surface stress, Y is the Young's modulus, γ is the Poisson's ratio, a_0 is the strain-free lattice parameter of bulk MgO, and a is the measured lattice parameter. The term $(a_0 - a)/a_0$ represents the relative lattice distortion. Since Y is expressed in GPa, while γ and $(a_0 - a)/a_0$ are dimensionless, the calculated intrinsic surface stress is also expressed in GPa. Negative values of α indicate compressive surface stress, whereas positive values correspond to tensile surface stress.

Figure 8 illustrates the variation of intrinsic surface stress with calcination temperature. The intrinsic surface stress becomes progressively more negative with increasing calcination temperature, indicating an increase in the magnitude of compressive surface stress. At 450 °C, the intrinsic surface stress is approximately $-2{,}30$ GPa, which is associated with incomplete crystallization, limited atomic diffusion, and a relatively high concentration of lattice defects. Increasing the calcination temperature to 650 °C results in a larger compressive stress of approximately $-15{,}0$ GPa due to improved lattice ordering and defect reduction. At 700 °C, the intrinsic surface stress reaches approximately $-19{,}8$ GPa, indicating enhanced grain densification, improved atomic packing, and greater structural stability. The progressive increase in compressive intrinsic surface stress demonstrates that calcination promotes lattice stabilization and improves the crystallinity of MgO nanoparticles [57].

The crystallographic Young's modulus was estimated from the intrinsic surface stress and the average microstrain using

$$E(\text{hkl}) = \frac{\sigma}{\langle \varepsilon \rangle}, \tag{15}$$

where σ is the intrinsic surface stress calculated using Eq. (16), and $\langle \varepsilon \rangle$ is the average microstrain obtained from the

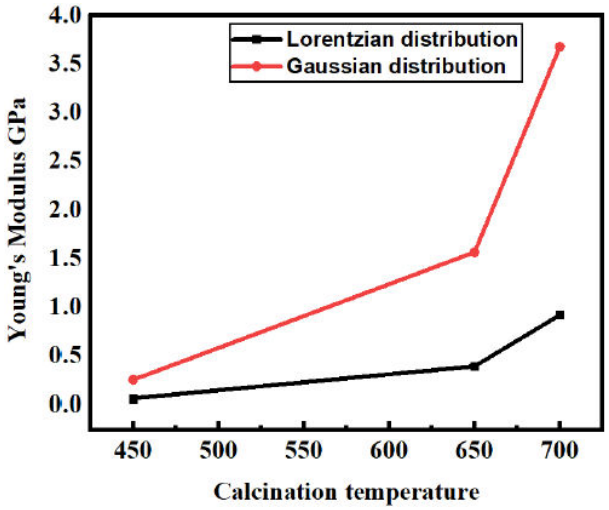


FIGURE 9. Variation of crystallographic Young's modulus of MgO nanoparticles obtained from Lorentzian and Gaussian Williamson–Hall analyses.

Williamson–Hall analysis [36]. The calculated values of $E(hkl)$ for each calcination temperature are presented in Fig. 9. These values provide information about the elastic response of the crystallographic planes.

Figure 9 shows the variation of Young's modulus with calcination temperature for both Lorentzian and Gaussian distributions. In both fitting methods, Young's modulus increases with increasing calcination temperature, indicating an enhancement in the elastic stiffness of the MgO nanoparticles. The Lorentzian values increase from 0.0631 to 0.9191 GPa, whereas the Gaussian values increase from 0.2523 to 3.6766 GPa as the calcination temperature increases from 450 to 700 °C. The higher values obtained from the Gaussian fitting indicate greater sensitivity to microstructural evolution. The increase in Young's modulus is consistent with the improvement in crystallinity, reduction of lattice defects, and enhanced atomic ordering produced by high-temperature calcination [58].

Table II summarizes the Williamson–Hall parameters of MgO nanoparticles. Increasing the calcination temperature results in a gradual increase in crystallite size and a corresponding decrease in lattice microstrain and dislocation density for both Lorentzian and Gaussian analyses. The reduction in microstrain and defect density indicates progressive lattice relaxation and improved structural ordering. These microstructural changes are accompanied by an increase in the magnitude of compressive intrinsic surface stress and an increase in Young's modulus, confirming that high-temperature calcination enhances the structural stability and elastic response of MgO nanoparticles [36,38].

TABLE II. Williamson–Hall parameters of MgO nanoparticles at different calcination temperatures.

Temp. (°C)	D_L (nm)	D_G (nm)	ε_L ($\times 10^{-3}$)	ε_G ($\times 10^{-3}$)	δ ($\times 10^{14}$ m^{-2})
450	5.8266	6.4741	3.6433	0.9108	22.256
650	7.5357	8.3730	2.8218	0.7054	13.305
700	9.9681	11.0757	2.1372	0.5343	7.605

3.7. Lattice strain estimation

Strain is the change in dimensions of a sample compared to its original length and can be either constant or irregular. Isotropic expansion or contraction of a unit cell, shifting XRD peaks without broadening, is due to uniform strain. Non-uniform strain, which is caused by defects, deformation, and incomplete crystallization, shifts atoms in an irregular manner and causes broadening of XRD peaks [59]. This strain is often expressed as:

$$\text{Lattice Strain} = \frac{\Delta a}{a_0}. \tag{16}$$

Here, Δa represents the deviation of the lattice parameter from the strain-free reference state a_0, which is taken as the equilibrium lattice parameter in the absence of applied stress or thermal strain. Lattice strain is associated with variations

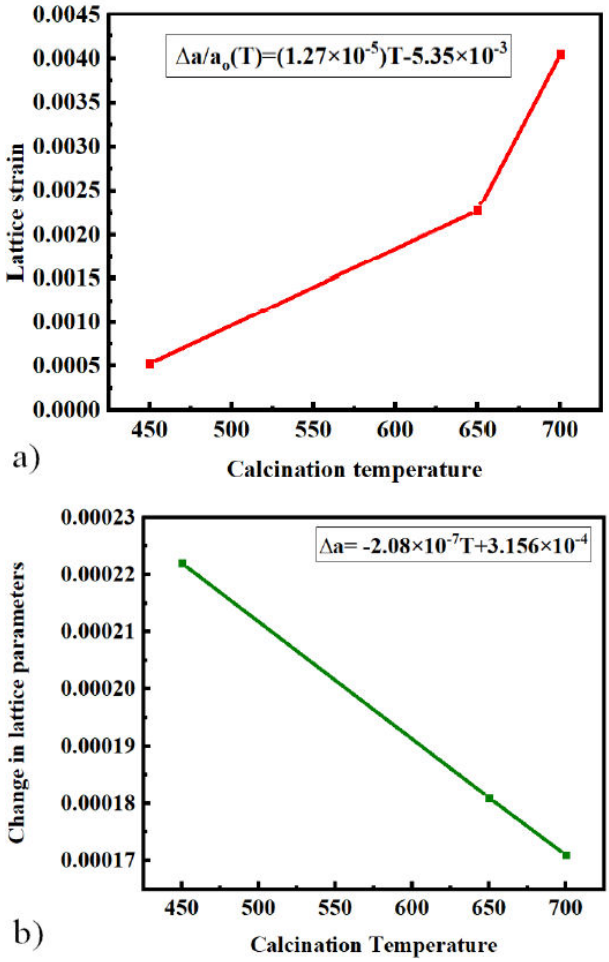


FIGURE 10. Variation of lattice strain ($\Delta a/a_0$) with calcination temperature for MgO nanoparticles.Evolution of the lattice parameter deviation (Δa) with calcination temperature.

in the lattice parameter ratio ($\Delta a/a_0$). Figure 10 shows that the lattice strain of MgO nanoparticles decreases progressively with increasing calcination temperature. The higher strain observed at 450 °C is attributed to incomplete crystallization, smaller crystallite size, and structural disorder due to lattice defects. Limited thermal energy at lower temperatures restricts atomic diffusion and lattice rearrangement, resulting in increased internal strain. At higher calcination temperatures (650 °C and 700 °C), enhanced thermal diffusion promotes crystallite growth and lattice relaxation, leading to reduced microstrain and improved structural ordering [60,61]. The Williamson-Hall analysis further indicates that increasing calcination temperature causes a slight increase in lattice deformation parameter (Δa), suggesting thermally induced lattice expansion and structural stabilization of the cubic MgO phase, as shown in Fig. 10. These results confirm that elevated calcination temperatures reduce lattice defects and improve the structural stability of MgO nanoparticles.

3.8. Dislocation density

Dislocation density refers to the total length of dislocation lines per unit volume and is an important parameter for defining structural imperfections in nanocrystalline materials. A high dislocation density indicates significant internal strain, lattice distortion, and low crystallinity. A reduced dislocation density indicates improved crystallinity, better structural ordering, and reduced lattice defects. The dislocation density (ρ) can be calculated from the Williamson-Smallman relation:

$$\rho = \frac{15\,\varepsilon}{aD}, \tag{17}$$

where ε represents the microstrain obtained from Williamson-Hall analysis, a denotes the lattice parameter, and D signifies the crystallite size. The equation incorporates both strain and crystallite size, thus enabling a more precise estimation of the defect density in strained nanomaterials.

As shown in Fig. 11, dislocation density for MgO nanoparticles decreases with an increase in calcination temperature and is observed for both Lorentzian and Gaussian distributions. Dislocation density is highest at 450 °C owing to the small crystallite size, high internal strain, and incomplete lattice ordering resulting from low-temperature calcination [62]. Calcination temperatures of 650 °C and 700 °C promote greater atomic ordering and grain growth, which leads to reduced lattice distortion and consequently a decrease in dislocation density, indicating improved structural and crystalline quality of MgO nanoparticles. This also confirms enhanced structural stability at higher temperatures. The Lorentzian profile shows higher dislocation density than the Gaussian profile, indicating that Lorentzian fitting corresponds to higher strain and more pronounced peak broadening compared to Gaussian fitting. A similar decrease in dislocation density and lattice defects with increasing calcination temperature has been reported for Cr-substituted Mg-Co

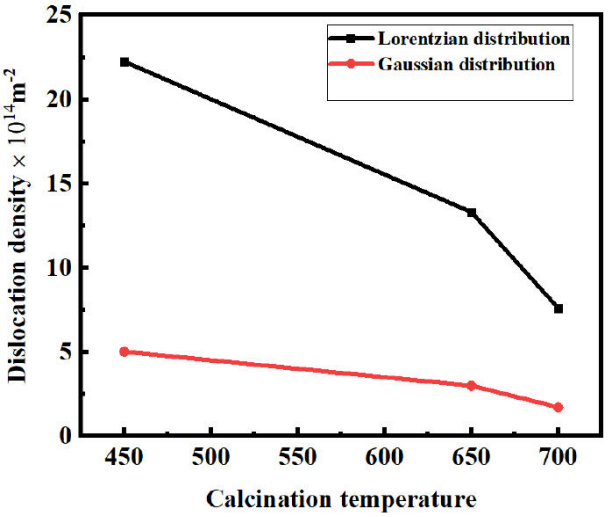


FIGURE 11. Variation of dislocation density (ρ) with calcination temperature for MgO nanoparticles, calculated using Lorentzian and Gaussian profiles via the Williamson-Smallman method.

ferrites by Chebbi *et al.* [25]. This was attributed to grain growth, strain relaxation, and improved structural ordering at higher temperatures. Jdey *et al.* [28] reported similar behavior in $Mg_{0,6}Cu_{0,4}FeCrO_4$ ferrites, while Harrabi *et al.* [37] demonstrated improved lattice stability and enhanced grain boundary coherence in Mg-Co-Cu ferrites at elevated calcination temperatures.Most of these studies focused on substituted ferrite systems with complex magnetic, electrical, and cation distribution effects, making interpretation of pure strain-driven systems more challenging. In contrast, the present work focuses on structurally simple cubic MgO nanoparticles, analyzing thermally induced defect evolution using comparative Lorentzian and Gaussian Williamson-Hall analysis [63]. The study demonstrates that increasing calcination temperature reduces lattice defects, enhances structural ordering, and improves the microstructural stability of MgO nanoparticles. The comparative analysis shows that present MgO nanoparticles and previously reported Mg-based ferrite systems have a lot in common. In those systems, higher calcination temperatures resulted in larger crystallite sizes, smaller lattice strains, and fewer defects due to thermally activated diffusion. Unlike ferrite materials that have complex structures and magnetic and cation distribution, our study focuses on MgO cubic nanoparticles, which have simpler structures. Our research also compares Lorentzian and Gaussian Williamson-Hall methods to evaluate thermally induced size-strain evolution.

4. Conclusion

This paper investigates the synthesis and post-synthesis characterization of MgO nanoparticles. MgO nanoparticles were synthesized via the co-precipitation method, followed by a post-synthesis morphology control procedure. The structural and microstructural changes of the calcined samples we-

re analyzed using X-ray diffraction (XRD), confirming the formation of a cubic single-phase MgO structure.Peak broadening observed in the XRD patterns indicates the presence of nanoscale crystallites, which were quantitatively analyzed using the Williamson-Hall (W-H) method. The W-H analysis reveals that calcination temperature significantly influences crystallite size and leads to a reduction in lattice microstrain, dislocation density, and structural defects through enhanced grain growth and strain relaxation mechanisms.Post-calcination XRD analysis at room temperature reveals that the crystallite size increases from 5–6 nm at 450 °C to 10–11 nm at 700 °C. Improved atomic ordering at elevated temperatures is further evidenced by shifts in XRD peak positions, indicating an increase in lattice parameter and unit-cell volume. Further analysis using Lorentzian and Gaussian peak fitting confirms these structural changes and supports the observed enhancement in crystallographic ordering. This study establishes a clear relationship between calcination temperature and crystallite size, defect concentration, and structural stability of MgO nanoparticles.The Williamson-Hall method is highlighted as a powerful tool for evaluating microstructural transformations in MgO nanomaterials. Overall, the results demonstrate that controlled calcination is an effective approach for tailoring the crystallite size, lattice strain, defect concentration, and structural stability of MgO nanoparticles for advanced functional applications.

1. M. S. Chavali and M. P. Nikolova, Metal oxide nanoparticles and their applications in nanotechnology, *SN applied sciences,* **1** (2019) 607.
2. Y. Yoon, P. L. Truong, D. Lee, and S. H. Ko, Metal-oxide nanomaterials synthesis and applications in flexible and wearable sensors, *ACS Nanoscience Au,* **2** (2021) 64-92.
3. N. Baig, I. Kammakakam, and W. Falath, Nanomaterials: A review of synthesis methods, properties, recent progress, and challenges, *Materials advances,* **2** (2021) 1821.
4. E. S. Araújo, M. F. Pereira, G. M. da Silva, G. F. Tavares, C. Y. Oliveira, and P. M. Faia, A review on the use of metal oxide-based nanocomposites for the remediation of organicscontaminated water via photocatalysis: fundamentals, bibliometric study and recent advances, *Toxics,* **11** (2023) 658.
5. A. Dey, Semiconductor metal oxide gas sensors: A review, *Materials science and Engineering: B,* **229** (2018) 206.
6. B. Saruhan, R. Lontio Fomekong, and S. Nahirniak, Influences of semiconductor metal oxide properties on gas sensing characteristics, *Frontiers in Sensors,* **2** (2021) 657931.
7. A. Asghar, K. Khan, O. Hakami, W. M. Alamier, S. K. Ali, T. Zelai, M. S. Rashid, A. K. Tareen, and E. A. Al-Harthi, Recent progress in metal oxide-based electrode materials for safe and sustainable variants of supercapacitors, *Frontiers in Chemistry,* **12** (2024) 1402563.
8. D. Dong, S. S. Dhanabalan, P. F. M. Elango, M. Yang, S.Walia, S. Sriram, and M. Bhaskaran, Emerging applications of metaloxide thin films for flexible and stretchable electronic devices, *Applied Physics Reviews,* **10** (2023).
9. A. M. Negrescu, M. S. Killian, S. N. Raghu, P. Schmuki, A. Mazare, and A. Cimpean, Metal oxide nanoparticles: review of synthesis, characterization and biological effects, *Journal of Functional Biomaterials,* **13** (2022) 274.
10. M. G. Kim, J. M. Kang, J. E. Lee, K. S. Kim, K. H. Kim, M. Cho, and S. G. Lee, Effects of calcination temperature on the phase composition, photocatalytic degradation, and virucidal activities of TiO2 nanoparticles, *ACS Omega,* **6** (2021) 10668.
11. M. Rabiei, A. Palevicius, A. Dashti, S. Nasiri, A. Monshi, A. Doustmohammadi, A. Vilkauskas, and G. Janusas, Xray diffraction analysis and williamson-hall method in USDM model for estimating more accurate values of stress-strain of unit cell and super cells of hydroxyapatite, confirmed by ultrasonic pulse-echo test, *Materials,* **14** (2021) 2949.
12. J. Hornak, P. Trnka, P. Kadlec, O. Michal, V. Mentlík, P. Šutta, G. M. Csányi, and Z. A. Tamus, Magnesium oxide nanoparticles: dielectric properties, surface functionalization and improvement of epoxy-based composites insulating properties, *Nanomaterials,* **8** (2018) 381.
13. M.-A. Gatou, E. Skylla, P. Dourou, N. Pippa, M. Gazouli, N. Lagopati, and E. A. Pavlatou, Magnesium oxide (MgO) nanoparticles: synthetic strategies and biomedical applications, *Crystals,* **14** (2024) 215.
14. S. E. Elashery, I. Ibrahim, H. Gomaa, M. M. El-Bouraie, I. A. Moneam, S. S. Fekry, and G. G. Mohamed, Comparative study of the photocatalytic degradation of crystal violet using ferromagnetic magnesium oxide nanoparticles and MgO-bentonite nanocomposite, *Magnetochemistry,* **9** (2023) 56.
15. M. Ludwig *et al*., Corrosion resistance of MgO,based refractory raw materials to pbo-rich cu slag determined by hot-stage microscopy and pellet corrosion test, *Materials,* **15** (2022) 725.
16. L. M. Al-Harbi, M. Ezzeldien, A. A. Elhenawy, and A. H. Said, Assessment of the bioactivity of bioinspired magnesium oxide nanoparticles from the azadirachta indica extract, *Frontiers in Bioengineering and Biotechnology,* **12** (2024) 1480694.
17. X. Li, J. Zhao, X. Hong, Y. Yang, X. Tang, Y. Zhu, and T. Li, Calcination-dependent surface defect variation and antibacterial activity of magnesium oxide nanoplates, *ChemistrySelect,* **5** (2020) 3201.
18. J. P. Singh, V. Singh, A. Sharma, G. Pandey, K. H. Chae, and S. Lee, Approaches to synthesize MgO nanostructures for diverse applications, *Heliyon*, **6** (2020).
19. D. Suhag, A. Thakur, and P. Thakur, Integrated nanomaterials and their applications. Springer, (2023).
20. D. Fischer, D. Zagorac, K. Küster, and J. C. Schön, Synthesis of two structurally different MgO Films containing dioxygen species: Dioxygen embedded at grain boundaries, and as components of a superfilled rock salt structure, *Coatings*, **14** (2024) 1563.
21. Y. Li *et al*., Photocatalytic water splitting on MgO with exceptional quantum efficiencies at elevated temperatures, *Nature Communications,* **10** (2019) 4421.

22. N. H. Khdary, A. S. Alayyar, L. M. Alsarhan, S. Alshihri, and M. Mokhtar, Metal oxides as catalyst/supporter for carbon dioxide capture and conversion, review, *Catalysts,* **12** (2022) 300.

23. N.-Y. T. Nguyen, N. Grelling, C. L. Wetteland, R. Rosario, and H. Liu, Antimicrobial activities and mechanisms of MgO nanoparticles against pathogenic bacteria, yeasts, and biofilms, *Scientific Reports,* **8** (2018) 16260.

24. A. Almontasser and A. Parveen, Probing the effect of nickel, cobalt, and iron doping concentrations on the antibacterial behaviors of MgO nanoparticles, *Scientific Reports,* **12** (2022) 7922.

25. M. Chebbi, S. Mansouri, S. Hcini, I. Ghiloufi, A. Mimouni, and L. El Mir, Investigating the impact of calcination temperature on the structural and optical properties of chromium-substituted Mg-Co ferrite nanoparticles, *Journal of Molecular Structure,* **1295** (2024) 136740.

26. W. Zarai *et al*., *Journal of Inorganic and Organometallic Polymers and Materials*, **36** (2025) 243.

27. M. Chebbi, S. Mansouri, S. Hcini, N. Hamdaoui, and L. El Mir, Study of sintering temperature effects on the structural and electrical properties of mg0. 6co0. 4fecro4 ferrites synthesized by the sol-gel method, *Journal of Inorganic and Organometallic Polymers and Materials*, **33** (2023) 1201.

28. W. Jdey, T. Mzoughi, N. Hamdaoui, S. Hcini, and S. Mansouri, Impact of the calcination temperature on structural, electrical and dielectric properties for spinel ferrites, *Journal of Inorganic and Organometallic Polymers and Materials,* **33** (2023) 3485.

29. T. V. Sagar, T. S. Rao, and K. C. B. Naidu, Effect of calcination temperature on structural, magnetic, and dielectric properties of mg0.75zn0.25al0.2fe1.8o4 ferrites, *Journal of Materials Science: Materials in Electronics,* (2024).

30. R. B. Rotti *et al*., Green synthesis of MgO nanoparticles and its antibacterial properties, *Frontiers in Chemistry,* **11** (2023) 1143614.

31. S. Yousefi, B. Ghasemi, and M. P. Nikolova, Morpho/optostructural characterizations and XRD-assisted estimation of crystallite size and strain in MgO nanoparticles by applying Williamson-Hall and size-strain techniques, *Journal of Cluster Science,* **33** (2022) 2197.

32. B. Himabindu, N. L. Devi, and B. R. Kanth, Microstructural parameters from x-ray peak profile analysis by Williamson- Hall models; a review, *Materials Today: Proceedings,* **47** (2021) 4891.

33. N. Rani, S. Chahal, A. S. Chauhan, P. Kumar, R. Shukla, and S. Singh, X-ray analysis of MgO nanoparticles by modified Scherer's Williamson-Hall and size-strain method, *Materials Today: Proceedings,* **12** (2019) 543.

34. R. Balakrishnan *et al.*, Thermal decomposition behavior and characterization of magnesium oxide nanoparticles synthesized by precipitation method, *Ceramics International,* **45** (2019) 18866.

35. G. Kasi *et al*., Effect of calcination temperatures on crystallite size, particle size, and antimicrobial activity of synthesized MgO and its cytotoxicity, *International Journal of Molecular Sciences,* **26** (2025) 4868.

36. X. Zhang, Y. Zheng, X. Feng, X. Han, Z. Bai, and Z. Zhang, Calcination temperature-dependent surface structure and physicochemical properties of magnesium oxide, *RSC advances,* **5** (2015) 86102.

37. D. Harrabi, S. Hcini, J. Dhahri, N. Hamdaoui, R. Charguia, M. Bouazizi, and S. Mansouri, Structural, magnetic, and dielectric properties for Mg0 spinel ferrites prepared under different calcination temperatures, *Journal of Superconductivity and Novel Magnetism,* **36** (2023) 1549.

38. W. Jdey, N. Hamdaoui, S. Hcini, S. Mansouri, and L. El Mir, Enhancement of the optical properties of Mgo. 6 Cuo. 4 FeCrO4 spinel ferrite via heat treatment, *Optical Materials,* **147** (2024) 114666.

39. M. Bura, G. Singh, D. Gupta, N. Malik, A. Salim, A. Kumar, R. Singhal, S. Kumar, and S. Aggarwal, Transition in the preferred orientation of RF sputtered ZnO/Si thin films by thermal annealing: Structural, morphological, and optical characteristics, *Optical Materials,* **133** (2022) 113024.

40. H. T. Sim, M. Gençaslan, and M. Merdan, Synthesis of MgO nanoparticles via the sol-gel method for antibacterial applications, investigation of optical properties and comparison with commercial magnisum oxide, *Discover Applied Sciences,* **6** (2024) 577.

41. J. P. Singh and K. H. Chae, Local electronic structure perspectives of nanoparticle growth: the case of MgO, *ACS Omega,* **4** (2019) 7140.

42. S. Dolabella, A. Borzì, A. Dommann, and A. Neels, Lattice strain and defects analysis in nanostructured semiconductor materials and devices by high-resolution X-ray diffraction: Theoretical and practical aspects, *Small Methods*, **6** (2022) 2100932 .

43. H. Zhang, J. Hu, J. Xie, S. Wang, and Y. Cao, A solid-state chemical method for synthesizing MgO nanoparticles with superior adsorption properties, *RSC Advances,* **9** (2019) 2011.

44. K. Ishimoto, T. Tanaka, Y. Ohki, Y. Sekiguchi, and Y. Murata, Thermally stimulated current in low-density polyethylene/mgo nanocomposite-on the mechanism of its superior dielectric properties, *IEEJ Transactions on Fundamentals and Materials,* **129** (2009) 97.

45. T. Kikuma, N. Fuse, T. Tanaka, Y. Murata, and Y. Ohki, Filler-content dependence of dielectric properties of lowdensity polyethylene/mgo nanocomposites, *IEEJ Transactions on Fundamentals and Materials*, **126** (2006) 1072.

46. S. Mehanathan *et al*., Magnesium oxide nanoparticles for the adsorption of pentavalent arsenic from water: Effects of calcination, *Membranes*, **13** (2023) 475.

47. C. Shi *et al*., Barium titanate nanoparticles: Short-range lattice distortions with long-range cubic order, *Physical Review B,* **98** (2018) 085421.

48. T. H. Ulucan, J. Wang, E. Onur, S. Chen, M. Behrens, and C. Weidenthaler, Unveiling the structure-property relationship of MgO-supported Ni ammonia decomposition catalysts from bulk to atomic structure by in situ/operando studies, *ACS Catalysis*, **14** (2024) 2828.

49. M.-A. Gatou, N. Bovali, N. Lagopati, and E. A. Pavlatou, MgO nanoparticles as a promising photocatalyst towards rhodamine B and rhodamine 6G degradation, *Molecules*, **29** (2024) 4299.

50. J. B. Nelson and D. P. Riley, An experimental investigation of extrapolation methods in the derivation of accurate unit-cell dimensions of crystals, *Proceedings of the Physical Society*, **57** (1945) 160.
51. P. Scardi *et al.*, Size-strain separation in diffraction line profile analysis, *Journal of Applied Crystallography*, **51** (2018) 831.
52. P. P. Rodenbough, C. Zheng, Y. Liu, C. Hui, Y. Xia, Z. Ran, Y. Hu, and S.-W. Chan, Lattice expansion in metal oxide nanoparticles: MgO, Co3O4, & Fe3O4, *Journal of the American Ceramic Society*, **100** (2017) 384.
53. B. Pathak, A. Yadav, P. Choudhary, M. Varshney, and A. Mishra, Structural and phonon modes study of nano ceramics coal2o4 synthesized by sol-gel route, *in AIP Conference Proceedings,* **2100** (2019) 020175.
54. V. Daniele, A. R. Volpe, P. Cesare, and G. Taglieri, MgO nanoparticles obtained from an innovative and sustainable route and their applications in cancer therapy, *Nanomaterials,* **13** (2023) 2975.
55. Savita, M. Jain, Manju, A. Vij, and A. Thakur, Impact of annealing on the structural properties of MgO nanoparticles by XRD analysis and Rietveld refinement, *in AIP Conference Proceedings*, **2093** (2019) 020024.
56. S. Abinaya and H. P. Kavitha, MgO nanoparticles: effective antilarvicidal and antibacterial agents, *ACS Omega,* **8** (2023) 5225.
57. L. Huang, Z. Yang, and S.Wang, Influence of calcination temperature on the structure and hydration of MgO, *Construction and Building Materials*, **262** (2020) 120776.
58. J. Karamdel et al., Structural, optical and mechanical properties of mgo nanoparticles: effect of calcination temperature, *Journal of Alloys and Compounds,* **735** (2018) 123.
59. J. Madhavi, Comparison of average crystallite size by X-ray peak broadening and Williamson-Hall and size-strain plots for VO2+ doped ZnS/CdS composite nanopowder, *SN Applied Sciences*, **1** (2019) 1509.
60. J. Hornak, Synthesis, properties, and selected technical applications of magnesium oxide nanoparticles: a review, International *Journal of Molecular Sciences*, **22** (2021) 12752.
61. D. Balzar *et al.*, Size-strain line-broadening analysis of the ceria roundrobin sample, *Journal of Applied Crystallography,* **37** (2004) 911.
62. S. Alias, A. Ismail, and A. Mohamad, Effect of pH on ZnO nanoparticle properties synthesized by sol-gel centrifugation, *Journal of Alloys and Compounds*, **499** (2010) 231.
63. G. Williamson and R. Smallman, Dislocation densities in some annealed and cold-worked metals from measurements on the X-ray debye-scherrer spectrum, *Philosophical magazine*, **1** (1956) 34.

Structural, electronic, magnetic, and optical properties of $CuMnInSe_3$ chalcogenide compound

W. Menasri, S. Fetah, and S. Didaoui

Laboratory of materials and renewable energy, Faculty of science, University Pole of M'sila, 28000 M'sila, Algeria.

A. Djerad

Laboratory of Pure and Applied Mathematics, Department of Mathematics, University Pole of Msila, 28000 M'sila, Algeria.

Received 22 November 2023; accepted 13 May 2026

Using density functional theory in conjunction with the FP-LAPW method under the generalized gradient approximation, specifically employing the Perdew 2008 functional GGA-PBEsol, spin-polarized density functional theory computations were conducted to investigate the structural, electronic, and magnetic properties of the quaternary chalcogenide $CuMnInSe_3$ crystal. Both experimental findings and the calculated equilibrium structural parameters exhibit strong concordance. Through an analysis of the spin-polarized band structures and density of states, the half-metallic nature of the studied compound was predicted, characterized by a total magnetic moment of $6\,\mu_B$ per unit cell and an energy gap of 0.644 eV. Furthermore, it was observed that the electronic structure is more accurately represented when incorporating the electronic exchange-correlation via the Tran–Blaha modified Becke–Johnson (TB-mBJ) potential, which was employed to precisely compute the band gap of the compound, resulting in an indirect band gap $(X$–$\Gamma)$ of 1.546 eV. Optical properties were predicted by analyzing the spectra of the real and imaginary components of the permittivity, the reflectivity function, and the absorption coefficient. These calculations suggest that this material has potential as an effective ultraviolet sensor.

Keywords: Quaternary chalcogenide; half-metal; magnetic and optical properties; DFT.

DOI: https://doi.org/10.31349/RevMexFis.72.061002

1. Introduction

$CuMnInSe_3$ is an emerging multifunctional semiconductor combining semiconducting and magnetic properties. It belongs to the I–II–III–VI_3 family of chalcogenides, materials well known for their adjustable band gaps, significant spin–orbit coupling, and varied magnetic behavior, which make them promising candidates for spintronics, nonlinear optics, and optoelectronic technologies [1, 2].

The crystal structure of $CuMnInSe_3$ has been experimentally characterized through X-ray powder diffraction analysis [3, 4]. The compound crystallizes in a tetragonal phase that is closely related to the chalcopyrite structure of $CuInSe_2$. In this structure, the symmetry is reduced from the $I\bar{4}2d$ space group to the closely related $P\bar{4}2c$ space group, which is isostructural with $CuFeInSe_3$ and belongs to the sphalerite-derived structural family [5]. Specifically, $CuMnInSe_3$ adopts a chalcopyrite-type tetragonal structure (space group No. 112) with lattice parameters $a = 5{,}7907$ Å, $c = 11{,}648$ Å, and $V = 390{,}58$ Å^3. These values are very similar to those reported for $CuInSe_2$ ($a = 5{,}781(1)$ Å and $c = 11{,}642(3)$ Å) [6, 7].

Even though $CuMnInSe_3$ has received considerably less attention than its parent compound $CuInSe_2$, it represents a valuable system for studying diluted magnetic semiconductors and holds potential for future technological applications [8]. While some structural data are available, its electronic and magnetic characteristics are still not well established. This gap provides the basis for the present theoretical study, which seeks to investigate the impact of Mn incorporation on structural stability, electronic behavior, and magnetic properties, in order to better understand its multifunctional character and possible applications.

The paper is organized as follows: Section 2 presents the computational details. The findings and their subsequent analysis are presented in Sec. 3. Finally, Sec. 4 summarizes the main conclusions of this study.

2. Computational details

The present study was performed using first-principles calculations within the framework of density functional theory (DFT), as incorporated in the WIEN2k computational package [9]. The calculations relied on the full-potential linearized augmented plane wave (FP-LAPW) method [10], which constitutes the foundation of the present *ab initio* analysis. The structural properties were thoroughly investigated using the generalized gradient approximation for solids (GGA-PBEsol) [11] to describe exchange–correlation effects, as this functional is recognized for its enhanced accuracy in solid-state systems.

To achieve a more accurate description of the electro-

nic structure, the Tran–Blaha modified Becke–Johnson (TB-mBJ) potential [12] was employed in addition to the GGA-PBEsol functional. Implemented within the WIEN2k framework, the TB-mBJ potential has been shown to significantly improve the prediction of band gaps in semiconductors and insulators compared with conventional GGA functionals such as PBE or PBEsol, particularly for materials containing localized d- and f-electrons [13]. Consequently, this potential was adopted to obtain a more reliable estimation of the band-gap energy by reducing the well-known underestimation associated with standard GGA approaches, and to provide a more accurate description of the electronic band structure and density of states of $CuMnInSe_3$, which contains a transition metal with partially occupied $3d$ states.

In this approach, the crystal unit cell is divided into non-overlapping muffin-tin (MT) spheres and an interstitial region separating them. The muffin-tin radii (R_{MT}) for Cu, Mn, In, and Se atoms were set to 2.11, 2.11, 1.99, and 2.00 bohr, respectively. The basic functions were partitioned into core and valence states, using an energy cutoff of $-6{,}0$ Ry to differentiate between the two regions. The Kohn–Sham equations were solved self-consistently. The core states were treated assuming a spherically symmetric charge density confined within the MT spheres, where only the spherical component of the potential was considered. For the valence states, the potential was expanded in spherical harmonics inside the spheres up to $l_{\max} = 10$. In the interstitial region, the wave functions were represented by plane waves. Brillouin zone integrations [14] were performed using 63 k-points in the irreducible Brillouin zone (IBZ), generated from a $12\times12\times6$ Monkhorst–Pack grid. Self-consistency was considered achieved when the total energy convergence reached a threshold smaller than 10^{-5} eV.

3. Results and discussion

3.1. Analysis of structural properties

The $CuMnInSe_3$ compound adopts a tetragonal crystal structure belonging to the space group $P\bar{4}2c$ (No. 112) with two formula units per unit cell ($Z = 2$) [3, 4]. The unit cell of the investigated material is illustrated in Fig. 1.

The total energy as a function of unit-cell volume was computed for the non-magnetic (NM), antiferromagnetic (AFM), and ferromagnetic (FM) configurations of $CuMnInSe_3$. The resulting energy–volume data were fitted

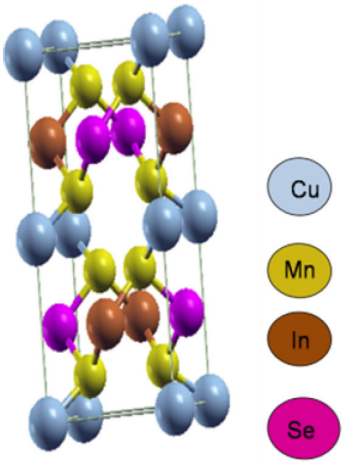


FIGURE 1. Representation of the $CuMnInSe_3$ chalcogenide crystal structure.

to the third-order Birch–Murnaghan equation of state [15], as presented in Fig. 2, to extract the equilibrium structural parameters comprising the equilibrium volume (V_0), the bulk modulus (B), and the pressure derivative (B') of the bulk modulus.

A comparison of the total energies shows that the AFM configuration is more stable than the NM state, whereas the FM configuration possesses the lowest total energy among the considered magnetic arrangements. These results indicate that the ferromagnetic configuration corresponds to the magnetic ground state of the compound. The stabilization of this magnetic state mainly originates from the exchange interactions associated with the Mn $3d$ electrons. Furthermore, the lattice parameters obtained for the FM ground state show excellent agreement with the available experimental data.

The optimized structural parameters, including the relaxed atomic positions, equilibrium lattice constants (a, c, and c/a), equilibrium unit-cell volume (V_0), bulk modulus (B), and pressure derivative (B'), are listed in Table I. The relative deviations between the calculated and experimental lattice constants are less than 1.90 % and 3.50 % for a and c, respectively, confirming the structural stability of the tetragonal phase. These values are also comparable to those of the parent chalcopyrite compound $CuInSe_2$ [7], indicating that Mn incorporation does not significantly affect the unit-cell volume.

TABLE I. Equilibrium structural parameters: lattice constants a (Å) and c (Å), ratio c/a, equilibrium volume per formula unit V_0 (Å^3), bulk modulus B (GPa), pressure derivative B', and relaxed atomic positions for $CuMnInSe_3$.

	a	c	c/a	V_0	B	B'	Atom	Site	x/a	y/b
$CuMnInSe_3$	5.68	11.24	1.98	362.629	56.375	5.475	Cu	$2c$	0	1/2
	5,7907[a]	11,648[a]	2,01[a]	390,58[a]	–	–	Mn	$2e$	0	0
							In	$2b$	1/2	0
							Se	$8n$	0.2509 (0,227[a])	0.2553 (0,255[a])

[a]Ref. [3]

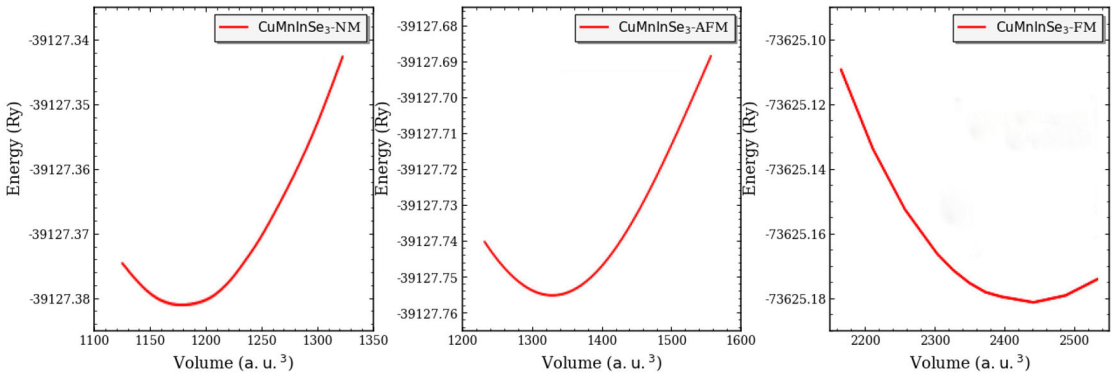


FIGURE 2. Total energy as a function of the unit-cell volume for $CuMnInSe_3$ calculated for different magnetic configurations: non-magnetic (NM), antiferromagnetic (AFM), and ferromagnetic (FM).

To the best of our knowledge, this work provides the first reported estimates of the bulk modulus ($B = 56{,}375$ GPa) and its pressure derivative ($B' = 5{,}475$) for $CuMnInSe_3$. The relatively moderate value of B indicates that the material is mechanically soft and exhibits appreciable compressibility, while B' reflects the variation of compressibility under applied pressure.

3.2. Electronic structure and magnetic behavior

The electronic and magnetic characteristics of $CuMnInSe_3$ were analyzed using spin-polarized calculations. The electronic properties of a crystalline material can be assessed through its band structure and density of states (DOS), which together provide detailed insight into its electronic behavior.

Spin-polarized total DOS and band structures were computed using the FP-LAPW method within the GGA-PBEsol and TB-mBJ frameworks, at the optimized equilibrium geometry. The band structures were plotted along the high-symmetry directions of the first Brillouin zone of the tetragonal lattice, separately for majority (spin-up) and minority (spin-down) channels, as shown in Figs. 3 and 4. The asymmetric distribution of spin-up and spin-down states confirms that $CuMnInSe_3$ is not paramagnetic. In the majority-spin channel, several bands cross the Fermi level, resulting in a high DOS and indicating metallic behavior. In contrast, the minority-spin channel exhibits a clear energy gap around the Fermi level, characteristic of semiconducting behavior. This combination confirms the half-metallic character of $CuMnInSe_3$.

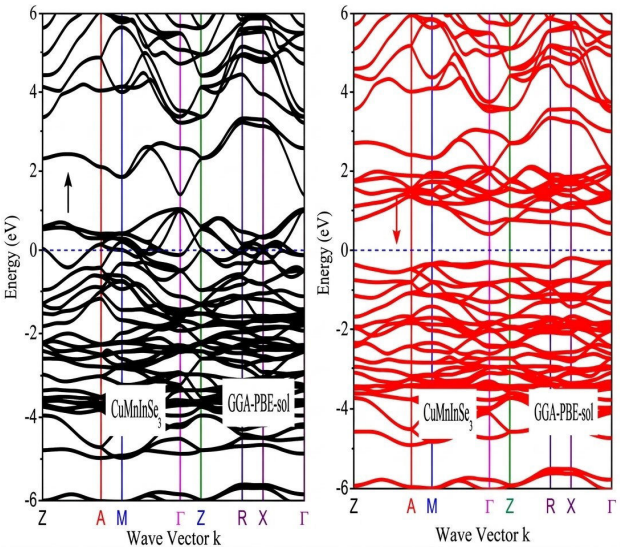


FIGURE 3. Electronic band structure of $CuMnInSe_3$ chalcogenide calculated by GGA-PBEsol.

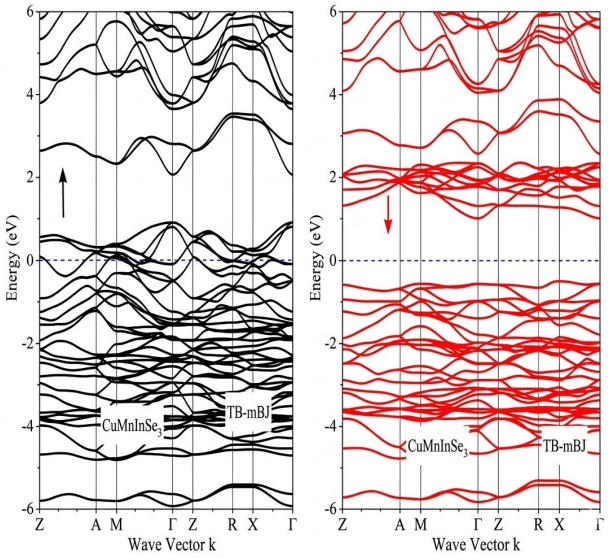


FIGURE 4. Electronic band structure of $CuMnInSe_3$ chalcogenide calculated by TB-mBJ.

The spin-resolved partial DOS, illustrated in Fig. 5, further clarifies the elemental contributions near the Fermi level. The $3d$ states of Cu and Mn dominate the top of the valence band for both spin channels, highlighting their crucial role in shaping the electronic properties of $CuMnInSe_3$. Conversely, the $3p$ states of Cu and Se contribute very little in this energy range. In the conduction band, the spin-down $3d$ states of Mn overwhelmingly dominate, with minimal participation from other atomic orbitals.

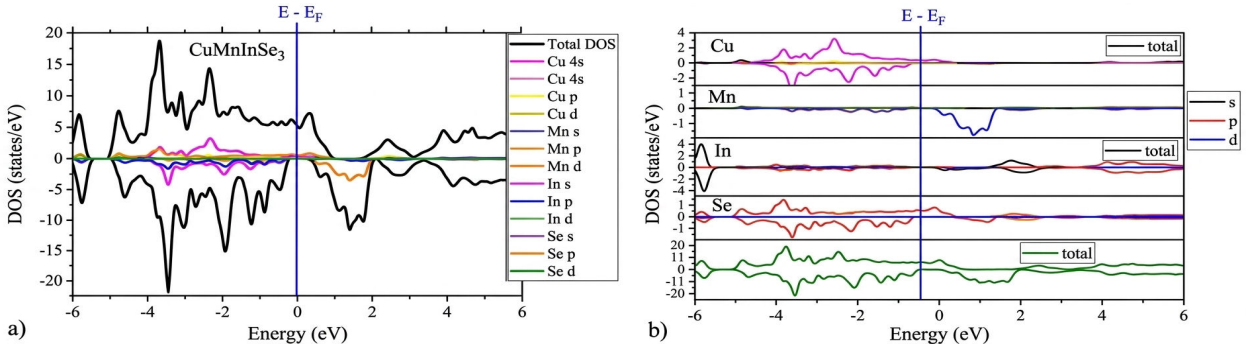


FIGURE 5. Calculated partial and total density of states of CuMnInSe$_3$ chalcogenide obtained by TB-mBJ.

TABLE II. Band gap energy E_g (eV), total and partial magnetic moments (μ_B) for CuMnInSe$_3$ chalcogenide.

	E_g (eV)	μ_{Tot}	μ_{Cu}	μ_{Mn}	μ_{In}	μ_{Se}
GGA-PBEsol	0.644	6.0025	−0,1407	3.18152	0.03756	−0,03756
TB-mBJ	1.546	6.002	−0,2707	3.11252	0.01756	−0,14756

The calculated band gap is indirect, with the valence band maximum located at the M point and the conduction band minimum at the Γ point. While the overall band-structure features obtained from GGA-PBEsol and TB-mBJ functionals are similar, the predicted band-gap values differ significantly, emphasizing the importance of the TB-mBJ potential for accurate band-gap estimation in systems containing transition-metal $3d$ states. Both Cu ($3d^{10}$) and Mn ($3d^5$) atoms have partially filled d-orbitals, which are prone to self-interaction errors in standard DFT. The Tran–Blaha TB-mBJ potential addresses this issue by introducing a semi-local approximation to the exchange potential, better reproducing the derivative discontinuity of the total energy with respect to electron number [12, 16]. For CuMnInSe$_3$, the GGA-PBEsol functional predicts a minority-spin band gap of 0.644 eV, while the inclusion of the mBJ correction increases it to 1.546 eV, bringing it closer to the range observed in related chalcopyrite compounds. The total magnetic moment remains nearly constant at $\sim 6\,\mu_B$ per unit cell, confirming the robustness of the magnetic configuration.

The energy-dependent spin polarization at the Fermi level $P(E_F)$ provides important information about the electronic behavior of a material. For half-metallic systems, $P(E_F)$ reaches unity (100 %) [17, 18]. It is defined as

$$P(E_F) = \frac{\rho^{\uparrow}(E_F) - \rho^{\downarrow}(E_F)}{\rho^{\uparrow}(E_F) + \rho^{\downarrow}(E_F)}, \tag{1}$$

where $\rho^{\uparrow}(E_F)$ and $\rho^{\downarrow}(E_F)$ are the total densities of states for spin-up and spin-down electrons at the Fermi level, respectively.

The electrons at the Fermi level are completely spin-polarized (100 %), since $\rho^{\downarrow}(E_F) = 0$, as illustrated in Fig. 5, confirming that CuMnInSe$_3$ exhibits half-metallic behavior.

The total magnetic moment (in μ_B) is defined as the difference between the number of occupied spin-up and spin-down states [18]. The atomic magnetic moments of Cu, Mn, In, and Se, along with the total integer magnetic moment μ_{tot} of CuMnInSe$_3$, were calculated using both the TB-mBJ and GGA-PBEsol methods and are summarized in Table II. Our results yield a total spin magnetic moment of 6 μ_B per unit cell from both computational approaches, satisfying the requirement for half-metallic materials [17]. Specifically, the Mn atom exhibits a magnetic moment of approximately 3,182 μ_B within GGA-PBEsol and 3,113 μ_B using the TB-mBJ approach. In contrast, Cu and Se atoms display small negative magnetic moments, while In atoms contribute only a very weak magnetic moment.

3.3. Optical properties and analysis

The optical properties of a solid describe the response of a material to incident electromagnetic radiation, leading to polarization effects and the excitation of conduction electrons. The interaction between photons and the electronic structure results in energy loss and charge polarization, constituting the optical response of the system. This can be described by the complex dielectric function

$$\varepsilon_{\alpha\beta}(\omega) = \varepsilon_1^{\alpha\beta}(\omega) + i\,\varepsilon_2^{\alpha\beta}(\omega), \quad \alpha, \beta = x, y, z. \tag{2}$$

The crystal symmetry of the compound implies the following relations for the dielectric tensor components:

$$\varepsilon_i^{xx}(\omega) = \varepsilon_i^{yy}(\omega) \equiv \varepsilon_i^{\parallel}(\omega), \qquad \varepsilon_i^{zz}(\omega) \equiv \varepsilon_i^{\perp}(\omega). \tag{3}$$

TABLE III. Energy ranges for the real part $\varepsilon_1^{xx(zz)}$ of the dielectric function.

	$\varepsilon_1 < 0$ (eV)	$\varepsilon_1 > 0$ (eV)	$\varepsilon_1 = 0$ (eV)
$E \parallel xx$	0.48-0.942, > 8,50	0.942-8.50	0.48, 0.942, 8.50
$E \parallel zz$	0.60-1.15, > 8,50	1.15-8.50	0.48, 0.942, 8.50

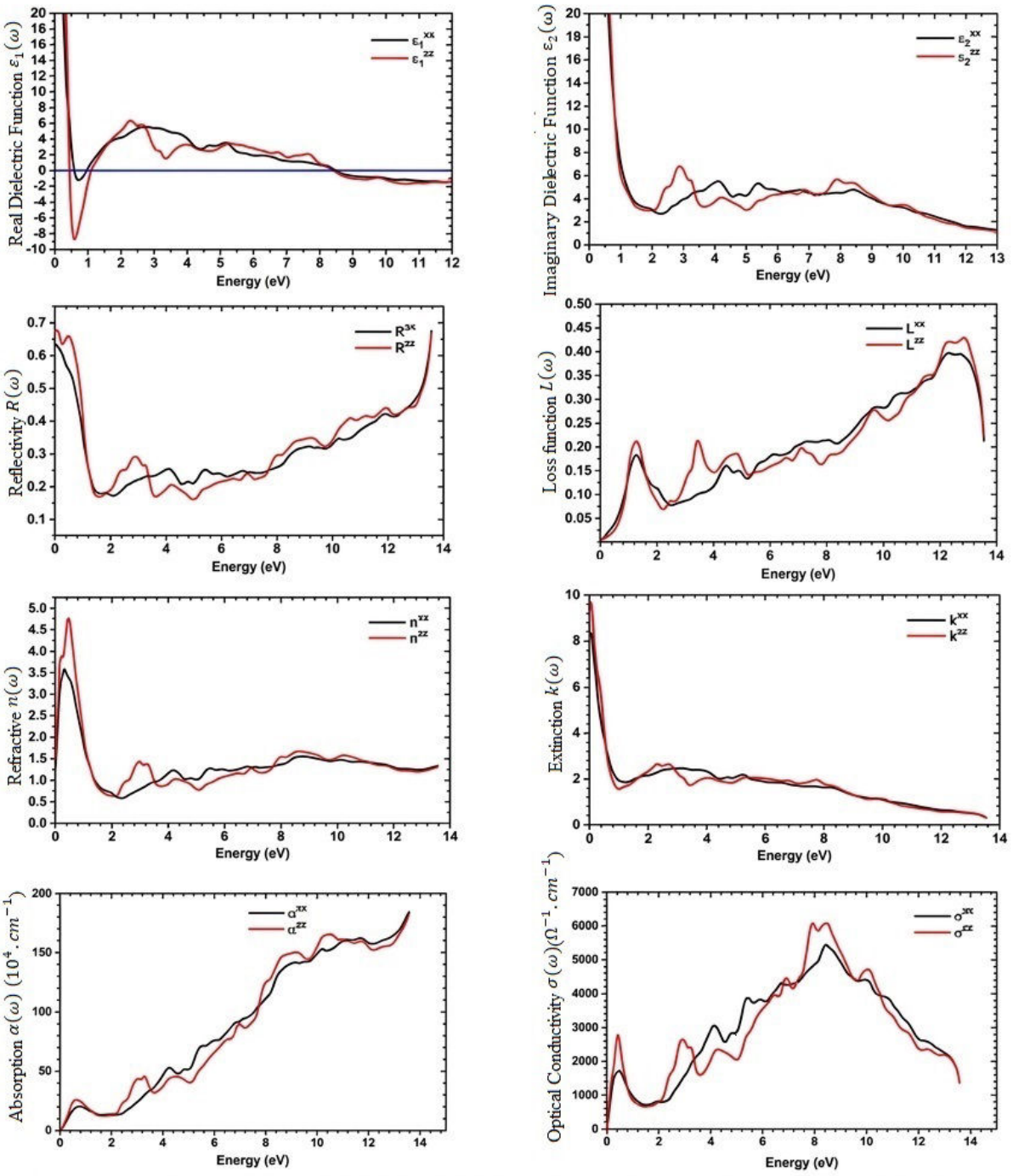


FIGURE 6. Variation of the optical parameters as a function of absorption energy for $CuMnInSe_3$ chalcogenide.

The calculated optical spectra are not identical along the xx and zz directions, indicating optical anisotropy in the compound. Figure 6 shows the variation of the optical parameters as a function of photon energy.

The real part $\varepsilon_1^{xx(zz)}(\omega)$ takes large positive values at low photon energies, reflecting strong electronic polarizability. As the photon energy increases, it gradually decreases. Negative values of $\varepsilon_1^{xx(zz)}$ indicate that electromagnetic waves cannot propagate inside the material in this energy region, resulting in strong reflection and absorption. The photon energies at which $\varepsilon_1^{xx(zz)}$ crosses zero correspond to plasma resonance frequencies. The energy ranges for the sign of the real part are summarized in Table III.

The imaginary part $\varepsilon_2^{xx(zz)}(\omega)$ describes absorption processes arising from interband electronic transitions. In the low-energy region (below $\approx$ 0,85 eV), the finite value of $\varepsilon_2^{xx(zz)}$ indicates the presence of free carriers, characteristic of metallic-like behavior. At higher photon energies, several

TABLE IV. Refractive index values $n_{xx(zz)}(0)$ and energies at which $n_{xx(zz)} = 1$.

$n_{xx}(0)$	$n_{zz}(0)$	$E(n_{xx} = 1)$ (eV)	$E(n_{zz} = 1)$ (eV)
1.26	1.59	1.42, 3.45	1.42, 2.75, 3.45, 5.63

pronounced peaks appear due to enhanced interband transitions. The main peaks are located at approximately 1.92 (2.84) eV, 4.08 (4.26) eV, 5.43 (6.89) eV, and 8.33 (8.02) eV for the xx and zz polarizations, respectively, corresponding to electronic transitions mainly in the visible and ultraviolet energy regions.

The most prominent peaks in the electronic energy loss spectrum occur in the ultraviolet region. The main peaks of $L_{xx}(\omega)$ and $L_{zz}(\omega)$ appear at 12.76 eV and 12.79 eV, respectively. Owing to the metallic nature of the compound, the reflectivity at zero frequency is relatively high, with $R_{xx}(0) = 62\,\%$ and $R_{zz}(0) = 68\,\%$ in the infrared region. In the visible range, the reflectivity reaches about 25 % and 28 % at photon energies of 4.14 eV and 2.91 eV for the xx and zz directions, respectively. A strong reflection of approximately 65 % at 13.54 eV in the ultraviolet region further confirms the metallic behavior and the absence of optical transparency.

The extinction coefficient $K(\omega)$ decreases significantly with increasing photon energy in the visible region and above 5.00 eV, whereas the refractive indices n_{xx} and n_{zz} increase and reach their maximum values at 0.29 eV and 0.45 eV, respectively (Table IV).

Consistent with this metallic behavior, the absorption coefficient starts at very low photon energies and increases rapidly across the visible and ultraviolet regions. The absorption spectrum reaches saturation around 8.47 eV, coinciding with the maximum in the optical conductivity spectrum. Overall, the calculated dielectric function, energy-loss spectrum, reflectivity, refractive indices, extinction coefficient, and absorption coefficient consistently indicate a metallic character, anisotropic optical response, and strong ultraviolet absorption of the compound.

4. Conclusion

The structural, electronic, optical, and magnetic properties of the novel half-metal chalcogenide quaternary compound $CuMnInSe_3$ have been investigated using first-principles calculations. The computed structural parameters were found to be in good agreement with available experimental data. The half-metallic nature of the material was confirmed through analysis of the spin-polarized band structures: the majority-spin channel shows metallic behavior while the minority-spin channel exhibits a semiconducting indirect band gap of 0.644 eV and 1.546 eV within the GGA-PBEsol and TB-mBJ approximations, respectively. A total magnetic moment of $6\,\mu_B$ was obtained from both computational approaches. Additionally, strong absorption in the visible and ultraviolet regions was observed, suggesting that the compound could serve as an effective UV sensor or far-ultraviolet photo-detector.

1. S. A. Chambers and Y. K. Yoo, New materials for spintronics, *MRS Bull.* **28** (2003) 706, https://doi.org/10.1557/mrs2003.210
2. G. A. Medvedkin *et al.*, Novel spintronic materials based on ferromagnetic semiconductor chalcopyrites, *Int. J. Nanosci.* **3** (2004) 39, https://doi.org/10.1142/S0219581X04001791
3. G. E. Delgado, J. A. Flores-Cruz, P. Grima-Gallardo, M. Quintero, and A. Moreno, Synthesis and crystal structure of three new quaternary compounds in the system Cu–Mn–III–Se_3 (III = Al, Ga, In), *Mater. Res.* **21** (2018) e20160748, https://doi.org/10.1590/1980-5373-MR-2016-0748
4. G. E. Delgado, P. Grima-Gallardo, M. Quintero, and C. Chacón, Preparation and structural characterization of the new diamond-like semiconductor $CuMnInSe_3$, *Rev. Téc. Fac. Ing. Univ. Zulia* **41** (2018) 25.
5. A. J. Mora, G. E. Delgado, and P. Grima-Gallardo, Crystal structure of $CuFeInSe_3$ from X-ray powder diffraction data, *Phys. Status Solidi A* **204** (2007) 547, https://doi.org/10.1002/pssa.200622395
6. S. Chen, X. G. Gong, A. Walsh, and S.-H. Wei, Electronic structure and stability of quaternary chalcogenide semiconductors derived from cation cross-substitution of II-VI and I-III-VI_2 compounds, *Phys. Rev. B* **79** (2009) 165211, https://doi.org/10.1103/PhysRevB.79.165211
7. K. S. Knight, The crystal structures of $CuInSe_2$ and $CuInTe_2$, *Mater. Res. Bull.* **27** (1992) 161, https://doi.org/10.1016/0025-5408(92)90209-I
8. Y.-J. Zhao and A. Zunger, Electronic structure and ferromagnetism of Mn-substituted $CuAlS_2$, $CuGaS_2$, $CuInS_2$, $CuGaSe_2$, and $CuGaTe_2$, *Phys. Rev. B* **69** (2004) 104422, https://doi.org/10.1103/PhysRevB.69.104422
9. K. Schwarz, P. Blaha, and G. K. H. Madsen, Electronic structure calculations of solids using the WIEN2k package for material sciences, *Comput. Phys. Commun.* **147** (2002) 71, https://doi.org/10.1016/S0010-4655(02)00206-0
10. P. Blaha, K. Schwarz, P. Sorantin, and S. B. Trickey, Full-potential, linearized augmented plane wave programs for crystalline systems, *Comput. Phys. Commun.* **59** (1990) 399, https://doi.org/10.1016/0010-4655(90)90187-6
11. J. P. Perdew *et al.*, Restoring the density-gradient expansion for exchange in solids and surfaces, *Phys. Rev. Lett.* **100** (2008) 136406, https://doi.org/10.1103/PhysRevLett.100.136406

12. F. Tran and P. Blaha, Accurate band gaps of semiconductors and insulators with a semilocal exchange-correlation potential, *Phys. Rev. Lett.* **102** (2009) 226401, https://doi.org/10.1103/PhysRevLett.102.226401

13. D. Koller, F. Tran, and P. Blaha, Merits and limits of the modified Becke–Johnson exchange potential, *Phys. Rev. B* **83** (2011) 195134, https://doi.org/10.1103/PhysRevB.83.195134

14. P. E. Blöchl, O. Jepsen, and O. K. Andersen, Improved tetrahedron method for Brillouin-zone integrations, *Phys. Rev. B* **49** (1994) 16223, https://doi.org/10.1103/PhysRevB.49.16223

15. F. D. Murnaghan, The compressibility of media under extreme pressures, *Proc. Natl. Acad. Sci.* **30** (1944) 244, https://doi.org/10.1073/pnas.30.9.244

16. D. Koller, F. Tran, and P. Blaha, Improving the modified Becke–Johnson exchange potential, *Phys. Rev. B* **85** (2012) 155109, https://doi.org/10.1103/PhysRevB.85.155109

17. I. Galanakis, P. H. Dederichs, and N. Papanikolaou, Slater–Pauling behavior and origin of the half-metallicity of the full-Heusler alloys, *Phys. Rev. B* **66** (2002) 174429, https://doi.org/10.1103/PhysRevB.66.174429

18. I. I. Mazin, How to define and calculate the degree of spin polarization in ferromagnets, *Phys. Rev. Lett.* **83** (1999) 1427. https://doi.org/10.1103/PhysRevLett.83.1427

Studying the properties of prepared kaolin/epoxy nanocomposites for flame retardancy

M. T. Abd and I. N. Kashkool

Bilad Al Rafidain University, College of Medical and Health Technology, Iraq.

Saif Khalel Jasim

Ministry of Education. Diyala Education Directorate, Diyala, Iraq.
e-mail: saifalaosy@gmail.com

Received 12 November 2025; accepted 8 June 2026

Numerous everyday goods, including fabrics, electrical appliances, vehicles, and airplanes, are currently undergoing extensive testing and inspection for their flammability features. The results of the study showed that adding 10 % by weight of nano-kaolin achieved the best flame resistance performance, recording the highest limiting oxygen index (LOI) and lowest rate of burn (RB) compared to pure epoxy, indicating the formation of an effective insulating char layer. By lowering the total fire risk associated with the use of highly flammable raw materials in goods such as textiles, apparel, composites, and plastics, flame retardants perform a critical protective role in preserving lives and property. In this study, kaolin and epoxy were used to prepare a nanocomposite flame retardant. The used kaolin was tested by X-ray diffraction and (AFM) tests. The results showed that the powders possess multi-phases (presence of quartz and goethite phases alongside kaolinite) and also have a mean grain size of (38 nm) according to AFM results showing a homogeneous distribution of particles and root mean square (RMS) of (12.25). Also, the energy-dispersive spectroscopy analysis (EDX) showed that the presence of the essential elements (Al, Si, O) plus trace amounts of Fe and Ti of these powders was accurate and clear. The nanocomposites were prepared by mixing the kaolin nanopowder with the epoxy resin by weight percentages of (2, 4, 6, 8 and 10 %). To determine the efficiency of these additives in flame retardants and to increase the combustion resistance of epoxy resin, different methods of measurement were used according to ASTM, average time of burning, average extent of burning, rate of burning, limiting oxygen index, maximum flame height and residue percentage succeeding combustion. Based flame retardant are commercially successful and they are more environmentally friendly as compared to halogenated and non-halogenated inorganic or organic types and they are being applied suitably with a crossinker and/or binder copolymer that makes the FRs more resistant to common weathering conditions and exposures. They also produce less or no obnoxious gases while burning.

Keywords: Flame Retardant; flammability properties; kaolin; limiting oxygen index; rate of burning.

DOI: https://doi.org/10.31349/RevMexFis.72.061003

1. Introduction

Flammable materials, such as polymers, that are used in a variety of aspects of human life pose a significant fire hazard. Flame retardants help to mitigate this risk while also assisting in the achievement of reasonable amounts of fire prevention [1,2]. There are advantages and disadvantages to each of these substances that have been in use for a long time [3]. It is dependent on a variety of factors as to how effective they are at attempting to reduce the flammability of various materials [4]. It can be said that these factors are material type, the application and the environment, which is the main container for these materials and applications [5,6]. The second factor is the compatibility/compliance of a flame retardant with a particular substance, as well as, the third factor is methodologies for processing [7,8]. When burned, some flame retardants produce toxic gases in space, and others can cause the premature degradation of some materials [9,10]. The hydrolysis of the product may be caused by some of them, which are hygroscopic [2]. When it comes to being effective, some fire retardants must be used in large quantities, which results in deterioration of mechanical properties as well as a decrease in interfacial adhesion between different components of the composite [11,12].

Nanoclays are receiving a lot of attention these days for their ability to act as fire-resistant added chemicals. Inorganic clay-based nanomaterials with the ability to integrate with a wide range of materials belong to this category [13]. Many minerals, such as hectorite, montmorillonite (MMT), kaolinite, halloysite, and bentonite, form silicate and perhaps aluminum-silicate constructions [14].

Nanoclays, with the exception of traditional flame retardants, are environmentally friendly, highly effective, and, most importantly, could indeed convey unique characteristics to a material [15]. The use of nanoclays in resins, such as MMT, has been shown to reduce flammability while also improving strength properties [16]. Tiny particles also make it harder for carbon chains to move around, which changes the nanocomposites' volume, surface, and characteristics [5].

Among nanoclays used to make UPRs, MMT is among the most commonly used ones. They are very big. It has a big

surface area and a lot of space between the longest and

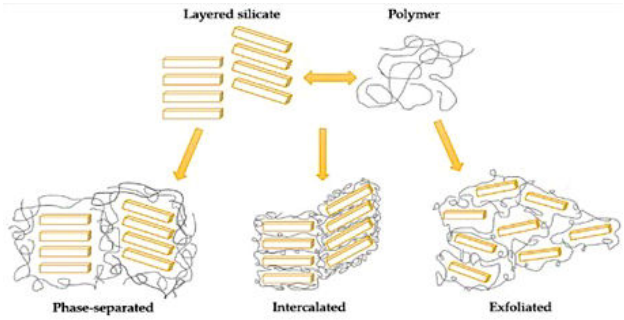


FIGURE 1. A scheme of dispersion states of the clay in the polymer matrix [6].

the smallest parts [8]. This improves the fire retardancy of the material, but only if the material is spread out well. A decrease in the specific surface area, on the other hand, may result in a reduction in the flame retardant attributes. It's possible to have the clay in one of three different dispersion states: phase-separation, intercalation, or exfoliation. As a result of its larger specific surface area, the last option is preferred. Figure 1 depicts all of the forms.

Since nanoclays have such a large surface area, they can decrease the amount of admixture by as much as a few percent. The mechanism of action is based on the formation of a char layer, which prevents heat transfer. In Ref. [7], it was shown that capturing free radicals is a common phenomenon for inorganic nanoclays. After being exposed to high temperatures, nanocomposites that included silicates or silica retain their structural integrity, and the decomposition of organic components takes place within the material, cutting the level of soot issued [8]. The accumulation of a carbonaceous-silicate char layer on the surface of the material results in the insulation of the material and the retardation of mass loss. By enhancing char formation and decreasing heat release, nano flame retardants have been found to reduce flammability as it was shown in Ref. [9].

The physical preparation method seems to be more productive if silicate layers of nanoclays are properly intercalated or exfoliated in the matrix. A labyrinth effect occurs when volatile species released during combustion are unable to diffuse freely because of the tortuous path formed by these layers [16,17].

2. Experimental

This part discusses the practical steps involved in preparing the materials used in flame retardant specimens' preparation, functionalization of kaolinite and preparation of the kaolin/epoxy resin nanocomposites.

2.1. Materials

Imported from the Sikadur-52 company in the United States, epoxy resin and hardener type (amine). For curing, this study used a 2:1 ratio of epoxy and hardener. The raw kaolinite was obtained from white stone produced and processed in the western desert mining division/Al-Rutbah/Al-Anbar governorate/ Iraq, with the chemical formula of $Al_2Si_2O_5(OH)_4$.

Functionalization of kaolinite: The kaolin nanopowder was prepared from its raw stones, which were crashed and grinded to obtain powders with a final fineness of fewer than 20 μm and used for size reduction, mixing and triturating. The kaolin nanoparticle was prepared by mixing (30 g) of ultra-fine powder with (300 mL) of ethanol, (100 mL) of distilled water and (10 mL) of HCl with a concentration of (36.5 %). After stirring for 14 hours, the mixture was filtered and washed several times by using distilled water to get rid of the effects of HCl. The importance of using HCl lies in activating the kaolin surface and removing carbonate impurities, thereby increasing its compatibility with epoxy resin. The solution containing the mixture was tested using the pH meter to confirm its equivalence then filtered, dried in air at room temperature and calcinated at 800 °C for 4 hours. To convert it into the chemically active form metacacoline. To remove the impurities which present in the powder. AFM, XRD and EDX tests were performed to prove the particle size of prepared powder on the nanoscale.

Pre-processing of the kaolin/epoxy resin nanocomposites: Hand lay-up molding was used to prepare the nanocomposites, to ensure effective dispersion and prevent agglomeration at high concentrations, intensive mechanical mixing was used to increase the penetration of polymer chains between the nanolayers. Molded cases in the form of sheets with sizes of $13 \times 13 \times 0.4$ cm^3. All samples were given sufficient time to harden (24 hours) to ensure that the chemical reaction in the presence of nanoparticles was complete. These epoxy resin sheets were made for each percentage weight of flame retardant substance (kaolin) nanopowder (0, 2, 4, 6, 8, and 10) wt. percent, respectively. Depending on the method of test, the samples were laser cut and obtained charming ends. The samples were chosen as 130 ± 5 mm for the limiting oxygen index (LOI) length, the height of flame (HF) length is equal to 125 ± 5 mm, and with the rate of burning (RB) length matches the LOI length. That is, the width of LOI was 6.5 ± 0.5 mm with a width of 10 ± 0.1 mm for the HF, while RB with set to 12.5 ± 0.5 mm. Furthermore, their thickness was equal to 3.0 ± 0.1 mm, as shown in Figure (2). It should be noted that the diagram shown in Fig. 2 represents an illustrative model of the mechanism of chemical interaction and bonding, where the step of 'silane grafting' in the diagram reflects the principle of surface activation achieved in this study

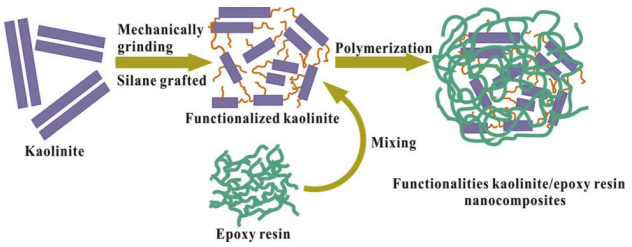


FIGURE 2. Diagram of pre-processing of the kaolin/epoxy resin nanocomposites.

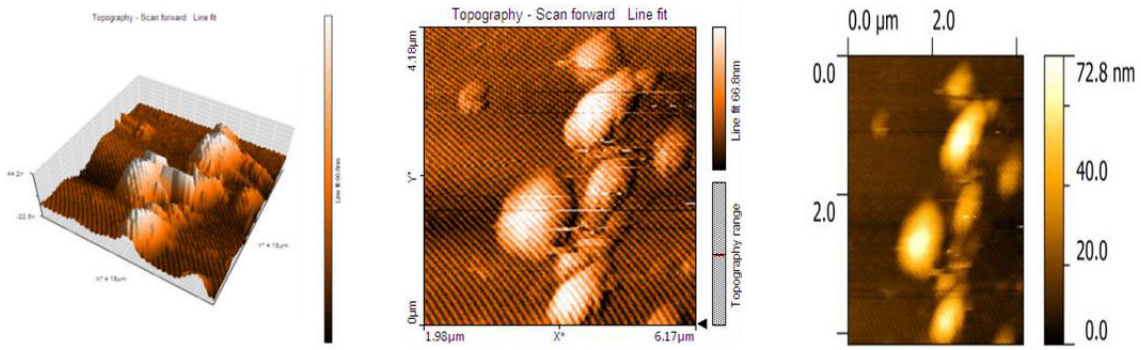


FIGURE 3. The surface topography of kaolin nanopowder.

by activating kaolin with hydrochloric acid (HCl) and calcining at 800 °C, which created strong and highly compatible bonds between the nanoparticles and the epoxy matrix.

Characterization: The acidity and alkalinity of the solution containing kaolin powder were measured individually by using the pH meter type (pH starer 2000). The surface topography of the prepared nanopowder was studied by using a German-made compact AFM. The crystalline structure of the prepared powder was identified by using X-ray diffraction type (Shimadzu XRD-6000) with the target (Cu) and wavelength (1.5406 Å). The chemical composition of the prepared powder was studied using a scanning electron microscope test, model (AIS 2300, USA). In order to determine the flammability of polymers, the limiting oxygen index (LOI), was used (ASTM: D-2863). It is necessary to monitor the RB, the average time of burning (ATB) and the average extent of burning (AEB) in accordance with (ASTM: D-635). While HF and the quantity of weight loss in the polymer are carried out in compliance with the scheme (ASTM: D-3014).

3. Result and discussion

3.1. PH meter test

The acidity and alkalinity for the solution of the nanopowder were measured, where kaolin solution has neutral PH.

3.2. Atomic force microscopy test

Surface morphology of prepared kaolin nanopowder image is illustrated in Fig. 3, where the particles appear with clear nanoscale dimensions and an average size of 38 nanometres, with peak heights reaching approximately 72.8 nanometres, which enhances the contact surface area between the nano and polymer.

TABLE I. Values of surface roughness, RMS and mean grain size of prepared powder.

Sample	Surface Roughness (nm)	RMS (nm)	Mean grain Size (nm)
Kaolin	12.251	8.5356	38

3.3. X-ray diffraction-test

From Table I, it was observed that the surface roughness and mean grain size of the preparation due to the large size of grain causes porosity during the molding, which is considered a weak area of the sample because it will be a store of oxygen. From Fig. 4, there are three phases are detected in the XRD pattern: kaolinite, goethite and quartz with crystalline phases triclinic, orthorhombic and hexagonal, respectively [18,19]. The average grain size for synthesized kaolin was determined by Scherrer's equation. It was found to be about (42.7 nm). This result is in full agreement with the results that were obtained in Table I.

3.4. Energy dispersive X-ray spectroscopy-test

The elemental composition in the reaction mixture of nanopowder material was analyzed by detecting X-ray emission due to the electron beam where the energy distribution of the X-ray emission was analyzed by (EDX). The EDX spectrum of raw material and prepared nanopowder and kaolin

TABLE II. XRD data of prepared nano-powder for the strongest three peaks.

Sample	$2\theta(^\circ)$	d(Å)	FWHM(°)
Kaolin	26.5912	3.34949	0.17050
	20.8054	4.26604	0.20240
	50.0568	1.82075	0.16990

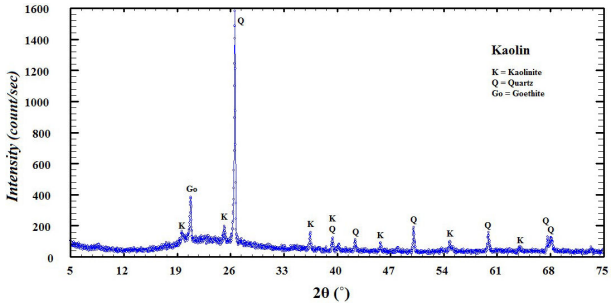


FIGURE 4. XRD pattern of kaolin nanopowder.

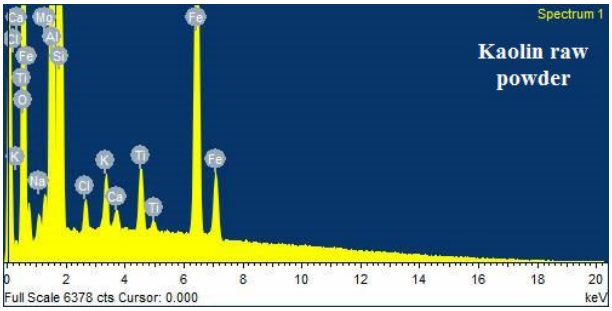


FIGURE 5. EDX spectrum of kaolin raw powder.

TABLE III. Chemical composition of kaolin raw powder.

Element	Weight %	Atomic %	Series
O	52.52	69.81	K
Mg	0.47	0.41	K
Al	12.64	9.96	K
Ca	0.26	0.14	K
Si	16.43	12.44	K
K	0.63	0.34	K
Ti	1.17	0.52	K
Fe	15.02	5.72	K
Na	0.47	0.44	K
Cl	0.39	0.22	K

shows in Figs. 5 and 6, respectively. The elements that constitute the raw material and prepared nanopowder are given in atomic and mass percentages in Tables III and IV, respectively. From Fig. 6, the kaolin nanopowder is composed mainly of Al_2O_3 and SiO_2, elements Al, Si, O , this result confirms that the kaolin clay is mainly composed of kaolinite and quartz clay minerals. Trace amounts of iron and titanium were also detected as natural impurities in the ore structure, this corresponds to the result of XRD. In the clay powder, (Al_2O_3) doesn't exist in its free form but is bound to the clay minerals.

3.5. LOI-test (limiting oxygen index)

The limiting oxygen index (LOI) model is the most commonly used method for determining the resistance to ignition and comparative flammability of polymeric materials. It was determined using the (ASTM: D-2863), and the results were determined by using the formula [20,21]:

$$n\,\% = \frac{V_{O_2}}{V_{O_2} + V_{N_2}} \times 100, \tag{1}$$

where $n\,\%$ stands for LOI, the volumetric speed flow of nitrogen in ml/sec is represented by V_{N_2}, while V_{O_2} refers to the volumetric speed of oxygen in ml/sec.

Table V shows the outcomes that were obtained. That is, in Table V, it is shown that LOI is increased when the reinforcement ratios of the added kaolin nanopowder to the epoxy (directly proportional) increase. This is due to the fact that

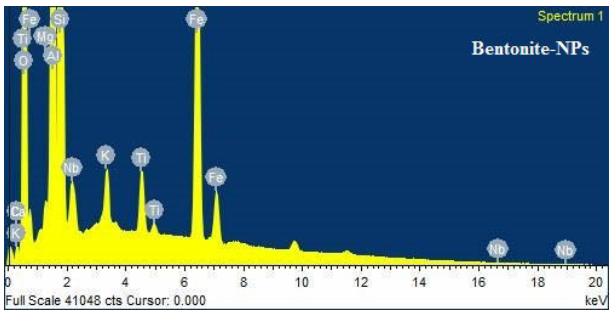


FIGURE 6. EDX spectrum of kaolin nanopowder.

TABLE IV. Chemical composition of kaolin nanopowder.

Element	Weight %	Atomic %	Series
O	51.95	67.47	K
Al	20.28	15.62	K
Si	19.38	14.34	K
K	0.79	0.42	K
Ti	0.89	0.39	K
Fe	1.75	0.65	K
Nb	4.96	1.11	L

these additives create an inert atmosphere, which diminishes and hinders the oxygen from getting to the flame zone, which really is essential to sustaining the ignition's stability.

As a result of the exposure of (kaolin/Epoxy) nanocomposites in the air and at atmospheric pressure, dehydroxylation occurs by an endothermic process at (550-700°C) to give a meta form called irregular metakaolin and a continuous loss of hydroxyl groups (OH^-) at temperatures (700-800°C), due to oxolation. Removal of hydroxyl from kaolin leads to a failure of the material and thus non-resistance to flame [22,23]. Kaolin works by heat absorption mechanism and cools the surface of the material to 700°C.

3.6. Burning rate-test

The test was measured using the (ASTM: D-635) manner and intended to use formula (2) and (3), [24,25], ATB in

minutes and AEB were calculated as follows:

$$ATB = \frac{\sum(t-30)}{N}, \tag{2}$$

$$ABE = \frac{\sum(100-X)}{N}. \tag{3}$$

TABLE V. Results of LOI for the epoxy without and with reinforcement ratio of kaolin nanopowder.

Type of additive	LOI vs. Additives %					
	0	2	4	6	8	10
Neat Epoxy	19.59	-	-	-	-	-
Epoxy + Kaolin	-	20.23	21.1	21.56	21.95	22.33

TABLE VI. ATB, AEB, RB, SE and NB for epoxy without and with reinforcement ratios of kaolin nanopowder.

Test	Additives %					
	Original	2	4	6	8	10
ATB	5.35	5.81	6.08	6.9	4.5	3.61
AEB	10.3	10.3	10.3	10.3	4.12	3.88
RB	1.92	2.02	1.91	1.83	1.65	1.34
SE	-	-	-	-	-	-
NB	-	-	-	-	-	-

In the last two expressions, the time in minutes is represented by t, when self-extinguishing occurs, the length of the not yet burned portion of the structure is evaluated in cm, which is represented by X, and N is the number of samples. A worthy mention here is that according to the (ASTM: D-635) methodology, RB is measured in cm/min. Moreover, the self-extinguishing is abbreviated by SE and NB stands for that after removing the heat source, the specimen's ignition does not continue.

The results of RB of epoxy with additive show a large drop in RB. The RB of epoxy samples was measured without and with additive in addition to the values of (ATB) and (AEB) were calculated by using Eqs. (2) and (3), respectively, as listed in Table VI. The decrease in the R.B is inversely relative to the growth in the reinforcement ratios of the added additive to the epoxy for the same reason mentioned in the LOI test.

3.7. HF maximum-test

The burning substantial residual weight percentage was determined using the strategy defined in (ASTM: D-3014) and determined by calculating using the equation given [25,26]:

$$PWR\% = \frac{W_1 - W_2}{W_1} \times 100. \tag{4}$$

In which, the weight of the specimen before combustion in gm is represented by W_1, W_2 stands for the weight of residual material succeeding the combustion also in gm, furthermore, PWR % is the residual percentage weight of the burning material.

Table VII summarizes the output of the HF measurement for EP including several kaolin weight proportions. The results showed that the increasing reinforcement ratios of the added additive lead to the decrease of (HF) (inversely proportional) and an increase in the effectiveness and retardancy (directly proportional) for the same reason mentioned in the LOI test.

TABLE VII. (HF) with reinforcement ratios of kaolin.

Test	H vs. percentage additives					
	Non	2	4	6	8	10
W1(gm)	4.56	4.76	4.85	5.23	5.31	5.36
W2(gm)	1.37	0.8	0.86	1.28	1.4	1.47
PWR %	69.95	83.19	82.26	75.52	73.63	72.57
HF(cm)	12.3	11.3	8.8	7.43	5.44	4.52

TABLE VIII. ATB, AEB, RB, SE and NB for EP.

Test	Additives %					
	Non	2	4	6	8	10
ATB	5.35	6.71	7.3	3.22	2.52	2.25
AEB	10.3	10.3	10.3	4.1	1.8	1.4
RB	1.92	1.73	1.69	1.2	0.57	0.49
SE	-	-	-	Yes	Yes	Yes
NB	-	-	-	-	-	-

4. Conclusions

The nanocomposites of functionalized kaolin/epoxy resin were synthesized using synthesized kaolin as padding. The used method was successful in preparing nanopowder for kaolin clay with an average grain size (38 nm). Limiting oxygen index (LOI) was increased and rate of burning (R.B) and maximum flame height (HF) were decreased for epoxy resin by increasing the reinforcement ratios of additive. They demonstrated that surface functionalization of kaolin is a straightforward but effective technique for producing elevated clay mineral-polymer nanocomposites.

Acknowledgment

The authors would like to thank the University of Diyala/College of Science/Department of Physics for the technical support to complete this work in their laboratories.

1. Y. Wang, T. Henriksen, M. Deo, and R. A. Mentzer, Factors contributing to US chemical plant process safety incidents from 2010 to 2020, *J. Loss Prev. Process Ind.* **71** (2021) 104512. https://doi.org/10.1016/j.jlp.2021.104512
2. S. S. Abdullah and F. L. Ahmed, Structural and optical studies on sliver nitrate doped polymer blend and effect on some pathogenic bacteria, *Rev. Mex. Fis.* **71** (2025) 041004. https://doi.org/10.30723/ijp.v19i49.625
3. S. Sonkaria and H. J. Kim, Nanoscale configuration of clay-interlayer chemistry: A precursor to enhancing flame retardant properties, *IntechOpen* (2021) 75385. https://www.intechopen.com/chapters/75385
4. T. Y. Sabri, S. K. Jasim, A. A. Habeeb, and A. S. Jasim, Preparation and Study Ag Nanoparticles via PLAL Technique: Influence of Different Number of Pulses, *Int. J. Nanoelectron. Mater.* **17** (2024) 45. https://doi.org/10.58915/ijneam.v17i1.458
5. S. K. Jasim, A. M. Shano, and S. K. Adnan, Zinc Oxide Poly Crystals Heterojunction and Infrared-Blind UV-Photodetector, *J. Nano- Electron. Phys.* **16** (2024) 01012. https://doi.org/10.21272/jnep.16(1).01012
6. K. Zheng, F. Zheng, J. Lin, Z. Ren, and Y. Lin, Utilization of red mud as copper substitute in eco-friendly resin-based brake composites: Performance evaluation and machine learning prediction, *Tribol. Int.* **214** (2026) 111324. https://doi.org/10.1016/j.triboint.2025.111324
7. N. Abu-Thabit *et al.*, Preparation of pH-Indicative and Flame-Retardant Nanocomposite Films for Smart Packaging Applications, *Sensors* **20** (2020) 5462. https://doi.org/10.3390/s20195462
8. S. K. Jasim, W. M. W. A. Kamil, A. A. Habeeb, and E. Ali, Effect of Cinnamon Nano/Micro Particles at Antibacterial Activity, *J. Phys. Sci.* **36** (2025) 43. https://doi.org/10.21315/jps2025.36.3.4
9. G. Jin *et al.*, A novel coarse-grained discrete element method for simulating failure process of strongly bonded particle materials, *Powder Technol.* **464** (2025) 121212. https://doi.org/10.1016/j.powtec.2025.121212
10. S. K. Jasim, S. M. A. Al Hussan, and M. T. Abd, Improving the Mechanical Properties of Dental Fillings by Adding TiO_2 NPs Prepared Laser Ablation, *Bio. Nano. Science* **15** (2025) 330. https://doi.org/10.1007/s12668-025-01970-y
11. S. K. Jasim, S. M. A. A. Hussan, A. S. Noori, and A. A. Habeb, Determine surface plasmon resonance and effect parameters laser ablation on Cu and Zn nanoparticles, *AIP Conf. Proc.* **3219** (2024) 060008. https://doi.org/10.1063/5.0236469
12. X. Li and Ma, Z., Inherent anisotropy of aeolian sand with different bedding angles in true-triaxial tests, *Eng. Geol.* **356** (2025) 108272. https://doi.org/10.1016/j.enggeo.2025.108272
13. F. Xu *et al.*, Novel high-efficiency casein-based P-N-containing flame retardants with multiple reactive groups for cotton fabrics, *ACS Sustainable Chem. Eng.* **7** (2019) 13999. https://doi.org/10.1021/acssuschemeng.9b02474
14. B. M. Dheyaa, W. H. Jassim, and N. A. Hameed, Evaluation of the epoxy/antimony trioxide nanocomposites as flame retardant, *J. Phys. Conf. Ser.* **1003** (2018) 012078. https://doi.org/10.1088/1742-6596/1003/1/012078
15. L. Su, X. Zeng, H. He, Q. Tao, and S. Komarneni, Preparation of functionalized kaolinite/epoxy resin nanocomposites with enhanced thermal properties, *Appl. Clay Sci.* **148** (2017) 103. https://doi.org/10.1016/j.clay.2017.08.017
16. Z. Luo *et al.*, Synergistic enhancement of heat resistance and mechanical performance of epoxy resin by introducing entanglement effect, *Composites Part A* **203** (2026) 109581. https://doi.org/10.1016/j.compositesa.2026.109581
17. S. A. Zaidan and M. H. Omar, The effects of bauxite, metakaolin, and porosity on the thermal properties of prepared Iraqi clays refractory mortars, *Appl. Phys. A* **124** (2018) 386. https://doi.org/10.1007/s00339-018-1759-2
18. C. Liu *et al.*, Phosphorous-Nitrogen Modification of Epoxy Grafted Poly-Acrylic Resin: Synergistic Flame Retardment Effect, *Polymers* **13** (2021) 2826. https://doi.org/10.3390/polym13162826
19. X. S. Wang, G. L. Xu, Y. Wang, Y. Liang, and J. Hu, Preparation of phosphorus-containing poly-acrylate resins and their flame resistant properties, *J. Chem. Eng. Chin. Univ.* **31** (2017) 186. http://dx.doi.org/10.3969/j.issn.1003-9015.2017.01.026
20. A. H. Ahmed, A. S. Jasima, and S. K. Jasim, Synthesis of Gold Nanoparticles by Pulsed Laser Ablation and its Study Physical and Mechanical Properties, *Int. J. Nanoelectron. Mater.* **17** (2024) 1465. https://doi.org/10.58915/ijneam.v17i4.1465
21. N. R. Kopparthi, J. Schuster, and Y. P. Shaik, Fabrication and Characterization of Bamboo-Epoxy Reinforced Composite for Thermal Insulation, *Open J. Compos. Mater.* **14** (2023) 15. https://doi.org/10.4236/ojcm.2024.141002
22. H. Ma *et al.*, Multifunctional Graphite Nanosheet-Hydrophilic Epoxy Anticorrosion Coatings via Size Confinement of Exfoliated Graphite, *Polymers* **17** (2025) 1803. https://doi.org/10.3390/polym17131803
23. C. Yan *et al.*, Additive manufacturing of hydroxyapatite and its composite materials: A review, *J. Micromech. Mol. Phys.* **5** (2020) 2030002. https://doi.org/10.1142/S2424913020300029
24. F. Heidari, M. Razavi, M. A. A. Zamani, M. Tahriri, and L. Tayebi, A comparison between the properties of natural hydroxyapatite produced by cold isostatic pressing and spark plasma sintering techniques, *J. Aust. Ceram. Soc.* **54** (2018) 337. https://doi.org/10.1007/s41779-017-0158-z
25. Y. Zheng and B. A. Baudet, Pore structure response of reconstituted kaolin and illite-smectite mixed-layer rich clay to 1D compression, *Appl. Clay Sci.* **276** (2025) 107892. https://doi.org/10.1016/j.clay.2025.107892
26. M. Altaf, M. N. Ahmed, A. Iqbal, and A. A. Khan, Synthesis and characterization of novel organoclay-epoxy based flame retardant nanocomposites, *J. Reinf. Plast. Compos.* **45** (2026) 32. https://doi.org/10.1177/07316844241272956

The pH effect on PEDOT: PSS/GO as a potential hole transport layer

M. D. Nurhafizah*, Tan You Zi, and B. Afzalina

School of Physics, Universiti Sains Malaysia,
11800 Minden, Penang, Malaysia
**Tel: +60194104058;*
e-mail: *mdnurhafizah@usm.my*
ORCID: 0000-0003-3660-5274*

Received 29 December 2025; accepted 19 May 2026

Poly(3,4-ethylenedioxythiophene)-polystyrenesulfonate (PEDOT: PSS) with secondary doping has been widely researched as a hole transport layer in solar cells because secondary doping can provide conformational change and improve the properties of PEDOT: PSS. PEDOT: PSS is doped with graphene oxide (GO) to form PEDOT: PSS/GO solution, and then, sodium hydroxide is added into the acidic PEDOT: PSS/GO solution. The novelty of this work relies on the pH effect of PEDOT: PSS/GO, which shows basic condition allows better dispersity of GO in water. The HRTEM result indicates the formation of PEDOT: GO. Besides, the two-point probe results show that both acidic and basic PEDOT: PSS/GO is more conductive than PEDOT: PSS and GO alone. This was due to the transformation of benzoid structure to quinoid structure which has been supported by the lower d-spacings of acidic PEDOT: PSS/GO (3.48 Å) and basic PEDOT: PSS/GO (3.44 Å) compared to PEDOT: PSS (3.56 Å) in the XRD result. Other than that, the UV-Vis absorbance result shows that the PSS chain absorbance peak in basic PEDOT: PSS/GO is around 13 % lower than that in acidic PEDOT: GO, indicating better replacement of insulating PSS chain and more successful formation of PEDOT: GO. In the EDX results, the basic PEDOT: PSS/GO shows higher oxygen content (93.34 %) than acidic PEDOT: PSS/GO (44.58 %) due to the increase of hydroxyl groups of GO in basic conditions caused by NaOH. Besides, the average resistance values of the basic PEDOT: PSS/GO and acidic PEDOT: PSS/GO layers are 3.72E+10 Ω and 1.30E+10 Ω, respectively. The Na^+ ion in NaOH resulted in the damages of unreacted PEDOT: PSS, making the basic PEDOT: PSS/GO sample more electrically resistant than the acidic PEDOT: PSS/GO sample. Despite some of the adverse effects of basic PEDOT: GO, it shows the lowest surface roughness (Rq: 2.52 nm) among all potential HTLs investigated, indicating the best deposition on glass and wettability for organic semiconductors (OSCs) which can be applied as a counter electrode in dye-sensitized solar cell (DSSC) application.

Keywords: Polymer; graphene oxide; acidic; basic; characterization; properties.

DOI: https://doi.org/10.31349/RevMexFis.72.061004

1. Introduction

Organic materials which are low-cost materials have been greatly utilized as third-generation solar cells such as the dye-sensitized solar cells and the perovskite solar cells [1]. The hole transport layer has been an important interlayer in organic solar cells [2] and perovskite solar cells to perform better hole extraction and transportation [3]. According to Yu et al. (2018), one of the very popular hole transport layers used in perovskite solar cells is poly(3,4-ethylenedioxythiophene)-polystyrenesulfonate (PEDOT: PSS) since it can form a smooth surface on the indium-tin oxide (ITO) electrode [4]. Even so, it has disadvantages like being very acidic which could cause corrosion on the perovskite layer and ITO electrode, because of that, the stability and the performance of perovskite solar cells based on PEDOT: PSS hole transport layer (HTL) can be adversely affected [4]. Other than perovskite solar cells, PEDOT: PSS can work as a hole transport layer for organic solar cells as well [5]. The PSS component in PEDOT: PSS is held with the PEDOT unit through an ionic bond and such interaction provides stabilization in aqueous media [6]. Ozcan et al. (2020) mentioned that the good aspect of PSS is that it can make PEDOT: PSS dispersive, however, PSS is insulating, thus, the conductivity of PEDOT: PSS is adversely affected by the PSS component, even so, it is possible to increase the conductivity through secondary doping [6].

One of the very popular types of materials to be combined or doped with PEDOT: PSS is the carbon material such as graphene [7,8], graphene oxide (GO) [9,10], and reduced graphene oxide (rGO) [11,12]. Among various graphene-based materials mentioned, although having conductivity lower than graphene and rGO, GO has the best wettability to deposit perovskite solution [13]. It has been reported that the removal of insulating PSS could increase the conductivity but the power conversion efficiency still decreases because the PEDOT-rich surface is unfavorable for the perovskite crystal growth [14]. The pros of GO for having strong wettability for perovskite deposition could outweigh its cons of being less conductive than graphene and rGO. Since acid is a hygroscopic [15], it can absorb moisture, resulting in poor stability of solar cells [16]. It has been widely known that the highly acidic PEDOT: PSS can degrade the perovskite layer in a perovskite solar cell, as a result, the efficiency and stability

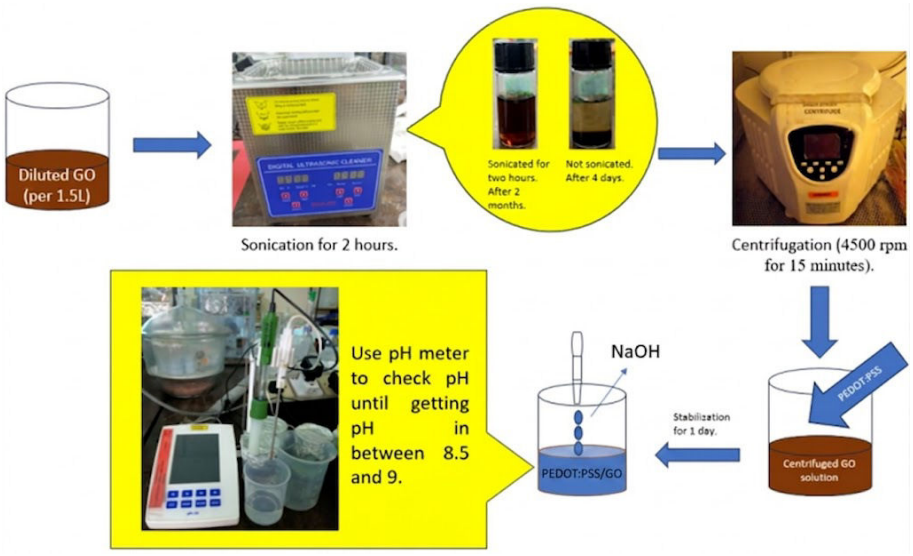


FIGURE 1. Modified synthesis of acidic and basic PEDOT: PSS/GO solutions.

of perovskite solar cells have been greatly reduced [17]. Furthermore, the acidity of PEDOT: PSS can harm the ITO electrode in organic solar cells as well [18]. So, research related to the effect of pH condition on PEDOT: PSS on the performance of perovskite solar cells has been conducted, and basic PEDOT: PSS hole transport layer has indicated better performance in terms of efficiency than the acidic PEDOT: PSS hole transport layer [17] Even so, it has been shown that basic PEDOT: PSS has lower wettability [17], and that can adversely affect the deposition of the perovskite solution in an inverted structure solar cell [19]. Thus, to increase the wettability, the addition of GO is a good choice because GO can increase the wettability of the composite [19]. Coincidently, the basic condition can make GO a more dispersive [20]. GO aggregates in acidic conditions and dissolves better in basic conditions because carboxyl groups of GO can be protonated in acidic conditions and that makes it less hydrophilic, thus forming an aggregation [20]. On the contrary, the carboxyl groups can be deprotonated in a basic condition which makes GO a more dispersive [20], due to the electrostatic repulsion between the deprotonated carboxyl groups [21].

In this study, the pH of basic PEDOT: PSS/GO solution was tuned by NaOH, and different potential hole transport materials which are GO, PEDOT: PSS, acidic, and basic PEDOT: PSS/GO were compared to study the electrical, structural, and optical properties. Besides, the pros and cons of acidic PEDOT: PSS/GO and basic PEDOT: PSS/GO were investigated.

2. Materials and methods

2.1. Sample Preparation

GO was synthesized with graphite (C0350) from HmbG Chemicals through a modified Hummer's method [22]. GO was kept in the solution form without drying into powder form and the solution was diluted to 1.5 L. The conductive grade poly(3,4-ethylenedioxythiophene)-poly(styrenesulfonate) (PEDOT: PSS) with 1.3 wt % dispersion in H_2O (483095-500G) was purchased from Sigma Aldrich. The PEDOT: PSS/GO solution synthesis process was modified from the method conducted by Yu *et al.* (2014) [23]. The graphene oxide solution was sonicated for 2 hours. Then, the sonicated solution was centrifuged at 4500 rpm for 15 minutes to remove any large GO nanosheets, which means the centrifuged solution was kept and the very little precipitate was removed. Next, the PEDOT: PSS solution was mixed with the GO solution directly with the volume ratio of 1: 1 and the mixture was left in the fridge (3°C) to be stabilized for one day. The original PEDOT: PSS/GO solution was acidic (pH between 2 and 2.5). After that, 0.1 M of NaOH was carefully added drop by drop with a dropper to the solution until the solution became basic (pH between 8.5 to 9). The pH meter was used to determine the pH of the solution intermittently until the desired pH. The acidic and basic PEDOT: PSS/GO mixture solutions were spin-coated onto the cleaned glass substrates at 4000 rpm for 45 seconds, then, the layer was annealed at 145°C for 15 minutes [23]. GO and PEDOT: PSS solutions were also deposited with the same procedure for further investigation.

2.2. Material characterizations

To provide a fundamental baseline for PEDOT: PSS/GO solutions, Agilent Technologies: Cary Series UV-Vis-NIR Spectrophotometer was used to obtain the absorbance spectra of various potential hole transport layer using solution-based measurement. The wavelength range scanned was between 200 nm and 800 nm using standard cuvette of 10 mm optical pathlength. High-Resolution Transmission Electron Microscopy (HRTEM) images were obtained by using JEOL JEM 2100F Field Emission Transmission Electron Microsco-

pe (FETEM) operated at an accelerating voltage of 200 kV. Bruker D8 DISCOVER featured with DAVINCI design was employed to obtain the X-ray diffraction (XRD) pattern, the radiation source is Cu-Kα, and 2θ was scanned from 10°C to 90°C. For XRD, the samples were drop-cast rather than spin-coated. The atomic force microscope (Bruker Dimension Edge) was used to study the surface morphology and roughness of the potential hole transport layers. The scan range for each spot was 5 micrometers and the scanning was run at 1 Hz. The spring constant and resonance frequency for the silicon cantilever were around 40 N/m and 250-300 kHz respectively.

A field emission scanning electron microscope (NOVA NANOSEM 450) was employed to obtain high-resolution images of deposited potential HTL particles and the elemental components by the EDX feature. The FESEM images were taken at the voltage of 10 kV with magnification of 10 kX and 100 kX. The EDX feature was run at 10 kV with a working distance of 5 mm and the magnification was 10 kX. KEITHLEY 4200-SCS two-point probe was employed to obtain the current-voltage (I-V) curves of different deposited potential hole transport layers. The working voltage range was -10 V to 10 V and the resistance values could be obtained from 1/gradient of the I-V curves.

3. Results and discussion

3.1. UV-Vis result

As shown in Fig. 2, the absorbance peaks of GO, PEDOT: PSS, basic PEDOT: PSS/GO, and acidic PEDOT: PSS/GO in between the regions of 200 nm to 800 nm are 231 nm, 224 nm, 225 nm, and 225 nm respectively. GO has an absorbance peak at around 231 nm which is very near to the previously reported result [24]. The absorbance peak around 230 nm is due to the electron transition at the carbon π bonds

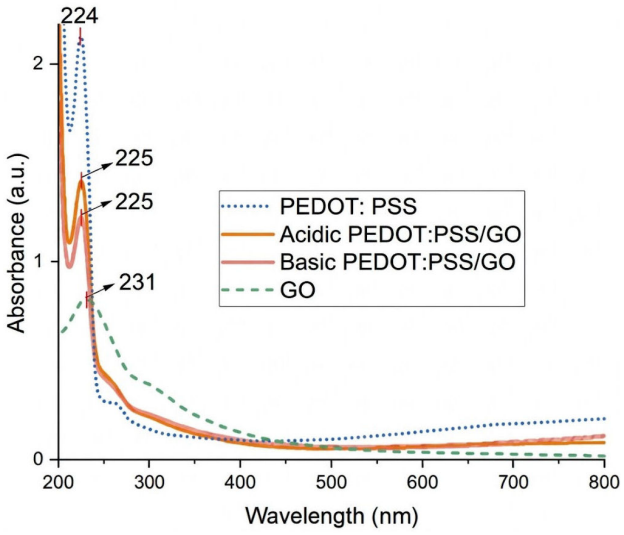


FIGURE 2. Absorbance spectra of potential HTL solutions.

[25]. According to Xia *et al.* (2012), the absorbance peak at around 224 nm is the absorbance peak of the aromatic ring of the PSS unit, thus, the decrement of the peak intensity around that region indicates more replacement of PSS with GO [26]. Based on this concept, it is seen in Fig. 2 that the peak intensity of basic PEDOT: PSS/GO at 225 nm is around 13 % lower than that of acidic PEDOT: GO, which shows more replacement of PSS in the basic PEDOT: PSS/GO solution. The reason can be that GO is more dispersive in basic conditions than in acidic conditions [20], thus, GO is more evenly mixed with PEDOT: PSS, so, the replacement of PSS with GO can be more widely done. The PSS chain detached from the PEDOT unit can be attached to GO through the hydrophilic-hydrophilic interaction [27]. Another possible reason behind the lower PSS chain absorbance of basic PEDOT: PSS/GO is that the Na^+ from NaOH can remove PSS from PEDOT: PSS to form Na^+PSS^- [28]. The reason for the red-shift of PSS chain peak from 224 nm in PEDOT: PSS absorbance spectrum to 225 nm in the acidic and basic PEDOT: PSS/GO absorbance spectra is possibly due to the effect of GO, which has a peak at 231 nm rather than 224 nm, thus, slightly red-shifting the peak. However, there was no peak shown at around 231 nm (GO absorbance peak) for both acidic and basic PEDOT: PSS/GO but the presence of a 225 nm peak for the PSS chain is distinct for both cases, which indicates the dominant presence of unreacted PEDOT: PSS in the PEDOT: PSS/GO solutions, although a portion of PEDOT: PSS has been transformed into PEDOT:/GO. This measurement confirms the interaction and mechanism between PEDOT: PSS and GO to produce acidic and basic PEDOT: PSS/GO.

3.2. HRTEM Result

Figure 3 shows the HRTEM images of GO and PEDOT: PSS/GO at different resolutions. The graphene oxide layer deposited can be observed in Fig. 3a). There are certain dark spots found on the GO layer in Fig. 3b) which are the PEDOT molecules bonded with GO. Figure 3d) shows a clearer image of PEDOT (dark) on GO (bright), which is similar to the image of PEDOT within rGO layers in previous literature [29]. The GO HRTEM image with 10 nm resolution is shown in Fig. 3e), which roughly indicates the hexagonal lattice structure of GO. There are also lines representing the crystallites of PEDOT on the GO layer in Fig. 3f), as indicated in the yellow box. The HRTEM result supports the UV-vis result where the UV-vis result shows the replacement of the PSS chain by GO [26] and the HRTEM result indicates the formation of PEDOT: GO.

The X-ray diffraction pattern has also been obtained as indicated in Fig. 4. As shown in Fig. 4, the graphene oxide indicates a peak at 21.325°C which indicates the interlayer spacing of 0.416 nm, which is not in correspondence to the normal GO XRD peak at around 10°C which represents the interlayer spacing of around 0.8 nm [30]. However, the UV-visible result shown in Fig. 2 indicates the GO absorbance peak at 231 nm which indicates the presence of a graphene

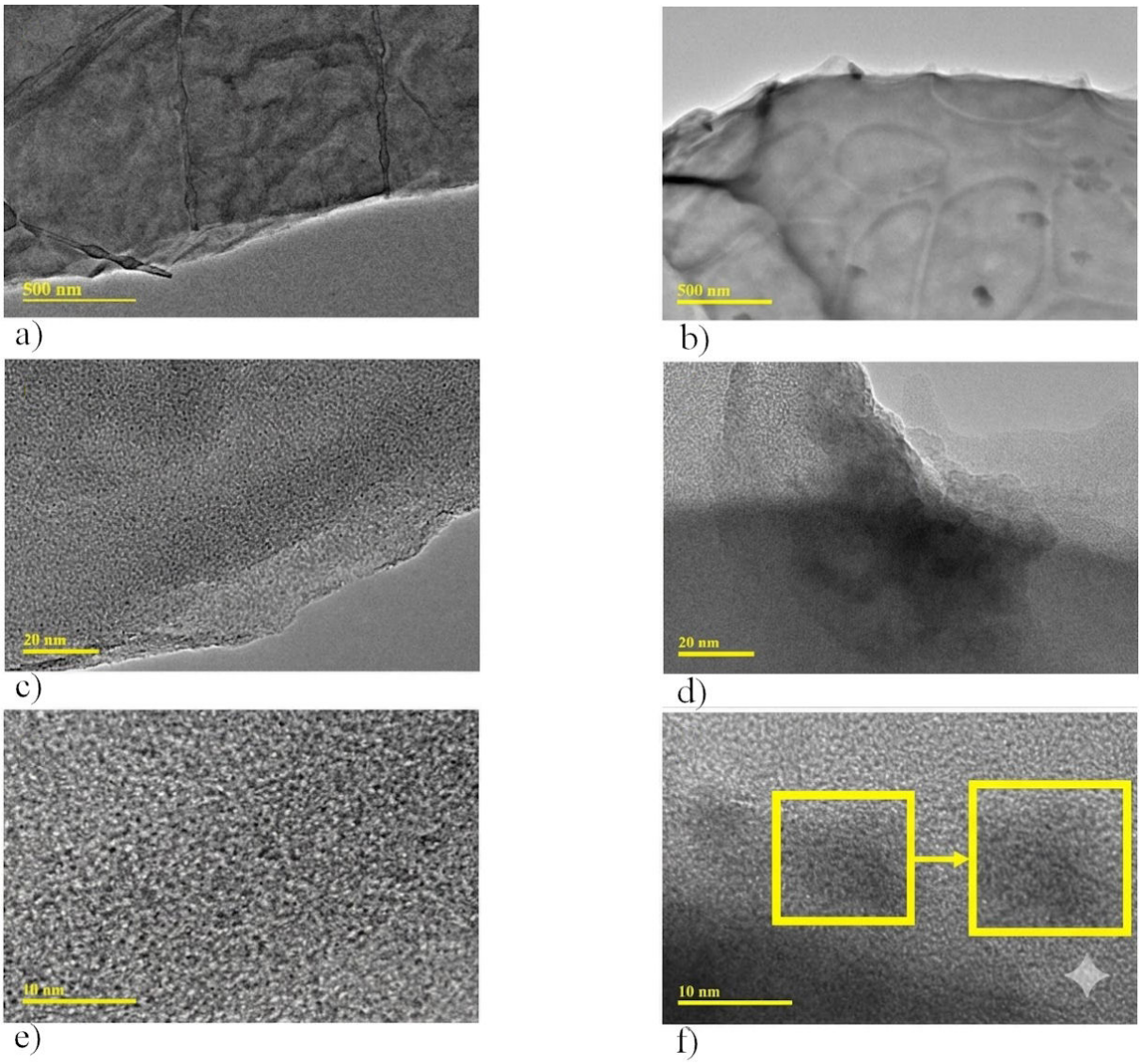


FIGURE 3. HRTEM images of a) GO (500 nm), b) PEDOT: PSS/GO (500 nm), c) GO (20 nm), d) PEDOT: PSS/GO (20 nm); e) GO (10 nm); f) PEDOT: PSS/GO (10 nm).

oxide [24], the reason is probably due to the effect of annealing because the UV-vis absorbance spectra are the results of the hole transport layer (HTL) solutions while the XRD results are obtained after drop-casting and annealing. With more oxygen functional groups, the interlayer spacing increases [31], thus, the lower interlayer spacing obtained shows fewer oxygen functional groups. According to [32], the drying process increases the GO 2θ peak in XRD, where the GO powder dried at 140°C for 30 minutes indicated the 2θ peak between 19 to 24°C because of the eradication of intercalated water and certain oxygen functional groups. Since the annealing temperature in this study is 145°C, the water and oxygen content can be reduced, making the interlayer spacing shorter.

As shown in Fig. 4, the XRD peaks for PEDOT: PSS, acidic PEDOT: GO, and basic PEDOT: PSS/GO are 25°C, 25.553°C, and 25.906°C respectively, indicating the interplanar spacing of 3.56 Å, 3.48 Å and 3.44 Å respectively. The interplanar spacing at around 3.5 Å is the pi-to-pi stacking (010) of PEDOT and the decrease in the pi-to-pi stacking distance can be attributed to the transformation of PEDOT structure from benzoid to quinoid form [33]. The PEDOT bonds with GO through pi-to-pi interactions [34] and for more pi-to-pi interactions to occur [35], the transformation of PEDOT structure from benzoid to quinoid occurs [36]. Because of that, the reduction of interplanar spacing from 3.56 Å to 3.48 Å shows the formation of PEDOT: PSS/GO after GO replaces the PSS chain. This can be supported by the reduction of the PSS chain absorbance peak in the UV absorbance result in Fig. 2 which indicates the replacement of the PSS chain by GO [26] and the HRTEM result in Fig. 3f) which indicates the formation of PEDOT: GO. Thus, lower interplanar spacing of basic PEDOT: PSS/GO (3.44 Å) than that of acidic PEDOT: PSS/GO (3.48Å) indicates more trans-

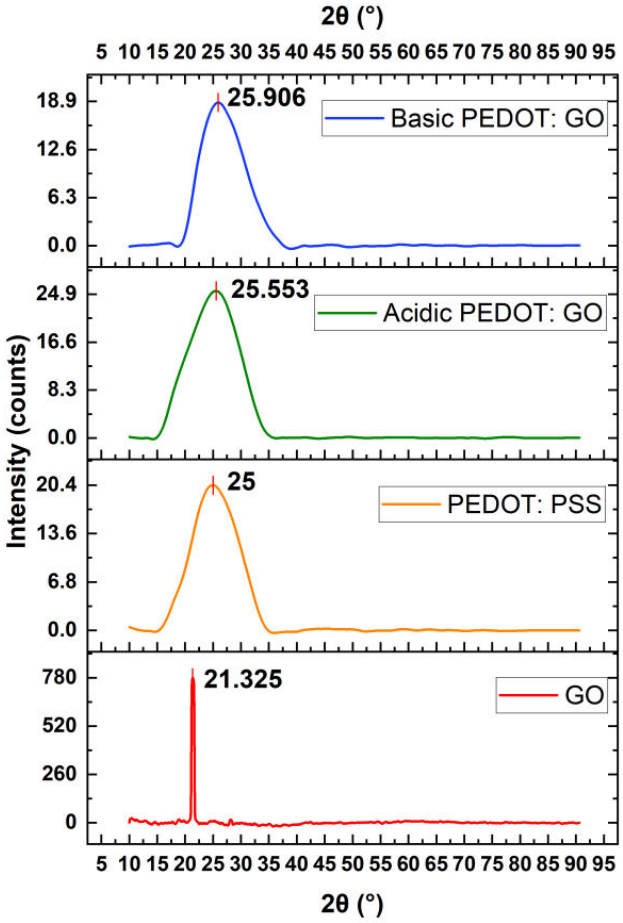


FIGURE 4. X-ray diffraction pattern for basic PEDOT: GO, acidic PEDOT: GO, PEDOT: PSS, and GO.

formation of PEDOT structure from benzoid to quinoid and more PEDOT: PSS/GO formation which corresponds to the lower PSS chain absorbance peak of basic PEDOT: PSS/GO in Fig. 2 that indicates more replacement of PSS chain. In Fig. 4, the GO peak at 21.325 degrees is not observed in the acidic and basic PEDOT: PSS/GO XRD patterns at all, this indicates the low presence of GO. Such phenomenon can be explained by the UV-Vis result in Fig. 2 where the peak of 225 nm which represents the PSS chain absorbance [26] in both acidic and basic PEDOT: PSS/GO is obvious while the GO absorbance peak is unseen. This shows the dominant presence of unreacted PEDOT: PSS even in the PEDOT: PSS/GO solutions.

Figure 5 shows the surface morphology of the four potential hole transport layers. The Rq (root-mean-square) values of two random points on each layer were taken and each average Rq value was calculated. The film thicknesses of PEDOT: PSS, GO, acidic PEDOT: GO, and basic PEDOT: PSS/GO are 32.9 nm, 18.6 nm, 45.0 nm and 49.5 nm, respectively. The surface roughness (Rq) of PEDOT: PSS, GO, acidic PEDOT: GO, and basic PEDOT: PSS/GO are 3.04 nm, 2.65 nm, 2.88 nm, and 2.52 nm, respectively. The low surface roughness result of PEDOT: PSS (3.04 nm) is consistent with the smooth surface characteristic of PEDOT: PSS (less than 5 nm) stated by Sun et al. (2015) [44]. According to Luo et al. (2017), the contact angle of the PEDOT: PSS/GO surface is smaller than the PEDOT: PSS surface, which shows that GO is more hydrophilic than the PSS chain unit [19]. That allows GO and GO-based materials to be deposited more evenly due to the stronger adhesion on glass. Thus, GO and both acidic and basic PEDOT: PSS/GO show lower surface roughness than PEDOT: PSS.

The basic PEDOT: PSS/GO surface with the Rq value of 2.52 nm is smoother than the acidic PEDOT: PSS/GO surface with the Rq value of 2.88 nm. That seems to contrast with the previous result [17], which showed that basic PEDOT: PSS has a higher contact angle than acidic PEDOT: PSS and neutral PEDOT: PSS. However, since the result shown in that literature does not involve GO, it does not take GO dispersity in basic conditions into account. GO is more dispersive in the basic condition [20]. Because of that, GO can spread in the solution more evenly, providing more possibility to react with PEDOT: PSS, thus, allowing more formation of PEDOT: PSS/GO molecules. Since PEDOT: PSS/GO is more hydrophilic than PEDOT: PSS [19], more PEDOT: PSS/GO formation allows the solution to be more hydrophilic. Higher hydrophilicity allows better adhesion on glass, thus, allowing more even deposition, because of that, basic PEDOT: PSS/GO shows lower surface roughness than acidic PEDOT: GO. That can be supported by the UV-vis result in Fig. 2, where the lower PSS chain peak absorbance of basic PEDOT: PSS/GO solution indicates more removal of PSS [26] and the XRD result, where the lower pi-to-pi stacking in basic PEDOT: PSS/GO indicates more benzoid to quinoid transformation [33] and thus, more PEDOT: PSS/GO formation [23].

However, there is also another possible reason for basic PEDOT: PSS/GO to be more dispersive than acidic PEDOT: GO, which is due to the damage of the epoxide group and the production of the hydroxyl group after lengthy mixing with NaOH, resulting in the formation of graphene hydroxide [37]. The epoxide group's contribution to solubility is smaller than the hydroxyl group due to the lower solubility of the R-O-R group than the R-OH group [38]. Thus, the increase of hydroxyl groups in GO makes the overall mixture of basic PEDOT: PSS/GO more dispersive than the mixture of acidic PEDOT: GO, causing better wettability and adhesion on glass, resulting in more even deposition and lower surface roughness. Since a rough surface can lead to interfacial recombination which is undesired in the solar cell application [39], basic PEDOT: PSS/GO with the lowest surface roughness can have the least interfacial recombination.

The elemental evolution of the (HTL) composites was quantitatively assessed via Energy-Dispersive X-ray (EDX) spectroscopy. From Fig. 6a), the analysis of pristine GO revealed a balanced atomic distribution of oxygen (49.22 %) and carbon (50.78 %), whereas pristine PEDOT: PSS showed in Fig. 6b) exhibited a significantly higher oxygen concentration of 85.1 %. This elevated oxygen content is intrinsic to the PEDOT: PSS structure, arising from the oxygen-dense ethylenedioxy groups in the PEDOT backbone and the sul-

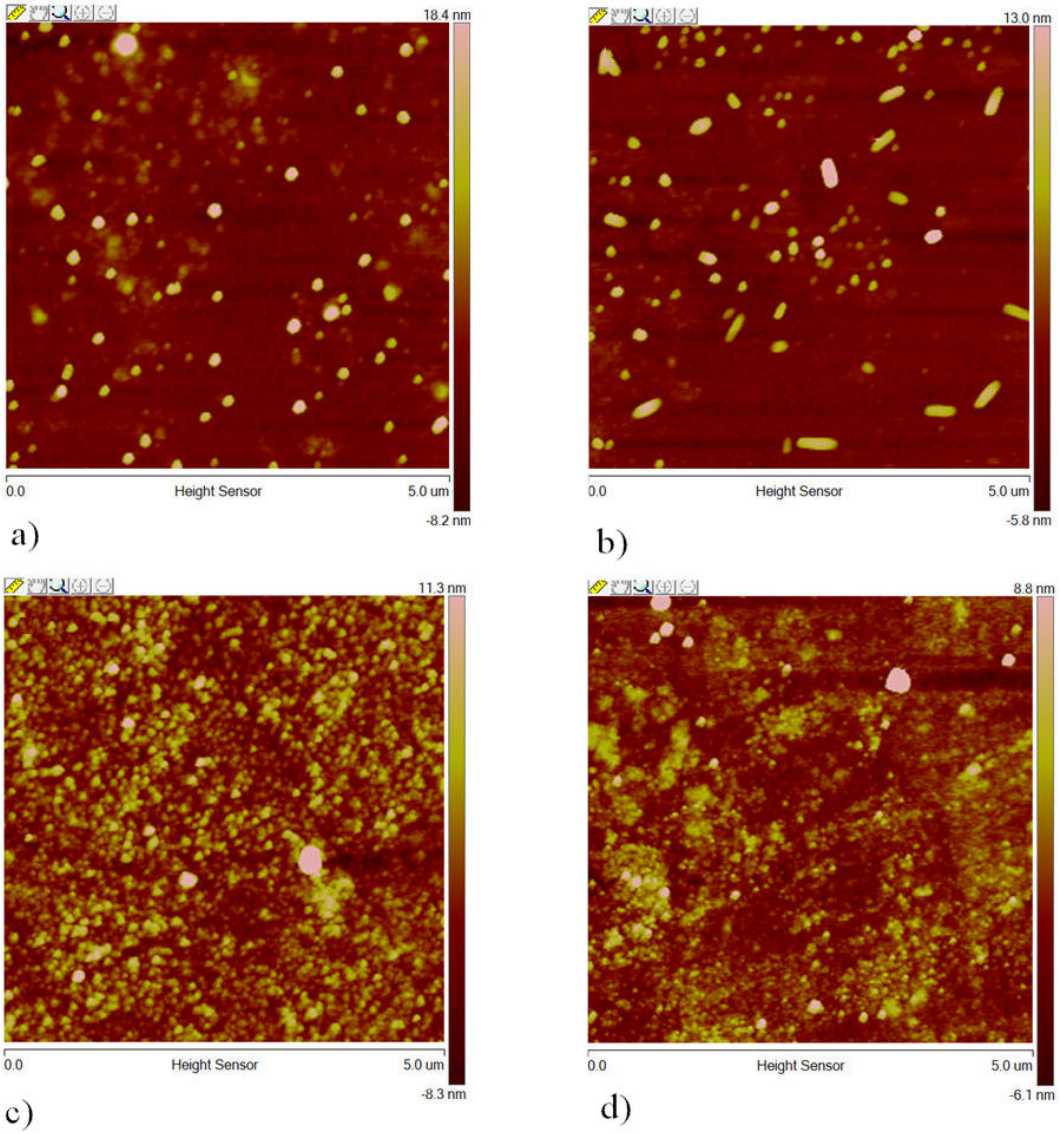


FIGURE 5. Atomic force microscopy results for a) PEDOT: PSS; b) GO; c) acidic PEDOT: GO; d) basic PEDOT: GO.

fonate groups of the PSS chains. Upon the integration of GO to form the acidic PEDOT: PSS/GO composite as in Fig. 6c), the carbon content increased markedly to 55.12 % compared to the 14.21 % observed in pristine PEDOT: PSS. This shift confirms the successful loading of the carbon-dense GO lattice within the polymer matrix. A profound elemental divergence was observed in the basic PEDOT: PSS/GO sample in Fig. 6d), which exhibited an anomalous oxygen concentration of 93.34 % and a depleted carbon fraction of 6.41 %.

This phenomenon is likely driven by two synergistic mechanisms. First, the enhanced dispersity of GO under alkaline conditions promotes more intimate mixing with the PEDOT: PSS matrix, facilitating the displacement of insulating PSS chains [20]. While UV-Vis spectroscopy confirmed a 13 % reduction in PSS absorbance which indicates successful PSS replacement by GO and Na^+ ions [26,28], the magnitude of the oxygen spike suggests a second, more dominant chemical transformation. Under basic conditions, the introduction of NaOH facilitates the ring-opening of the epoxy groups on the GO basal plane, leading to a proliferation of hydroxyl functionalities and the formation of graphene hydroxide species [37]. This chemical restructuring is further supported by the sulfur (S) content trends. The atomic percentage of sulfur decreased from 0.3 % in the acidic composite to 0.24 % in the basic variant. This reduction is attributed to the interaction of Na^+ ions with the PSS^- polyanion, forming Na^+PSS^- complexes that effectively decouple the PSS from the PEDOT: PSS/GO system [28,34]. Since the PSS chains typically maintain stability through hydrogen bonding with the GO oxygen groups, their displacement by Na^+ results in a localized reduction of the sulfur signature. These elemental shifts, combined with the observed reduction in XRD d-spacing from 3.56Å to 3.44Å, underscore a transition from a coiled benzoid to a planarized quinoid conformation, ultimately governing the optoelectronic performance of the resulting HTL.

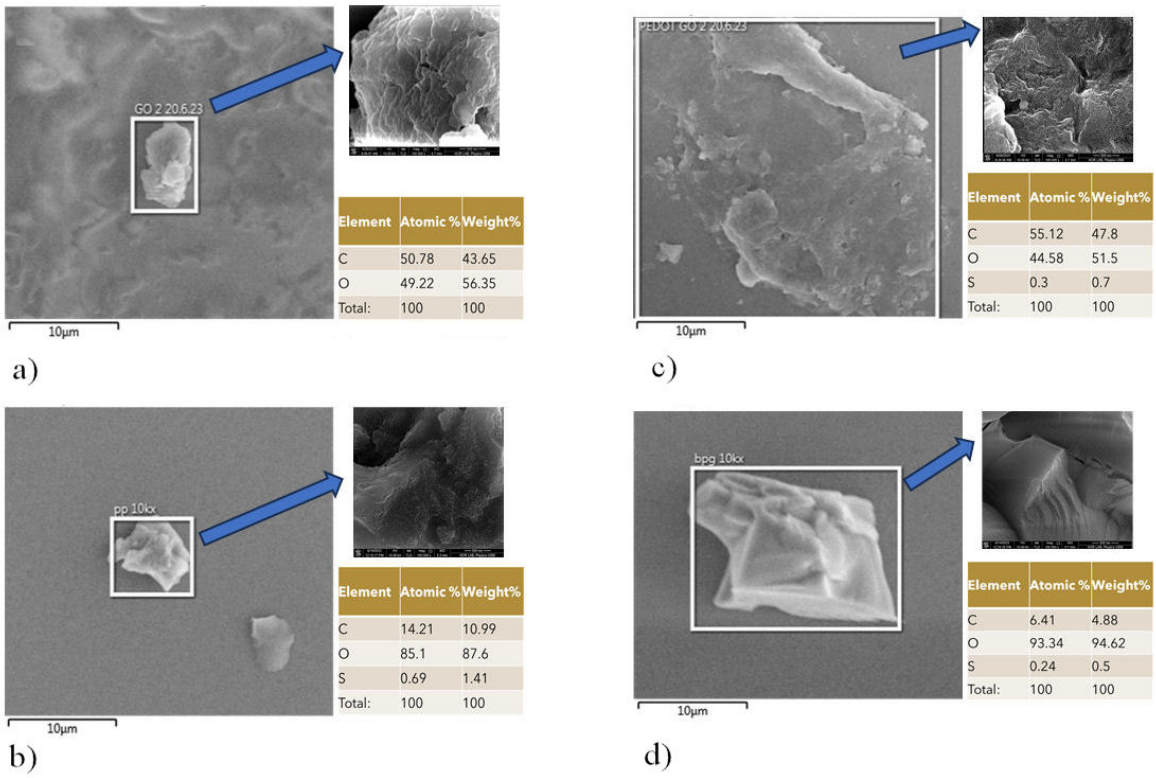


FIGURE 6. FESEM and EDX results at 10kX for a) GO; b) PEDOT: PSS; c) acidic PEDOT: PSS/GO and d) basic PEDOT: GO. Insets are the FESEM images at 100kX.

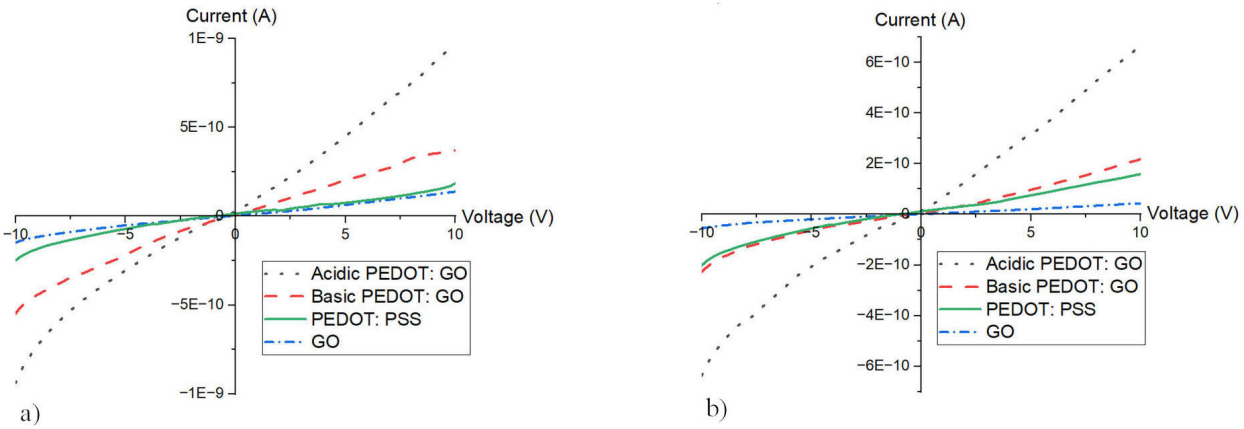


FIGURE 7. Two-point probe results for each HTL; a) random region 1; b) random region 2.

3.3. I-V result

Figure 7 shows the I-V curves for each HTL at two random regions. The average resistance value for each HTL was calculated and tabulated as shown in Table I. As shown in Fig. 7, GO has the lowest curve among all which means it is the least conductive potential hole transport layer, with the highest average resistance of 1.55E+11 Ω and lowest bulk conductivity of 8.58E-09 S/cm as shown in Table I. Due to the existence of the oxygen functional groups, GO has a low electrical conductivity [40]. PEDOT is a conjugated polymer [41] and its conductivity can be contributed to the conjugated bonds with pi electrons which are delocalized [42]. After PEDOT: PSS reacts with GO, GO replaces the insulating PSS to form PEDOT: GO, and PEDOT combines with GO through the pi-to-pi interaction [34]. During this process, PEDOT transforms from a benzenoid structure to a quinoid structure to allow more pi-to-pi interactions [35,36]. This can be supported by the lower pi-to-pi stacking of basic PEDOT: PSS/GO (3.44Å) and acidic PEDOT: GO (3.48Å) than that of PEDOT: PSS

TABLE I. Average resistance and bulk conductivity for each HTL.

HTL material	Resistance (Ω) First region	Resistance (Ω) Second region	Average Resistance (Ω)	Sheet Resistance (Ω/sq)	Bulk Conductivity, σ(S/cm)
Acidic PEDOT: PSS/GO	1.06E+10	1.54E+10	1.30E+10	1.95E+10	1.03E-07
Basic PEDOT: PSS/GO	2.76E+10	4.69E+10	3.72E+10	5.58E+10	3.58E-08
PEDOT: PSS	5.86E+10	6.79E+10	6.33E+10	9.50E+10	2.11E-08
GO	7.39E+10	2.37E+11	1.55E+11	2.33E+10	8.58E-09

(3.56Å) in the XRD result which reflects the transformation of PEDOT structure from benzoid to quinoid [33]. The increase of pi-to-pi interactions provides more paths for electron transfer [43], facilitating the electron transport process [44], thus, making PEDOT: PSS/GO more conductive than PEDOT: PSS with the values of 3.58E-08 S/cm and 2.11E-08 S/cm respectively. Meanwhile, the acidic PEDOT: PSS/GO and basic PEDOT: GO showed average resistance values of 1.30E+10 Ω and 3.72E+10 Ω showing lower electrically resistance than PEDOT: PSS, which has an average resistance value of 6.33E+10 Ω. Basic PEDOT: PSS/GO shows better conductivity than acidic PEDOT: GO with the value of 2.11E-08 S/cm and 1.03E-07 S/cm respectively. However, the results in Fig. 7 show that basic PEDOT: PSS/GO has a lower I-V curve than acidic PEDOT: GO, thus, it is less conductive than acidic PEDOT: GO.

Moreover, Table I shows that the basic PEDOT: PSS/GO has an average resistance value of 3.72E+10 Ω, which is higher than acidic PEDOT: PSS/GO which has an average resistance value of 1.30E+10 Ω. The PSS chain is significant in stabilizing the PEDOT: PSS molecule, thus, the loss of PSS which destabilizes PEDOT: PSS can adversely affect the charge carrier concentration [45]. When NaOH is present, Na^+ reacts with the PSS chain to form Na^+PSS^- [28], thus, the PEDOT: PSS which loses the PSS component is destabilized. Although many of the PEDOT: PSS have been transformed into PEDOT: PSS/GO in the basic PEDOT: PSS/GO solution, there are unreacted PEDOT: PSS molecules that can contribute to the conductivity as well. In fact, by referring to the absorbance spectra in Fig. 2, the peak of 225 nm which represents the PSS chain absorbance [26] in both acidic and basic PEDOT: PSS/GO is distinct, showing the dominant presence of unreacted PEDOT: PSS. When NaOH is used as a base, the NaOH destroys the unreacted PEDOT: PSS molecules, making them destabilized [28]. Thus, although there are more PEDOT: PSS/GO molecules formed in the basic condition than those formed in the acidic condition, the overall conductivity contributed by both PEDOT: PSS/GO and unreacted PEDOT: PSS is higher in the acidic PEDOT: PSS/GO layer than that in the basic PEDOT: PSS/GO layer, making the basic PEDOT: PSS/GO layer more electrically resistant than the acidic PEDOT: PSS/GO layer.

As compared to commercial ITO electrodes (10–100 Ω/sq); (1.0 x 10^3 S/cm), the optimized Acidic PEDOT: PSS/GO film exhibits a highly resistive profile that is 9 orders of magnitude higher in sheet resistance and 12 orders of magnitude lower in bulk conductivity, a divergence consistent with its role as a charge-selective interface rather than a bulk current collector. Consequently, this multi-order of magnitude difference does not hinder device performance. While the underlying ITO layer is engineered exclusively for low-loss bulk current extraction, these ultra-thin polymer blends are optimized for energy level alignment, targeted hole extraction, and electron blocking at the active layer boundary.

4. Conclusion

In a nutshell, PEDOT: PSS, as a commonly employed hole transport layer can be doped with carbon materials such as graphene oxide to improve its performance. The PEDOT: PSS/GO synthesized from the mixture of PEDOT: PSS and GO has shown better electrical properties, being more conductive than PEDOT: PSS and GO. However, the acidic PEDOT: GO, with a lower average resistance value of 1.30E+10 Ω and conductivity value of 1.03E-07 S/cm is more conductive than the basic PEDOT: PSS/GO which has higher average resistance value of 3.72E+10 Ω due to the damage of unreacted PEDOT: PSS caused by NaOH. Based on the UV-Vis absorbance result, the PSS chain absorbance peak of the basic PEDOT: PSS/GO is around 13 % less than that of the acidic PEDOT: GO, indicating more replacement of the PSS chain and better formation of PEDOT: GO. The XRD result further supports the UV-vis result. The basic PEDOT: PSS/GO has lower pi-to-pi stacking (3.44Å) than acidic PEDOT: PSS/GO (3.48Å) which indicates more benzoid to quinoid transformation and more PEDOT: PSS/GO formation in basic PEDOT: GO. The EDX results indicate higher oxygen content in the basic PEDOT: PSS/GO (93.34 %) than in the acidic PEDOT: PSS/GO (44.58 %) due to the presence of NaOH which generates more hydroxyl groups in GO. Even so, based on the AFM result, the basic PEDOT: PSS/GO still shows the lowest surface roughness (Rq: 2.52 nm) among all potential HTLs, which can lead to the lowest interfacial recombination among all. That is due to the better wettability of basic PEDOT: PSS/GO because of the higher dispersity of GO in basic condition, thus, making the adhesion on glass better. Therefore, the potential usage of basic PEDOT: PSS/GO in the organic semiconductors (OSCs) such as film deposited onto ITO as counter electrode for dye-sensitized solar cell (DSSC).

Acknowledgment

The authors would like to express their profound gratitude for the financial support received from the Ministry of Higher Education Malaysia for Fundamental Research Grant Scheme with Project Code: (FRGS/1/2022/STG07/USM/02/8), and the Bridging Grant (RUI), USM (grant number: R501-LR-RND003-0000002174-0000).

Authors contribution

M.D. Nurhafizah: Writing-original draft; supervision; resources
Tan You Zi: Methodology, formal analysis
B. Afzalina: Writing-review and editing, formal analysis

Conflict of interest

There is no conflict of interest.

1. S. Katoon *et al.*, Perovskite solar cell's efficiency, stability and scalability: A review, *Materials Science for Energy Technologies* **6** (2023) 437, https://doi.org/10.1016/j.mset.2023.04.007
2. H. Xu *et al.*, Hole transport layers for organic solar cells: recent progress and prospects, *Journal of Materials Chemistry A* **8** (2020) 11478, https://doi.org/10.1039/d0ta03511d
3. S. Li *et al.*, A brief review of hole transporting materials commonly used in perovskite solar cells, *Rare Metals* **40** (2021) 2712, https://doi.org/10.1007/s12598-020-01691-z
4. J.C. Yu *et al.*, Highly efficient and stable inverted perovskite solar cell employing PEDOT:GO composite layer as a hole transport layer, *Scientific Reports* **8** (2018) 1070, https://doi.org/10.1038/s41598-018-19612-7
5. Y. Wang *et al.*, High-performance hole transport layer based on WS_2 doped PEDOT: PSS for organic solar cells, *Organic Electronics* **99** (2021) 106305, https://doi.org/10.1016/j.orgel.2021.106305
6. S. Ozcan *et al.*, Graphene oxide-doped PEDOT: PSS as hole transport layer in inverted bulk heterojunction solar cell, *Journal of Materials Science: Materials in Electronics* **31** (2020) 3576, https://doi.org/10.1007/s10854-020-02906-w
7. W. Li *et al.*, Boost the performance of inverted perovskite solar cells with PEDOT: PSS/Graphene quantum dots composite hole transporting layer, *Organic Electronics* **78** (2020) 105575, https://doi.org/10.1016/j.orgel.2019.105575
8. C. Redondo-Obispo *et al.*, Enhanced stability and efficiency in inverted perovskite solar cells through graphene doping of PEDOT: PSS hole transport layer, *Materials & Design* **191** (2020) 108587, https://doi.org/10.1016/j.matdes.2020.108587
9. D.-Y. Lee, S.-I. Na, and S.-S. Kim, Graphene oxide/PEDOT: PSS composite hole transport layer for efficient and stable planar heterojunction perovskite solar cells, *Nanoscale* **8** (2016) 1513, https://doi.org/10.1039/C5NR05271H
10. J. Niu *et al.*, Graphene-oxide doped PEDOT: PSS as a superior hole transport material for high-efficiency perovskite solar cell, *Organic Electronics* **48** (2017) 165, https://doi.org/10.1016/j.orgel.2017.05.044
11. A. Giuri *et al.*, UV Reduced Graphene Oxide PEDOT: PSS Nanocomposite for Perovskite Solar Cells, *IEEE Transactions on Nanotechnology* **15** (2016) 725, https://ieeexplore.ieee.org/abstract/document/7398111/
12. S. Wang *et al.*, Hybrid UV-Ozone-Treated rGO-PEDOT: PSS as an Efficient Hole Transport Material in Inverted Planar Perovskite Solar Cells, *Nanoscale Research Letters* **12** (2017) 619, https://doi.org/10.1186/s11671-017-2393-1
13. X. Huang *et al.*, Moderately reduced graphene oxide/PEDOT: PSS as hole transport layer to fabricate efficient perovskite hybrid solar cells, *Organic Electronics* **39** (2016) 288, https://doi.org/10.1016/j.orgel.2016.10.013
14. X.-Y. Li *et al.*, The solvent treatment effect of the PEDOT: PSS anode interlayer in inverted planar perovskite solar cells, *RSC Advances* **6** (2016) 24501, https://doi.org/10.1039/c5ra25787e
15. C. Peng, M.N. Chan, and C.K. Chan, The Hygroscopic Properties of Dicarboxylic and Multifunctional Acids: Measurements and UNIFAC Predictions, *Environmental Science & Technology* **35** (2001) 4495, https://doi.org/10.1021/es0107531
16. R. Tariq Ahmedhamdi *et al.*, Humidity impact on photovoltaic cells performance: *A review*, **35** (2018), http://www.ijrerd.com/papers/v3-i11/5-IJRERD-C264.pdf
17. Q. Wang *et al.*, Modulation of PEDOT: PSS pH for Efficient Inverted Perovskite Solar Cells with Reduced Potential Loss and Enhanced Stability, *ACS Applied Materials & Interfaces* **8** (2016) 32068, https://doi.org/10.1021/acsami.6b11757
18. F.J. Lim *et al.*, Influence of a novel fluorosurfactant modified PEDOT: PSS hole transport layer on the performance of inverted organic solar cells, *Journal of Materials Chemistry* **22** (2012) 25057, https://doi.org/10.1039/C2JM34484K
19. H. Luo *et al.*, Efficient and Air-Stable Planar Perovskite Solar Cells Formed on Graphene-Oxide-Modified PEDOT: PSS Hole Transport Layer, *Nano-Micro Letters* **9** (2017) 39, https://doi.org/10.1007/s40820-017-0140-x
20. C.-J. Shih *et al.*, Understanding the pH-Dependent Behavior of Graphene Oxide Aqueous Solutions: A Comparative Experimental and Molecular Dynamics Simulation Study, *Langmuir* **28** (2012) 235, https://doi.org/10.1021/la2036079

21. J.L. Suter and P.V. Coveney, Principles governing control of aggregation and dispersion of aqueous graphene oxide, *Scientific Reports* **11** (2021) 22460, https://doi.org/10.1038/s41598-021-01643-4

22. E.H. Sujiono *et al*., Graphene oxide based coconut shell waste: synthesis by modified Hummers method and characterization, *Heliyon* **6** (2020) e04568, https://doi.org/10.1016/j.heliyon.2020.e04568

23. J.C. Yu *et al*., Highly Efficient Polymer-Based Optoelectronic Devices Using PEDOT: PSS and a GO Composite Layer as a Hole Transport Layer, *ACS Applied Materials & Interfaces* **6** (2014) 2067, https://doi.org/10.1021/am405231b

24. T.F. Emiru and D.W. Ayele, Controlled synthesis, characterization and reduction of graphene oxide: A convenient method for large scale production, *Egyptian Journal of Basic and Applied Sciences* **4** (2017) 74, https://doi.org/10.1016/j.ejbas.2016.11.002

25. V.B. Mbayachi *et al.*, Graphene synthesis, characterization and its applications: A review, *Results in Chemistry* **3** (2021) 100163, https://doi.org/10.1016/j.rechem.2021.100163

26. Y. Xia, K. Sun, and J. Ouyang, Highly conductive poly(3,4-ethylenedioxythiophene):poly(styrene sulfonate) films treated with an amphiphilic fluoro compound as the transparent electrode of polymer solar cells, *Energy & Environmental Science* **5** (2012) 5325, https://doi.org/10.1039/c1ee02475b

27. F.-P. Du *et al.,* PEDOT: PSS/graphene quantum dots films with enhanced thermoelectric properties via strong interfacial interaction and phase separation, *Scientific Reports* **8** (2018) 6441, https://doi.org/10.1038/s41598-018-24840-y

28. T.-C. Tsai *et al*., A facile dedoping approach for effectively tuning thermoelectricity and acidity of PEDOT: PSS films, *Organic Electronics* **15** (2014) 641, https://doi.org/ https://doi.org/10.1016/j.orgel.2013.12.023

29. F. Abd-Wahab, H.F. Abdul Guthoos, and W.W.A. Wan Salim, Solid-State rGO-PEDOT: PSS Transducing Material for Cost-Effective Enzymatic Sensing, *Biosensors* **9** (2019) 6, https://doi.org/10.3390/bios9010036

30. G. Surekha *et al*., FTIR, Raman and XRD analysis of graphene oxide films prepared by modified Hummers method, *Journal of Physics: Conference Series* **1495** (2020) 012012, https://doi.org/10.1088/1742-6596/1495/1/012012

31. N.G. de Barros *et al.*, Graphene Oxide: A Comparison of Reduction Methods, C **9** (2023) 73, https://doi.org/10.3390/c9030073

32. S.B. Singh and S.A. Dastgheib, Physicochemical transformation of graphene oxide during heat treatment at 110-200°, *Carbon Trends* **10** (2023) 100251, https://doi.org/10.1016/j.cartre.2023.100251

33. X. Wang *et al*., Enhancement of thermoelectric performance of PEDOT: PSS films by post-treatment with a superacid, *RSC Advances* **8** (2018) 18334, https://doi.org/10.1039/c8ra02058b

34. R.K. Sharma *et al*., Graphene oxide modified PEDOT: PSS as an efficient hole transport layer for enhanced performance of hybrid silicon solar cells, *Surfaces and Interfaces* **36** (2023) 102577, https://doi.org/10.1016/j.surfin.2022.102577

35. B. Piro *et al*., Fabrication and Use of Organic Electrochemical Transistors for Sensing of Metabolites in Aqueous Media, *Applied Sciences* **8** (2018) 928, https://doi.org/10.3390/app8060928

36. J. Ouyang *et al*., On the mechanism of conductivity enhancement in poly(3,4-ethylenedioxythiophene):poly(styrene sulfonate) film through solvent treatment, *Polymer* **45** (2004) 8443, https://doi.org/10.1016/j.polymer.2004.10.001

37. D. Lee and J. Seo, Three-dimensionally networked graphene hydroxide with giant pores and its application in supercapacitors, *Scientific Reports* **4** (2014) 7419, https://doi.org/10.1038/srep07419

38. V.V. Neklyudov *et al*., New insights into the solubility of graphene oxide in water and alcohols, *Physical Chemistry Chemical Physics* **19** (2017) 17000, https://doi.org/10.1039/C7CP02303C

39. J. Eun Song *et al*., A Thin In_2S_3 Interfacial Layer for Reducing Defects and Roughness of $Cu_2ZnSn(S,Se)_4$ Thin-Film Solar Cells, *Chem.Sus.Chem.* **15** (2022) e202102350, https://doi.org/10.1002/cssc.202102350

40. T. Tene *et al*., Optical properties of graphene oxide, Frontiers in *Chemistry* **11** (2023) 1152865, https://doi.org/10.3389/fchem.2023.1214072

41. T. Kim *et al*., Highly conductive PEDOT: PSS with enhanced chemical stability, *Organic Electronics* **74** (2019) 77, https://doi.org/ https://doi.org/10.1016/j.orgel.2019.06.033

42. S.A. Umoren, M.M. Solomon, and V.S. Saji, Chapter 19 - Conducting polymers, in Polymeric Materials in Corrosion Inhibition, S.A. Umoren, M.M. Solomon, and V.S. Saji, *Editors.* **2022** (2022) 443, https://doi.org/10.1016/C2020-0-00555-4

43. G. Skorupskii *et al*., Electrical conductivity through π–π stacking in a two-dimensional porous gallium catecholate metal–organic framework, *Annals of the New York Academy of Sciences* **1518** (2022) 226, https://doi.org/10.1111/nyas.14867

44. B. Sun *et al.*, Electron Transfer Facilitated by π–π Stacking during the Nitrobenzene Recognition Process of an MOF Sensor, *The Journal of Physical Chemistry C* **125** (2021) 12433, https://doi/10.1021/acs.jpcc.1c02942%20

45. S.H. Kim, Control of the Charge Carrier Concentration and Hall Mobility in PEDOT: PSS Thermoelectric Films, *Bulletin of the Korean Chemical Society* **38** (2017) 1460, https://doi.org/10.1002/bkcs.11327

Structural, morphological, optical and electrical properties of Al-doped ZnO thin films prepared by Sol-Gel spin coating

A. Carrero[a,b,c,*], P. Perillo[a,b], D. Rodríguez[a,b], and M. Barrera[a,b,c]

[a]*Comisión Nacional de Energía Atómica, Centro Atómico Constituyentes, e-mail: aneelyc@gmail.com*

[b]*Instituto de Nanociencia y Nanotecnología, CNEA–CONICET,*

[c]*Departamento Energía Solar, CAC–CNEA.*

Received 17 April 2026; accepted 4 August 2026

Undoped and aluminum-doped ZnO (AZO) thin films were prepared by the sol-gel method using spin coating. The films exhibited the characteristic wurtzite crystal structure of ZnO with a preferential orientation along the c-axis. Surface and cross-sectional morphologies were analyzed by scanning electron microscopy (SEM), revealing noticeable differences between the doped and undoped films. The optical transmittance was approximately 77 % in the 450-750 nm range. Electrical resistivity decreased from $1{,}9\times10^{5}$ Ω·cm (ZnO) to $1{,}0\times10^{2}$ Ω·cm (AZO). These results suggest that low-level Al doping enhances the electrical properties while preserving good optical transparency in AZO thin films. Furthermore, the results highlight the correlation between structural, optical, and electrical properties in ZnO and AZO thin films.

Keywords: Al-Doped ZnO; Sol–Gel; spin coating technique; structural properties; optical transparency.

DOI: https://doi.org/10.31349/RevMexFis.72.061005

1. Introduction

Zinc oxide (ZnO) is a II-VI semiconductor with a wide direct band gap of approximately 3.37 eV at room temperature. In addition, it exhibits a high exciton density due to its large exciton binding energy (60 meV). ZnO is also characterized by high optical transparency in the visible and near-ultraviolet regions, highlighting its strong potential for optoelectronic applications [1-3]. Furthermore, ZnO has been extensively investigated for applications in photocatalysis [4], piezoelectric devices [5], solar cells [6], and as a transparent conductive contact [7-8]. The electrical, optical, and morphological properties of ZnO can be tailored through doping [2,6]. In this material, doping can be achieved by substituting cationic sites Zn^{2+} with metals or anionic sites O^{2-} with non-metals [6,9]. In particular, doping with group III elements, such as Al, Ga, or In, has proven to be an effective strategy for enhancing the electrical properties of ZnO. AZO thin films exhibit increased electrical conductivity while maintaining high optical transmittance, making them attractive candidates for transparent electronics applications [1]. Moreover, AZO thin films stand out due to their thermal stability, low cost, and excellent transparency, which make them especially suitable for electro-optical applications [10-11] Various deposition techniques have been employed to fabricate AZO films, including pulsed laser deposition [12-13], molecular beam epitaxy (MBE) [14], and RF or DC magnetron sputtering [15-16]. However, these methods typically require complex and expensive equipment. On the other hand, AZO films can be synthesized using the sol-gel method, which has attracted significant attention due to its simplicity, low cost, and potential for large-area coating [2,17-18]. Moreover, the structural, optical, and electrical properties of the resulting films are strongly influenced by several parameters, such as the substrate, solvent, annealing temperature, doping concentration, aging time, and precursor molar concentration [2,19-21]. On the other hand, obtaining AZO films with preferential orientation along the c-axis prepared by the sol-gel method is a challenge due to the various processing parameters. AZO films with preferential orientation are of great interest for applications in photovoltaic or optoelectronic devices [18,22-23]. In this work, ZnO and AZO thin films with preferential orientation along the c-axis were prepared by a sol-gel spin-coating route and deposited onto glass substrates. The films were comparatively analyzed in terms of their structural, morphological, optical, and electrical properties. This study aims to provide further insight into the effect of low aluminum concentration on the properties of ZnO thin films, contributing to a better understanding of how subtle compositional modifications influence their performance and potential application in optoelectronic devices.

2. Materials and methods

2.1. Preparation of ZnO and Al-Doped ZnO precursor sols

Undoped ZnO and aluminum-doped ZnO sols were synthesized via the sol-gel method. Zinc acetate dihydrate ($Zn(CH_3COO)_2{\cdot}2H_2O$) was used as the zinc precursor, absolute ethanol as the solvent, monoethanolamine (MEA) as the stabilizing agent, and aluminum nitrate nonahydrate ($Al(NO_3)_3{\cdot}9H_2O$) as the dopant source. For the AZO sols, aluminum was introduced at a nominal concentration of 0.8 at %. A 0.2 M solution was prepared by dissolving 0.02 mol of zinc acetate in 100 mL of ethanol. While the solution was

stirred and heated to 80°C, MEA was added dropwise at a fixed MEA:Zn molar ratio of 1:1, inducing a transition from a whitish to a transparent solution. Subsequently, aluminum nitrate was added, and the mixture was refluxed for 3 h. Finally, the resulting sol was aged for 48 h prior to thin-film deposition.

2.2. Thin-film deposition and thermal treatment

Thin films were deposited onto cover glass substrates by spin coating. Prior to deposition, the substrates were sequentially cleaned with acetone, isopropyl alcohol, and deionized water, and then dried under a nitrogen stream. Spin coating was carried out at 2000 rpm for 40 s. After each coating step, the films were preheated on a hot plate at 100°C for 10 min to promote solvent evaporation and remove residual organic species. This coating-drying cycle was repeated six times to obtain the desired film thickness. Finally, the films were annealed in a furnace at 500°C for 2 h with a heating rate of 5°C/min and then allowed to cool naturally to room temperature.

The deposition conditions were optimized, and the films reported here were obtained under these optimized, controlled, and reproducible parameters.

2.3. Film characterization

The crystallinity of the films was analyzed by X-ray diffraction (XRD) using a Panalytical Empyrean diffractometer operating in parallel-beam geometry with CuKα radiation. Surface and cross-sectional morphologies were examined by scanning electron microscopy (SEM) using a Carl Zeiss Supra 40 Gemini microscope. Optical properties were characterized by UV–Vis spectroscopy using a GBC UV–Vis 920 spectrophotometer. Electrical resistance was measured using the standard four-point probe technique.

3. Results and discussion

3.1. Structural and morphology of the films

Figure 1 shows the X-ray diffraction (XRD) patterns of undoped ZnO and Al-doped ZnO films grown on cover glass. The crystalline planes present in the films were identified using Miller indices (*hkl*). The diffraction peaks match well with the JCPDS PDF card No. 00-036-1451, confirming that the films exhibit the typical wurtzite structure of ZnO, are polycrystalline, and show a preferential orientation along the (002) direction. Moreover, no additional crystalline phases, such as aluminum oxide or other impurities, were detected.

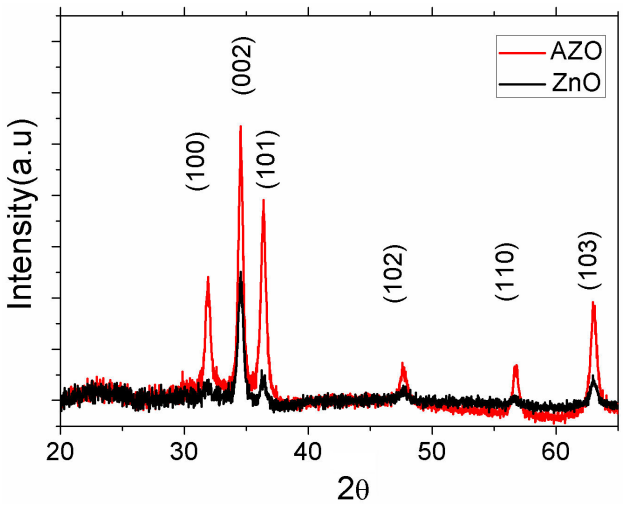


FIGURE 1. XRD patterns of undoped and Al-doped ZnO thin films.

The lattice parameters were calculated from the diffractogram using the following relations [24-26]:

$$\frac{1}{d_{hkl}^2} = \frac{4}{3}\left(\frac{h^2+hk+k^2}{a^2}\right) + \frac{l^2}{c^2}, \tag{1}$$

$$d_{hkl} = \frac{\lambda}{2\sin\theta}, \tag{2}$$

where d_{hkl} denotes the interplanar spacing for the (hkl) planes, and a and c represent the lattice constants. The calculated lattice parameters for the undoped ZnO and AZO films are presented in Table I. No significant changes in the lattice parameters are observed after Al incorporation, which can be attributed to the relatively low aluminum concentration used in this work. This behavior is consistent with previous reports on doped ZnO films [2,21]. Moreover, the c/a ratio is in agreement with the typical value for ZnO, confirming the hexagonal wurtzite crystal structure of the films. The crystallite size was estimated using the Debye-Scherrer equation [21,27-28], employing the full width at half maximum (FWHM) of the most intense diffraction peak (see Table I). The larger crystallite size observed for the doped film suggests that Al incorporation may have modified the growth kinetics, possibly through enhanced atomic mobility, reduced grain boundary energy, and decreased microstrain and defect density.

TABLE I. Crystallite size (D), lattice constants (a, c), and c/a ratio of ZnO and AZO films determined from XRD analysis.

Parameter	ZnO	AZO
$a = b$ (Å)	3.242 (2)	3.242 (4)
c (Å)	5.191 (1)	5.191 (6)
c/a	1.601	1.601
D (nm)	10.6 (3)	17.0 (7)

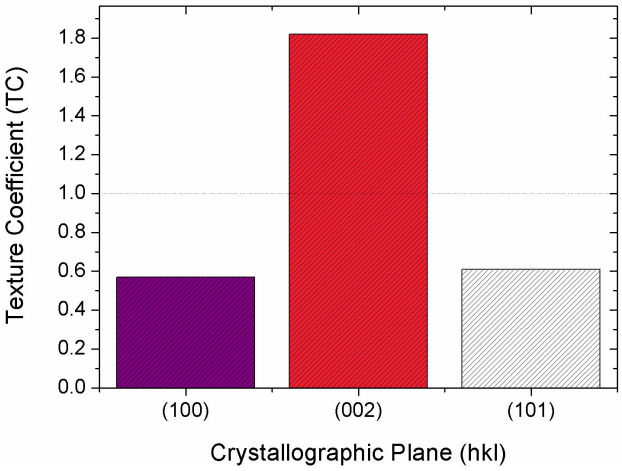


FIGURE 2. Texture coefficients of the (100), (002), and (101) planes of the AZO thin film.

In order to examine the preferred orientation of the crystal structure, the texture coefficient (TC) was calculated from the XRD data using the following equation [2,21,27-28]:

$$TC_{\text{hkl}} = \frac{I_{(\text{hkl})}/I_{0(\text{hkl})}}{\frac{1}{N}\sum_n \left(I_{(\text{hkl})}/I_{0(\text{hkl})}\right)}, \tag{3}$$

where $I_{(\text{hkl})}$ is the measured intensity of the (hkl reflection and $I_0(\text{hkl})$ is the corresponding standard intensity and N is the number of diffraction peaks considered. A $TC > 1$ indicates preferential growth of the film along the corresponding crystallographic plane.

In Fig. 2 the texture coefficient (TC) values indicate that the AZO film exhibits preferential growth along the (002) crystallographic plane ($TC_{002} = 1{,}82$), consistent with the XRD diffractogram. This preferential orientation along the c-axis indicates a higher degree of crystallographic alignment and may favor the development of more ordered crystalline domains. This structural feature can contribute to the functional properties of the AZO film, including its electrical performance.

The SEM images of the surface of undoped and aluminum-doped ZnO thin films are shown in Fig. 3a) and 3b), respectively. The undoped ZnO film exhibits a porous morphology with a granular structure and an average grain size of approximately 40 nm. In contrast, the AZO film displays a denser and more homogeneous surface, consisting of grains with an average size of about 49 nm, as determined from the micrograph analysis using ImageJ software.

The cross-sectional SEM images are shown in Figs. 3c) - 3d). Both thin films exhibit a granular structure [29], and the grains display a preferred growth orientation, as they are not completely spherical [30-31]. This observation is consistent with the preferential growth inferred from the XRD analysis. The undoped ZnO film appears less homogeneous, with higher surface roughness and a less densely packed structure compared to the Al-doped ZnO film, suggesting that the dopant plays a significant role in influencing the film morphology [2,6]. The film thicknesses estimated from the cross-sectional SEM images were approximately 170 nm for the undoped ZnO film and 163 nm for the AZO film.

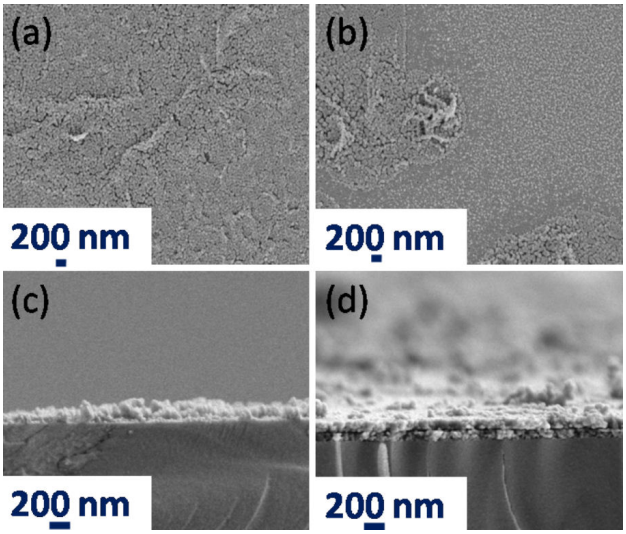


FIGURE 3. SEM top-view images of undoped ZnO a) and AZO b), and cross-sectional images of undoped ZnO c) and AZO d) films on cover glass substrates.

3.2. Optical characterization

Figure 4 shows the transmittance spectra of the undoped ZnO film, the Al-doped ZnO film, and the glass coverslip substrate. Two main features can be identified in the spectra. First, the absorption edge of both ZnO films (undoped and Al-doped) appears around 390 nm, which is associated with the fundamental band-to-band transition of ZnO. Additionally, a shoulder with a maximum around 330 nm is observed in the UV region. Second, in the visible region (450–750 nm), the undoped ZnO film exhibits an average transmittance of approximately 94 %, slightly higher than that of the glass coverslip substrate (∼92 %). This behavior could be

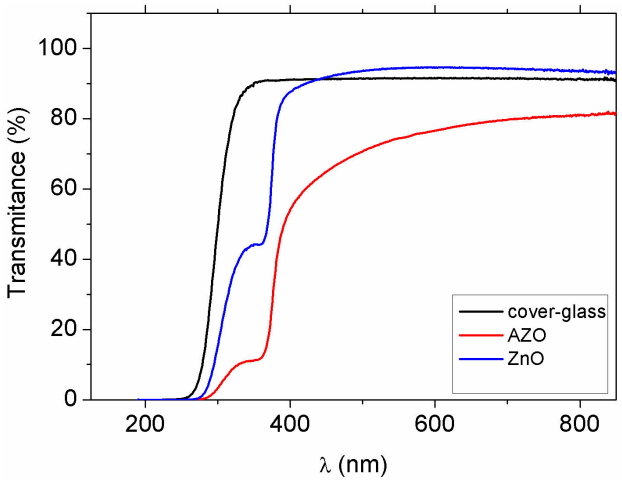


FIGURE 4. Transmittance spectra of undoped ZnO, AZO thin films and the cover glass substrate.

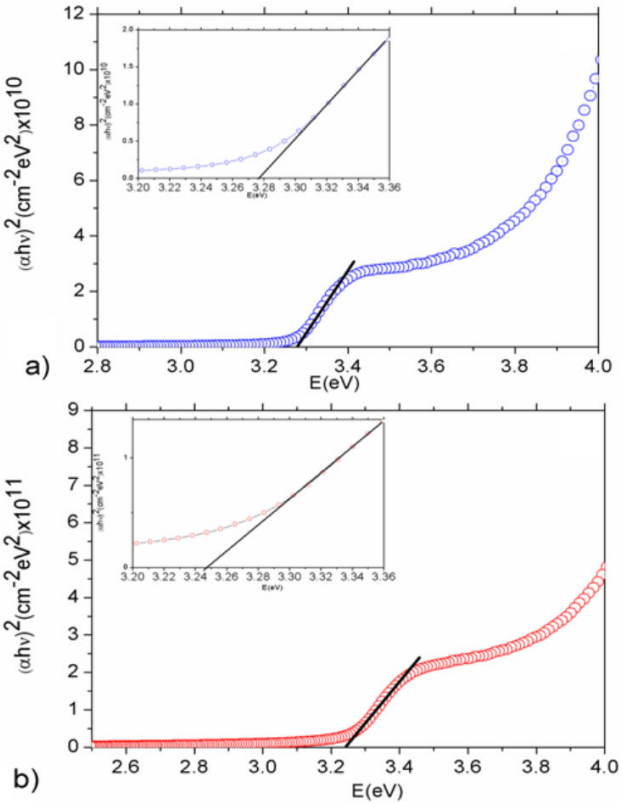


FIGURE 5. Optical band gap energy of undoped ZnO a) and AZO b) thin films.

be related to the thickness of the ZnO film (≈ 170 nm, estimated from SEM images), which is close to the optical optimum for antireflection conditions, as well as to its morphology characterized by the presence of voids, which may promote a partial antireflection effect in the air/film/glass system [32-33]. In contrast, the Al-doped ZnO film shows a lower transmittance (77 %) in the visible range (450–750 nm). This difference may be associated with the more compact and homogeneous morphology of the AZO film compared with the undoped ZnO film, as revealed by the SEM images [Fig. 3c) and 3d)] [33,34-36].

The energy band gap value was determined from transmittance measurements. The optical absorption coefficient was calculated using the Beer-Bouguer-Lambert law, according to the expression $\alpha = -(1/d)\ln(T)$, where d is the thickness of the film [37-39]. The energy gap of the films was estimated by using the Tauc relation [40-41], given by: $\alpha h\nu = A(h\nu - Eg)^{1/2}$, Where $h\nu$ is the photon energy, α is the absorption coefficient, Eg is the band gap energy and A is a constant. Fig. 5 shows that the band gap energy was determined by extrapolating the straight line of the curve to the point where $(\alpha h\nu)^2 = 0$. The obtained values were 3.28 eV and 3.24 eV for the undoped and doped ZnO films, respectively. The slight reduction in the optical band gap may be attributed to Al incorporation, which can introduce shallow donor states near the conduction band as well as defect- or disorder-related states within the band gap [10,41]. These

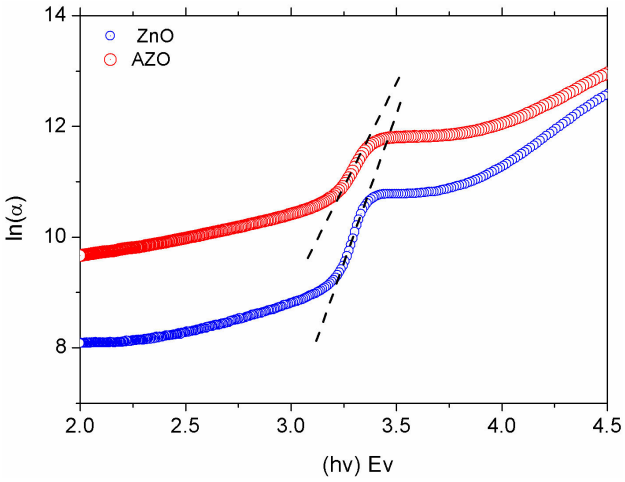


FIGURE 6. $\ln(\alpha)$ versus photon energy for undoped ZnO and AZO thin films.

effects can lead to band tailing and a shift of the absorption edge toward lower energies, as will be further discussed in relation to the Urbach energy analysis. Although Al doping is often associated with increased carrier concentration and a Burstein-Moss shift leading to an apparent band gap widening, the observed behavior suggests that band-gap narrowing mechanisms dominate in the present case. This may be related to the relatively low Al concentration and the presence of structural disorder or defect states, which can mask the Burstein-Moss effect.

In semiconductors, the optical absorption below the band-edge energy exhibits an exponential behavior, known as the Urbach tail. The energy associated with this tail is referred to as the Urbach energy (Eu) and provides information about the degree of disorder present near the band edge. The Urbach energy can be described by the following relation [42-43]:

$$\alpha = \alpha_0 \exp\left(\frac{h\nu}{E_u}\right), \tag{4}$$

where α_0 is a constant and hν represents the photon energy. The value of Eu was obtained from the plot of the natural logarithm of the absorption coefficient, $\ln(\alpha)$, as a function of the photon energy (hν), as shown in Fig. 6. The linear region of the curve was fitted, and Eu was determined from the inverse of the slope. The obtained values were 102 meV and 207 meV for the undoped ZnO and Al-doped ZnO thin films, respectively, suggesting that the incorporation of Al increases the electronic disorder of the system. These values are in good agreement with those reported for ZnO and AZO thin films in the literature [44-45].

3.3. Electric characterization

The electrical resistivity ρ of the thin films was determined using the relation

$$\rho = \frac{\pi}{\ln 2}\frac{V}{I}t, \tag{5}$$

TABLE II. Main structural, optical, and electrical parameters for ZnO and AZO thin films.

Parameter	ZnO	AZO
Crystallite size (nm)	10,6	17,0
Thickness (nm)	170	163
Transmittance (%) (450-750nm)	94	77
Resistivity ($\Omega \cdot$ cm)	$1{,}9 \times 10^5$	$1{,}0 \times 10^2$

where $\pi/\ln 2$, is the geometrical correction factor for thin films and t is the film thickness [46]. The resistivity values obtained were $1{,}9\times10^5\ \Omega\cdot$cm and $1{,}0\times10^2\ \Omega\cdot$cm for the undoped ZnO and Al-doped ZnO films, respectively. These results indicate that Al doping reduces the resistivity of the ZnO film by approximately three orders of magnitude. Similar resistivity values have been reported for AZO thin films deposited on glass substrates by the sol-gel method [3,23,47]. This decrease in resistivity suggests that Al incorporation modifies the electrical properties of ZnO, possibly through donor-like behavior. A commonly proposed mechanism is the substitution of Zn^{2+} by Al^{3+} ions acting as donor centers [3]. However, in the absence of direct evidence of substitution Al incorporation (*e.g.*, Hall-effect measurements or compositional analysis), this interpretation should be regarded as plausible rather than definitive. Additionally, the improved crystallinity and denser morphology of the doped films may also contribute to the enhanced electrical conductivity [39,43].

A summary about the main results is presented in Table II.

4. Conclusions

ZnO and AZO thin films with a nominal Al concentration of 0.8 at. % were successfully prepared by the sol-gel method using spin coating. The films exhibit the characteristic wurtzite crystal structure of ZnO, are polycrystalline and show a preferential c-axis orientation, with improved structural ordering observed upon Al incorporation.

SEM analysis revealed that the AZO film is more uniform, denser, and compact than the undoped ZnO film. The optical transmittance of the AZO film is approximately 77 % in the visible range (450-750 nm), being lower than that of the undoped ZnO film. A slight decrease in the optical band gap was observed, from 3.28 eV for ZnO to 3.24 eV for AZO. A significant decrease in electrical resistivity was observed, $1{,}9 \times 10^5\ \Omega \cdot$ cm (ZnO) to $1{,}0 \times 10^2\ \Omega \cdot$ cm (AZO).

In summary, ZnO and AZO thin films were obtained using a simple and low-cost method. The results show that Al doping leads to a significant improvement in the electrical properties while maintaining good optical transparency. These results provide further insight into the effect of low-level Al doping on ZnO thin films by correlating their structural, morphological, optical, and electrical properties and support their potential use in optoelectronic applications.

Acknowledgments

This work was financed by the Argentine National Atomic Energy Commission (CNEA), the Argentinian National Council for Scientific and Technical Research (CONICET) and the National Agency for Scientific and Technological Promotion (ANPCyT) through grant PICT-2021-I-A-00206. The authors gratefully acknowledge the Crystallography Group at CNEA for their support. In particular, we thank Diego Lionello and Daniel Vega for their collaboration in carrying out the crystallographic measurements.

1. Z. Wang *et al*., Vacancy cluster in ZnO films grown by pulsed laser deposition, *Sci. Rep.* **9** (2019) 3534, https://doi.org/10.1038/s41598-019-40029-3.
2. T. Ivanova *et al*., Sol-Gel synthesis of ZnO:Li thin films: Impact of annealing on structural and optical properties, *Crystals* **14** (2023) 6, https://doi.org/10.3390/cryst14010006.
3. S. Mridha, D. Basak, Aluminium doped ZnO films: electrical, optical and photoresponse studies, *J. Phys. D: Appl. Phys.* **40** (2007) 6902, https://doi.org/10.1088/0022-3727/40/22/008.
4. K. M. Mohamed *et al*., Recent advances in ZnO-based nanostructures for photocatalytic degradation, *Crystals* **13** (2023) 329, https://doi.org/10.3390/cryst13020329.
5. S. Ghosh *et al*., Piezoelectric-based bioactive ZnO-cellulose acetate mats, *Front. Immunol.* **14** (2023) 1245343, https://doi.org/10.3389/fimmu.2023.1245343.
6. A. Wibowo *et al*., ZnO nanostructured materials for solar cell applications, *RSC Adv.* **10** (2020) 42838, https://doi.org/10.1039/D0RA07689A.
7. N. Zhang *et al*., ZnO transparent conductive films with upconversion function, *Mater. Sci. Eng. B* **325** (2026) 119076, https://doi.org/10.1016/j.mseb.2025.119076
8. Y. C. Kao *et al*., Performance comparison of III-V multijunction solar cells, *Sci. Rep.* **9** (2019) 4308, https://doi.org/10.1038/s41598-019-40727-y.
9. D. Zhao *et al*., n-Type conducting P-doped ZnO thin films, *RSC Adv.* **10** (2020) 34527, https://doi.org/10.1039/D0RA05667G.
10. I. Jellal *et al*., Comparative study of Al- and Nidoped ZnO films, *Opt. Quantum Electron.* **55** (2023) 620, https://doi.org/10.1007/s11082-023-04798-6.
11. L. E. Morinigo *et al*., Aluminum-doped zinc oxide thin films,

Mater. Sci. Eng. B **318** (2025) 118279, https://doi.org/10.1016/j.mseb.2025.118279.

12. Q. A. Drmosh *et al*., Cu-doped ZnO thin films by PLD, *Appl. Surf. Sci.* **270** (2013) 104, https://doi.org/10.1016/j.apsusc.2012.12.126.
13. N. K. Temizer *et al*., Ferromagnetism in Al-doped ZnO films, *AIP Adv*. **14** (2024) 105331, https://doi.org/10.1063/5.0224007.
14. L. He *et al.*, Topological insulator thin films, *Phys. Status Solidi RRL* **7** (2013) 50, https://doi.org/10.1002/pssr.201307003.
15. Y. Shen *et al*., Blue light emission from ZnO/GaN heterojunction, *Curr. Appl. Phys*. **14** (2014) 345, https://doi.org/10.1016/j.cap.2013.12.011.
16. W. Yang *et al*., Al-doped ZnO films by sputtering, *Appl. Surf. Sci.* **255** (2009) 5669, https://doi.org/10.1016/j.apsusc.2008.12.021.
17. Y. Ammaih *et al*., ZnO:Al thin films properties, Opt. Quantum Electron. **46** (2014) 229, https://doi.org/10.1007/s11082-013-9757-2.
18. X. Zi-qiang *et al*., Al-doping effects in ZnO films, *Mater. Sci. Semicond. Process.* **9** (2006) 132, https://doi.org/10.1016/j.mssp.2006.01.082.
19. H. M. Hussein, Cu-doped ZnO thin films, *Results Opt*. **13** (2023) 100543, https://doi.org/10.1016/j.rio.2023.100543.
20. H. Stroescu *et al*., Sol-gel AZO thin films, *Materials* **16** (2023) 3329, https://doi.org/10.3390/ma16093329.
21. K. D. A. Kumar *et al.,* Sol-gel Al-doped ZnO films, *Appl. Phys. A* **123** (2017) 801, https://doi.org/10.1007/s00339-017-1426-z.
22. K. Baba *et al*., ZnO films by spray plasma, *Thin Solid Films* **595** (2015) 129, https://doi.org/10.1016/j.tsf.2015.10.072.
23. D. Zhang *et al*., Al-doped ZnO films, *J. Am. Ceram. Soc*. **93** (2010) 3291, https://doi.org/10.1111/j.1551-2916.2010.03847.x.
24. M. S. Nadeem *et al*., Co, Ni co-doped ZnO nanorods, *Opt. Mater.* **111** (2021) 110606, https://doi.org/10.1016/j.optmat.2020.110606.
25. A. A. Aboud *et al*., Doping effects on ZnO thin films, *RSC Adv.* **9** (2019) 7729, https://doi.org/10.1039/C8RA10599E.
26. B. D. Cullity, S. R. Stock, Elements of X-ray Diffraction, Prentice Hall, Upper Saddle River, NJ (2001).
27. M. S. Nadeem et al., Sr-doped ZnO thin film, *Opt. Mater.* **157** (2024) 116106, https://doi.org/10.1016/j.optmat.2024.116106.
28. A. Kumar, M. I. Ahmad, Role of defects in Al-doped ZnO films, *J. Mater. Sci*. **57** (2022) 7877, https://doi.org/10.1007/s10853-022-07136-5.
29. M. Khiari *et al*., ZnO thin films by liquid deposition, *Coatings* **12** (2022) 65, https://doi.org/10.3390/coatings12010065.
30. R. G. B. Madera *et al*., ZnO thin films using sintered targets, *Physica B* **698** (2025) 416733, https://doi.org/10.1016/j.physb.2024.416733.
31. M.W. Zhu *et al*., Sol-gel ZnO films, *J. Non-Cryst. Solids* **354** (2008) 2416, https://doi.org/10.1016/j.jnoncrysol.2007.10.037.
32. Y. Demirhan, Anti-reflective coatings, Opt. Quantum Electron. **58** (2026) 75, https://doi.org/10.1007/s11082-026-08675-w.
33. W. Li *et al*., Anti-reflection ZnO coatings, *Mater. Lett*. **243** (2019) 108, https://doi.org/10.1016/j.matlet.2019.01.158.
34. Y. Li *et al*., Superhydrophobic coatings, *Chem. Commun*. (2009) 2730, https://doi.org/10.1039/B900804G.
35. S. Salam *et al*., Sol-gel ZnO films, *Thin Solid Films* **529** (2013) 242, https://doi.org/10.1016/j.tsf.2012.10.079.
36. H. Zhou *et al*., Al-doped ZnO films, *Thin Solid Films* **515** (2007) 6909, https://doi.org/10.1016/j.tsf.2007.01.041.
37. K. Shalimova, Physics of Semiconductors, Mir, Moscow (1975).
38. G. L. Kabongo *et al*., Holmium-doped ZnO, *Nanomaterials* **11** (2021) 2611, https://doi.org/10.3390/nano11102611.
39. N. Al-Khalli *et al*., ZnO thin films properties, *Mater. Trans.* **62** (2021) 915, https://doi.org/10.2320/matertrans.MT-M2020350.
40. J. Tauc, Optical properties of amorphous semiconductors, *Mater. Res. Bull*. **3** (1968) 37.
41. A. López-Suárez *et al*., Mn-doped ZnO films, *J. Mater. Sci.*: *Mater. Electron.* **31** (2020), https://doi.org/10.1007/s10854-019-02830-8.
42. M. R. Islam, M. G. Azam, Mg-doped ZnO films, *Surf. Eng.* **37** (2021) 775, https://doi.org/10.1080/02670844.2020.1801143.
43. F. Urbach, Absorption edge in solids, *Phys. Rev.* **92** (1953) 1324, https://doi.org/10.1103/PhysRev.92.1324.
44. R. C. Rai, Urbach tails in ZnO, *J. Appl. Phys*. **113** (2013) 153508, https://doi.org/10.1063/1.4801900.
45. P. Potera et al., Co-doped ZnO films, *Appl. Sci.* **13** (2023) 2701, https://doi.org/10.3390/app13042701.
46. F. M. Smits, Four-point probe method, *Bell Syst. Tech*. J. **34** (1958) 711.
47. K. M. Salman et al., Mg-doped ZnO films, *Opt. Mater*. **158** (2025) 116460, https://doi.org/10.1016/j.optmat.2024.116460.

Improvement I-V characteristics of (GaAs/Ge) heterojunction at different thicknesses and annealing temperatures by thermal evaporation method

I. N. Kashkool[a], Saif Khalel Jasim[b,*] A. K. Mohammed[a], M. T. Abd[a], and A. M. Shano[a]

[a]*Department of Radiological Tech., Bilad Alrafidain University College, Diyala, 32001, Iraq.*
[b]*Ministry of Education. Diyala Education Directorate, Diyala, Iraq.*
[*]*e-mail: saifalaosy@gmail.com*

Received 14 March 2025; accepted 19 June 2026

In the present work we are reporting the preparation conditions of GaAs thin films and the technique employed to produce films deposited on Ge wafers substrate at constant substrate temperature by thermal evaporation method. Also it includes photovoltaic measurements which are presented by current voltage characteristics, photocurrent, shortcircuit, open - circuit voltage of GaAs/Ge heterojunction, at room temperature and different annealing temperatures. All the samples were prepared under constant conditions (pressure, substrate temperature and rate of deposition); the main parameters that control the nature of the film properties are thickness (0.4, 0.7, 1.0 and 1.5 μm) and annealing temperature (473 and 523 K). The dark current decreases with increasing of thickness; whereas increases slightly with increasing of annealing temperatures. Under illumination, the photocurrent increases with increasing of annealing temperatures and decreases with increasing of thickness except at thickness equal to 1.5 μm. There is a linear increasing in the first part of the relation between Isc and Voc with incident power intensity and then the saturation region appeared. The Isc and Voc decrease with increasing of thickness, while increase with increase of annealing temperatures.

Keywords: GaAs; solar cell; I_V characteristics; thickness; thin films.

DOI: https://doi.org/10.31349/RevMexFis.72.061007

1. Introduction

Germanium (Ge) has been one of the most studied materials as its properties benefit many applications. Ge was the choice of material used in the first bipolar invented transistor in 1949 by Bardeen, Brattain, and Shockley [1,2]. Due to its small energy band gap 0.66 eV, Ge is also used in optical and optoelectronic devices, (such as photodetectors, solar cells,and waveguides) [3]. In addition, Ge films can be grown epitaxially on the GaAs heterostructures typically used for fabrication of a number of types of electronic devices, such as photodetectors, diodes and sensors of temperature, magnetic field and strain [4,5]. Ge and GaAs have almost the same lattice parameter at room temperature [6]. GaAs/Ge epitaxial heterostructures have received a great deal of attention as starting materials for the fabrication of space quality solar cells and their potential application in electronic and optoelectronic devices.

Due to its high mechanical strength, Ge is an optimized substrate material in terms of its power - to power ratio for high efficiency GaAs/Ge photovoltaic devices. As large area, minority carrier devices, III-V/Ge cells are extremely sensitive to defects [7,8]. GaAs devices fabricated on a Ge substrate can have higher resistance to thermal burn out than those fabricated on a GaAs substrate, as Ge has thermal conductivity compared to GaAs [9,10]. The devices on Ge will be more economical as the cost of Ge wafers is less than that of GaAs wafers [11,12]. The elimination of antiphase domains (APDs), which are characteristic of polar-on-non polar epitaxy, and suppression of large - scale inter diffusion across the GaAs/Ge heterointerface remain key challenges for increase yield, reliability, and performance [13,14].

From a commercial perspective, the utilization of thermal evaporation for GaAs/Ge heterojunction fabrication offers a highly cost-effective and scalable alternative to expensive epitaxy techniques like MBE or MOCVD, making it attractive for mass-produced terrestrial and space solar applications [15]. In the present work we are reporting the preparation conditions of GaAs thin films and the technique employed to produce films deposited on Ge wafers substrate at constant substrate temperature by thermal evaporation method [16]. Also, it includes photovoltaic measurements which are presented by current - voltage characteristics, photocurrent, short - circuit, open - circuit voltage of GaAs/Ge heterojunction, at room temperature and different annealing temperatures.

2. Experimental procedure

Two types of substrates were used in this study: glass slides which were used to study the structural, electrical and optical properties of GaAs films; and p-type Ge wafer substrate with crystal orientation (100), with electrical resistivity of 55.5 Ω·cm, free carriers concentration 3.3×10^{13} cm^{-3} and thickness of 450 μm. The Ge substrate forms with GaAs film the heterojunction. To ensure accurate electrical characteri-

zation of the GaAs layer and avoid parasitic conduction from the substrate, separate GaAs films were deposited on insulating glass slides under identical conditions for Hall effect measurements. Flash evaporation technique was used to prepare GaAs films to avoid the segregation problem. This technique, which involves instantaneous evaporation of the material with minimum time of contact with the evaporator, has been successfully used for growing precisely stoichiometric films of compounds whose constituents have widely different vapor pressures.

In this technique, the finely powdered evaporating material is allowed to drop grain by grain onto a hot surface whose temperature is maintained well above the evaporation temperature of the least volatile constituent of the evaporant. The preparation of GaAs films with satisfactorily reproducible properties demands special technological procedures. Therefore, flash evaporation techniques were chosen in the present investigation [17,18]. The required weight of GaAs powder was charged into a funnel structure which was fixed in the holder and the boat was mounted under the funnel between two electrodes in the vacuum chamber. The substrates were fixed on a spherical holder and placed in position at height of about 12 cm above the boat.

Before starting the evaporation process, the substrate was heated to about 433 K. The temperature was monitored by using a digital thermometer. When the system was pumped down to a vacuum of 10^{-5} mbar, an electric current was passed through the boat gradually to prevent breaking the boat, when the boat temperature reached the required temperature the deposition process starts with constant deposition rate. After these steps the current supply was switched off and the samples were left in the high vacuum for one day, and then the air was admitted to the chamber, and the films were taken out from the coating unit and kept in the vacuum desiccators until the measurements were made.

All the samples were prepared under constant conditions (pressure, substrate temperature and rate of deposition); the main parameters that control the nature of the film properties are thickness (0.4, 0.7, 1.0 and 1.5 μm) and annealing temperature (473 and 523 K). There are many methods used to determine the film thickness. In this part two experimental methods of thickness measurements were used. Weighting Method I-V measurements have been done under illumination for the GaAs/Ge heterojunction which was prepared with different thicknesses and annealing temperatures at forward and reverse conditions with different intensities (30-105 mW/cm^2) by using Halogen lamp type Philips of 120 W. The current-voltage measurements in the dark were done for the GaAs/Ge heterojunction by using Keithley digital electrometer 616 and D.C. power supply. The bias voltage was varied in the range of (0-1 V) in the case of forward and reverse bias.

3. Results and discussions

3.1. Structural properties

The structural properties of the deposited GaAs thin films were investigated using X-ray diffraction (XRD). As shown in Fig. 1, the XRD patterns exhibit three distinct peaks at 2θ values of approximately 27.5°, 45.5°, and 53.5°, corresponding to the (111), (220), and (311) planes of the cubic zincblende structure.

The structural properties of the deposited GaAs thin films were investigated using X-ray diffraction (XRD). As shown in Fig. 1, the XRD patterns exhibit three distinct peaks at 2θ values of approximately 27.5°, 45.5°, and 53.5°, corresponding to the (111), (220), and (311) planes of the cubic zincblende structure.

A significant increase in peak intensity and a reduction in the Full Width at Half Maximum (FWHM) were observed as the annealing temperature increased from 303 K to 523 K. This indicates an enhancement in crystallinity and an increase in grain size, as detailed in Table I. The improved grain size

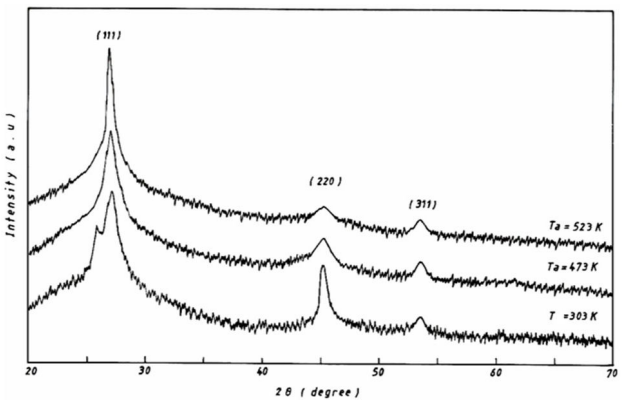


FIGURE 1. X-ray diffraction patterns of GaAs thin films (1.0 μm thickness) deposited on Ge substrates at room temperature (303 K) and after annealing at different temperatures (473 K and 523 K).

TABLE I. Structural parameters of GaAs thin films at different annealing temperatures.

D(Å)	(hkl)	a(Å)	d_{exp} (Å)	2θ (degree)
GaAs Films at T = 303 K				
37.550	111	5.611	3.240	27.5
107.352	220	5.632	1.991	45.5
97.007	311	5.674	1.711	53.5
GaAs Films at T_a = 473 K				
54.881	111	5.611	3.240	27.5
48.481	220	5.632	1.991	45.5
103.474	311	5.674	1.711	53.5
GaAs Films at T_a = 523 K				
155.211	111	5.611	3.240	27.5
65.345	220	5.632	1.991	45.5
118.908	311	5.674	1.711	53.5

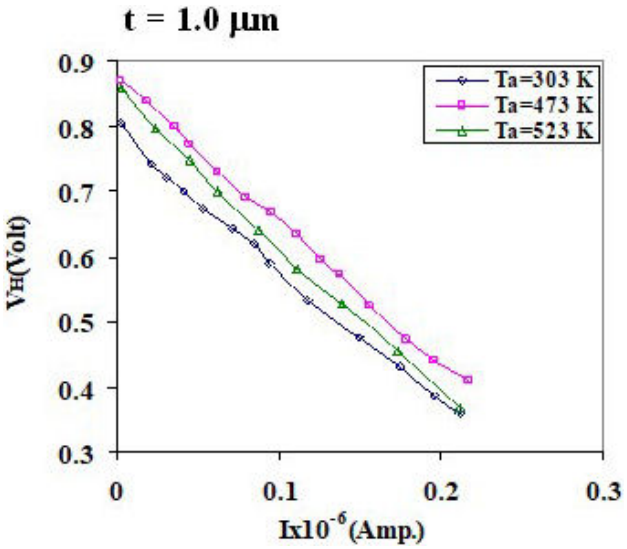


FIGURE 2. Hall potential (V_H) as a function of current for thin GaAs films of thickness (1.0 μm) at room temperature and different annealing temperatures (473 K and 523 K).

(reaching 155.2 Å at 523 K) reduces grain boundary scattering and recombination centers, which directly correlates with the enhanced I-V characteristics of the GaAs/Ge heterojunction.

3.2. Hall effect measurements

Hall effect measurements on GaAs films deposited on glass substrates confirmed n-type conductivity with a negative Hall coefficient. Figure 2 displays the linear Hall voltage (V_H) and current for the 1.0 μm film, where the increase in V_H with annealing temperature (T_a) indicates a modification in free carrier density and mobility. These results provide experimental evidence for the formation of an n-GaAs/p-Ge heterojunction when deposited on p-Ge wafers.

3.3. Characteristics for GaAs/Ge Heterojunction under dark

One of the important parameters of diode measurement is a current-voltage characteristic which explains the behavior of the resultant current with the applied forward and reverse bias voltages. Figure 3 shows I-V characteristics for GaAs/Ge heterojunction at forward and reverse bias voltages for different thicknesses and annealing temperatures.

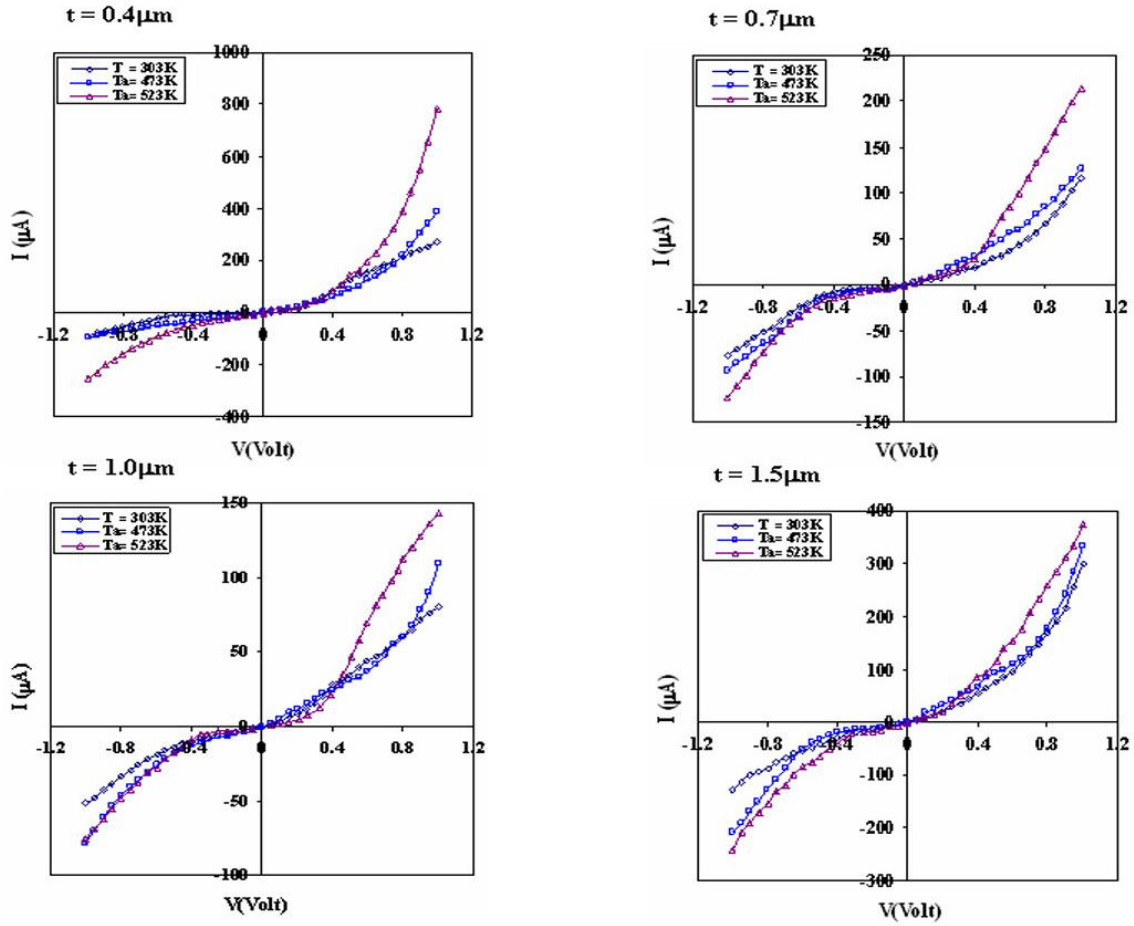


FIGURE 3. I-V characteristics for GaAs/Ge heterojunction at forward and reverse bias voltages for different thicknesses and annealing temperatures.

In general, the forward dark current is generated due to the flow of majority carriers and the applied voltage injects majority carriers which lead to the decrease of the built - in potential, as well as the width of the depletion layer. As the majority and minority carrier concentration is higher than the intrinsic carrier concentration ($n_i^2 < np$) which generate the recombination current at the low voltage region (0-0.3 V). This is because the excitation of electrons from valence band (V.B.) to conduction band (C.B.) will recombine them with the holes which are found at the V.B., and this is observed by the little increase in recombination current at low voltage region [15,16]. On the other hand, tunnelling current is present at the high voltage region ($>$ 0,3 V). After that there is a fast exponential increase in the current magnitude with increasing of the voltage and this is called diffusion current, which dominates [19].

The reverse bias current also contains two regions. In the first region of low voltages ($<$ 0,3 V), the current slightly increases with increasing of the applied voltage, and the generation current dominates, while at second high voltage region ($>$ 0,3 V), the diffusion current dominates [20]. Also we can observe from this figure that the value of the current decreases with increasing of thickness of GaAs films which is attributed to evolving defects and dislocations that have an effect on the mobility of charge carriers. Also these defects evolutions allow energy levels to be within the energy gap, these defects are within the depletion region and act as active recombination centers, and consequently they decrease current flow across the junction. This behavior is similar for all the film thicknesses except at thickness equal to 1.5 μm. We also observed that the current increases slightly with increasing of annealing temperature because the increasing of temperatures causes a rearrangement of the interface atoms and reduce the dangling bond which leads to improvement of the junction characteristics [21,22].

3.4. Short circuit current and open circuit voltage measurement for GaAs/Ge heterojunction

The variation of I_{sc} as a function of incident power intensity for GaAs/Ge heterojunction at different thicknesses (0.4, 0.7,

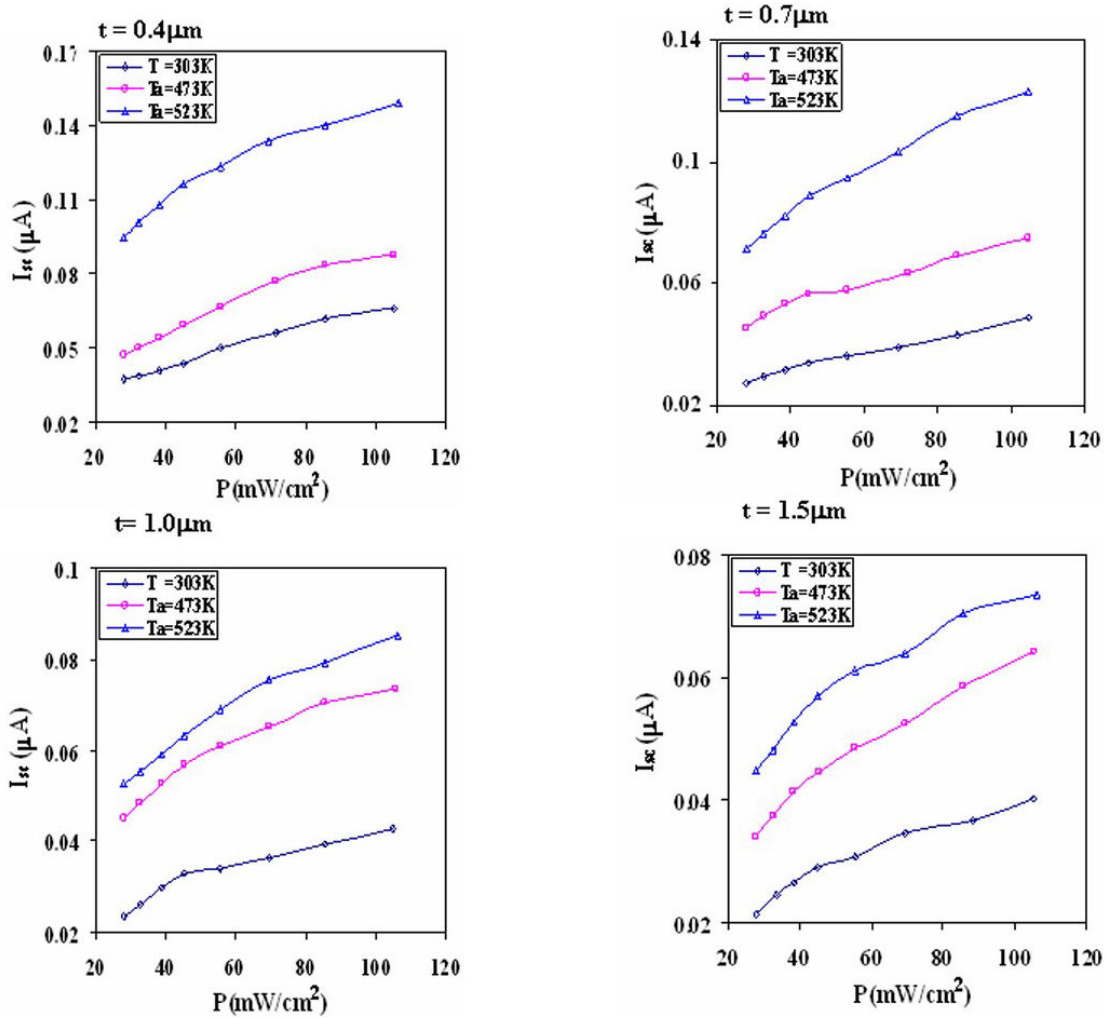


FIGURE 4. The variation of I_{sc} as a function of incident power intensity for GaAs/Ge heterojunction at different thicknesses and annealing temperatures.

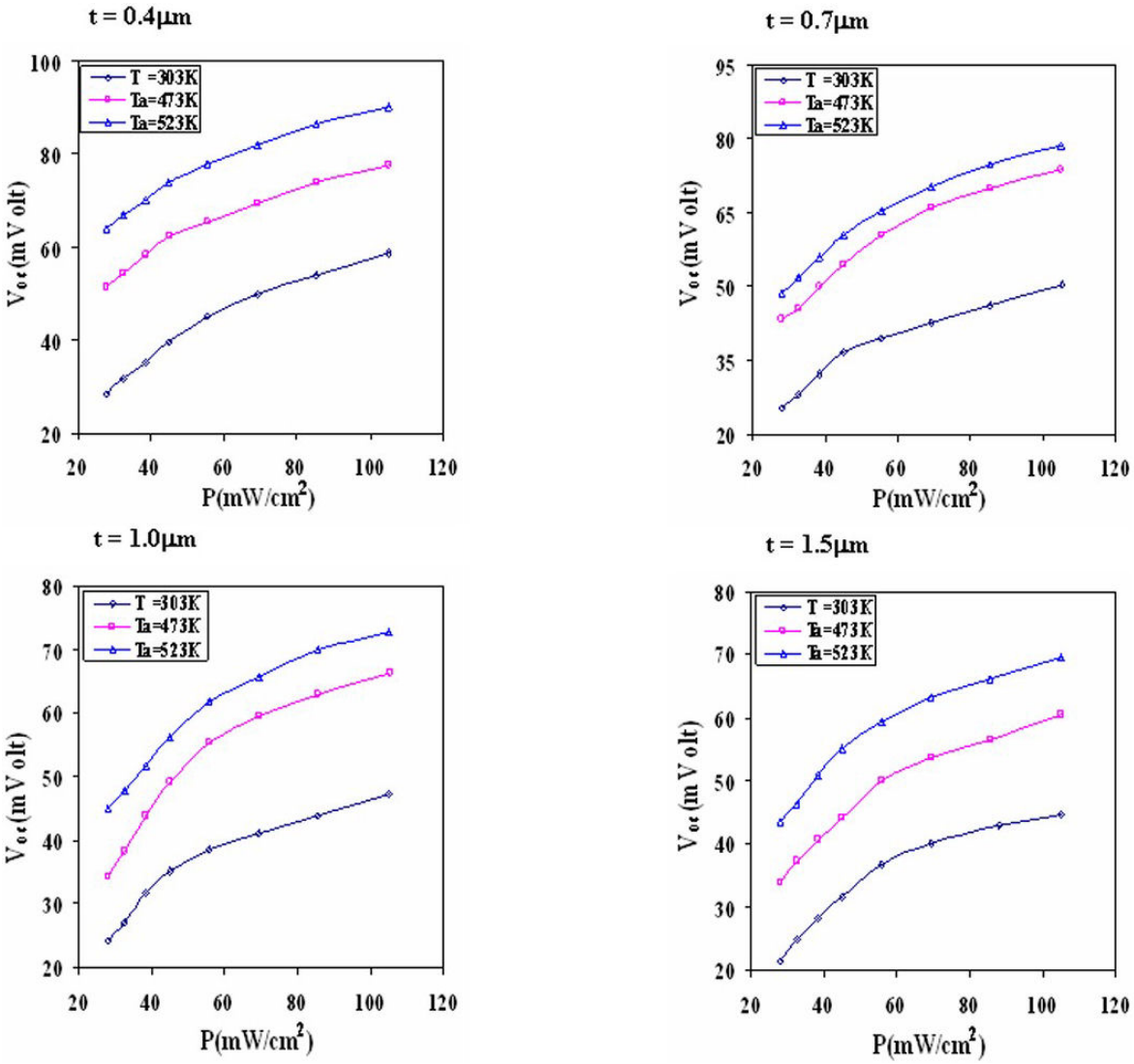


FIGURE 5. The variation of V_{oc} as a function of incident power intensity for GaAs/Ge heterojunction at different thicknesses and annealing temperatures.

1.0 and 1.5 μm) at R.T and annealing temperatures (473 and 523 K) is shown in Fig. 4.

We can observe from this figure that the I_{sc} increases with increasing of the incident power intensity. The behavior of I_{sc} is linear at the first portion and this is attributed to the incident power intensity. In the second portion there is a tendency to saturation with increasing of the incident power intensity at a limited range, due to the recombination effect [23,24]. We can observe that I_{sc} decreases with increasing of thickness of GaAs films about two times. This is attributed to the defects which act as capture centers to the generation of carriers, leading to an increase of the recombination process and a decrease of the current value. I_{sc} increases with increasing of annealing temperature due to the decrease of the defects by annealing and the improvement of the structure [25,26]. The observed enhancement in solar cell parameters via simple thermal evaporation underscores the potential for low-cost commercial photovoltaic devices.

The variation of V_{oc} as a function of power light intensity for GaAs/Ge heterojunction at different thicknesses (0.4, 0.7, 1.0 and 1.5 μm) and at R.T and annealing temperatures (473 and 523 K) is shown in Fig. 5.

Also we can divide this figure into two regions: a linear region at low illumination intensities, and a tendency for a saturation region at high illumination intensities. The V_{oc} decreases with increasing of thickness due to recombination processes at traps centers inside the materials or at the surface. The V_{oc} increases with increasing of annealing temperature due to the reduction of the defects and localized states and increasing of the mobility.

4. Conclusions

From the obtained results of the present work, we conclude that the mechanism of the forward current coincides with the recombination- tunneling mechanism. The dark current

decreases with increasing of thickness; whereas increases slightly with increasing of annealing temperatures.

Under illumination, the photocurrent increases with increasing of annealing temperatures and decreases with increasing of thickness except at thickness equal to 1.5 μm. There is a linear increasing in the first part of the relation between I_{sc} and V_{oc} with incident power intensity and then the saturation region appeared. The I_{sc} and V_{oc} decrease with increasing of thickness, while increase with increase of annealing temperatures. The results demonstrate that thermal evaporation is a viable, economical method for fabricating GaAs/Ge solar cells with promising performance, offering a significant reduction in production costs for large-scale energy applications.

Acknowledgment

The authors would like to thank the University of Diyala/College of Science/Department of Physics for the technical support to complete this work in their laboratories, and Universiti Sains Malaysia.

Conflict of interest

The authors declare that they have no conflict of interest.

1. Y. H. Hu, M. J. Li, Y. P. Zhou, H. Xi, and T. C. Hung, Multiphysics investigation of a GaAs solar cell based PV-TE hybrid system with a nanostructured front surface, *Sol. Energy* **224** (2021) 102-111. https://doi.org/10.1016/j.solener.2021.06.003
2. T. Y. Sabri, S. K. Jasim, A. A. Habeeb, and A. S. Jasim, Preparation and study Ag nanoparticles via PLAL technique: Influence of different number of pulses, *Int. J. Nanoelectron. Mater*. **17** (2024) 45-51. https://doi.org/10.58915/ijneam.v17i1.458
3. C. Wang, Z. Zhang, X. Jing, Z. Yang, and W. Xu, Optimization of multistage femtosecond laser drilling process using machine learning coupled with molecular dynamics, *Opt. Laser Technol*. **156** (2022) 108442. https://doi.org/10.1016/j.optlastec.2022.108442
4. E. S. Goh, T. P. Chen, C. Q. Sun, and Y. C. Liu, Thickness effect on the band gap and optical properties of germanium thin films, *J. Appl. Phys.* **107** (2010) 023506. https://doi.org/10.1063/1.3291103
5. C. Han *et al*., Microstructure evolution and ductility improvement of additively manufactured biodegradable zinc-magnesium alloys via annealing, *Int. J. Bioprint.* **10** (2024) 3034. https://doi.org/10.36922/ijb.3034
6. J. Peng *et al*., Numerical simulation and process parameter optimization of laser spot welding for ultra-thin sheets, *Opt. Laser Technol*. **193** (2026) 114240. https://doi.org/10.1016/j.optlastec.2025.114240
7. S. K. Jasim, A. M. Shano, and S. K. Adnan, Zinc oxide poly crystals heterojunction and infrared-blind UV-photodetector, *J. Nano-Electron. Phys.* **16** (2024) 01012. https://doi.org/10.21272/jnep.16(1).01012
8. Y. Zhang, Z. Zhang, X. Zhang, K. Wu, R. Riedel, D. Hu, and J. Sun, Machine learning guided design and ablation behavior of ZrC-TaC-SiC ternary coatings, *Corros. Sci.* **260** (2026) 113499. https://doi.org/10.1016/j.corsci.2025.113499
9. S. K. Jasim, S. M. A. Al Hussan, and M. T. Abd, Improving the mechanical properties of dental fillings by adding TiO_2 NPs prepared laser ablation, *BioNanoScience* **15** (2025) 330. https://doi.org/10.1007/s12668-025-01970-y
10. R. Kumar *et al*., Realization of high-quality InGaAs/GaAs quantum dot growth on Ge substrate and improvement of optical property through ex-situ ion implantation, *J. Lumin.* **223** (2020) 117208. https://doi.org/10.1016/j.jlumin.2020.117208
11. Y. Jiang, H. Shen, T. Pu, C. Zheng, Q. Tang, K. Gao, and Y. Liu, High efficiency multi-crystalline silicon solar cell with inverted pyramid nanostructure, *Sol. Energy* **142** (2017) 91-96. https://doi.org/10.1016/j.solener.2016.12.007
12. I. Hilmi, M. K. Adam, J. Purwadi, Q. M. B. Soesanto, and D. Y. Kusuma, Influence of annealing on the physical and optical properties of Ge thin films deposited using thermal evaporation, *J. Phys. Appl*. **7** (2025) 28-32. https://doi.org/10.14710/jpa.v7i2.24517
13. A. H. Ahmed, A. S. Jasima, and S. K. Jasim, Synthesis of gold nanoparticles by pulsed laser ablation and its study physical and mechanical properties, *Int. J. Nanoelectron. Mater*. **17** (2024) 634-644. https://doi.org/10.58915/ijneam.v17i4.1465
14. I. Demir, A. E. Kasapoğlu, H. F. Budak, E. Gür, and S. Elagoz, Influences of thickness and temperature of low temperature GaAs buffer layer on two-step MOVPE grown GaAs/Ge heterostructures, *Eur. Phys. J. Appl. Phys*. **90** (2020) 20301. https://doi.org/10.1051/epjap/2020190216
15. W. Kou, J. Gou, J. Gao, J. Zhu, Z. Li, and J. Wang, Effects of arc oscillation on interface behavior and properties of additive-manufactured 2319/5356 dissimilar aluminum alloy, *Mater. Today Commun*. **47** (2025) 113068. https://doi.org/10.1016/j.mtcomm.2025.113068
16. S. K. Jasim, S. M. A. A. Hussan, A. S. Noori, and A. A. Habeb, Determine surface plasmon resonance and effect parameters laser ablation on Cu and Zn nanoparticles, *AIP Conf. Proc*. **3219** (2024) 060008. https://doi.org/10.1063/5.0236469
17. Y. Zhou, W. Liu, S. Zhang, H. Liu, Z. Wu, and X. Wang, Eco-friendly flame-retardant phase-change composite films based on polyphosphazene/phosphorene hybrid foam and paraffin

wax for light/heat-dual-actuated shape memory, ACS *Appl. Mater. Interfaces* **16** (2024) 7754-7767. https://doi.org/10.1021/acsami.3c16953

18. J. Zhou *et al*., GaAs/GeSn/Ge n-i-p diodes and light emitting diodes formed via grafting, *J. Vac. Sci. Technol. B* **42** (2024). https://doi.org/10.1116/6.0003619

19. E. Erofeev and V. Kagadei, Formation of Ge/Cu ohmic contacts to n-GaAs with atomic hydrogen pre-annealing step, *Proc. SPIE* **7521** (2010) 176-181. https://doi.org/10.1117/12.853639

20. I. Kabacelik, M. Kulakci, and R. Turan, Structural and electrical analysis of poly-Ge films fabricated by e-beam evaporation for optoelectronic applications, *Mater. Sci. Semicond. Process.* **56** (2016) 368-372. https://doi.org/10.1016/j.mssp.2016.09.023

21. N. A. Pakhanov and M. Z. Shvarts, Designing of lightweight and ultrathin III-V/Ge solar cells for flexible space and terrestrial photovoltaic blankets, *Phys. Status Solidi A* **221** (2024) 2300709. https://doi.org/10.1002/pssa.202300709

22. R. Naik, A. Aparimita, D. Alagarasan, S. Varadharajaperumal, and R. Ganesan, Linear and nonlinear optical properties change in Ag/GeS heterostructure thin films by thermal annealing and laser irradiation, *Opt. Quantum Electron*. **52** (2020) 136. https://doi.org/10.1007/s11082-020-2245-6

23. X. Zhang, J. Sun, Y. Zhang et al., Machine learning for phase prediction of high entropy carbide ceramics from imbalanced data, *npj Comput. Mater*. (2026). https://doi.org/10.1038/s41524-025-01873-2

24. G. Cai, Y. Huang, Y. Qing, and R. D. K. Misra, Investigation of microstructure and texture evolution of nickel-saving duplex stainless steels containing Y, *J. Mater. Res. Technol*. (2026). https://doi.org/10.1016/j.jmrt.2026.01.109

25. Z. Zhang *et al*., Synergistic radiation effect of 300 MeV proton and heavy ion on electrical characteristics of β-Ga_2O_3 SBD, *IEEE Trans. Nucl. Sci*. (2026). https://doi.org/10.1109/TNS.2026.3666502

26. Y. Liu *et al*., Effect of annealing temperature on microstructure and properties of stainless steel/copper composite strips, *Adv. Compos. Hybrid Mater.* **9** (2026) 103. https://doi.org/10.1007/s42114-026-01648-3

Ising-type ferroelectric switching and piezoelectric response in wurtzite KMgP: First-principles study

A. Labdelli[a,b,*], and A. Benbedra[b]

[a]*Biodiversity, Water and Soil Conservation Laboratory (LBCES), University of Mostaganem, Algeria,*
[b]*Faculty of Medicine, University of Mostaganem, Algeria*
[*]*e-mail: abbes.labdelli@univ-mosta.dz*

Received 24 june 2026; accepted 27 july 2026

The present paper employs first-principles calculations based on density functional theory to investigate the structural, electronic, ferroelectric, and piezoelectric properties of KMgP in the wurtzite LiGaGe-type phase. The thermodynamical, mechanical and dynamical stability of the compound are confirmed through the formation energy, elastic coefficients and phonon spectrum, respectively. Our results reveal that wurtzite KMgP is a semiconductor with a direct band gap of 1.25 eV within the local-density approximation. We use the Berry-phase approach to evaluate the polarization properties inherent to the polar structure of KMgP, yielding a spontaneous polarization of 0.385 C/m^2 and Born effective charges near their nominal ionic values. The ferroelectric nature of the material is demonstrated by the characteristic double-well potential associated with Ising-type polarization reversal. With a high Curie temperature (385.32 K) and low switching energy barrier (0.0568 eV) and coercive electric field (2.78 MV/cm), we predict that wurtzite KMgP possesses highly reversible polarization, making it a promising candidate for novel ferroelectric applications. Moreover, we find that KMgP is an anomalous piezoelectric compound with a negative longitudinal piezoelectric coefficient (modulus) of $-0{,}75$ C/m^2 ($-52{,}66$ pC/N).

Keywords: Wurtzite crystals; electric polarization; Berry phase; ferroelectricity; piezoelectricity.

DOI: https://doi.org/10.31349/RevMexFis.72.061008

1. Introduction

Materials that are both piezoelectric and ferroelectric [1] have revolutionized the landscape of solid-state devices. This is due to their unique ability to interconvert electric polarization into mechanical strain on one hand [2,3], and maintain a switchable polarization on the other hand [4,5]. The electromechanical conversion is indispensable for a broad range of applications, including transducers [6], energy harvesters [7], pressure sensors [8] and surface/bulk acoustic wave resonators [9]. Furthermore, the ferroelectric switching is the basis of non-volatile random-access memories, for which 1 and 0 bits correspond to "up" and "down" polarized states [10,11].

Historically, materials crystallizing in the wurtzite structure have been key players in the piezoelectric industry. Binary III-nitrides (such as AlN and GaN) and II-oxides (such as ZnO), along with their various alloys, are widely employed owing to their significant piezoelectric response [12-14]. While these binary compounds are naturally piezoelectric due to their non-centrosymmetric structure, they typically lack the ability for ferroelectric switching under an applied electric field. However, recent studies have demonstrated that some wurtzite crystals can exhibit ferroelectricity [15-19], and thus sparking an interest in identifying new ferroelectric wurtzite compounds.

Promising candidates in that respect are new ternary ABC compounds that crystallize in the wurtzite-like LiGaGe-type phase. Unlike their binary counterparts, these ternary systems offer greater chemical flexibility and a polar ground state that supports both piezoelectricity and ferroelectricity. Bennett *et al*. [20] used first-principles calculations to identify 17 compounds in this structural family, including LiBeP, NaMgAs, NaZnSb and KMgSb. These wurtzite ferroelectrics may be promising for the development of newhigh-performance systems for practical piezoelectric and ferroelectric applications.

In this work, we introduce and investigate the new ternary wurtzite compound KMgP. As far as we know, this material has never been studied before in the literature, particularly regarding its ferroelectric and piezoelectric behaviour. We carry out a density-functional theory (DFT) simulation to predict some physical properties of wurtzite KMgP. We provide results for the structural optimization via total-energy calculations and assess the structural stability through formation energy, elastic constants and phonon frequencies.We further characterize the electronic structure in terms of the band structure and density of states (DOS). A central focus is placed on properties related to electric polarization, namely the spontaneous polarization, Born effective charges and piezoelectric coefficients, all calculated using the Berry-phase theory.We also investigate the Ising-type ferroelectric switching by mapping the double potential well, which allows us to provide critical ferroelectric parameters such as the switching barrier energy, Curie temperature and the coercive electric field. The remainder of the paper is structured as follows. Section 2 details the numerical parameters of the DFT simulation. Section 3 presents our results, subdivided into three key parts: Sec. 3.1 covers structural optimization, Sec. 3.2 examines structural stability, Sec. 3.3 describes the electro-

nic structure, and Sec. 3.4 explores the ferroelectric switching mechanism and polarization-related quantities. Finally, our findings and concluding remarks are summarized in Sec. 4.

2. Computational details

Ab-initio calculations for wurtzite KMgP are performed within the framework of DFT [21,22] using the WIEN2k package [23], based on the full-potential linearized augmented plane wave plus local orbitals (FP-LAPW+lo) method [24]. In this approach, the unit cell is divided into non-overlapping muffin-tin (MT) spheres and an interstitial region. Inside the MT spheres, the wave functions are expanded in spherical harmonics and radial functions, while plane waves are used in the interstitial region [24]. The exchange-correlation effects are treated using the local-density approximation (LDA) [25]. This choice was adopted to maintain consistency with the seminal first-principles study of LiGaGe-type ferroelectric semiconductors by Bennett *et al.* [20], in which LDA was successfully employed to describe the equilibrium crystal structures, spontaneous polarization, and ferroelectric switching of this class of materials. Since the present work focuses on the ferroelectric and piezoelectric properties of the LiGaGe-type KMgP compound, the use of the same exchange-correlation functional enables a direct and meaningful comparison with the reference study.

Regarding the convergence parameters, the maximum angular momentum inside the MT spheres is set to $l_{\text{máx}} = 10$. The plane wave cutoffs are chosen as $RMTK_{\text{máx}} = 7$ and $G_{\text{máx}} = 12$, where RMT , Kmax and Gmax are defined in Ref. [23]. The core-valence energy separation is fixed at -6 Ry. The valence electron configurations considered are K ($4s^1$), Mg ($3s^2$), and P ($3s^23p^3$). The radii RMT of MT spheres of individual elements are chosen as follows: 2.4, 1.9, and 1.85 Bohr for K, Mg, and P, respectively. The Brillouin zone is sampled using 4000 k-points. Total-energy is considered to be converged when the difference is less than 10^{-4} Ry and the forces on atoms are below 10^{-4} Ry/Bohr. The elastic constants are calculated using the energy-strain method as implemented in the IRelast code [26]. Phonon frequencies are obtained using the finite-displacement supercell approach with the Phonopy package [27]. Finally, the polarization properties are evaluated using the BerryPI code [28], interfaced with WIEN2k, within the framework of the modern theory of polarization based on the Berry-phase formalism. The Berry-phase calculations were performed using the converged self-consistent electronic structure obtained with an energy convergence criterion of 10^{-4} Ry. A dense $10 \times 10 \times 40$ Monkhorst-Pack k-point mesh was employed to ensure the numerical convergence of the calculated spontaneous polarization.

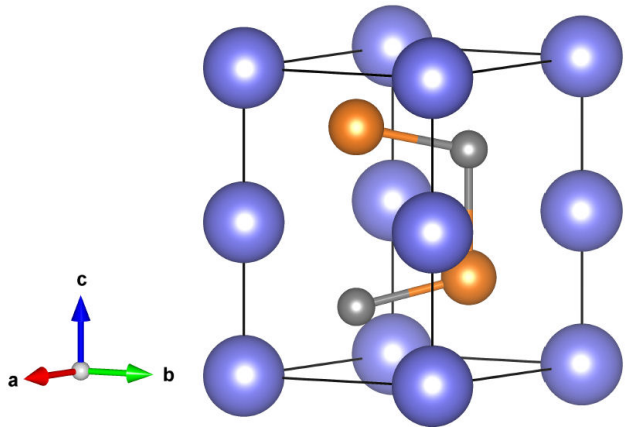


FIGURE 1. Unit cell of KMgP in the non-centrosymmetric polar wurtzite structure. The violet, orange and gray spheres represent K, Mg and P atoms, respectively. The Wyckoff positions are: K at $2a$ (0, 0, 0), Mg at $2b$ (1/3, 2/3, u) and P at $2b'$ (1/3, 2/3, v). The lattice axes a, b, and c are indicated on the left.

3. Results and discussion

3.1. Structural optimization

KMgP is experimentally observed to adopt the tetragonal structure (space group P4/nmmorNo. 129) [29]. Here,we investigate KMgP within the hexagonal wurtzite structure, also known as the LiGaGe-type phase (space groupP63mc, No. 186), whose unit cell is shown in Fig. 1. This structure is described by two independent lattice constants a and c (the lattice angle $\gamma = 120°$). In this case, the equilibrium structural parameters are determined by minimizing the total energy with respect to the unit-cell volume and the lattice constant ratio c/a [30]. The total energy is obtained from self-consistent solutions of the Kohn-Sham equation [31]. The variations of energy as a function of volume and c/a ratio are presented in Fig. 2.

The $E(V)$ data [Fig. 2a)] is fitted using the Murnaghan equation of state [32]:

$$E(V) = E_0 + \frac{BV}{B'}\left[\frac{1}{B'-1}\left(\frac{V}{V_0}\right)^{B'} + 1\right] - \frac{BV_0}{B'-1'}, \quad (1)$$

where E_0 and V_0 denote the equilibrium energy and volume, respectively, B is the bulk modulus, and B' is the first derivative of B with respect to pressure.

On the other hand, the $E(c/a)$ data [Fig. 2b)] is fitted to a fourth-order polynomial of the form:

$$E\left(\frac{a}{c}\right) = k_0 + k_1\left(\frac{a}{c}\right) + k_2\left(\frac{a}{c}\right)^2 + k_3\left(\frac{a}{c}\right)^3 + k_4\left(\frac{a}{c}\right)^4, \quad (2)$$

where k_i are fitting coefficients. The equilibrium lattice constants are obtained from the minimum of the total energy,

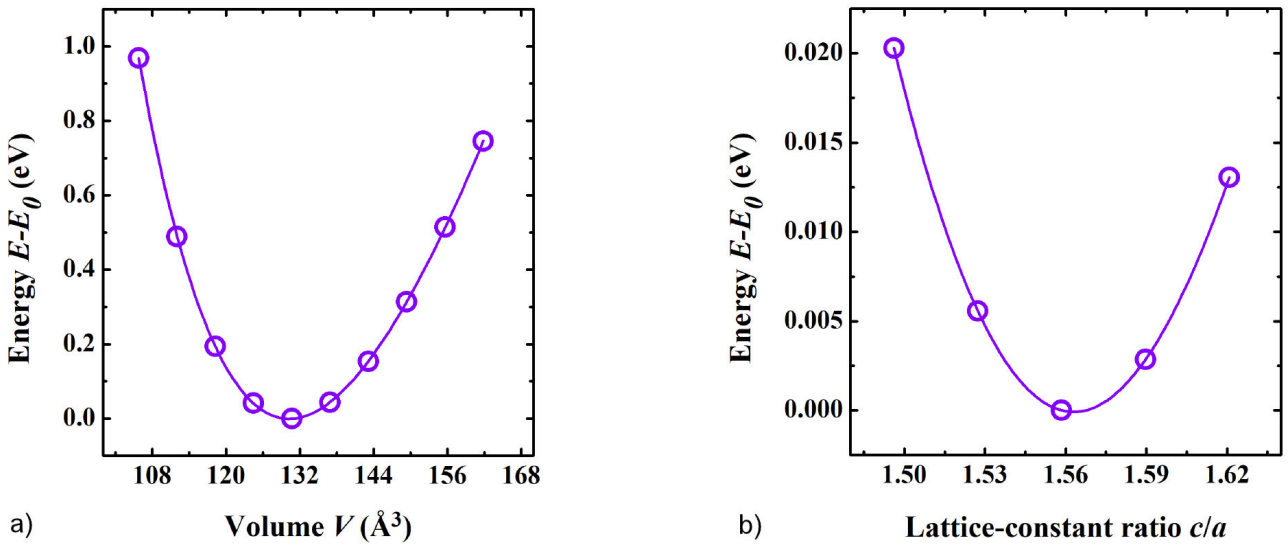


FIGURE 2. Total energy of wurtzite KMgP as a function of a) unit-cell volume and b) lattice-constant ratio c/a. In both cases, the energy scale is referenced to the minimum energy E_0. The curve in a) is a fit to the Murnaghan equation, whereas that in b) corresponds to a fourth-order polynomial fit.

TABLE I. Calculated equilibrium cell volume V, lattice constants a and c, bulk modulus B, its pressure derivative B', and internal parameter u (in units of c) for wurtzite KMgP within the LDA. These values are obtained from total-energy calculations.

KMgP	$V(^3)$	a (Å)	c (Å)	B (GPa)	B'	u	v
	879.9547	4.58	7.16	45.5453	4.309	0.307	0.705

corresponding to the optimal volume V_0 and lattice-constant ratio $(c/a)0$.

For the wurtzite structure, the unit-cell volume is given by

$$V_0 = \frac{\sqrt{3}}{2} a^2 c, \tag{3}$$

from which the lattice constants a and c are determined by:

$$a = \left[\frac{2V_0}{\sqrt{3}(c/a)_0}\right]^{1/3}, \quad c = a(c/a)_0. \tag{4}$$

In addition to the lattice parameters, wurtzite KMgP possesses internal structural degrees of freedom associated with the atomic positions: two internal parameters u and v corresponding to the non-ideal fractional coordinates of the Mg and P atoms along the c-axis [20-33], which cannot be expressed as simple rational fractions.

The equilibrium values of the internal parameters are determined by minimizing the forces acting on the atoms, in accordance with the Hellmann-Feynman theorem [34], *i.e.*, by evaluating the gradients of the total energy with respect to the atomic coordinates. The atomic positions are fully relaxed until the forces converge to negligible values. Note that the K atom occupies the ideal Wyckoff positions (0,0,0) and therefore is not subjected to relaxation.

The calculated equilibrium volume, lattice constants, bulk modulus, its pressure derivative, and the internal parameters for wurtzite KMgP are summarized in Table I. There is no data to compare our values with, since this work is the first to report the structural parameters of wurtzite KMgP. The calculated pressure derivative of the bulk modulus B' is 4.309, which is consistent with the general trend that this parameter remains below 5 for most crystalline solids [35]. The internal parameter $u(v)$ is greater (lesser) than the ideal values 0.25 (0.75).

3.2. Structural stability

Whether or not a material is thermodynamically stable depends on its formation energy (E_f). At $T = 0$ K, it is calculated from total energies as [36]:

$$E_f = E_{\mathrm{KM_gP}} - \sum_i n_i E_i, \tag{5}$$

where $E_{\mathrm{KM}_g P}$ is the energy of $\mathrm{KM}_g\mathrm{P}$ in the wurtzite structure, $n_i = 2$ is the number of K, Mg and P atoms within KMgP and E_i is the energy per atom of each element in its ground-state bulk structure (tetragonal for K, hexagonal for Mg and orthorhombic for P). We find a formation energy of -1.55 eV per formula unit (f.u.). The negative value indicates that wurtzite KMgP is thermodynamically stable relative to its isolated constituent elements and confirms the possibility of synthesis in the laboratory [36]. We note that KMgP has been experimentally realized only in the tetragonal phase.

Next, we investigate the mechanical stability. This is determined by the elastic constants (C_{ij}). Having hexagonal

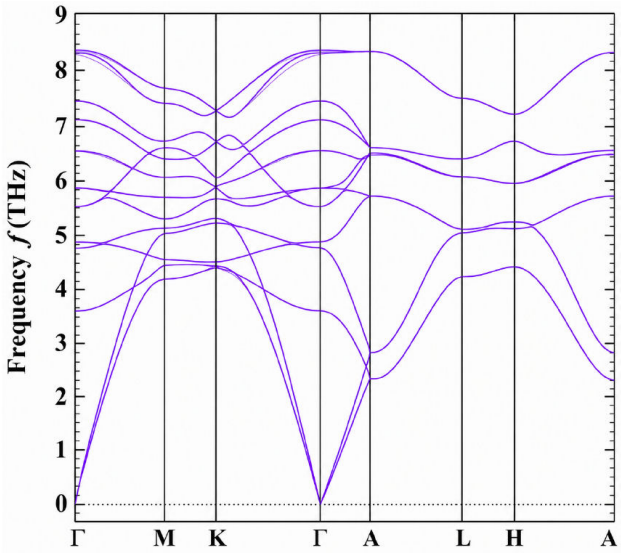


FIGURE 3. Phonon spectrum of KMgP in the wurtzite structure. The horizontal dotted line indicates zero frequency.

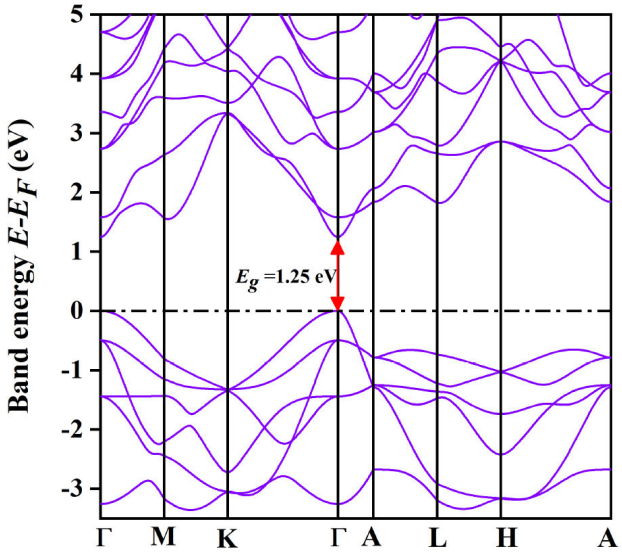


FIGURE 4. Band structure of wurtzite KMgP at the level of LDA. The energy bands are plotted relative to the Fermi level E_F (presented by the dashed horizontal line). The red double arrow indicates the band gap E_g.

symmetry, KMgP has five independent elastic constants. The determination of C_{ij} relies on evaluating the energy under appropriate deformations [37]. We implement such deformations using the IRelast code [26]. The calculated elastic constants of wurtzite KMgP are: $C_{11} = 92{,}88$ GPa, $C_{12} = 32{,}33$ GPa, $C_{13} = 31{,}42$ GPa, $C_{33} = 41{,}16$ GPa and $C_{44} = 45{,}31$ GPa.

The elastic constants are doubly interesting. On the one hand, they provide access to several elastic properties that describe the mechanical behaviour of materials, such as the bulk modulus and Poisson ratio. On the other hand, they make it possible to verify the mechanical stability of the system via the Born stability criteria. For a hexagonal crystal, these criteria are [38]:

$$\begin{aligned} C_{11} - C_{12} &> 0, \\ C_{33}(C_{11} + C_{12}) - 2C_{13}^2 &> 0, \\ C_{44} &> 0. \end{aligned} \tag{6}$$

According to our numerical data, the elastic constants satisfy the stability conditions, which implies that the ternary compound KMgP in the wurtzite structure is mechanically stable [38], in the sense that it will not collapse under applied strain.

Finally, we check the dynamical stability. To do so, we calculate the phonon frequencies from the force constants via the Phonopy code [27]. The phonon dispersion curves for wurtziteKMgPare plotted in Fig. 3. The key observation is the absence of any negative (imaginary) frequencies: all phonon modes have positive values of frequency across the entire Brillouin zone, confirming the dynamical stability of KMgP crystallizing in the wurtzite LiGaGe-type phase [39]. In this context, dynamical stability refers to the fact that the crystal structure is stable against its own atomic vibrations.

3.3. Electronic properties

The physical properties of a material are largely governed by its electronic structure. Therefore, understanding the band structure and DOS is essential for identifying materials with potential technological applications.

3.3.1. Band structure

Figure 4 shows the electronic band structure of wurtzite KMgP calculated along the high-symmetry directions of the hexagonal Brillouin zone, with the Fermi level set to zero. As observed in Fig. 4, the valence-band maximum and the conduction-band minimum are both located at the Γ point, revealing a direct band gap. This confirms the semiconducting nature of KMgP. The LDA-predicted band gap is approximately 1.25 eV. The presence of a direct band gap is particularly advantageous for optoelectronic applications, as it enables efficient interband optical transitions. The valence bands, located below the Fermi level, exhibit moderate dispersion, suggesting a mixture of localized and delocalized electronic states. In contrast, the conduction bands are more dispersive, indicating relatively low electron effective masses and potentially high carrier mobility. Furthermore, the variation in band dispersion along different high-symmetry paths $\Gamma - M - K - \Gamma - A - L - H - A$ highlights the anisotropic electronic behaviour associated with the hexagonal wurtzite structure.

3.3.2. Density of states

The total DOS and partial DOS (PDOS) of wurtzite KMgP are shown in Figs. 5 and 6, respectively. The absence of elec-

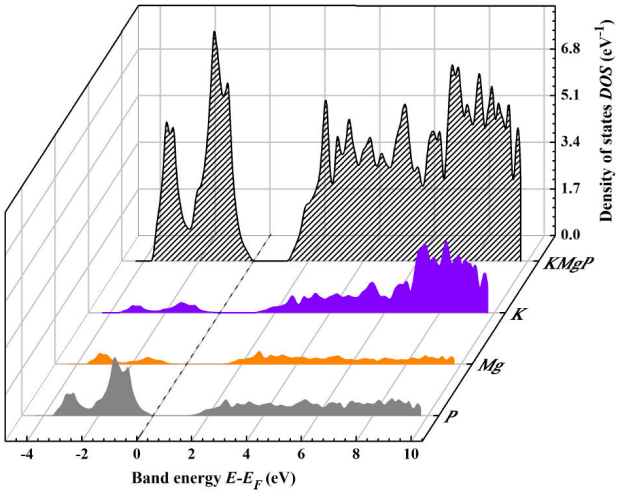


FIGURE 5. Total and atomic-projected DOS for KMgP in the wurtzite structure (within LDA). The dashed area represents the total DOS of the system. The violet, orange, and grey areas are the K , Mg, and P contributions, respectively. As in Fig. 4, the energy is referenced to the Fermi level dashed black line that passes the zero energy.

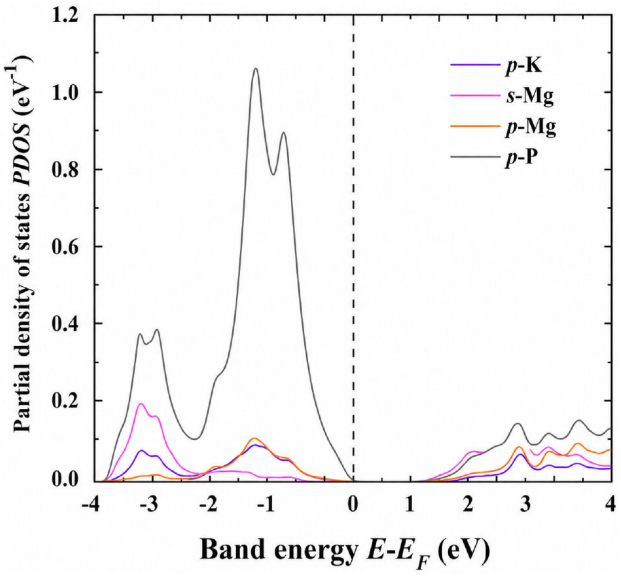


FIGURE 6. Orbital-projected PDOS of wurtzite KMgP. The vertical dashed line indicates the Fermi level.

tronic states at the Fermi level confirms the semiconducting nature of our compound, in agreement with the band-structure results. By inspecting Fig. 6, we observe that the valence band region (from approximately -4 eV to 0 eV) is mainly dominated by P-p states, which provides the major contribution near the valence-band maximum. Smaller contributions from K-s and Mg-s states are also observed, indicating a certain degree of hybridization between P and the metallic atoms. This hybridization suggests a mixed bonding character with partial covalent features. In the conduction band region (above the Fermi level), the electronic states are primarily composed of Mg-s, Mg-p, and P-p states, with minor contributions from K-p states. This indicates that the conduction-band minimum is mainly derived from the metal atoms, consistent with the relatively dispersive conduction bands observed in the band structure. Moreover, the sharp peaks in the DOS correspond to localized states, while the broader features indicate more delocalized electronic states.

3.4. Electric polarization

3.4.1. Spontaneous polarization

The spontaneous polarization (PSP) of a crystalline solid is the value of polarization at equilibrium, *i.e.* in the absence of external perturbations such as electric field and mechanical strain. The theoretical framework to define and compute the electric polarization is the Berry-phase theory [40,41], which is based on two fundamental hypotheses [42,43]: (i) the only physically meaningful values of polarization are polarization differences between two different states, and (ii) such polarization differences are calculated as a Berry phase of the system wavefunction. For the spontaneous polarization, the two states correspond to a non-centrosymmetric structure and its high-symmetry counterpart, also referred to as the reference structure [42,43].

In the specific case of our compound KMgP, the non-centrosymmetric structure is wurtzite whereas the structure that serves as a reference is the layered-hexagonal phase [20-44]. The latter structure can be constructed from the wurtzite phase by putting the cations and anions on the same atomic plane (*i.e.* $u = 0{,}25$ and $v = 0{,}75$) [20]. Hence the spontaneous polarization is calculated as the difference between the polarization of the wurtzite (LiGaGe-type) and layered-hexagonal (ZrBeSi-type) structures:

$$P_{\mathrm{SP}} = P_{\mathrm{WZ}} - P_{\mathrm{LH}}, \tag{7}$$

where P_{WZ} and P_{LH} refer to the wurtzite and layered-hexagonal polarization values, respectively, both of which are evaluated as a Berry phase of the Bloch-like orbitals via the BerryPI code.

The value of the spontaneous polarization of wurtzite KMgP is found to be 0.385 C/m^2. Note that polarization is a vector quantity. Due to hexagonal symmetry, the polarization vector is always along the vertical c-axis. The positive value of P_{SP} indicates that the spontaneous polarization vector points to the [0001] direction.

The spontaneous polarization of KMgP is benchmarked to previously reported LiGaGe-type ferroelectrics. We choose the two related materials KMgSb and NaMgP as comparative case-studies. This allows us to investigate the effect of chemical substitution on polarization properties. The spontaneous polarization is (0.370 C/m^2) for KMgSb [45] and (0.490 C/m^2) for NaMgP [20]. Both values are within the same order of magnitude as the value calculated for KMgP (0.385 C/m^2).

TABLE II. Born effective charges Z^* (in unit of e) of individual ions (K, Mg and P) for wurtzite KMgP with their nominal values Z.

	K	Mg	P
Z^*	0.71	2.1	−2,80
Z	1	2	−3

3.4.2. *Born effective charge*

The Born effective charge (Z^*) describes the polarization induced by ionic displacements [45]. Within the Berry-phase method, the calculation of the Born effective charge is done by studying the variation of polarization as the different ions are displaced from their equilibrium positions [46,47]:

$$Z_i^* = \frac{V}{e}\frac{\Delta P_i}{\Delta r_i}, \tag{8}$$

where V is the unit cell volume, e is the electron charge, ΔP_i is the change in polarization that results from the ionic displacement Δr_i and i runs over each ion (K, Mg and P). In our study, we introduce for each ion a small displacement of $\pm 0{,}1\,\%$ along the c-axis and calculate the corresponding polarizations as Berry phases. The results for the Born effective charges of wurtzite KMgP are gathered in Table II. The nominal ionic charges Z are also included for the sake of comparison.

It can be seen that the effective charge of each ion has the same sign as and is very close to the nominal value (especially for Mg and P). It is established that the approximate equivalence of Z^* and Z is an indicator of a strong ionic character of the chemical bonds [47,48], which aligns with the large value of the spontaneous polarization reported above. In order to verify the validity of our simulation we check the acoustic sum rule, which states that the sum of the effective charge of all ions in the unit cell is zero [49]. Our values of Z^* obey this rule to a negligible error (see Table II).

3.4.3. *Ferroelectric switching*

Acondensed system is ferroelectric if its polarization vector can be reversed by an external electric field [50]. In what follows, we demonstrate that KMgP is one of the wurtzite materials that support ferroelectricity. For this purpose, we present in Fig. 7 the variation of energy as a function of the reaction coordinate.We observe a double potentialwell that characterizes the Ising-type polarization reversal by 180°. There exist other ferroelectric switching mechanisms such as the Bloch- and Néel-types, in which the polarization vector does not vanish but rather rotates by an angle [51]. The reaction coordinate x describes the shift of the cation Mg and anion P up and down the c-axis, with $x = 1$ and $x = -1$ corresponding to the ferroelectric wurtzite structures with opposite polarization (the two minima in Fig. 7) [52]. To study ferroelectric switching a paraelectric state of well-defined polarization is needed. For wurtzite ferroelectrics, a straightforward choice would be the layered-hexagonal configuration, for which $x = 0$ [52] (the saddle point in Fig. 7).

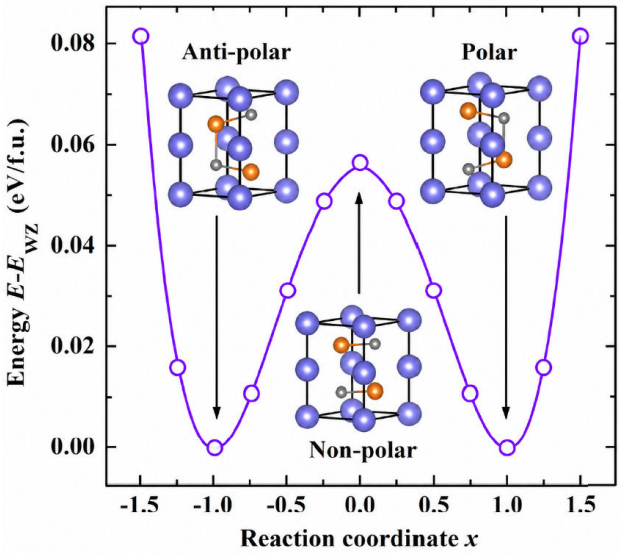


FIGURE 7. Energy per formula unit of wurtzite KMgP as a function of the reaction coordinate x, which controls ionic displacements along the c-axis. The origin of energy is taken to be the energy of the ferroelectric configuration E_{WZ}. The inset shows hexagonal unit cells corresponding to the polar wurtzite (1), layered-hexagonal (2), and anti-polar wurtzite (3) structures.

The energy profile allows us to extract important parameters associated with the ferroelectric effect. The height of the potentialwell is the energy barrier (US) against polarization switching, which is equal to the energy difference between the ferroelectric and paraelectric states [53]:

$$U_S = E_{\mathrm{LH}} - E_{\mathrm{WZ}}, \tag{9}$$

where LH and WZ denote the layered-hexagonal (paraelectric) and wurtzite (ferroelectric) values, respectively. Our prediction of U_S for KMgP is 0.0568 eV/f.u. This energy barrier is small enough that an applied electric field can reverse the polarization vector. For the sake of comparison, the switching barrier of wurtzite KMgSb and NaMgP is reported to be 0.093 [45] and 0.20 eV/f.u. [20], respectively. Another ferroelectric parameter is the Curie temperature (TC), defined as the temperature beyond which the material loses its ferroelectric behaviour [54]. For typical ferroelectric compounds, the value of TC can be approximated by:

$$T_C = \frac{U_S}{k_B}, \tag{10}$$

with k_B being the Boltzmann constant. Using this formula, the Curie temperature of wurtziteKMgPis 385.32 K, which is higher than room temperature (300 K). This is essential for practical applications, since KMgP-based ferroelectric devices usually operate under normal conditions of pressure and temperature. The Curie temperature for KMgSb and NaMgP were not reported in Refs. [20,45]. However, we can use the switching barriers and Eq. (9) to predict its value for both systems: 1078.26 K for KMgSb and 2318.84 KforNaMgP. The

value of T_C can be seen to be much larger for KMgSb and NaMgP than for KMgP. This is consistent with the trend identified earlier, since the switching barrier increases in going from KMgP to KMgSb and NaMgP, and it is obvious from Eq. (9) that this effect tends to increase the Curie temperature.

It is important to emphasize that Eq. (9) provides only a rough qualitative estimate of the Curie temperature. Because it relies on a local mean-field approximation, it does not account for spatial thermal fluctuations and long-range dipole-dipole interactions. For a quantitative and physically rigorous determination of T_C, more sophisticated statistical mechanics approaches, such as constructing an effective Hamiltonian or performing large-scale Monte Carlo simulation [56], are required. Nevertheless, this simple relation gives a first approximation for the value of T_C for KMgP and similar wurtzite ferroelectrics.

Finally, we define the coercive electric field (E_C) to be the minimum field required to switch the polarization. Using the values of P_{SP} and U_S, the intensity of E_C is estimated via [57]:

$$E_C = \frac{8}{3\sqrt{3}} \frac{U_S}{V P_{\text{SP}}}. \tag{11}$$

We point out that this value represents the ideal intrinsic coercive field derived from assuming a homogeneous switching mechanism across a defect-free crystal. In real experimental measurements, polarization reversal typically occurs at significantly lower electric fields [57] . This discrepancy is well known in ferroelectrics and stems from the fact that experimental switching is a heterogeneous process mediated by the nucleation and motion of domains at defects, impurities and grain boundaries. This leads to a reduced energy barrier and, consequently, reduced coercivity compared to the homogenous process.

We find that a coercive field of about 2.78 MV/cm is needed to reverse the polarization from "up" to "down" and vice versa. Because this coercive field is moderate, polarization in wurtzite KMgP is expected to switch before reaching the dielectric breakdown limit (the threshold where the material fails as an insulator and its polarization vanishes).

Based on the values of PSP and US given in Refs. [20,45], the intrinsic coercive field for KMgSb and NaMgP is computed to be 3.56 and 8.63MV/cm, respectively. Both values are smaller than that of KMgP. This ordering is consistent with the values of the switching barrier and spontaneous polarization for the three materials [see Eq. (10)].

3.4.4. Piezoelectric coefficients

Piezoelectricity is the property of some materials to exhibit an electric polarization (called piezoelectric polarization) upon the application of a mechanical deformation [56]. Wurtzite crystals such as KMgP display this effect since their symmetry does not allow a centre of inversion [57]. The piezoelectric response of wurtzite materials is quantified by three independent piezoelectric constants, namely e_{33}, e_{31} and e_{15} [57]. The coefficients e_{33} and e_{31} measure the polarization induced by uniaxial and biaxial strain, respectively. The coefficient e_{15}, on the other hand, links the polarization to shear strain. Given the complexity to implement shear deformation,we carry out calculation of e_{33} and e_{31}. In order to do so,we investigate the evolution of polarization as small strains are applied. A finite difference then leads to values of e_{ij} as follows [58]:

$$e_{3j} = \frac{\Delta P_3}{\Delta \epsilon_j}, \tag{12}$$

where $\Delta\epsilon_j = 1\,\%$ is the applied strain and ΔP_3 is the polarization difference (along the c-axis) between the 0.5 % and $-0{,}5\,\%$ strained wurtzite structures. The strain index j denotes Cartesian axes within the Voigt notation ($x = 1$ for e_{31} and $z = 3$ for e_{33}). The piezoelectric coefficients of wurtzite KMgP are calculated to be $e_{33} = -0{,}75$ C/m^2 and $e_{31} = 1{,}19$ C/m^2. We see that e_{33} (e_{31}) is negative (positive), in sharp contrast with typical wurtzite binaries like AlN, GaN and ZnO, where the signs are reversed between the two coefficients. e_{33} is also negative for KMgSb ($-0{,}42$ C/m^2 [61]) but is positive for NaMgP (0.58 C/m^2 [61]).

For the longitudinal piezoelectric constant e_{33}, the negative sign implies that stretching the crystal along the c-axis reduces the polarization, or equivalently, the polarization opposes the applied tensile strain. This unusual piezoelectric behaviour stems from the combination of low Born effective charges (see Table II) and small strain sensitivity of the internal parameters $\partial u/\partial\epsilon\epsilon_3$ and $\partial v/\partial\epsilon_3$ [59]. Indeed, the response of the internal coordinates of KMgP to the applied strain is extremely low, namely $\partial u/\partial\epsilon\epsilon_3 = -0{,}045$ and $\partial v/\partial\epsilon\epsilon_3 = 0{,}018$.

The experimental evaluation of the piezoelectric response usually relies on the piezoelectric moduli d_{ij}, rather than the piezoelectric coefficients e_{ij}. The relation between d_{ij} and e_{ij} can readily be found from the elastic coefficients C_{ij} [60]:

$$d_{33} = \frac{e_{33}(C_{11}+C_{12}) - 2e_{31}C_{13}}{(C_{11}+C_{12})C_{33} - 2C_{13}^2},$$
$$d_{31} = \frac{e_{31}C_{33} - e_{33}C_{13}}{(C_{11}+C_{12})C_{33} - 2C_{13}^2}. \tag{13}$$

We obtain the values $d_{33} = -52{,}66$ pC/N and $d_{31} = 22{,}72$ pC/N. Due to the absence of prior literature on the piezoelectric coefficients and moduli of this system, a comparative analysis of our results is not possible. We can only compare the present results with previously studied similar compounds. The value of d_{33} is $-19{,}15$ pC/N for KMgSb and 7.80 pC/N for NaMgP [61] (there is no data on d_{31}).

4. Conclusion

In this paper, we have conducted a comprehensive first-principles investigation of the structural, electronic, ferroelectric and piezoelectric properties of KMgP within the wur-

tzite LiGaGe-type structure. Our results suggest thatKMgPis a theoretically viable candidate as a functional material in both ferroelectric and piezoelectric applications. The mechanical and dynamical stability of the wurtzite phase was verified, as the calculated elastic constants satisfy the Born criteria and the phonon spectrum exhibit no imaginary frequencies. Electronic-structure calculations identify wurtzite KMgP as a direct-gap semiconductor. DOS analysis revealed that the valence band is primarily composed of P orbitals, while the conduction band is dominated by a mixture of P and Mg states.

Regarding the ferroelectric behaviour of our compound, we employed the Berry-phase technique to determine the spontaneous polarization and the Born effective charges for each constituent ion. Next, we modelled the ferroelectric switching via the double-well potential energy profile. The calculated energy barrier and coercive field indicate that polarization reversal is energetically feasible, confirming the potential forKMgPto be utilized in practical ferroelectric devices.

Finally, we reported the piezoelectric coefficients and moduli, and discussed the counterintuitive negative longitudinal piezoelectric constants e_{33} and d_{33}. Future work will focus on a more comprehensive investigation of the dielectric response, electron localization function (ELF), and hybrid-functional calculations to provide further insight into the electronic structure, chemical bonding, and ferroelectric properties of KMgP.

Competing interests

The authors declare no competing interests.

Data availability statement

The data that support the findings of this study are available from the corresponding author upon reasonable request.

1. R. Machado, M. G. Stachiotti, R. L. Migoni and A. H. Tera, Estructura electrónica y origen de la ferroelectricidad en el Bi4Ti3O12, por medio de cálculos de primeros principios, *Rev. Mex. Fis.* **51** (2005), https://rmf.smf.mx/ojs/index.php/rmf/article/view/3357.
2. M. De Jong, W. Chen, H. Geerlings, M. Asta and K. A. Persson, A database to enable discovery and design of piezoelectric materials, *Sci. Data* **2** (2015), https://doi.org/10.1038/sdata.2015.53.
3. X. Guo, Z. Li, J. Peng, H. Dong, R. Wang, Y. Yang and F. Wu, Piezoelectric properties of novel group III-VI TiA2X4 (A = Ga, Al; X = S, Se, Te) monolayers: First-principles calculations, *Phys. Lett. A* **572** (2026) 131365, https://doi.org/10.1016/j.physleta.2026.131365.
4. H. Fu and R. E. Cohen, Polarization rotation mechanism for ultrahigh electromechanical response in single-crystal piezoelectrics, *Nature* **403** (2000) 281, https://doi.org/10.1038/35002022.
5. X. Ding, J. B. Si, Y. Zhang, L. Tang, J. H. Ma, Y. H. Xie and X. Q. Deng, Electronic properties and device design of ferroelectric Al2O3/GaN heterostructure, *Phys. Lett. A* **497** (2024) 129328, https://doi.org/10.1016/j.physleta.2024.129328.
6. D. A. Aldahiry, D. A. Bajaba, N. M. Basalamah and M. M. Ahmed, Piezoelectric Transducer as an Energy Harvester: A Review, Yemeni *J. Eng. Sci.* **19** (2022) 30, https://doi.org/10.53370/001c.33771.
7. H. Liu, J. Zhong, C. Lee, S.-W. Lee and L. Lin, A comprehensive review on piezoelectric energy harvesting technology: Materials, mechanisms, and applications, *Appl. Phys. Rev.* **5** (2018) 041306, https://doi.org/10.1063/1.5074184.
8. J. Li, L. Fang, B. Sun, X. Li and S. H. Kang, Review-Recent Progress in Flexible and Stretchable Piezoresistive Sensors and Their Applications, *J. Electrochem. Soc.* **167** (2020) 037561, https://doi.org/10.1149/1945-7111/ab6828.
9. L. Wang, C. Wang, Y. Wang, A. Quan, M. Keshavarz, B. P. Madeira, H. Zhang, C. Wang and M. Kraft, A Review on Coupled Bulk Acoustic Wave MEMS Resonators, *Sensors* **22** (2022), https://doi.org/10.3390/s22103857.
10. Y. Arimoto and H. Ishiwara, Current Status of Ferroelectric Random-Access Memory, *MRS Bull.* **29** (2004) 823, https://doi.org/10.1557/mrs2004.235.
11. Y. Kato, T. Yamada and Y. Shimada, 0.18-μm nondestructive readout FeRAM using charge compensation technique, IEEE Trans. *Electron Devices* **52** (2005) 2616, https://doi.org/10.1109/TED.2005.859688.
12. K. R. Talley, R. Sherbondy, A. Zakutayev and G. L. Brennecka, Review of high-throughput approaches to search for piezoelectric nitrides, *J. Vac. Sci. Technol. A* **37** (2019) 060803, https://doi.org/10.1116/1.5125648.
13. N. Gogneau, N. Jamond, P. Chrétien, F. Houzé, E. Lefeuvre and M. Tchernycheva, From single III-nitride nanowires to piezoelectric generators: New route for powering nomad electronics, *Semicond. Sci. Technol.* **31** (2016) 103002, https://doi.org/10.1088/0268-1242/31/10/103002.
14. R. K. Pandey, J. Dutta, S. Brahma, B. Rao and C.-P. Liu, Review on ZnO-based piezotronics and piezoelectric nanogenerators: aspects of piezopotential and screening effect, *J. Phys. Mater.* **4** (2021) 044011, https://doi.org/10.1088/2515-7639/ac130a.
15. Y. Shimomura, S. Ohno, K. Hayashi and H. Akamatsu, Quadruple-well ferroelectricity and moderate switching barrier in defective wurtzite α-Al2S3: a first-principles study, *npj Comput. Mater.* **11** (2025) 38, https://doi.org/10.1038/s41524-025-01519-3.
16. C.-W. Lee, K. Yazawa, A. Zakutayev, G. L. Brennecka and P. Gorai, Switching it up: New mechanisms revealed in wurtzite-type ferroelectrics, *Sci. Adv.* **10** (2024) eadl0848, https://doi.org/10.1126/sciadv.adl0848.

17. S. Fichtner, N. Wolff, F. Lofink, L. Kienle and B. Wagner, AlScN: A III-V semiconductor based ferroelectric, *J. Appl. Phys.* **125** (2019) 114103, https://doi.org/10.1063/1.5084945.

18. D.Wang *et al.*, FerroelectricYAlN grown by molecular beam epitaxy, *Appl. Phys. Lett.* **123** (2023) 033504, https://doi.org/10.1063/5.0159562.

19. A. Konishi, T. Ogawa, C. A. J. Fisher, A. Kuwabara, T. Shimizu, S. Yasui, M. Itoh and H. Moriwake, Mechanism of polarization switching in wurtzite-structured zinc oxide thin films, *Appl. Phys. Lett.* **109** (2016) 102903, https://doi.org/10.1063/1.4962440.

20. J. W. Bennett, K. F. Garrity, K. M. Rabe and D. Vanderbilt, Hexagonal ABC Semiconductors as Ferroelectrics, *Phys. Rev. Lett*. **109** (2012) 167602, https://doi.org/10.1103/PhysRevLett.109.167602.

21. P. Hohenberg and W. Kohn, Inhomogeneous Electron Gas, *Phys. Rev.* **136** (1964) B864, https://doi.org/10.1103/PhysRev.136.B864.

22. R. O. Jones, Density functional theory: Its origins, rise to prominence, and future, *Rev. Mod. Phys.* **87** (2015) 897, https://doi.org/10.1103/RevModPhys.87.897.

23. P. Blaha, K. Schwarz, F. Tran, R. Laskowski, G. K. H. Madsen and L. D. Marks, WIEN2k: An APW+lo program for calculating the properties of solids, *J. Chem. Phys.* **152** (2020) 074101, https://doi.org/10.1063/1.5143061.

24. E. Sjöstedt, L. Nordström and D. J. Singh, An alternative way of linearizing the augmented plane-wave method, *Solid State Commun*. **114** (2000) 15, https://doi.org/10.1016/S0038-1098(99)00577-3.

25. J. P. Perdew and A. Zunger, Self-interaction correction to density-functional approximations for many-electron systems, *Phys. Rev. B* **23** (1981) 5048, https://doi.org/10.1103/PhysRevB.23.5048

26. M. Jamal, M. Bilal, I. Ahmad and S. Jalali-Asadabadi, IRelast package, *J. Alloys Compd.* **735** (2018) 569, https://doi.org/10.1016/j.jallcom.2017.10.139.

27. A. Togo, First-principles Phonon Calculations with Phonopy and Phono3py, *J. Phys. Soc. Jpn*. **92** (2023) 012001, https://doi.org/10.7566/JPSJ.92.012001.

28. S. J. Ahmed, J. Kivinen, B. Zaporzan, L. Curiel, S. Pichardo and O. Rubel, BerryPI: A software for studying polarization of crystalline solids with WIEN2k density functional all-electron package, *Comput. Phys. Commun.* **184** (2013) 647, https://doi.org/10.1016/j.cpc.2012.10.028.

29. R. Vogel and H.-U. Schuster, Neue elektrovalente ternäre Verbindungen des Kaliums mit Magnesium und Elementen der 5. Hauptgruppe, *Z. Naturforsch.* B **34** (1979) 1719, https://doi.org/10.1515/znb-1979-1219.

30. Y.-N. Xu and W. Y. Ching, Electronic, optical, and structural properties of some wurtzite crystals, *Phys. Rev. B* **48** (1993) 4335, https://doi.org/10.1103/PhysRevB.48.4335.

31. W. Kohn and L. J. Sham, Self-Consistent Equations Including Exchange and Correlation Effects, *Phys. Rev.* **140** (1965) A1133, https://doi.org/10.1103/PhysRev.140.A1133.

32. F. D. Murnaghan, The Compressibility of Media under Extreme Pressures, *Proc. Natl. Acad. Sci. U.S.A.* **30** (1944) 244, https://doi.org/10.1073/pnas.30.9.244.

33. F. Casper, C. Felser, R. Seshadri, C. P. Sebastian and R. Pöttgen, Searching for hexagonal analogues of the half-metallic half-Heusler XYZ compounds, *J. Phys. D: Appl. Phys.* **41** (2008) 035002, https://doi.org/10.1088/0022-3727/41/3/035002.

34. R. P. Feynman, Forces in Molecules, *Phys. Rev.* **56** (1939) 340, https://doi.org/10.1103/PhysRev.56.340.

35. A. M. Hofmeister, Pressure derivatives of the bulk modulus, *J. Geophys. Res. Solid Earth* **96** (1991) 21893, https://doi.org/10.1029/91JB02157.

36. V. Stevanović, S. Lany, X. Zhang and A. Zunger, Correcting density functional theory for accurate predictions of compound enthalpies of formation: Fitted elemental-phase reference energies, *Phys. Rev. B* **85** (2012) 115104, https://doi.org/10.1103/PhysRevB.85.115104.

37. D. Holec, M. Friák, J.Neugebauer and P. H.Mayrhofer, Trends in the elastic response of binary early transition metal nitrides, *Phys. Rev. B* **85** (2012) 064101, https://doi.org/10.1103/PhysRevB.85.064101.

38. F. Mouhat and F.-X. Coudert, Necessary and sufficient elastic stability conditions in various crystal systems, *Phys. Rev. B* **90** (2014) 224104, https://doi.org/10.1103/PhysRevB.90.224104.

39. G. Petretto *et al*., High-throughput density-functional perturbation theory phonons for inorganic materials, *Sci. Data* **5** (2018) 180065, https://doi.org/10.1038/sdata.2018.65.

40. R. D. King-Smith and D. Vanderbilt, Theory of polarization of crystalline solids, *Phys. Rev. B* **47** (1993) 1651, https://doi.org/10.1103/PhysRevB.47.1651.

41. R. Resta, Theory of the electric polarization in crystals, *Ferroelectrics* **136** (1992) 51, https://doi.org/10.1080/00150199208016065.

42. R. Resta, Macroscopic Electric Polarization as a Geometric Quantum Phase, *Europhys. Lett.* **22** (1993) 133, https://doi.org/10.1209/0295-5075/22/2/010.

43. R. Resta and D. Vanderbilt, Theory of Polarization: A Modern Approach, in Physics of Ferroelectrics: A Modern Perspective (Springer, Berlin, 2007), pp. 31-68, https://doi.org/10.1007/978-3-540-34591-6_2.

44. C. E. Dreyer, A. Janotti, C. G. Van de Walle and D. Vanderbilt, Correct Implementation of Polarization Constants in Wurtzite Materials and Impact on III-Nitrides, *Phys. Rev. X* **6** (2016) 021038, https://doi.org/10.1103/PhysRevX.6.021038.

45. E. H. Abbes, A. Benbedra, I. Bouhamou, L. Latreche, H. Abbassa and S. Meskine, Stability, Electronic Structure and Ferroelectric Switching of Wurtzite KMgSb, *Phys. Status Solidi B* **263** (2026) e202500633, https://doi.org/10.1002/pssb.202500633.

46. A. Dal Corso *et al*., Ab initio study of piezoelectricity and spontaneous polarization in ZnO, *Phys. Rev. B* **50** (1994) 10715, https://doi.org/10.1103/PhysRevB.50.10715.

47. F. Bernardini, V. Fiorentini and D. Vanderbilt, Spontaneous polarization and piezoelectric constants of III-V nitrides, *Phys. Rev. B* **56** (1997) R10024, https://doi.org/10.1103/PhysRevB.56.R10024.

48. S. Massidda *et al*., Polarization and dynamical charge of ZnO within different one-particle schemes, *Phys. Rev. B* **52** (1995) R16977, https://doi.org/10.1103/PhysRevB.52.R16977.

49. X. Gonze and C. Lee, Dynamical matrices, Born effective charges, dielectric permittivity tensors, and interatomic force constants from density-functional perturbation theory, *Phys. Rev. B* **55** (1997) 10355, https://doi.org/10.1103/PhysRevB.55.10355.

50. K. F. Garrity, High-throughput first-principles search for new ferroelectrics, *Phys. Rev. B* **97** (2018) 024115, https://doi.org/10.1103/PhysRevB.97.024115.

51. D. Lee, R. K. Behera, P. Wu, H. Xu, Y. L. Li, S. B. Sinnott, S. R. Phillpot, L. Q. Chen and V. Gopalan, Mixed Bloch-Néel-Ising character of 180° ferroelectric domain walls, *Phys. Rev. B* **80** (2009) 060102, https://doi.org/10.1103/PhysRevB.80.060102.

52. S. J. Ahmed, S. Pichardo, L. Curiel and O. Rubel, First-principle modelling of the ferroelectric switching in BaTiO3: concurrent switching versus domain wall motion, *Model. Simul. Mater. Sci. Eng*. **22** (2014) 055014, https://doi.org/10.1088/0965-0393/22/5/055014.

53. J. Cole, S. J. Ahmed, L. Curiel, S. Pichardo and O. Rubel, Marble game with optimal ferroelectric switching, *J. Phys.: Condens. Matter* **26** (2014) 135901, https://doi.org/10.1088/0953-8984/26/13/135901.

54. K. M. Rabe, M. Dawber, C. Lichtensteiger, C. H. Ahn and J.-M. Triscone, Modern Physics of Ferroelectrics: Essential Background, in Physics of Ferroelectrics: A Modern Perspective (Springer, Berlin, 2007), pp. 1-30, https://doi.org/10.1007/978-3-540-34591-6_1.

55. S. P. Beckman, X.Wang, K. M. Rabe and D.Vanderbilt, Ideal barriers to polarization reversal and domain-wall motion in strained ferroelectric thin films, *Phys. Rev. B* **79** (2009) 144124, https://doi.org/10.1103/PhysRevB.79.144124.

56. M. C. Sekhar, E. Veena, N. S. Kumar, K. C. B. Naidu, A. Mallikarjuna and D. B. Basha, A Review on Piezoelectric Materials and Their Applications, *Cryst. Res. Technol.* **58** (2023) 2200130,https://doi.org/10.1002/crat.202200130.

57. P. J. Dobson, Physical Properties of Crystals - Their Representation by Tensors and Matrices, *Phys. Bull.* **36** (1985) 506, https://doi.org/10.1088/0031-9112/36/12/027.

58. P. Gopal, N. A. Spaldin and U. V. Waghmare, First-principles study of wurtzite-structure MnO, *Phys. Rev. B* **70** (2004) 205104, https://doi.org/10.1103/PhysRevB.70.205104.

59. S. Liu and R. E. Cohen, Origin of Negative Longitudinal Piezoelectric Effect, *Phys. Rev. Lett.* **119** (2017) 207601, https://doi.org/10.1103/PhysRevLett.119.207601.

60. M. Catti, Y. Noel and R. Dovesi, Full piezoelectric tensors of wurtzite and zinc blende ZnO and ZnS by first-principles calculations, *J. Phys. Chem. Solids* **64** (2003) 2183, https://doi.org/10.1016/S0022-3697(03)00219-1.

Antenas pre-fractales en medicina: fundamentos geométricos, desempeño electromagnético y aplicaciones diagnósticas

L. González-Zamora[a] S. S. Hidalgo-Tobón[a,b,*] y M. A. Quiroz-Juarez[c]

[a] *Departamento de Física, Universidad Autónoma Metropolitana-Iztapalapa (UAM-I), Ciudad de México, 09340, CDMX, México.*
orcid: 0000-0001-7207-4576

[b] *Departamento de Imagenología, Hospital Infantil de México Federico Gómez, Ciudad de México, 06720, CDMX, México.*
[*] *e-mail: shid@xanum.uam.mx*
orcid: 0000-0002-3025-0989

[c] *Centro de Física Aplicada y Tecnología Avanzada, Universidad Nacional Autónoma de México, Boulevard Juriquilla 3001, Querétaro, 76230, México.*
orcid: 0000-0002-5995-9510

Received 11 March 2026; accepted 15 June 2026

Las antenas pre-fractales, basadas en geometrías auto-semejantes de tipo Sierpinski y Koch, han emergido como una alternativa atractiva para el diseño de dispositivos de radiofrecuencia en escenarios donde se requiere miniaturización, operación multibanda y control del diagrama de radiación. En este trabajo se presenta una revisión enfocada específicamente en aplicaciones médicas, en contraste con revisiones previas de carácter más general sobre antenas fractales orientadas a comunicaciones inalámbricas. Se integran tres niveles complementarios: i) el uso de la geometría y de la dimensión fractal para describir estructuras biológicas complejas y analizar imágenes médicas, ii) los fundamentos electromagnéticos necesarios para entender la radiación y el acoplamiento campo-tejido de antenas pre-fractales, y iii) estudios recientes que emplean geometrías pre-fractales y metafractales en detección temprana de cáncer de piel y de mama, sensores portátiles flexibles tipo "tatuaje electrónico" y bobinas para imagen por resonancia magnética multinuclear. Se discuten las ventajas en términos de tamaño, comportamiento multibanda y adaptabilidad mecánica, así como las principales limitaciones asociadas a la presencia de tejido biológico (desintonización, pérdidas y restricciones de SAR), la complejidad del modelado y los retos de fabricación. Esta visión unificada pretende servir como puente entre la física de antenas y la instrumentación biomédica, y como guía para el diseño de nuevas antenas pre-fractales orientadas a aplicaciones clínicas y preclínicas.

Descriptores: Antenas pre-fractales; geometría fractal; telemetría implantable; detección de cáncer; electrónica flexible; imagen por resonancia magnética.

Pre-fractal antennas based on self-similar geometries such as Sierpinski and Koch have emerged as an attractive alternative for designing radiofrequency devices in scenarios that demand miniaturization, multiband operation, and control of the radiation pattern. This work presents a review specifically focused on medical applications, in contrast to previous, more general reviews on fractal antennas aimed at wireless communication systems. Three complementary levels are integrated: (i) the use of fractal geometry and fractal dimension to describe complex biological structures and to analyze medical images, (ii) the electromagnetic foundations required to understand radiation and field-tissue coupling in pre-fractal antennas, and (iii) recent studies that employ pre-fractal and metafractal geometries for early detection of skin and breast cancer, flexible "electronic tattoo" wearable sensors, and coils for multinuclear magnetic resonance imaging. We discuss the advantages in terms of size reduction, multiband behavior, and mechanical adaptability, as well as the main limitations associated with the presence of biological tissue (detuning, additional losses, and SAR constraints), the complexity of modeling, and fabrication challenges. This unified perspective is intended to bridge antenna physics and biomedical instrumentation and to guide the design of new pre-fractal antennas oriented towards clinical and preclinical applications.

Keywords: Pre-fractal antennas; fractal geometry; implantable telemetry; cancer detection; flexible electronics; magnetic resonance imaging.

DOI: https://doi.org/10.31349/RevMexFis.72.061101

1. Introducción

Las antenas de radiofrecuencia empleadas en aplicaciones médicas suelen diseñarse para operar en bandas específicas, lo que limita su ancho de banda y restringe su uso a un conjunto reducido de frecuencias [1,2]. Esta situación ha motivado la búsqueda de estructuras capaces de combinar miniaturización, operación multibanda y buen control de los diagramas de radiación, entre las cuales las geometrías fractales han adquirido un papel destacado en las últimas décadas [3-10]. Diversos estudios han mostrado que el uso de configuraciones fractales permite reducir el tamaño físico de la antena y, al mismo tiempo, habilitar resonancias en múltiples bandas, con aplicaciones potenciales en comunicaciones

inalámbricas y sistemas biomédicos [3-7]. A diferencia de trabajos previos sobre geometría fractal y su aplicación al diseño de antenas orientados principalmente a sistemas de comunicación inalámbrica [11], el presente trabajo se distingue en varios aspectos fundamentales. En primer lugar, el enfoque está dirigido de manera explícita y exclusiva a aplicaciones médicas, integrando tres niveles complementarios que no se consideran de forma conjunta en la literatura previa: el uso de la dimensión fractal para describir y analizar estructuras biológicas complejas, los fundamentos electromagnéticos de la radiación y el acoplamiento campo–tejido, y las aplicaciones diagnósticas y de monitorización más recientes. En segundo lugar, se incorporan geometrías metafractales y estudios publicados hasta 2024, incluyendo bobinas fractales para imagen por resonancia magnética multinuclear, sensores flexibles tipo "tatuaje electrónico" y antenas compactas para detección de cáncer de piel y de mama, aplicaciones no abordadas en revisiones anteriores [11].

El término *fractal* fue acuñado por Mandelbrot en 1975 para describir figuras compuestas por partes similares a la forma completa, es decir, estructuras auto-semejantes a distintas escalas [12-14]. Estas formas se construyen a partir de reglas geométricas relativamente simples, pero pueden exhibir una complejidad muy elevada, con patrones que se repiten de manera recursiva en múltiples niveles de aumento [12,15]. La geometría fractal ha revolucionado la forma en que entendemos y medimos la complejidad de objetos irregulares, como el cuerpo humano, al proporcionar una caracterización más precisa de la irregularidad mediante la dimensión fractal, una medida numérica que cuantifica el nivel de complejidad más allá de las dimensiones enteras tradicionales [12,15]. Desde el punto de vista geométrico, se adopta la dimensión fractal auto-semejante para describir la complejidad de los patrones utilizados. Para construcciones ideales, la dimensión fractal puede escribirse como

$$D = \frac{\log(N)}{\log(1/r)}, \tag{1}$$

donde N es el número de copias auto-semejantes en que puede descomponerse la figura, es decir, cuántas piezas de menor tamaño reproducen exactamente la forma completa, y r es el factor de escala lineal entre cada copia y la figura original; un valor $r = 1/2$ indica que cada copia tiene la mitad del lado de la figura completa. La dimensión fractal D cuantifica numéricamente cuán eficientemente la estructura llena el espacio: valores entre 1 y 2 corresponden a figuras más complejas que una línea, pero menos densas que una superficie.

Para el triángulo de Sierpinski, por ejemplo, $N = 3$ y $r = 1/2$, lo que da $D = \log(3)/\log(2) \approx 1.585$ [8]. En el caso de geometrías de tipo Sierpinski, como la preforma triangular mostrada esquemáticamente en la Fig. 1, esta formulación permite relacionar, al menos cualitativamente, el orden de iteración con la aparición de nuevos caminos de corriente y, en consecuencia, con la aparición de nuevas

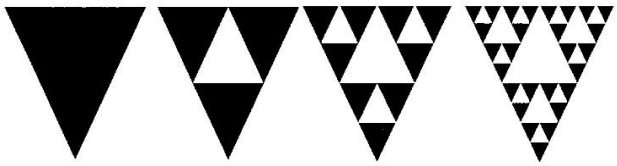


FIGURE 1. Construcción esquemática del triángulo de Sierpinski a partir de un triángulo equilátero inicial (iteración 0), eliminando recursivamente el subtriángulo central en cada iteración.

frecuencias de resonancia en la respuesta de la antena [1,5,12,15].

Las características principales de un fractal incluyen la auto-semejanza, donde una parte de la figura se asemeja a la forma completa, la dimensión fractal, usualmente fraccionaria y asociada con su complejidad, la construcción recursiva mediante iteraciones sucesivas, y la presencia de bordes y contornos altamente irregulares que lo distinguen de las figuras geométricas clásicas [14,15]. Ejemplos como la curva de Koch ilustran cómo una curva puede situarse entre una línea y una superficie en términos de complejidad, lo cual se refleja en valores de dimensión fractal mayores que uno y menores que dos [15]. En muchos casos, los fractales pueden considerarse de complejidad prácticamente ilimitada, puesto que surgen nuevos detalles estructurales conforme aumenta la resolución de observación [12,15].

En el ámbito médico, la dimensión fractal se ha empleado para caracterizar de manera más fiel estructuras biológicas intrínsecamente complejas, como neuronas, pulmones, intestinos y vasos sanguíneos, así como para analizar imágenes microscópicas y radiológicas con fines de diagnóstico y clasificación [16-20]. Esta capacidad de cuantificar la irregularidad ha dado lugar a nuevas herramientas para la detección y evaluación de enfermedades, en particular en oncología, donde el análisis fractal de masas y contornos celulares se ha utilizado para distinguir entre tejidos sanos y patológicos y para apoyar la clasificación de procesos metastásicos [16,17,19,20]. Un ejemplo representativo es el trabajo de Klein *et al.*, quienes emplearon análisis fractal de imágenes obtenidas mediante microscopía de contraste de interferencia en reflexión para diferenciar células tumorales pancreáticas, mostrando que la dimensión fractal de los contornos celulares permite distinguir líneas celulares tumorales con alta precisión. Estos estudios ilustran cómo la fractalidad actúa como descriptor de la morfología tisular, consolidándose como herramienta práctica para el diagnóstico de procesos patológicos complejos [20]. Ejemplos de estas aplicaciones suelen ilustrarse mediante imágenes de estructuras biológicas complejas, como las mostradas en la Fig. 2, donde la organización ramificada recuerda a los patrones fractales [18-20].

La misma propiedad de auto-semejanza que permite describir y cuantificar la complejidad de estructuras biológicas como vasos sanguíneos, pulmones y neuronas resulta intrínsecamente ventajosa en el diseño de antenas destinadas a operar en entornos biológicos [16,18]. Por un lado, la geometría pre-fractal permite incrementar la longitud eléctrica

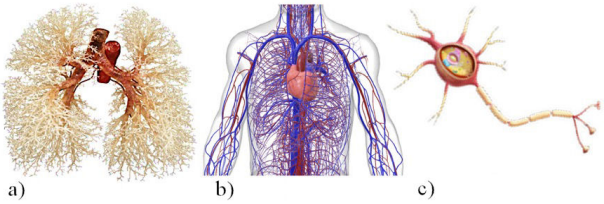


FIGURE 2. Ejemplos de estructuras biológicas que exhiben patrones ramificados con morfología de tipo fractal: a) árbol bronquial, b) red vascular, c) arborización dendrítica.

efectiva de la antena sin aumentar proporcionalmente sus dimensiones físicas, lo que facilita la miniaturización necesaria para integrar antenas en dispositivos implantables o portátiles [3-7]. Por otro lado, la coexistencia de múltiples escalas geométricas dentro de una misma estructura favorece la aparición de resonancias en varias bandas de frecuencia de interés diagnóstico o terapéutico [4,5,9,10]. En este sentido, la fractalidad no es únicamente una herramienta descriptiva de la morfología biológica, sino también un principio de diseño que permite adaptar las propiedades electromagnéticas de la antena a los requerimientos específicos del entorno médico. En la práctica, las estructuras fractales ideales no pueden construirse físicamente, por lo que se recurre a aproximaciones de orden finito denominadas *pre-fractales*, obtenidas tras un número limitado n de iteraciones del proceso geométrico generador [8,15]. Por su parte, los *metafractales* combinan geometrías pre-fractales con materiales con propiedades electromagnéticas especiales (metamateriales), con el objetivo de optimizar parámetros como la ganancia, el ancho de banda y la eficiencia en diseños compactos [21]. A lo largo de este trabajo se emplea el término *pre-fractal* para referirse a estas implementaciones físicas de orden finito; no obstante, se conserva la terminología original cuando se describen trabajos de otros autores, quienes en muchos casos utilizan el término *fractal* de manera general. En el campo de las antenas, la geometría fractal ha encontrado una aplicación particularmente relevante en el diseño de antenas miniaturizadas y multibanda. La propiedad de auto-semejanza, mediante la cual cada parte reproduce la forma global a distintas escalas, convierte a los patrones fractales en una solución natural para desarrollar antenas capaces de operar en múltiples bandas de frecuencia sin incrementar de manera significativa el tamaño del dispositivo [3-10]. En este contexto, las antenas pre-fractales constituyen una aproximación práctica a las estructuras fractales ideales, ya que implementan un número finito de iteraciones geométricas en configuraciones como el triángulo de Sierpinski y otras geometrías relacionadas [4,5,9,10,22]. Un ejemplo representativo de una antena pre-fractal basada en este tipo de geometría y orientada a aplicaciones médicas se muestra en la Fig. 3, donde puede apreciarse la evolución de la estructura con el orden de iteración [4,5,9,10].

Estas propiedades resultan especialmente atractivas en aplicaciones médicas, donde las antenas deben integrarse en espacios reducidos, cumplir con restricciones de seguridad (como los límites de SAR) y mantener un desempeño ade-

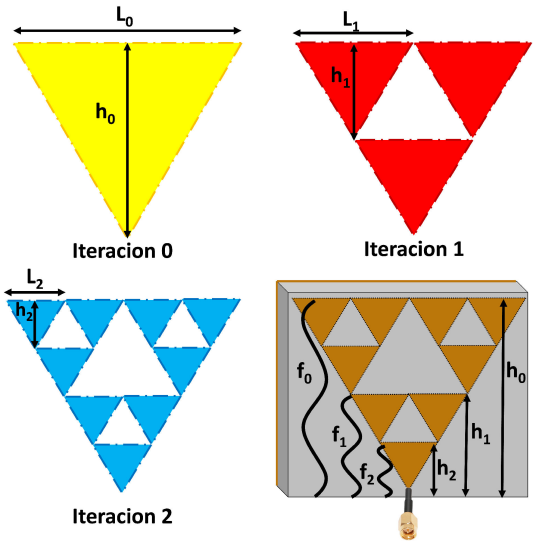


FIGURE 3. Antena pre-fractal de tipo Sierpinski: evolución geométrica en las iteraciones 0 (amarillo), 1 (rojo) y 2 (azul), donde h_0, h_1 y h_2 son las alturas de las ramas dominantes en cada orden de iteración. El panel derecho muestra la implementación física sobre sustrato dieléctrico con alimentación mediante conector SMA, ilustrando la correspondencia entre cada escala geométrica y su frecuencia de resonancia asociada f_0, f_1 y f_2.

cuado en bandas de interés diagnóstico o terapéutico [2,21,23-29]. En los últimos años, se han propuesto antenas y bobinas con geometría fractal o pre-fractal para aplicaciones que incluyen imagen por resonancia magnética, detección de cáncer de piel y de mama, telemetría implantable y sensores portátiles flexibles, aprovechando la miniaturización, el comportamiento multibanda y la adaptabilidad mecánica que proporcionan estos diseños [21,23-25,27-29]. Configuraciones típicas de estas antenas en escenarios biomédicos, por ejemplo, colocadas sobre fantomas tisulares o integradas en plataformas flexibles se esquematizan en la Fig. 4, destacando la interacción entre la antena pre-fractal y el entorno biológico [21,25,27,28].

En el contexto de aplicaciones médicas, algunos de estos conceptos han sido abordados en un trabajo orientado a un

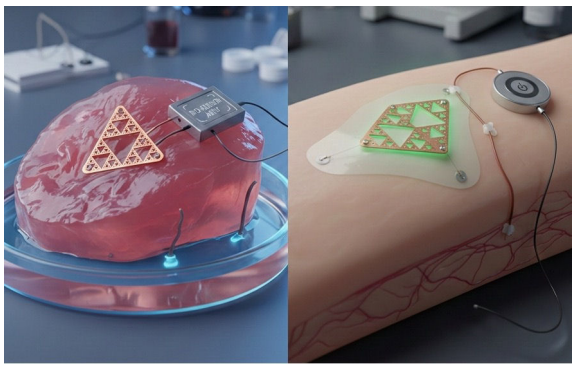


FIGURE 4. Configuraciones típicas de antenas pre-fractales de tipo Sierpinski en escenarios biomédicos, como su colocación sobre fantomas tisulares y su integración en plataformas flexibles, que ilustran su interacción con el entorno biológico circundante.

público principalmente clínico [30]. El presente artículo amplía y actualiza de manera sustancial dicha contribución, integrando una revisión más extensa de la literatura reciente y una discusión más detallada sobre los fundamentos físicos de la radiación, la interacción campo-tejido y las implicaciones biomédicas del uso de antenas pre-fractales en medicina.

2. Metodología

La metodología de este trabajo combina una revisión sistemática de la literatura con un marco de análisis electromagnético basado en las ecuaciones de Maxwell y en modelos simplificados para antenas pre-fractales. El objetivo es integrar, en una descripción coherente, los aspectos geométricos fractales, los fundamentos de la radiación y los resultados experimentales y numéricos reportados en aplicaciones médicas.

En primer lugar, se realizó una búsqueda focalizada de literatura en libros y artículos especializados sobre geometría fractal [12-15], aplicaciones médicas de la dimensión fractal [16-20] y diseño de antenas fractales y pre-fractales para comunicaciones y uso biomédico [3-10,21,23-25,27-29]. A diferencia de revisiones generales sobre antenas fractales para telecomunicaciones [11], los trabajos seleccionados en esta revisión se centran en aplicaciones médicas, criterio que guió tanto la búsqueda bibliográfica como el análisis presentado en las secciones siguientes, y reportan: (i) miniaturización de antenas mediante geometrías fractales, (ii) comportamiento multibanda o de banda ancha, (iii) integración de antenas en dispositivos implantables, portátiles o flexibles, y (iv) uso de bobinas fractales en imagen por resonancia magnética.

En segundo lugar, se revisaron los fundamentos del análisis electromagnético de antenas a partir de las ecuaciones de Maxwell, tomando como punto de partida la forma diferencial de la ley de Ampère–Maxwell:

$$\nabla \times \vec{B} = \mu_0 \vec{J} + \mu_0 \varepsilon_0 \frac{\partial \vec{E}}{\partial t}, \tag{2}$$

y de la ley de inducción de Faraday:

$$\nabla \times \vec{E} = -\frac{\partial \vec{B}}{\partial t}. \tag{3}$$

Aquí, $\vec{B}$ es el campo magnético, $\vec{J}$ es la densidad de corriente, $\vec{E}$ es el campo eléctrico y μ_0, ε_0 son la permeabilidad y la permitividad del vacío, respectivamente [22]. Al combinar estas expresiones con la ecuación de Gauss para el campo eléctrico en un medio lineal y homogéneo, se obtiene la ecuación de onda vectorial general para el campo eléctrico:

$$\nabla^2 \vec{E} + k^2 \vec{E} = -j\omega\mu\vec{J} + \frac{\nabla \rho}{\varepsilon}, \tag{4}$$

donde k es el número de onda del medio, ω la frecuencia angular, μ la permeabilidad, ρ la densidad volumétrica de carga libre y ε la permitividad del medio [1,22]. En aplicaciones de antenas, el medio conductor que forma la estructura radiante es macroscópicamente neutro, de modo que $\rho = 0$ y la ecuación anterior se reduce a:

$$\nabla^2 \vec{E} + k^2 \vec{E} = -j\omega\mu\vec{J}. \tag{5}$$

La solución formal de esta ecuación puede escribirse como una integral de volumen de la densidad de corriente ponderada por una función de Green escalar para campos monocromáticos en medios homogéneos,

$$g(\vec{r}, \vec{r}\,') = \frac{e^{jkR}}{4\pi R}, \tag{6}$$

donde $R = |\vec{r} - \vec{r}\,'|$ es la distancia entre la fuente y el punto de observación [22]. En esta revisión, estas formulaciones se utilizan de manera conceptual para vincular la distribución de corriente sobre la geometría pre-fractal con el diagrama de radiación resultante, tal como se discute en los textos clásicos de análisis y diseño de antenas [1,22].

A partir del campo eléctrico radiado,la directividad de las antenas consideradas se describe en términos de la densidad de potencia radiada $U(\theta, \phi)$ y de la referencia isotrópica $U_{\rm iso} = P_{\rm rad}/(4\pi)$, de modo que

$$D(\theta, \phi) = \frac{U(\theta, \phi)}{U_{\rm iso}} = \frac{4\pi\, U(\theta, \phi)}{P_{\rm rad}}, \tag{7}$$

donde $P_{\rm rad}$ es la potencia total radiada [1,22]. En el contexto de esta revisión, la directividad se utiliza principalmente como un parámetro para comparar cualitativamente el comportamiento angular de antenas pre-fractales con diseños convencionales reportados en la literatura [3-10].

Como se discutió en la Ec. (1), la dimensión fractal autosemejante se utiliza aquí como un descriptor geométrico de la complejidad de la antena. En geometrías de tipo Sierpinski, como la preforma triangular mostrada esquemáticamente en la Fig. 1, el orden de iteración se asocia con la aparición de nuevos caminos de corriente y, en consecuencia, con nuevas frecuencias de resonancia en la respuesta de la antena [1,5,12,15].

Desde un punto de vista constructivo, una antena pre-fractal basada en el triángulo de Sierpinski parte de un triángulo equilátero inicial (iniciador) de lado L_0 y altura $h_0 = \sqrt{3}L_0/2$, que se comporta como un monopolo o parche triangular convencional en su modo fundamental, tal como se representa en la Fig. 3 [4,5]. La primera iteración se obtiene al dividir el triángulo inicial en cuatro subtriángulos equiláteros congruentes y eliminar el triángulo central; las iteraciones sucesivas repiten este procedimiento sobre cada uno de los subtriángulos restantes, generando una jerarquía de huecos y brazos conductores de diferentes longitudes efectivas [4,5,9,10]. En la práctica, las antenas empleadas en aplicaciones médicas son pre-fractales de orden finito n, de modo que la estructura conserva una longitud y un área totales compatibles con las restricciones geométricas del dispositivo [3-7].

Para un monopolo triangular de Sierpinski alimentado en la base, la auto-semejanza implica que, además del modo fundamental asociado a la altura h_0 (frecuencia f_0), aparecen resonancias adicionales ligadas a subtriángulos de altura $h_0/2$,

$h_0/4$, etc., presentes en cada iteración, como se esquematiza en la Fig. 1 [4,5,9,10]. De manera aproximada, la relación entre la altura efectiva h_{eff} de cada rama dominante y su frecuencia de resonancia f sigue la dependencia inversa típica de antenas tipo monopolo o parche,

$$f \approx \frac{c}{4h_{\text{eff}}\sqrt{\varepsilon_{\text{eff}}}}, \tag{8}$$

donde c es la velocidad de la luz en el vacío y ε_{eff} es la permitividad efectiva del medio que rodea a la *antena* (combinación del sustrato y del entorno dieléctrico, que en aplicaciones médicas incluye tejido biológico) [1,22]. En este contexto, una *rama dominante* se refiere al tramo de la geometría de la *antena* por el que circula la mayor parte de la corriente en un modo resonante dado, de modo que su longitud efectiva controla, de manera aproximada, la posición de la correspondiente frecuencia de resonancia. Así, los subtriángulos más pequeños generan resonancias en múltiplos superiores de f_0, mientras que las ramas de mayor longitud producen resonancias cercanas o ligeramente desplazadas respecto a f_0 [4,5,9,10]. En consecuencia, al aumentar el orden de iteración n se enriquece el espectro de caminos de corriente y se obtienen respuestas multibanda o de banda ancha sin necesidad de incrementar la altura total de la antena, lo que resulta especialmente útil en diseños compactos para aplicaciones biomédicas [3-7].

En los estudios numéricos y experimentales analizados, los parámetros de desempeño de las antenas -como la respuesta en frecuencia, la ganancia, la eficiencia de radiación y el coeficiente de reflexión S_{11}- se obtienen mediante simulaciones de onda completa y, cuando es posible, se validan con prototipos físicos [3-7,9,10]. En el contexto biomédico se hace especial énfasis en el uso de fantomas tisulares y modelos estratificados para evaluar el acoplamiento de impedancias, las distribuciones de campo en el interior del tejido y las restricciones de la tasa de absorción específica (SAR) [2,21,23-29].

Además de su descripción geométrica, las antenas pre-fractales deben caracterizarse en términos de parámetros convencionales de antena, como impedancia de entrada, coeficiente de reflexión, ancho de banda, diagrama de radiación y ganancia [1,22]. Una métrica simple pero útil es el coeficiente de reflexión Γ, que relaciona la impedancia de entrada de la antena Z_{in} con la impedancia característica de la línea de alimentación Z_0 mediante

$$\Gamma = \frac{Z_{\text{in}} - Z_0}{Z_{\text{in}} + Z_0}, \tag{9}$$

tal como se discute en los textos estándar de teoría de antenas y líneas de transmisión [1,22]. A partir de Γ se obtienen la razón de ondas estacionarias de voltaje (VSWR) y el ancho de banda operacional, que definen el intervalo de frecuencias en el cual la antena transfiere potencia de manera eficiente al espacio libre [1]. Por otra parte, parámetros como la ganancia y la eficiencia de radiación cuantifican qué tan eficazmente la antena fractal convierte la potencia de entrada en radiación en una dirección dada, lo cual es crítico en aplicaciones médicas donde deben satisfacerse simultáneamente el presupuesto de enlace y las restricciones de seguridad (por ejemplo, límites de SAR) [2,22,25]. Por tanto, una caracterización electromagnética adecuada de las antenas pre-fractales proporciona la base para comparar diferentes diseños, optimizar su geometría y asegurar que la miniaturización o la operación multibanda no comprometan el desempeño en las bandas de interés diagnóstico o terapéutico [1,22].

Con esta metodología, el presente trabajo integra una revisión crítica de la literatura, el marco geométrico basado en la dimensión fractal y las formulaciones electromagnéticas clásicas, con el fin de ofrecer una visión unificada del papel de las antenas pre-fractales en aplicaciones relacionadas con la salud.

3. Estado del arte

El uso de la geometría fractal en medicina se remonta al trabajo pionero de West, quien introdujo el concepto de *fisiología fractal* para describir la organización jerárquica y autosemejante de diversos sistemas biológicos, desde las redes vasculares hasta las estructuras pulmonares [18]. En este enfoque, la dimensión fractal se interpreta como un descriptor cuantitativo de la complejidad de los procesos fisiológicos y morfológicos, lo que abrió la puerta a modelos más realistas de transporte, intercambio de masa y dinámica de fluidos en el organismo. En paralelo, se desarrollaron y aplicaron técnicas de análisis fractal y multifractal a imágenes biomédicas, demostrando su utilidad para caracterizar patrones patológicos, por ejemplo en la clasificación de enfermedad ósea metastásica y en la detección y diagnóstico de lesiones mamarias [16,17].

En el ámbito de los dispositivos, la idea de explotar patrones fractales o pre-fractales se ha extendido a la electrónica flexible y a los sistemas portátiles de monitorización de la salud. El trabajo de Rogers y colaboradores sobre materiales y mecánica para electrónica estirable mostró cómo el uso de trazas serpentinas y diseños que se aproximan a estructuras fractales permite fabricar circuitos y sensores que se adaptan mecánicamente a la piel o a superficies deformables, manteniendo la integridad eléctrica bajo deformación [23]. Posteriormente, Fan *et al.* profundizaron en conceptos de diseño fractal para electrónica flexible, destacando que estas geometrías minimizan la formación de lazos cerrados y el acoplamiento indeseado con campos de radiofrecuencia, lo cual es particularmente ventajoso en entornos de imagen por resonancia magnética [24]. Estos enfoques han impulsado el desarrollo de sensores portátiles y plataformas tipo "tatuaje electrónico" capaces de medir parámetros fisiológicos de manera continua y mínimamente invasiva, con potencial de



FIGURE 5. Configuraciones representativas de electrónica flexible y trazas de tipo fractal empleadas en sensores portátiles y plataformas para monitorización de la salud [21,23,24].

integración en redes de telemedicina y sistemas de monitorización remota [21,23,24].

De forma más específica en oncología, la geometría fractal y sus derivados han resultado relevantes tanto en la etapa diagnóstica como en el diseño de antenas para detección. Kaur y Kaur diseñaron una antena fractal alimentada por CPW para detección no invasiva de cáncer de piel, aprovechando la capacidad de estas estructuras para rellenar espacio y operar en regímenes de banda ancha [27].

En este tipo de dispositivos, la física subyacente de la detección depende tanto de las propiedades dieléctricas del tejido como, en técnicas de resonancia magnética, de la respuesta de los núcleos bajo excitación por RF. En microondas, la presencia de una lesión modifica la permitividad relativa ε_r y la conductividad σ del tejido, lo que altera la impedancia vista por la antena y, por tanto, el coeficiente de reflexión S_{11} y la potencia reflejada en determinadas bandas de frecuencia [27,28,31,32]. Al barrer la frecuencia y registrar los cambios en S_{11} o en la señal dispersada, se obtiene un contraste electromagnético que puede correlacionarse con la presencia de lesiones. Esta interacción campo–tejido tiene también implicaciones de seguridad relevantes: la energía de RF depositada en el tejido se cuantifica mediante la tasa de absorción específica (SAR, en W/kg), y concentraciones locales elevadas pueden provocar incrementos de temperatura y quemaduras por radiofrecuencia, por lo que los diseños de antenas destinados a operar en contacto o en proximidad con el cuerpo deben respetar los límites de SAR establecidos en las normas de seguridad y evaluarse mediante modelos y fantomas apropiados [2,25,26,33].

Para detección de cáncer de mama, Lala *et al.* utilizaron una antena miniaturizada en la banda ISM de 5.72-5.82 GHz, basada en la técnica DGS, mostrando que estructuras compactas cuidadosamente adaptadas al tejido mamario pueden proporcionar un contraste significativo entre tejido sano y tumoral [28]. En este caso, la antena se coloca en contacto o en proximidad a *fantomas* mamarios que emulan las propiedades dieléctricas de los distintos tejidos, y se analizan la distribución del campo electromagnético y la tasa de absorción específica (SAR) en el volumen del fantoma. Más recientemente, Marzouk *et al.* desarrollaron una antena fractal compacta de ultra-ancho de banda que, además de aplicaciones en WiMAX y WLAN, fue evaluada como herramienta para la detección de tumores mamarios mediante fantomas mamarios; el contraste en campo y en potencia absorbida entre regiones sanas y simuladas como tumorales se emplea como métrica para valorar la capacidad de detección [29]. En configuraciones tomográficas, arreglos de antenas compactas alrededor del fantoma permiten reconstruir mapas espaciales de propiedades dieléctricas que pueden correlacionarse con la presencia de lesiones.

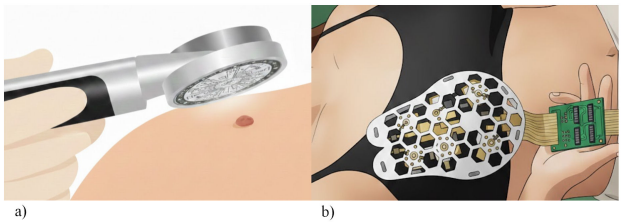


FIGURE 6. Ejemplos de antenas compactas empleadas en la literatura para la detección de a) cáncer de piel y b) cáncer de mama mediante técnicas de microondas [27-29].

En imagen por resonancia magnética, la física subyacente es cualitativamente distinta a la detección por microondas: la respuesta de los núcleos ante un pulso de RF depende no solo de la frecuencia de Larmor del núcleo (por ejemplo, ^{1}H, ^{23}Na) sino también del microentorno en que se encuentran. Para núcleos de hidrógeno (^{1}H), los tiempos de relajación T_1 y T_2 difieren significativamente entre materia gris, materia blanca y tejido tumoral, generando el contraste intrínseco de las imágenes de RM [2,25]. Esta variación refleja diferencias en el contenido de agua, la organización celular y la densidad de membranas lipídicas en cada tipo de tejido. En este contexto, la geometría fractal ha mostrado ventajas específicas en el diseño de bobinas: Nowikow *et al.* analizaron bobinas de radiofrecuencia con geometría de copo de nieve de Koch para RM de sodio, demostrando que estas estructuras pueden reducir la inductancia mutua entre elementos en fase y mejorar la uniformidad de campo y la eficiencia [25]. Este tipo de bobina resulta particularmente atractivo para estudios multinucleares, donde las restricciones de espacio y la necesidad de minimizar artefactos son críticas [2,25,26], y donde el diseño debe optimizarse además en términos de homogeneidad del campo B_1 y relación señal-ruido para distinguir tejidos con propiedades de relajación próximas [2,25,26]. Por otro lado, Sabban presentó una familia de sensores y antenas portátiles *metafractales* para aplicaciones médicas, comunicaciones 5G e IoT, en los que las geometrías fractales se combinan con metamateriales para optimizar la ganancia, el ancho de banda y la eficiencia, manteniendo diseños compactos y ligeros [21].

La Tabla I resume algunas de las contribuciones más representativas sobre el uso de geometrías fractales y pre-frac-

TABLE I. Resumen de trabajos representativos que emplean geometrías fractales o pre-fractales en aplicaciones médicas.

Referencia	Geometría/tipo	Banda o frecuencia	Aplicación principal	Característica clave
West (1990) [18]	Modelos fisiológicos fractales	–	Fisiología fractal, sistemas biológicos complejos	Introduce el marco de fisiología fractal para describir redes y procesos en el organismo.
Klein *et al.* (2013) [20]	Análisis fractal de contornos celulares	–	Fenotipado de células tumorales pancreáticas	Uso de la dimensión fractal para distinguir líneas celulares tumorales con alta precisión.
Rogers *et al.* (2010) [23]	Trazas flexibles tipo fractal	RF baja-media	Electrónica flexible y sensores sobre piel	Diseños deformables que mantienen continuidad eléctrica y compatibilidad mecánica.
Fan *et al.* (2014) [24]	Conceptos fractales para electrónica estirable	RF / RMN	Electrónica flexible, compatibilidad con RMN	Geometrías fractales que minimizan lazos cerrados y el acoplamiento RF en entornos de imagen.
Nowikow *et al.* (2021) [25]	Bobina de RF tipo copo de nieve de Koch	RMN de sodio	Imagen por resonancia magnética de sodio	Bobinas fractales con menor inductancia mutua y mejor desempeño en estudios multinucleares.
Kaur & Kaur (2021) [27]	Antena fractal alimentada por CPW	Microondas	Detección temprana de cáncer de piel	Antena compacta y de banda ancha para diagnóstico no invasivo.
Lala *et al.* (2023) [28]	Antena miniaturizada con DGS	5.72-5.82 GHz (ISM)	Detección de cáncer de mama	Antena miniaturizada optimizada para contraste entre tejido sano y tumoral.
Marzouk *et al.* (2023) [29]	Antena fractal UWB compacta	2.8-9.37 GHz	Comunicaciones y detección de tumores	Antena UWB compacta evaluada con fantomas mamarios para imagen.
Sabban (2024) [21]	Antenas y sensores metafractales	Varias bandas (5G, IoT)	Dispositivos portátiles médicos, 5G, IoT	Combinación de geometría fractal y metamateriales para alta eficiencia y ganancia en dispositivos portátiles.

tales en aplicaciones médicas recientes, destacando la diversidad de configuraciones, bandas de operación y objetivos clínicos.

En conjunto, estos trabajos revelan una tendencia clara hacia el uso de estructuras pre-fractales y metafractales en el diseño de antenas y bobinas para diagnóstico, monitorización y comunicación en entornos médicos, aprovechando su capacidad de miniaturización, operación multibanda y adaptabilidad a configuraciones biológicas complejas [21,23-25,27-29]. Este cuerpo de evidencia proporciona el contexto necesario para analizar, en las siguientes secciones, las ventajas y limitaciones de las antenas pre-fractales en aplicaciones específicas como la detección de cáncer, la telemetría implantable y la imagen por resonancia magnética multinuclear.

4. Discusión: ventajas y limitaciones de las antenas pre-fractales en medicina

Los trabajos revisados muestran que las antenas con geometrías fractales y pre-fractales ofrecen un conjunto claro de ventajas frente a diseños convencionales, especialmente en contextos donde el espacio disponible es limitado y se requiere operación en múltiples bandas de frecuencia [3-10,27-29]. La auto-semejanza de patrones como los de Sierpinski o Koch permite incrementar de manera efectiva la longitud eléctrica de la antena sin un aumento proporcional de sus dimensiones físicas, lo que se traduce en una mayor miniaturización para una frecuencia de operación dada [3-10]. Asimismo, la coexistencia de distintas escalas geométricas dentro de una misma estructura favorece la aparición de múltiples

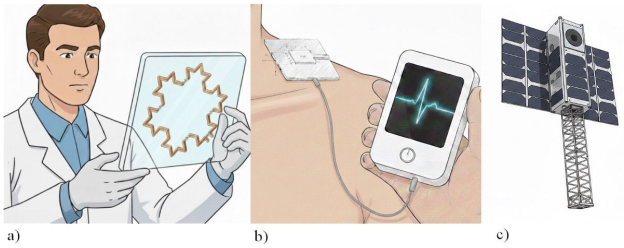


FIGURE 7. Esquema de a) bobina de RF con geometría de copo de nieve de Koch para RMN de sodio, b) antenas metafractales portátiles orientadas a aplicaciones médicas y c) IoT [21,25].

frecuencias de resonancia, de modo que una sola antena puede cubrir operación multibanda o de banda ancha, como se ha demostrado en aplicaciones de comunicaciones y en configuraciones evaluadas para el diagnóstico de cáncer de piel y de mama mediante microondas [27-29].

En el contexto de dispositivos implantables y portátiles, estas propiedades resultan particularmente atractivas. Por un lado, la miniaturización facilita la integración de antenas en volúmenes muy restringidos, como cápsulas ingeribles o implantes subcutáneos, donde la reducción del tamaño de la antena es un requisito crítico [2,21,23-26,28,29]. Por otro lado, las capacidades multibanda y de banda ancha permiten que un solo elemento pueda cubrir funciones de comunicación, sensado y, en algunos casos, imagen, reduciendo la necesidad de emplear múltiples antenas o transductores [21,25,27-29]. Adicionalmente, en diseños flexibles y portátiles, las geometrías fractales proporcionan caminos de corriente que se adaptan mejor a la deformación mecánica sin pérdida de continuidad eléctrica, característica que se ha aprovechado en plataformas tipo "tatuaje electrónicoz en sensores textiles integrados [21,23,24]. En bobinas para imagen por resonancia magnética, configuraciones fractales como el copo de nieve de Koch ayudan además a reducir la inductancia mutua y a mejorar la uniformidad del campo B_1 en estudios multinucleares [25].

No obstante, la adopción de antenas pre-fractales en aplicaciones médicas también presenta limitaciones y retos importantes. Desde el punto de vista electromagnético, la presencia de tejido biológico con alta permitividad y conductividad introduce desintonización, pérdidas adicionales y cambios en la distribución de campo que pueden degradar la eficiencia y la ganancia efectiva de la antena, especialmente en configuraciones implantables o en contacto cercano con el cuerpo [2,21,23-29]. Esto hace necesario llevar a cabo procesos de optimización específicos para el entorno de operación, que incluyen el uso de *fantomas* realistas y simulaciones de onda completa que consideren la dispersión dieléctrica del tejido. Del mismo modo, la evaluación de la tasa de absorción específica (SAR) se convierte en un aspecto central, ya que la concentración de campo en regiones de alta densidad de corriente puede incrementar localmente la deposición de potencia en el tejido [25,26,28,29].

Desde una perspectiva tecnológica, la fabricación de geometrías pre-fractales de alto orden plantea desafíos relacionados con la resolución de los procesos de manufactura y las tolerancias de los materiales empleados. A escalas micrométricas, pequeñas desviaciones en las dimensiones pueden provocar desplazamientos apreciables en las frecuencias de resonancia y variaciones en el acoplamiento entre elementos, lo que exige procesos de fabricación precisos y reproducibles [3-7,9,10]. Además, en dispositivos implantables o en contacto directo con el cuerpo, deben considerarse cuestiones como la biocompatibilidad de sustratos y conductores, la estabilidad a largo plazo en entornos biológicos y la necesidad de encapsulados que protejan tanto a la antena como al tejido circundante [2,21,23-26,28. En electrónica flexible, la fatiga mecánica debida a ciclos repetidos de flexión o estiramiento añade requisitos adicionales sobre la robustez mecánica de las trazas fractales y de las interfaces entre capas [21,23,24].

Finalmente, desde la perspectiva de diseño de sistema, el uso de antenas pre-fractales en medicina requiere un equilibrio cuidadoso entre los beneficios de la miniaturización y la operación multibanda, y la complejidad del modelado y la integración. Aunque las geometrías fractales ofrecen un espacio de diseño amplio, su comportamiento electromagnético puede ser menos intuitivo que el de antenas convencionales, lo que demanda estrategias de optimización asistidas por simulación y una validación experimental cuidadosa [3-10,21,25,27-29]. En este sentido, la evidencia disponible sugiere que las antenas pre-fractales son especialmente prometedoras en escenarios donde el compromiso entre tamaño, número de bandas y adaptabilidad mecánica es crítico -como en sensores portátiles, telemetría implantable e imagen por resonancia magnética multinuclear-, pero su adopción generalizada en entornos clínicos aún depende de avances en materiales, técnicas de fabricación y protocolos de validación adaptados a cada aplicación específica.

5. Conclusiones

Las antenas pre-fractales, basadas en geometrías autosemejantes de tipo Sierpinski y Koch, representan una alternativa robusta para el diseño de dispositivos de radiofrecuencia en el ámbito médico, ya que combinan de forma natural la miniaturización, la operación multibanda y la capacidad de controlar los diagramas de radiación. Las propiedades de auto-semejanza y relleno de espacio características de estas estructuras permiten obtener longitudes eléctricas efectivas mayores sin incrementar de manera significativa el tamaño físico, lo cual resulta particularmente útil en escenarios donde el volumen disponible es limitado, como implantes, sensores portátiles y bobinas para imagen por resonancia magnética.

Este trabajo integra tres niveles complementarios que permiten una visión unificada del tema. En primer lugar, el uso de la dimensión fractal como herramienta para describir y analizar estructuras biológicas complejas, desde redes vasculares y árboles bronquiales hasta contornos celulares tumorales, reforzando el uso de la dimensión fractal como criterio de análisis de la morfología tisular con aplicaciones diagnósticas concretas. En segundo lugar, los fundamentos electro-

magnéticos de la radiación y el acoplamiento campo–tejido en antenas pre-fractales, donde las leyes de Ampère-Maxwell y de Faraday, junto con la condición de medio macroscópicamente neutro, proporcionan el marco formal para relacionar la geometría de la antena con su respuesta en frecuencia y su diagrama de radiación. En tercer lugar, las aplicaciones recientes que emplean geometrías pre-fractales y metafractales en detección temprana de cáncer de piel y de mama, sensores portátiles flexibles tipo "tatuaje electrónico" y bobinas para imagen por resonancia magnética multinuclear, donde las ventajas de tamaño, comportamiento multibanda y adaptabilidad mecánica han sido demostradas experimentalmente.

No obstante, la implementación práctica de antenas pre-fractales en entornos clínicos reales sigue enfrentando desafíos importantes. La presencia de tejido biológico con alta permitividad y conductividad introduce desintonización, pérdidas adicionales y modificaciones en la distribución de campo que pueden degradar la eficiencia y la ganancia efectiva. A esto se suman los requisitos estrictos en la evaluación de SAR y biocompatibilidad, y las exigencias de precisión en la fabricación cuando se trabaja a escalas micrométricas. Además, el comportamiento electromagnético de las geometrías pre-fractales puede resultar menos intuitivo que el de las antenas convencionales, lo cual obliga a apoyarse en herramientas avanzadas de simulación y en protocolos detallados de validación experimental.

De cara al futuro, las líneas de investigación más prometedoras incluyen la integración de antenas pre-fractales con materiales flexibles y biocompatibles, la combinación con conceptos de metamateriales para mejorar aún más la eficiencia y la ganancia, y el desarrollo de diseños adaptados a aplicaciones de imagen por resonancia magnética multinuclear y sistemas de telemetría implantable de largo plazo. La consolidación de estos avances, junto con protocolos de evaluación estandarizados en fantomas y estudios preclínicos, será clave para que las antenas pre-fractales evolucionen de demostraciones de laboratorio a soluciones robustas y de uso rutinario en la práctica clínica.

Agradecimientos

Los autores agradecen sinceramente el apoyo financiero proporcionado por el Consejo Nacional de Humanidades, Ciencias y Tecnologías (CONAHCYT), México, a través de una beca doctoral.

Financiamiento

Este trabajo fue apoyado por el Consejo Nacional de Humanidades, Ciencias y Tecnologías (CONAHCYT), México, mediante una beca doctoral.

Conflicto de intereses

Los autores declaran que no tienen conflictos de intereses relacionados con el contenido de este artículo.

1. C. A. Balanis, Antenna Theory: Analysis and Design, 2nd ed. (John Wiley and Sons, New York, 1997).

2. J. Mispelter, M. Lupu, and A. Briguet, NMR Probeheads for Biophysical and Biomedical Applications (Imperial College Press, London, 2015), https://doi.org/10.1142/p438

3. T. A. Elwi, A. I. Imran, and Y. Al-Naiemy, A miniaturized lotus shaped microstrip antenna loaded with EBG structures for high gain bandwidth product applications, *Progress In Electromagnetics Research C* **60** (2015) 157, https://doi.org/10.2528/PIERref5101804

4. S. A. Hamzah *et al*., Size Reduction and Multiband Characteristic Using Koch Fractal Dipole, In 2006 International RF and Microwave Conference (IEEE, Putrajaya, Malaysia, 2006) pp. 140-142, https://doi.org/10.1109/RFM.2006.331055

5. N. N. Kumar *et al*., Compact modified Sierpinski fractal monopole antenna for multiband wireless applications, In IEEE Conference Publications (2014) pp. 1264-1266, https://doi.org/10.1109/ICCSP.2014.6950054.

6. A. K. Panda, M. K. Panda, and S. S. Patra, A compact multiband gasket enable rectangular fractal antenna, In International Conference on Computational Intelligence and Communication Systems (IEEE, Gwalior, India, 2011) pp. 11-14, https://doi.org/10.1109/CICN.2011.3.

7. N. Cohen, Tuning Fractal Antennas and Fractal Resonators, U.S. Patent 6,104,349 (2000).

8. N. Cohen, Fractal Antenna Applications in Wireless Telecommunications, In Professional Program Proceedings: Electronic Industries Forum of New England (IEEE, 1997) pp. 43-49, https://doi.org/10.1109/EIF.1997.605374.

9. C. A. Figueroa-Torres *et al*., A novel fractal antenna based on the Sierpinski structure for super wide-band applications, *Microwave and Optical Technology Letters* **59** (2017) 1148, https://doi.org/10.1002/mop.30489

10. A. Sundaram, M. Maddela, and R. Ramadoss, Koch-fractal folded-slot antenna characteristics, *IEEE Antennas and Wireless Propagation Letters* **6** (2007) 219, https://doi.org/10.1109/LAWP.2007.895293

11. M. R. Jena, Mishra *et al.*, Fractal Geometry and Its Application to Antenna Designs, *International Journal of Engineering and Advanced Technology* **9** (2019) 109119, https://doi.org/10.35940/ijeat.A9793.109119

12. B. B. Mandelbrot, The Fractal Geometry of Nature, vol. **1** (W. H. Freeman, New York, 1982).

13. B. Mandelbrot, Los objetos fractales: Forma, azar y dimensión (Tusquets Editores, Barcelona, 1993).

14. J. Harte, The Fractalist: Memoir of a Scientific Maverick, *American Journal of Physics* **81** (2013) 477, https://doi.org/10.1119/1.4795315

15. K. Falconer, Fractal Geometry: Mathematical Foundations and Applications (John Wiley and Sons, Chichester, 2003), https://doi.org/10.1002/0470013850.

16. J. Vasiljevic *et al*., Application of multifractal analysis on microscopic images in the classification of metastatic bone disease, *Biomedical Microdevices* **14** (2012) 541, https://doi.org/10.1007/s10544-012-9631-1

17. S. M. Beheshti *et al*., An efficient fractal method for detection and diagnosis of breast masses in mammograms, *Journal of Digital Imaging* **27** (2014) 661, https://doi.org/10.1007/s10278-013-9654-z

18. B. J. West, Fractal Physiology and Chaos in Medicine (World Scientific, Singapore, 1990), https://doi.org/10.1142/1025.

19. J. D. Jackson, Classical Electrodynamics, 3rd ed. (Wiley, New York, 1998).

20. K. Klein *et al*., Marker-free phenotyping of tumor cells by fractal analysis of reflection interference contrast microscopy images, *Nano Letters* **13** (2013) 5474, https://doi.org/10.1021/nl4030402

21. A. Sabban, Novel Meta-Fractal Wearable Sensors and Antennas for Medical, Communication, 5G, and IoT Applications, *Fractal and Fractional* **8** (2024) 100, https://doi.org/10.3390/fractalfract8020100

22. A. Cardama *et al*., Antenas, 2nd ed. (Edicions UPC, Barcelona, 2002).

23. J. A. Rogers *et al*., Materials and Mechanics for Stretchable Electronics, *Science* **327** (2010) 1603, https://doi.org/10.1126/science.1182383

24. J. Fan *et al*., Fractal design concepts for stretchable electronics, *Nature Communications* **5** (2014) 3266, 1 https://doi.org/10.1038/ncomms4266

25. C. E. Nowikow, P. Polak, et al., Network and Field Analysis of Koch Snowflake Fractal Geometry Radiofrequency Coils for Sodium MRI, *Frontiers in Physics* **9** (2021), https://doi.org/10.3389/fphy.2021.697104

26. J. C. Weinreb, et al., Use of Intravenous Gadolinium-based Contrast Media in Patients with Kidney Disease: Consensus Statements from the American College of Radiology and the National Kidney Foundation, *Radiology* **298** (2021) 28, https://doi.org/10.1148/radiol.2020202903

27. K. Kaur and A. Kaur, Fractal geometry based CPW fed antenna for early stage skin cancer detection, In 2021 IEEE Indian Conference on Antennas and Propagation (InCAP) (IEEE, 2021) pp. 517-520, https://doi.org/10.1109/InCAP52216.2021.9726481.

28. A. E. V. D. B. O. K. Lala and F. M. Mbango, A Miniaturized Antenna for Breast Cancer Detection at the 5.72-5.82 GHz ISM Band Based on the DGS Technique, *Progress In Electromagnetics Research B* **98** (2023) 87, https://doi.org/10.2528/PIERB23011004

29. M. Marzouk *et al*., Ultra-wideband compact fractal antenna for WiMAX, WLAN, C and X band applications, *Sensors* **23** (2023) 4254, https://doi.org/10.3390/s23094254

30. L. González Zamora and S. S. Hidalgo-Tobón, Antenas fractales y su aplicación en la medicina, In Congreso Nacional de Tecnología Aplicada a Ciencias de la Salud (CONTACS), vol. **5**, (Puebla, México, 2023) pp. 14-22, https://doi.org/10.10.1063/5.0308613.

31. C. Gabriel, S. Gabriel, and E. Corthout, The dielectric properties of biological tissues: I. Literature survey, *Physics in Medicine and Biology* **41** (1996) 2231, https://doi.org/10.1088/0031-9155/41/11/001

32. S. Gabriel, R.W. Lau, and C. Gabriel, The dielectric properties of biological tissues: II. Measurements in the frequency range 10 Hz to 20 GHz, *Physics in Medicine and Biology* **41** (1996) 2251, https://doi.org/10.1088/0031-9155/41/11/002

33. C. Baker *et al*., Systematic review of MRI safety literature in relation to radiofrequency thermal injury prevention, *Journal of Medical Radiation Sciences* **71** (2024) 445, https://doi.org/10.1002/jmrs.800

Wavelength-dependent optical bleaching in Al_2O_3:C nanoDot optically stimulated luminescence dosimeters

Isabel Morales-Peña and Miguel Ángel Camacho-López

Laboratorio de Fotomedicina, Biofotónica y Espectroscopia Láser de Pulsos Ultracortos, Facultad de Medicina, Universidad Autónoma del Estado de México (UAEMex), Toluca, Mexico.

Olivia Amanda García-Garduño

Laboratorio de Física Médica, Instituto Nacional de Neurología y Neurocirugía, Mexico City, Mexico.

Rosalia Contreras-Bulnes

Facultad de Odontología, Universidad Autónoma del Estado de México (UAEMex), Toluca, Mexico.

Received 7 April 2026; accepted 12 June 2026

The reusability of Al_2O_3:C-based optically stimulated luminescence dosimeters (OSLDs) relies on efficient removal of the stored signal through optical irradiation. Wavelength-dependent optical bleaching was evaluated in nanoDot^{TM} dosimeters using 3 W LED matrices centered at 463 and 516 nm, with irradiances of 587.7 and 457.7 mW·cm^{-2}, respectively. Dosimeters irradiated with 6 MV photons were subjected to successive 5-min bleaching cycles with intermediate microStar readouts. The 463 nm system produced faster signal reduction and higher bleaching efficiency than the 516 nm system. A residual component persisted after prolonged irradiation, indicating incomplete depletion of optically accessible trapping states under the evaluated conditions. These results support wavelength selection as a key parameter for optimizing nanoDot reuse protocols.

Keywords: Optically stimulated luminescence dosimeters; optical bleaching; wavelength dependence; Al_2O_3:C; residual signal; clinical dosimetry.

DOI: https://doi.org/10.31349/RevMexFis.72.061102

1. Introduction

Optically stimulated luminescence (OSL) is a widely used technique in ionizing radiation dosimetry due to its high sensitivity, stability, and capability for repeated, non-destructive readout [1]. In particular, Al_2O_3:C-based dosimeters, such as nanoDot^{TM} devices, have demonstrated robust performance in clinical applications owing to their wide dynamic range and reproducibility [2].

At the microscopic level, OSL behavior in Al_2O_3:C is associated with crystal defects induced by carbon doping, which introduce energy levels within the bandgap. Among these defects, F and F^+ centers—related to oxygen vacancies acting as electron traps—as well as recombination centers responsible for luminescent emission, play a key role [3]. Upon irradiation with ionizing radiation, charge carriers are promoted to the conduction band and subsequently trapped in metastable states. Optical stimulation releases these electrons, producing a luminescent signal proportional to the absorbed dose [4].

The removal of the stored signal, known as bleaching, is essential for OSLD reuse. However, its efficiency is strongly influenced by the energy distribution of traps in the material. In Al_2O_3:C, both shallow traps—efficiently emptied by optical irradiation—and deep traps—limiting complete signal removal—coexist [5].

The probability of optical release of trapped electrons depends on the photon energy, introducing a direct wavelength dependence in the bleaching process. Shorter wavelengths (higher photon energy) generally enhance photoionization rates, increasing bleaching efficiency, whereas longer wavelengths are less effective in depopulating certain trap populations [6].

Additionally, phototransfer phenomena have been reported, in which electrons trapped in deep levels are promoted to optically active traps, contributing to residual signal even after prolonged optical irradiation [7]. This behavior imposes limitations on bleaching efficiency and measurement reproducibility.

From a kinetic standpoint, the reduction of the OSL signal during optical irradiation can be approximated by effective exponential models, which allow characterization of trap depopulation dynamics through time constants and related parameters such as the process half-life [8]. These parameters provide useful metrics for comparing bleaching efficiency under different experimental conditions.

In this context, the present study aims to evaluate the bleaching efficiency of Al_2O_3:C nanoDot^{TM} dosimeters under optical irradiation at 463 nm and 516 nm. The analysis is based on normalized signal evolution, monoexponential fitting of decay curves, and determination of characteristic parameters such as half-life and residual signal, in order to establish a quantitative comparison between both irradiation systems. The primary objective of this work is to provide a quantitative assessment of monochromatic LED-based optical bleaching systems and their applicability to

nanoDot^{TM} reuse protocols under controlled experimental conditions, rather than to identify the fundamental trapping mechanisms responsible for the observed luminescence behavior.

Theoretical framework

The characterization of the optical bleaching process in optically stimulated luminescence dosimeters requires a quantitative description of signal decay under optical irradiation. From an experimental perspective, the primary objective is to compare the rate and efficiency of signal removal through measurable parameters, rather than relying solely on qualitative descriptions of signal reduction. In this context, the analysis of normalized decay curves and their fitting using exponential functions constitutes a widely adopted approach for describing the effective dynamics of electron trap depopulation [4, 8].

When the signal decay is governed by an effective population of traps, the behavior can be approximated by a monoexponential model:

$$I(t) = I_b + A\exp(-t/\tau),$$

where $I(t)$ is the measured signal after a cumulative optical irradiation time t, I_b corresponds to the baseline signal of the system, A represents the removable signal amplitude, and τ is the characteristic time constant of the process. This formulation allows bleaching to be described as an effective decay process without explicitly accounting for the individual contributions of each trap population present in the material [4, 9].

From this expression, the half-life of the process is defined as:

$$t_{1/2} = \tau \ln 2,$$

The half-life provides a direct parameter for comparison between different experimental conditions, as it represents the time required for the signal to decrease to half of its initial value. In OSL dosimetry studies, this parameter is commonly used as a practical metric to evaluate bleaching rate and compare different optical stimulation systems [8].

Since the initial OSL signal depends on the absorbed dose, normalization is required to compare results across different conditions. The ratio $I(t)/I_0$, where I_0 is the initial signal prior to bleaching, allows analysis of the remaining signal fraction independently of absolute signal magnitude. This approach is consistent with methodologies reported in the literature for analyzing decay processes in OSL dosimetry [1,5].

However, when the residual signal approaches values close to the detection limit, the contribution of the system baseline becomes significant. For this reason, the ratio $I(t)/I_b$, where I_b represents the experimentally determined background signal, provides a useful metric to evaluate the degree of approach to the baseline state of the dosimeter. This relationship is particularly relevant for defining the practical limit of bleaching, as a residual signal approaching I_b indicates effective emptying of optically accessible traps [1, 2, 9].

The inclusion of the term I_b in the decay model also allows discrimination between actual signal removal and limitations imposed by the measurement system. In this sense, the baseline signal should not be interpreted solely as instrumental noise, but rather as an experimental reference defining the minimum observable signal level in the reader–dosimeter system [9].

Although the actual bleaching process may involve multiple trap populations and complex kinetics, the use of a monoexponential model is appropriate when the objective is to perform quantitative comparisons between experimental conditions. This type of approximation has been widely employed to describe effective decay processes in luminescent materials, enabling the extraction of reproducible parameters without overfitting the data [10, 11].

Under this framework, bleaching efficiency can be evaluated based on three primary parameters: the time constant τ, the half-life $t_{1/2}$, and the residual term associated with the baseline signal.

2. Materials and methods

2.1. Materials

Twenty Al_2O_3:C optically stimulated luminescence dosimeters (nanoDot^{TM}, Landauer Inc.) were used in this study. All dosimeters were selected from the same batch in order to minimize sensitivity variations. The detectors were divided into two groups of ten units, assigned to optical irradiation conditions at wavelengths of 463 nm and 516 nm.

OSL signal readout was performed using a microStar reader, which provides an integrated signal corresponding to the luminescent emission during the readout cycle.

Prior to experimental use, the dosimeters were subjected to optical irradiation cycles to reduce residual signals associated with manufacturing and storage conditions, thereby establishing reproducible initial conditions. All handling and experimental procedures were conducted in accordance with the recommendations of the AAPM TG-191 report [13].

2.2. Irradiation

Irradiations were performed using a clinical linear accelerator TrueBeam STx (Varian Medical Systems, USA) delivering a 6 MV photon beam.

Beam calibration was carried out following the TRS-398 protocol established by the International Atomic Energy Agency (IAEA), using a Farmer-type ionization chamber as the reference detector [14].

The nanoDot^{TM} dosimeters were irradiated with absorbed doses ranging from 0.25 to 5 Gy using a 6 MV photon beam generated by a Varian TrueBeam STx linear accelerator (Varian Medical Systems, USA). Irradiations were performed

in a Solid Water phantom under reference dosimetry conditions following the IAEA TRS-398 protocol. The dosimeters were positioned at a depth of 5 cm, with 5 cm of Solid Water above and 5 cm below the detectors, at a source-to-surface distance (SSD) of 100 cm and using a 10×10 cm^2 irradiation field. These conditions ensured accurate and reproducible dose delivery throughout the study.

After irradiation, the dosimeters were stored under controlled lighting conditions to prevent unintended optical exposure prior to the bleaching process.

2.3. Optical irradiation system

For the optical bleaching process, LED-based irradiation modules were developed. Each module consisted of a 5×2 matrix arrangement of high-power LEDs mounted on a 20×15 cm acrylic base.

Two independent modules were constructed with central wavelengths of 463 nm and 516 nm, corresponding to the blue and green spectral regions, respectively. The LEDs used were commercial 3 W devices connected in series.

To ensure reproducible geometry, laser-cut acrylic positioning plates were incorporated, allowing precise placement of the dosimeters during optical irradiation.

This configuration provided an approximately uniform optical irradiance over the sensitive area of the detectors. The irradiance at the dosimeter position was estimated to be 587.7 mW·cm^{-2} for the 463 nm module and 457.7 mW·cm^{-2} for the 516 nm module.

2.4. Experimental protocol for optical bleaching

The dosimeters were initially irradiated with a 6 MV photon beam at the prescribed dose levels. Following the recommendations of AAPM TG-191, all dosimeters were allowed to stabilize for 15 min after irradiation before the initial readout. This delay was kept constant throughout the study. The signal measured after this stabilization period was defined as I_0 and used as the reference value for normalization.

Subsequently, each dosimeter was subjected to optical irradiation in successive 5-minute cycles. After each irradiation interval, the dosimeters were removed from the optical irradiation system and allowed to stabilize for 15 min before readout, following the same procedure adopted for the initial measurement. The corresponding signal I(t) was then recorded for each cumulative optical irradiation time.

This optical irradiation–readout sequence (as illustrated in Fig. 1) was repeated sequentially until a total accumulated irradiation time of 60 minutes was reached, generating a discrete dataset of OSL signal as a function of time.

2.5. OSL signal definition and curve construction

Based on the described experimental protocol, the OSL signal $I(t)$ corresponds to the integrated value provided by the reader at each measurement interval, where t represents the cumulative optical irradiation time. Each data point represents the mean value obtained from ten dosimeters.

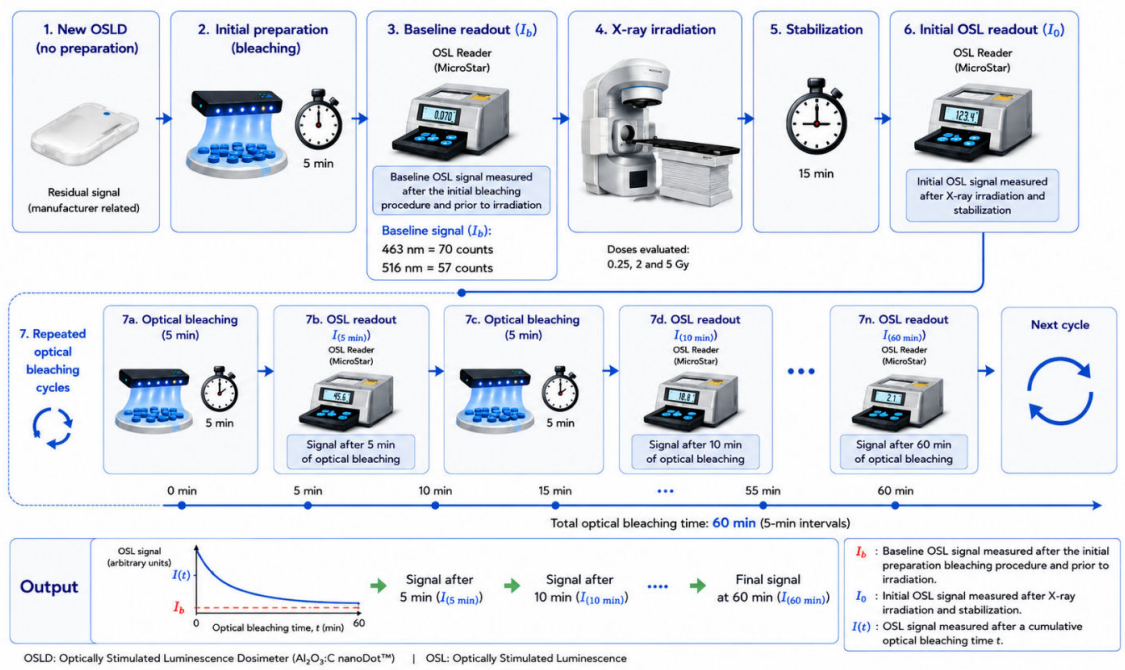


FIGURE 1. Schematic representation of the experimental protocol used for optical bleaching of Al_2O_3:C nanoDot^{TM} OSL dosimeters under 463 nm and 516 nm irradiation. I_b denotes the baseline OSL signal measured after the initial preparation bleaching procedure and prior to irradiation, I_0 denotes the initial OSL signal measured after X-ray irradiation and stabilization, and $I(t)$ represents the OSL signal measured after a cumulative optical bleaching time t.

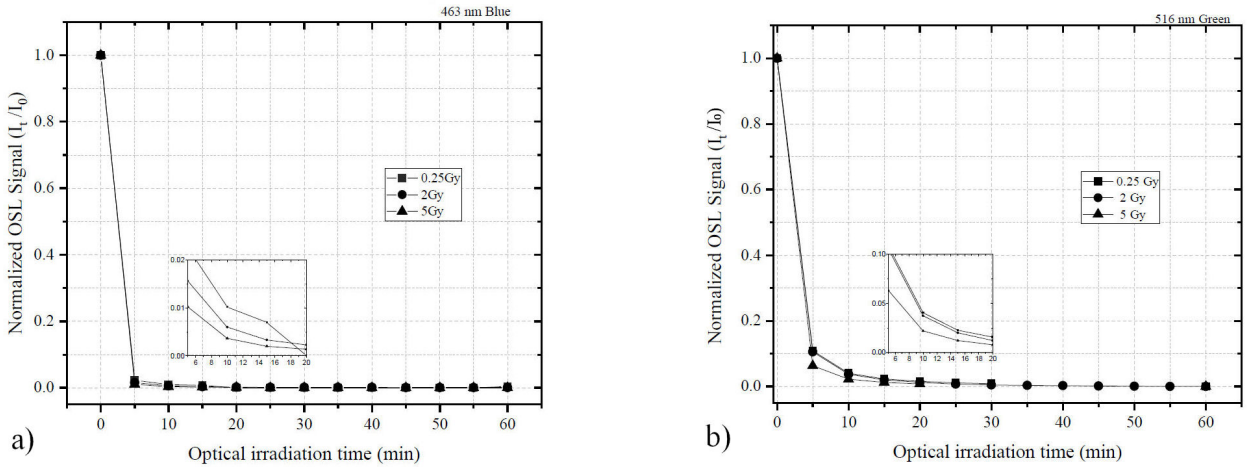


FIGURE 2. Decay of the normalized OSL signal in Al_2O_3:C nanoDot^{TM} dosimeters under optical irradiation at a) 463 nm and b) 516 nm. The curves show the evolution of the remaining signal as a function of cumulative optical irradiation time for the evaluated dose levels.

The initial signal I_0 was defined as the readout obtained immediately after irradiation with 6 MV photons and prior to optical bleaching. The background signal I_b was determined from non-irradiated dosimeters previously conditioned, establishing the baseline level of the measurement system.

To compare the evolution of the bleaching process under different experimental conditions, the ratios $I(t)/I_0$ and $I(t)/I_b$ were calculated. The former represents the fraction of remaining signal relative to the initial signal, while the latter indicates the relationship between the measured signal and the baseline level.

Bleaching efficiency was calculated as:

$$\text{Efficiency}(\,\%) = \left(1 - \frac{I(t)}{I_0}\right) \times 100.$$

These quantities were used to construct normalized decay curves and comparative tables of residual signal and bleaching efficiency as a function of time and dose.

TABLE I. Normalized residual signal and bleaching efficiency for Al_2O_3:C nanoDot^{TM} dosimeters under optical irradiation at 463 nm. Values are reported as mean ± standard deviation.

Dose (Gy)	Time (min)	$I(t)/I_0$ (mean ± SD)	Efficiency (%)
0.25	5	0,0226 ± 0,0087	97.74
	10	0,0102 ± 0,0013	98.98
	15	0,0070 ± 0,0005	99.30
2	5	0,0156 ± 0,0039	98.44
	10	0,0060 ± 0,0014	99.40
	15	0,0046 ± 0,0008	99.54
5	5	0,0102 ± 0,0015	98.98
	10	0,0036 ± 0,0005	99.64
	15	0,0020 ± 0,0002	99.80

TABLE II. Normalized residual signal and bleaching efficiency for Al_2O_3:C nanoDot^{TM} dosimeters under optical irradiation at 516 nm. Values are reported as mean ± standard deviation.

Dose (Gy)	Time (min)	$I(t)/I_0$ (mean ± SD)	Efficiency (%)
0.25	5	0,1135 ± 0,0188	88.65
	10	0,0457 ± 0,0067	95.43
	15	0,0279 ± 0,0034	97.21
2	5	0,1037 ± 0,0024	89.63
	10	0,0378 ± 0,0003	96.22
	15	0,0234 ± 0,0001	97.66
5	5	0,1212 ± 0,0224	87.88
	10	0,0447 ± 0,0026	95.53
	15	0,0276 ± 0,0033	97.24

3. Results

3.1. Bleaching efficiency

Bleaching efficiency, calculated from the ratio $I(t)/I_0$, shows a clear dependence on the optical irradiation wavelength. The corresponding results are summarized in Tables I and II.

For the 463 nm system, bleaching efficiency exceeds 98 % within the first 5 minutes of irradiation, increasing to values between 98.98 % and 99.80 % at 10–15 minutes, depending on the delivered dose. In contrast, the 516 nm system exhibits lower initial efficiencies, with values ranging from 87.88 % to 89.63 % at 5 minutes, and from 95.43 % to 97.66 % at 10–15 minutes.

These results demonstrate that optical irradiation at 463 nm enables a more efficient removal of the OSL signal compared to 516 nm across all evaluated times.

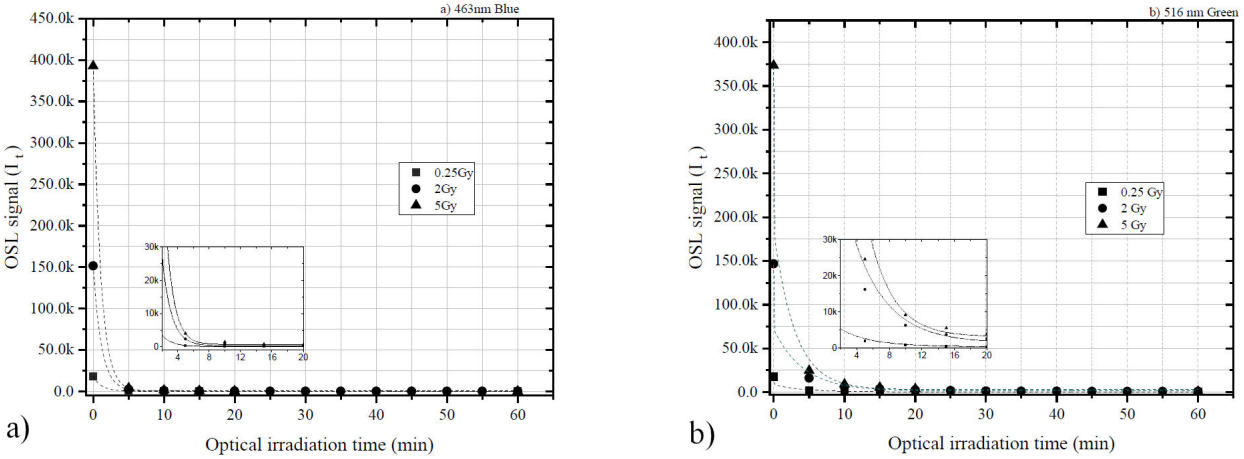


FIGURE 3. Evolution of the OSL signal, $I(t)$, as a function of cumulative optical irradiation time for Al_2O_3:C nanoDot^{TM} dosimeters under optical irradiation at a) 463 nm and b) 516 nm for absorbed doses of 0.25, 2, and 5 Gy. Dashed lines represent monoexponential fits. Insets show the 2–20 min region.

Furthermore, the variation in efficiency with dose is minimal for both wavelengths, indicating that the bleaching process remains consistent within the analyzed dose range.

3.2. Background signal and baseline level

Figure 3 presents the evolution of the OSL signal in absolute units (counts) as a function of optical irradiation time for both wavelengths. A progressive reduction of the signal is observed for all dose levels, with clear differences in decay rate between the two irradiation systems.

The relationship between the residual signal and the system baseline, expressed as $I(t)/I_b$, is summarized in Table III. For the 463 nm system, this ratio decreases rapidly with increasing irradiation time. For a dose of 0.25 Gy, the ratio decreases from 5.86 at 5 minutes to 1.80 at 15 minutes, indicating a close approach to the baseline level. Similarly, for a dose of 5 Gy, values decrease from 57.4 at 5 minutes to 11.1 at 15 minutes.

TABLE III. Residual signal relative to the baseline for Al_2O_3:C nanoDot^{TM} dosimeters. Baseline values were $I_b = 70$ counts at 463 nm and $I_b = 57$ counts at 516 nm.

λ (nm)	Dose (Gy)	Time (min)	$I(t)$ (counts, mean $\pm$ SD)	$I(t)/I_b$
463	0.25	5	410 ± 157	5.86
		10	185 ± 22	2.64
		15	126 ± 8	1.80
	2	5	2364 ± 589	33.8
		10	905 ± 203	12.9
		15	692 ± 116	9.89
	5	5	4012 ± 556	57.4
		10	1423 ± 194	20.3
		15	777 ± 69	11.1
516	0.25	5	1993 ± 330	35.0
		10	802 ± 117	14.1
		15	489 ± 59	8.59
	2	5	$16173{,}93 \pm 1597{,}43$	283.9
		10	$6241{,}60 \pm 684{,}23$	109.6
		15	$3685{,}93 \pm 417{,}09$	64.7
	5	5	24559 ± 3319	431.1
		10	9144 ± 736	160.5
		15	5501 ± 463	96.6

In contrast, the 516 nm system exhibits significantly higher residual-signal ratios throughout the entire time interval. Based on the values of the ratio $I(t)/I_b$ summarized in Table III, the ratio decreases from 35.0 at 5 minutes to 8.59 at 15 minutes for 0.25 Gy, whereas for 5 Gy the corresponding values are 431.1 and 96.6, respectively. These values indicate that, despite the progressive reduction of the OSL signal shown in Fig. 3, the residual signal remains substantially above the baseline level, particularly at higher absorbed doses.

These results indicate that, although both systems reduce the signal over time, irradiation at 463 nm enables a faster approach to the baseline level, whereas at 516 nm a considerably higher residual signal persists across the entire dose range.

This behavior suggests differences in the decay dynamics, which can be further quantified through curve fitting and the determination of characteristic parameters such as the time constant and half-life.

3.3. Monoexponential fitting and half-life

Monoexponential fitting was performed on the normalized decay curves shown in Fig. 2, yielding the parameters τ, $t_{1/2}$, and the residual term, as summarized in Tables IV and V.

For the 463 nm system, the time constant values range approximately from 1.07 to 1.30 min, corresponding to half-life values between 0.74 and 0.90 min. In contrast, for the 516 nm system, the time constants are significantly higher, ranging from 2.14 to 2.35 min, with half-life values between 1.49 and 1.63 min.

This difference indicates that the signal decay process occurs in approximately half the time under 463 nm irradiation compared to 516 nm across the entire evaluated dose range.

The coefficient of determination (R^2) exceeds 0.99 in all cases, indicating an excellent agreement between the monoexponential model and the experimental data.

These results are consistent with the higher bleaching efficiency and faster approach to the baseline level previously observed for the 463 nm irradiation.

TABLE IV. Monoexponential fitting parameters obtained from normalized decay curves under optical irradiation at 516 nm.

Dose (Gy)	τ (min)	$t_{1/2}$ (min)	Residual term	R^2
0.25	$2{,}27 \pm 0{,}12$	1.57	$0{,}0101 \pm 0{,}0039$	0.9983
0.5	$2{,}35 \pm 0{,}12$	1.63	$0{,}0088 \pm 0{,}0037$	0.9984
1	$2{,}14 \pm 0{,}08$	1.49	$0{,}0119 \pm 0{,}0024$	0.9993
2	$2{,}21 \pm 0{,}09$	1.53	$0{,}0119 \pm 0{,}0027$	0.9991
3	$2{,}15 \pm 0{,}08$	1.49	$0{,}0107 \pm 0{,}0025$	0.9993
5	$2{,}19 \pm 0{,}25$	1.52	$0{,}0092 \pm 0{,}0081$	0.9937

TABLE V. Monoexponential fitting parameters obtained from normalized decay curves under optical irradiation at 463 nm.

Dose (Gy)	τ (min)	$t_{1/2}$ (min)	Residual term	R^2
0.25	$1{,}30 \pm 0{,}06$	0.90	$0{,}00186 \pm 0{,}00105$	0.9999
0.5	$1{,}22 \pm 0{,}05$	0.84	$0{,}00211 \pm 0{,}00082$	0.9999
1	$1{,}17 \pm 0{,}04$	0.81	$0{,}00241 \pm 0{,}00054$	0.9999
2	$1{,}17 \pm 0{,}03$	0.81	$0{,}00182 \pm 0{,}00046$	0.9999
3	$1{,}12 \pm 0{,}03$	0.78	$0{,}00145 \pm 0{,}00037$	0.9999
5	$1{,}08 \pm 0{,}03$	0.75	$0{,}00065 \pm 0{,}00035$	0.9999

3.4. Temporal behavior

The shape of the decay curves suggests the presence of multiple trap populations with different emptying probabilities. The rapid initial decrease in signal is associated with shallow traps, while the slower decay region indicates the contribution of deeper or less optically accessible traps.

4. Discussion

The results obtained in this work demonstrate a clear dependence of the optical bleaching process on the irradiation wavelength. Irradiation at 463 nm produced a faster decrease of the OSL signal than irradiation at 516 nm, as shown by the normalized curves $I(t)/I_0$, the bleaching efficiency values, and the kinetic parameters obtained from monoexponential fitting. This behavior indicates that the reduction of the stored signal is strongly influenced by the photon energy of the stimulating light.

From a physical perspective, this wavelength dependence can be associated with the spectral response of optically active traps in Al_2O_3:C. Shorter wavelengths correspond to higher photon energies and therefore increase the probability of optical release of trapped electrons. This interpretation is consistent with the general OSL mechanism described for Al_2O_3:C, where optical stimulation promotes trapped charge carriers into the conduction band or into recombination pathways that produce luminescence [1,5]. In addition, comparative studies of blue and green stimulation in Al_2O_3:C have reported higher stimulation efficiency in the blue spectral region, supporting the stronger bleaching effect observed at 463 nm [6].

Although the higher bleaching efficiency observed at 463 nm is consistent with the greater photon energy and higher optical stimulation efficiency reported for blue stimulation in Al_2O_3:C, the difference in irradiance between the two optical modules must also be considered. The irradiance at the dosimeter plane was 587.7 mW·cm^{-2} for the 463 nm module and 457.7 mW·cm^{-2} for the 516 nm module, corresponding to an approximately 28 % higher irradiance for the 463 nm system. Therefore, the observed differences in bleaching

efficiency cannot be attributed exclusively to wavelength effects. The higher optical power density of the 463 nm module may have contributed partially to the faster signal reduction. Nevertheless, under the experimental conditions evaluated in this work, the 463 nm system produced consistently shorter time constants, lower residual signals, and higher bleaching efficiencies than the 516 nm system. Future studies using power-matched optical irradiation conditions would be necessary to separate the relative contributions of wavelength and irradiance.

The present results demonstrate that optical bleaching significantly reduces the residual OSL signal, facilitating the practical reuse of nanoDot$^{\mathrm{TM}}$ dosimeters within the investigated dose range. However, the long-term lifespan of the detectors was not directly evaluated in this study. The primary objective of this work was to characterize and compare the optical bleaching efficiency of Al_2O_3:C nanoDot$^{\mathrm{TM}}$ dosimeters under 463 nm and 516 nm irradiation, rather than to assess sensitivity degradation or cumulative effects associated with repeated irradiation–bleaching cycles.

Therefore, although the proposed bleaching protocol facilitates dosimeter reuse by reducing the residual signal, conclusions regarding long-term detector lifespan or sensitivity changes cannot be drawn from the present data. Future studies should investigate the effects of repeated irradiation and bleaching cycles on the long-term performance and stability of nanoDot$^{\mathrm{TM}}$ dosimeters.

The kinetic analysis reinforces this interpretation. The time constants obtained for 463 nm irradiation, approximately 1.08–1.30 min, were about half of those obtained for 516 nm irradiation, approximately 2.14–2.35 min. This indicates that the characteristic time scale of trap depopulation is significantly shorter under 463 nm irradiation. Similar wavelength-dependent behavior has been reported for Al_2O_3:C OSL detectors exposed to 6 MV photon beams, where different bleaching wavelengths produced distinct effects on detector response and sensitivity [8].

An important observation is the weak dependence of the normalized decay behavior on dose. The overlap of the normalized curves and the relatively stable values of τ and $t_{1/2}$ across the evaluated dose range suggest that the bleaching kinetics are mainly governed by optically induced transition probabilities rather than by the initial population of trapped charge carriers. This behavior is consistent with continuous-wave OSL descriptions, in which the decay curve reflects the emptying of optically accessible trap populations under a given stimulation condition [1,4,5].

The analysis of the ratio $I(t)/I_b$ provides additional insight into the residual signal. For 463 nm irradiation, the rapid decrease of this ratio indicates that the residual signal approaches the baseline level of the reader–dosimeter system within relatively short irradiation times. In contrast, the higher $I(t)/I_b$ values observed for 516 nm, particularly at higher doses, suggest that a fraction of the trapped charge remains in levels that are not efficiently emptied under lower photon energy stimulation.

This behavior can be interpreted in terms of a distribution of trap depths in Al_2O_3:C. Shallow and optically accessible traps are emptied more rapidly and contribute to the initial fast decay of the signal, whereas deeper or less optically accessible traps contribute to the slower residual component.

The presence of multiple trapping and recombination pathways in Al_2O_3:C has been widely discussed in luminescence models and is consistent with the non-zero residual signal observed after prolonged optical irradiation [1,4,10,11].

Additionally, the persistence of residual signal may also be related to phototransfer processes. Such behavior has been reported in Al_2O_3:C under infrared stimulation, where multiple optically stimulated components have been observed, indicating the participation of different trapping states in the luminescence response [7]. The existence of multiple trapping and recombination centers in Al_2O_3:C has been widely discussed in the literature and may contribute to the persistence of residual signal after optical bleaching [1,10,11]. However, the specific mechanisms responsible for the residual signal observed in the present study were not directly investigated.

Overall, the results suggest that the observed optical bleaching behavior in Al_2O_3:C nanoDot$^{\mathrm{TM}}$ dosimeters is influenced by the interaction between photon energy, trap-depth distribution, and the photoionization probability of trapped carriers.

The shorter wavelength of 463 nm provides more efficient access to optically active trap populations, leading to faster signal decay, higher bleaching efficiency, and a closer approach to the baseline level. In contrast, irradiation at 516 nm produces slower bleaching and a higher residual signal, suggesting incomplete depopulation of deeper or less optically accessible traps.

5. Conclusions

In this work, the efficiency of the optical bleaching process in Al_2O_3:C nanoDot$^{\mathrm{TM}}$ dosimeters was evaluated using optical irradiation at 463 nm and 516 nm. The results demonstrate that the irradiation wavelength significantly influences both the rate of OSL signal decay and the residual signal level achieved.

Irradiation at 463 nm showed higher bleaching efficiency compared to 516 nm, reaching values above 99 % within short irradiation times. This behavior was consistently reflected in the normalized curves, in the efficiency values, and in the $I(t)/I_b$ ratio, where a closer approach to the system baseline level was observed, particularly at low doses.

Kinetic analysis based on monoexponential fitting revealed that the decay process occurs on a significantly shorter time scale for 463 nm, with half-life values approximately two times lower than those obtained for 516 nm. Additionally, the kinetic parameters exhibited low dependence on dose within the evaluated range, suggesting that the bleaching process is primarily governed by optical interaction probability rather than by the initial population of charge carriers.

In contrast, irradiation at 516 nm showed a significant persistence of residual signal, particularly at higher doses, indicating lower efficiency in the emptying of electron traps under these conditions. This effect was evidenced by both the higher values of $I(t)/I_b$ and the longer characteristic times of the process.

Overall, the results confirm that the selection of the optical irradiation wavelength is a determining factor in the optimization of the bleaching process in OSL dosimeters. These findings have direct implications for the design of reuse protocols, enabling a reduction in conditioning times without compromising the stability of the dosimetric response in clinical applications.

1. E.G. Yukihara and S.W.S. McKeever, *Optically Stimulated Luminescence: Fundamentals and Applications* (Wiley, Chichester, 2011).
2. P.A. Jursinic, Characterization of optically stimulated luminescent dosimeters (OSLDs) for clinical dosimetric measurements, *Med. Phys.* **34** (2007) 4594, https://doi.org/10.1118/1.2804555.
3. M.S. Akselrod, V.S. Kortov, D.J. Kravetsky and V.I. Gotlib, Highly sensitive thermoluminescent anion-defective α-Al_2O_3:C single crystal detectors, *Radiat. Prot. Dosim.* **32** (1990) 15.
4. S.W.S. McKeever, *Thermoluminescence of Solids* (Cambridge University Press, Cambridge, 1985).
5. E.G. Yukihara and S.W.S. McKeever, Optically stimulated luminescence (OSL) dosimetry in medicine, *Phys. Med. Biol.* **53** (2008) R351, https://doi.org/10.1088/0031-9155/53/20/R01.
6. N.K. Umisedo, E.G. Yukihara and S.W.S. McKeever, Comparison between blue and green stimulated luminescence of Al_2O_3:C, *Radiat. Meas.* **45** (2010) 181, https://doi.org/10.1016/j.radmeas.2010.02.001.
7. E. Bulur and W. Wahl, Infrared stimulated luminescence from Al_2O_3:C, *Radiat. Meas.* **29** (1998) 639, https://doi.org/10.1016/S1350-4487(98)00059-0.
8. A.A. Omotayo, J.E. Cygler and G.O. Sawakuchi, The effect of different bleaching wavelengths on the sensitivity of Al_2O_3:C optically stimulated luminescence detectors exposed to 6 MV photon beams, *Med. Phys.* **39** (2012) 5457, https://doi.org/10.1118/1.4742865.
9. P.A. Jursinic, Changes in optically stimulated luminescent dosimeter dosimetric characteristics with accumulated dose, *Med. Phys.* **37** (2010) 132, https://doi.org/10.1118/1.3267489.
10. A.J.J. Bos, Theory of thermoluminescence, *Radiat. Meas.* **33** (2001) 737, https://doi.org/10.1016/S1350-4487(01)00106-0.
11. V. Pagonis, G. Kitis and C. Furetta, *Numerical and Practical Exercises in Thermoluminescence* (Springer, New York, 2006).
12. M. Jain, K.J. Thomsen, L. Bøtter-Jensen and A.S. Murray, Thermal transfer and apparent dose distributions in OSL dating of quartz, *Radiat. Meas.* **38** (2004) 101, https://doi.org/10.1016/j.radmeas.2003.10.003.
13. A.A. Mowlavi et al., AAPM Task Group 191: Clinical use of luminescent dosimeters, *Med. Phys.* **47** (2020) e19, https://doi.org/10.1002/mp.13839.
14. International Atomic Energy Agency, *Absorbed Dose Determination in External Beam Radiotherapy: An International Code of Practice for Dosimetry Based on Standards of Absorbed Dose to Water (TRS-398)* (IAEA, Vienna, 2000).

A dynamical system approach to modified point kinetics equations

T. M. Tiscareño Sánchez

Unidad Académica de Física, Universidad Autónoma de Zacatecas, Calzada Solidaridad esquina Paseo la Bufa s/n, Zacatecas, Zac., México.

S. L. Hinojosa Ruiz

Unidad Académica de Física, Universidad Autónoma de Zacatecas, Calzada Solidaridad esquina Paseo la Bufa s/n, Zacatecas, Zac., México.

H. Tototzintle Huitle

Unidad Académica de Física, Universidad Autónoma de Zacatecas, Calzada Solidaridad esquina Paseo la Bufa s/n, Zacatecas, Zac., México.

Received 22 November 2023; accepted 13 May 2026

We apply the formalism of dynamical systems and the Kosambi-Kartan-Chern theory to perform an extensive stability analysis of solutions to modified point kinetics equations, a set of two differential equations used in nuclear physics to describe the temporal behavior of a fission nuclear reactor. It is known that the stability of the system depends on reactivity, which appears in the equations as a parameter ρ, and the functional form of this parameter can describe different situations that may occur in a nuclear reactor, making the equations nonlinear or even nonautonomous in certain cases. We present a comparative study between linear stability and Jacobi stability, pointing out the usefulness of the geometrodynamical approach.

Keywords: Dynamical systems; Lyapunov stability; Jacobi stability; Kosambi-Cartan-Chern theory, reactor point-kinetics.

DOI: https://doi.org/10.31349/RevMexFis.72.061201

1. Introduction

The point-kinetic model is a set of coupled differential equations that have been widely used to describe the temporal behavior of nuclear fission reactors and can be derived directly from the neutron transport equation, the neutron diffusion equation or by heuristic procedures [1-3]. The stability of the system has been studied using different methods [4-7]. Recently, new modifications have been formulated for this set of equations, such as Refs. [8,9]. The Modified Point Kinetics Equations (MPK) [10] arise when the derivative of the neutron density is incorporated into the derivation of the set of equations.

By considering this set of equations, we perform a stability analysis on the critical points of the system. Considering a functional form of reactivity depending on time and an integral over neutron number, we have a set of nonlinear nonautonomous equations which, due to nonautonomous nature, is difficult to analyze because the conventional techniques such as linearization about critical points, the Hartman-Grobman theorem or Lyapunov-Poincare theorem can not be applied directly. Furthermore, the system becomes integrodifferential in some cases. Nevertheless, global stability of the system can be studied by constructing an appropriate Lyapunov function $V(x,t)$ that satisfies the conditions of the Lyapunov theorem and, thereby determining the asymptotic stability of the solutions. Additionally, we employ the Kosambi-Cartan-Chern (KCC) theory to assess the Jacobi (in)stability of critical points, particularly in cases where the application of Lyapunov stability becomes intricate due to the nature of critical points or difficulties that arose for certain functional forms of reactivity ρ. Some authors refer tho the combined use of dinamycal systems theory and differential geometry as geometrodynamical approach to dynamical systems. This framework has been applied in a wide range scientific fields, and some of its earlier applications arose in biology, where Antonelli *et al.* [11] conducted a stability analysis of Tayson's equations for the cell-division cycle. The authors studied Jacobi stability of the model trough the deviation curvature tensor. In recent years, the method has gained popularity in the field of gravitation and cosmology [12], in part, due to familiarity of concepts inherent to mathematical framework used in this theories and the differential geometrical approach provided by KCC theory. Some recent investigation made comparative studies of stability using Lyapunov stability and Jacobi stability of circular orbits around black holes in modified theories of gravity [13-16].

This paper is structured as follows. Section 2 contains a brief introduction to dynamical systems and KCC theory. Section 3 provides the mathematical model considered. In Sec. 4, we present a stability analysis of MPK equations by considering some functional forms of reactivity ρ. Section 5 is devoted to a discussion of our main results, concluding that the geometrodynamical approach provides a robust framework for studying complex dynamical systems.

2. Mathematical background

The purpose of this section is to provide the essential mathematical insights for analyzing the stability of MPK equations. For dynamical systems theory, the reader is referred to classic texts such as [17-23]. For a complete description of the KCC framework, see [12,13,15,24].

The first part of this section is devoted to apply dynamical systems theory to the study of differential equations of the form

$$\dot{x} = f(x), \tag{1}$$

where $x \in \mathbb{R}^n$, $E \in R^n$ and $f : E \to \mathbb{R}^n$. Critical points x_c of Eq. (1) are those that satisfy $f(x_c) = 0$.

The critical points correspond to equilibrium solutions of the system, that is, $x(t) = x_c$ satisfies the equation for all time. The study of these points and solutions in their neighborhood is of particular interest. Through the application of linearization around the critical points, Eq. (1) can be approximated as a linear equation

$$\dot{x} = Ax, \tag{2}$$

where A is the Jacobian matrix of $f(x)$. The fundamental theorem of linear systems establishes the existence and uniqueness of solutions of this kind of systems with initial conditions $x(0) = x_0$, which is given as $x(t) = e^{tA}x_0$. As a consequence, from the eigenvalues of A we can obtain important qualitative information about the behavior of solution curves near critical points in the phase space. Some examples can be found in Refs. [22,25-28]. Generally, the process starts with a linearization around its critical points, as it is the simplest approach; however, a nonlinear analysis of the dynamical system is necessary to gain a more comprehensive understanding of the behavior of the entire system.

The stability of critical points of any nonlinear system can be analyzed from the characteristic roots of the Jacobian matrix, provided that they are distinct from zero, and its solutions can be classified in terms of nodes, focus, saddle or center behavior. The system is said to be stable if the eigenvalues of the corresponding Jacobian matrix are negative, have negative real part, or are pure imaginary; otherwise, the system is unstable, and its solutions can be classified in terms of nodes, focus, saddle, or center behavior. It should be pointed out that if the system has eigenvalues equal to zero, other methods should be used to determine stability or instability in the system, such as the Floquet theorem or the Lyapunov theorem.

Other features of nonlinear systems can be viewed by making bifurcation analysis, which consists of studying changes in the behavior of the system from the variation of parameters appearing in the equations. In the case where the independent variable appears in the equations, which for physical systems usually corresponds to time, the system is said to be nonautonomous. This kind of system should be treated carefully, as the theory of autonomous systems does not work the same. Although some of the existent theorems cover few special cases, a general theory for nonautonomous systems have not been completely developed yet [17-23,29].

Furthermore, the Kosambi-Cartan-Chern (KCC) theory is a powerful mathematical method for investigating the characteristics of dynamical systems. The KCC theory utilizes a geometric depiction of the time evolution of dynamical systems, where the solution curves are described trough techniques similar to those found in the study of geodesics in Finsler spaces. In this framework, stability of solutions of second order differential equations of the form

$$\frac{d^2x^i}{dt^2} + 2G^i(x^j, y^j, t) = 0, \quad i = 1, 2, ..., n, \tag{3}$$

is studied [30]. Here x^i are the dynamical variables defined on a smooth manifold $\mathcal{M}$, usually $\mathcal{M} = \mathbb{R}^n$. Let Ω be a subset of the Euclidian $(2n+1)-$dimensional space on which the coordinate system $(x^i, y^i, t), i = 1, 2, ..., n$, is introduced, $y^i = (dx^i/dt)$. The main idea of KCC theory is that the evolution and behavior of trajectories of the system (A.1) can be analyzed using tools of differential geometry.

The study of geometrical properties associated to the dynamical system defined by Eq. (A.1) is possible by introducing the nonlinear connection N with coefficients N^i_j defined as:

$$N^i_j = \frac{\partial G^i}{\partial y^j}. \tag{4}$$

The KCC-covariant differential of a vector field ξ^i is introduced trough the definition

$$\frac{D\xi^i}{dt} = \frac{d\xi^i}{dt} + N^i_j\xi^j. \tag{5}$$

For $\xi^i = y^i$ is obtained

$$\frac{Dy^i}{dt} = N^i_j y^j - 2G^i = -\epsilon^i, \tag{6}$$

where ϵ^i is called the first KCC invariant.

By introducing a nonlinear connection, KCC theory provides a geometric interpretation of the evolution of a dynamical system, thereby facilitating the construction of the KCC covariant derivative of an arbitrary field χ

$$\frac{D^2\chi^i}{dt^2} = P^i_j\chi^j, \tag{7}$$

where the deviation curvature tensor is

$$P^i_j = -2\frac{\partial G^i}{\partial x^j} - 2G^l G^i_{jl} + y^l\frac{\partial N^i_j}{\partial x^l} + N^i_l N^l_j + \frac{\partial N^i_j}{\partial t}. \tag{8}$$

The Berwald connection is

$$G^i_{jl} \equiv \frac{\partial N^i_j}{\partial y^l}. \tag{9}$$

The third, fourth and fifth invariant are constructed according to definitions

$$P^i_{jk} \equiv \frac{1}{3}\left(\frac{\partial P^i_j}{\partial y^k} - \frac{\partial P^i_k}{\partial y^j}\right),$$

$$P^i_{jkl} \equiv \frac{\partial P^i_{jk}}{\partial y^l}, \qquad D^i_{jkl} \equiv \frac{\partial G^i_{jk}}{\partial y^l}. \tag{10}$$

In this theory, the properties of any dynamical system can be explained using the five invariants depicted, the second invariant determining the Jacobi stability of the system. In KCC theory, these five invariants are the basic mathematical quantities that describe the geometrical properties and interpretation of an arbitrary system of second-order differential equations [12,13,24].

KCC theory and its relation with chaos in 3D systems is explored by Somanath Roy *et al.* [31], showcasing the KCC theory as a powerful tool to capture nuanced dynamics. Other contributions has been made in the study of 2D systems [32]. Furthermore, some particular systems which exhibits chaotic behavior have been studied as Liu system [33], the Lorentz model [34], a Lorentz type model [35], Rössler system [36], just to name some examples.

It should be noticed that Lyapunov stability analysis (linearization, lyapunov function, center manifold) and KCC stability (Jacobi stability) differ in the type of stability that is determined by each. The former studies how solution curves evolve near critical points; it could be an attractor (repulsor), which means that solution curves are attracted (repealled) to it when $t \to \infty$. An attractor can be stable (unstable) in the sense of Lyapunov; that is, solution curves remain close starting from slightly different initial conditions and stay in a neighborhood for all t.

On the other hand, Jacobi stability is an extension of the concept of stability in geodesic flows on manifolds with Riemannian or Finslerian metrics. It examines the robustness of a second-order differential equation, where robustness is a measure of the system's and environment's sensitivity to changes in its internal parameters. From a mathematical point of view, KCC theory looks at the variations in nearby trajectories as geodesics in a Finsler space, allowing for an estimation of the perturbations that can be tolerated around the equilibrium solutions of a second-order differential equation. This is especially useful in physical applications, where determining areas with both Lyapunov and Jacobi stability is of great importance. Further discussion of the differences between these two methods can be found in Refs. [37,38]. A good correlation exists between the linear stability and Jacobi stability of critical points, nevertheless this is not always true. A critical point can be Lyapunov stable and Jacobi unstable and vice versa, and in consequence some discrepancies in the results of these two stability methods arise.

3. Mathematical model

One of the simplest ways to determine the time behavior of nuclear power in nuclear fission reactors is through the solution of point kinetics equations, which are a set of nonlinear nonautonomous coupled differential equations in the most general form. The character of nonautonomous and nonlinear is given by the functional form of the reactivity $\rho(n,t)$. Such equations can be derived from various procedures. The one that concerns us is that obtained from the neutron transport equation; this derivation needs several approximations, including weak angular dependence of the angular distribution of the neutrons, isotopic sources of neutrons, and disregarding the derivative of the neutron current density [1,2]. Recently, new modifications had been formulated for this set of equations taking into account the temporal derivative of the neutron current density for the analysis of behavior and solutions, giving as a result the Modified Point Kinetics (MPK).

TABLE I. Parameters and variables appearing in MPK model.

Parameter	Description	Value
$n(t)$	Neutron number	
$c_i(t)$	Precursor number	
$\rho(n,t)$	Reactivity	
f_D	Transport frequency	$3 \times 10^5 s^{-1}$
f_A	Neutron absorption frequency	$4{,}167 s^{-1}$
β	Fraction of delayed neutrons	0.007
Λ	Mean generation time	0.002s
λ_i	Decay constant	$0{,}0810958 s^{-1}$

The MPK equations are

$$\frac{d^2n(t)}{dt^2} + M\frac{dn(t)}{dt} = Pn(t) + f_D\sum_{i=1}^{6}\lambda_i c_i(t) + \sum_{i=1}^{6}\lambda_i\frac{dc_i}{dt}$$

$$\frac{dc(t)_i}{dt} = \frac{\beta_i}{\Lambda}n(t) - \lambda_i c_i(t), \tag{11}$$

where $M = (f_D + f_A - [1-\beta/\Lambda])$, $P = (f_D/\Lambda)(\beta - \rho)$. For a detailed derivation, see [10]. In this investigation, the system was analyzed and solutions for constant reactivity were derived using an analytical method involving the construction of a third-order differential equation and using the Laplace transform method to solve it. This system is comparable to the traditional Point-Kinetics (PK) model, which is referred to as the "classical point kinetics" when the limit of $1/f_d$ approaches zero. Variables $n(t), c(t)$ and parameters $f_D, f_A, \beta, \Lambda, \lambda_i, \rho(n,t)$ are listed in Table I. Stability analysis for this system is performed in the next section.

4. Stability analysis

As stated earlier, stability analysis can be derived in two ways, in this section is considered first the cases that can be studied using Lyapunov stability, then some cases of nonlinear reactivity are considered using KCC theory.

The first of the Eqs. (11) is second-order and includes the derivative of precursors C. We are interested into write this equation in the form of Eq. (1) in order to apply stability analysis. From this system, the set of three first-order coupled differential equations can be constructed as follows:

Considering one group of precursors in the Eq. (11), substituting in the first equation, and taking the change of variables $x_1 = n$, $x_2 = \dot{x_1} = \dot{n}$ and $x_3 = c$, the first equation can

be stated as two coupled first order equations, and together with the second equation one obtains the following system of three coupled equations of the form of Eq. (1)

$$\begin{aligned}\dot{x}_1 &= x_2,\\ \dot{x}_2 &= -Mx_2 + Px_1 + f_D\lambda x_3 + \lambda\left(\frac{\beta}{\Lambda}x_1 - \lambda x_3\right),\\ \dot{x}_3 &= \frac{\beta}{\Lambda}x_1 - \lambda x_3,\end{aligned} \tag{12}$$

with initial conditions

$$\left.\frac{dc(t)}{dt}\right|_{t=0} = 0, \tag{13}$$

$$c(0) = \frac{\beta}{\lambda\Lambda}n(0) = 0, \tag{14}$$

$$n(0) = n_0. \tag{15}$$

As stated before, the stability of MPK equations and, therefore, of nuclear reactors depends on the functional form of the reactivity $\rho(n,t)$. Depending on this functional form, various cases can be considered: the system becomes linear, nonlinear and nonautonomous. Due to the complexity that exhibits the system, is suitable to analyze it using the mathematical tools described in Sec. 2.

4.1. Constant reactivity

The simplest case of MPK equations is when the reactivity has a constant value $\rho(n,t) = cte$.

4.1.1. One group of precursors

In this case, the system becomes lineal and has the form $\dot{x} = Ax$, where $x \in \mathbb{R}^3$, and A is a 3×3 matrix with constant coefficients

$$A = \begin{pmatrix} 0 & 1 & 0 \\ P + \frac{\lambda\beta}{\Lambda} & -M & \lambda(f_D - \lambda) \\ \frac{\beta}{\Lambda} & 0 & -\lambda \end{pmatrix}. \tag{16}$$

A stability analysis can be carried out by computing the correspondent eigenvalues of this matrix from the eigenvalue equation $\omega_i = det|A - \omega\mathbb{I}| = 0$:

$$-\omega(M+\omega)(\lambda+\omega) + (\lambda+\omega)N = 0, \tag{17}$$

where $N = P + [\lambda\beta/\Lambda]$ and whose solutions are

$$\omega_1 = -\lambda, \qquad \omega_{2,3} = -\frac{1}{2}(M \pm \sqrt{M^2 + 4N}). \tag{18}$$

TABLE II. Eigenvalues for the MPK system.

Reactivity	ω_1	ω_2	ω_3
$\rho = -0{,}5$	-0.7997577974	-255.41000694	-9925259105
$\rho = 0$	0.0000002597	-3.59852555	-99504.48257
$\rho = 0{,}5$	-0.08224688231	247.1062989	-99755.10515

The parameter N depends on reactivity ρ, so the solutions depends too. The eigenvalues were computed for some particular cases of reactivity covering the cases of critical, subcritical, and supercritical that can occur in a nuclear reactor.

The findings of this study are in agreement with those obtained from a comparable examination of the traditional point kinetics equations.

4.2. Nonlinear reactivity

Some authors [39] consider a nonlinear reactivity by introducing temperature feedback reactivity, in this case

$$\frac{d\rho}{dt} = \frac{d\gamma(t)}{dt} - Bn(t), \tag{19}$$

where $\gamma(t)$ is the prescribed reactivity. The dynamical system formed is of the form $\dot{x} = f(x,t)$, where $x \in \mathbb{R}^4$ and

$$f(x,t) = \begin{pmatrix} x_2 \\ Qx_1 - Mx_2 + Rx_3 - \frac{f_D}{\Lambda}\rho x_1 \\ \frac{\beta}{\Lambda}x_1 - \lambda_i x_3 \\ \frac{d\gamma(t)}{dt} - Bx_1 \end{pmatrix}, \tag{20}$$

where $R = f_D\lambda_i - \lambda_i^2$, $Q = (\beta/\Lambda)(f_d + \lambda)$.

The simplest case is when the prescribed reactivity is constant $\gamma(t) = cte$, and the equation becomes

$$f(x,t) = \begin{pmatrix} x_2 \\ Qx_1 - Mx_2 + Rx_3 - \frac{f_D}{\Lambda}\rho x_1 \\ \frac{\beta}{\Lambda}x_1 - \lambda_i x_3 \\ -Bx_1 \end{pmatrix}. \tag{21}$$

This system is nonlinear, and has infinite critical points given by $(0,0,0,x_4)^t$, however, all of this critical points are nonhyperbolic and the stability analysis is carried out using a suitable Lyapunov function. One simple function that satisfies the criteria of Lyapunov theorem

$$V(x) = x_1^2 + x_2^2 + x_3^2 + x_4^2. \tag{22}$$

This function has negative definite orbital derivative and is positively definite in a neighbourhood of $x = 0$, sufficient conditions to establish that the origin is asymptotically stable.

For different forms of prescribed reactivity, this system can be nonlinear and autonomous, or nonautonomous. some cases are considered next. As the reactivity ρ appears in the

second and fourth equation as its derivative, analyzing this problem gives place to a integro differential equation. In order to study this cases KCC theory can be applied. For this purpose, we compute the derivative of function $f(x,t)$ in Eq. (20) with respect time to obtain a equation in the form of Eq. (A.1), where

$$G^i = \frac{1}{2}\begin{pmatrix} \dot{x}_2 \\ (Q-\frac{f_D}{\Lambda})\dot{x}_1 - M\dot{x}_2 + R\dot{x}_3 - \frac{f_D}{\Lambda}x_1\dot{\rho} \\ \frac{\beta}{\Lambda}\dot{x}_1 - \lambda\dot{x}_3 \\ \frac{d^2\gamma}{dt^2} - B\dot{x}_1 \end{pmatrix}. \quad (23)$$

Components of the first KCC invariant are constructed using Eq. (2)

$$\epsilon = \begin{pmatrix} \epsilon^1 \\ \epsilon_2 \\ \epsilon_3 \\ \epsilon_4 \end{pmatrix} = \frac{1}{2}\begin{pmatrix} \dot{x}_2 \\ (Q-\frac{f_D}{\Lambda})\dot{x}_1 - M\dot{x}_2 + R\dot{x}_3 - \frac{f_D}{\Lambda}x_1\dot{\rho} \\ \frac{\beta}{\Lambda}\dot{x}_1 - \lambda\dot{x}_3 \\ \frac{d^2\gamma}{dt^2} - B\dot{x}_1 \end{pmatrix}. \quad (24)$$

In this case, the first invariant coincides with the function G^i. Deviation curvature tensor can be obtained as

$$P^i_j = \frac{1}{2}\sum_{k=1}^{n} f^i_{jk}(x^1,...,x^n)y^k + \frac{1}{4}\sum_{l=1}^{n} f^i_l(x^1,...,x^n)f^l_j(x^1,...,x^n), \quad (25)$$

where f^n are the components of $f(x,t)$. The components of this tensor different from 0 are

$$P^1_1 = \frac{Q-Sx_4}{4};\quad P^1_2 = \frac{-M}{4};\quad P^1_3 = \frac{R}{4};\quad P^1_4 = \frac{3x_1}{4},$$

$$P^2_1 = -\frac{S}{2}\dot{x}_4 + \frac{1}{4}(MSx_4 - MQ + RT - BSx_1),$$

$$P^2_2 = \frac{1}{4}(Q - Sx_4 + M^2);\qquad P^2_3 = -\frac{R}{4}(M+\lambda),$$

$$P^2_4 = \frac{S\dot{x}_1}{2} - \frac{MSx_1}{4};\qquad P^3_1 = \frac{-\lambda\beta}{4\Lambda};$$

$$P^3_2 = \frac{\beta}{a\Lambda};\qquad P^3_3 = \frac{\lambda^2}{4},$$

where $S = f_D/\Lambda$ and

$$P = \begin{pmatrix} P^1_1 & P^1_2 & P^1_3 & P^1_4 \\ P^2_1 & P^2_2 & P^2_3 & P^2_4 \\ P^3_1 & P^3_2 & P^3_3 & 0 \\ 0 & 0 & 0 & 0 \end{pmatrix}. \quad (26)$$

The eigenvalues of this tensor indicate the Jacobi stability of the system; if they are negative, the system is stable and unstable otherwise. One of the eigenvalues of this tensor is zero, which implies that the system is Jacobi unstable.

The third, fourth and fifth invariants are constructed following the definitions (10). In the case of the third invariant we found that the only elements distinct from cero are

$$P^2_{14} = P^2_{41} = \frac{S}{3}. \quad (27)$$

The elements of the fourth invariant are partial derivatives of P^i_{jk} with respect to y^j, and since the elements of P^i_{jk} are constants, thus elements of fourth invariant are equal to 0.

On the other hand, for the fifth invariant, since elements of N^i_j depend at most of x_i, then, partial derivatives of this elements with respect to y^l are equal to 0, thus, elements of fifth invariant are equal to 0.

Under this approach of stability different types of reactivity can be considered in Eq. (12) including step ramp insertion $\gamma = at$, periodic reactivity $\gamma = \rho_0\cos(\omega t)$, and pulse type reactivity $\gamma = 4\beta e^{-2t^2}$. Deviation curvature tensor has the same form, with the last row consisting of zeros. Therefore, the eigenvalues of this tensor have similar values, including 0. By taking this into account, the instability of critical points can be determined. It should be noted that each case of prescribed reactivity leads to different critical points that appear in the set of Eqs. (12), some of them are nonhyperbolic, but all of these critical points exhibit the same behavior, that is, the presence of a zero eigenvalue in the deviation curvature tensor.

4.2.1. *Periodic prescribed reactivity*

Some authors consider the case where the reactivity has a periodic variation, in this case $\gamma(n,t) = \rho_0\sin(\omega t)$. Thus, the system has the form $\dot{x} = A(t)x$. In the case where only one group of precursors is considered, this system has critical points given by

$$\left(\frac{\omega\rho_0\cos(\omega t)}{B}, 0, \frac{\omega\rho_0\beta\cos(\omega t)}{\lambda\Lambda B}, \frac{Q\Lambda}{f_D} - \frac{R\beta}{B\lambda\Lambda}\right),$$

the system can be analyzed using Floquet's theorem. On the other hand, it can be studied with KCC theory.

4.2.2. *Step ramp insertion*

Introducing the case of step ramp insertion reactivity $\gamma = at$ in Eq. (20) gives

$$f(x,t) = \begin{pmatrix} x_2 \\ Qx_1 - Mx_2 + Rx_3 - \frac{f_D}{\Lambda}\rho x_1 \\ \frac{\beta}{\Lambda}x_1 - \lambda_i x_3 \\ a - Bx_1 \end{pmatrix}. \quad (28)$$

This system has two critical points $x_{01} = (a/B, 0, \beta/\lambda\Lambda a/B, 2\beta)^t$ and $x_{02} = (a/B, 0, \beta/\lambda\Lambda a/B, 0)^t$, both of which are nonhyperbolic.

4.2.3. Pulse type prescribed reactivity

Introducing the case of pulse type reactivity $\gamma = 4\beta e^{-2t^2}$ in Eq. (20) gives

$$f(x,t) = \begin{pmatrix} x_2 \\ Qx_1 - Mx_2 + Rx_3 - \frac{f_D}{\Lambda}\rho x_1 \\ \frac{\beta}{\Lambda}x_1 - \lambda_i x_3 \\ 16t\beta e^{-2t^2} - Bx_1 \end{pmatrix}. \quad (29)$$

This case of reactivity has critical point at $([16te^{-2t^2}/B], 0, [\beta 16te^{-2t^2}/\lambda\Lambda B], Q\Lambda/f_D - R\beta/B\lambda\Lambda)$, in which curvature tensor is evaluated, given the same functional form with a zero eigenvalue.

5. Results and discussions

The aim of this investigation is apply geometrodynamical approach provided by Lyapunov and Jacobi stability to the study of complex dynamical systems. MPK equations, due to functional form of reactivity are suitable for this analysis, allowing us to explore the scope of the theory. The conducted analysis enables a comparative examination between the "classical" point kinetics equations and the modified point kinetics equations, which is consistent with previous findings. Moreover, the KCC theory was successfully employed to identify additional characteristics, such as the Jacobi stability of the MPK system, that cannot be easily discerned through the classical dynamical systems approach. The combined methods of stability enable us to perform a deeper study of the dynamics of equations, and allowing us to gain fuller insights in the behavior of solutions.

The stability analysis in the sense of Lyapunov is performed for the case of constant reactivity and one group of precursors for the point kinetics equations coincides with a similar examination of the classical point kinetics equations. As a complementary study, in the future this results must be extended to the case of more than one precursor, and compared with other analytical methods as well numeric solutions.

Also, introducing the temperature feedback reactivity some cases can be studied using Lyapunov theorem; however, for the nonlinear reactivity feedback cases of step ramp insertion, periodic reactivity and pulse type reactivity, the stability analysis is carried out by means of the deviation curvature tensor, whose eigenvalues give information about Jacobi instability of the system. Nevertheless, to gain a complete description of behavior of solutions these results must be contrasted with numerical solutions. Furthermore, only the case with one group of precursors has been studied, while the case of two or more precursors is worth further investigation.

Acknowledgments

The authors appreciate the support provided by CONAHCyT through grant 519369 which made this research possible.

1. A. F. Henry and E. Melkonian, Nuclear-Reactor Analysis, 1st ed. (The MIT Press, 1977), pp. 297-300.
2. J. Duderstadt and L. Hamilton, Nuclear Reactor Analysis, 1st ed. (Wiley, 1991), pp. 237-239.
3. T. W. Kerlin and B. R. Upadhyaya, Dynamics and Control of Nuclear Reactors, 1st ed. (Academic Press, 2019), pp. 21-25.
4. G. G. Theler and F. J. Bonetto, On the stability of the point reactor kinetics equations, Nucl. Eng. Des. **240** (2010) 1443, https://doi.org/10.1016/j.nucengdes.2010.03.007
5. V. Pandey and S. Singh, Detailed bifurcation analysis with a simplified model for advance heavy water reactor system, *Commun. Nonlinear Sci. Numer. Simul.* **20** (2015) 186, https://doi.org/10.1016/j.nucengdes.2010.03.007
6. R. Vora, A. Chakraborty, and S. Singh, Bifurcation analysis of out-of-phase oscillations in boiling water reactors using multipoint neutron kinetics, *Prog. Nucl. Energy* **120** (2019), https://doi.org/10.1016/j.pnucene.2019.103218
7. C. Z. Petersen *et al.*, An analytical solution of the point kinetics equations with time variable reactivity by the decomposition method, *Prog. Nucl. Energy*, **53** (2011) 1091, https://doi.org/10.1016/j.pnucene.2011.01.001
8. A. Gandini and M. Salvatores, The Physics of Subcritical Multiplying Systems., *J. Nucl. Sci. Tech.* **39** (2002) 673, https://doi.org/10.1080/18811248.2002.9715249
9. A. E. Aboanber and A. A. Nahla, A novel fractional technique for the modified point kinetics equations, *J. Nucl. Sci. Tech.* **24** (2016) 666, https://doi.org/10.1016/j.joems.2016.02.001
10. A. Nunes *et al.*, A New Formulation to the Point Kinetics Equations Considering the Time Variation of the Neutron Currents, *WJNST* **05** (2015) 57, http://dx.doi.org/10.4236/wjnst.2015.51006
11. P. Antonelli, S. Rutz, and S. Sabau, A Transient-State Analysis of Tyson's Model for the Cell Division Cycle by Means of KCC-Theory, *Open Syst. Inf. Dyn.* **9** (2002) 223, https://doi.org/10.1023/A:1019752327311
12. C. Boehmer, T. Harko, and S. Sabau, Jacobi stability analysis of dynamical systems - applications in gravitation and cosmology, *Adv. Theor. Math. Phys.* **16** (2010) 1145, https://dx.doi.org/10.4310/ATMP.2012.v16.n4.a2
13. C. Blaga, P. Blaga, and T. Harko, Jacobi and Lyapunov stability analysis of circular geodesics around a spherically symmetric dilaton black hole, *Symmetry* **15** (2023) 319, https://doi.org/10.3390/sym15020329

14. P. Singh *et al*., Stability of circular geodesics in equatorial plane of Kerr spacetime, *Eur. Phys. J. Plus.* **137** (2022), http://dx.doi.org/10.1140/epjp/s13360-022-02477-1

15. Tiscareño, Tonatiuh, Rodríguez, Benito, and Chagoya, Javier, Stability analysis of geodesics in dynamical Chern-Simons black holes: a geometrical perspective, *Eur. Phys. J. C* **85** (2025) 439, https://doi.org/10.1140/epjc/s10052-025-14137-6

16. C. Blaga and P. A. Blaga, Jacobi Stability of Circular Orbits Around Conformally InvariantWeyl Gravity Black Holes, *Universe* **12** (2026) 114, http://dx.doi.org/10.3390/universe12040114

17. M. W. Hirsch and S. Smale, Ecuaciones Diferenciales, Sistemas Dinámicos y Algebra lineal, 1st ed. (Alianza Editorial, España, 1983).

18. L. Perko, Differential equations and dynamical systems, 3rd ed. (Springer Verlag, New York, 2001).

19. E. A. Coddington and N. Levinston, Theory of Ordinary Differential equations, 1st ed. (Dover publications, United states of America, 1987).

20. F. Verhulst, Nonlinear Differential Equations and Dynamical Systems, 1st ed. (Springer Verlag, Berlin, 1990).

21. P. E. Kloeden and R. Martin, Nonautonomous Dynamical Systems (American Mathematical Society, Providence, Rhode Island, 2011).

22. V. Marinca and N. Herisanu, Nonlinear Dynamical Systems in Engineering: Some Approximate Approaches (Springer Verlag, 2011).

23. T. Caraballo and X. Han, Aplied Nonautonomous and Random Dynamical Systems Aplied Dymanical Systems (Springer Verlag, Switzerland, 2016).

24. T. Harko, P. Pantaragphong, and S. V. Sabau, Kosambi-Cartan-Chern (KCC) theory for higher-order dynamical systems, *Int. J. Geom. Methods Mod. Phys.* **13** (2016) 1650014, https://doi.org/10.1142/S0219887816500146

25. W. Krabs, A General Predator-Prey Model, *Math. Comput. Model. Dyn. Syst.* **9** (2003) 387, http://dx.doi.org/10.1076/mcmd.9.4.387.27896

26. M. Lines and A. Medio, Nonlinear Dynamical Systems in Economics (Springer-Verlag Wien, 2005).

27. K. Rateitschak and O. Wolkenhauer, Thresholds in transient dynamics of signal transduction pathways, *J. Theor. Biol.* **264** (2010) 334, https://doi.org/10.1016/j.jtbi.2010.02.001

28. M. Crucifix and J. Rougier, On the use of simple dynamical systems for climate predictions, *Eur. Phys. J. Spec.* **174** (2009) 11, https://doi.org/10.1140/epjst/e2009-01087-5

29. P. E. Kloeden and C. Pötzsche, Nonautonomous Dynamical Systems in the Life Sciences, 1st ed. (Springer Verlag, Switzerland, 2013).

30. M. Fels, The Equivalence Problem for Systems of Second- Order Ordinary Differential Equations, *Proc. Lond. Math. Soc.* **71** (1995) 221, https://doi.org/10.1112/plms/s3-71.1.221

31. S. Roy, A. Ray, and A. R. Chowdhury, Kosambi-Cartan-Chern perspective on chaos: Unveiling hidden attractors in nonlinear autonomous systems, *Phys. Rev. E* **109** (2024) 044205, https://link.aps.org/doi/10.1103/PhysRevE.109.044205

32. F. Wang *et al.*, Jacobi Stability Analysis and the Onset of Chaos in a Two-Degree-of-Freedom Mechanical System, Int. J. Bifurc. Chaos Appl. Sci. Eng. 31 (2021) 2150075, https://doi.org/10.1142/S0218127421500759

33. Q. Liu and X. Zhang, Jacobi Stability Analysis of Liu System: *Detecting Chaos, Mathematics* **12** (2024), https://doi.org/10.3390/math12131981

34. T. Harko *et al*., Jacobi stability analysis of the Lorenz system, Int. J. Geom. Methods Mod. Phys. **12** (2015) 1550081, https://doi.org/10.1142/S0219887815500814

35. Y. Chen and Z. Yin, The Jacobi Stability of a Lorenz-Type Multistable Hyperchaotic System with a Curve of Equilibria, *Int. J. Bifurc. Chaos Appl. Sci. Eng*. **29** (2019) 1950062, https://doi.org/10.1142/S0218127419500627

36. M. K. Gupta and C. K. Yadav, Jacobi Stability Analysis of Rössler System, *Int. J. Geom. Methods. Mod. Phys.* **27** (2017) 1750056, https://doi.org/10.1142/S0218127417500560

37. H. Abolghasem, Liapunov Stability Versus Jacobi Stability, *J. Dyn. Syst. Geom. Theor.* **10** (2012) 13, https://doi.org/10.1080/1726037X.2012.10698604

38. S. Sabau, Some remarks on Jacobi stability, *Nonlinear Anal. Theory Methods Appl.* **63** (2005) 143, https://doi.org/10.1016/j.na.2005.02.061

39. Y. Cai *et al.*, A numerical solution to the nonlinear point kinetics equations using Magnus expansion, *Ann. Nucl. Energy*. **89** (2016) 84, https://doi.org/10.1016/j.anucene.2015.11.021

Numerical modeling of spin-dependent phase shifts in nucleon-nucleon scattering

P. Sahoo

Department of Physics, Dharanidhar University, Keonjhar, Odisha, 758001, India,
e-mail: nlphy.pati7@gmail.com

Received 7 January 2026; accepted 15 June 2026

Scattering phase shifts for quantum mechanical potential scattering can be derived directly from the scattering amplitude, bypassing the need to solve the Schrödinger equation explicitly. This can be achieved by numerically integrating the phase equation from the origin to the asymptotic limit. The Phase Function Method (PFM) is considered an effective approach for computing scattering phase shifts in quantum mechanics. The PFM is applied to analyze the Pöschl-Teller potential along with spin-orbit interactions. The strategy includes employing a five-parameter potential model to fit the calculated scattering phase shift curves to the established data for elastic scattering phase shifts. Numerical scattering phase shifts for nucleon-nucleon systems align well with prior research results.

Keywords: Phase function method; Pöschl-Teller plus spin-orbit interaction; scattering phase shifts; nucleon-nucleon systems.

DOI: https://doi.org/10.31349/RevMexFis.72.061202

1. Introduction

Researchers have been investigating how to accurately predict the magic numbers by identifying necessary corrections to existing nuclear models. This involves refining potential energy calculations, adjusting interaction strengths among nucleons, and incorporating effects like deformation and pairing interactions. Correcting these potentials helps improve the predictions for the stability and structure of nuclei, especially those far from stability, such as superheavy elements. Advances in theoretical models, along with experimental data from facilities studying exotic nuclei, are crucial for achieving a more comprehensive understanding of nuclear structure and the underlying forces at play. Ultimately, in 1949, Mayer [1], Haxel [2], and their colleagues demonstrated that incorporating a spin-orbit potential could effectively separate the subshells as required. Initially, the concept of spin-orbit coupling was employed by atomic physicists to account for the fine structure observed in spectral lines. This phenomenon occurs as a result of the electromagnetic interaction between the magnetic field produced by electrons orbiting the nucleus and the magnetic moment of the electrons themselves. While electromagnetic spin-orbit effects [3] are generally quite minor, on the order of one part in 10^5 in atomic level spacing, they are insufficient to produce the significant changes in nuclear level spacing needed to explain the observed magic numbers. Consequently, a similar framework is employed to the nuclear potential as used in the atomic spin-orbit concept. One-gluon exchange (OGE) [4] serves as a plausible origin for velocity-dependent potentials, such as spin-orbit coupling, which is evidenced by the significant polarization observed in nucleon-nucleus scattering and the notable splitting between doublet levels explained within the shell model framework. The exact dynamical origin of the strong nuclear spin-orbit force remains unclear [5], but parallels drawn from atomic physics suggest it may be a relativistic effect. Empirical evidence indicates that static (velocity-independent) nuclear potentials predominantly govern interactions at relatively low energies for the incoming particles. However, at elevated energies, the forces are influenced by the relative momentum $P = P_1 - P_2$ of the nucleons. In this context, P_1 and P_2 represent the momenta of the individual nucleons, and based on Galilean invariance, the interaction is solely dictated by their relative motion, rather than their absolute motion at any specific moment during the interaction. Therefore, for two body interaction, the only viable spin-orbit coupling is $V_{SO}(s)((\vec{s}\times\vec{P})\cdot\vec{S})$. In this context, $V_{SO}(s)$ refers to the spin-orbit potential, characterized by a form factor similar to that of the central potential but with distinct parameters, while 's' represents the relative distance between the nucleons. The expectation value of the spin-orbit interaction is proportional to $2 < \vec{L}\cdot\vec{S} >= J(J+1)-L(L+1)-S(S+1)$ where the notations L, S and J stand for the orbital angular momentum, spin angular momentum and the total angular momentum, respectively. Although the spin-orbit potential is traditionally treated as a surface term, being proportional to $\frac{1}{s}\frac{dV}{ds}$ [6–8], its effect is strongest at the nuclear surface because the spin density vanishes inside the nucleus. However, we adapt the Pöschl-Teller [9–15] like spin-orbit term, added with the central Pöschl-Teller potential, hypothesizing that it will take care of the varying effects of the interior and surface of the nucleus with suitable parameterization of the potential. It is also well known that the form of the potential in spin-orbit term $V_{SO}(s)(\vec{L}\cdot\vec{S})$ is not that vital, but it is the $(\vec{L}\cdot\vec{S})$ factor which contributes significantly to reordering the levels. A significant spin-orbit coupling potential appears to be advantageous in explaining high-energy data.

When particles undergo scattering, the manner in which they deflect provides valuable insight into the underlying interaction mechanisms. The outgoing particle effectively encodes information about the forces it has experienced. However, achieving a precise and universally accepted description of the nuclear force remains a significant challenge in

nuclear physics. To reconcile theoretical predictions with experimental observations, many researchers have developed phenomenological models that incorporate various aspects of nucleon-nucleon interactions. The investigation of three-nucleon systems plays a crucial role in advancing our understanding of nuclear forces. Consequently, considerable theoretical and experimental attention has been devoted over the past several decades to studying such systems [16–20]. Extensive efforts have aimed at extracting reliable information about nuclear interactions and accurately describing scattering observables [21–27]. In particular, the inclusion of the Coulomb interaction in three-body calculations has proven to be technically demanding, especially in proton-deuteron scattering. To address this issue, different computational approaches and potential models have been proposed to consistently incorporate electromagnetic effects while preserving the accuracy of nuclear force descriptions. A central quantity in scattering theory is the differential cross-section, which represents the likelihood of scattering into a specific solid angle at a given energy. By examining its angular dependence, along with observables such as analysing powers, one can deduce important characteristics of the interaction, including whether the scattering process is isotropic or exhibits directional preferences. More recently, significant progress has been achieved through the development of nuclear forces based on chiral effective field theory. In particular, work by Epelbaum *et al*. [28] has introduced a new generation of interactions employing semi-local regularization schemes. These studies provide a clear conceptual framework for chiral effective field theory and demonstrate its applicability to two- and few-nucleon systems.

In the realm of non-relativistic quantum scattering theory [29], exploring the energy spectra and wave functions of quantum systems influenced by different potentials is a captivating area of study, as it provides essential insights into the behavior of the system. The Pöschl-Teller [9–15] diatomic molecular potential, introduced by Pöschl and Teller, was designed to model the vibrational excitations in molecular systems. In this study, the Pöschl-Teller potential is employed in the nuclear context to investigate nucleon-nucleon interactions with spin-orbit effect, utilizing the PFM [30] effectively. Several authors [9–15, 29–33] have explored the Pöschl-Teller potential in various quantum mechanical contexts, applying several standard approximation methods to find solutions in both relativistic and non-relativistic frameworks. Using this potential, Dong *et al*. [12] derived the exact solutions of the Schrödinger equation through conventional methods, while Infield *et al*. [34] employed the factorization method for their analysis. Recently, Aktas and Sever [35] as well as Diaz *et al*. [36] explored the supersymmetric solutions of the modified Pöschl-Teller potential. Therefore, the Pöschl-Teller potential presents a compelling option for theoretical physicists, particularly in its applications to molecular dynamics [9–13, 31–33]. Numerous studies have been conducted in this area using the PFM [15, 37–40]. In a relatively recent study, Behera *et al*. [40] investigated nucleon-nucleon and alpha-nucleon elastic scattering within the Manning-Rosen potential, while Sahoo *et al*. [39] examined nucleon-nucleon scattering for F- and G-partial waves using the Hulthén potential, both employing the Phase Function Method effectively. This text focuses on the analysis of nucleon-nucleon phase shifts using the variable phase method [30], which is briefly outlined in Sec. 2. Section 3 presents the results and discussions, while Sec. 4 offers the concluding remarks.

2. Methodology

PFM [30] is a valuable numerical approach that provides a strong alternative to the standard methods used to solve the Schrödinger equation. The methodology relies on the potential transformation of second-order linear homogeneous equations into first-order nonlinear Riccati equations or phase equations, as illustrated below. The function $\delta_\ell(k,r)$, referred to as the phase function, represents the accumulated phase shift at a distance r, effectively modeling the scattering caused by a truncated version of the potential up to that range. If the potential is completely cut off, no phase shift occurs, implying $\delta_\ell(k,r) = 0$. This framework transforms the original second-order linear differential equation into a first-order nonlinear equation-commonly a Riccati-type equation-thereby simplifying the computational treatment of the scattering problem. The radial Schrödinger equation for a given potential $V(r)$ is given as:

$$\frac{d^2}{dr^2}u_l(k,r) + \left[k^2 - \frac{l(l+1)}{r^2}\right] u_l(k,r) = V(r)\, u_l(k,r). \tag{1}$$

We Solve Eq. (1) using PFM, as it is a useful special method to solve the radial Schrödinger equation.

The regular free particle Green's function reads as,

$$G_l(r,r') = \begin{cases} -\frac{1}{k}\left[\hat{j}_l(kr)\,\hat{\eta}_l(kr') - \hat{j}_l(kr')\,\hat{\eta}_l(kr)\right], & r' < r, \\ 0, & r' > r. \end{cases} \tag{2}$$

Using Eq. (2), the solution to Eq. (1) is given by

$$u_l(k,r) = \hat{j}_l(kr) - \frac{1}{k}\,\hat{j}_l(kr)\int_0^r dr'\,\hat{\eta}_l(kr')\,V(r')\,u_l(k,r'), + \frac{1}{k}\,\hat{\eta}_l(kr)\int_0^r dr'\,\hat{j}_l(kr')\,V(r')\,u_l(k,r'). \tag{3}$$

Let

$$S_l(r) = -\frac{1}{k}\int_0^r dr'\,\hat{j}_l(kr')\,V(r')\,u_l(k,r'), \tag{4}$$

$$C_l(r) = 1 - \frac{1}{k}\int_0^r dr'\,\hat{\eta}_l(kr')\,V(r')\,u_l(k,r'). \tag{5}$$

Also, $S_l(r) \xrightarrow{r\to 0} 0$ and $C_l(r) \xrightarrow{r\to 0} 1$. Using Eqs. (4) and (5), Eq. (3) becomes

$$u_l(k,r) = \hat{j}_l(kr)\,C_l(r) - \hat{\eta}_l(kr)\,S_l(r). \tag{6}$$

As

$$\hat{j}_l(kr) \xrightarrow[r\to\infty]{} \sin\left(kr - \frac{l\pi}{2}\right), \quad kr \gg l, \tag{7}$$

$$\hat{\eta}_l(kr) \xrightarrow[r\to\infty]{} -\cos\left(kr - \frac{l\pi}{2}\right), \quad kr \gg l, \tag{8}$$

$C_l(r) \xrightarrow{r\to\infty} C_l(\infty)$ and $S_l(r) \xrightarrow{r\to\infty} S_l(\infty)$.

$$\therefore\ u_l(k,r) \xrightarrow{r\to\infty} C_l(\infty)\,\sin\left(kr - \frac{l\pi}{2}\right) + S_l(\infty)\,\cos\left(kr - \frac{l\pi}{2}\right). \tag{9}$$

However,

$$u_l(k,r) \xrightarrow{r\to\infty} \text{Const.} \times \sin\left(kr - \frac{l\pi}{2} + \delta_l\right) = A\left[\sin\left(kr - \frac{l\pi}{2}\right)\cos\delta_l + \cos\left(kr - \frac{l\pi}{2}\right)\sin\delta_l\right]. \tag{10}$$

From Eqs. (9) and (10)

$$A\left[\sin\left(kr - \frac{l\pi}{2}\right)\cos\delta_l + \cos\left(kr - \frac{l\pi}{2}\right)\sin\delta_l\right] = C_l(\infty)\,\sin\left(kr - \frac{l\pi}{2}\right) + S_l(\infty)\,\cos\left(kr - \frac{l\pi}{2}\right). \tag{11}$$

Equating the coefficient of $\sin(kr - [l\pi/2])$ and $\cos(kr - [l\pi/2])$ on both sides, one gets

$$A\cos\delta_l = C_l(\infty), \tag{12}$$

$$A\sin\delta_l = S_l(\infty), \tag{13}$$

which gives

$$\tan\delta_l = \frac{S_l(\infty)}{C_l(\infty)}. \tag{14}$$

Hence the knowledge of the asymptotic limit of $S_l(\infty)$ and $C_l(\infty)$ gives an idea about the tangent of scattering phase shifts. Let us define a new function

$$t_l(r) = \frac{S_l(r)}{C_l(r)}. \tag{15}$$

From Eqs. (4) and (5), it is clear that $t_l(r)$ vanishes at $r \longrightarrow 0$. At the same time asymptotic behaviour of $t_l(r)$ gives the value of tangent of scattering phase shifts

$$\lim_{r\to\infty} t_l(r) = t_l(\infty) = \tan\delta_l. \tag{16}$$

From Eq. (4)

$$S_l'(r) = -\frac{1}{k}\,V(r)\,\hat{j}_l(kr)\,u_l(k,r), \tag{17}$$

and

$$C_l'(r) = -\frac{1}{k}\,V(r)\,\hat{\eta}_l(kr)\,u_l(k,r). \tag{18}$$

Differentiating Eq. (15) and substituting Eqs. (17) and (18),

$$\frac{d}{dr}\left(\frac{S_l(r)}{C_l(r)}\right) = \frac{C_l(r)\,S_l'(r) - S_l(r)\,C_l'(r)}{C_l^2(r)}, \tag{19}$$

we get,

$$t_l'(r) = -\frac{1}{k}\,V(r)\left[\hat{j}_l(kr) - t_l(r)\,\hat{\eta}_l(kr)\right]^2. \tag{20}$$

Again,

$$t_l(r) = \tan\delta_l. \tag{21}$$

Differentiating Eq. (21), we get,

$$t_l'(r) = \frac{\delta_l'(r)}{\cos^2\delta_l(r)}. \tag{22}$$

Substituting Eq. (22) in Eq. (20), we get,

$$\delta_\ell'(k,r) = -k^{-1}V(r) \times [\cos\delta_\ell(k,r)\hat{j}_\ell(kr) - \sin\delta_\ell(k,r)\hat{\eta}_\ell(kr)]^2, \tag{23}$$

where $\hat{j}_\ell(kr)$ and $\hat{\eta}_\ell(kr)$ are the Riccati-Bessel functions [41]. The resulting phase equations [30, 41] for $\ell = 0, 1$ and 2 read as

$$\delta_0'(k,r) = -k^{-1}V(r)[\sin(\delta_0(k,r) + kr)]^2, \tag{24}$$

$$\delta_1'(k,r) = -\frac{V(r)}{k^3r^2}\left[\sin(\delta_1(k,r) + kr) - kr\cos(\delta_1(k,r) + kr)\right]^2, \tag{25}$$

and

$$\delta_2'(k,r) = -k^{-1}V(r)\left[(\frac{3}{k^2r^2} - 1)\sin(\delta_2(k,r) + kr) - \frac{3}{kr}\cos(\delta_2(k,r) + kr)\right]^2. \tag{26}$$

Here, k represents the center of mass momentum, which is related to the center of mass energy E as $k = \sqrt{2\mu E/\hbar^2}$. The term $\delta_\ell(k,r)$ is referred to as the phase function, which satisfies the phase equation described in Eq. (1). This represents the phase shift of the wave function as it scatters off the potential at each point, ultimately truncated at a distance 'r'. With the initial condition provided, the phase equations described by Eqs. (2-4) are solved numerically for the potential under consideration to align the scattering phase shifts across various states with the established data.

The effective Pöschl-Teller potential [9–15] in all partial waves is written as

$$V_{PT}(r) = \frac{V_1 - V_2\cosh(\alpha r)}{\sinh^2(\alpha r)} + \frac{\ell(\ell+1)}{r^2}, \tag{27}$$

and the effective spin orbit coupling is taken as

$$V_{SO}(r) = \frac{V_1' - V_2'\cosh(\alpha r)}{\sinh^2(\alpha r)}(\vec{L}\cdot\vec{S}). \tag{28}$$

$$\tag{29}$$

The effective equivalent nuclear potential under investigation for uncharged hadrons is thus

$$V(r) = V_{\rm PT}(r) + V_{\rm SO}(r). \tag{30}$$

$$\tag{31}$$

The strength parameters V_1, V_2, V_1', V_2' of the total potential $V(r)$ have the unit of fm^{-2} and α is the inverse range parameter with dimension of fm^{-1}. To address charged hadron systems, it is necessary to incorporate an electromagnetic interaction alongside the nuclear potential

$$V(r) = V_{\rm PT}(r) + V_{\rm SO}(r) + V_C(r). \tag{32}$$

$$\tag{33}$$

The pure Coulomb potential theoretically allows for an infinite range of interaction. However, in practice, it becomes screened beyond a certain distance, rendering the Coulomb potential negligible after a finite range. Motivated by this the electromagnetic potential is taken as screened atomic Hulthén potential [42–45]

$$V_C(r) = V_0 \frac{\exp(-r/a)}{[1-\exp(-r/a)]}, \tag{34}$$

with V_0, the strength and a , the screening radius of the potential with $V_0 a = 0{,}03472 fm^{-1}$ for nucleon-nucleon systems.

3. Results and discussion

The parameterization of the nuclear Pöschl-Teller potential, including the spin-orbit term as outlined in Eqs. (29) and (30), to match the available standard phase parameters [46] for various states of the (n-p) and (p-p) systems through the numerical solution of the differential equations (24-26). The best fitted parameters for the (n-p) and (p-p) systems across various states is presented in Table I.

TABLE I. List of parameters for (n-p) system.

States	α	V_1	V_2	V_1'	V_2'
$^3P_0$	0.92	9.02	11.25	0.50	2.70
$^3P_1$	2.24	4.35	0.15	0.08	15.60
$^3P_2$	0.96	9.25	8.89	0.51	1.27
$^3D_1$	2.03	8.65	2.05	1.85	6.70
$^3D_2$	0.96	2.031	32.065	8.05	18.27
$^3D_3$	1.26	6.36	8.65	18.69	31.35

TABLE II. List of parameters for (p-p) system.

States	α	V_1	V_2	V_1'	V_2'
$^3P_0$	0.86	9.05	8.92	0.5	1.70
$^3P_1$	2.46	4.34	0.17	0.08	15.50
$^3P_2$	0.82	10.08	0.82	2.02	2.29

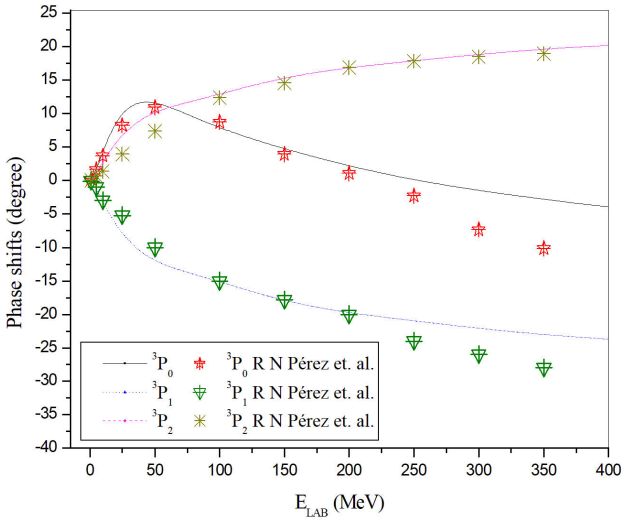


FIGURE 1. Variation of (n-p) P-wave scattering phase shifts with laboratory energy.

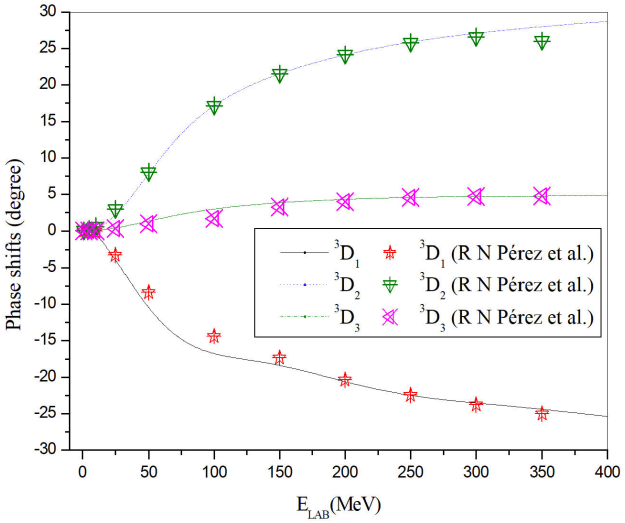


FIGURE 2. Variation of (n-p) D-wave scattering Phase shifts with laboratory energy.

For numerical adjustments of the phase shift results, we have utilized $\hbar^2/2\mu = 41{,}47$ MeV fm^2 specific to the (n-p) and (p-p) systems, respectively. Here, μ denotes the reduced mass of the corresponding systems. In this article, we examine the scattering phase shifts for neutron-proton (n-p)

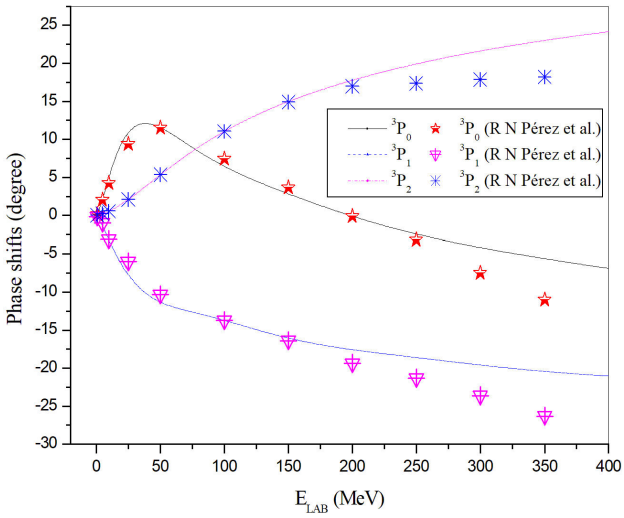


FIGURE 3. Variation of (p-p) P-wave scattering phase shifts with laboratory energy.

and proton-proton (p-p) interactions for angular momenta $\ell = 1\,\&\,2$. Figures 1-3 illustrate the computed phase shift values in comparison with the established results [46] for various (n-p) and (p-p) triplet scattering states, as detailed in Tables I and II. As shown in Figs. 1 and 2, the analysis for the P- and D-wave states in the (n-p) system aligns well with the established phase parameters up to a laboratory energy of 350 MeV, closely matching the findings of Perez *et al.* [46]. The phase parameters for p-p scattering, as depicted in Fig. 3, show strong agreement with the results of Perez *et al.* [46] up to a laboratory energy of 350 MeV. The strength parameters for the p-p triplet states $^3P_0$, $^3P_1$ and $^3P_2$ are kept consistent with those of the n-p states $^3P_0$, $^3P_1$ and $^3P_2$. A slight adjustment has been introduced for the inverse range parameter 'α' leading to minor effects on both the central nuclear and spin-orbit terms, but the changes are not considerable. The strength values remain unchanged because the nuclear force treats n-p and p-p interactions similarly, considering both neutrons and protons as equivalent nucleons. Therefore, it is reasonable to expect analogous parameterization of the strong nuclear environment for two-nucleon interactions in similar states, regardless of their charge. However, the Coulomb force is relevant for p-p interactions, and we have addressed this by incorporating additional Coulomb terms into the existing nuclear and spin-orbit terms, as shown in Eq. (8). As the nuclear potential is greatly influenced by spin and varies with different states, it is necessary to individually parameterize each state of the P and D waves in n-p interactions and the P-wave states in p-p interactions to accurately reflect the real inter-nucleon interaction field.

We assessed the goodness of fit by computing the χ^2 per degree of freedom (reduced χ^2 values) for different states in the n-p and p-p systems, considering (8-5) = 3 degrees of freedom. The calculated reduced χ^2 values for the $^3P_0$, $^3P_1$, $^3P_2$,$^3D_1$,$^3D_2$,$^3D_3$ states of the n-p system are 0.684, 0.923, 0.527, 0.125, 0.571, and 1.186, respectively. For the p-p system, the reduced χ^2 values for $^3P_0$, $^3P_1$ and $^3P_2$states are 0.812, 0.136, and 1.136, respectively. Overall, these reduced chi-square values are either below or around 1, suggesting that the model provides a good fit to the standard data for all states of the n-p and p-p systems. Also, we have verified the R-square values for different states which are close to unity. Thus, the inclusion of the Pöschl-Teller and Pöschl-Teller like spin-orbit interaction successfully modifies the phase shifts to match the established data [46] for the n-p and p-p systems, demonstrating the robustness and reliability of this approach. As the energy increases, the probability of the projectile accessing the nuclear range of interaction also grows, allowing for a more pronounced spin-orbit effect, which is crucial for accurately modelling the real nuclear phenomenological field. Beyond 200 MeV the phase parameters for $^3P_0$, $^3P_1$ and $^3P_2$ states differ from those of standard values by maximum of 6 degree. It is argued that the discrepancy in phase shifts at higher energies is largely reduced if the short-range part of the LS force in the nucleon-nucleon potential is modified. Since nucleon- nucleon scattering at energies below 15 MeV is almost purely S-wave scattering which arises from the interference between S- and P-waves, is very small. Contrarily, the P-wave nucleon-nucleon interactions are very important in scattering and PJ state contribution [47–49] must be included. The lack of PJ state in the proposed potential employed in this calculation may be the cause of the discrepancies in the phase parameters beyond 200 MeV.

At higher incident energies near 200 MeV, a reversal of the phase shift for the $^3P_0$ state is evident in both (n-p) and (p-p) scattering in Figs. 1 and 3, implying the influence of a repulsive hardcore.

4. Conclusion

This study tests the phase shift analysis of charged and uncharged nucleon-nucleon interactions in the context of the Pöschl-Teller [9–15] plus Pöschl-Teller like spin-orbit interaction field [Eq. 6], focusing on higher incident particle energies up to 350 MeV and higher partial waves using phase function methodology [30]. Using a five-parameter potential, we achieve excellent fitting of the phase shift parameters for all P-wave and D-wave triplet states in n-p scattering, as well as for the P-wave triplet states in p-p scattering, in line with the results of [46]. The reduced χ^2 values suggest that the quality of the adjustment is quite satisfactory. This confirms that the model effectively calibrates the phase shifts for both n-p and p-p systems. The results demonstrate that high-energy scattering data up to 350 MeV can be interpreted if the nuclear interaction exhibits two main traits: a robust spin-orbit coupling possibly in the outer region, similar to the exchange character of pion theoretical potential, along with a hard-core-like repulsive force in the inner region. Encouraged by the success of this work, I am motivated to advance to the calculation of polarization effects for scattered particles with unpolarized incident and target particles. Nonetheless, assessing polarization will involve calculating the phase parameters for the triplet state ($^3S_1$ state), despite the absence of any spin-orbit

contribution for this particular state. I am eager to explore spin-orbit coupling, particularly through the incorporation of second-order momentum approximations.

Data availability statement

The author declares that the data supporting the findings of this study are available within the paper.

Funding

There is no funding source for this work.

Conflict of interest

The author declares that there exists no competing financial interest or personal relationships that could have appeared to influence the work reported in this paper.

1. M. G. Mayer, On closed shells in nuclei, *Physical Review* **74** (1948) 235.
2. O. Haxel, J. H. D. Jensen, and H. E. Suess, On the "Magic Numbers" in Nuclear Structure, *Physical Review* **75** (1949) 1766-1766, https://doi.org/10.1103/physrev.75.1766.2
3. K. Krane, Introductory Nuclear Physics (Wiley John Sons, New York, 1988).
4. H. Hong-Xia, *et al*., Influence of Spin-Orbit Force on Nucleon-Nucleon Scattering in the Quark Delocalization Colour Screening Model, *Chinese Physics Letters* **25** (2008) 1617-1620, https://doi.org/10.1088/0256-307x/25/5/026
5. N. Kaiser, Nuclear spin-orbit interaction from chiral pion-nucleon dynamics, *Nuclear Physics A* **709** (2002) 251-274, https://doi.org/10.1016/s0375-9474(02)01044-8
6. M. Sajedi and Z. Kargar, Shifted Deng-Fan potential and cluster structure in 19Ne, *Nuclear Physics A* **1015** (2021) 122314, https://doi.org/10.1016/j.nuclphysa.2021.122314
7. L. Kumar, A. Khachi, and O. Sastri, Phase Shift Analysis for Neutron-Alpha Elastic Scattering Using Phase Function Method with Local Gaussian Potential, Journal of Nuclear Physics, Material Sciences, *Radiation and Applications* **9** (2022) 215-221, https://doi.org/10.15415/jnp.2022.92032
8. F. Brieva and J. Rook, Nucleon-nucleus optical model potential, *Nuclear Physics A* **297** (1978) 206-230, https://doi.org/10.1016/0375-9474(78)90272-5
9. G. Poschl and E. Teller, Bemerkungen zur Quantenmechanik des anharmonischen Oszillators, *Zeitschrift fur Physik* **83** (1933) 143-151, https://doi.org/10.1007/bf01331132
10. G.-F. Wei and S.-H. Dong, The spin symmetry for deformed generalized Pöschl-Teller potential, *Physics Letters A* **373** (2009) 2428.
11. Y. You, *et al*., Solutions of the Second Pöschl-Teller Potential Solved by an Improved Scheme to the Centrifugal Term, *Few-Body Systems* **54** (2013) 2125-2132, https://doi.org/10.1007/s00601-013-0725-y
12. S. H. Dong and J. Garcia Ravelo, Exact solutions of the Schrodinger equation with the second poschl-teller-like potential, *Modern Physics Letters B* **23** (2009)
13. S. H. Dong, W. C. Qiang, and J. Garcia Ravelo, Analytical approximations to the Schrödinger equation for a second Pöschl-Teller-like potential with centrifugal term, *International Journal of Modern Physics A* **23** (2008) 1537
14. P. Sahoo, Evaluation of n-p and n-d Analyzing Powers Through the Jost Formalism, Brazilian Journal of Physics 54 (2023)
15. P. Sahoo and U. Laha, Phase shift and cross section analysis of nucleon-nucleon and nucleon-nucleus scattering using second Pöschl-Teller potential, *Canadian Journal of Physics* **101** (2023) 441-452
16. L. D. Faddeev, Scattering Theory for a Three-Particle System, *Sov. Phys. JETP* **12** (1961) 1014.
17. E. Alt, P. Grassberger, and W. Sandhas, Reduction of the three-particle collision problem to multi-channel two-particle Lippmann-Schwinger equations, *Nuclear Physics B* **2** (1967) 167-180, https://doi.org/10.1016/0550-3213(67)90016-8
18. K. Sekiguchi, *et al*., Resolving the Discrepancy of 135 MeV P-D Elastic Scattering Cross Sections and Relativistic Effects, *Physical Review Letters* **95** (2005), https://doi.org/10.1103/physrevlett.95.162301
19. E. Stephan, *et al.*, Vector and tensor analyzing powers in deuteron-proton breakup at 130 MeV, *Physical Review C* **82** (2010), https://doi.org/10.1103/physrevc.82.014003
20. S. Kistryn, *et al*., Evidence of three-nucleon force effects from 130mev deuteron-proton breakup cross section measurement, *Physical Review C* **68** (2003), https://doi.org/10.1103/physrevc.68.054004
21. S. Ishikawa, Low-Energy Proton-Deuteron Scattering with a Coulomb-Modified Faddeev Equation, *Few-Body Systems* **-1** (2003) 1-1, https://doi.org/10.1007/s00601-003-0001-7
22. A. Deltuva, A. C. Fonseca, and P. U. Sauer, Momentumspace treatment of the Coulomb interaction in three-nucleon reactions with two protons, *Physical Review C* **71** (2005), https://doi.org/10.1103/physrevc.71.054005
23. A. Deltuva, *et al*., Benchmark calculation for proton-deuteron elastic scattering observables including the Coulomb interaction, *Physical Review C* **71** (2005), https://doi.org/10.1103/physrevc.71.064003
24. P. Sahoo, U. Laha, and A. K. Behera, p-C12 and pd Scattering within the Separable Model of Interaction, *Physics of Atomic Nuclei* **83** (2020) 802-810, https://doi.org/10.1134/s1063778820660072

25. P. Sahoo, U. Laha, and B. Khirali, On the p-d and po16 elastic scattering, *Pramana* **95** (2021), https://doi.org/10.1007/s12043-021-02188-9

26. B. Swain, *et al*., Phase function method for Hulthén-distorted separable non-local potentials in all partial waves, *Pramana* **96** (2022), https://doi.org/10.1007/s12043-022-02410-2

27. B. Swain, U. Laha, and A. K. Behera, Low and intermediate energy cross section analysis of p-p and p-d elastic scattering using modified phase amplitude method for electromagnetic distorted nuclear interaction, *Physica Scripta* **98** (2023) 105308, https://doi.org/10.1088/1402-4896/acfb47

28. E. Epelbaum, H. Krebs, and P. Reinert, High-precision nuclear forces from chiral EFT: State-of-the-art, challenges, and outlook, *Frontiers in Physics* **8** (2020) 98

29. R. G. Newton, Scattering theory of waves and particles., 2nd ed. (Springer Verlag, New York, NY, 1982).

30. F. Calogero, Variable Phase Approach to Potential Scattering by F Calogero, Mathematics in Science and Engineering (Elsevier Science, 1967), https://books.google.co.in/books?id=fmjuIREIN8gC.

31. D. Agboola, Solutions to the modified Pöschl-Teller potential in D-dimensions, *Chinese Physics Letters* **27** (2010) 040301.

32. M. Hamzavi and A. Rajabi, Exact S-wave solution of the trigonometric pöschl-teller potential, *International Journal of Quantum Chemistry* **112** (2012) 1592.

33. S. H. Dong and A. Gonzalez Cisneros, Energy spectra of the hyperbolic and second Pöschl-Teller like potentials solved by new exact quantization rule, *Annals of Physics* **323** (2008) 1136.

34. L. Infeld and T. E. Hull, The Factorization Method, *Reviews of Modern Physics* **23** (1951) 21-68.

35. M. Aktas and R. Sever, Exact supersymmetric solution of Schrödinger equation for central confining potentials by using the Nikiforov-Uvarov method, *Journal of Molecular Structure: Theochem* **710** (2004) 223.

36. J. I. Díaz, *et al*., The supersymmetric modified Pöschl-Teller and delta well potentials, *Journal of Physics A: Mathematical and General* **32** (1999) 8447-8460.

37. B. Khirali, *et al*., Phase function metod for elastic nucleon-nucleon scattering using Hellmann plus Coulomb potential, *Rev. Mex. Fis.* **69** (2023), https://doi.org/10.31349/revmexfis.69.061201

38. B. Khirali, *et al*., Numerical phase shift analysis of nucleonnucleon systems with Hellmann plus spin dependence, *Rev. Mex. Fis.* **71** (2025), https://doi.org/10.31349/revmexfis.71.031202

39. P. Sahoo, *et al*., Nuclear Hulthen potentials for F and G Partial waves Research & Reviews, Research Reviews: *J. Phys* **10** (2021) 31.

40. A. K. Behera, *et al*., Study of nucleon-nucleon and alphanucleon elastic scattering by the Manning-Rosen potential, *Communications in Theoretical Physics* **72** (2020) 075301, https://doi.org/10.1088/1572-9494/ab8a1a

41. G. N. Watson, A treatise on the theory of Bessel functions, vol. 3 (The University Press, 1922).

42. P. SAHOO, *et al*., THE ANALYTIC T-MATRIX FOR THE HULTHÉN POTENTIAL IN ALL PARTIAL WAVES, *Reports on Mathematical Physics* **88** (2021) 295-311, https://doi.org/10.1016/s0034-4877(21)00082-3

43. P. Sahoo, U. Laha, and B. Khirali, Hulthén off-shell transition matrix for nuclear systems, *Chinese Journal of Physic*s **73** (2021) 561-568, https://doi.org/10.1016/j.cjph.2021.07.008

44. P. Sahoo and U. Laha, Treatment of hadronic systems involving two potentials under a new approximation scheme, *Pramana* **96** (2022) 15.

45. P. Sahoo and U. Laha, Exact solutions of the Schrödinger equation for Manning-Rosen plus Yamaguchi potential, *Physica Scripta* **96** (2021) 095302, https://doi.org/10.1088/1402-4896/ac07b8

46. R. N. Pérez, J. E. Amaro, and E. R. Arriola, The low-energy structure of the nucleon-nucleon interaction: statistical versus systematic uncertainties, *Journal of Physics G: Nuclear and Particle Physics* **43** (2016) 114001, https://doi.org/10.1088/0954-3899/43/11/114001

47. J. L. Friar, *et al*., Benchmark solutions for n-d breakup amplitudes, *Physical Review C* **51** (1995) 2356-2359, https://doi.org/10.1103/physrevc.51.2356

48. A. Kievsky, M. Viviani, and S. Rosati, Cross section, polarization observables, and phase-shift parameters in p-d and nd elastic scattering, *Physical Review C* **52** (1995) R15-R19, https://doi.org/10.1103/physrevc.52.r15

49. A. Kievsky, M. Viviani, and S. Rosati, scattering above the deuteron breakup threshold, *Physical Review C* **56** (1997) 2987-2991, https://doi.org/10.1103/physrevc.56.2987

Testing the effects of ultraviolet radiation on biological samples using laser interferometry

G. Frausto-Rea and M. del S. Hernández-Montes
Centro de Investigaciones en Óptica, A.C.,
Loma del Bosque 115, Col. Lomas del Campestre, León, Guanajuato, 37150, México.

Received 13 October 2025; accepted 27 July 2026

Laser interferometry is used to analyze biological samples non-invasively before and after exposure to ultraviolet B (UVB) radiation. The objective is to ascertain the damage induced by this type of radiation by quantifying displacements across the entire surface of the samples. The analysis of those displacements, with a resolution of a few micrometers, is presented. Displacements are induced by applying a sound load to the sample with and without radiation. The results are displayed as fringe patterns and displacement maps, where changes caused by UVB radiation exposure can be observed. It was found that displacement values decrease and fringe patterns change slightly due to the radiation. Displacement data is useful as it is an indicator of the biological sample's elasticity. This work contributes to the understanding of the impact of UVB irradiation on sample elasticity, which can be assessed non-invasively.

Keywords: Radiation; ultraviolet; laser interferometry; fringe patterns; displacements.

DOI: https://doi.org/10.31349/RevMexFis.72.061301

1. Introduction

The sun energy, or solar energy, which is present on Earth as electromagnetic radiation. The electromagnetic spectrum encompasses different wavelengths, which can be divided mainly into visible (400 to 700 nm), infrared (750 nm to 1 mm), and ultraviolet (200 to 400 nm), the latter of which is considered in this paper. In turn, the ultraviolet range can be divided into three types: UVA, UVB, and UVC. In the case of UVC and much of the UVB spectrum, radiation is absorbed by the atmosphere ozone layer. However, UVA radiation passes through the ozone layer and reaches the Earth's surface. Due to the deterioration of the ozone layer in recent years [1-4], there has been an increase in UVB radiation on Earth, leading to various problems for living beings [5-7]. Alterations in mechanical properties due to exposure to ultraviolet radiation have been demonstrated in synthetic materials and biological tissues. Some studies have shown that in both natural and synthetic materials, such as Glass/polyester composite, poly methyl methacrylate (PMMA), epoxy laminate, and elastic material, among others, distinct changes in their mechanical properties can be attributed to UV radiation [8-12]; for example, in the case of PMMA, exposure to ultraviolet light caused surface damage that made mechanical parameters degrade, as was the case of strength and strain at rupture [13]. Regarding biological tissues, specifically porcine skin, samples were subjected to two different doses of UV radiation which were high and lasted for prolonged periods, and were then analyzed to obtain the rigidity coefficients before and after radiation, resulting in a loss of skin elasticity [14]. Focusing on humans, high exposure to UVB rays can cause various skin problems, such as premature aging, darkening or burns, and in the long term, it could lead to skin cancer [15-20]. On the other hand, it should be noted that UVA radiation is used to treat certain dermatological diseases such as psoriasis, atopic dermatitis and mycosis fungoides, among others [21-25], or for aesthetic purposes, such as in tanning beds [26-28]. In such cases, the radiation is used while taking precautions with regard to the duration of exposure to solar radiation. It is important to be able to analyze changes to the skin, primarily caused by UVB radiation, and there are multiple options to do so. One is the use of non-invasive optical techniques, such as confocal laser microscopy [29, 30], optical coherence tomography [31-36], digital holographic interferometry (DHI) and digital speckle pattern interferometry (DSPI) [37-39]. At present, laser interferometry is a non-destructive and non-invasive optical technique that allows a sample to be analyzed without manipulation. This ensures that the measurements are not altered, thus producing highly accurate results. Laser interferometry uses the phenomenon of interference and monochromatic light sources, such as lasers, to measure displacements, deformations, shapes, vibrations, distances, and refractive indices, among other parameters. It is important to note that laser interferometry is a two-state technique. This means that it is necessary to capture an image without deformation and/or load, which is called a reference, and a second image with a disturbed state (with a modification in the sample). In the present study, we propose using an optical interferometric technique to examine a biological sample before and after exposure to UVB radiation in order to demonstrate its elasticity variations. We will present images of the optical phase, as well as the quantification of the displacements and the change in fringe patterns. Changes in displacement are used to indicate the variation in elasticity that the sample undergoes due to radiation.

2. Optical method and experimental setup

Laser interferometry is a non-destructive optical technique that allows one to analyze a sample without manipulation, yielding highly accurate measurements. To analyze the biological sample, an optical setup based on laser interferometry was required. Figure 1 shows the optical configuration based on the interference phenomenon. The optical configuration includes a Cobolt Samba laser source with a wavelength of 532 nm, and a power output of 1 W. The laser beam is directed towards a beam splitter (BS), which separates it into two beams: the reference beam and the object beam. To avoid illumination loss, both beams are coupled to single-mode optical fibers (FO1 and FO2). The object beam's optical fiber output (FO2) illuminates the sample under study. The backscattered light is collected by an aperture and lens system, and then sent to a combiner cube (CC), where it is merged with the reference beam (FO1). The two beams are then recombined, producing wave superposition and generating an interference pattern [40-43], and the overlap of those two beams is captured by the camera sensor; the camera used was a PCO pixelfly with a resolution of 800 x 600 pixels. To perform the interferometric measurements, an acoustic load (sinusoidal sound waves) was applied to the sample by placing a loudspeaker behind it [44]. This was controlled by a function generator (GF), which allowed controlling the type of signal, as well as the frequency, amplitude and phase, see Fig. 1. In order to discover the characteristic vibration modes in response to the application of sound load, a frequency sweep was performed on the sample, and with the help of a homemade interface, it was possible to visualize its behavior and identify the vibration modes in real time to confirm that the sample was responding effectively. This stage of the experiment was vital in order to obtain the fringe patterns in response to sound and observe the changes due to the UVB radiation.

To record a digital speckle pattern or hologram, the object and reference beams must be recorded simultaneously on the camera sensor using the setup shown in Fig. 1. The intensity of the recorded hologram can be expressed as follows:

$$I(x,y) = a(x,y) + b(x,y)cos[\Delta\phi(x,y)]. \tag{1}$$

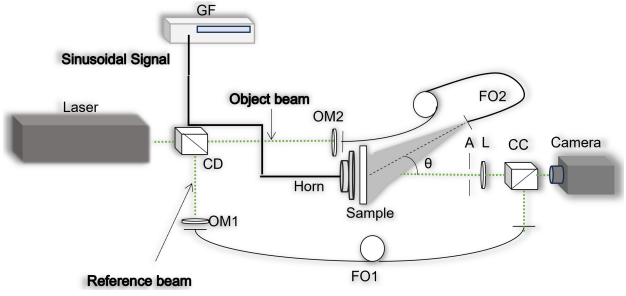


FIGURE 1. Optical setup.

where a, b y $\Delta\phi$ are the background signal, modulation and phase difference, respectively. The latter contains information about the object under study in the form of interference patterns.

In order to find out the fringe vibration pattern of the sample, *i.e.*, to identify its characteristic vibration mode, the sample was subjected to acoustic sound from the rear. To achieve this, it was necessary to record two holograms: one without (I_R) and another with (I_V) the acoustic load. Here, I_R is the so-called reference hologram, which is subtracted from I_V in order to obtain the fringe pattern, showing the intensity modulation by means of:

$$I_F = |I_V - I_R| \tag{2}$$

Subsequently, the optical phase can be recovered from the fringe patterns using the spatial carrier method, which involves the Fourier transform [45-47]. To quantify the displacements $(w(x,y))$ on a micrometric scale the next relationship is used,

$$w(x,y) = \frac{\lambda}{2\pi(1+cos\theta)}\Delta\varphi \tag{3}$$

where $\Delta\varphi$ is the unwrapped optical phase difference, λ is the wavelength of the illumination source used in the optical system, and θ is the illumination angle existing between the observation and illumination directions.

It is important to note that the above process is followed to study samples with and without the exposure to UVB radiation.

3. Results and analysis

Numerous tests were performed to corroborate the repeatability of the process. It is important to note that the biological sample had an uneven thickness and a diameter of 20 mm, which it was placed in an optomechanical circular support. As mentioned before, a frequency sweep was performed to identify the resonant frequencies of the sample, and an interesting finding was that more than two vibration modes were identified, which points to the elasticity of the sample. Before the exposure to UV radiation, the sample was placed in the position displayed in Fig. 1, and two images were captured: one before and another after the application of sound to the sample; it is important to note that the same process is to be followed when UV radiation is applied to the sample.

First, the first vibration mode was obtained using Eq. (2); subsequently, the wrapped phase, unwrapped phase, and displacement maps are obtained [48-53]. Figure 2a) presents the fringe pattern obtained at a frequency of 850 Hz before the application of radiation, while Fig. 2b) shows the fringe pattern when the sample was subjected to a UVB radiation dose of 0.0014 J/cm^2. The vibration frequency of the first mode of the sample remained the same, but it is noticeable that the vibration pattern underwent minor changes, such as a slight rotation of the fringe observed in Fig. 2a), *i.e.*, the

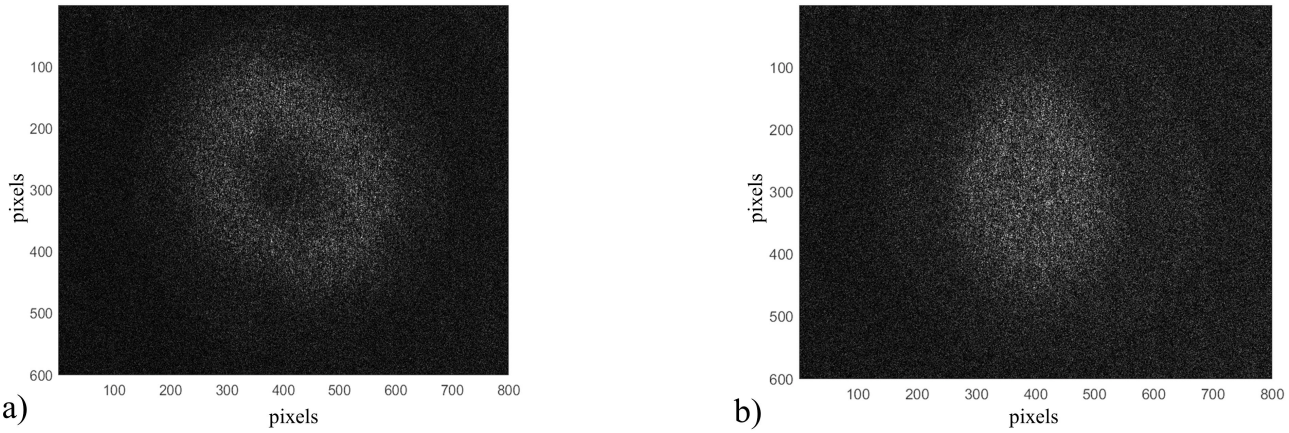


FIGURE 2. Vibration pattern to 850 Hz for the biological sample: a) before and b) after UVB radiation. A slight modification in the fringe pattern is noticeable.

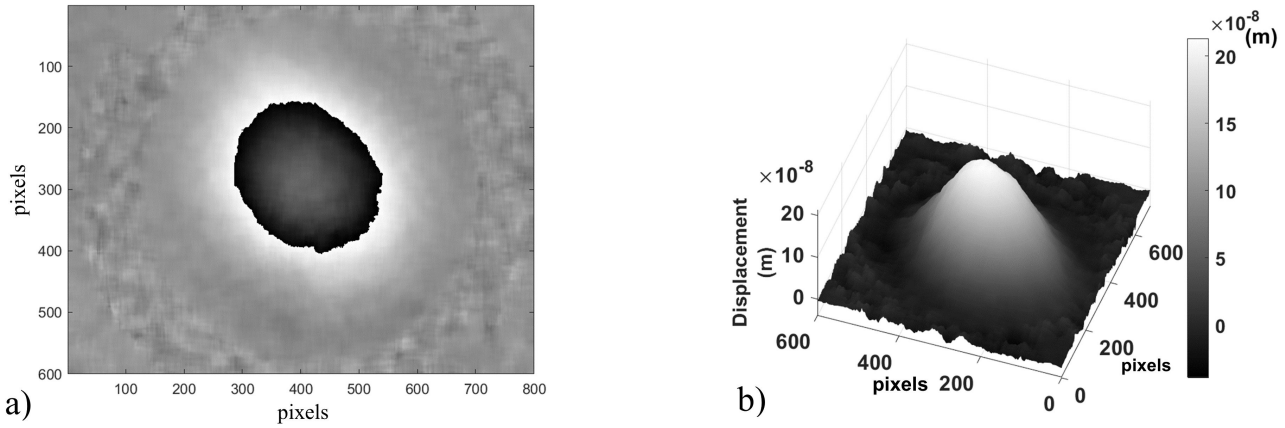


FIGURE 3. Biological sample before UVB radiation, a) wrapped phase and b) displacement map.

fringe appears slightly tilted. In addition, the fringe in Fig. 2a) has dark and bright fringes, while in Fig. 2b) only a bright fringe is visible. This finding suggests that, under the same sound load conditions, the initiation of fringe formation occurs prior to the onset of visible signs of damage, thereby providing an indirect indication of sample elasticity loss after radiation.

A Fourier transform method was applied to the images shown in Fig. 2 to obtain the object's optical phase information; Fig. 3a) presents the wrapped phase, and the displacement map is displayed in Fig. 3b). It is important to mention that the images in Fig. 3 were obtained without using UVB radiation. Meanwhile, Fig. 4 presents the results after the sample had been irradiated; Figs. 4a) and 4b) present the wrapped phase and the displacement map, respectively. To obtain the displacement map shown in Figs. 3b) and 4b), Eq. (3) was used, which depends on the value of λ used, the value of the angle between the observation and illumination directions, θ measured in the optical array, and the unwrapped phase map, $\Delta\varphi$; from these maps, the maximum displacements of the object before and after the application of the radiation dose were obtained and used to construct Table I. The displacement value decreased after UVB irradiation indicating that the sample loses elasticity, *i.e*. the sample is more rigid than at the beginning of the test, when it was in its initial state (without radiation). The displacement value decreased after UVB irradiation, indicating that the sample lost elasticity, *i.e.*, the rigidity increased in the sample compared to the data obtained in its initial state (without radiation).

Analyzing Figs. 3a) and 4b), slight changes in the wrapped phase map are observed. For example, in Fig. 3a), the black fringe is oval and tilted shape, while in Fig. 4a) the dark fringe is smaller than the fringe in Figs. 3a) and it is not tilted. Furthermore, the scale bar in Fig. 3b) is a bit larger compared to Fig. 4b), indicating that the displacement value decreased when the biological sample was subjected to UV radiation, and this is confirmed with the data of Table I, where the maximum displacement of the sample irradiated with UV

TABLE I. Maximum displacement for the first vibration mode found at 850 Hz.

Without UVB radiation	With UVB radiation
$0{,}210 \pm 0{,}015$ μm	$0{,}160 \pm 0{,}010$ μm

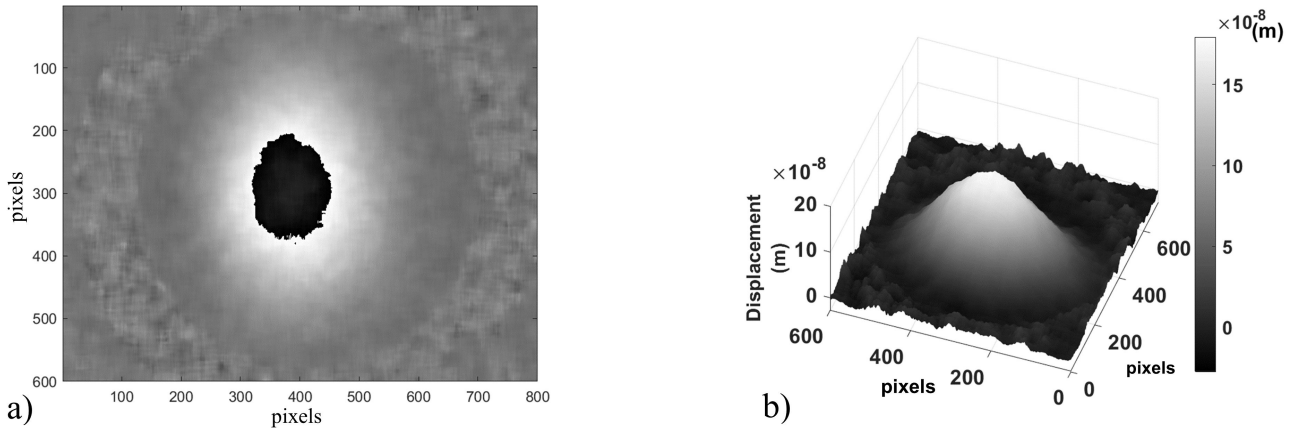


FIGURE 4. Biological sample after application of a UVB radiation dose of 0.0014 J/cm^2, a) wrapped phase and b) displacement map.

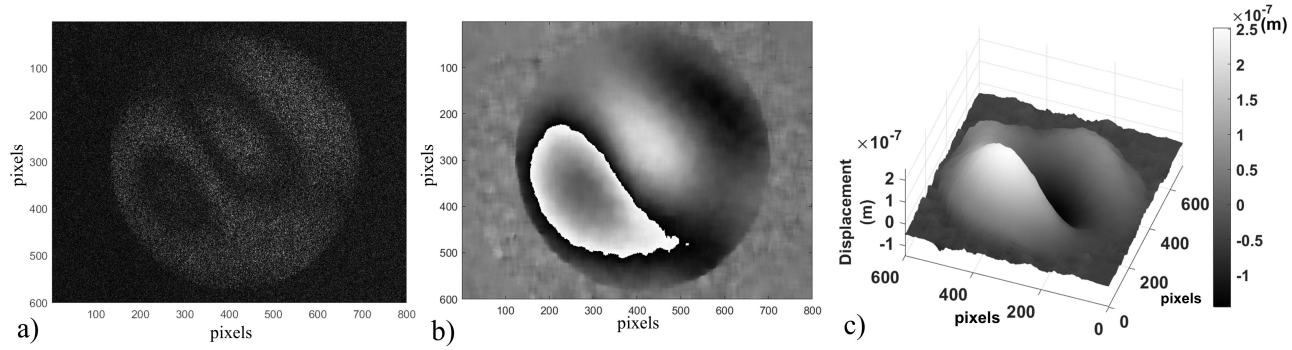


FIGURE 5. Biological sample at a frequency of 1 kHz and without UVB radiation, a) vibration pattern, b) wrapped phase, and c) displacement map.

rays is lower than that of the sample without UV radiation. This assertion is substantiated by the data presented in Table I, which reveals that the maximum displacement of the UVB-irradiated sample is less pronounced than that of the sample not exposed to UVB radiation.

On the other hand, it is important to note that the difference of displacement between sample data with and without UVB radiation is small, exactly $0{,}05 \pm 0{,}018$ μm, due to the low dose of UVB radiation applied to the tissue. If the UVB radiation had been higher, the difference in displacement would have been greater, which could indicate greater damage caused by radiation.

According to the literature, the increased rigidity in biological tissue is associated with higher frequencies and, consequently, lower displacements. Conversely, softer or elastic skin results in lower frequencies, and therefore, greater deformations. Viscoelasticity also plays a role in the tests, as it dampens the sinusoidal signal, leading to modifications in the vibration modes. Another important factor is tissue hydration; as the sample dehydrates, it loses elasticity, which increases its stiffness [54-58]. Thus, after irradiation of the sample with UVB rays, a change occurred in the biological tissue that caused dehydration and/or aging, which caused the displacement values to change for the same frequency.

Another vibration pattern was found at a frequency of 1 kHz. The results obtained when sound was applied to the sample are presented in Fig. 5, without UVB radiation, and 6 with radiation. It is noticeable that the patterns and the displacements are altered upon exposure to the UVB dose. The maximum displacements are shown in Table II.

Examining the vibration pattern images in Figs. 5a) and 6a), the vibration mode appears to be a (1,1) mode, and it is notorious that there are changes in their shapes. For example, in Fig. 5a), bright and dark fringes are presented in a particular position; apparently, the fringes are rotated. However, when the sample is irradiated, the pattern is modified, displaying a pair of dark and bright fringes that are separated and not rotated compared with the pattern without UVB radiation. On the other hand, the displacement maps and the scale bar showed that the displacement value is slightly higher in the sample without radiation, which agrees with the maximum displacement values shown in Table II.

A further result of the experiment was the discovery of a complex vibration pattern found at 1.62 kHz for the sample

TABLE II. Maximum displacements at a frequency of 1 kHz.

Without UVB radiation	With UVB radiation
$0{,}252 \pm 0{,}0014$ μm	$0{,}248 \pm 0{,}0011$ μm

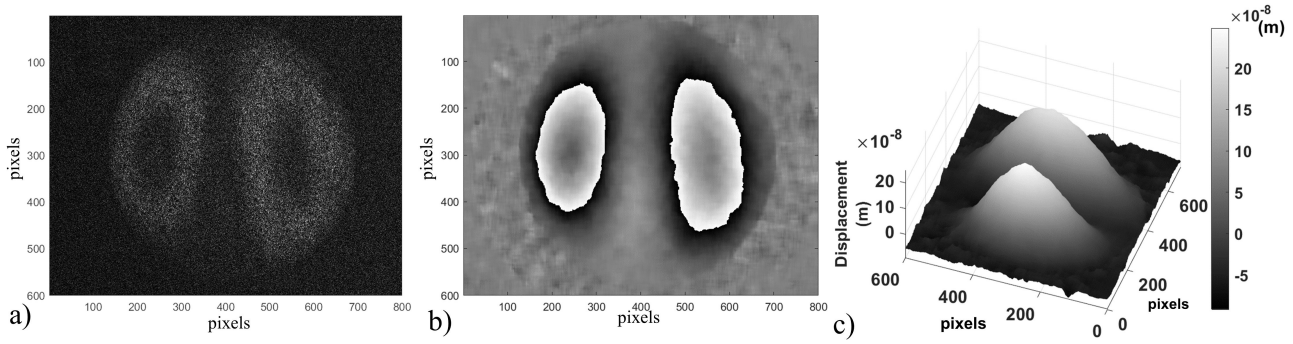


FIGURE 6. Biological sample at a frequency of 1 kHz and with a dose of 0.0014 J/cm^2 of UVB radiation, a) fringe pattern, b) wrapped phase, and c) displacement map.

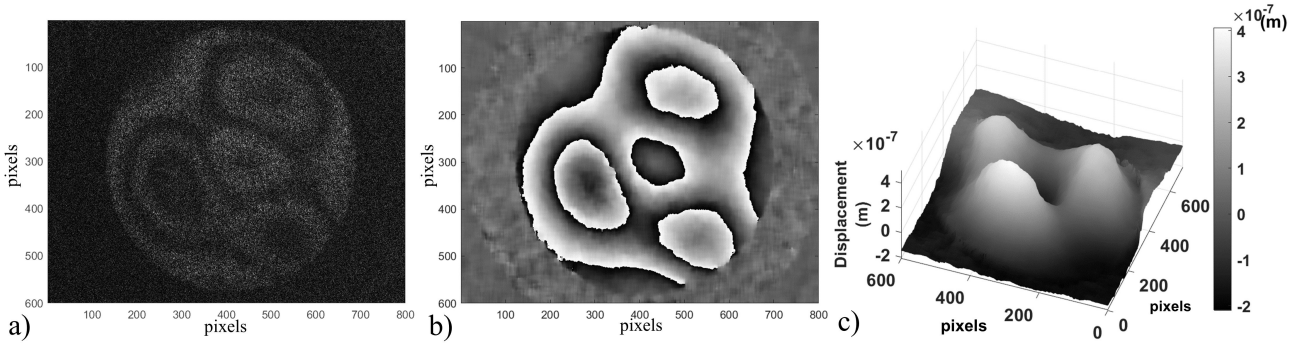


FIGURE 7. Biological sample at a frequency of 1.62 KHz and without UV radiation, a) fringe pattern, b) wrapped phase, and c) displacement map.

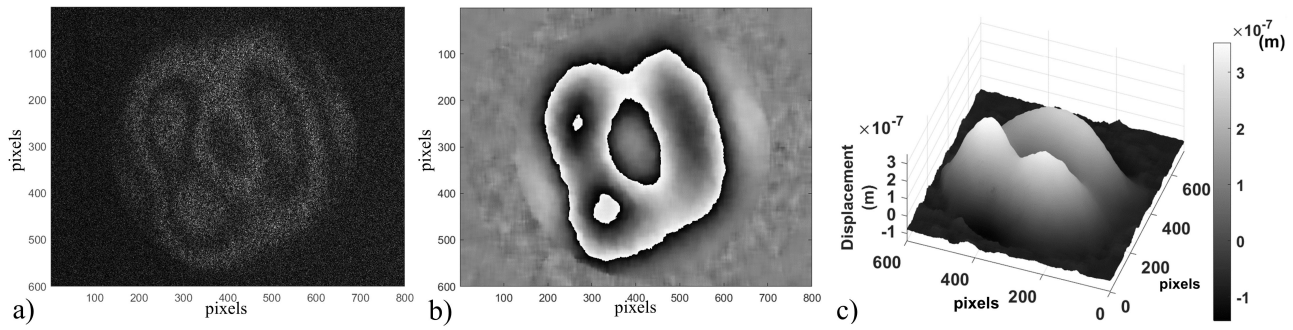


FIGURE 8. Biological sample with a UVB radiation at a frequency of 1.75 KHz, a) fringe pattern, b) wrapped phase, and c) displacement map.

prior to exposure to radiation, as illustrated in Fig. 7. However, following the application of UVB radiation to the sample, it was inspected at 1.62 kHz and did not vibrate at this frequency. Consequently, an exhaustive search for the vibration pattern was carried out, which was found at 1.75 kHz. This indicates that there was a change in frequency, as well as a decrease in the magnitude of the displacement, which is an indicator that the sample is affected after being irradiated, as illustrated in Fig. 8.

A maximum displacement of $0{,}407 \pm 0{,}0013$ μm was quantified for the biological sample without UVB radiation at 1.62 kHz, and a maximum displacement of $0{,}350 \pm 0{,}0012$ μm was determined for the biological sample with UVB radiation dose at a frequency of 1.75 kHz.

The vibration frequency of biological tissue depends on the mechanical properties inherent to its viscoelastic nature. It is worth noting that the biological sample used in this work exhibited various vibration modes at different frequencies, indicating that it cannot be considered a homogeneous system and that its internal structure is complex.

In addition, the alteration of the sample with UVB radiation caused slight changes in the displacement information and the vibration patterns detected by optical techniques.

4. Conclusions

The research presented allowed us to analyze biological tissue using a non-invasive optical technique, which facilita-

ted the quantification of micro-displacements and changes in them caused by UVB radiation applied to the sample. The laser interferometry technique permitted the biological sample to be evaluated without manipulation, which helped to avoid external alterations that could influence the measurements. Furthermore, the optical technique used in this work lets us see superficial variations and/or modifications in the biological sample that are not perceptible to the naked eyed. In this regard, changes in the outer layer of the sample due to UVB radiation can be seen in the 3D displacement maps.

It was imperative to discover the vibration modes of the tissue prior to its quantitative analysis, and consequently, tissue information was obtained and analyzed before and after UVB radiation. The displacement in the tissue before UVB radiation was greater in comparison to the displacement values obtained with the irradiated sample; additionally, when the sample was subjected to UVB radiation, the fringe patterns and elasticity were modified, as UVB rays generate an increase in viscoelastic stiffness on the tissue surface, indicating photoaging and dehydration, as well as possible internal alterations in elastin, fragmentation, and collagen reorganization [15]. Thus, in the first and second vibration modes found, the frequency of the sound load at which they were found remained the same for both sample conditions with and without radiation. However, the behavior of the phase and displacement maps changed, and a decrease in the displacement values of the irradiated sample was observed. In a complex vibration pattern, in addition to the change in displacement, the frequency also changed from 1.62 kHz to 1.75 kHz due to the effects of UVB radiation on the tissue.

It should be noted that the difference in maximum displacement between the irradiated and non-irradiated samples was small due to the low dose of radiation that was applied; these small changes of the order of microns can be detected with the technique presented. In future work, focus will be on obtaining mechanical parameters such as stiffness, Young's modulus, and Poisson's ratio, among others, in order to better understand the damage that prolonged exposure to UVB rays can cause to human skin.

Acknowledgments

The authors acknowledge support from their institution.

1. US EPA, O. (2015) Sun safety, US EPA. Available at: https://www.epa.gov/sunsafety, (Consulted: december 12th, 2025).
2. El deterioro de la capa de ozono, problema vigente (2019). Gaceta UNAM.
3. Agotamiento de la capa de ozono (2019) National Geographic. Available at: https://www.nationalgeographicla.com/espacio/2019/01/agotamiento-de-la-capa-de-ozono, (Consulted: december 12th, 2025).
4. F. López Figueroa, Implicaciones dermatológicas del cambio climático y de la disminución de la capa de ozono, *Actas Dermo-Sifiliográficas*, **102** (2011), 311-315, https://doi.org/10.1016/j.ad.2010.12.006.
5. S. A. Umar and S. A. Tasduq, Ozone Layer Depletion and Emerging Public Health Concerns - An Update on Epidemiological Perspective of the Ambivalent Effects of Ultraviolet Radiation Exposure, *Front. Oncol.,* **12**, (2022), 1-11, https://doi.org/10.3389/fonc.2022.866733.
6. K. R. Solomon, Effects of ozone depletion and UV-B radiation on humans and the environment, Atmosphere-Ocean, **46** (2008) 185-202, https://doi.org/10.3137/ao.460109.
7. E Kovács, and Á Keresztes, Effect of gamma and UV-B/C radiation on plant cells, Micron, **33** (2002) 199-210, https://doi.org/10.1016/S0968-4328(01)00012-9.
8. A. L. Andrady, A. M. Heikkilä, K. K. Pandey, L. S. Bruckman, C. C. White, M. Zhu, and L. Zhu, Effects of UV radiation on natural and synthetic materials. *Photochem Photobiol Sci*, **22** (2023) 1177-1202, https://doi.org/10.1007/s43630-023-00377-6.
9. M. M. Shokrieh, and A. Bayat, Effects of Ultraviolet Radiation on Mechanical Properties of Glass/Polyester Composites. Journal of Composite Materials, **41** (2007) 2443-2455, https://doi.org/10.1177/0021998307075441.
10. A. Leal-Junior, R. Pires-Junior, A. Frizera, and C. A. F. Marques, (2022). Influence of UV radiation on mechanical properties of polymer optical fibers, *Polymers,* **14** (2022), 4496, https://doi.org/10.3390/polym14214496.
11. R. Naveen, M. Kumar, M. Ramesh, R. Abinaya, and M. S. Prasath, An investigation on effect of ultraviolet (UV) rays on mechanical properties of epoxy laminates, Materials Today: Proceedings, (2023), https://doi.org/10.1016/j.matpr.2023.06.257.
12. S. Muñoz Solís, M. S. Hernández-Montes, and F. Mendoza Santoyo, Measurement of Young's modulus in an elastic material using 3D digital holographic interferometry, *Appl. Opt.,* **50**, (2011), 3383-3388.
13. S. Eve, and J. Mohr, Effects of UV-irradiation on the thermomechanical properties of optical grade poly(methyl methacrylate), *Applied Surface Science,* **256** (2010), 2927-2933, https://doi.org/10.1016/j.apsusc.2009.11.052.
14. L. Silva Acosta, M. S. Hernández-Montes, F. Mendoza Santoyo, M. H. De la Torre, J. M. Flores, G. Frausto, and S. Muñoz, Study of skin rigidity variations due to UV radiation using digital holographic interferometry, *Opt. Lasers Eng.*, **126** (2020) 105909.
15. R. P. Gallagher and T. K. Lee, Adverse effects of ultraviolet radiation: A brief review, *Progress in Biophysics and Molecular Biology,* **92**, (2006), 119-131, https://doi.org/10.1016/j.pbiomolbio.2006.02.011.

16. D'Orazio, S. Jarrett, A. Amaro-Ortiz and T. Scott, UV radiation and the skin. *Int. J. Mol. Sci.*, **14** (2013), 12222-12248, https://doi.org/10.3390/ijms140612222.

17. R.P. Gallagher, T. K. Lee, C. D. Bajdik and M. Borugian, Ultraviolet radiation. *Chronic Dis Can.*, **29** (2010), 51-68, https://doi.org/10.24095/hpcdp.29.S1.04.

18. C. Nishigori, N. Yamano, M. Kunisada, A. Nishiaki-Sawada, H. Ohashi and T. Igarashi, Biological Impact of Shorter Wavelength Ultraviolet Radiation-, *Photochemistry y Photobiology,* **99** (2023), 335-343, https://doi.org/10.1111/php.13742.

19. K. A. Merin, M. Shaji, and R. Kameswaran, A review on sun exposure and skin diseases, *Indian Journal of Dermatology*, **67** (2022), 625, https://doi.org/10.4103/ijd.ijd_1092_20.

20. F. Papaccio, S. Caputo and B. Bellei, Focus on the contribution of oxidative stress in skin aging. *Antioxidants*, **11** (2022) 1121, https://doi.org/10.3390/antiox11061121.

21. S. L. Yu, and S. K. Lee, Ultraviolet radiation: DNA damage, repair, and human disorders, *Mol. Cell. Toxicol.*, **13**, (2017), 21-28, https://doi.org/10.1007/s13273-017-0002-0.

22. C. Green, B. L. Diffey and J. L. M. Hawk, Ultraviolet radiation in the treatment of skin disease, *Physics in Medicine and Biology,* **37** (1992), 1-20, https://doi.org/10.1088/0031-9155/37/1/001.

23. E. B. M. Kroft, N. J. G. Berkhof, P. C. M. van de Kerkhof, R. M. J. P. Gerritsen and E. M. G. J. de Jong, Ultraviolet A phototherapy for sclerotic skin diseases: A systematic review, *Journal of the American Academy of Dermatology,* **59** (2008), 1017-1030, https://doi.org/10.1016/j.jaad.2008.07.042.

24. F. Breuckmann, T. Gambichler, P. Altmeyer and A. Kreuter, UVA/UVA1 phototherapy and PUVA photochemotherapy in connective tissue diseases and related disorders: a research based review, BMC Dermatol, **4** (2004), 1-14, https://doi.org/10.1186/1471-5945-4-11.

25. M. Šitum, V. Bulat, K. Majcen, A. Džapo and J. Ježovita, Benefits of Controlled Ultraviolet Radiation in the Treatment of Dermatological Diseases, *Coll. Antropol,* **38** (2014) 1249-1253.

26. W. L. Scarlett, Ultraviolet radiation: sun exposure, tanning beds, and vitamin D levels. What you need to know and how to decrease the risk of skin cancer, *JAOA.*, **103** (2003), 371-375, https://doi.org/10.7556/jaoa.2003.103.8.371.

27. R. P. Gallagher, J. J. Spinelli and T. K. Lee, Tanning Beds, Sunlamps, and Risk of Cutaneous Malignant Melanoma, *Cancer Epidemiol Biomarkers Prev.*, **14**((2004), 562-566, https://doi.org/10.1158/1055-9965.EPI-04-0564.

28. K. P. Radack, M. E. Farhangian, K. L. Anderson and S. E. Feldman, A Review of the Use of Tanning Beds as a Dermatological Treatment, *Dermatol Ther (Heidelb),* **5** (2015) 37-51, https://doi.org/10.1007/s13555-015-0071-8.

29. A. Gerger, S. Koller, T. Kern, C. Massone, K. Steiger, E. Richtig, H. Kerl, and J. Smolle, Diagnostic Applicability of In Vivo Confocal Laser Scanning Microscopy in Melanocytic Skin Tumors, *Journal of Investigative Dermatology,* **124** (2005) 493-498, https://doi.org/10.1111/j.0022-202X.2004.23569.x.

30. M. A. Ilie, C. Caruntu, M. Lupu, D. Lixandru, M. Tampa, S-R. Georgescu, A. Bastian, C. Constantin, M. Neagu, S. Andrada Zurac, and D. Boda, Current and future applications of confocal laser scanning microscopy imaging in skin oncology (Review), *Oncology Letters,* **17** (2019), 4102-4111, https://doi.org/10.3892/ol.2019.10066.

31. O. Babalola, A. Mamalis, H. Lev-Tov, and J. Jagdeo, Optical coherence tomography (OCT) of collagen in normal skin and skin fibrosis. *Arch Dermatol Res*, **306**, (2014), 1-9, https://doi.org/10.1007/s00403-013-1417-7.

32. M. Mogensen, L. Thrane, T.M. Joergensen, P.E. Andersen, and G.B.E. Jemec, Optical Coherence Tomography for Imaging of Skin and Skin Diseases, *Annals of Clinical Psychiatry*, **28** (2016), 196-202, https://doi.org/10.1177/104012371602800309.

33. J. Welzel, Optical coherence tomography in dermatology: a review, *Skin Research and Technology,* **7** (2001) 1-9, https://doi.org/10.1034/j.1600-0846.2001.007001001.x.

34. K. V. Larin and D. D. Sampson, Optical coherence elastography - OCT at work in tissue biomechanics [Invited], *Biomedical Optics Express*, **8** (2017) 1172-1202, https://doi.org/10.1364/BOE.8.001172.

35. J. Rogowska, N. Patel, S. Plummer, and M. E. Brezinski, Quantitative optical coherence tomographic elastography: method for assessing arterial mechanical properties, *British Journal of Radiology,* **79** (2006) 707-711, https://doi.org/10.1259/bjr/22522280.

36. I. A. Sigal, J. L. Grimm, J. S. Schuman, L. Kagemann, H. Ishikawa, and G. Wollstein, A Method to Estimate Biomechanics and Mechanical Properties of Optic Nerve Head Tissues From Parameters Measurable Using Optical Coherence Tomography. *IEEE Transactions on Medical Imaging*, **33** (2014) 1381-1389, https://doi.org/10.1109/TMI.2014.2312133.

37. D. S. Zhang, and D. D. Arola, Applications of digital image correlation to biological tissues, *Journal of Biomedical Optics*, **9** (2004), 691-699, https://doi.org/10.1117/1.1753270.

38. G. Pedrini, I. Alexeenko, P. Zaslansky, H. J. Tiziani, and Wolfgang Osten, Digital holographic interferometry for investigations in biomechanics, Proc. SPIE 5776, *Eighth International Symposium on Laser Metrology*, (2005) 325-332, https://doi.org/10.1117/12.611633.

39. L. Silva Acosta, F. Mendoza Santoyo, J. M. Flores, M. S. Hernández-Montes, M. H. De la Torre, G. Frausto, S. Muñoz, and E. E. Lozada, Study of skin aging effects induced by near UV radiation using time average digital holographic interferometry, *Opt. Lasers Eng.*, **137**, (2020), 106345.

40. P. K. Rastogi, Holographic Interferometry Principles and Methods. Springer Series in Optical Sciences, 1st edition, (1994) 7-32, https://doi.org/10.1007/978-3-540-48078-5.

41. G. H. Kauffmann, Advances in Speckle Metrology and Related Techniques, Wiley-VCH, (2011).

42. S. S. Andrews, Light and Waves: A Conceptual Exploration of Physics, Springer Nature Switzerland, (2023) 43-70.

43. K. J. Gasvik, Optical metrology. John Wiley & Sons, Ltd, (2002), 37-65.

44. J. Clinton, and K. P. Wani, Extracting Vibration Characteristics and Performing Sound Synthesis of Acoustic Guitar to Analyze Inharmonicity, *Open Journal of Acoustics*, **10** (2020), 41-50, https://doi.org/10.4236/oja.2020.103003.

45. M. Takeda, H. Ina, y S. Kobayashi, Fourier-transform method of fringe-pattern analysis for computer-based topography and interferometry, *J. Opt. Soc. Am,* **72**(1), (1982), 156-160, https://doi.org/10.1364/JOSA.72.000156

46. Y. I. Ostrovsky, V. P. Shchepinov, and V. V. Yakovlev, Holographic interferometry, in Holographic Interferometry in Experimental Mechanics, Springer Series in Optical Sciences, 1st edition, **Vol. 60**, Springer, Berlin, Heidelberg, (1991), 24-87.

47. T. Kreis, Handbook of Holographic Interferometry: Optical and Digital Methods, Wiley, (2004), 185-218.

48. M. Servin, J. A. Quiroga and M. Padilla, Fringe Pattern Analysis for Optical Metrology: Theory, algorithms and applications, Wiley, (2014).

49. S. Zhang, Composite phase-shifting algorithm for absolute phase measurement. *Opt. Laser Eng*., **50** (2012), 1538-1541, https://doi.org/10.1016/j.optlaseng.2012.06.005.

50. K. Itoh, Analysis of the Phase Unwrapping algorithm, *Appl. Opt.*, **21** (1982), 2470, https://doi.org/10.1364/AO.21.002470.

51. J. M. Huntley, Noise Immune Phase Unwrapping Algorithms, *Appl. Opt.*, **28** (1989), 3268-3270, https://doi.org/10.1364/AO.28.003268.

52. J. M. Huntley, and J. R. Buckland, Characterization of sources of 2π discontinuities in speckle interferograms, *J. Opt. Soc. Am. A,* **12** (1995), 1990-1996, https://doi.org/10.1364/JOSAA.12.001990.

53. D. C. Ghiglia, and L. A. Romero, Minimum Lp-Norm Two-Dimensional Phase Unwrapping, *J. Opt. Soc. Am. A,* **13** (1996), 1999-2013, https://doi.org/10.1364/JOSAA.13.001999.

54. K. Moon Jeong, K. Bo-seung, H. Sejin, and Y. Hong Hee, Experimentally derived viscoelastic properties of human skin and muscle in vitro, *Medical Engineering & Physics,* **61** (2018) 25-31, https://doi.org/10.1016/j.medengphy.2018.08.001.

55. S. Sakaguchi, and M. Konyo, Skin viscoelasticity effects on the periodic mechanical stimuli propagation between skin layers. *Journal of the Mechanical Behavior of Biomedical Materials.* **152**, (2024), 106416, https://doi.org/10.1016/j.jmbbm.2024.106416.

56. M. L. Crichton, X. Chen, H. Huang, M. A.F. Kendall, Elastic modulus and viscoelastic properties of full thickness skin characterised at micro scales, *Biomaterials*, **34** (2013), 2087-2097, https://doi.org/10.1016/j.biomaterials.2012.11.035.

57. H. Koruk, and S. Rajagopal, A Comprehensive Review on the Viscoelastic Parameters Used for Engineering Materials, Including Soft Materials, and the Relationships between Different Damping Parameters, *Sensors (Basel)*, **24** (2024) 6137, https://doi.org/10.3390/s24186137.

58. R. Lakes, Viscoelastic Materials, Cambridge University Press, (2009), 236-237, 341-376.

Topological modes for light propagation inside a 2D photonic square lattice crystal with $p4$ symmetry

M. A. Tun-Carrillo

Posgrado en Ciencias-IICBA, Universidad Autónoma del Estado de Morelos, Av. Universidad No. 1001, 62209, Cuernavaca, Morelos, México; e-mail: marco.tun@uaem.edu.mx Orcid: 0009-0008-4813-5365

J. A. Medina-Vázquez

Facultad de Ingeniería, Universidad Autónoma de Chihuahua, Circuito Número I s/n, Nuevo Campus Universitario, Nte. 2, 31125, Chihuahua, Chihuahua, México. Orcid: 0000-0001-6012-7933

M. E. Mora-Ramos*

*Centro de Investigación en Ciencias-IICBA, Universidad Autónoma del Estado de Morelos, Av. Universidad No. 1001, 62209, Cuernavaca, Morelos, México, *e-mail: memora@uaem.mx Orcid: 0000-0002-6232-9958*

H. A. Gómez-Urrea

Instituto de Ciencias Básicas, Universidad de Medellín, 050026, Medellín, Colombia, Orcid: 0000-0003-0611-2428

I. V. Pérez-Quintana

Facultad de Ingeniería, Universidad Autónoma de Yucatán, Industrias No Contaminantes S/N, Sin Nombre de Col 27, 97302, Mérida, Yucatán, México. Orcid: 0000-0003-2802-4760

Received 12 January 2026; accepted 2 October 2026

We investigate a two-dimensional all-dielectric silicon photonic crystal with a square lattice based on $p4$ space group wallpaper symmetry, demonstrating dual-functional electromagnetic response. By employing group-theoretical symmetry indicators, we characterize the topological phase hierarchy of the lower ten transverse magnetic (TM) bands for two complementary unit cell configurations (UC1 and UC2). The topological non-triviality of UC2 enables the emergence of robust edge and corner modes within the telecommunication window ($\sim$ 1,84 THz / 1,6 μm) at the interface with the trivial UC1 phase. Additionally, an accidental p–p–d band degeneracy forming a Dirac-like cone at the Γ point yields a near-zero refractive index (NZRI) regime in the mid-infrared region ($\sim$ 1,03 THz / 2,9 μm). We discuss the interplay between time-reversal symmetry-protected degeneracies and the absence of monopolar (s-like) symmetry, which results in directional impedance variations and non-ideal wave-front flattening. These findings highlight the potential of simple square-lattice geometries for integrated topological routing, directional optical sensing, and light manipulation.

Keywords: Higher-order topological modes; photonic crystal; topological edge and corner states; light localization.

DOI: https://doi.org/10.31349/RevMexFis.72.061302

1. Introduction

In modern photonics, efficient control of light propagation is essential for applications in telecommunications, sensors, information processing, and optical computing [1-3]. Traditionally, waveguides have been designed using refractive index contrasts, confining light to specific regions through total internal reflection or periodic structures such as photonic crystals [4]. However, these methods are typically sensitive to manufacturing imperfections, misalignments, and structural disorders, which hinder their robustness and scalability.

In contrast, topological boundaries in photonic systems offer a revolutionary alternative based on the principles of solid-state physics, specifically band topology. These waveguides form at the boundaries between two materials with different topological invariants, allowing the emergence of topologically protected edge modes. Such modes can propagate without dispersion, even in the presence of defects, curvatures, or irregularities, giving them unprecedented robustness against disorder [1,5-7].

The realization of topological boundaries in optical waveguides not only enhances tolerance to structural defects but

also enables the development of more compact, efficient, and robust integrated photonic devices. Notably, the influence of edge and corner states on light propagation exhibits a strong analogy with the behavior of electronic transport in dislocation pathways within graphene structures [7-9].

Modern topological photonics have made incredible advances regarding hexagonal and more exotic cell structures; from a technological perspective squared lattices may be a more feasible way to implement topological wave guides, given the simplicity of it's geometry [6,10,11]. This type of geometry is compatible with standard manufacturing techniques, such as electron lithography or deep etching, facilitating their integration into photonic chips. By breaking certain spatial symmetries-such as rotational symmetries-in a square lattice, it is possible to induce topological phases that support robust edge modes.

Modern material science, in particular the engineering of metamaterials, have made the ideal playground for the study of photonic structures that may present multiple functionalities through the appearance of different phenomena, such as Near Zero Refractive Index (NZI) and topological light propagation [12-14].

In this article, we propose a particular example of a two-dimensional photonic crystal (2DPC) with square lattice geometry based on the $p4$ symmetry (a type characterized by 90° rotations), which allows for the propagation of high-sensitivity corner and border modes, considered topological borders. Photonic properties, such as band structure and transmission, are discussed within the framework of the analysis as well.

2. Design and methodology

The design –perhaps the simplest wallpaper-like– resembles that of a pinwheel that tiles the plane. Both unitary cells correspond to a pattern that clearly presents fourth-order rotational symmetry (90° rotation) around the center, without horizontal, vertical, or diagonal reflection clearly being a $p4$ symmetry [15]. A schematic view of the dielectric structure

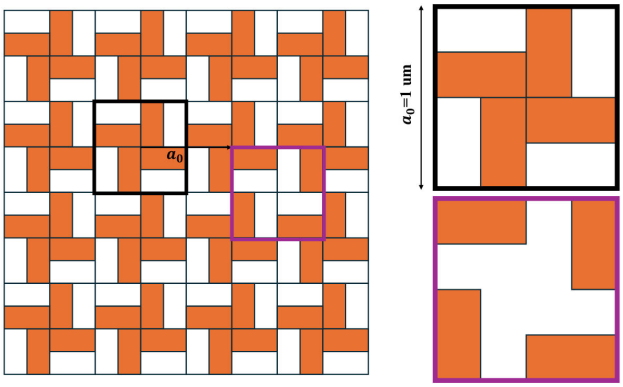


FIGURE 1. On the left we observe the pattern as it tiles the plane. On the right we see the two possible primitive cells that make the pattern, UC1 (Top) and UC2 (Bottom).

is displayed in Fig. 1. Simulations are carried out using COMSOL package [16]. The materials of choice are air (white areas) and silicon (orange areas) using $\varepsilon_{Si} = 12{,}25$. Technologically speaking, this design would be simple and easy to produce using traditional methods of deposition, such as RF sputtering.

In the case of topological mode propagation, we need to identify which unitary cell (UC) is trivial and which one is non-trivial, according to the accepted classification. The topological characterization of a photonic crystal band relies on identifying how its Bloch eigenmodes transform under the crystalline symmetries of the lattice. In what follows, we shall provide a detailed description of the procedure.

The topological characterization of photonic crystal bands under crystalline symmetries is fundamentally rooted in the representation theory of space groups applied to the Maxwell eigen-problem [17]. In a periodic dielectric medium, the electromagnetic modes are described by Bloch functions of the form.

$$\mathbf{E}_{n,\mathbf{k}}(\mathbf{r}) = e^{i\mathbf{k}\cdot\mathbf{r}}\mathbf{u}_{n,\mathbf{k}}(\mathbf{r}), \tag{1}$$

where $\mathbf{u}_{n,\mathbf{k}}(\mathbf{r})$ represents the periodic part of the electric field that satisfies the lattice periodicity condition, $\mathbf{k}$ is the Bloch wave vector defined within the first Brillouin zone, n is the label for the given band, and $\mathbf{r}$ is the position vector in real space.

Inside the band diagram, there are certain points of high symmetry (HSP's) in the Brillouin zone, which define nontrivial point group symmetries. At these high symmetry points (HSPs), the corresponding little group contains point-group operations-such as discrete rotations-that commute with the Maxwell operator, allowing the Bloch modes to be chosen as simultaneous eigen-states of these symmetry operations as well [18]. For a $n-$fold rotational symmetry, the action of the rotation operator $\hat{C}_n$ over the periodic part of the electric field is given as

$$(\hat{C}_n)(\mathbf{r}) = R_n u(R_n^{-1}\mathbf{r}), \tag{2}$$

where R_n is the matrix corresponding to a rotation by an angle of $2\pi/n$ about the symmetry axis. R_n accounts for the transformations of the vector field components under rotation. As mentioned, at the HSP points, the rotation operator and the Maxwell operator must commute. Therefore, the eigenmodes can be chosen to transform according to irreducible representations of the rotation group. To extract the rotation eigenvalues λ in a gauge-invariant manner, we compute the normalized expectation value

$$\lambda = \frac{\langle u \mid \hat{C}_n u\rangle}{\langle u \mid u\rangle}, \tag{3}$$

Here, the operator $< \mid >$ denotes the inner product over the unit cell, defined as

$$< f|g >= \int_{UC} f^*(\mathbf{r}) \bullet g(\mathbf{r}) d\mathbf{r}.$$

The normalization in the denominator ensures that λ is independent of the absolute field amplitude and invariant under global phase transformations $u \to e^{i\phi}u$.

This operation returns a phase factor of the form $e^{2\pi ip/n}$ when the field is an irreducible eigenstate of the symmetry operation. Because the Maxwell operator commutes with $\hat{C}_n$ only at the HSPs, the extraction of these eigenvalues at Γ, X, M, K, provides a symmetry-protected and gauge-independent fingerprint for the transformation properties of the investigated modes [19].

Once the rotation eigenvalues $\lambda_{n,\mathbf{k}}$ have been calculated for each band at each HSP, the next step consists in assembling these local symmetry data into global, gauge-invariant topological quantities known as symmetry-based invariants or symmetry indicators. These invariants capture the obstruction to providing a complete classification of crystalline topological phases within the symmetry class under consideration [17,19].

Let K be the set of all high-symmetry points (HSPs) invariant under a given rotational symmetry C_n. For each $\mathbf{k} \in K$, one can define the integer multiplicities:

$$N_p^{\mathbf{k}}, \quad p \in \{0, 1, \ldots, n-1\}. \tag{4}$$

Here, $N_p^{\mathbf{k}}$ counts the number of bands below the band gap (or within the chosen frequency range) whose rotation eigenvalue equals $\lambda_p = e^{2\pi ip/n}$. These multiplicities define a representation vector in the free Abelian group $\mathbb{Z}^{|K|\times n}$. Further details on this topological classification framework can be found in the work by Vaidya *et al.* [20].

To isolate genuinely topological features, one must therefore construct quantities in which all atomic-limit contributions cancel out. This is naturally achieved by forming differences between representation multiplicities at different high-symmetry points that share the same symmetry or belong to the same little group, leading to robust symmetry-based invariants [21].

The canonical way to define such differences is in the form

$$[\Pi_p^{(n)}] = \Pi_p^{(\Pi)} - \Pi_p^{(\Gamma)}, \tag{5}$$

where Γ denotes the Brillouin zone center and Π denotes another HSP invariant under the same rotation invariance, such as M in lattices with C_4 symmetry. For any elementary band representation induced from localized Wannier functions, the number of states transforming with a given angular momentum p is identical at all HSPs connected by symmetry. Consequently, atomic bands contribute equally to $N_p^{(\Gamma)}$ and $N_p^{(\Pi)}$, causing their difference to vanish identically [17]. Therefore, a nonzero value of $[\Pi_p^{(n)}]$ signals a genuine topological obstruction.

Now, the topological characterization of the photonic modes can be formulated in terms of the geometric phase accumulated under crystalline rotations at high-symmetry points in the Brillouin zone [20,22]. This is defined by the following equation:

$$\chi^{(4)} = ([X_1^{(2)}], [M_1^{(4)}], [M_2^{(4)}]). \tag{6}$$

The total phase accumulated when the mode is rotated is obtained by summing these discrete phase contributions weighted by their multiplicities at each high-symmetry point. For the twofold-symmetric X point, this construction leads to the invariant

$$[X_1^{(2)}] = \left(n_{X,+} - n_{X,-}\right) \text{ mód } 2,$$

which corresponds to a quantized geometric phase $\phi = \pi$, and $n_{X,+}, n_{X,-}$ are the even and odd number of modes, for a non-trivial case this should be 0. This phase reflects a parity inversion of the electromagnetic mode and remains invariant under any smooth, symmetry-preserving deformation of the system.

A similar phase-based interpretation applies at the fourfold-symmetric M point, where the rotation eigenvalues are given by $\lambda_j = e^{i\pi j/2}$ with $j = 0, 1, 2, 3$. The invariant

$$[M_1^{(4)}] = \left(n_{M,1} - n_{M,3}\right) \text{ mód } 4,$$

measures the imbalance between conjugate rotational eigenvalues and is associated with a total accumulated phase $\phi = \pi/2$, characteristic of modes with opposite angular circulation. $n_{M,j}$ is defined as the multiplicity of eigen values, in simple words, in counts how many bands are associated with the $e^{i\pi j/2}$ phase. In contrast, the invariant

$$[M_2^{(4)}] = \left(n_{M,2} - n_{M,0}\right) \text{ mód } 4,$$

corresponds to a phase $\phi = \pi$, linked to field configurations that change sign under a fourfold rotation. From this viewpoint, these symmetry-based invariants provide a compact and physically transparent description of the rotational phase winding of photonic modes, without invoking more elaborate topological constructs.

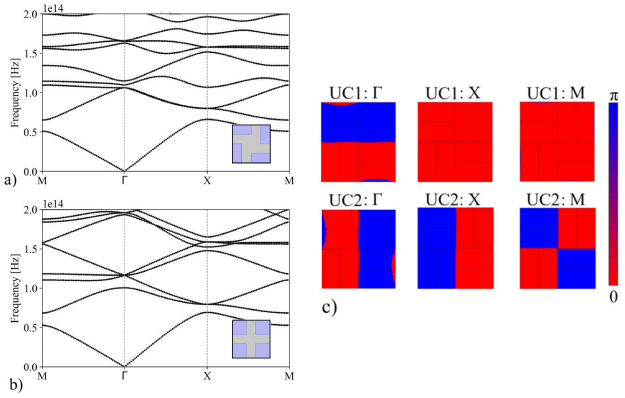


FIGURE 2. a) Band diagram for both UC1 and UC2 calculated with $a_1 = 0 = 1$, b) Shows the band diagram for the symmetric unitary call (see inset), obtained by setting $a_1 = -0{,}5$, according to the description in the text. c) Shows the phase diagram for each point through the Brillouin Zone of both UC1 and UC2.

In addition, through this work, the phase diagrams will serve as a tool for understanding how electromagnetic modes organize and interact within the unit cell, offering an analogy to electronic orbitals in solid-state systems.

3. Results

Once the plane is tiled, two distinct primitive cells emerge, UC1 and UC2. Both of these crystal cells generate the same 2D lattice and can be regarded as inverse representations of each other. When the side length and the lattice vector of these primitive cells are set to $a_0 = 1$ μm, both UC1 and UC2 generate the same photonic band diagram [see Fig. 2a)]. The TM mode band diagram showcases two gaps, the main one centered around $0{,}5 \times 10^{14}$ Hz (approximately 6000 nm) and a secondary, much smaller gap at around $1{,}9 \times 10^{14}$ Hz (about 1600 nm), as seen in Fig. 3. There is also a partial Dirac point that spans four distinct bands at a frequency around 1×10^{14} Hz.

To clarify the origin of the secondary gap relevant to the topological states, we analyze a continuous geometrical deformation of the unit cell through the parameter a_1, as shown in Fig. 2. For $a_1 = -0{,}5$, the silicon elements form a cross-like geometry, the unit cell symmetry is C_{4v} and its space group is $p4mm$, and the corresponding band structure exhibits the Dirac-like degeneracy associated with this higher-symmetry configuration. The parameter a_1 is introduced as a dimensionless translation factor that governs the spatial displacement of the rectangular air voids within the silicon matrix. In the finite element simulation, the position of these voids is modified by a displacement vector parameterized by a_1: $\vec{r}' = \vec{r} + a_1 L_1 \hat{u}$, where L_1 is a characteristic length of the geometry (*e.g.*, a shift along the vertical would be $\Delta y = a_1 L_1$). This acts strictly as an analytical tool to explore the geometric symmetries of the lattice. As shown in Fig. 2, setting $a_1 = -0{,}5$ forces the air voids to converge into a central cross-like geometry, introducing mirror symmetry and a corresponding Dirac-like degeneracy. The integer values $a_1 = 0$ and $a_1 = 1$ exactly recover the perfect corner-sharing configurations of the primitive cells UC1 and UC2, respectively.

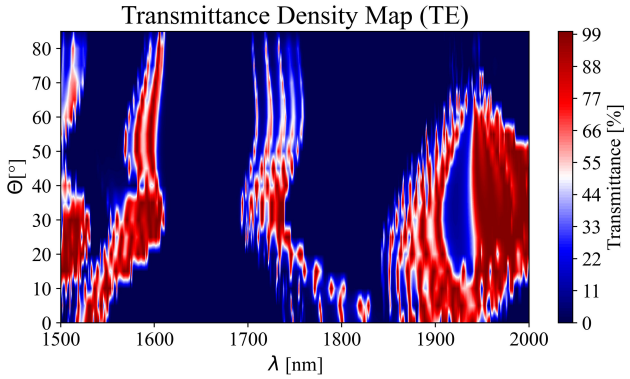


FIGURE 3. Transmittance density map showcasing the omnidirectional band gap that forms at around 1600 nm, in agreement with the band structure shown in Fig. 2.

It is important to note that for intermediate fractional values (e.g., $0 < a_1 < 1$), the translation disrupts the seamless tiling of the pinwheel pattern, resulting in disjointed geometries where the squares do not perfectly fit together. Therefore, the continuous sweep of a_1 does not represent a physically realizable crystalline phase, but rather a theoretical mechanism to demonstrate how breaking the higher-symmetry configuration lifts the degeneracy and opens the relevant topological band gap between bands 8 and 9.

In the periodic Bloch calculation, UC1 and UC2 describe the same underlying square lattice and yield equivalent bulk band structures, while the symmetry analysis of their eigenmodes distinguishes their topological character. The gap between bands 8 and 9 is therefore the relevant bulk gap in which the topological boundary and corner states are subsequently identified.

Phase diagrams are a useful tool for predicting not only topological phenomena but also other light-matter interactions. In this context, they serve as analogs to atomic orbitals in electronic theory. In combination with band diagrams, they provide information about how light propagates along the structure. For example, while both UC1 and UC2 generate the same band structure, propagating modes for each cell can be different for the same given k-number; they may reach the same destination, yet the way they reach it is what makes both UCs distinct.

The phase diagrams shown in Fig. 2c), reveal that both UC1 and UC2 present a p-like orbital at the Γ point, p_x for UC1 and p_y for UC2. For the other points, UC1 exhibits s orbital configurations, whereas UC2 at the X point remains as a p_x orbital. Furthermore, at the M point, it has a d_{xy}-like orbital phase configuration. This showcases evidence that, while both unitary cells produce the same band diagram, the phase analysis indicates a difference in which modes can propagate through each structure.

The band structure and symmetry analysis therefore provide a consistent picture of the two complementary primitive-cell configurations. In particular, the opening of the gap upon departing from the higher-symmetry configuration provides the bulk spectral region in which the topological properties of the corresponding bands can be analyzed.

Tables I and II showcase the topological invariants made to both UC1 and UC2. Given that our point of interest is located very high in the frequency domain, nearly at 2×10^{14} Hz, it is of great importance that we consider the topological class from all the bands below, including the one of interest.

So, from Table I we can see that although a subset of bands in UC1 (bands 3, 5, 7, and 9) display stable topological invariants, the majority of the low-lying bands yield the trivial vector $(0, 0, 0)$, which corresponds to fragile topology. This predominance of fragile indicators, together with the absence of robust non-trivial symmetry indices in most bands, supports the interpretation of UC1 as the topologically trivial unit cell. In contrast, the analysis of Table II, focused on UC2, reveals a predominance of stable indicators, with bands 1, 2, 3, 5, 6, and 10 displaying non-trivial vectors of the form

TABLE I. Symmetry vector for the first ten bands for UC1.

Band	UC1 ($[X_1^{(2)}], [M_1^{(4)}], [M_2^{(4)}]$)	UC1 Class.
1	$(0,0,0)$	Trivial
2	$(0,0,0)$	Trivial
3	$(+1,0,-1)$	Stable
4	$(0,0,0)$	Trivial
5	$(-1,0,+1)$	Stable
6	$(0,0,0)$	Trivial
7	$(-1,0,+1)$	Stable
8	$(0,0,0)$	Trivial
9	$(-1,0,+1)$	Stable
10	$(0,0,0)$	Trivial

$(\pm 1,0,\mp 1,0)$. These configurations cannot be decomposed into non-negative combinations of atomic limits, confirming their stable topological nature. Although a few bands (4, 7, 8, and 9) exhibit fragile indicators with trivial vectors $(0,0,0)$, the overall band structure is dominated by stable topological signatures. This establishes UC2 as the non-trivial unit cell, in sharp contrast to UC1; all of this in agrement with the literature [23,24].

TABLE II. Symmetry vector for the first ten bands for UC2.

Band	UC2 ($[X_1^{(2)}], [M_1^{(4)}], [M_2^{(4)}]$)	UC2 Class.
1	$(-1,0,+1)$	Stable
2	$(+1,0,-1)$	Stable
3	$(-1,0,+1)$	Stable
4	$(0,0,0)$	Trivial
5	$(-1,0,+1)$	Stable
6	$(+1,0,-1)$	Stable
7	$(0,0,0)$	Trivial
8	$(0,0,0)$	Trivial
9	$(0,0,0)$	Trivial
10	$(+1,0,-1)$	Stable

3.1. Topological edge states

Once the trivial and non-trivial hierarchy between UC1 and UC2 is established, we can construct the finite crystal supercell. In Fig. 4, we show the design of the combined UC1-UC2 finite photonic system, suitably combining lattices with trivial and non-trivial unit cells. The system consists of a 20×20 array of UC1 unit cells, within which a smaller 10×10 region composed of UC2 unit cells is embedded. The UC1 subregion is positioned such that its bottom-left corner is centered

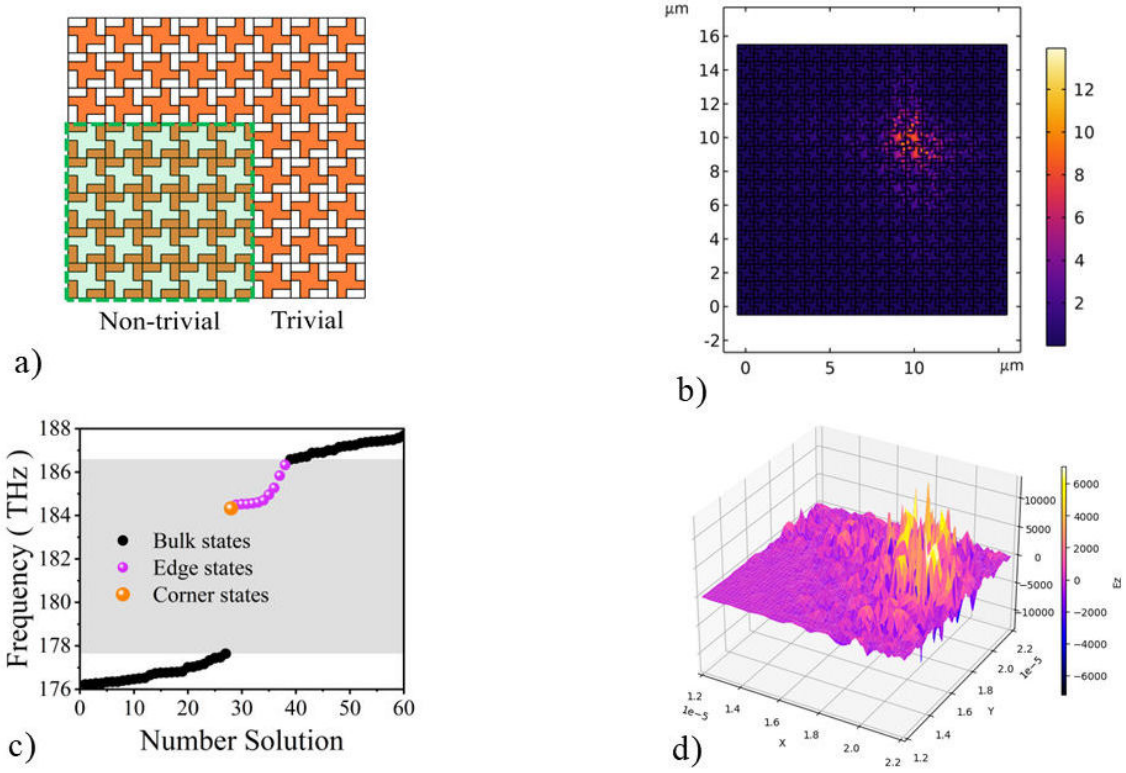


FIGURE 4. a) Representation of the finite crystal, centered around one of the corners. b) Localized edge state for the light mode of frequency $1{,}8471\times10^{14}$ Hz, for the E_z component of the electric field. c) Graph for the eigen frequencies and number of solutions of our system. d) Height map for the Ez component at the edge state.

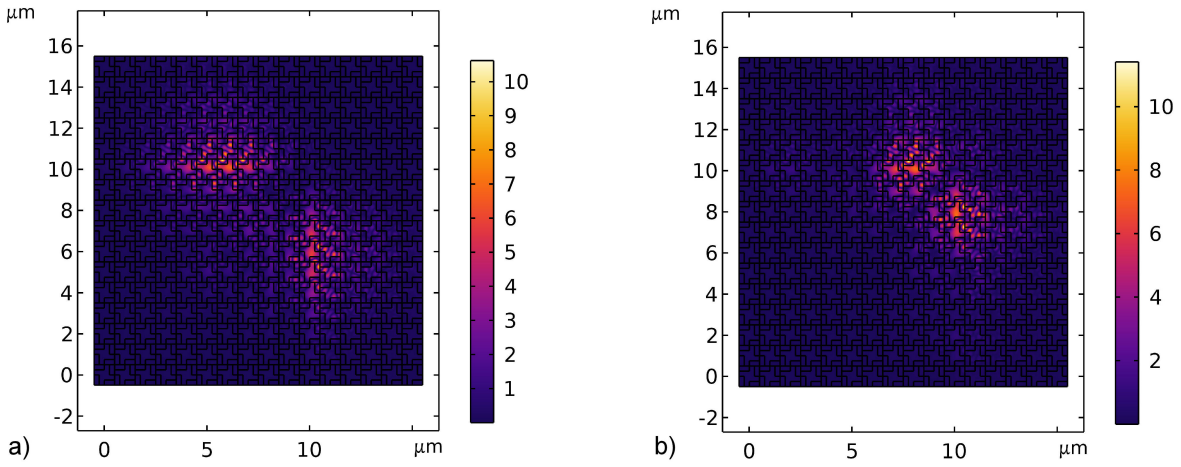


FIGURE 5. a) shows an edge that appears at a frequency of $1{,}8449 \times 10^{14}$ Hz, and goes around the dislocation, b) a more concentrated edge state at around $1{,}8433 \times 10^{14}$ Hz.

is centered at the coordinate origin, $(0, 0)$ [see Fig. 4a)]. We assume the incidence of a Gaussian-like light beam from the negative x-direction. It is possible to observe a localized, corner-like mode of light propagation [Fig. 4b)], corresponding to a frequency of $\sim 1{,}8471 \times 10^{14}$ Hz, correctly predicted by the number of solutions. Figure 4c) shows the diagram of frequency against the number of solutions, illustrating a clear bulk band gap in which localized states emerge, consistent with a nontrivial topological phase in the two-dimensional photonic crystal [22]. Bulk modes form two separated continua, while edge states appear within the gap and smoothly connect the bands, indicating topologically protected boundary propagation. Additionally, an isolated corner state is observed inside the gap, spectrally separated from the edge branch. Finally, a plot of the z-component of the electric field [Fig. 4d)] shows quite strong localization of its amplitude on both sides of the edge, although there is still some non-zero intensity away from it along the edges toward the frontier of the system. From the frequency of this mode alone, one can see that our design is highly sensitive to the frequency, in part due to its location in the band diagram, as well as the unitary cells themselves. We have also identified the presence of a well defined topological border-like state at around $1{,}8471 \times 10^{14}$ Hz [see Fig. 5a)]. There, as well as for the aforementioned corner-like state, we are firmly within the 10th photonic band. Therefore, it was convenient to calculate the topological invariant not only for the first band but also for the lowest ten bands, as reported in Tables I and II for each of the unit cells involved. In Fig. 5, we represent additional topological states that showcase the propagation of light through the boundary. Fig. 5a) shows an edge mode that appears at a frequency of $1{,}8449 \times 10^{14}$ Hz and goes around the dislocation; however, it does not exhibit the cardioid-like structure at the corner. In addition, Fig. 5b) shows another edge state at around $1{,}8433 \times 10^{14}$ Hz, respectively. Unlike the main mode, which is highly localized around the corner of the embedded square, these other modes propagate around the lattice edges.

3.2. Near-zero refractive index

By observing the photonic band diagram, it is possible to note that at the Γ point, around 1×10^{14} Hz, there is a collection of bands that form a Dirac cone. Zooming into this region reveals four bands in close proximity. Two of these bands - colored orange and green, [see the lowest depicted ones in Fig. 6a)]- are particularly relevant, with a third band appearing near the Dirac point. This arrangement resembles configurations typically observed in near-zero index (NZI) phenomena. Such systems allow for unique wave propagation properties, such as uniform phase across space or enhanced tunneling, and often involve specific band structures near the Γ point that resemble Dirac-like dispersions [25,26].

One key distinction, however, lies in the orbital composition of the bands involved. While NZI systems often feature an $s - p - p$ or monopole-dipole-dipole orbital distribution, the case examined here may differ in the exact orbital character of the bands forming the Dirac cone. This difference in orbital symmetry can have important implications for both the photonic behavior and potential topological properties of the system.

In an ideal NZI crystal, the electric field must be uniform at the scale of the unit cell, with a uniform phase across the supercell and omnidirectional propagation [27-29]. From the perspectives of symmetry and photonic band theory, our orbital dipole-dipole-quadrupole ($p - p - d$) distribution fully satisfies these criteria. At the Γ point, the point group symmetry is C_4. While C_4 is an Abelian group with strictly one-dimensional irreducible representations, the double degeneracy of the p_x/p_y modes is guaranteed by time-reversal symmetry, which pairs the two complex-conjugate one-dimensional representations. And is, therefore, symmetry-protected to be degenerate, while the quadrupole mode (d_{xy}, belonging to B_1 or B_2) can naturally lie above them if the geometry or material parameters invert the conventional $s - p - p$ ordering.

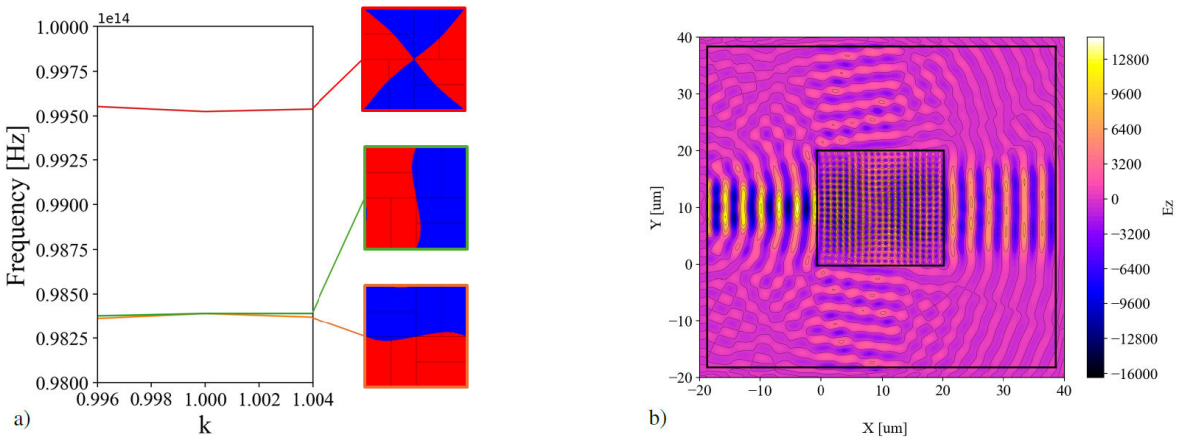


FIGURE 6. a) Band diagram of the two bands that form the Dirac point near a third upper band, the phase diagrams represent the orbitals; from up to bottom we have, d_xy, p_y and p_x orbitals. b) 20×20 supercell simulation showcasing a near-zero refractive index using a $1{,}031 \times 10^{14}$ Hz Gaussian beam.

If we consider the effective impedance Z_{eff}, defined as

$$Z_{\text{eff}} = \sqrt{\frac{\mu_{\text{eff}}}{\varepsilon_{\text{eff}}}}, \tag{7}$$

an ideal zero-refractive-index condition for the given mode would occur when both the effective permeability and permittivity vanish simultaneously, $\mu_{\text{eff}} = \epsilon_{\text{eff}} = 0$. The resulting finite, non-zero effective impedance Z_{eff} ensures high transmittance matching the incident medium. In our system, the p_x/p_y mode degeneracy at the Γ point is symmetry-protected by the C_4 lattice and time-reversal symmetry. However, obtaining a zero-index response requires bringing these modes into spectral overlap with an additional band. Here, the quadrupole (d) band is positioned above the p-doublet, signaling a band inversion rather than the canonical triple ($s + p + p$) accidental degeneracy [13,30]. This structural configuration yields an effective near-zero-index regime characterized by a non-ideal evanescent field profile and residual internal reflections [30].

By simulating a UC1 20x20 supercell, we can achieve a near-zero refractive index using a $1{,}031 \times 10^{14}$ Hz (2900 nm) Gaussian beam, [see Fig. 6b)]. As commented, compared to other 2D geometries [25], our finite crystal cannot be viewed as a perfect example of a near zero index case: When such a Gaussian beam is shot from the k_x direction, the electric field at the top of the crystal does not propagate parallel to the surface of the lattice; instead, it does so in a slightly tilted way, as seen in Fig. 6b). As a result, when a beam is shot from both the k_x and k_y directions, the effect of an outgoing plane wave is not as pronounced as when the beam comes from a single direction (see Fig. 7).

In short, while the linear dispersion and associated orbital configuration with p_x/p_y degeneracy at a Dirac point can drive the effective refractive index n_{eff} toward zero, it does not inherently produce a stable near-zero-index (NZI) effect. The resulting impedance is often unstable and highly direction-dependent. As established in the literature, achieving a robust, isotropic NZI condition requires a monopolar contribution, which is absent in simple Dirac cone degeneracies [30]. Considering the relation between topological protection and effective electromagnetic properties [17], despite the Dirac cone associated with the p_x/p_y band inversion is topologically allowed and protected, this absence prevents the crystal from behaving as a fully homogeneous zero-index material, leading to a regime that can be described as a near-zero-index phase that is topologically permitted but electromagnetically incomplete. This highlights a fundamental distinction between topological robustness in momentum space and the effective behavior of the medium and its properties [17,30,31].

4. Conclusions

Squared lattices are notorious for their difficulty in generating topological photonic phenomena. Through this work, we present a squared lattice that can produce both topological and near-zero index propagation using a simple star-like design made of silicon rectangular bars. Technologically speaking, our design is suitable for reproduction using well known techniques, such as RF sputtering.

As for the optical results, the design represents a case of *jack of all trades, master of none*, since the optical phenomena observed are both of perspective interest; however, the way they manifest lacks the refinement of a device specifically made for such a task. For example, the NZI effect observed at $1{,}031 \times 10^{14}$ Hz shows a slight deviation in the perpendicular propagation of a Gaussian beam. Making this types of devices ideal for uses in cloaking both transmission and reflection [32].

The same can be expected for the propagation of topological modes. To begin with, the frequency at which the effect can be observed appears around the 10th band in the photonic dispersion relation. This already proves difficult to diagnose its presence, thus forcing the calculation of the symmetry vector for all bands below it [20,33]. Initial results showcase a clear tendency for the unit cells labeled UC2 and UC1

to behave as non-trivial and trivial, respectively. Yet, some points within this analysis present irregularities (see Tables I and II). As a result, the stability of the topological propagation is quite low. Moreover, when simulating a boundary between two unit cells, the edge state appears to be quite sensitive to the frequency of the input signal and is surrounded by multiple cases of low propagation profiles.

Nonetheless, given the presence of two different kinds of *exotic* light propagation modes-topological and near-zero index-the photonic structure under study can be considered promising. Given the simplicity of the photonic crystal design, paired with satisfactory results for both identified phenomena, we can confidently refer to this possible device as having strong potential for applications in areas such as high-sensitivity optical sensing and signal modulation. A systematic study, perhaps involving automatic learning to improve the geometry by means of rotations or re-dimensioning [34], could lead to a 'ready to apply' design oriented to topological photonics.

Acknowledgments

MEMR, MATC, HAGU and IVPQ acknowledge Mexican SECIHTI for its support through Research Grant CBF-2025-I-1058.

1. S.-Q. Wu *et al*., All-dielectric photonic crystal with unconventional higher-order topology, Photonics Research (2021), https://doi.org/10.1364/PRJ.418689
2. J. Ma *et al*., Manipulating Second Harmonic Generation in Higher-Order Topological Photonic Crystals, Annalen der Physik **533** (2021), https://doi.org/10.1002/andp.202100191
3. B. Xie *et al*., Visualization of Higher-Order Topological Insulating Phases in Two-Dimensional Dielectric Photonic Crystals., Physical review letters **122** (2018) 233903, https://doi.org/10.1103/PhysRevLett.122.233903
4. E. Y. González-Ramírez *et al.*, All-optical photonic switch via the higher-order topological spin Hall effect, *Phys. Rev. Appl.* **21** (2024) 044038, https://doi.org/10.1103/PhysRevApplied.21.044038
5. J. A. Medina-Vázquez, E. Y. González-Ramírez, and J. G. Murillo-Ramírez, Corner states in photonic higher-order Dirac semimetals, *Phys. Rev. A* **107** (2023) 053511, https://doi.org/10.1103/PhysRevA.107.053511
6. F. Zangeneh-Nejad and R. Fleury, Topological Fano Resonances, *Phys. Rev. Lett.* **122** (2019) 014301, https://doi.org/10.1103/PhysRevLett.122.014301
7. Z. Wang *et al*., Higher-order Dirac semimetal in a photonic crystal, *Physical Review B* (2022), https://doi.org/10.1103/physrevb.105.l060101
8. S. G. y. García *et al*., Atomically Thin Current Pathways in Graphene through Kekulé-O Engineering, *Nano Letters* **24** (2024) 2322, https://doi.org/10.1021/acs.nanolett.3c04703
9. M. Li *et al*., Higher-order topological states in photonic kagome crystals with long-range interactions, *Nature Photonics* **14** (2020) 89, https://doi.org/10.1038/s41566-019-0561-9
10. L. Xiong *et al*., Topological Properties of a Two-Dimensional Photonic Square Lattice without C4 and Mx(y) Symmetries, ACS Photonics (2022), https://doi.org/10.1021/acsphotonics.2c00571
11. Z.-K. Lin *et al*., Anomalous quadrupole topological insulators in two-dimensional nonsymmorphic sonic crystals, *Phys. Rev. B* **102** (2020) 035105, https://doi.org/10.1103/PhysRevB.102.035105
12. S. A. Horsley and M. Woolley, Zero-refractive-index materials and topological photonics, *Nature Physics* **17** (2020) 348-355, https://doi.org/10.1038/s41567-020-01082-2
13. X. Huang *et al*., Dirac cones induced by accidental degeneracy in photonic crystals and zero-refractive-index materials., *Nature materials* **10** (2011) 582, https://doi.org/10.1038/nmat3030
14. H. Tang *et al*., Low-Loss Zero-Index Materials., *Nano letters* (2020), https://doi.org/10.1021/acs.nanolett.0c03575
15. V. Sasse, Classification of the 17 Wallpaper Groups, https://math.uchicago.edu/ may/REU2020/ REUPapers/Sasse.pdf (2020), REU Paper, University of Chicago.
16. COMSOL AB, COMSOL Multiphysics Reference Manual, COMSOL AB, Stockholm, Sweden (2023), v. 6.2.
17. B. Bradlyn *et al*., Topological quantum chemistry, *Nature* **547** (2017) 298.
18. L. Lu, J. D. Joannopoulos, and M. Soljačić, Topological photonics, *Nature Photonics* **8** (2014) 821-829, https://doi.org/10.1038/nphoton.2014.248
19. H. C. Po, A. Vishwanath, and H. Watanabe, Symmetry-based indicators of band topology in the 230 space groups, *Nat. Commun.* **8** (2017) 50.
20. S. Vaidya *et al*., Topological phases of photonic crystals under crystalline symmetries, *Phys. Rev. B* **108** (2023) 085116, https://doi.org/10.1103/PhysRevB.108.085116
21. C. Fang and L. Fu, New classes of topological crystalline insulators having surface rotation anomaly, *Sci. Adv* **5** (2019)
22. W. A. Benalcazar, T. Li, and T. L. Hughes, Quantization of fractional corner charge in C-n- symmetric higher-order topological crystalline insulators, *Physical Review B* **99** (2019), https://doi.org/10.1103/physrevb.99.245151

23. Y. Chen, J. Li, and J. Zhu, Topology optimization of quantum spin hall effect-based second-order phononic topological insulator, *Mechanical Systems and Signal Processing* **164** (2022) 108243, https://doi.org/10.1016/j.ymssp.2021.108243

24. B. Xie *et al*., Second-order photonic topological insulator with corner states, *Phys. Rev. B* **98** (2018) 205147, https://doi.org/10.1103/PhysRevB.98.205147

25. L. Vertchenko *et al*., Near-Zero Index Photonic Crystals with Directive Bound States in the Continuum, *Laser & Photonics Reviews* **15** (2021) 2000559, https://doi.org/10.1002/lpor.202000559

26. L. Vertchenko, M. Nikitin, and A. Lavrinenko, Near-zero-index platform in photonics: tutorial, *J. Opt. Soc. Am. B* **40** (2023) 1467, https://doi.org/10.1364/JOSAB.489055

27. M. W. Ashraf and M. Faryad, On the mapping of Diraclike cone dispersion in dielectric photonic crystals to an effective zero-index medium, *J. Opt. Soc. Am. B* **33** (2016) 1008, https://doi.org/10.1364/JOSAB.33.001008

28. I. Liberal and N. Engheta, Near-zero refractive index photonics, *Nature Photonics* **11** (2017) 149-158, https://doi.org/10.1038/nphoton.2017.13

29. M. Minkov *et al*., Zero-Index Bound States in the Continuum., *Physical review letters* **121** (2018) 263901, https://doi.org/10.1103/physrevlett.121.263901

30. X. Huang *et al*., Dirac cones induced by accidental degeneracy in photonic crystals and zero-refractive-index materials, *Nature Materials* **10** (2011) 582-586, https://doi.org/10.1038/nmat3030

31. G.-G. Wei *et al*., Zero refractive index properties of twodimensional photonic crystals with Dirac cones, *Chinese Physics Letters* **36** (2019) 034203, https://doi.org/10.1088/0256-307x/36/3/034203

32. T. Luo *et al*., Transmission and reflection cloaking by using a zero-refractive-index photonic crystal in the microwave region., *Applied optics* **60** (2021) 7492, https://doi.org/10.1364/ao.430234

33. M. D. de Paz *et al*., Engineering fragile topology in photonic crystals: Topological quantum chemistry of light, *Physical Review Research* (2019), https://doi.org/10.1103/physrevresearch.1.032005

34. J. G. Cardona *et al*., Flat band fine-tuning in photonic crystals via unsupervised shape artificial intelligence, *Optik* (2024) 172669.

Plasma-Activated Fenton Chemistry for Acid Blue 9 dye removal: Kinetics, physicochemical dynamics, and G_{50} optimization

J. Vergara[a], E. Gutiérrez[a], C. Torres[b,*], E. Montiel[b], B. Bazaldua[c], A. Gómez[d], P. G. Reyes[d], and H. Martínez[e]

[a]*Laboratorio de Ingeniería Ambiental, Facultad de Ciencias Químicas e Ingeniería, Universidad Autónoma del Estado de Morelos, Av. Universidad 1001, Chamilpa, Cuernavaca, Morelos, 62210, México.*

[b]*Laboratorio de Análisis y Sustentabilidad Ambiental, Escuela de Estudios Superiores de Xalostoc, Universidad Autónoma del Estado de Morelos, Av. Nicolás Bravo S/N, Ayala, Morelos, 62715, México.*

[c]*Escuela de Estudios Superiores de Atlatlahucan, Universidad Autónoma del Estado de Morelos, Galeana 146, San Antonio, Atlatlahucan, Morelos, 62840, México.*

[d]*Laboratorio de Física Avanzada, Facultad de Ciencias, Universidad Autónoma del Estado de México, Instituto Literario No. 100 Col. Centro, Toluca, Estado de México, 50000, México.*

[e]*Laboratorio de Espectroscopia, Instituto de Ciencias Físicas, Universidad Nacional Autónoma de México, Apartado Postal 48-3, Cuernavaca, Morelos, 62251, México.*

[*]*e-mail: cesar.torres@uaem.mx*

Received 22 June 2026; accepted 7 July 2026

Industrial effluents containing synthetic dyes represent one of the most persistent sources of surface water contamination, largely because conventional treatment processes fail to achieve their complete removal. In this work, we evaluated the degradation efficiency of a Non-Thermal Atmospheric-Pressure Plasma (NTAPP) system toward Acid Blue 9 (AB9) dye, using $FeSO_4$ as a catalytic additive at concentrations ranging from 0.2 to 1.0 mM. Degradation was monitored by UV-Vis absorbance at 630 nm, and solution physicochemical parameters pH, electrical conductivity, salinity, total dissolved solids (TDS), and bulk solution temperature were recorded throughout treatment. After 30 minutes of plasma exposure, near complete decolorization was achieved, with optimal catalytic performance observed at 0.6 mM $FeSO_4$. The enhanced degradation at this concentration is consistent with a Fenton-type mechanism, in which Fe^{2+} ions react with plasma-generated H_2O_2 to produce additional ·OH radicals. TOC analysis confirmed a dye mineralization efficiency exceeding 90 %. These results demonstrate the potential of catalytically intensified NTAPP as an effective strategy for the treatment of dye contaminated water.

Keywords: Non-thermal plasma; AB9; triarylmethane dye.

DOI: https://doi.org/10.31349/RevMexFis.72.061501

1. Introduction

Textile industry effluents are among the most chemically complex wastewaters generated by any industrial sector. A recurring problem is the discharge of synthetic dyes that resist conventional biological and physicochemical treatment Acid Blue 9 (AB9) being a well-documented example [1]. During fabric dyeing, an estimated 10–15 % of the dye applied fails to bind to the fiber substrate; this unbound fraction is flushed out in process wastewater and eventually reaches surface water bodies, where its persistence becomes an ecological liability [2].

What makes synthetic dyes particularly problematic is not just their color. These compounds are designed to resist fading, which means they also resist environmental degradation. In aquatic systems, their high solubility keeps them in the water column rather than settling out, while their structural stability allows them to persist for extended periods [3]. Over time, bioaccumulation through the food chain becomes a concern, and some dyes break down into transformation products that are more acutely toxic than the original molecule [4]. The ecological consequences are tangible: dye-contaminated water absorbs and scatters light, suppressing photosynthesis in aquatic plants and disrupting the base of freshwater food webs [1,5].

Beyond the ecosystem, the human health implications are serious. AB9, specifically, has been classified as a potentially carcinogenic and mutagenic compound. Subcutaneous administration in rat models produced carcinogenic effects, and oral ingestion was associated with a higher incidence of renal tumors [1,6]. Given that human exposure can occur through consumption of contaminated drinking water or trophic transfer, treatment strategies that fully mineralize this dye, rather than simply transferring it to another phase, are not optional; they are necessary [6,7].

Dye removal from wastewater is therefore both an environmental and a public health imperative. It also bears directly on freshwater availability: in regions facing water scarcity, the ability to treat and reuse industrial effluents could substantially reduce demand on freshwater reserves. Conventional methods of biological treatment, coagulation, and adsorption have well-known limitations when applied to recal-

citrant dyes. They either fail to achieve complete removal or generate secondary waste streams that require further management [8,9].

Advanced Oxidation Processes (AOPs) address these limitations through a fundamentally different mechanism: the in-situ generation of hydroxyl radicals (·OH), which are among the most powerful oxidizing agents known in aqueous chemistry [10]. Unlike biological processes, ·OH radicals do not select their targets; they attack aromatic rings, conjugated bonds, and other organic structures indiscriminately, driving mineralization to CO_2, H_2O, and inorganic salts [11]. This makes AOPs well suited for compounds that have specifically evolved, so to speak, to resist biological attack.

Among the AOP family, non-thermal atmospheric-pressure plasma (NTAPP) occupies a distinctive position. Rather than relying on a single reactive species, plasma discharge simultaneously generates a cocktail of reactive oxygen and nitrogen species (RONS), including ·OH, O_3, H_2O_2, and UV photons, without consuming chemical reagents or producing hazardous byproducts [12,13]. The system operates at atmospheric pressure and can be switched on and off on demand, which simplifies reactor design and operational control relative to other AOP configurations. In AOPs, the mineralization of contaminants occurs in successive stages. The first stage involves the generation of reactive species (O_3, H_2O_2), primarily the hydroxyl radical (·OH). This pathway begins with the dissociation of water molecules by energetic electrons generated during plasma discharge:

$$e^- + H_2O \rightarrow \cdot OH + H^{\bullet} + e^-. \quad (1)$$

The ·OH radicals produced in Eq. (1) can subsequently recombine in the bulk solution to form hydrogen peroxide:

$$\cdot OH + \cdot OH \rightarrow H_2O_2. \quad (2)$$

This accumulated H_2O_2 becomes a secondary source of ·OH when a ferrous iron catalyst is present. The addition of $FeSO_4$ triggers a Fenton-type reaction that regenerates radicals from the peroxide pool:

$$Fe^{2+} + H_2O_2 \rightarrow Fe^{3+} + \cdot OH + OH^-. \quad (3)$$

Once these reactive species are generated, oxidative attack occurs on the contaminants (AB9) present in the medium. The ·OH radical reacts non-specifically with the contaminant molecule, initiating oxidation and destabilizing its chemical structure. The oxidation of AB9 is primarily due to highly reactive species such as the hydroxyls (·OH) generated during discharge, leading to the formation of intermediate compounds and partial mineralization products [11,12,14], as represented in Eqs. (4) and (5):

$$AB9 + \cdot OH \rightarrow \text{oxidation intermediate}. \quad (4)$$

Finally, these unstable structures fragment into intermediates, which ultimately break down into their most basic and harmless mineral components:

$$\text{oxidation intermediate} \rightarrow CO_2 + H_2O + \text{inorganic ion}. \quad (5)$$

This coupling between plasma-generated H_2O_2 and Fe^{2+}-driven Fenton chemistry creates a synergistic amplification of the oxidative capacity of the system [14]. The resulting radical flux attacks the chromophoric structure of AB9, specifically the conjugated π-system and the aromatic rings associated with its triarylmethane backbone. The species preferentially attack the central carbon atom and the aromatic rings of the AB9 molecule, which constitute its chromophore system. This attack leads to the disruption of the triarylmethane structure and promotes the breaking of conjugated π bonds and the opening of the aromatic rings, resulting in the formation of several low molecular weight organic intermediates. This leads to progressive decolorization and, ultimately, mineralization.

AB9 (Brilliant Blue FCF; MW = 792.86 g/mol; CAS 3844-45-9; $C_{37}H_{34}N_2Na_2O_9S_3$; CI 42090) is an appropriate model contaminant for this study for several reasons. It is widely used across food, cosmetic, pharmaceutical, and textile applications [15,16], which ensures its practical relevance. Its well defined absorption maximum at 630 nm allows straightforward spectrophotometric monitoring. And its documented toxicological profile, including carcinogenicity in animal models, makes its effective removal a meaningful benchmark for treatment performance.

In this work, we evaluate the efficiency of an NTAPP system for the degradation of AB9, using $FeSO_4$ as a catalytic additive at concentrations ranging from 0.2 to 1.0 mM. The specific objective is to identify the optimal catalyst concentration and to characterize the physicochemical changes in the treated solution throughout the plasma exposure period.

2. Material and methods

A batch reactor (Fig. 1) was used to generate a corona discharge at the surface of the liquid sample. The discharge was generated by a DC power supply (Advanced Energy, PNCL PLUS+) operating at a frequency of 5 kHz and a power input of 40 W.

The following physicochemical parameters were monitored throughout the treatment: pH, electrical conductivity, total dissolved solids (TDS), salinity, and bulk solution temperature, using a Hach HQ40d multiparameter meter. UV- Vis absorbance of the treated solutions was measured at discrete $FeSO_4$ concentrations ranging from 0.2 to 1.0 mM (in

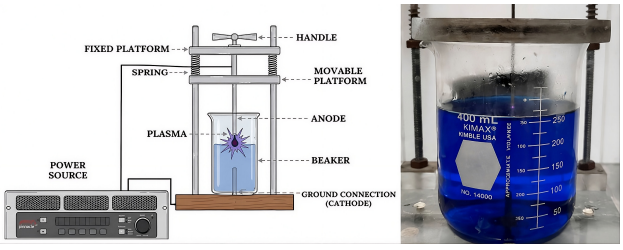


FIGURE 1. Batch reactor used for plasma treatment of AB9 dye solutions.

0.2 mM increments) using a Hach DR3900 spectrophotometer. The maximum absorption wavelength (λ_{max}) of AB9 was determined to be 630 nm, which was used as the analytical wavelength for all absorbance measurements.

Total organic carbon (TOC) was determined using the Hach TNT plus low-range vial method.

2.1. Reactor configuration

The plasma generation reactor consists of a beaker containing two tungsten electrodes. The anode is positioned on the surface of the beaker holding the sample, and the cathode is placed on the surface of the sample to be treated (2 mm). The beaker has an acrylic lid, and the cathode passes through the lid via a 3 mm diameter hole. The beaker is placed inside an acrylic container.

2.2. Sample preparation

Samples were prepared with a concentration of 0.1 mM in a volume of 250 mL. For this purpose, 0.0198 g of Acid Blue 9 dye was weighed. The mass was transferred to a 250 mL beaker containing 100 mL of distilled water, stirring constantly for 5 minutes. Subsequently, the solution was transferred to a 250 mL volumetric flask where the catalyst was added using a 5 mL pipette with the aid of a precision pipette, and the flask was filled to the mark with distilled water. The degradation of AB9 dye was investigated at an initial dye concentration of 0.1 mM, varying volumes of the catalyst stock solution were added to each sample, which was subsequently diluted to a total volume of 250 mL. Plasma treatment was applied for 30 minutes in all experiments. The catalyst was prepared at a concentration of 50 mM ($FeSO_4$) + 1.0 M (H_2SO_4). For its preparation, 3.47 g of ferrous sulfate were weighed and 1.4 mL of H_2SO_4 were added to a 250 mL beaker containing 100 mL of distilled water. The solution was stirred for 30 minutes. It was then transferred to a 250 mL volumetric flask and diluted to the mark with distilled water. Different volumes of the catalyst were added to the solution, from 1 mL (0.2 mM) up to 5 mL (1.0 mM). At the end of each treatment, the samples were stored in 250 mL amber glass bottles, in order to avoid any type of contamination; each experiment was performed 5 times.

3. Results

3.1. Decolorization of AB9 by Plasma Treatment

Figure 2 illustrates the progressive decolorization of AB9 dye solutions over increasing plasma treatment times. AB9 belongs to the triarylmethane class of synthetic dyes, whose intense blue coloration originates from a conjugated π-electron system centered on a central sp^3 carbon bonded to three aromatic rings. As treatment progressed, the optical absorbance at 630 nm declined steadily until the solution became virtually colorless after 30 minutes of plasma exposure. This

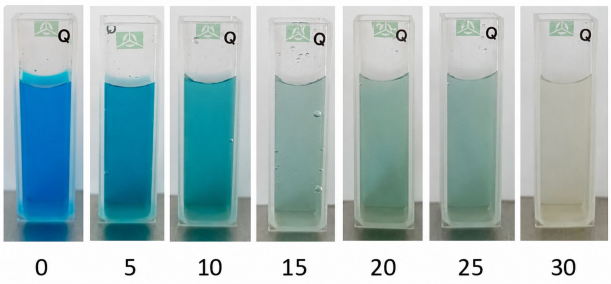


FIGURE 2. Progressive decolorization of AB9 dye solution as a function of plasma treatment time.

progressive loss of color reflects the disruption of the chromophore system through cleavage of the conjugated π-bonds responsible for visible-light absorption. The reduction in the characteristic absorption band at 630 nm confirms that AB9 degradation is driven by the RONS generated during plasma discharge, principally ·OH, O_3, and H_2O_2, which collectively promote the oxidative breakdown of the dye molecule [17,18].

3.2. Effect of $FeSO_4$ Concentration on Degradation Efficiency

Figure 3 present the UV-Vis absorbance spectra of AB9 at each $FeSO_4$ concentration tested [3a) to 3e)]. In all cases, the absorbance band at $\lambda_{max} = 630$ nm decreased progressively with treatment time, confirming that plasma-driven oxidation was active across the entire concentration range studied. The rate and extent of decolorization varied markedly with catalyst dosage, however, revealing a well-defined optimum. At the lowest catalyst concentration tested, 0.2 mM $FeSO_4$ [Fig. 3a)], absorbance decreased only modestly over 30 minutes and complete decolorization was not achieved. The limited performance is consistent with insufficient Fe^{2+} availability: with little Fe^{2+} present, decomposition of plasma-produced H_2O_2 into ·OH radicals is constrained, and the overall oxidative capacity remains below the threshold required for complete chromophore destruction. Increasing the catalyst concentration to 0.4 mM $FeSO_4$ [Fig. 3b)] produced a noticeably greater reduction in absorbance, indicating that higher Fe^{2+} availability translated into more effective ·OH generation via H_2O_2 decomposition. Nevertheless, decolorization remained incomplete at 30 minutes [19]. At 0.6 mM $FeSO_4$ [Fig. 3c)], representing the optimal condition, the most pronounced decline in band intensity was observed. By 30 minutes, the absorption band at 630 nm had disappeared entirely, indicating near complete degradation of the AB9 chromophore. This result demonstrates that 0.6 mM is the optimal catalyst dosage, at which Fenton-type coupling between Fe^{2+} and plasma-generated H_2O_2 achieves maximum ·OH production [19]. At 0.8 mM $FeSO_4$ [Fig. 3d)], the decolorization rate was lower than at the optimum, and a residual absorption band persisted after 30 minutes. This decline is attributed to the radical scavenging effect of excess Fe^{2+}: at supraoptimal concentrations, Fe^{2+} competes with organic substrates for ·OH radicals through the reaction

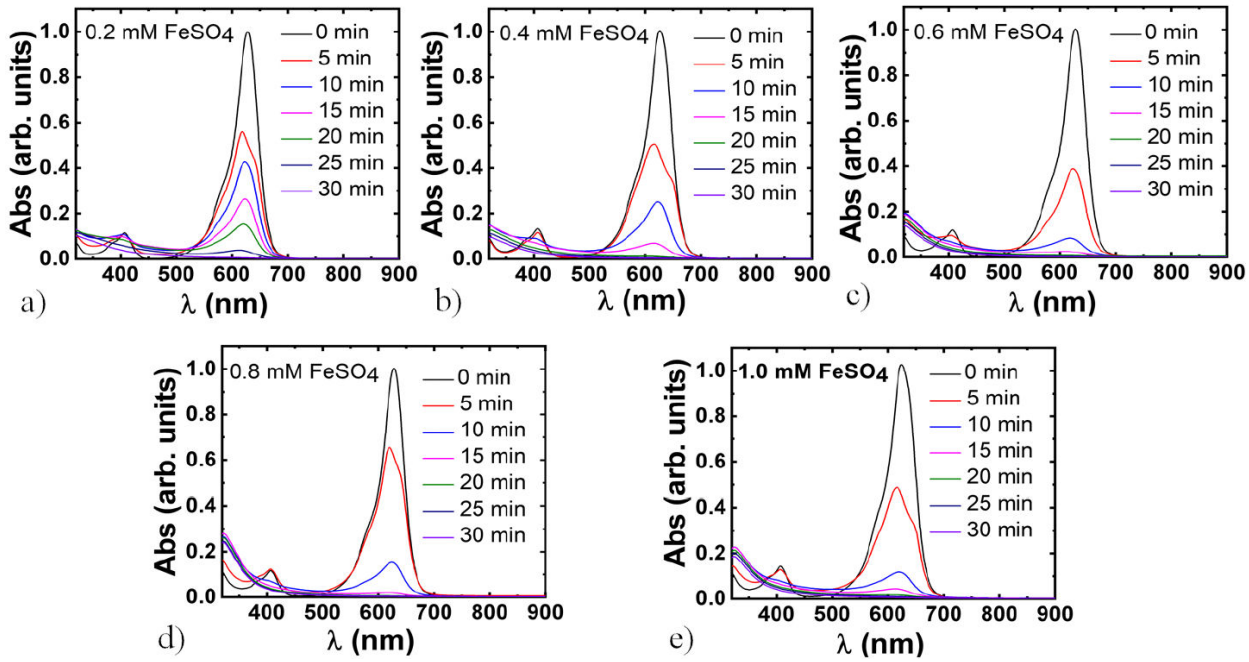


FIGURE 3. UV-Vis absorbance spectra of AB9 during plasma treatment at $FeSO_4$ concentrations of (A) 0.2 to (E) 1.0 mM.

$Fe^{2+} + \cdot OH \rightarrow Fe^{3+} + OH^-$ [18]. The highest catalyst concentration,1.0 mM $FeSO_4$ [Fig. 3e)], yielded the poorest decolorization among the supraoptimal conditions. The overabundance of Fe^{2+} intensifies radical scavenging competition, suppressing ·OH availability and limiting oxidative attack on the dye. These results collectively confirm that the relationship between $FeSO_4$ concentration and degradation efficiency is non-monotonic, with a well-defined maximum at 0.6 mM.

3.3. Mineralization and reaction kinetics

The normalized TOC/TOC_0 ratio as a function of plasma exposure time is shown in Fig. 4. In all cases, TOC/TOC_0 decreased progressively with treatment time, confirming actual mineralization of AB9. The steepest decline occurred during the initial phase, particularly at 0.6 mM $FeSO_4$. As treatment proceeded, the rate of TOC removal slowed characteristic of AOPs systems where recalcitrant intermediates exhibit lower reactivity toward ·OH than the parent compound [18]. At 0.6 mM $FeSO_4$, mineralization efficiency exceeded 90 % within 30 minutes. Decolorization followed an apparent pseudo-first-order model, with rate constants of: $\kappa = 0{,}0895\ \text{min}^{-1}$ (0.2 mM), $0{,}1499\ \text{min}^{-1}$ (0.4 mM), $0{,}2093\ \text{min}^{-1}$ (0.6 mM), $0{,}1371\ \text{min}^{-1}$ (0.8 mM), and $0{,}1202\ \text{min}^{-1}$ (1.0 mM). The maximum rate constant at 0.6 mM is consistent with the optimal Fenton-type catalytic condition.

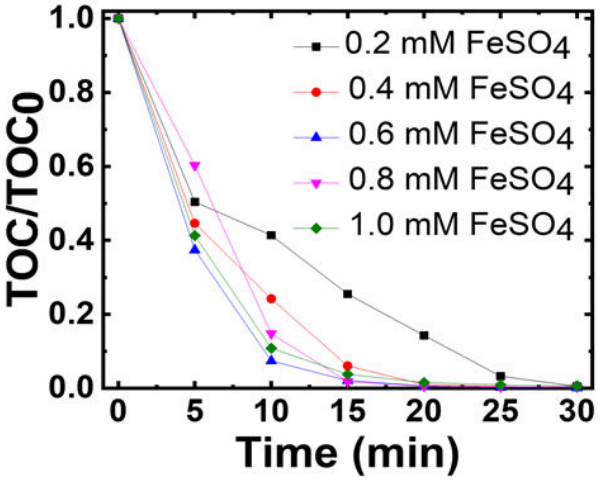


FIGURE 4. Normalized TOC/TOC_0 profiles as a function of plasma exposure time.

3.4. Physicochemical Evolution of the Treated Solution

The bulk solution temperature rose from approximately 22°C to 45°C over the 30-minute treatment [Fig. 5a)]. The most rapid increase occurred during the first 10–15 minutes, after which the system approached quasi-thermal equilibrium. This response results from the transfer of energy from plasma-generated species into the liquid phase through excitation-relaxation and ion-neutral collision processes at

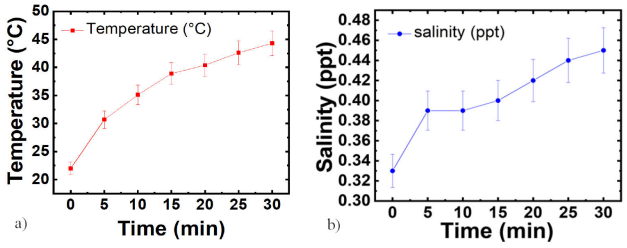


FIGURE 5. a) Bulk solution temperature and b) salinity as a function of plasma treatment time.

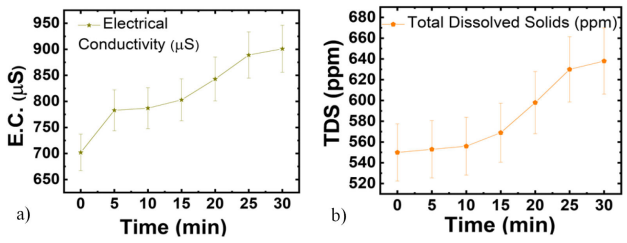


FIGURE 6. a) Electrical conductivity and b) total dissolved solids (TDS) as a function of plasma treatment time.

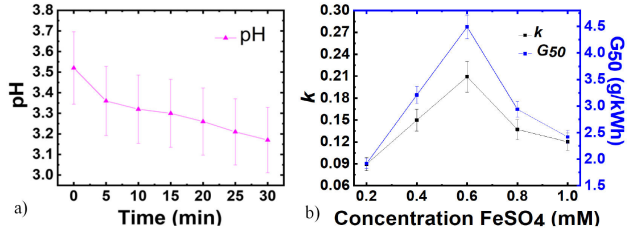


FIGURE 7. a) pH variation and b) rate constant (κ) and G_{50} as a function of $FeSO_4$ concentration.

the plasma-liquid interface [20]. Concurrently Salinity increased from approximately 0.33 to 0.45 ppt [Fig. 5b)], reflecting progressive accumulation of dissolved ionic species from oxidative fragmentation of AB9 and plasma-driven RONS formation, consistent with the initial stages of organic mineralization in AOPs systems [21].

Electrical conductivity increased from approximately 702 to 901 μS/cm [Fig. 6a)], driven by ionic species released during plasma-driven oxidative degradation of AB9. As the dye's aromatic structure is fragmented, ionic degradation products accumulate in solution, continuously feeding the conductivity increase throughout treatment [22]. TDS values increased from approximately 550 to 640 ppm [Fig. 6b)], closely paralleling the conductivity trend. Together, these parameters confirm ongoing mineralization: both increase as large organic structures are converted into low-molecular-weight ionic species [22].

Solution pH declined progressively from 3.52 to 3.17 [Fig. 7a)]. This acidification is primarily driven by the formation of HNO_3 and HNO_2 from gas-phase reactions between atmospheric nitrogen, water vapor, and plasma-generated species, supplemented by intermediate organic acids formed during AB9 fragmentation [19].

3.5. Energy efficiency: G_{50} parameter

A parameter for measuring energy efficiency in the degradation of pollutants is the G_{50}, which is defined as the amount of pollutant removed per unit of energy consumed to achieve 50 % degradation [23,24]. The energy efficiency of the decolorization process was evaluated using the G_{50} parameter:

$$G_{50} = 1{,}8 \times 10^6 \frac{C_0 V_0 M}{P t_{50}}. \quad (6)$$

TABLE I. Comparison of G_{50} values for plasma-based degradation processes [24,25].

System	Contaminant	Catalyst / Conditions	G_{50}
NTAPP + $FeSO_4$ (this work)	Acid Blue 9	$FeSO_4$ (0.6 mM)	4.49
Non-thermal plasma	Acid Blue 25	Without catalyst	2.40
Dielectric Barrier Discharge (DBD)	Carbamazepine	Without catalyst	1.60
Dielectric Barrier Discharge (DBD)	2,4-Dinitrophenol	Without catalyst	0.94

For this study, $C_0 = 1{,}0 \times 10^{-4}$ M, $V_0 = 0{,}25$ L, $M = 792{,}86$ g/mol, and $P = 40$ W. The experimentally determined t_{50} values were 465, 277.8, 198.6, 303, and 268.4 s for 0.2, 0.4, 0.6, 0.8, and 1.0 mM $FeSO_4$, respectively, yielding G_{50} values of 1.92, 3.21, 4.49, 2.94, and 2.42 g/kWh [Fig. 7b)]. The maximum G_{50} of 4.49 g/kWh was achieved at 0.6 mM $FeSO_4$.

3.6. Comparative analysis of energy efficiency

Table I compares the G_{50} values obtained system achieves the highest energy efficiency among all entries listed, attributed to the synergistic interaction between plasma-generated RONS and the Fenton-type reaction at 0.6 mM $FeSO_4$ [24,25]. The availability of Fe^{2+} ions is sufficient to promote the decomposition of H_2O_2 generated by the plasma, increasing the production of ·OH radicals. At low concentrations (0.2 and 0.4 mM), the process is limited by insufficient catalyst availability, resulting in lower hydroxyl radical generation and a slower degradation rate. Conversely, at higher $FeSO_4$ concentrations (0.8 and 1.0 mM), the excess Fe^{2+} ions act as scavengers of ·OH radicals. This decreases the oxidative capacity and reduces the overall degradation efficiency.

3.7. Operating energy cost

Under optimal conditions (0.6 mM $FeSO_4$; $t_{1/2} = 198{,}6$ s; $P = 40$ W), the energy consumed to treat 250 mL was 0.00220 kWh. Applying CFE domestic electricity tariffs (0.987-3.218 MXN/kWh) [26], the estimated operating cost is 0.00217-0.00710 MXN per 250 mL, equivalent to 17.4-56.8 MXN/m^3 or approximately 0.50-1.64 USD/m^3.

From an operational standpoint, the energy cost analysis places the proposed system at 0.50-1.64 USD/m^3 under optimal conditions, which compares favorably with UV/H_2O_2, ozone-based, and photocatalytic systems reported in the literature. The reactor operates at atmospheric pressure, requires no chemical dosing beyond the catalytic $FeSO_4$ additive, and generates reactive species on demand without producing hazardous secondary byproducts. These characteristics collectively reduce the barriers to practical implementation, par-

TABLE II. Operating costs of the NTAPP + $FeSO_4$ system and other advanced oxidation processes reported in the literature [26-32].

Technology	Cost (USD/m^3)
NTAPP + $FeSO_4$ (0.6 mM)	0.50 – 1.64
UV/H_2O_2	∼5.80
O_3/H_2O_2	∼8.64
O_3/UV	up to 240
TiO_2/UV	4 – 12
Conventional ozone treatment	6 – 15

ticularly in decentralized or small-scale treatment contexts where reagent logistics and reactor complexity are limiting factors.

4. Conclusions

This study set out to evaluate whether $FeSO_4$ could meaningfully enhance the performance of a non-thermal atmospheric-pressure plasma system for degrading Acid Blue 9. The results confirm that it can but only within a narrow concentration window. At 0.6 mM $FeSO_4$, the system achieved near-complete decolorization and a mineralization efficiency exceeding 90 % within 30 minutes, with a pseudo-first-order rate constant of $\kappa = 0{,}2093\ \text{min}^{-1}$ and an energy efficiency of $G_{50} = 4{,}49$ g/kWh. What these results demonstrate, more broadly, is that the combination of plasma-generated H_2O_2 and Fenton chemistry is not simply additive it is synergistic. Plasma alone produces RONS, but the integration of $FeSO_4$ converts a fraction of the accumulated H_2O_2 into additional ·OH radicals, extending the reactive lifetime of the system and enabling a level of mineralization that plasma alone, under the same power input and treatment time, would not achieve. The triarylmethane backbone of AB9 which confers both its chromophoric properties and its resistance to biological degradation is effectively dismantled under these conditions.

The broader implication is that NTAPP, when catalytically intensified, represents a technically sound and economically competitive option for the treatment of dye-contaminated wastewater. In a context where textile industry effluents continue to pose a documented risk to surface water quality and human health, and where freshwater scarcity makes wastewater reuse increasingly important, systems that achieve genuine mineralization, rather than phase transfer or partial decolorization, deserve serious consideration. The data reported here supports that case.

Acknowledgments

The authors wish to thank Herlinda Z. Pichardo Morales for technical support in the development of this work, as well as the following funding sources for their support: PRODEP DSA/103.5/15/6986, CA-5511-6/18-8304, and UAEMex 7440/2026CIB.

1. M. Berradi, R. Hsissou, M. Khudhair, M. Assouag, O. Cherkaoui, A. El Bachiri and A. El Harfi, Textile finishing dyes and their impact on aquatic environs, *Heliyon* **5** (2019) e02711, https://doi.org/10.1016/j.heliyon.2019.e02711
2. G. Kavitha, M. Govindhan, and S. Premkumar, Dye pollution and its implications for human health, aquatic ecosystems, and sustainable wastewater treatment: A comprehensive review, *J. Water Process Eng*. **80** (2025) 109071, https://doi.org/10.1016/j.jwpe.2025.109071
3. E. Forgacs, T. Cserhati, and G. Oros, Removal of synthetic dyes from wastewaters: A review, *Environ. Int*. **30** (2004) 953, https://doi.org/10.1016/j.envint.2004
4. T. Robinson and G. McMullan and R. Marchant and P. Nigam, Remediation of dyes in textile effluent: A critical review on current treatment technologies with a proposed alternative, *Bioresour. Technol.* **77** (2001) 247, https://doi.org/10.1016/s0960-8524(00)00080-8
5. S. Samsami and M. Mohamadizaniani and M. H. Sarrafzadeh and E. R. Rene and M. Firoozbahr, Recent advances in the treatment of dye-containing wastewater from textile industries: Overview and perspectives, *Process Saf. Environ. Prot.* **143** (2020) 138, https://doi.org/10.1016/j.psep.2020.05.034
6. H. Zollinger, Color chemistry: Syntheses, properties, and applications of organic dyes and pigments, 3rd ed. (Wiley-VCH, 2003), pp. 1-367.
7. M. A. Shannon and P. W. Bohn and M. Elimelech and J. G. Georgiadis and B. J. Mariñas and A. M. Mayes, Science and technology for water purification in the coming decades, *Nature* **452** (2008) 301, https://doi.org/10.1038/nature06599
8. V. Katheresan, J. Kansedo, and S. Y. Lau, Efficiency of various recent wastewater dye removal methods: A review, *J. Environ. Chem. Eng*. **6** (2018) 4676, https://doi.org/10.1016/j.jece.2018.06.060
9. J. A. Garrido-Cardenas and B. Esteban-García and A. Agüera and J. A. Sánchez-Pérez and F. Manzano-Agugliaro, Wastewater treatment by advanced oxidation processes and their worldwide research trends, *Int. J. Environ. Res. Public Health* **17** (2020) 170, https://doi.org/10.3390/ijerph17010170
10. Y. Deng and R. Zhao, Advanced oxidation processes (AOPs) in wastewater treatment, *Curr. Pollut. Rep.* **1** (2015) 167, https://doi.org/10.1007/s40726-015-0015-z
11. M. A. Oturan and J. J. Aaron, Advanced oxidation processes in water/wastewater treatment: Principles and applications. A re-

view, *Crit. Rev. Environ. Sci. Technol*. **44** (2014) 2577, https://doi.org/10.1080/10643389.2013.829765

12. A. Barjasteh and Z. Dehghani and P. Lamichhane and N. Kaushik and E. H. Choi and N. K. Kaushik, Recent progress in applications of non-thermal plasma for water purification, *Appl. Sci*. **11** (2021) 3372, https://doi.org/10.3390/app11083372
13. P. Bruggeman and C. Leys, Non-thermal plasmas in and in contact with liquids, *J. Phys. D: Appl. Phys*. **42** (2009) 053001, https://doi.org/10.1088/0022-3727/42/5/053001
14. H. Zeghioud and P. Nguyen-Tri and L. Khezami and A. Amrane and A. A. Assadi, Review on discharge plasma for water treatment: Mechanism, reactor geometries, active species and combined processes, *J. Water Process Eng*. **38** (2020) 101664, https://doi.org/10.1016/j.jwpe.2020.101664
15. J. Sánchez, J. Beltrán, and M. T. Rodríguez, Removal of Erioglaucine (Acid Blue 9) with a new coagulant agent from Acacia mearnsii tannin extract, *Coloration Technol.* **128** (2012) 15, https://doi.org/10.1111/j.1478-4408.2011.00342.x
16. M. Flury and H. Flühler, Tracer characteristics of Brilliant Blue FCF, *Soil Sci. Soc. Am. J.* **59** (1995) 22, https://doi.org/10.2136/sssaj1995.03615995005900010003x
17. A. V. Borhade, D. R. Tope, and G. B. Dabhade, Removal of Erioglaucine dye from aqueous medium using ecofriendly synthesized ZnMnO3, e-J. *Surf. Sci. Nanotechnol*. **15** (2017) 74, https://doi.org/10.1380/ejssnt.2017.74
18. E. Brillas, I. Sirés, and M. A. Oturan, Electro-Fenton process and related electrochemical technologies based on Fenton's reaction chemistry, *Chem. Rev.* **109** (2009) 6570, https://doi.org/10.1021/cr900136g
19. J. J. Pignatello, E. Oliveros, and A. MacKay, Advanced oxidation processes for organic contaminant destruction based on the Fenton reaction and related chemistry, *Crit. Rev. Environ. Sci. Technol*. **36** (2006) 1, https://doi.org/10.1080/10643380500326564
20. A. Fridman, Plasma chemistry (Cambridge University Press, 2008), https://doi.org/10.1017/cbo9780511546075
21. H. Ghodbane and A. Y. Nikiforov and O. Hamdaoui and P. Surmont and F. Lynen and G. Willems and C. Leys, Non-thermal plasma degradation of anthraquinonic dye in water: Oxidation pathways and effect of natural matrices, *J. Adv. Oxid. Technol*. **17** (2014) 372, https://doi.org/10.1515/jaots-2014-0223
22. A. Babuponnusami and K. Muthukumar, A review on Fenton and improvements to the Fenton process for wastewater treatment, *J. Environ. Chem. Eng*. **2** (2014) 557, https://doi.org/10.1016/j.jece.2013.10.011
23. M. Rahimpour and M. Rahimpour and H. Taghvaei and S. Zafarnak and M. R. Rahimpour and M. R. Rahimpour and S. Raeissi, Post-discharge DBD plasma treatment for degradation of organic dye in water: A comparison with different plasma operation methods, *J. Environ. Chem. Eng*. **7** (2019) 103220, https://doi.org/10.1016/j.jece.2019.103220
24. M. A. Malik, Water purification by plasmas: Which reactors are most energy efficient?, *Plasma Chem. Plasma Process.* **30** (2009) 21, https://doi.org/10.1007/s11090-009-9202-2
25. Y. Cao and G. Qu and T. Li and N. Jiang and T. Wang, Review on reactive species in water treatment using electrical discharge plasma: Formation, measurement, mechanisms and mass transfer, P*lasma Sci. Technol*. **20** (2018) 103001, https://doi.org/10.1088/2058-6272/aacff4
26. CalcUle MX, Precio kWh CFE 2026: Tarifas 1, 1B, 1C, DAC y Recibo, https://www.calcule.com/guias/cfe/ tarifas-electricas/ (2026).
27. Y. Zhang and K. Shaad and D. Vollmer and C. Ma, Treatment of textile wastewater using advanced oxidation processes-A critical review, *Water* **13** (2021) 3515, https://doi.org/10.3390/w13243515
28. N. Azbar, T. Yonar, and K. Kestioglu, Comparison of various advanced oxidation processes and chemical treatment methods for COD and color removal from a polyester and acetate fiber dyeing effluent, *Chemosphere* **55** (2003) 35, https://doi.org/10.1016/j.chemosphere.2003.10.046
29. S. Mehdizadeh and S. Sadjadi and S. J. Ahmadi and M. Outokesh, Removal of heavy metals from aqueous solution using platinum nanoparticles/Zeolite-4A, *J. Environ. Health Sci. Eng.* **12** (2014) 7, https://doi.org/10.1186/2052-336x-12-7
30. E. N. Kadioglu and H. A. Eroglu and H. Ozturk and F. Akbal and A. Kuleyin, Enhanced degradation of textile wastewater by activated carbon-assisted Fenton oxidation: Economic analysis and ANN-based optimization, *Biomass Conv. Bioref.* **15** (2025) 17775, https://doi.org/10.1007/s13399-025-06599-1
31. M. N. Chong and B. Jin and C. W. Chow and C. Saint, Recent developments in photocatalytic water treatment technology: A review, *Water Res*. **44** (2010) 2997, https://doi.org/10.1016/j.watres.2010.02.039
32. K. Ikehata and M. G. El-Din, Aqueous pesticide degradation by ozonation and ozone-based advanced oxidation processes: A review (Part I), *Ozone: Sci. Eng*. **27** (2005) 83, https://doi.org/10.1080/01919510590925220

Deep learning based identification of solvents from post-desiccation patterns

J. I. Morán-Cortés* and F. Pacheco-Vázquez

Instituto de Física, Benemérita Universidad Autónoma de Puebla,
Apartado Postal J-48, Puebla 72570, Mexico,
**e-mail: jmoran@ifuap.buap.mx; fpacheco@ifuap.buap.mx*

Received 8 January 2026; accepted 29 May 2026

We introduce an optimized Deep learning protocol for fracture pattern classification to identify the solvent involved in the desiccation cracking process of starch-liquid slurries, even after its complete evaporation. For this purpose, image analysis techniques were used to characterize patterns obtained from drying suspensions using single solvents (water, ethanol, acetone) and two-component solvents (water-ethanol mixtures at different concentrations). Frequency histograms were generated based on nine morphological features, taking into account their size, shape, geometry and orientational ordering. Subsequently, we used these histograms as input data in different artificial neural network variants to determine which set of features leads to the highest accuracy in solvent identification. An average accuracy of up to $96(\pm1)\,\%$ was achieved in the classification when all solvents were considered in the analysis. The highest accuracy was obtained with sets that include the crack area, $A_{\mathrm{cr}N}$, a feature barely considered in the literature. We found that $A_{\mathrm{cr}N}$ can be related to the cohesive energy associated with hydrogen bond interactions. Taking this into account, we estimated some physicochemical properties of two-component solvents (specifically, the Hansen and Kamlet-Taft parameters) based solely on the features of patterns obtained from the individual components, achieving an error within $15\,\%$ compared to the values determined from the literature. The proposed protocol could help to encode some implicit parameters and the optimal combination of features for pattern recognition in other fields of science and engineering.

Keywords: Solvent identification; pattern recognition protocol; cracking process; desiccation; neural networks; deep learning.

DOI: https://doi.org/10.31349/RevMexFis.72.061701

1. Introduction

In different scientific fields, neural networks stand out for their effectiveness and efficiency in automatically classifying patterns based on their morphological features [1-10]. Ponomarev *et al*. [4,5] used an automatic classification method of immunofluorescent images for autoimmune disease diagnostics based on the number, size, shape, and localization of individual cells in medical tests, achieving an average accuracy of $84(\pm6)\,\%$ and showing performance comparable to that of the texture-based method [6]. Umer *et al*. [7] proposed a person identification system based on multiscale morphology to extract structural and textural features from human iris images, with average accuracy of $99(\pm1)\,\%$. Wang et al. [8] developed a model for material property classification based on X-ray and neutron diffraction patterns of crystal structures, reaching accuracies of $66(\pm14)\,\%$ for the perovskite family ABO_3. Fan *et al*. [9] propose a model for classifying multi-defect wafer map patterns by combining a densities clustering method with geometric features, including form factor (area/perimeter) and eccentricity, obtaining average accuracy of up to $94\,\%$, whereas more recently, Choi and Suh [10] achieved over $98\,\%$ accuracy for the same purpose with a model focused on the active contour. Although neural networks with statistical approaches are feasible tools for pattern recognition, a correct selection of parameters is essential to avoid overfitting and increase the accuracy and efficiency of the method.

Desiccation patterns are probably the most common examples of how nature spontaneously generates configurations through complex processes that occur over multiple time and length scales. For example, at microscopic scale, slow evaporation of gold nanoparticle suspensions results in microwire patterns induced by drying liquid bridges [11]. Evaporation of blood droplets produces dendritic patterns with radial fissures in the periphery related to a high concentration of lipids [12]. On a much larger scale, drying processes in basins and lakes generate polygonal salt patterns [13], while the shrinkage of frozen ground (permafrost) creates ice-filled crevices and soil [14]. Furthermore, these polygonal patterns are not limited to Earth alone, but are also found on the surface of Mars [14-19] and the Moon [17]. Such patterns exhibit great morphological diversity due to the influence of multiple factors during their formation; however, they can be effectively analyzed and classified using image analysis and Deep learning techniques (for example, to predict the number of cracks in the soil based on the initial moisture content, layer thickness, and sample size [20]), provided that adequate selection of parameters is made.

Thin layers of colloidal suspensions have been extensively used at laboratory scale to explore desiccation processes. On the one hand, it has been shown that the morphology of the resulting cracking patterns depends significantly on the thickness h of the layer. Theoretically, thin films crack upon reaching a critical stress, which relaxes over a distance proportional to h [21], while the crack spacing L follows a power scaling with exponent $n = 2/3$ [17,22], in reasonable agreement with experiments ($n = 0{,}65 \pm 0{,}01$ for silica particles [23,24], $n = 0{,}71 \pm 0{,}01$ for cornstarch and $n = 0{,}53 \pm 0{,}02$ with clay [17]), for which the characte-

ristic lengths $L_1 = \sqrt{A_c/N_c}$ and $L_2 = A_c/L_T$ have been proposed, where A_c is the size of the container, N_c the number of cells, and L_T the total length of the cracks. In addition, the average displacement of the pattern vertices increases linearly with h during repeated wetting and drying cycles [21]. Likewise, the characteristic area A of the patterns is directly proportional to $h^{4/3}$ when using cornstarch with water, as well as calcium carbonate ($CaCO_3$) with different solvents such as water, isopropanol and silicone oil [16,17]. On the other hand, Choudhury *et al*. [25] studied the desiccation cracking process in bentonite-chloride salt slurries. Bentonite can exhibit strong swelling and dispersion due to water absorption, but the presence of dissolved salts affects shrinkage properties, surface tension and internal stress distribution by altering the ionic concentration, osmotic effects, and physicochemical properties. All these results evidence the influence of solute/solvent interactions on the morphological features of fracture patterns.

In order to classify fracture patterns, frequency histograms are a useful tool to represent their morphological distribution. A variety of parameters exists to characterize the geometry and topology of these patterns based on radial density profile [12], average areas [16,26-29], lengths [17,19,23,24,27,30], number of neighbors [19,29,31], fractal dimension [32,33] and lacunarity [33], to name a few, but only some studies include a large dataset of measurements. However, histograms based on the normalized isoperimetric ratio, defined as $\lambda = 4\pi A/P^2$, where A is the area and P is the perimeter of the patterns, have been proposed by Roy *et al*. [29] as the most efficient parameter to distinguish between fracture patterns, which they qualitatively evidenced in cracked materials of natural mud, clays (such as laponite and bentonite), corn and potato starch extracts, polymers (such as PDMS), among others. From a statistical point of view, this should hold true even if the successive cleavage of the fracture patterns does not follow a regular or uniform process [31]. For this reason, histograms of the area−perimeter set and other morphological features may contribute to the automated identification of such patterns, but the effectiveness and efficiency of these features for classification is still unknown.

In this work, we propose an optimized Deep learning protocol that uses neural networks to recognize and classify fracture patterns produced during the desiccation of cornstarch-liquid slurries involving different solvents. For this purpose, an experimental array (described in Sec. 2) was used to follow the evaporation process of thin layers of the slurries until the fracture patterns appear. The experimental results are discussed in Sec. 3. The methodology used for the morphological analysis is described in Sec. 4, where the set of features are represented in frequency histograms to characterize fracture patterns from their size, shape, geometry and orientational ordering. On the one hand, the size is characterized using the area and perimeter of the cells and the area of the cracks, all normalized by characteristic values, while shape is described by the eccentricity. On the other hand, the geometry is determined by the number of neighbors, obtained from Voronoi diagrams; while ordering is determined by an order parameter, defined as a function of these neighbors and the centroids of the cells. In Sec. 5, we outline the framework of the proposed protocol, emphasizing the construction, training, and accuracy calculation of an Artificial Neural Network (ANN) to classify experimental sample classes. Subsequently, in Sec. 6, the accuracy of the classification was evaluated considering each individual feature as well as combinations of different sets of features, identifying those sets that lead to the highest accuracies. We also discuss why the feature A_{cr} becomes relevant for the classification based on its correlation with hydrogen bonding solute-solvent interactions. In Sec. 7, a possible application of the protocol focused on the estimation of physicochemical properties is presented. The conclusions are finally summarized in Sec. 8. Additionally, an Appendix section is provided to explain why the accuracy of the model can be compromised in the analysis.

2. Experimental setup

The experimental design is sketched in Fig. 1a), and it is similar to previous systems used in the literature [26,27]. A given mass of cornstarch-liquid slurry is deposited in a cylindrical aluminium container of diameter $D_c = 100$ mm, and the container is placed on an analytical balance (OHAUS PX423). The system allows for recording the mass of the slurry during the desiccation process every minute, and a digital thermometer-hygrometer placed inside the balance chamber was used to register the temperature T (°C) and the relative ambient humidity RH (%) every five minutes. A digital camera (NIKON D3200) is positioned to record images from a top view of the container and to capture the final morphology of the fracture patterns.

The mixtures were prepared with an initial concentration $\phi_0 = 1/2$, defined as $\phi_0 = m_{liq}/(m_{liq} + m_{cs})$ [34], where m_{liq} is the mass of the liquid (solvent) and m_{cs} corresponds to dry cornstarch (solute), obtained from a commercial brand (Maizena). A mass $m_0 = 40{,}0\,(\pm 0{,}1)$g of the homogeneous mixture was prepared for each experiment using equal masses of liquid (20,0g) and cornstarch (20,0g), obtaining average densities $\rho = 1{,}20(\pm 0{,}01)\,\mathrm{g/cm^3}$ for cornstarch-

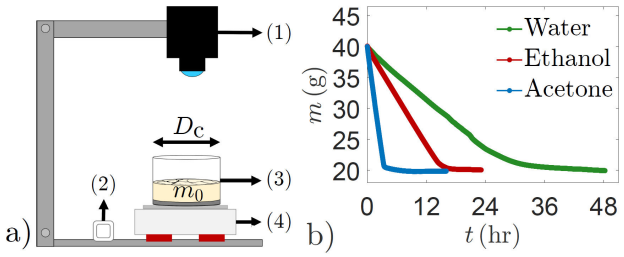


FIGURE 1. a) Experimental setup components: (1) digital camera, (2) digital thermometer-hygrometer (3) aluminum container with initial mass m_0 of a specific mixture, and (4) analytical balance. b) Remanent mass m of the mixtures as a function of time t during the drying process, for three different solvents.

water slurry and $\rho = 1{,}03(\pm 0{,}01)\,\mathrm{g/cm^3}$ for both cornstarch-ethanol and cornstarch-acetone slurries. The mixture is deposited in the center of the container, and it extends radially, forming a thin horizontal liquid layer of thickness $h_0 \sim 4-5$ mm $\ll \mathrm{D_c}$. Once the solvent evaporation is completed, the layer thickness (and therefore, the volume of the layer) is reduced by $16(\pm 1)\,\%$, and the patterns are recorded for subsequent analysis.

Following the procedure described above, 75 liquid layers were prepared using single solvents, distributed in 25 samples for each solvent: deionized water, ethanol (CTR Scientific) and acetone (CTR Scientific). The samples were left to evaporate naturally for 48, 24, and 12 hours for the water, ethanol, and acetone mixtures, respectively. The latter substances are more volatile and require less time for total evaporation, which is considered to occur when $m \approx 20$ g, *i.e.* when all the liquid has been evaporated and only the solute remains in the container. Environmental conditions remained nearly constant throughout the experiments, with an average relative humidity of $\mathrm{RH_{env}} = 39(\pm 6)\,\%$ and an average room temperature of $T_{\mathrm{env}} = 28(\pm 1)^{\circ}\mathrm{C}$.

3. Experimental results

3.1. Evaporation process

Figure 1b) shows how the mass of the mixture m decreases with time t for the three samples of water, ethanol and acetone. From the moment of deposition, evaporation proceeds in two stages [26,35,36]. First, the mass decreases linearly with time (constant evaporation rate) until a wet cornstarch layer seems to settle at the bottom of the container, which is characterized by the notorious change of curvature in the plots. At this moment, the layer adheres to the substrate and begins to contract until it detaches from the container walls. This process is consistent for different solutes in water, such as cornstarch [16,30], granular polymers [37], Romainville clay [27], hard and soft nanolatex spheres [26,31], Sisal fiber and soil [38], sand and kaolinite clay [32], among others. Subsequently, two types of cracks appear that divide the layer into primary and secondary patterns according to their order of appearance [16,30]. Primary patterns arise from a critical h_c layer thickness and they are formed in the first evaporation stage due to capillary contraction of the material [16]. During the second evaporation stage for the case of cornstarch in water, secondary patterns emerge in large amounts and simultaneously within the primary patterns due to dehydration of the hygroscopic cornstarch particles [16,31], even when the layer thickness is $h < h_c$. For the case of ethanol and acetone, only one kind of cracks appear during the evaporation process and the resulting patterns are more homogeneous, as we discuss in the following section.

3.2. Fracture patterns produced by different solvents

Figure 2 shows that the final fracture patterns depend on the solvent used. For the case of water, primary thicker fractures are clearly observed (secant lines crossing almost the whole layer), which are not observed with ethanol or acetone. There are also numerous small secondary thinner fractures associated with columnar joints in water [21,35,36], while the number of cells decreases significantly in ethanol and acetone, causing an increase in their size, as shown in Fig. 2a). Furthermore, the secondary cells are larger in acetone than in ethanol, whereas in water they are noticeably smaller and more irregular. Consequently, the samples in Fig. 2a) can in principle be easily distinguished from one another.

The change in pattern features can be associated to changes of the physicochemical properties of the solvent. To explore this aspect, we considered 50 additional liquid layers with binary solvents consisting of mixtures of water and

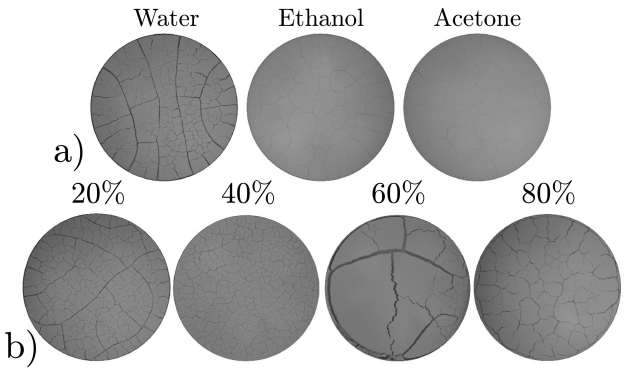


FIGURE 2. Fracture patterns observed in experimental samples of mixtures using solvents of a) pure liquids and b) water-ethanol mixtures with the indicated percentages of ethanol.

TABLE I. Some properties of pure solvents and ethanol-water binary solvents used in this study, including: the surface tension σ, density ρ and viscosity η at 25°C [39-43]. Volume fraction v and mole fraction X of ethanol ($M = 46{,}07$) in water ($M = 18{,}02$), depending on the indicated percentage of ethanol mass in the mixture, where M denotes the molar mass.

Property	Water	20 %	40 %	60 %	80 %	Ethanol	Acetone
σ (mN/m)	72.01	37.97	30.16	26.23	23.82	21.82	23.02
ρ (g/cm^3)	0.9971	0.9663	0.9316	0.8882	0.8398	0.7856	0.7843
η (mPa·s)	0.8907	1.7803	2.3586	2.2411	1.7302	1.0907	0.3050
v	0	0.241	0.458	0.656	0.835	1	-
X	0	0.089	0.207	0.370	0.610	1	-

ethanol at different concentrations (see Table I). The characteristic patterns of the transition from pure water to pure ethanol are shown in Fig. 2b) using water-ethanol mixtures at 20, 40, 60 and 80 % of ethanol content. On the one hand, for concentrations close to pure liquids, the number of patterns and the size of the cracks appear similar to those of the dominant liquid, although contrasting morphological features arise due to the recessive liquid. On the other hand, mixtures with comparable proportions of water and ethanol can be clearly distinguished from the other samples. For instance, at 40 % ethanol, primary cracks disappear with respect to 20 %, but the number of secondary cells looks similar. A particular pattern appears at 60 % ethanol, in which case the pattern size and width of the cracks seem considerably larger. However, in the mixture of 80 % ethanol, a clear competition arises between the morphological features obtained with pure liquids; the presence of water produces thicker fractures, but with an ordering and geometry of cells similar to those observed in pure ethanol. Therefore, the number of patterns, the spatial distribution, their average area and perimeter, and the thickness of the cracks are morphological features of the patterns determined by the solvent, which have to be considered in the classification and identification protocol.

4. Morphological analysis

Figure 3 illustrates the methodology used for the morphological analysis of fracture patterns. Images of all experimental samples are first captured, as illustrated in Fig. 3a). Then, using the software FIJI ImageJ®, each image is binarized to show exclusively the cracks that outline the boundaries of the patterns as depicted by the red borders in Fig. 3b). By performing this image analysis iteratively for each of the experimental samples, five main features can be estimated: the number N_c of patterns in each experimental sample, the area A, perimeter P, centroid $C\,(x, y)$, and eccentricity ε of the patterns. After applying Voronoi tesselation, the total length L_T was obtained. Furthermore, each image was divided in $n = 64$ circular sectors to account for variations in the crack distribution, and the number of pixels conforming the cracks in each sector was estimated, which allows to obtain the area A_{cr} of the cracks. These morphological features characterize the size (area−perimeter) and shape (eccentricity) of the fracture patterns.

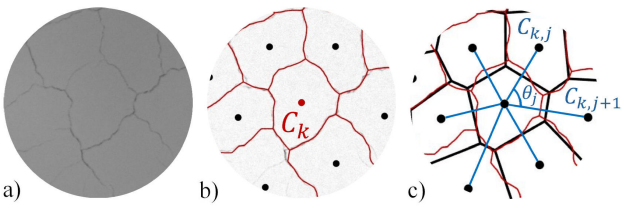


FIGURE 3. Image processing. a) Picture of a fracture pattern. b) Corresponding centroids (black dots) and c) Voronoi diagram (black edges) from the real fracture pattern (red edges) after image processing.

On the other hand, centroids [Fig. 3b)] allow to infer geometrical and ordering features of the patterns, which show a high correspondence with the Voronoi diagrams [black edges in Fig. 3c)] [29]. Using MATLAB®, if we focus on the Voronoi diagram of the centroid C_k of some pattern [see Fig. 3b)], we can compute its number of neighbors $N_{B,k}$ with the associated Voronoi diagram to know its geometry. In addition, such centroid can be linked to two adjacent and consecutive centroids $C_{k,j}$ and $C_{k,j+1}$ by straight lines [blue lines in Fig. 3c)] to calculate the angle θ_j between them. Therefore, the associated bound orientational parameter (BOP) $\psi_{k,n}$ of each $k-$th pattern [44], defined as a function of the number $N_{B,k}$ and the angles θ_j for each $j = 1, \ldots, N_{B,k}$, can be computed by:

$$\psi_{k,n} = \frac{1}{N_{B,k}} \left| \sum_{j=1}^{N_{B,k}} \exp\left(in\theta_j\right) \right|, \quad 0 \leq \theta_j < 2\pi, \tag{1a}$$

with

$$\theta_j = \arccos\left[\frac{(C_{k,j+1} - C_k) \cdot (C_{k,j} - C_k)}{|C_{k,j+1} - C_k| \cdot |C_{k,j} - C_k|} \right]. \tag{1b}$$

By applying the morphological analysis to all fracture patterns, we initially estimate the average values of such morphological features. On the one hand, since the area of the container $A_c = 7854$ mm^2 is constant, then the average area $\overline{A}$ of the patterns is inversely proportional to $\overline{N}_c$, such that: $\overline{A} \approx A_c/\overline{N}_c = L_1^2$. On the other hand, the measurements obtained from the image analysis also reveal that $\overline{P} \approx 8A_c/\overline{L}_T = 8L_2$. Additionally, the patterns exhibit similar characteristics; they follow the normalized isoperimetric ratio with an average value of $\lambda = 0{,}70 \pm 0{,}03$, and they show comparable average values of eccentricity ($\varepsilon = 0{,}67 \pm 0{,}07$) and order parameter ($\psi = 0{,}47 \pm 0{,}17$). Therefore, normalized quantities for the sizes of the patterns and cracks can be defined relative to these characteristic lengths, *i.e.*, $A_N = A/L_1^2$, $P_N = P/(8L_2)$, and $A_{crN} = A_{cr}/L_3^2$, respectively, where $L_3 \equiv L_1^2/L_2 = L_T/N_c$. Then, a set of normalized features can be used for the morphological characterization of the fracture patterns.

Figure 4 displays the size and shape measurements in the form of frequency histograms of normalized features, which help to identify those parameters that can be useful to classify the experimental samples. To obtain the histograms, the methodology described above was iteratively applied to the samples [see Figs. 4A)-4B)], with the goal of extracting and characterizing nearly $24,000$ individual cells. In the histograms, one can notice that the measurements for ethanol are more homogeneous than for the case of water (which shows a wider distribution). For the mixture of 20 % water and 80 % ethanol, two maxima appear in the distributions of A_N and P_N indicating a superposition of the effects of both solvents. There is also a noticeable shift to the left in the maximum of the A_{crN} distribution for more volatile liquids. This indicates thinner cracks for acetone and ethanol compared to water.

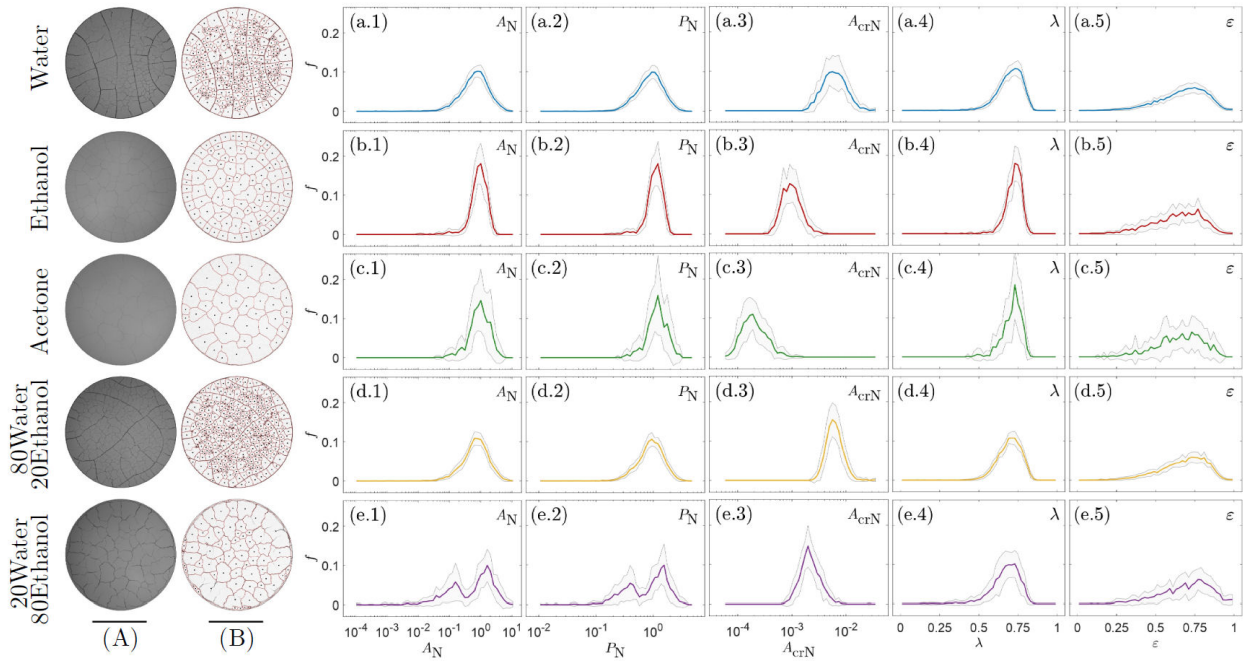


FIGURE 4. Size-shape analysis. (A) Final patterns observed after the desiccation process of layers of cornstarch and the indicated solvent. (B) Corresponding processed images used to identify the cracks (red edges) and their centroids (black dots). In A and B the scale bar is 50 mm. (a-e) Histogram distribution of (1) pattern area A_N, (2) perimeter P_N, (3) crack area A_{crN}, (4) isoperimetric ratio λ, and (5) eccentricity ε, obtained using as solvent: (a) water, (b) ethanol, (c) acetone, and (d) $80/20\,\%$ and (e) $20/80\,\%$ water/ethanol. Colored lines represent the average value and the gray shaded area represents the standard deviation.

For the binary mixtures, the maximum is between the values corresponding to the pure solvents, and the shift depends on the ethanol concentration, suggesting that A_{crN} could be one of the most relevant parameters for the classification and identification of the solvents.

Figure 5 shows histograms corresponding to ordering parameters (ψ_4, ψ_5, ψ_6) and number of neighbors N_B, where it is more difficult to distinguish by eye the differences between the distributions. The histograms show that the patterns have between 4 and 7 neighbors, while on average they tend toward hexagonal geometries $(N_B = 6 \pm 1)$ in samples with pure water and, $80\,\%$ water and $20\,\%$ ethanol mixture, but they tend toward pentagonal geometries $(N_B = 5 \pm 1)$ in those with pure ethanol, pure acetone and, $20\,\%$ water and $80\,\%$ ethanol mixture [see Fig. 5A)]. On the other hand, the order parameter is used to analyze whether the centroids of the patterns are organized in an ordered (BOP $\to 1$) or disordered (BOP $\to 0$), but from Figs. 5A)-5D) one finds that the $47\,(\pm 2)\,\%$ of the patterns present values of BOP between 0,35 and 0,65 [see Fig. 5B)], which are around their mean value; therefore, it is concluded that the centroids do not manifest a predominant symmetry associated with square, pentagonal or hexagonal structures.

5. Deep learning implementation

Let us now describe the Deep learning approach used to identify the solvent involved in the desiccation process (see framework in Fig. 6). First, we apply the fracture pattern analysis described in the previous section to obtain the frequency histograms [Fig. 6a)]. Then, the Artificial Neural Networks (ANNs) is trained in MATLAB® using a 5-fold cross-validation [Fig. 6b)], where the dataset is divided into five equal parts: four of them $(80\,\%)$ are used as the training set, and the remaining one $(20\,\%)$ as a test set (shown in yellow), and the latter is rotated until all five possible combinations are covered [10,45]. Then, a multilayer perceptron (MLP) neural network with a given number of neurons N is employed, which consists of fully connected layers: an input layer (IL), one or more hidden layers (HL $= 1 - 10$), and an output layer (OL). Here, the frequency histograms are used as input data $(f_1, f_2, \ldots, f_n)$ and the different solvents are defined as output data $(C_1, \ldots, C_5)$. Subsequently, the neural network is trained using the Scaled Conjugate Gradient (SCG) backpropagation algorithm, which iteratively adjusts weights and biases to minimize errors, with three predefined random seeds to ensure the reproducibility. For each hidden layer, the hyperbolic tangent sigmoid function $\tanh(x) = 2/(1 + \exp(-2x)) - 1$ is used as the activation function, while the softmax transfer function $y_i = \exp(x_i)/\left[\sum_{j=1}^{N} \exp(x_j)\right]$ is assigned to the output layer. Using an initial number of neurons N, ranging from 60 to 120 in increments of 2 neurons, 31 neural network variants are evaluated for each individual feature $\{X_1, \ldots, X_9\}$ across ten hidden layers with steps of $p = 6$ neurons. The confusion matrix highlights the correctly classified samples (shown in green),

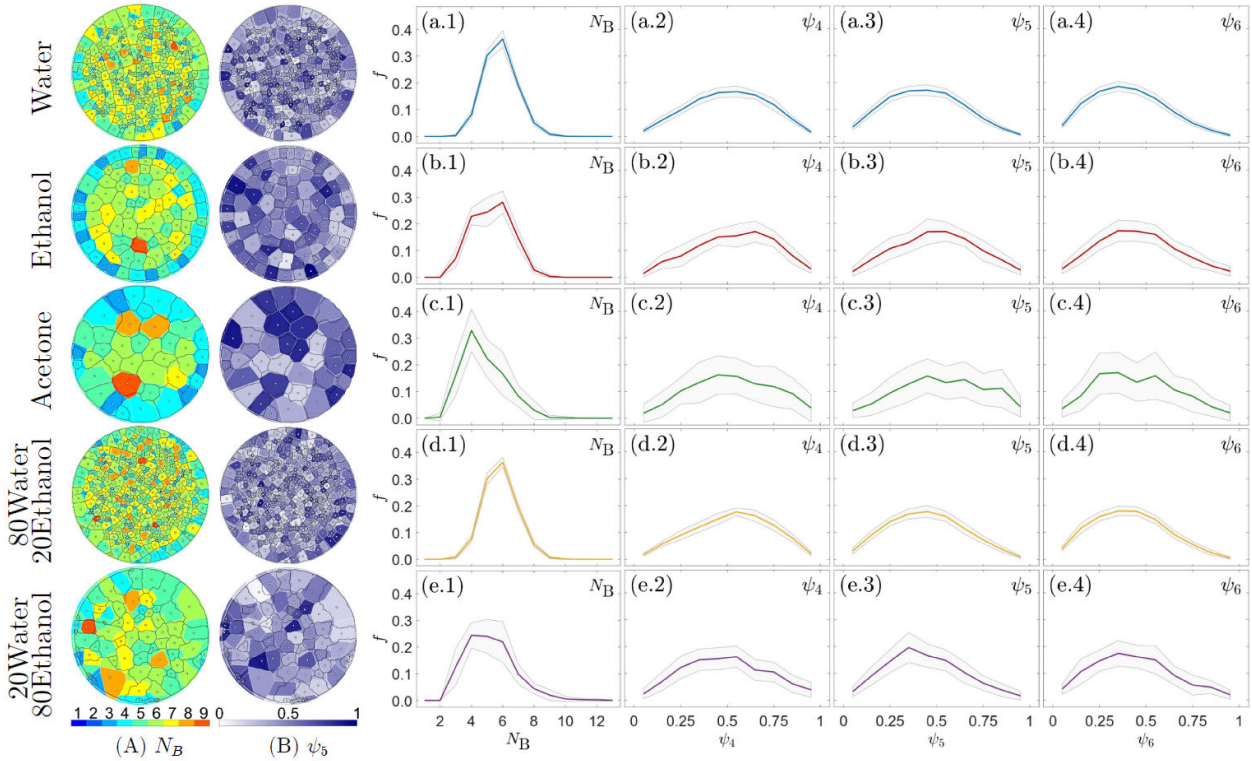


FIGURE 5. Orientational ordering analysis. (A-B) Voronoi diagrams (colored cells) and centroids (white dots) obtained from the actual patterns (black lines) depending on the solvent. Colors are used to indicate A) the number of neighbors N_B and B) the orientational order (here ψ_5 is shown for visualization) according to the color bars. (1-4) Frequency histograms of 1) nearest neighbors, and different order parameters 2) ψ_4, 3) ψ_5 and 4) ψ_6, depending on the solvent indicated in the same row. Colored lines represent the mean values and the gray shaded areas the corresponding standard deviations.

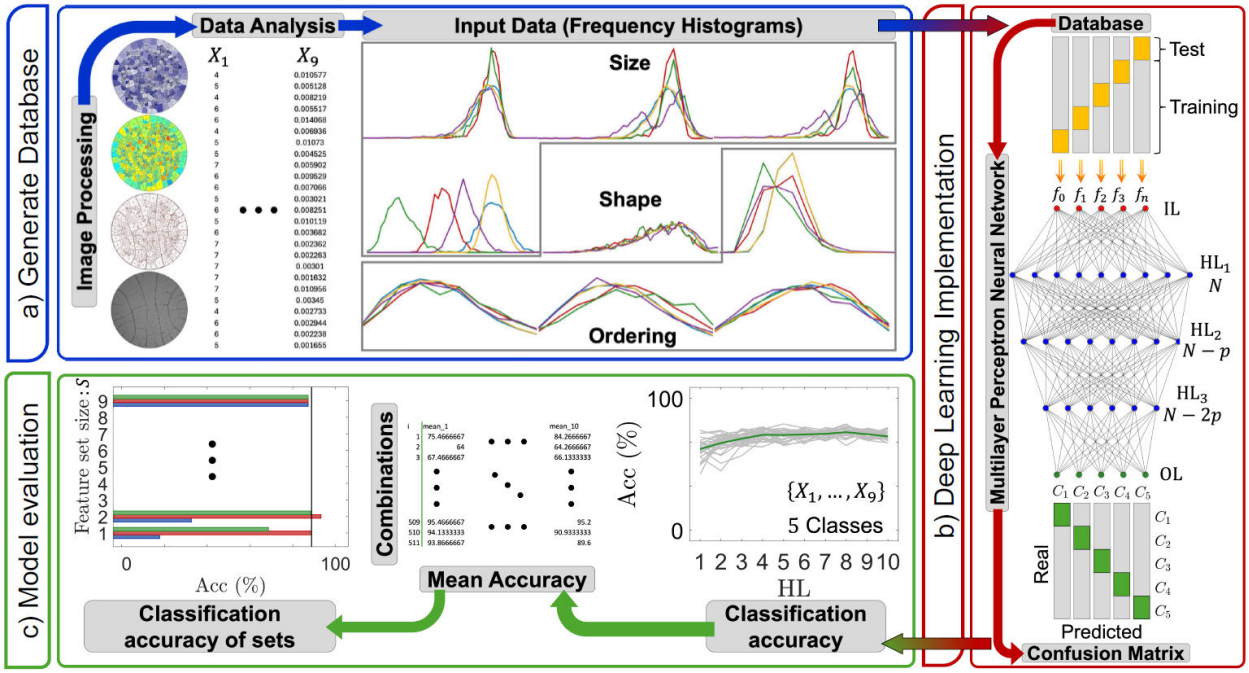


FIGURE 6. Framework of the proposed protocol, including: a) database construction, b) Deep learning implementation, and c) model evaluation.

which vary for each neural network variant, and the classification accuracy is calculated as the ratio of the number of correct predictions to the total number of tests. While the mean diagonal of the confusion matrix is used to determine the accuracy, the model confusion is given by the off-diagonal elements. From 465 runs per hidden layer (5 folds $\times$ 3 seeds $\times$ 31 variants), an average accuracy curve is obtained, illustrated by the green curve of the Acc vs HL plot in Fig. 6c). This process is performed with all the size, shape, and ordering features to determine which of them lead to a higher classification accuracy, individually or forming feature sets of different size ($S = 1, \ldots, 9$).

6. Model evaluation

6.1. Accuracy of individual features

Figure 7 shows the variation in the accuracy of the classification as a function of the number of hidden layers. The upper curves (higher accuracy) in each plot correspond only to

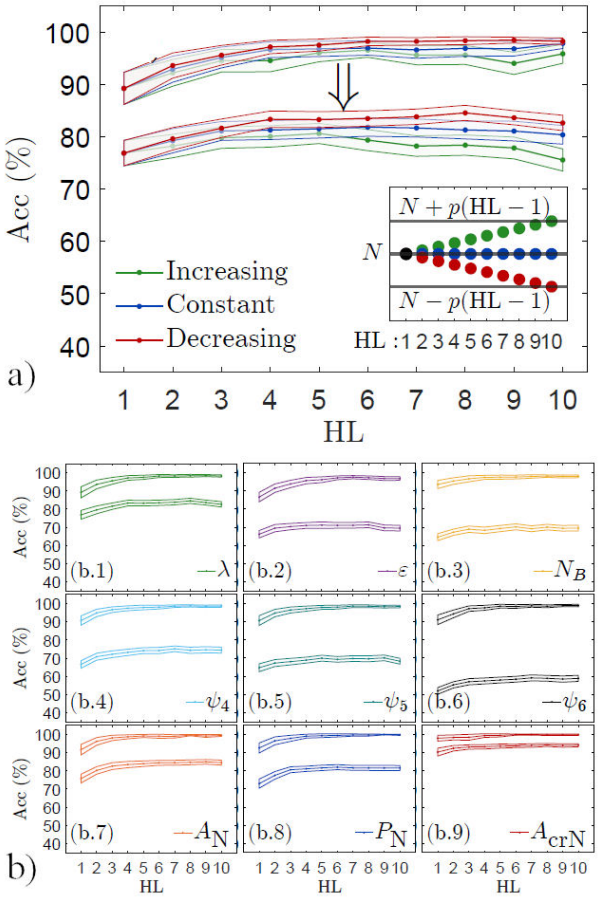


FIGURE 7. Classification accuracy. Performance of a) the normalized isoperimetric ratio λ in three MLP neural network configurations depicted in the inset: increasing, constant, and decreasing architectures as a function of the number of hidden layers (HL). b) Performance of each feature in the decreasing architecture. Solid lines indicate mean values, and shaded areas represent the corresponding standard deviations.

the classification of single solvents (water, ethanol, and acetone), while the bottom curves (lower accuracy) also include binary solvents. In particular, using the isoperimetric ratio, Fig. 7a) exemplifies the accuracy reached for three MLP neural network configurations obtained by decreasing, keeping constant, or increasing the number of neurons in each hidden layer (as shown in the inset). One can notice that the decreasing MLP neural network achieves the highest accuracy [red symbols in Fig. 7a)]. Thus, we can improve the accuracy of the classification by choosing this architecture, which is the one used in the rest of this study. The decrease of accuracy when binary solvents are included is due to an increase on confusion in the analysis generated by the overlapping of the frequency histograms and the similar microscopic physicochemical properties of the solvents (see Appendix section).

Figures 7b) present a comparison of the classification accuracy achieved using nine individual features $(\lambda, \varepsilon, N_{\mathrm{B}}, \psi_4, \psi_5, \psi_6, A_N, P_N, A_{\mathrm{crN}})$ as input to the 31 variants of the decreasing MLP neural network, in order to identify those parameters contributing to higher or lower predictive performance. When all the solvents are included (lower curves), the order parameter ψ_6 yields the lowest performance, with accuracies ranging from $51(\pm 2)\,\%$ to $59(\pm 2)\,\%$; ε,N_{B}, ψ_4 and ψ_5 achieve values from $64(\pm 2)\,\%$ to $75(\pm 2)\,\%$. In comparison, the normalized parameters λ, P_N and A_N reach higher values from $73(\pm 3)\,\%$ to $85(\pm 1)\,\%$. Notably, the normalized crack area A_{crN} yields the highest performance, ranging from $90(\pm 2)\,\%$ to $94(\pm 1)\,\%$; therefore, this is a key parameter to maximize the accuracy of the classification.

6.2. Improving accuracy with set of features

The combination of features can be used to improve even more the classification accuracy, using concatenated histograms as input data of the decreasing MLP neural network. By combining the features, there are $2^9 - 1 = 511$ possible sets with at least one feature. Thus, we calculated the average accuracy of each combination to identify the set of features that maximizes the accuracy, and avoid sets with overfitting that decrease its overall value. Figure 8 presents those sets with the lowest (blue), intermediate (green) and highest (red) average accuracies, depending on the number of parameters conforming the set. For the case of single solvents [Fig. 8a)], the combination of parameters leads to very high accuracies $> 95\,\%$. Even with a two-feature set $(\psi_4, A_{\mathrm{crN}})$, the highest accuracy is reached $(100{,}0\,\%)$, but using the full nine-features set results in overfitting, with a slight decrease of accuracy and inconvenient longer processing time. On the other hand, including binary solvents in the analysis [see Fig. 8b)], the classification is certainly less accurate. In this case, the two-feature set (ψ_5, ψ_6) yields the lowest classification performance, with an accuracy of $66{,}1(\pm 2{,}8)\,\%$. In contrast, the four-feature set $(\lambda, \psi_4, \psi_5, A_{\mathrm{crN}})$ yields the highest accuracy of $97{,}0(\pm 1{,}2)\,\%$, slightly better than the two-feature set $(\psi_4, A_{\mathrm{crN}})$, which accuracy is $96{,}8(\pm 1{,}4)\,\%$. The use of all the parameters also results in overfitting in this case, with

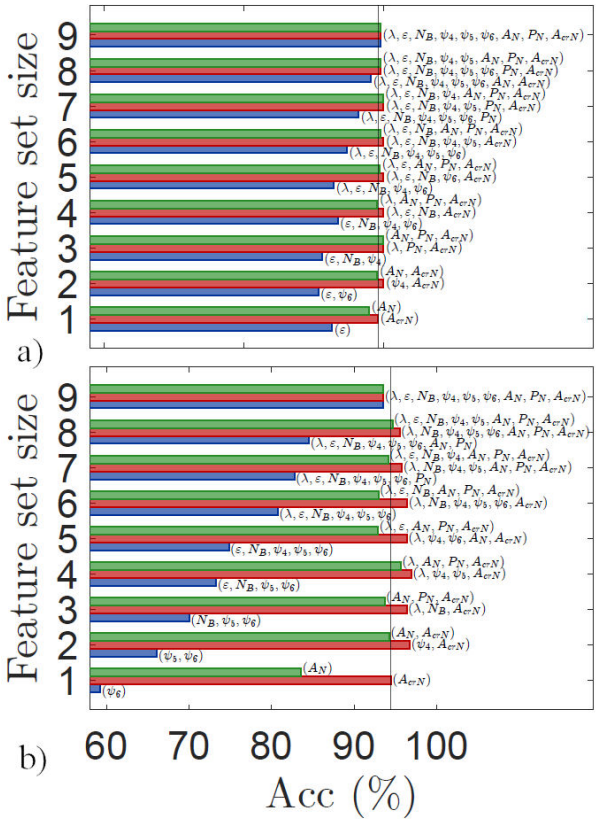


FIGURE 8. Classification accuracy for some sets of features (with $N = 60$ neurons), comparing a) three classes corresponding to single solvents (water, ethanol, and acetone) and b) five classes including the single solvents and binary solvents (20 % and 80 % ethanol content in water). For sets with the same number of elements, the worst, intermediate and best accuracies are indicated by blue, green and red bars, respectively. For comparison, green bars correspond to the same sets in both cases a) and b). The vertical black line corresponds to the accuracy using only $A_{\mathrm{cr}N}$, which leads to the highest value obtained with an individual feature.

an accuracy of $93{,}6(\pm 1{,}6)\,\%$. Therefore, the most suitable set of features for the classification in both groups of solvents is $(\psi_4, A_{\mathrm{cr}N})$, associated with the orientational ordering and the area of the cracks. It is important to remark that the measurement and subsequent analysis of data is simpler for those features that can be easier to determine. For instance, an adequate feature set to analyze unknown samples of fractured dried layers that requires less processing time is the set associated with size $(\lambda, A_N, P_N, A_{\mathrm{cr}N})$ which achieves an average accuracy of $96(\pm 1)\,\%$, very close to the highest value.

6.3. What makes A_{cr} a powerful feature for pattern classification? Towards a microscopic perspective

In the previous sections, we show that A_{cr} can perform better as a morphological feature for classification than most of features sets, and those sets leading to higher accuracy also include A_{cr}. In order to understand why this parameter plays such a fundamental role in the classification, it is necessary to discuss the origin of crack formation and the role of physichochemical properties involved in the process.

The consolidation of particles during the evaporation of colloidal and granular suspension produces an increase of the tensile stresses due to the competition between the compressive capillary pressure and substrate constraints [46], nucleating cracks to dissipate stored elastic energy. This process is fundamentally governed by the Griffith's criterion [21,47-49]. According to this criterion, primary cracks form in the direction that maximizes the condition: $\mathcal{G} - \mathcal{G}_c \geq 0$, where $\mathcal{G}$ is the strain energy release rate and $\mathcal{G}_c$ denotes the critical energy required to create new fracture surfaces. The critical value $\mathcal{G}_c$ depends on the surface energy per unit area γ_s and the plastic work per unit area γ_p [49].

In our system of cornstarch-water slurries, both primary and secondary cracks are observed. This is in agreement with previous studies [16,28]. Thick primary cracks appear first sequentially, while thinner secondary cracks appear later simultaneously within primary cells. The first ones typically form T-junctions, while the second ones form Y- or V-junctions. According to Refs. [16,28], capillary-induced film shrinkage promotes primary cracks. As the water evaporates, solvent menisci form between individual particles, generating a Laplace pressure that scales as $\Delta P \sim \sigma/R$, where $R \sim 6\ \mu$m is the mean size of cornstarch particles [16,28]. Therefore, the induced capillary stress is ~ 12 kPa. The secondary cracks are generated by the deswelling of the hygroscopic cornstarch particles [16]. In contrast, only one kind of cracks is observed for cornstarch with ethanol or acetone ($\sigma \sim 22$ mN/m), where the induced capillary stress (~ 4 kPa) is not enough to generate large primary cracks. Similar results were found for potato starch in water [28], where primary cracks are suppressed and only secondary cracks are formed, in which case, the reduction in capillary stress comes from the particle size ($R \sim 15\ \mu$m). Since primary cracks disappear using binary solvents between the range of 20-40 % of ethanol in water mixtures ($\sigma \sim 30 - 38$ mN/m), one can roughly estimate a critical stress of ~ 6 kPa. Additionally, we have to consider that changes in the rheology of the suspension could contribute to generate changes in the observed patterns. It was recently reported that the suspension behavior changes continuously with ethanol concentration from dynamic shear thickening for pure water to low viscosity shear thinning for pure ethanol, passing through a yield-stress-fluid phase for intermediate mixtures, with a maximum solubility (cosolvency effect) at 50-75 % concentration [50]. This effect could be associated to the remarkable change in the pattern at 60 % concentration in Fig. 2.

The above discussion suggests that changes in desiccation patterns for the cornstarch slurry could be mainly due to surface tension and solubility effects, which are determined by atomic and molecular interactions within the material. At atomic and molecular scales, solute-solvent interactions results in cohesive energy. In cornstarch-liquid slurries, starch (mainly amylose and amylopectin [51,52]) contains hydroxyl groups that form strong hydrogen bonds [53] with solvents

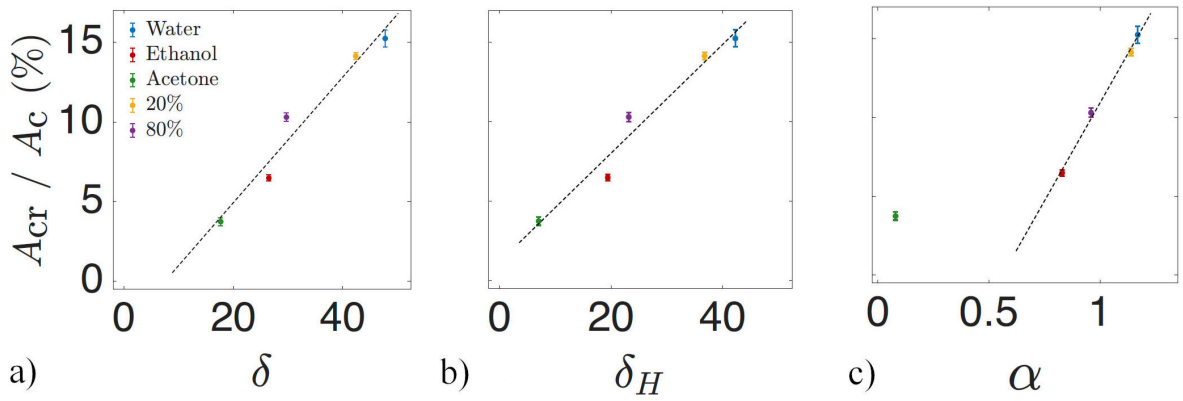


FIGURE 9. Crack area values per solvent. Crack area A_{cr} normalized to container size $A_c = (\pi/4)D_c^2$ with respect to a) Hildebrand parameter δ b) Hydrogen bonding, δ_H (Hansen parameter), and (c) hydrogen-bond donor, α (Kamlet-Taft parameter). Linear fits of experimental data corresponding to a) $(A_{cr}/A_c)\times 100\,\% = 0{,}39\,\delta - 2{,}95$, b) $(A_{cr}/A_c)\times 100\,\% = 0{,}34\,\delta_H + 1{,}19$, and c) $(A_{cr}/A_c)\times 100\,\% = 24{,}86\,\alpha - 13{,}94$.

TABLE II. Hansen parameters δ_D, δ_P and δ_H [54], and Kamlet-Taft parameters α, β and π^* [55,56] of the indicated pure solvents and ethanol-water binary solvents. The corresponding parameters for binary solvents were calculated using the linear approximation: $\delta_{i,\text{mix}} = v\delta_{i,\text{ethanol}} + (1-v)\delta_{i,\text{water}}$ [54] and $\kappa_{\text{mix}} = X\kappa_{\text{ethanol}} + (1-X)\kappa_{\text{water}}$, with $i \in \{D, P, H\}$ and $\kappa \in \{\alpha, \beta, \pi^*\}$ [56], with the values of v and X for ethanol in water provided in Table I.

Property	Water	80/20 %	20/80 %	Ethanol	Acetone
δ_D (MPa$^{1/2}$)	15.50	15.57	15.75	15.80	12.50
δ_P (MPa$^{1/2}$)	16.00	14.27	9.98	8.80	10.40
δ_H (MPa$^{1/2}$)	42.30	36.78	23.17	19.40	7.00
δ (MPa$^{1/2}$)	47.81	42.42	29.74	26.52	17.70
α	1.17	1.14	0.96	0.83	0.08
β	0.18	0.23	0.54	0.77	0.48
π^*	1.09	1.04	0.75	0.54	0.71

with high hydrogen-bonding parameters. This implies that polar protic solvents (*e.g.*, water) can induce granule swelling, whereas polar aprotic solvents (*e.g.*, acetone) do not. Consequently, the type of solvent affects the effective volume of the slurry. As the solvent evaporates, the layer contracts significantly more with water than with acetone, leading to different levels of cohesive energy buildup and variations in the crack area. The cohesive energy density can be estimated from the ratio of the energy of vaporization and the molar volume of the solvent through the the Hildebrand solubility parameter, δ [54]. Since the solute (cornstarch) was the same in our experiments, we focus on the solvents to assess the influence of cohesive energy in the slurries. This parameter can be decomposed into three main contributions:

$$\delta^2 = \delta_D^2 + \delta_P^2 + \delta_H^2, \tag{2}$$

where δ_D, δ_P and δ_H are the Hansen parameters (HSP) associated with (atomic) dispersion, (molecular) polar and (molecular) hydrogen bonding interactions, respectively [54]. The Kamlet-Taft parameters (KTP) also provide additional insight into swelling by describing the hydrogen-bond donor (α), hydrogen-bond acceptor (β), and dipolarity/polarizability (π^*) of solvents [55]. These parameters are shown in Table II for the different pure liquids and binary mixtures analyzed in our experiments.

A higher Hildebrand solubility parameter leads to greater cohesive energy buildup by intensifying the constrained shrinkage of the slurry during the drying process, suggesting that higher values of δ can lead to a higher fracture density (*i.e.*, smaller cells) and more prominent crack openings, which release accumulated cohesive energy. Indeed, Fig. 9a) shows that the crack area increases nearly lineraly with δ, and, due to the presence of hydroxyl (OH) groups in starch, the δ_H value of the solvents is clearly the parameter that exerts the greatest contribution [Fig. 9b)]. Additionally, Fig. 9c) shows that A_{cr} also increases with the solvent ability to donate hydrogen bonds, given by α. The fact that acetone is not properly described by the same trend is because this solvent leaks of hydroxil groups and cannot donate a proton in a solvent-to-solute hydrogen bond [55]. The marked dependence of A_{cr} on the atomic/molecular interactions helps to understand why this geometric parameter is so relevant for solvent classification.

7. Estimating physicochemical properties from fracture patterns

The connection between geometric pattern features and microscopic-level interactions discussed in the previous sec-

TABLE III. Classification of physicochemical properties using the four-feature set $(\lambda, A_N, P_N, A_{\mathrm{cr}N})$ and $N = 60$ neurons. Eight hidden layers are used to estimate the six-property set $(\sigma, \rho, \eta, \delta_D, \delta_P, \delta_H)$, while five hidden layers are used to estimate the three-property set (α, β, π^*). (0,00 denotes an error $< 0{,}005$.)

Property / Liquid	Water	80/20 %	20/80 %	Ethanol	Acetone
σ (mN/m)	$68{,}16 \pm 11{,}06$	$41{,}15 \pm 9{,}96$	$24{,}26 \pm 1{,}99$	$21{,}85 \pm 0{,}17$	$22{,}99 \pm 0{,}21$
ρ (g/cm^3)	$0{,}9938 \pm 0{,}0113$	$0{,}9680 \pm 0{,}0126$	$0{,}8410 \pm 0{,}0202$	$0{,}7858 \pm 0{,}0014$	$0{,}7843 \pm 0{,}0006$
η (mPa·s)	$0{,}9970 \pm 0{,}2890$	$1{,}6913 \pm 0{,}2675$	$1{,}7008 \pm 0{,}2119$	$1{,}0897 \pm 0{,}0254$	$0{,}3087 \pm 0{,}0155$
δ_D (MPa$^{1/2}$)	$15{,}52 \pm 0{,}10$	$15{,}56 \pm 0{,}06$	$15{,}71 \pm 0{,}16$	$15{,}79 \pm 0{,}06$	$12{,}51 \pm 0{,}05$
δ_P (MPa$^{1/2}$)	$15{,}77 \pm 0{,}56$	$14{,}40 \pm 0{,}62$	$10{,}03 \pm 0{,}45$	$8{,}81 \pm 0{,}04$	$10{,}40 \pm 0{,}04$
δ_H (MPa$^{1/2}$)	$41{,}72 \pm 1{,}85$	$37{,}14 \pm 2{,}01$	$23{,}20 \pm 1{,}63$	$19{,}39 \pm 0{,}26$	$7{,}04 \pm 0{,}16$
α	$1{,}17 \pm 0{,}02$	$1{,}14 \pm 0{,}02$	$0{,}95 \pm 0{,}07$	$0{,}83 \pm 0{,}01$	$0{,}08 \pm 0{,}01$
β	$0{,}19 \pm 0{,}03$	$0{,}23 \pm 0{,}03$	$0{,}54 \pm 0{,}07$	$0{,}77 \pm 0{,}00$	$0{,}48 \pm 0{,}00$
π^*	$1{,}08 \pm 0{,}02$	$1{,}04 \pm 0{,}03$	$0{,}75 \pm 0{,}07$	$0{,}54 \pm 0{,}00$	$0{,}71 \pm 0{,}00$

tion suggests that the proposed Deep learning protocol not only classifies patterns, but is also indirectly detecting the mechanical consequences of solute-solvent chemical affinity. Let us now describe a possible application of our study, specifically, an estimation of the physicochemical properties of solvents based on the morphological features of the final fracture patterns.

To reach this goal, the physicochemical properties are defined as output variables $(P_1, \ldots, P_9)$, while a linear transfer function $y_i = x_i$ is used as the activation function in the output layer to obtain free parameter values. Subsequently, the neural network is trained applying the Levenberg-Marquardt (LM) backpropagation algorithm using the data of Tables I and II, to iteratively adjusts weights and biases to minimize errors. Data adquisition and network architecture remain unchanged. First, we trained the neural network using all the data set. After an implicit classification using a 5-fold cross-validation (80 % training, 20 % test), we obtained the data shown in Table III. In line with the traditional classification (described in Secs. 5 and 6), the largest deviations are observed for water and the 80/20 % water/ethanol. Nevertheless, most estimates have low error, typically below 2 %. This indicates that the association of images of the fracture patterns with the physicochemical parameters is possible. After such corroboration, we estimated the physicochemical properties for binary solvents using the model trained exclusively with single solvents. The results are shown in Table IV. Although the model is not so accurate in determining some macroscopic properties, the microscopic properties of two-component solvents, as the Hansen and Kamlet-Taft parameters, can be estimated within a reasonable error ($< 15\,\%$).

TABLE IV. Estimation of physicochemical properties of binary solvents based on the analysis of patterns obtained with single solvents, using the four-feature set $(\lambda, A_N, P_N, A_{\mathrm{cr}N})$ and $N = 60$ neurons. Two hidden layers are used to estimate each three-property set: (σ, ρ, η), $(\delta_D, \delta_P, \delta_H)$ and (α, β, π^*), respectively.

Property / Liquid	80/20 %	20/80 %
σ (mN/m)	$69{,}67 \pm 4{,}23$	$32{,}90 \pm 11{,}67$
ρ (g/cm^3)	$0{,}9822 \pm 0{,}0161$	$0{,}8347 \pm 0{,}0342$
η (mPa·s)	$0{,}8576 \pm 0{,}0673$	$0{,}9482 \pm 0{,}1648$
δ_D (MPa$^{1/2}$)	$15{,}42 \pm 0{,}41$	$15{,}38 \pm 0{,}60$
δ_P (MPa$^{1/2}$)	$15{,}65 \pm 0{,}56$	$10{,}53 \pm 1{,}19$
δ_H (MPa$^{1/2}$)	$40{,}49 \pm 2{,}4$	$22{,}69 \pm 6{,}51$
α	$1{,}12 \pm 0{,}12$	$0{,}82 \pm 0{,}22$
β	$0{,}20 \pm 0{,}04$	$0{,}61 \pm 0{,}10$
π^*	$1{,}05 \pm 0{,}04$	$0{,}68 \pm 0{,}12$

8. Conclusions

We developed a protocol that integrates image analysis, statistics, and Deep learning techniques to classify fracture patterns of cornstarch with five different solvents, specifically focused on improving the accuracy in determining the solvent used in a desiccation process. First, the fracture patterns were characterized based on morphological features. Then, frequency histograms were generated from a normalized dataset and used to train a large number of MLP neural network variants. Our results show that: (1) classification accuracy improves when the number of neurons decreases progressively across hidden layers; (2) crack area is the most informative feature for solvent identification; and (3) accuracy is further enhanced when this parameter is combined with additional morphological features. To balance performance and computational efficiency, the four-feature set $(\lambda, A_N, P_N, A_{\mathrm{cr}N})$ is recommended, achieving an average accuracy of $96(\pm 1)\,\%$ in identifying the solvent in starch-liquid desiccation processes. These findings suggest that existing classification approaches across science, engineering, and medicine, often based on single parameters, could benefit from adopting similar protocols to determine optimal feature sets. Finally, we provide a microscopic perspective in which a linear dependence of the crack Area on the cohesive energy of hydrogen bonds of the solvent and on its ability to donate hydrogen bonds was found. Based on that, we propose that the physicoche-

mical properties of two-component solvents can be estimated indirectly using a model trained on patterns obtained from individual components.

Appendix

A. Origin of model confusion

As discussed in Sec. 6, most of individual features lead to less accurate results in the classification than a set of features, but in some cases, in particular $A_{\rm cr}$, a single parameter can perform better than most of features sets. This can be explained by analyzing the confusion matrices, which hide information about fracture pattern morphology and solute-solvent physicochemical interactions. The discriminative capacity of the model depends on morphological characteristics (see Fig. 7), but this is compromised when all solvents are included. Furthermore, the model accuracy is evaluated using confusion matrices for each feature. Figure 10 shows the histograms and confusion matrices for three features, sorted from the lowest accuracy (corresponding to ordering) to the highest accuracy (corresponding to crack area). A visual inspection of the input data suggests that the main reason for low accuracy is the overlap between frequency histograms, while well differentiated histograms lead to high accuracy. Nevertheless, the discriminative capacity of the model is compromised in the case of well-defined class pairs: (a/d, b/e, c/e). For all other class pairs, the error is less than 4 %, regardless of the overlap in the input data. For instance, (c/a) has 0 % error for these three features despite the histograms overlap. This implies that the accuracy of the model depends not only on the morphology of the fracture patterns, but also on the solute-solvent physicochemical interactions. These interactions play an important role in classification, even though they are not explicitly included in the model. Since the solute (cornstarch) was the same in our experiments, it can be concluded that the model's accuracy also depends on the similarity of the physicochemical properties of the solvents. For this reason, we propose a distance metric M based on the physicochemical properties of solvent pairs to explain which pairs of classes compromise the model's overall accuracy, in order to map the physicochemical space of the solvents to the space of the confusion matrix.

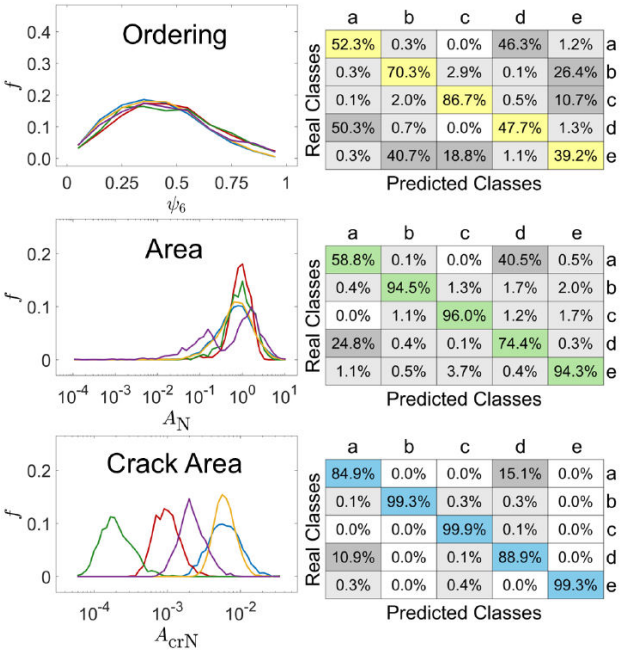


FIGURE 10. Frequency histograms and corresponding confusion Matrices for ordering (ψ_6), area (A_N) and crack area (A_{crN}). Corresponding solvents are: (a) water –, (b) ethanol –, (c) acetone –, (d) 80/20 % water/ethanol – and (e) 20/80 % water/ethanol –. Same labels are used in the matrices to indicate the real and predicted solvent in rows and columns, respectively. In a confusion matrix, the colored diagonal shows the correct predictions, while elements out of the diagonal indicate the percentage of error in the classification between pairs of classes.

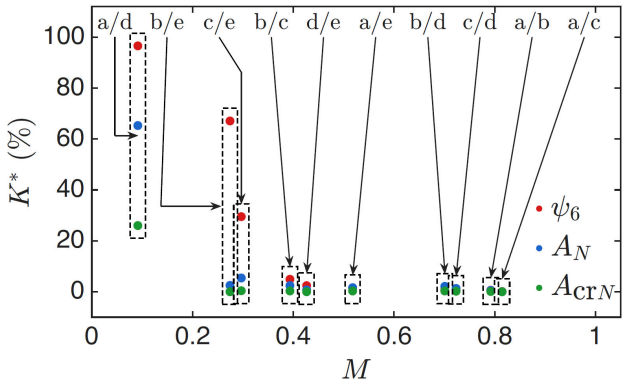


FIGURE 11. Correlation of the model confusion K^* and the metric M given by Eqs. (A.1) for ψ_6 (red), A_N (blue), and A_{crN} (green) using the values of the physicochemical properties given in Table II. Upper labels indicate the corresponding class pairs.

In this context, M was defined as:

$$M(i,j) = \sum_{k=1}^{9} \omega_k \cdot d_k(i,j), \tag{A.1a}$$

where

$$d_k(i,j) = \frac{|P_k(i) - P_k(j)|}{\max\limits_{p,q} |P_k(p) - P_k(q)|}, \tag{A.1b}$$

and

$$1 = \sum_{k=1}^{9} \omega_k. \tag{A.1c}$$

Here, P denotes the physicochemical properties of Tables I and II, i and j denote different solvents, and $\omega_k \geq 0$ are the weights for each physicochemical property $k = 1, \ldots, 9$ $(\sigma, \rho, \eta, \delta_D, \delta_P, \delta_H, \alpha, \beta, \pi^*)$.

The model confusion is defined as $K^*(i,j) = K(i,j) + K(j,i)$, where $K(i,j)$ represents the percentage error between class pairs in the confusion matrix. In this context, the aim is to establish an inverse correlation whereby, as $M \to 0$, there is a high confusion $(K^* \to 100\,\%)$, and as $M \to 1$, there is low confusion $(K^* \to 0\,\%)$. Thus, we look for the combination of weights such that the Spearman's correlation

coefficient r_s (which determines the degree to which two variables are monotonically related) tends to (-1) [57,58]. The combination that most faithfully reproduces the descending order of the model confusion is given by $(w_{\delta_H}, w_\alpha, w_{\pi^*}) = (0{,}20,\ 0{,}20,\ 0{,}60)$, with the remaining weights equal to zero. Using these values, we compute $M(i,j)$ using Eqs. (A.1), and $K^*(i,j)$ using the percentages indicated in the confusion matrices of Fig. 10. Figure 11 shows $K^*(i,j)$ vs $M(i,j)$. Indeed, $K^*(i,j)$ decreases as M increases, and it allows to determine the most relevant cases in which the model's discriminatory capacity is compromised (mainly for a/d, b/e and c/e), as discussed previously. Additionally, K^* and M follow strong (negative) correlation for ψ_6 and A_N (corresponding to $r_s = -0{,}9879$ and $-0{,}9030$, respectively), while $A_{\mathrm{cr}N}$ shows moderate correlation ($r_s = -0{,}4536$). These results indicate that the neural network successfully encodes relationships between the physicochemical parameters based on the frequency histograms. Therefore, the microscopic properties play a more relevant role for a correct classification than macroscopic ones. If the microscopic properties considered in this study are very similar, the confusion will be high, independently of how close the macroscopic properties are. For instance, ethanol and acetone have very similar values of σ and ρ (see Table I) but dissimilar values of δ_H and α (see Table II) and the corresponding confusion K^* is very low (see class pair b/c in Fig. 11). Consequently, the model accuracy depends on solute-solvent molecular interactions associated to the ability of forming hydrogen bonds and effective polarity.

Acknowledgments

The authors gratefully acknowledge financial support from CONACyT Mexico (now SECIHTI) and VIEP-BUAP project 2024 and 2025. J. I. M. C. acknowledges Ph.D. scholarship 1079089 ("Becas nacionales CONAHCyT 2024").

1. F. Moreh, *et al.*, Deep neural networks for crack detection inside structures, *Sci. Rep*. **14** (2024) 4439, https://doi.org/10.1038/s41598-024-54494-y+
2. T. Mashayekhbakhsh *et al.*, SRU-Net: a novel spatiotemporal attention network for sclera segmentation and recognition, Pattern *Anal. Applic.* **27** (2024) 90, https://doi.org/10.1007/s10044-024-01301-z
3. J. Wang, M. Zhao, and C. Xia, An improved classification diagnosis approach for cervical images based on deep neural networks, *Pattern Anal. Applic.* **27** (2024) 79, https://doi.org/10.1007/s10044-024-01300-0
4. G. V. Ponomarev *et al*., ANA HEp-2 cells image classification using number, size, shape and localization of targeted cell regions, *Pattern Recognit*. **47** (2014) 2360, https://doi.org/10.1016/j.patcog.2013.09.027
5. G. V. Ponomarev and M. D. Kazanov, Classification of ANA HEp-2 slide images using morphological features of stained patterns, *Pattern Recognit. Lett*. **82** (2016) 79, https://doi.org/10.1016/j.patrec.2016.03.010
6. R. Nosaka and K. Fukui, HEp-2 cell classification using rotation invariant co-occurrence among local binary patterns, *Pattern Recognit*. **47** (2014) 2428, https://doi.org/10.1016/j.patcog.2013.09.018
7. S. Umer, B. C. Dhara, and B. Chanda, Iris recognition using multiscale morphologic features, *Pattern Recognit. Lett*. **65** (2015) 67, https://doi.org/10.1016/j.patrec.2015.07.008
8. Y. Wang *et al*., Learning the crystal structure genome for property classification, *Phys. Rev. Res*. **4** (2022) 023029, https://doi.org/10.1103/PhysRevResearch.4.023029
9. M. Fan, Q. Wang, and B. van der Waal, Wafer defect patterns recognition based on OPTICS and multi-label classification, In 2016 IEEE Advanced Information Management, Communicates, Electronic and Automation Control Conference (IMCEC) (2016) pp. 912-915, https://doi.org/10.1109/IMCEC.2016.7867343.
10. J. Choi and D. Suh, A depthwise convolutional neural network model based on active contour for multi-defect wafer map pattern classification, *Eng. Appl. Artif. Intell*. **139** (2025) 109707, https://doi.org/10.1016/j.engappai.2024.109707
11. I. U. Vakarelski *et al.*, Assembly of Gold Nanoparticles into Microwire Networks Induced by Drying Liquid Bridges, *Phys. Rev. Lett*. **102** (2009) 058303, https://doi.org/10.1103/PhysRevLett.102.058303
12. M. Ancheyta-Palacios *et al*., Dried Droplets of Diluted Blood to Detect a High Concentration of Lipids, *Processes* **11** (2023), https://doi.org/10.3390/pr11072047
13. J. Lasser *et al*., Salt Polygons and Porous Media Convection, *Phys. Rev. X* **13** (2023) 011025, https://doi.org/10.1103/PhysRevX.13.011025
14. P. Bacchin *et al.*, Drying colloidal systems: Laboratory models for a wide range of applications, *Eur. Phys. J. E* **41** (2018) 1, https://doi.org/10.1140/epje/i2018-11712-x
15. N. Mangold, High latitude patterned grounds on Mars: Classification, distribution and climatic control, *Icarus* **174** (2005) 336, https://doi.org/10.1016/j.icarus.2004.07.030
16. X. Ma, J. Lowensohn, and J. C. Burton, Universal scaling of polygonal desiccation crack patterns, *Phys. Rev. E* **99** (2019) 012802, https://doi.org/10.1103/PhysRevE.99.012802
17. A. Montigny, D. Walwer, and C. Michaut, The origin of hierarchical cracks in floor-fractured craters on Mars and the Moon, *Earth Planet. Sci. Lett*. **600** (2022) 117887, https://doi.org/10.1016/j.epsl.2022.117887

18. W. Rapin *et al*., Sustained wet-dry cycling on early Mars, *Nature* **620** (2023) 299, https://doi.org/10.1038/s41586-023-06220-3
19. P. Pina *et al*., Polygonal terrains on Mars: A contribution to their geometric and topological characterization, *Planet. Space Sci.* **56** (2008) 1919, https://doi.org/10.1016/j.pss.2008.09.020
20. T. Choudhury and S. Costa, Prediction of Parallel Clay Cracks Using Neural Networks - A Feasibility Study, In S. Hemeda and M. Bouassida, eds., Contemporary Issues in Soil Mechanics (Springer International Publishing, Cham, 2019) pp. 214-224, https://doi.org/10.1007/978-3-030-01941-9_19.
21. L. Goehring, Evolving fracture patterns: columnar joints, mud cracks and polygonal terrain, *Phil. Trans. R. Soc. A* **371** (2013) 20120353, https://doi.org/10.1098/rsta.2012.0353
22. T. S. K. Sasa, Pattern Selection of Cracks in Directionally Drying Fracture, *Jpn. J. Appl. Phys*. **36** (1997) 391, https://doi.org/10.1143/JJAP.36.391
23. C. Allain and L. Limat, Regular Patterns of Cracks Formed by Directional Drying of a Collodial Suspension, *Phys. Rev. Lett*. **74** (1995) 2981, https://doi.org/10.1103/PhysRevLett.74.2981
24. W. P. Lee and A. F. Routh, Why Do Drying Films Crack?, *Langmuir* **20** (2004) 9885, https://doi.org/10.1021/la049020v
25. M. D. Choudhury *et al*., Effect of chloride salts on desiccation cracks in bentonite, *Colloid Polym. Sci.* **304** (2026) 823-836, https://doi.org/10.1007/s00396-026-05570-4
26. L. Pauchard, B. Abou, and K. Sekimoto, Influence of Mechanical Properties of Nanoparticles on Macrocrack Formation, *Langmuir* **25** (2009) 6672, https://doi.org/10.1021/la9001384
27. C.-S. Tang *et al*., Desiccation and cracking behaviour of clay layer from slurry state under wetting-drying cycles, *Geoderma* **166** (2011) 111, https://doi.org/10.1016/j.geoderma.2011.07.018
28. Y. Akiba *et al*., Morphometric analysis of polygonal cracking patterns in desiccated starch slurries, *Phys. Rev. E* **96** (2017) 023003, https://doi.org/10.1103/PhysRevE.96.023003
29. A. Roy *et al*., Combinatorial topology and geometry of fracture networks, *Phys. Rev. E* **105** (2022) 034801, https://doi.org/10.1103/PhysRevE.105.034801
30. S. Bohn *et al*., Hierarchical crack pattern as formed by successive domain divisions. II. From disordered to deterministic behavior, *Phys. Rev. E* **71** (2005) 046215, https://doi.org/10.1103/PhysRevE.71.046215
31. S. Bohn, L. Pauchard, and Y. Couder, Hierarchical crack pattern as formed by successive domain divisions., *Phys. Rev. E* **71** (2005) 046214, https://doi.org/10.1103/PhysRevE.71.046214
32. K. F. DeCarlo and N. Shokri, Effects of substrate on cracking patterns and dynamics in desiccating clay layers, *Water Resour. Res.* **50** (2014) 3039, https://doi.org/10.1002/2013WR014466
33. J. Baer, T. Kent, and S. Anderson, Image analysis and fractal geometry to characterize soil desiccation cracks, *Geoderma* **154** (2009) 153, https://doi.org/10.1016/j.geoderma.2009.10.008
34. H.-A. Crostack *et al*., Analysis of crack patterns in drying corn starch by in-situ radiography and X-ray computer tomography, *Exp. Mech.* **52** (2012) 917, https://doi.org/10.1007/s11340-011-9581-1
35. L. Goehring, S.W. Morris, and Z. Lin, Experimental investigation of the scaling of columnar joints, *Phys. Rev. E* **74** (2006) 036115, https://doi.org/10.1103/PhysRevE.74.036115
36. L. Goehring, Drying and cracking mechanisms in a starch slurry, *Phys. Rev. E* **80** (2009) 036116, https://doi.org/10.1103/PhysRevE.80.036116
37. J. Liaudat and S. Muraro, Drying of silty soil treated with superabsorbent hydrogels: Retention behaviour and cracking, *Eng. Geol.* **331** (2024) 107433, https://doi.org/10.1016/j.enggeo.2024.107433
38. F. Bu *et al*., Enhancement of water-retaining property and cracking resistance of soil under wetting-drying cycles: Synergistic effect of sisal fiber and polyacrylamide, *Constr. Build. Mater*. **435** (2024) 136841, https://doi.org/10.1016/j.conbuildmat.2024.136841
39. G. Vazquez, E. Alvarez, and J. M. Navaza, Surface Tension of Alcohol + Water from **20 to 50** C, *J. Chem. Eng. Data* **40** (1995) 611, https://doi.org/10.1021/je00019a016
40. A. Cervantes-Álvarez *et al.*, Air entrainment and granular bubbles generated by a jet of grains entering water, *J. Colloid Interface Sci.* **574** (2020) 285, https://doi.org/10.1016/j.jcis.2020.04.009
41. S. Enders, H. Kahl, and J. Winkelmann, Surface Tension of the Ternary System Water + Acetone + Toluene, *J. Chem. Eng. Data* **52** (2007) 1072, https://doi.org/10.1021/je7000182
42. B. González *et al*., Density, dynamic viscosity, and derived properties of binary mixtures of methanol or ethanol with water, ethyl acetate, and methyl acetate at T=(293.15, 298.15, and 303.15)K, *J. Chem. Thermodyn.* **39** (2007) 1578, https://doi.org/10.1016/j.jct.2007.05.004
43. R. M. Pires *et al*., Viscosity and Density of Water + Ethyl Acetate + Ethanol Mixtures at 298.15 and 318.15 K and Atmospheric Pressure, *J. Chem. Eng. Data* **52** (2007) 1240, https://doi.org/10.1021/je600565m
44. F. López-González, F. Pacheco-Vázquez, and F. Donado, Ordering of a granular layer of cubes under strain-induced shear and vibration, *Phys. A* **620** (2023) 128768, https://doi.org/10.1016/j.physa.2023.128768
45. J.-Y. Kim, *et al*., Classification and concentration estimation of CO and NO2 mixtures under humidity using neural network-assisted pattern recognition analysis, *J. Hazard. Mater*. **459** (2023) 132153, https://doi.org/10.1016/j.jhazmat.2023.132153
46. L. Goehring, *et al*., Desiccation Cracks and their Patterns: Formation and Modelling in Science and Nature (Wiley-VCH, Weinheim, Germany, 2015), pp. 69-144, https://doi.org/10.1002/9783527671922

47. A. A. Griffith, VI. The phenomena of rupture and flow in solids, *Phil. Trans. R. Soc. A* **221** (1921) 163, https://doi.org/10.1098/rsta.1921.0006

48. J. Beuth, Cracking of thin bonded films in residual tension, *Int. J. Solids Struct.* **29** (1992) 1657, https://doi.org/10.1016/0020-7683(92)90015-L

49. T. L. Anderson, Fracture Mechanics: Fundamentals and Applications, 4th. edition. (CRC Press, Boca Raton, FL, 2017), pp. 25-39, https://doi.org/10.1201/9781315370293.

50. L. Oyarte Gálvez, *et al*., Dramatic effect of fluid chemistry on cornstarch suspensions: Linking particle interactions to macroscopic rheology, *Phys. Rev. E* **95** (2017) 030602, https://doi.org/10.1103/PhysRevE.95.030602

51. E. Bertoft, Understanding Starch Structure: Recent Progress, *Agronomy* **7** (2017) 56, https://doi.org/10.3390/agronomy7030056

52. M. Dogenski, *et al*., Starch-Based Aerogels Obtained via Solvent-Induced Gelation, *Gels* **6** (2020) 32, https://doi.org/10.3390/gels6030032

53. J. Clayden, N. Greeves, and S. Warren, Organic Chemistry, 2nd. edition. (Oxford University Press, Oxford, UK, 2012), pp. 29-67.

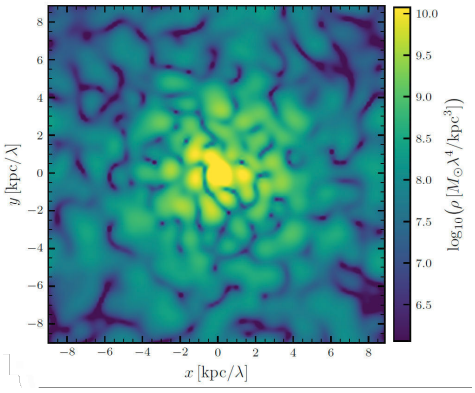
54. C. M. Hansen, Hansen Solubility Parameters: A User's Handbook, 2nd. edition. (CRC Press, Boca Raton, FL, 2007), pp. 1-38.

55. M. J. Kamlet, *et al*., Linear solvation energy relationships. 23. A comprehensive collection of the solvatochromic parameters, .alpha., and .beta., and some methods for simplifying the generalized solvatochromic equation, *J. Org. Chem.* **48** (1983) 2877, https://doi.org/10.1021/jo00165a018

56. K. A. Fletcher and S. Pandey, Solvatochromic Probe Behavior within Ternary Room-Temperature Ionic Liquid 1-Butyl-3-methylimidazolium Hexafluorophosphate + Ethanol + Water Solutions, *J. Phys. Chem. B* **107** (2003) 13532, https://doi.org/10.1021/jp0276754

57. C. Spearman, The Proof and Measurement of Association between Two Things, *Am. J. Psychol*. **15** (1904) 72, https://doi.org/10.2307/1412159

58. E. G. Olds, Distributions of Sums of Squares of Rank Differences for Small Numbers of Individuals, *Ann. Math. Statist.* **9** (1938) 133, https://doi.org/10.1214/aoms/1177732332



Volume 72

Number 6

Nov-Dec 2026

© Sociedad Mexicana de Física